University of Liège
Faculty of Applied Sciences

Hydro-mechanical analysis of the fracturing induced by the excavation of nuclear waste repository galleries using shear banding

Thesis submitted to obtain the degree of
Philosophiae Doctor in Engineering Sciences by

Benoît Pardoen

September 2015

Jury

Angélique Léonard	Professor	Université de Liège, president
Frédéric Collin	Associate Professor	Université de Liège, supervisor
Robert Charlier	Professor	Université de Liège
Bertrand François	Associate Professor	Université libre de Bruxelles
Séverine Levasseur	PhD, Research Engineer	Ondraf/Niras
Frédéric Nguyen	Associate Professor	Université de Liège
Darius M. Seyedi	PhD, Research Engineer	Andra
Jian-Fu Shao	Professor	Université Lille 1
Richard Wan	Professor	University of Calgary

This research was funded by:

FRIA - F.R.S. - FNRS
Fonds pour la formation à la Recherche dans l'Industrie et dans l'Agriculture
Rue d'Egmont, 5
B-1000, Bruxelles

Acknowledgements

I would like to express my sincere gratitude to Frédéric Collin, supervisor of the thesis, whose help and advices have largely contributed to the completion of this research. His pertinent remarks and his availability have been a great support all along the research. My sincere thanks also go to the Professor Robert Charlier for welcoming me in the geomechanics department at ULg and for his various comments which have contributed to the improvement of this work. Many thanks also to all members of the geomechanics department who have provided me with some precious advices every now and then.

The present work has been motivated by the scientific research programs of the French national agency for radioactive waste management (Andra) which I thank as well for their collaboration and partnership. Furthermore, I am grateful to all members of the jury who have read this manuscript thoroughly. Finally, I thank my relatives for their unconditional support.

Abstract

The long-term management of high-level nuclear wastes is envisaged by deep geological repository. Due to the safety function of the host formation, the behaviour of the Excavation Damaged Zone (EDZ) that develops around underground galleries during their drilling is of paramount importance. The EDZ is dominated by fracturing process which engenders irreversible modifications of the hydro-mechanical properties of the porous rock. In this zone, a significant hydraulic permeability increase of several orders of magnitude is observed. It may alter the safety function of the host formation by creating preferential flow paths for the migration of radionuclides towards the biosphere. Consequently, the understanding and the prediction of the EDZ hydro-mechanical behaviour are crucial issues for the long-term management of nuclear wastes. Among the different low-permeability media that are envisaged for the deep repository, the Callovo-Oxfordian claystone is studied.

The fracturing behaviour, the water transfers, and the coupled processes that occur around the underground galleries are most particularly addressed, especially in the EDZ. The fractures induced by the excavation process are reproduced with strain localisation in shear bands. An appropriate model allowing to properly reproduce the strain localisation in geomaterials with finite element methods is used. It is an enhanced model for microstructure media called the coupled local second gradient model and which involves a regularisation method. Its application is extended to unsaturated anisotropic rocks with compressible solid grains. The numerical modelling of the fractured zone with shear banding provides information about its shape, extent, fracturing structure, and behaviour that are in good agreement with *in situ* measurements. In particular, the shape of the EDZ in the Callovo-Oxfordian claystone is governed by its anisotropy and the gallery convergence strongly depends on the appearance of the shear bands.

The fluid transfers and the coupled processes are investigated in the EDZ. The impact of the rock fracturing on its hydraulic properties is addressed by taking into account strain localisation effects at macroscale. The evolution of the intrinsic water permeability is expressed by a strain-dependent relation which engenders a more pronounced increase of the permeability inside the shear bands. In agreement with experimental measurements, an important increase is reproduced in the excavation damaged zone. After gallery excavation, the hydraulic transfers in the rock surrounding the galleries are investigated by considering the interaction between the rock and the gallery air. These transfers are studied at large-scale during the reproduction of gallery air ventilation. Depending on the air hygrometry, the gallery ventilation implies drainage and desaturation of the surrounding rock which affect the shear banding development. The hydraulic

transfers in the rock which depend on the water exchanges at gallery wall are also studied.

The proposed approach aims to highlight the important hydro-mechanical aspects to take into account for the reproduction of the EDZ behaviour in unsaturated biphasic media with shear banding. The focus is resolutely on the large-scale numerical modelling of the EDZ as well as on the reproduction of the mechanical and hydraulic experimental measurements performed around galleries.

Keywords: Excavation damaged zone - Fracturing - Numerical modelling - Strain localisation - Shear banding - Unsaturated anisotropic rock

Contents

List of symbols and notations

Units are omitted if they are multiple.

General notations

The indicial notation is used and a double index corresponds to a summation index.

$\dot{a}$	Time derivative of quantity a	s^{-1}
$a^e,\ a^p,\ a^{vp}$	Elastic, plastic, and viscoplastic components of quantity a	$-$
$^\sharp a$	Quantity a in orthotropic axes	$-$
$a_\parallel,\ a_\perp$	Quantity a in parallel and perpendicular directions to the isotropic planes	$-$
$a_0,\ a_f$	Initial and final values of quantity a	$-$
a^t	Current value of quantity a at a given time t	$-$
$a^\tau,\ a^{\tau 1},\ a^{\tau 2}$	Quantity a at the end of time step in numerical iterative procedures	$-$
a^*	Virtual quantity a	$-$
$a^0,\ a^1$	Quantity a outside and inside a shear band	$-$
da	Variation of quantity a in numerical iterative procedures	$-$
Da	Normal derivative of quantity a	m^{-1}
$\frac{Da}{Dx_i}$	Tangential derivative of quantity a	m^{-1}

Greek letters

α	Orientation of isotropic planes	$^\circ$
α_i	Euler's rotation angles around the orthotropic axes e_i	$^\circ$
$\alpha_{\varsigma n}$	Shear band mode angle	$^\circ$
α_v	Vapour mass transfer coefficient	m/s
α^{vp}	Viscoplastic hardening function	$-$
α_0^{vp}	Initial threshold for the viscoplastic flow	$-$
β	Lode angle	$^\circ$
β_{per}	Evolution parameter for intrinsic water permeability	$-$
β^{vp}	Viscoplastic potential parameter	$-$
γ	Fluidity coefficient for viscoplasticity	s^{-1}
γ_0	Reference fluidity	s^{-1}
γ_1	Temperature parameter for the fluidity	J/mol
γ_{per}	Deformation parameter for the evolution of intrinsic water permeability	$-$
Γ	Porous material boundary	m^2

Γ_σ	Part of Γ on which external traction forces $\overline{t}_i$ and $\overline{T}_i$ are applied	m^2
Γ_{q_w}	Part of Γ on which input water mass $\overline{q}_w$ is prescribed	m^2
Γ_{q_a}	Part of Γ on which input air mass $\overline{q}_a$ is prescribed	m^2
Γ_t	Part of Γ on which classical external traction force $\overline{t}_i$ is applied	m^2
Γ_T	Part of Γ on which external double force $\overline{T}_i$ is applied	m^2
$d\Gamma$	Infinitesimal boundary	m^2
δ_{ij}	Kronecker symbol	$-$
$\Delta_1^{\tau 1}$, $\Delta_2^{\tau 1}$, $\Delta_3^{\tau 1}$	Non-equilibrium forces (residuals) of balance equations in numerical iterative procedures	Nm
ε_a, ε_1, ε_y	Axial or vertical strain in compression tests	$-$
ε_{ij}	Total macro-strain field	$-$
ε_{ij}^p	Plastic strain field	$-$
ε_{ij}^{vp}	Viscoplastic strain field	$-$
$\hat{\varepsilon}_{ij}$	Deviatoric total strain field	$-$
$\hat{\varepsilon}_{ij}^p$	Deviatoric plastic strain field	$-$
$\hat{\varepsilon}_{eq}$	Von Mises' equivalent deviatoric total strain (total deviatoric strain)	$-$
$\hat{\varepsilon}_{eq}^p$	Von Mises' equivalent deviatoric plastic strain	$-$
ε_{eq}^{vp}	Equivalent viscoplastic strain (generalised viscoplastic distortion)	$-$
$\bar{\varepsilon}_{ij}^{vp}$	Viscoplastic distortion	$-$
ε_{ij}^m	Micro-strain field	$-$
$\overline{\varepsilon}_{ij}$	Relative deformation of the microstructure	$-$
ε_p	Deformation of a bar in traction at yield stress	$-$
ε_r	Final deformation of a bar in traction for diffuse failure	$-$
ε_v	Volumetric strain	$-$
ζ	Stress deconfinement rate for gallery excavation	$-$
ζ_w	Pore water pressure deconfinement rate for gallery excavation	$-$
η	Yield surface convexity parameter	$-$
θ	Orthoradial coordinate	m
Θ	Shear band orientation	$^\circ$
Θ_A, Θ_C, Θ_R	Arthur's, Coulomb's, and Roscoe's angles for the shear band orientation	$^\circ$
κ_{eq}	Deviatoric strain increment	$-$
κ_i	Coordinate axis of parent finite element	m
$\varkappa_i$	Hardening and softening variables	$^\circ$ or Pa
$\overline{\lambda}$	Wavelength of a bar in traction	m
λ_{ij}	Lagrange multiplier field	Pa
λ^p	Plastic multiplier	$-$
μ_a	Dry air dynamic viscosity	$Pa\ s$
μ_g	Gas dynamic viscosity	$Pa\ s$
μ_v	Water vapour dynamic viscosity	$Pa\ s$
μ_w	Water dynamic viscosity	$Pa\ s$
ν	Poisson's ratio	$-$
νij	Poisson's ratios for anisotropic materials	$-$
$\nu_{\parallel\perp}$, $\nu_{\parallel\parallel}$, $\nu_{\perp\parallel}$	Poisson's ratios for transversely isotropic materials	$-$
ξ	Normal coordinate axis of a shear band	m
ξ_c	Ratio of cohesion softening	$-$
ϖ_1^{-1}, ϖ_2^{-1}, ϖ_3^{-1}	Internal length scales for the bar and the thick-walled problems	m
ρ	Homogenised mixture density of porous material	kg/m^3
ρ_a	Dry air density	kg/m^3
ρ_d	Dry density of porous material	kg/m^3

ρ_{da}	Dissolved air density	kg/m^3
ρ_g	Gas density	kg/m^3
ρ_s	Solid grain density	kg/m^3
ρ_v	Water vapour density	kg/m^3
ρ_v^0	Saturated water vapour density	kg/m^3
ρ_v^a	Water vapour density of the air for drying test	kg/m^3
$\rho_v^{0,a}$	Saturated water vapour density of the air for drying test	kg/m^3
ρ_v^Γ	Water vapour density of the material surface or gallery wall	kg/m^3
$\rho_v^{0,\Gamma}$	Saturated water vapour density of the sample surface for drying test	kg/m^3
ρ_v^{cav}	Water vapour density of the gallery air	kg/m^3
ρ_w	Water density	kg/m^3
σ	Mean total stress	Pa
$\sigma^{'},\ p^{'}$	Mean effective stress	Pa
$\sigma_i,\ \sigma_x,\ \sigma_y,\ \sigma_z$	Principal total stresses	Pa
$\sigma_i^{'}$	Principal effective stresses	Pa
$\sigma_1,\ \sigma_y$	Axial or vertical stress in compression tests	Pa
$\sigma_3,\ \sigma_x$	Confining stress in compression tests	Pa
σ_h	Minor horizontal principal total stress of the Callovo-Oxfodian claystone	Pa
σ_H	Major horizontal principal total stress of the Callovo-Oxfodian claystone	Pa
σ_v	Vertical principal total stress of the Callovo-Oxfodian claystone	Pa
σ_{ij}	Cauchy total stress field	Pa
$\sigma_{ij}^{'}$	Effective stress field	Pa
$\tilde{\sigma}_{ij}^{'}$	Jaumann effective stress rate	Pa/s
$\hat{\sigma}_{ij}$	Deviatoric total stress field	Pa
$\hat{\sigma}_{ij}^{'}$	Deviatoric effective stress field	Pa
σ_p	Yield stress of a bar in traction	Pa
$\sigma_{r,0}$	Initial total radial stress at gallery wall	Pa
σ_r^Γ	Fictive total radial stress at gallery wall	Pa
Σ_{ijk}	Double stress or second order stress	N/m
$\tilde{\Sigma}_{ijk}$	Jaumann double stress rate	$N/m\ s$
ς_i	Velocity gradient field of a shear band	s^{-1}
$\overline{\tau}$	Tortuosity of porous material	$-$
$\tau,\ \tau 1,\ \tau 2$	Times at the end of time step in numerical iterative procedures	s
τ_{ij}	Microstructure stress field (microstress)	Pa
υ_{ij}	Microkinematic gradient field (micro-deformation field)	$-$
Υ	Elastic determinant	Pa^{-3}
φ	Friction angle	$^\circ$
φ_{bif}	Friction angle at bifurcation	$^\circ$
φ_c	Compression friction angle	$^\circ$
$\varphi_{c,0},\ \varphi_{c,f}$	Initial and final compression friction angles	$^\circ$
φ_e	Extension friction angle	$^\circ$
$\varphi_{e,0},\ \varphi_{e,f}$	Initial and final extension friction angles	$^\circ$
Φ	Porosity	$-$
χ	Effective Bishop's stress parameter	$-$
χ_w^{-1}	Water compressibility	Pa^{-1}
ψ	Dilatancy angle	$^\circ$
ψ_{bif}	Dilatancy angle at bifurcation	$^\circ$
ψ_c	Compression dilatancy angle	$^\circ$

ψ_e	Extension dilatancy angle	$^\circ$
Ψ	Weight function for non-local approach	m^{-3}
ω_{ij}	Spin rate tensor	s^{-1}
Ω	Porous material configuration (representative elementary unit volume)	m^3
$\Omega^{\tau 1},\ \Omega^{\tau 2}$	Porous material configurations at the end of the time step in numerical iterative procedures	m^3
Ω^m	Micro-volume of a microscale particles	m^3
Ω_g	Gas volume inside Ω	m^3
Ω_p	Porous volume inside Ω	m^3
Ω_w	Water volume inside Ω	m^3
$d\Omega$	Infinitesimal volume	m^3

Roman letters

$I_{\sigma'}$	First stress invariant	Pa
$II_{\hat{\sigma}'}$	Second deviatoric stress invariant	Pa
$II^p_{\hat{\sigma}'}$	Second deviatoric stress invariant at plastic state	Pa
$III_{\hat{\sigma}'}$	Third deviatoric stress invariant	Pa
a_{ij}	Microstructure fabric tensor for cohesion	Pa
$\hat{a}_{ij}$	Deviatoric microstructure fabric tensor for cohesion	Pa
A	Constant section of a bar in traction	m^2
A^{vp}	Internal friction coefficient for viscoplasticity	$-$
$A_1,\ A_2$	Elastic and softening plastic slopes	Pa
A_d	External surface of a sample submitted to drying	m^2
A_{ij}	Reduced deviatoric microstructure fabric tensor for cohesion	$-$
$A_\parallel$	Component of A_{ij} in the isotropic planes	$-$
$A^{\tau 1}_{ijk}$	Terms of the coupling matrix $\left[K^{\tau 1}_{MW}\right]$	$kg/m^2\ s$
A^J_{ijkl}	Jaumann's correction tensor for large strains and rotations	Pa
$\mathcal{A}_{ijkl}$	Elastoplastic constitutive tangent tensor for large strains and rotations	Pa
$\wedge_{ij}$	Acoustic tensor	Pa
b	Generalised Biot's coefficient or Biot's coefficient for isotropic material	$-$
b_{ij}	Biot's tensor	$-$
$b_\parallel,\ b_\perp$	Biot's coefficients for transversely isotropic materials	$-$
$b_1,\ b_2$	Cohesion evolution parameters	$-$
B_φ	Friction angle hardening coefficient	$-$
B_c	Cohesion softening coefficient	$-$
$B^I,\ B^K$	Modified Bessel functions	$-$
B^{vp}	Viscoplastic hardening function parameter	$-$
$[B]$	Transformation matrix for finite element methods	$-$
c	Cohesion	Pa
$c_\parallel,\ c_\perp,\ c_\alpha$	Cohesion for transversely isotropic materials	Pa
$c_0,\ c_f$	Initial and final cohesions	Pa
$\bar{c}$	Cohesion under isotropic loading	Pa
c_i	Constants for the solution of the thick-walled problem	
C	Compressibility of the poroelastic material	Pa^{-1}
C_{ijkl}	Elastoplastic constitutive tangent tensor for small strains and rotations	Pa
C^e_{ijkl}	Hooke elastic stiffness tensor	Pa

C^p_{ijkl}	Plastic constitutive tangent tensor	Pa
C_p	Compressibility of the pores	Pa^{-1}
C_s	Compressibility of the solid phase	Pa^{-1}
C^{vp}	Cohesion coefficient for viscoplasticity	$-$
$C^{\tau 1}$	Term of the coupling matrix $\left[K^{\tau 1}_{MW}\right]$	$kg/m^3\ s$
$d_1,\ d_2$	Yield surface parameters	$-$
D	Second gradient elastic modulus	N
D_{da-w}	Diffusion coefficient for the dissolved air in liquid water	m^2/s
D_{v-a}	Diffusion coefficient for the gaseous mixture	m^2/s
D^e_{ijkl}	Compliance elastic tensor	Pa^{-1}
D_{ijklmn}	Elastic constitutive tangent tensor for the second gradient law	N
$\left[D^{\tau 1}\right]$	Part of the local element stiffness matrix corresponding to D_{ijklmn}	N
dec_φ	Friction angle hardening shifting	$-$
dec_c	Cohesion softening shifting	$-$
e_i	Orthotropic coordinate axes	m
e_{ijk}	Alternating tensor	$-$
$e_r,\ e_\theta,\ e_z$	Cylindrical coordinates axes	m and $^\circ$
E	Young's modulus	Pa
$\bar{E}$	Evaporation flow at gallery wall	$kg/m^2\ s$
E_i	Young's moduli for anisotropic materials	Pa
$E_\parallel,\ E_\perp$	Young's moduli for transversely isotropic materials	Pa
$\left[E^{\tau 1}\right]$	Local stiffness matrix of the current finite element	
$\left[E^{\tau 1}_{1/2/3/4}\right]$	Parts of the local element stiffness matrix	
$f_{a,i}$	Mass flow of dry air	$kg/m^2\ s$
$f_{da,i}$	Mass flow of dissolved air	$kg/m^2\ s$
$f_{v,i}$	Mass flow of water vapour	$kg/m^2\ s$
$f_{w,i}$	Mass flow of liquid water	$kg/m^2\ s$
F	Axial load	N
F^p	Yield surface	Pa
F^{vp}	Viscoplastic loading surface	Pa
F_{ij}	Macro-deformation field	$-$
$\overline{F}_{ij}$	Jacobian matrix of the transformation between two material configurations	$-$
$\left[f^{\tau 1}_{OB}\right]$	Vector of the elementary out of balance forces	
$\left[F^{\tau 1}_{OB}\right]$	Vector of the global out of balance forces	
g_i	Gravity acceleration vector	m/s^2
g	Gravity acceleration norm	m/s^2
$g(\beta)$	Influence of the Lode angle for viscoplasticity	$-$
G	Shear modulus	Pa
G^p	Plastic potential	Pa
G^{vp}	Viscoplastic potential	Pa
G_i	Gravity volume force	N/m^3
G_{ij}	Shear moduli for anisotropic materials	Pa
$G_{\parallel\perp}$, $G_{\parallel\parallel}$, $G_{\perp\parallel}$	Shear moduli for transversely isotropic materials	Pa
Gr	Green's function	m^{-3}
$\left[G^{\tau 1}_{1/2}\right]$	Gravity volume force matrices	
h_{ijk}	Microkinematic second gradient field	m^{-1}
H	Total height of a sample under compression	m
H_s	Shear band thickness in a sample under compression	m
ΔH	Shortening of a sample under compression	m

H_a	Henry's coefficient for dissolved air	$-$
$i_{a,i}$	Diffusion flux of dry air	$kg/m^2\ s$
$i_{da,i}$	Diffusion flux of dissolved air	$kg/m^2\ s$
$i_{v,i}$	Diffusion flux of water vapour	$kg/m^2\ s$
$J^{\tau 1}$	Jacobian matrix of the transformation between parent and current finite elements	$-$
$k_{r,g}$	Gas relative permeability	$-$
$k_{r,w}$	Water relative permeability	$-$
k_w	Intrinsic water permeability	m^2
$\overline{k}_w$	Water permeability for unsaturated conditions	m^2
$k_{w,ij}$	Intrinsic water permeability tensor	m^2
$k_{w,h},\ k_{w,v}$	Horizontal and vertical intrinsic water permeabilities	m^2
$k_{w,\parallel},\ k_{w,\perp}$	Intrinsic water permeabilities for transversely isotropic materials	m^2
K	Bulk modulus of the poroelastic material	Pa
K_{da}^{eq}	Equilibrium constant for dissolved air	Pa
K_{ij}^{c}	Cosserat's micro-rotation gradient field (curvature)	m^{-1}
K_p	Pores bulk modulus	Pa
K^{pen}	Numerical penalty coefficient for the seepage at gallery wall	s^3/kg
K_s	Isotropic bulk modulus of the solid grains	Pa
$K_{w,ij}$	Hydraulic conductivity	m/s
$\mathcal{K},\ \overline{\mathcal{K}},\ \overline{\overline{\mathcal{K}}}$	Constants for the solution of a bar in traction	m
$\left[k^{\tau 1}\right]$	Local element stiffness matrix	
$\left[K^{\tau 1}\right]$	Global stiffness matrix	
$\left[K_{MW}^{\tau 1}\right]$	Coupling matrix of the mechanic influence on the fluid	
$\left[K_{WM}^{\tau 1}\right]$	Coupling matrix of the fluid influence on the mechanics	
$\left[K_{WW}^{\tau 1}\right]$	Classical stiffness matrix of the flow problem	
$\left[K_{k}^{\tau 1}\right]$	Matrix of the evolution of intrinsic water permeability	$kg/m^2\ s$
$\overline{l}$	Characteristic length parameter for non-local approach	m^2
l_c	Internal length scale for non-local approach	m
l_i	Generalised loading vector	$-$
ℓ_i	Parameters for the Rice criterion	Pa
L	Length of a bar in traction	m
L_s	Length of a bar under softening plastic loading	m
L_h	Length of a bar under elastic unloading	m
L_{ij}	Macro-velocity gradient field	s^{-1}
m	Yield surface parameter	$-$
m_a	Molar mass of dry air	kg/mol
m_v	Molar mass of water vapour	kg/mol
m_G	Plastic potential parameter	$-$
$\overline{m}_i$	Parameters for the evolution of intrinsic water permeability	
M	Elastic P-wave modulus	Pa
M_a	Dry air mass inside unit volume Ω	kg/m^3
M_{da}	Dissolved air mass inside unit volume Ω	kg/m^3
M_s	Solid mass inside unit volume Ω	kg/m^3
M_v	Water vapour mass inside unit volume Ω	kg/m^3
M_w	Liquid water mass inside unit volume Ω	kg/m^3
$\mathcal{M}$	van Genuchten coefficient	$-$
n_i	Normal unit vector	$-$
$N_1,\ N_2$	Constant normal stresses for a bar in traction	N
$\mathcal{N}$	Creep curve shape parameter	$-$
p_a	Partial pressure of dry air	Pa

p_{atm}	Atmospheric pressure	Pa
p_c	Capillary pressure	Pa
p_g	Gas pressure	Pa
p_v	Partial pressure of water vapour	Pa
p_v^0	Pressure of saturated water vapour	Pa
p_w	Pore water pressure	Pa
p_w^Γ	Pore water pressure at gallery wall	Pa
p_w^{cav}	Pore water pressure in the gallery	Pa
P_r	van Genuchten air entry pressure	Pa
$\overline{P}_{ij}$	External double traction force	N/m
q	Deviatoric stress	Pa
$\underline{q}$	Deviatoric stress in compression tests	Pa
$q_{g,i}$	Advective flux of the gaseous phase	m/s
$q_{l,i}$	Advective flux of the liquid phase	m/s
$q_{w,i}$	Advective flux of the liquid water	m/s
$\overline{q}_w$	Input water mass per unit area on the porous material boundary	$kg/m^2\ s$
$\overline{q}_a$	Input air mass per unit area on the porous material boundary	$kg/m^2\ s$
Q_a	Total sink term of air mass	$kg/m^3\ s$
Q_w	Total sink term of water mass	$kg/m^3\ s$
r	Gallery radius	m
r_c	Compression reduced radius of the yield surface	$-$
$r_{c,G}$	Compression reduced radius of the plastic potential	$-$
r_e	Extension reduced radius of the yield surface	$-$
$r_{e,G}$	Extension reduced radius of the plastic potential	$-$
r_i^c	Cosserat's local rotations	$-$
r_{ij}	Macro-rotation field	$-$
r_{ij}^c	Cosserat's micro-rotation field	$-$
r_{ij}^m	Micro-rotation field	$-$
$r,\ \theta,\ z$	Cylindrical coordinates	
R	Universal gas constant	$J/mol\,K$
$\bar{R}$	Resistance parameter for viscoplasticity	Pa
R_c	Uniaxial compressive strength	Pa
R^{ext}	External radius of a thick-walled cylinder	m
R^{int}	Internal radius of a thick-walled cylinder	m
R_{ij}	Rotation matrix	$-$
RH	Relative humidity of the gaseous phase (air)	$-$
s	Matric suction	Pa
s^{tot}	Total suction	Pa
$\underline{s}$	Shear band mode parameter	$-$
$\bar{S}$	Seepage flow at gallery wall	$kg/m^2\ s$
S_{max}	Maximum degree of water saturation	$-$
S_{res}	Residual degree of water saturation	$-$
$S_{r,w}$	Degree of water saturation	$-$
$S_{r,g}$	Gas degree of saturation	$-$
S_{ijkl}	Jaumann's correction tensor for large strains and rotations	$-$
t	Current time	s
t_i	Interface traction force per unit area on a shear band	Pa
$\bar{t}_i$	Classical external traction force per unit area on the porous material boundary	Pa
T	Absolute temperature	K
T_a	Air temperature for drying test	K

T_w	Wet-bulb temperature	K
$\overline{T}_i$	External double force per unit area on the porous material boundary	N/m
Δt	Finite time step in numerical iterative procedures	s
$\left[T^{\tau 1}\right]$	Transformation matrix for finite element methods	$-$
u_a	Axial displacement	m
u_i	Macroscale displacement field	m
u_i^m	Microscale displacement field	m
u_r	Radial displacement	m
$u_r^\Gamma,\ u_x^\Gamma,\ u_y^\Gamma$	Radial, horizontal, and vertical displacements of the gallery wall	m
$\Delta u_r,\ \Delta u_x,\ \Delta u_y$	Relative radial, horizontal, and vertical displacements to the gallery wall	m
U	Elongation of a bar in traction	m
U_f	Final elongation of a bar in traction	m
$\left[U^{*,\tau 1}_{(x_1,x_2)}\right]$	Vector of the virtual nodal variables for the current finite element	
$\left[U^{*,\tau 1}_{Node}\right]$	Vector of the virtual nodal variables	
$\left[dU^{\tau 1}_{(x_1,x_2)}\right]$	Vector of the unknown increments of nodal variables for the current finite element	
$\left[dU^{\tau 1}_{(\kappa_1,\kappa_2)}\right]$	Vector of the unknown increments of nodal variables for the parent finite element	
$\left[dU^{\tau 1}_{Node}\right]$	Vector of the unknown increments of nodal variables	
$\left[\delta U^{\tau 1}_{Node}\right]$	Global correction vector of the nodal variables	
v	Local variable	
$\mathring{\text{v}}$	Non-local variable	
V	Weight function integral for non-local approach	$-$
$\|\|v\|\|$	Velocity norm	m/s
w	Water content	$-$
W^*_{ext}	Virtual work of external forces	Nm
$W^*_{ext,v}$	Virtual work of external volume forces	Nm
$W^*_{ext,c}$	Virtual work of external contact forces	Nm
w^*_{int}	Virtual volume work of internal forces	Nm/m^3
W^*_{int}	Virtual work of internal forces	Nm
x_{da}	Mole fraction of dissolved air	$-$
x_i	Global Cartesian coordinates and axes (x,y,z)	m
y_i	Coordinate vector for non-local approach	m
YI	Yield index	$-$
YI^{thr}	Yield index threshold for the evolution of intrinsic water permeability	$-$

Chapter 1

Introduction

1.1 Underground waste repository

Nuclear energy is a leading energy source used nowadays all over the world. The energy production process inevitably generates radioactive wastes that are hazardous to most forms of life, including the human being and its environment. To limit the risks, long-term nuclear waste management is considered and adapted depending on the nuclear waste activity and half-life period (IAEA, 1983, 2009). In fact, the more harmful the waste, the more isolated from the biosphere it should be stored. Various radioactive waste management agencies are responsible for assessing, achieving, and attesting adequate and sustainable disposal solutions (Andra, 2005a). Actually, surface, shallow, and deep geological facilities are envisaged with an increasing insulation related to the increasing waste harmfulness.

The deep geological disposal (NEA, 2008) is considered for long-lived intermediate-level and high-level wastes of types B and C which constitute the most significant part of the radioactivity generated by nuclear wastes. This mode of disposal consists of a repository in stable geological media providing good confining characteristics, such as a low permeability (IAEA, 2003). It is designed to delay and slow down the radionuclide migration on a time-scale consistent with the radioactive decay period, thereby avoiding to affect the biosphere and the living organisms. A multi-barriers confinement concept with a series of engineered and natural barriers is adopted to contain the nuclear wastes (NEA, 2003; Kim et al., 2011). For the high-level wastes, a vitrification process is firstly realised, then they are placed in steel canisters, which are in turn possibly placed in concrete containers or in a bentonite engineered barrier. Finally, the waste packages are placed in underground structures composed of many galleries, with the last and highest level barrier being the natural geological formation.

Different low-permeability host materials are envisaged such as argillaceous (Félix et al., 1996; Neerdael and Boyazis, 1997), granite (Bäckblom, 1991), and salt (Langer, 1999; Behlau and Mingerzahn, 2001) formations. They are privileged in different countries depending on the geological properties of their underground. Among these materials, a particular attention is paid to the Callovo-Oxfordian claystone (COx) which is the geological medium envisaged in France by the national radioactive waste management agency Andra (Andra, 2005a). The Andra is in charge of the long-term management of the French radioactive wastes and has been entrusted of the conception of a safe and reversible disposal system through the Cigéo project (Labalette et al., 2013). The deep geological repository facility will be composed of horizontal cells containing the radioactive nuclear wastes as illustrated in Fig. 1.1.

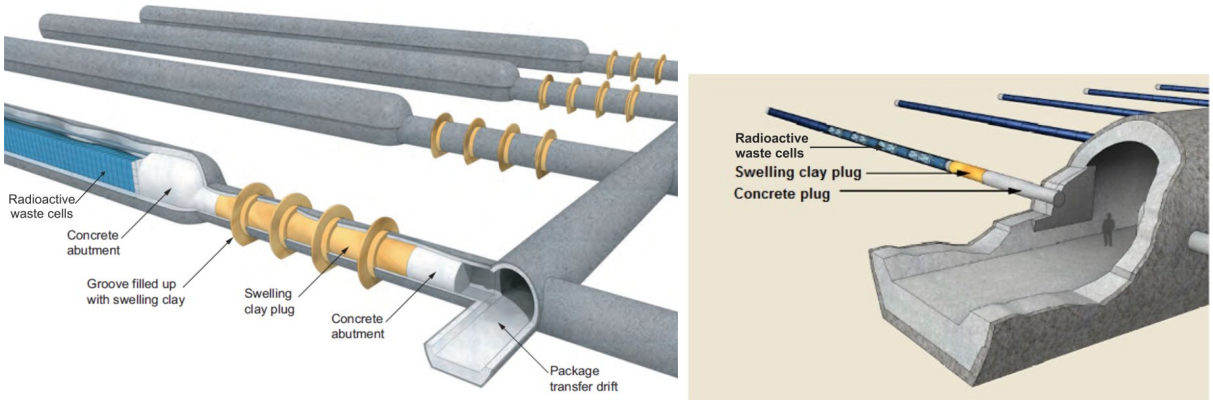

(a) (b)

Fig. 1.1: General concept of the repository layout in Callovo-Oxfordian claystone for nuclear waste of (a) type B and (b) type C after sealing (Andra, 2005a).

1.2 Fracturing and coupled processes

Long-term repository of radioactive wastes in deep geological media requires a good understanding of the host formation behaviour and of the coupled processes occurring during the different storage phases. Diverse phases are in fact achieved during the underground repository. The first one is the construction phase that consists of the excavation of the different galleries composing the underground disposal structures. The drilling process inevitably generates stress modifications, cracks, and eventually fractures in the surrounding medium (Fig. 1.2 (a)). The cracks and fractures concentrate in the gallery's vicinity and an Excavation Damaged Zone (EDZ) is created around the nuclear waste cells (Tsang et al., 2005) with important modifications of the hydro-mechanical properties (Bossart et al., 2002). In this zone, a significant hydraulic permeability increase of several orders of magnitude is observed experimentally (Fig. 1.2 (b)). This increase may alter the safety function of the host formation by creating preferential flow paths for the migration of radionuclides towards the biosphere.

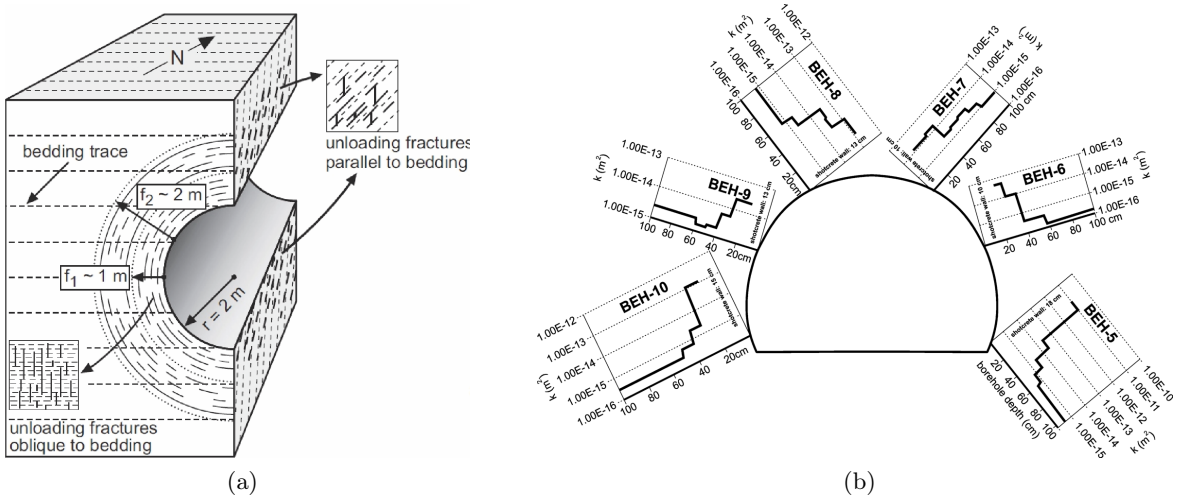

(a) (b)

Fig. 1.2: Excavation damaged zone around a gallery in Opalinus clay: (a) mechanical fracturing and (b) permeability evolution (Bossart et al., 2002).

Secondly, a maintenance phase occurs with air ventilation performed inside the galleries. Such ventilation may affect the material behaviour by draining its water and causing desaturation, especially in the damaged zone. If negative pore water pressure (suction) occurs close to the gallery, it could affect the damaged zone (Matray et al., 2007) by, for instance, modifying its fracturing structure and transport properties. The damaged zone can thus be influenced by air-material interactions due to gallery air ventilation.

After the construction and maintenance phases, the repository phase is realised. The nuclear waste packages are placed in their cells which are sealed with swelling clay and concrete (Fig. 1.1). At this stage, the dominant process taking place around nuclear cells is hydraulic resaturation. In fact, the pore water pressure in the far field engenders water flows directed towards the damaged zone which will progressively resaturate. Later, the heat generation which is characteristic of high-level wastes activity will create thermal effects, and gas migration will also appear due to radiolyse or steel corrosion. Both processes may also modify the host material behaviour in the long term (François, 2008; Gerard, 2011).

1.3 Objectives

The fluid transfers occurring around underground galleries are of paramount importance when envisaging the long-term sustainability of underground structures for nuclear waste disposal. These transfers are mainly conditioned by the behaviour of the surrounding unsaturated material and by its interactions with the gallery air. The hydro-mechanical behaviour of the excavation damaged zone, which develops around galleries due to the drilling process, is thenceforward critical because it is composed of fractures having a significant irreversible impact on flow characteristics and transfer kinetics. Consequently, it is obvious that understanding and predicting the behaviour of the excavation damaged zone is a major issue (Blümling et al., 2007).

The first objective is to improve the description of the fractures and of the EDZ development during excavation. Different methods could be taken into consideration to reproduce the drilling effects in geomaterials, from diffuse material damage to fracture onsets and open macrocracks (Barenblatt, 1962; Krajcinovic, 1996; Hajiabdolmajid et al., 2002; Jia et al., 2007; Zhu et al., 2008; Lisjak et al., 2014). Among the different methods, an appropriate method has to be chosen for the particular treated application.

Then, because sedimentary geomaterials frequently exhibit a transversely isotropic behaviour, a constitutive mechanical model incorporating the material anisotropy has to be taken into account. At repository scale, experimental measurements have also highlighted that the material anisotropy plays an important role in the onset of fractures and in the fractured zone pattern (Armand et al., 2014). This role will be analysed.

The third major objective is the description of the fluid transfers and of the material hydro-mechanical behaviour around galleries, especially in the damaged zone. The impact of fracturing on the transport properties has to be addressed to reproduce the significant hydraulic permeability increase observed in the excavation damaged zone. After gallery excavation, the material interaction with the gallery air conditions the hydraulic transfers, the water drainage, and the possible desaturation or resaturation of the rock. The hydraulic interactions at gallery walls as well as a hydro-mechanical model under partial saturation conditions, capable to reproduce experimental observations on clay rocks, are therefore developed.

In addition to these hydro-mechanical aspects, thermal effects will also be generated around the nuclear waste cells and will have an impact on the response of the host formation and of the EDZ (François et al., 2009; Dizier, 2011). Yet the heat generation of the wastes is not analysed and the focus is on the hydro-mechanical aspects.

Finally, the developed models are used to address numerical modelling at repository scale, including excavation and gallery air ventilation experiment in the Callovo-Oxfordian claystone. The modelling objective is to better understand how the fracturing and the hydro-mechanical coupling influence the host formation response during the different phases of the underground repository. The numerical modelling is performed with the non-linear finite element code Lagamine developed at the University of Liège (Charlier, 1987; Collin, 2003).

More broadly, the developments and applications that follow are oriented towards the modelling of the excavation damaged zone and of the hydro-mechanical coupling occurring in partially saturated low-permeability rocks. They are realised in partnership with the Andra which conducts various scientific research programs to ensure the feasibility of a safe repository in the Callovo-Oxfordian claystone and to characterise the claystone behaviour. The study of the EDZ behaviour is motivated mainly by two of theses research programs. The first one is the study of the Saturation Damaged Zone (SDZ) experiment that is realised in the context of the Group of Laboratories (GL) for gas transfer established by the Andra. The experiment consists of a large-scale gallery air ventilation test performed in the Andra's Underground Research Laboratory (URL). Its purpose is to investigate the rock-atmosphere interactions and the possible EDZ desaturation at repository scale (Cruchaudet et al., 2010a). The second is the benchmark named "Transversal action - Models" that is realised in the context of the Andra's Group of Laboratories for geomechanics. It consists in developing and calibrating numerical models for the Callovo-

Oxfordian claystone, and to use them to model underground structures by the reproduction of the drilling phase (Seyedi et al., 2012, 2013).

1.4 Outline

The thesis global frame consists of five main chapters that are articulated following the major objectives and published research articles. Numerical applications are realised all along the different chapters, improving the complexity of the material behaviour at each step. Globally, each chapter is based on an article but it is written with more developments and results to gain a global coherence. In that sense, the global frame of the document is slightly unusual because it does not corresponds exactly to a thesis by publication, nor to a complete coherent monograph. The different research articles are recalled in the abstracts of the chapters and are listed in the appendix B. The chapters are succinctly summarised as follows:

Chapter 2 states the starting point of the research. It includes the global properties of the considered argillaceous rock as well as experimental evidences of excavation damaged zone and air-rock interaction. A general framework for unsaturated porous media is detailed, then preliminary numerical modelling of the EDZ and of gallery air ventilation is performed.

Chapter 3 presents how the fracturing description is improved and details the chosen method. Because localised deformations can generally appear in materials prior to cracks and material ruptures in a large number of situations, the fractures are represented with shear strain localisation in band mode. An appropriate model allowing to properly reproduce the strain localisation in geomaterials with finite element methods is defined. The chosen model is an enhanced model for microstructure media which is called the coupled local second gradient model.

Chapter 4 contains the numerical modelling of an excavation fractured zone with shear banding. Some improvements of the coupled local second gradient model are included for unsaturated and compressible media. The numerical results provide information about the fractured zone extension, structure, and behaviour. A theoretical gallery air ventilation is also reproduce to highlight its effect on shear banding.

Chapter 5 is devoted to the transversely isotropic behaviour of the rock. The behaviour of anisotropic materials depends on the direction of loading with respect to their microstructure. This directional dependence is commonly observed both on elastic and plastic characteristics which will be envisaged in the model. The influence of transverse isotropy on shear banding remains an important issue that is investigated through numerical applications. Additionally, viscosity effect is also included in the modelling to improve the reproduction of long-term deformation.

Chapter 6 concerns the fluid transfers and the material coupled behaviour, especially in the EDZ. It regroups the precedent aspects (shear band and anisotropy descriptions) and incorporates permeability variation as well as air-rock interaction. A gallery air ventilation experiment is numerically reproduced to study its influence on hydraulic transfers.

Lastly, general conclusions and outlooks are stated and evidence the main contributions of the thesis.

Chapter 2

Excavation damaged zone and air interaction in argillaceous rock

Abstract The hydro-mechanical material behaviour and the fluid transfers taking place around underground galleries are addressed in this chapter. Firstly, the global characteristics of the considered argillaceous rock are summarised. Then, the excavation damaged zone development and the effects of exchanges between air and rock are detailed. The water transfers are most particularly analysed through a gallery air ventilation test. The modelling of such experiment requires to develop a general framework for unsaturated porous media including hydro-mechanical behaviour. Lastly, the ventilation test is numerically reproduced and the preliminary results that are obtained highlight the future challenges about EDZ and transfer modelling. For more details about this preliminary modelling, please refer to the scientific paper of Charlier et al. (2013b).

Article Charlier, R., Collin, F., Pardoen, B., Talandier, J., Radu, J. P., and Gerard, P. (2013). An unsaturated hydro-mechanical modelling of two in-situ experiments in Callovo-Oxfordian argillite. *Eng Geol*, 165:46-63. doi: 10.1016/j.enggeo.2013.05.021.

2.1 Callovo-Oxfordian claystone

Among the different materials suitable for deep geological repository of nuclear wastes, the behaviour of the Callovo-Oxfordian claystone will be most particularly studied. This geological medium is envisaged by the French national radioactive waste management agency (Andra) (Andra, 2005a). The Callovo-Oxfordian claystone, also called argillite, is part of the Paris Basin, a geological area in France filled with a thick accumulation of sedimentary formations. This basin is constituted of a succession of quasi-horizontal sedimentary layers of clay, limestone, and marls (Fig. 2.1). The Callovo-Oxfordian claystone is a quite homogeneous indurated clay formation with very low permeability, located between 400 and 600 m depth. It is a stiff rock exhibiting good retaining ability of radionuclides and its mineralogical composition is mainly made of illite-smectite clay minerals (Gaucher et al., 2004), quartz, and carbonate. The carbonate cements give good mechanical strength and contribute together with the high content of clay minerals to the very low permeability of this rock (Distinguin and Lavanchy, 2007). The proportions of the different minerals evolve in the rock layer with the depth.

The understanding of the geomechanical behaviour of the possible host formations is a crucial issue to evaluate and ensure the feasibility of a safe repository. This is why many Underground Research Laboratories (URL) have been developed around the world (Kickmaier and McKinley, 1997; Gens et al., 1998; Croisé et al., 2004; Rutqvist et al., 2005; Delay et al., 2007). The research programs in the different laboratories must allow an accurate characterisation of the confining properties of suitable geological formations. In France, the Andra developed an URL at Bure, in the Meuse/Haute-Marne area, at an average depth of 490 m corresponding to the median depth of the Callovo-Oxfordian formation. At this site location, the geological layers dip slightly to the West and the North-West. This low dip allows to assume that if an anisotropic behaviour of the claystone is observed, the main orientations of anisotropy are located in the horizontal sedimentary planes and along the vertical direction. The underground facility illustrated in Fig. 2.2 is composed of several galleries in which a series of experiments are conducted to characterise the formation. These *in situ* experiments cover various aspects, such as the mechanical, the hydraulic or the thermal behaviours of the host rock as well as its retention and diffusion properties of radioactive elements.

At the URL level, the material features anisotropic characteristics. This behaviour is due firstly to the material mode of deposition (inherent anisotropy). A layered structure is observed for sedimentary materials because they were usually deposited vertically in a succession of horizontal layers and were subjected to stress. Over time, this structure can lead to the creation of weakness planes called bedding planes due to metamorphism or diagenetic processes (Blümling et al., 2007). A second possible type of anisotropy is an induced anisotropy that results of the loading history and deformation following the material deposition (Arthur et al., 1977a).

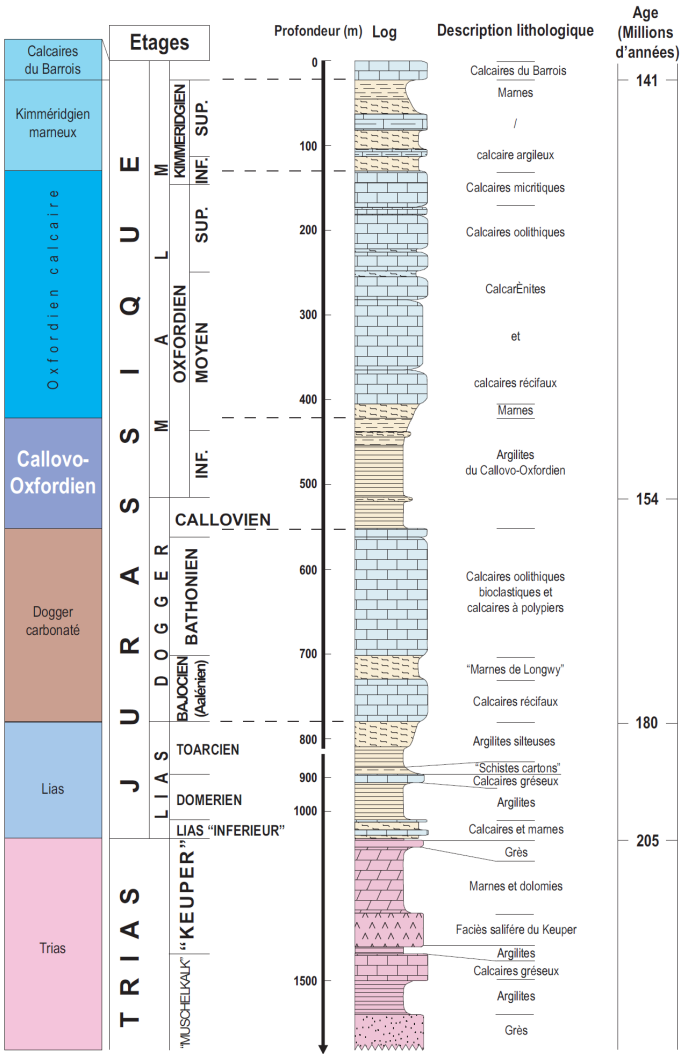

Fig. 2.1: Geological cross-section at the Meuse/Haute-Marne underground research laboratory site (Andra, 2005a).

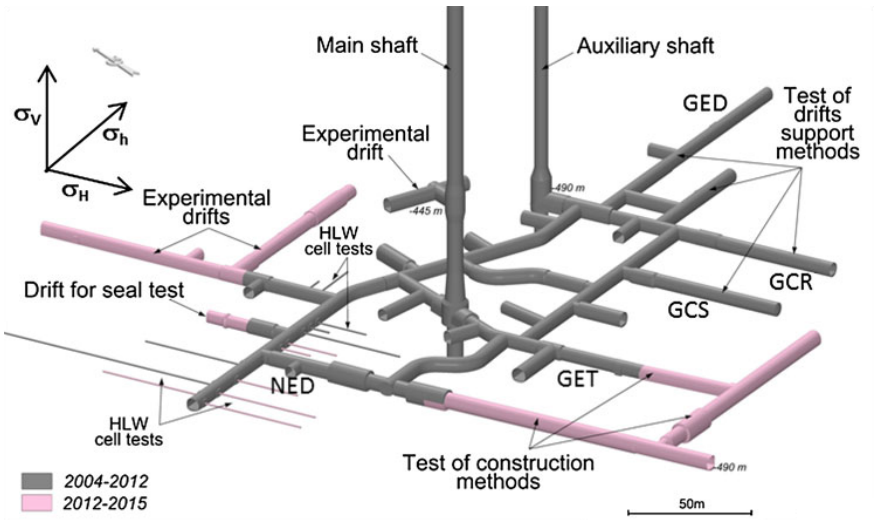

Fig. 2.2: Gallery network of the Meuse/Haute-Marne underground research laboratory developed in Callovo-Oxfordian claystone (Armand et al., 2014).

Lithological conditions (overburden pressure), rheological properties, and tectonic processes can of course play an important role (Wileveau et al., 2007).

For the considered claystone, the anisotropy is observed on the hydro-mechanical properties and on the *in situ* stress state. The anisotropic stress state in the clayey rock at the main level of the laboratory highlights an important horizontal stress and is defined as follows (Wileveau et al., 2007):

$$\sigma_v = 12 - 12.7\ MPa$$

$$\sigma_h = 12 - 12.4\ MPa$$

$$\sigma_H = 14.4 - 16.1\ MPa$$

$$\frac{\sigma_H}{\sigma_h} = 1.2 - 1.3$$

$$p_w = 4.5 - 4.7\ MPa$$

where σ_v is the vertical principal total stress, σ_h is the minor horizontal principal total stress, σ_H is the major horizontal principal total stress, and p_w is the pore water pressure. The usual value that is considered for the ratio σ_H/σ_h is closer to 1.3, even if it varies with the rheological material properties and the depth (Armand et al., 2013, 2014).

The hydraulic permeability of the rock is lower than $10^{-19}\ m^2$ with a more important value along the quasi-horizontal bedding planes which is in a ratio of about 3 with the vertical permeability. The mechanical characteristics also differ depending on the orientation. For instance, the ratio of elastic Young's modulus parallel to the bedding planes and in the vertical direction ranges from 1.05 to 1.4 (Andra, 2005b), and the uniaxial compressive strength of the material also depends on the orientation. Table 2.1 presents some typical values of some basic properties of Callovo-Oxfordian claystone and highlights the low porosity and the high strength of this material.

Symbol	Name	Value	Unit
E	Young's modulus	$4 - 5.6$	GPa
ν	Poisson's ratio	$0.18 - 0.37$	$-$
b	Biot's coefficient	0.6	$-$
ρ	Density	$2300 - 2400$	kg/m^3
ρ_d	Dry density	$2210 - 2330$	kg/m^3
Φ	Porosity	$15 - 18$	%
w	Water content	$3 - 7$	%
φ	Friction angle	$20 - 25$	$^\circ$
ψ	Dilatancy angle	$0 - 0.5$	$^\circ$
c	Cohesion	$3 - 7$	MPa
R_c	Uniaxial compressive strength	$20 - 30$	MPa

Table 2.1: Geomechanical characteristics of Callovo-Oxfordian claystone (Gens et al., 2007; Wileveau and Bernier, 2008; Malinsky, 2009; Andra, 2005a,b).

2.2 Excavation damaged zone

The process of underground excavation generates *in situ* stress modification and damage propagation in the surrounding medium. When the damage threshold is reached, microcracks initiate, then accumulate, propagate (distributed damage), and can lead to the onset of macrocracks (interconnected fractures). Different modes of fractures exist: opening or tensile fractures, shear fractures, and mixed-mode fractures which are a combination of the two previous modes (Jenq

and Shah, 1988). In the rock mass around underground galleries, distinct brittle failure mechanisms can occur due to the damage accumulation and microcracks coalescence (Diederichs, 2003). The failure mechanisms consist of macroscale shear failure in case of high-stress environment, spalling in case of low-stress environment, and unravelling which corresponds to tensile failure (Fig. 2.3). The author also mentions that dilating cracks appear close to the excavation wall because it is not restraint. Similar failure mechanisms are observed on small-scale laboratory tests.

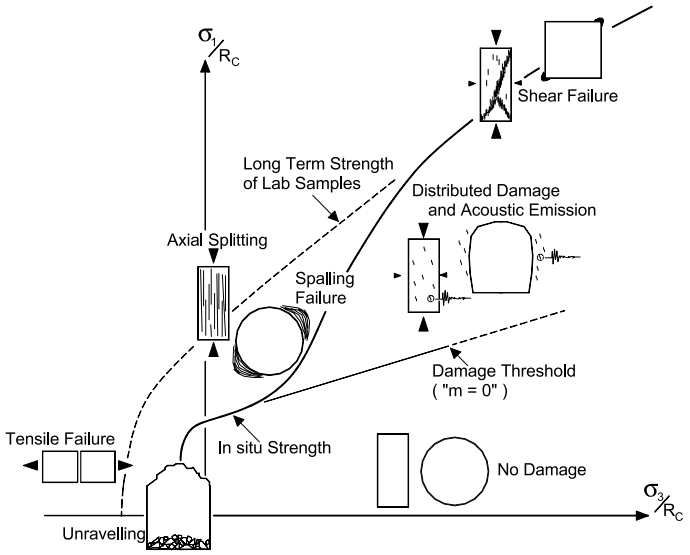

Fig. 2.3: Mechanisms of rock mass brittle failure around gallery (Diederichs, 2003).

An Excavation Damaged Zone (EDZ) therefore develops close to the drift wall with distributed damage as well as hypothetical macro-scale fractures. Emsley et al. (1997) and Tsang and Bernier (2004) define it as a zone dominated by geochemical and hydro-mechanical property changes that are mainly irreversible and which induce important modifications in flow and transport properties (Bossart et al., 2004; Tsang et al., 2005; Armand et al., 2007), such as permeability increase. These property modifications could alter the safety function of the rock; therefore, the EDZ behaviour is a major issue concerning the long-term management of nuclear waste repository. The EDZ has been carefully investigated in URL through, for instance, *in situ* observations, fracture measurements, permeability analyses, and fluid transfers.

Hereafter, the excavation damaged zone in Callovo-Oxfordian claystone is defined by focusing on experimental evidences of induced mechanical fracturing and permeability evolution.

2.2.1 Rock fracturing

For the Callovo-Oxfordian claystone, many *in situ* observations and measurements of fractures induced by the drilling are conducted in the vicinity of the Andra's URL. To characterise the fractured zone, the fractures located at the front, on the sidewalls, and in the rock around experimental galleries are of particular interest and are studied through a structural analysis. The geological survey of the galleries is performed after the excavation with two principal methods: three-dimensional scan measurements of the drifts' faces and sidewalls, and a structural analysis of core samples coming from boreholes. The scan measurements provide the senses, the strikes, and the dips of the superficial fractures. The fractures at the gallery fronts are illustrated in Fig. 2.4 for galleries parallel to both major and minor horizontal principal stresses. In addition to the scans, boreholes are drilled in the rock from the gallery walls and in different directions. The fracturing analyses realised on the borehole cores provide the EDZ extent and a description of the fracturing pattern as illustrated in Fig. 2.5. The description includes the cracks density

and the type of fractures (Armand et al., 2014).

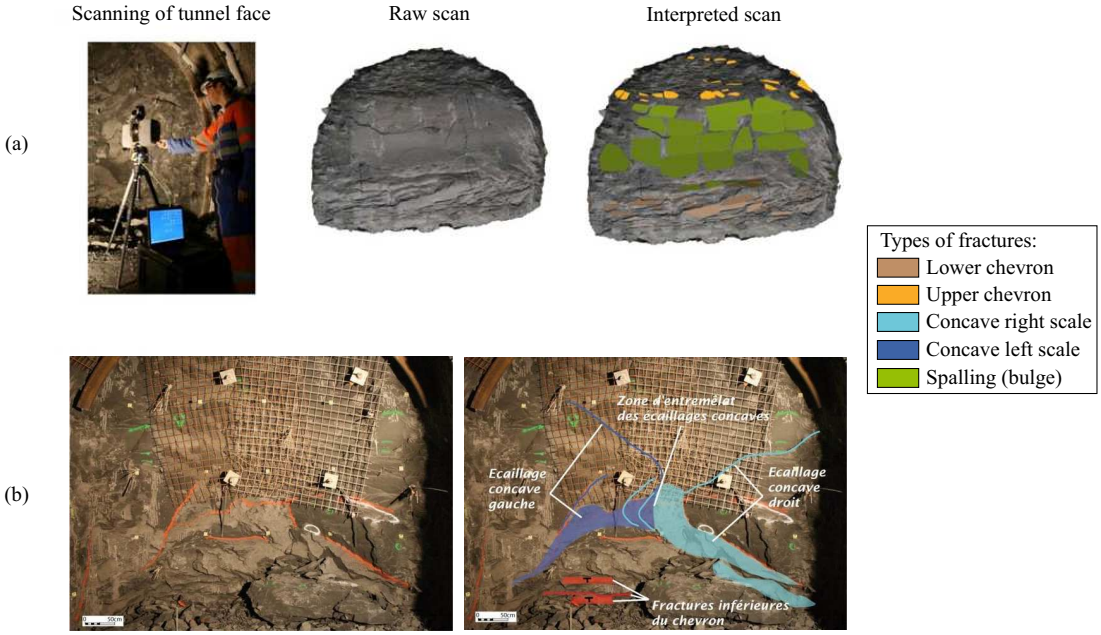

Fig. 2.4: Fractures at the front of the galleries parallel to (a) the major and (b) the minor horizontal principal stresses in the Andra's URL (according to Armand et al. (2014) and Cruchaudet et al. (2010a)).

Armand et al. (2014) indicate that extension (spalling) and shear fractures in chevrons are detected around the galleries as well as at the excavation front face (Figs. 2.4 and 2.5). For this material, shearing is the principal failure mechanism because of the high *in situ* stress environment (Diederichs, 2003). It has been evaluated, from core sample analyses, that approximately 75 % of the total number of fractures are shear fractures (mode II, Armand et al. (2014)). In the gallery axial direction, the shear chevron fractures initiate during the drilling in the rock ahead of the excavation front. Spalling and extensional failures appear during gallery convergence but remain less developed. Therefore, in the gallery cross-section, both types of fractures are detected close to the galleries but only shear fractures in chevrons are present deeper in the rock (Fig. 2.5). The extent of the fractured zone can then be separated in two sub-zones as shown in Fig. 2.5: a zone with mixed fractures (shear and extension) close to the gallery and a zone with only shear fractures further in the rock. The Fig. 2.6 illustrates a synthesis of the conceptual model of the induced fractures for both gallery orientations in Callovo-Oxfordian claystone.

Furthermore, the excavation fractured zone in Callovo-Oxfordian claystone has an elliptical extension that can reach several meters with a significantly larger extent in one direction. The shape of the fractured zone differs for the two main drifts orientations because of the stress state anisotropy as illustrated in Fig. 2.6. In fact, for galleries oriented in the direction of the minor horizontal principal stress, the anisotropy of the stress state in the plane perpendicular to the gallery axis seems to control the fracturing patterns in the rock. Nevertheless, the development of fractures in the rock has been observed even for galleries oriented in the direction of the major horizontal principal stress (Fig. 2.6) that present an isotropic or quasi-isotropic stress state in their perpendicular plane (gallery section). In this case, the anisotropic extent of the fractured zone around drifts suggests that the material anisotropy plays an important role in the onset of fractures.

The orientations of the galleries, the stress state anisotropy, and the fracturing pattern have also an influence on the convergence of the galleries. Fig. 2.7 illustrates the convergence measurements of drifts parallel to each principal horizontal stress from Armand et al. (2013). A

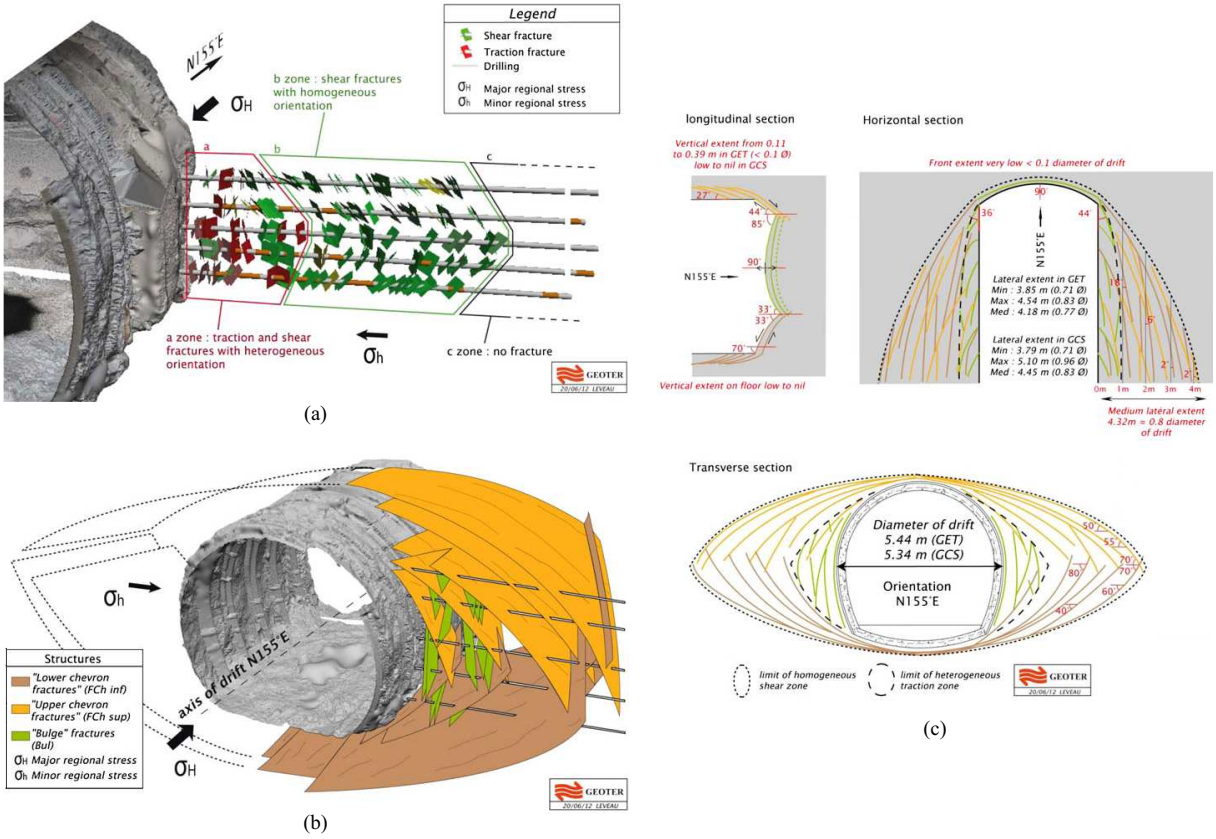

Fig. 2.5: Fractures in the rock around the galleries parallel to the major horizontal principal stress in the Andra's URL: (a) tree-dimensional visualisation of the fracture network (GET drift) and (b,c) conceptual model of the induced fractures (Armand et al., 2014).

convergence anisotropy develops in all drifts, for both gallery orientations, with the major convergence measured in the same direction than the location of the fractured zone. Nonetheless, the convergence and its anisotropy are larger for the drifts oriented parallel to the minor horizontal stress, where the stress anisotropy in the gallery section is more important with a ratio of $\sigma_H/\sigma_v \approx 1.3$.

Other low-permeability geological formations are envisaged for nuclear waste repository. For instance, two clayey formations that are considered in Europe are the Boom clay (Belgium) and the Opalinus clay (Switzerland). The chevron or herringbone fracture pattern observed in the Callovo-Oxfordian claystone is similar to what is observed in Boom clay around galleries and borehole cores (Blümling et al., 2007; Wileveau and Bernier, 2008), but no extensional failure is observed in this plastic clay. The Opalinus clay is an indurated clay studied in Switzerland on the Mont Terri site (Jura Canton). This clay exhibits comparable characteristics to the Callovo-Oxfordian claystone, with similar mineralogical composition, transfer, and mechanical properties. It features a strong material anisotropy with bedding planes inclined at about 45° with the horizontal (Martin and Lanyon, 2004). It has been observed for this material that the development of the fractures is dominated by pre-existing features (tectonic faults), extension, and bedding plane instabilities (Marschall et al., 2008). The extension is the prevailing mechanism of failure resulting from high differential stress and from a lower *in situ* stress state at laboratory level than for the Callovo-Oxfordian claystone. Moreover, the material anisotropy is a crucial factor in the determination of the excavation damaged zone geometry in Opalinus clay because instabilities, such as bedding slip or buckling, can initiate due to the material weakness along the bedding planes.

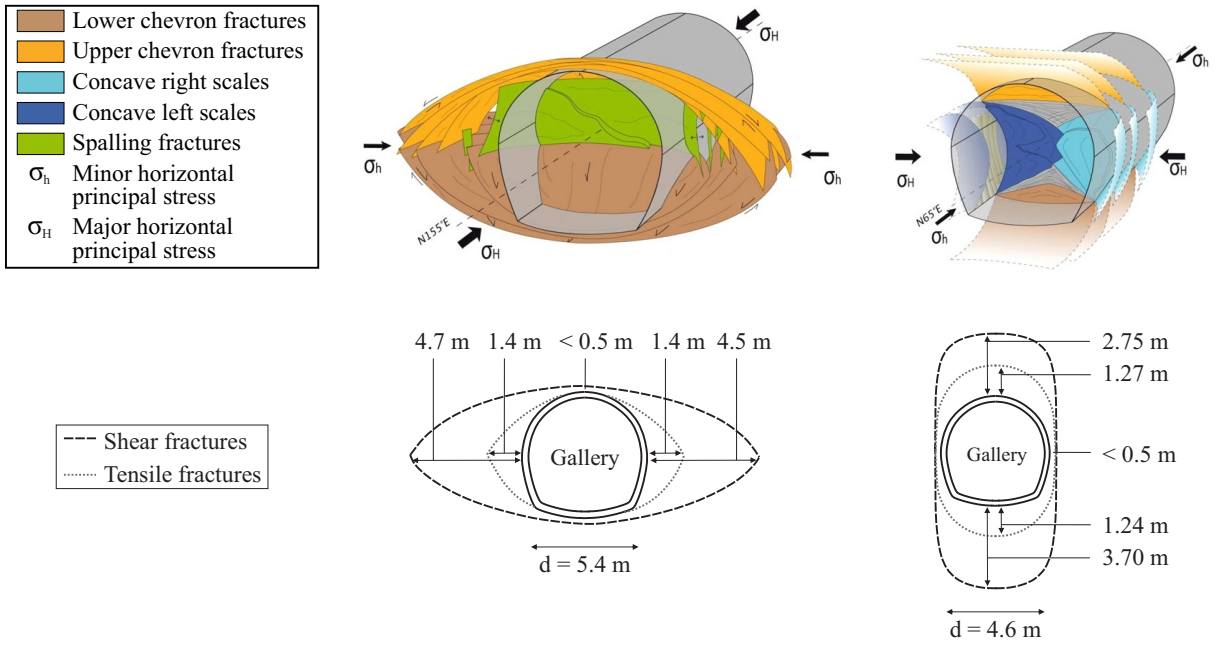

Fig. 2.6: Conceptual model of the induced fractures in Callovo-Oxfordian claystone around drifts parallel to the (a) major and (b) minor horizontal principal stresses (according to Armand et al. (2014)).

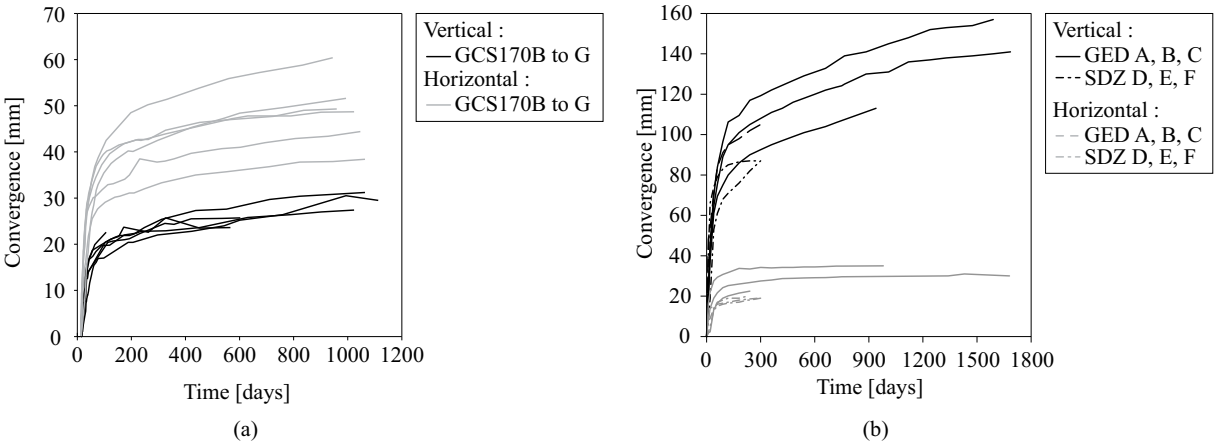

Fig. 2.7: Evolution of the convergence of drifts parallel to the (a) major and (b) minor horizontal principal stresses.

2.2.2 Permeability evolution

In the fractured zone, the hydraulic permeability is inhomogeneous and can severely increase up to several orders of magnitude, especially due to the presence of interconnected extensional fractures (Armand et al., 2014). This increase has been highlighted by measurements (Fig. 2.8) performed under saturated conditions in boreholes drilled around the galleries in different orientations (Armand et al., 2014). In the fractured zone, these measurements are representative of the fracture permeability, not of the continuous rock matrix permeability. Three zones can be defined in Callovo-Oxfordian claystones (Cruchaudet et al., 2010b): an undisturbed zone with a permeability lower than 10^{-19} m^2, a slightly disturbed zone with a permeability ranging from 10^{-19} m^2 to 10^{-17} m^2, and a highly disturbed zone close to the gallery with a permeability higher

than 10^{-17} m^2 (increase higher than 2 orders of magnitude). The extents of the zones are detailed in Fig. 2.9 and are superposed to the experimental data in Fig. 2.8. A parallelism between hydraulic measurements and fracture measurements can be evidenced and the permeability zones can then be related to the induced shear and tensile fracture zones (Fig. 2.9). Therefore, the shape of the permeability zones also differs depending on the gallery orientations and the stress state anisotropy (Armand et al., 2014).

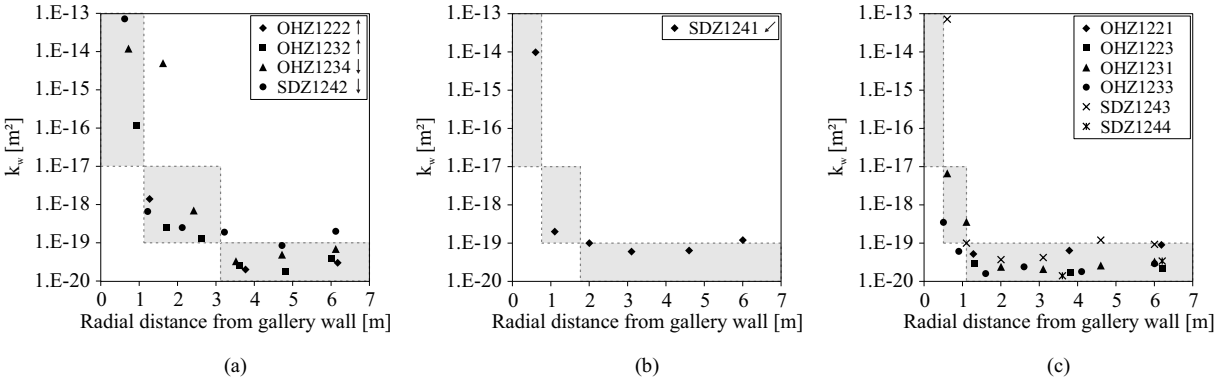

Fig. 2.8: Evolution of hydraulic permeability along (a) vertical, (b) oblique at 45°, and (c) horizontal boreholes drilled around a gallery (GED) parallel the minor horizontal principal stress in Callovo-Oxfordian claystone.

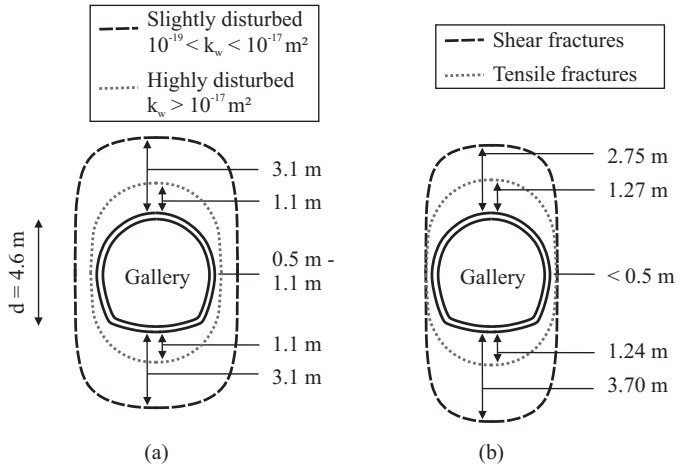

Fig. 2.9: Extensions of (a) hydraulic permeability and (b) fracture zones measured around a gallery (GED) parallel to the minor horizontal principal stress in Callovo-Oxfordian claystone.

2.3 Air-rock interaction

When a material is in contact with the atmosphere, transfers between them take place at their interface. These interface exchanges have to be carefully studied because they can lead to material drainage, desaturation, and stress modification. Such effects can affect the hydraulic transfer kinetics as well as the fracturing structure. For porous materials like soils and rocks, liquid and gaseous transfers can occur and may significantly modify the water saturation, especially close to the contact interface. The liquid exchange is a seepage flow directed towards the atmosphere that takes place if the porous surface of the material is fully saturated. Gaseous (water vapour) transfer occurs when water evaporates at the surface of the material or if water vapour reaches the contact interface. The latter is realised by fluid transfers (gas flows) inside the material that

are mainly governed by capillary forces.

At nuclear waste repository scale, air ventilation is performed in the underground galleries during the excavation and maintenance phases. This ventilation could impact the short-term behaviour of the underground structures because it may drain the water from the rock. In case of important drainage, it can even lead to rock desaturation, stress modification, as well as modification of the fracturing structure close to the drifts. As a consequence, the damaged zone behaviour could be affected (Matray et al., 2007).

2.3.1 Small-scale drying experiment

Different laboratory experiments are developed on a small scale to study the material evolution induced by material-atmosphere interaction and to emphasise the effect of shrinkage and desiccation on cracking (Peron et al., 2009a,b). In classical techniques, derived from chemical engineering methods, the suction in the material is controlled. One technique is to control the vapour phase by submitting samples to a relative humidity regulated with salt solutions in a desiccator (Young, 1967; Delage et al., 1998; Romero et al., 2001). Another technique that reproduces air circulation is the convective drying test, during which air is blown at the material surface (Léonard et al., 2005; Ta, 2009; Gerard et al., 2010). Generally, the relative humidity, the temperature, and the speed of the air are controlled during the drying. For example, Fig. 2.10 shows the result of a drying test that leads to the fracturing of a clay. In addition, an efficient tool to characterise the development and evolution of cracks during drying tests performed on small-scale samples is X-ray microtomography coupled to image analysis (Léonard et al., 2002, 2003). It also allows the determination of internal moisture profiles and geometrical changes that describe the shrinkage process.

Fig. 2.10: Cracks network on the surface of the Romainville clay after drying (Ta, 2009).

2.3.2 Large-scale ventilation experiment

In order to investigate the rock-atmosphere interactions at repository scale, large-scale ventilation experiments are performed in underground research laboratories. Among them are the Ventilation Experiment (VE) carried out at Mont Terri URL (Mayor et al., 2007) and the Saturation Damaged Zone experiment (SDZ) conducted in Andra's URL (Charlier et al., 2013b; Guillon, 2011; Pardoen et al., 2012a). The major objective is to characterise the influence of a controlled ventilation on the hydro-mechanical behaviour of the rock mass and on the hydraulic transfers taking place around the galleries, especially in the excavation damaged zone. A particular attention is paid to the material deformation, drainage, and desaturation processes during the tests.

The considered ventilation experiment is the SDZ test, which will be studied and reproduced numerically. It is performed at the end of the GED experimental gallery which is oriented parallel to the minor horizontal principal stress (Fig. 2.11). An experimental zone is isolated from the rest of the laboratory and is subjected to a controlled ventilation. Different levels of hygrometry are

applied in order to highlight the effect of drainage and wetting, or of desaturation and possible resaturation. The experimental zone, presented in Fig. 2.11, is divided in two parts: one with concrete covering and impervious geotextile on the gallery wall, and another without covering where the air-rock exchanges can be directly studied. An airlock is also present to isolate the experimental zone from the rest of the laboratory. The ventilation can be sequenced in different phases (Fig. 2.12): (1) the first phase corresponds to the global laboratory ventilation before the airlock closure, (2) once the airlock is closed the ventilation is stopped in the experimental zone and the exchanges with the GED gallery occur through the excavation damaged zone, later a controlled ventilation is imposed with hygrometric conditions of (3) 30 % of relative humidity and 23°C then of (4) 60 % of relative humidity and 22°C. The air temperature T and relative humidity RH evolutions are monitored in the experimental zone in different gallery sections. The measurements are illustrated in Fig. 2.12 with the four different ventilation phases.

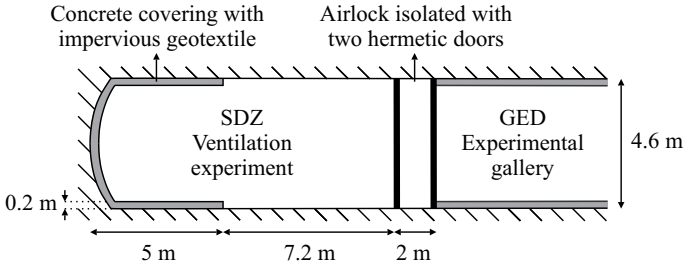

Fig. 2.11: Geometry of the SDZ experimental zone located at the end of the GED drift in Callovo-Oxfordian claystone.

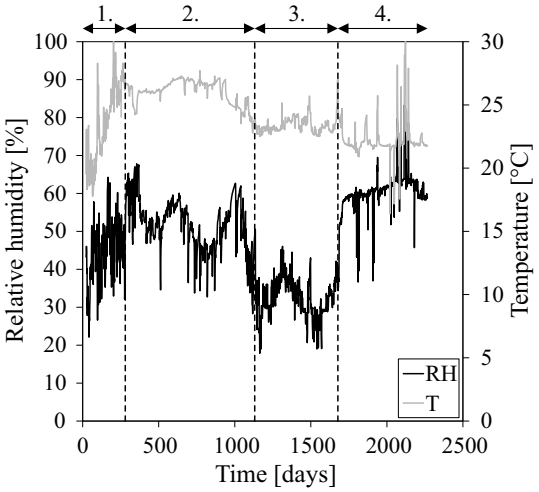

Fig. 2.12: Evolutions of temperature and relative humidity in the SDZ experimental zone.

Several *in situ* experimental measurements are realised during the test. Only the main experimental observations are presented hereafter, more complete results can be found in (Cruchaudet et al., 2010a). The pore water pressure evolution inside the rock mass is monitored in different boreholes having different orientations (Charlier et al., 2013b) as illustrated in Fig. 2.13. The sensors are set up at different depths and can acquire measurements in a range going from 0 to 10 MPa. The measurements around the experimental zone without covering are illustrated in Fig. 2.14 and give information on the progressive drainage of the material. One can observe that the drainage is not important in the far field where the pore water pressures are close to the initial rock water pressure of 4.5 MPa. It is more important close to the experimental zone where the measurements are close to the atmospheric pressure (in a 3 m ring). This is due to the deterioration of the permeability in the damaged zone, not in the far-field rock mass.

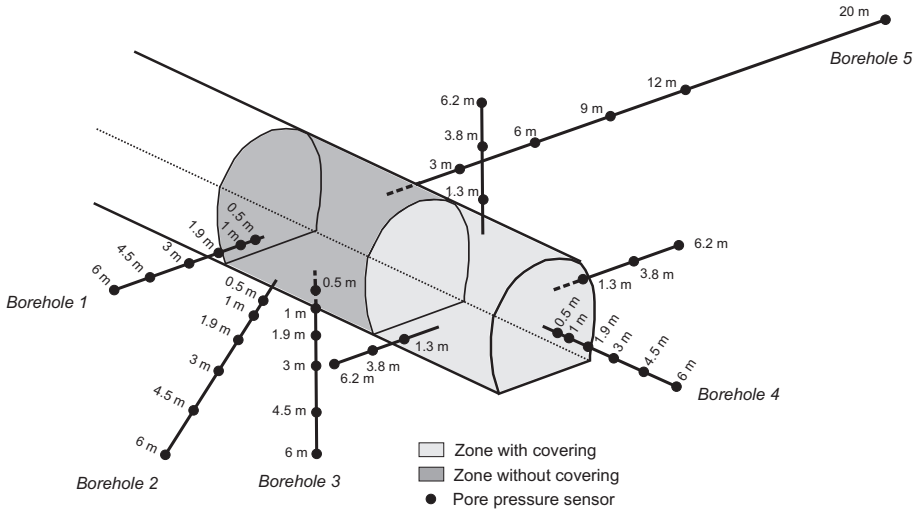

Fig. 2.13: Position of the pore water pressure sensors around the SDZ experimental zone with depths measured from the gallery wall (Charlier et al., 2013b).

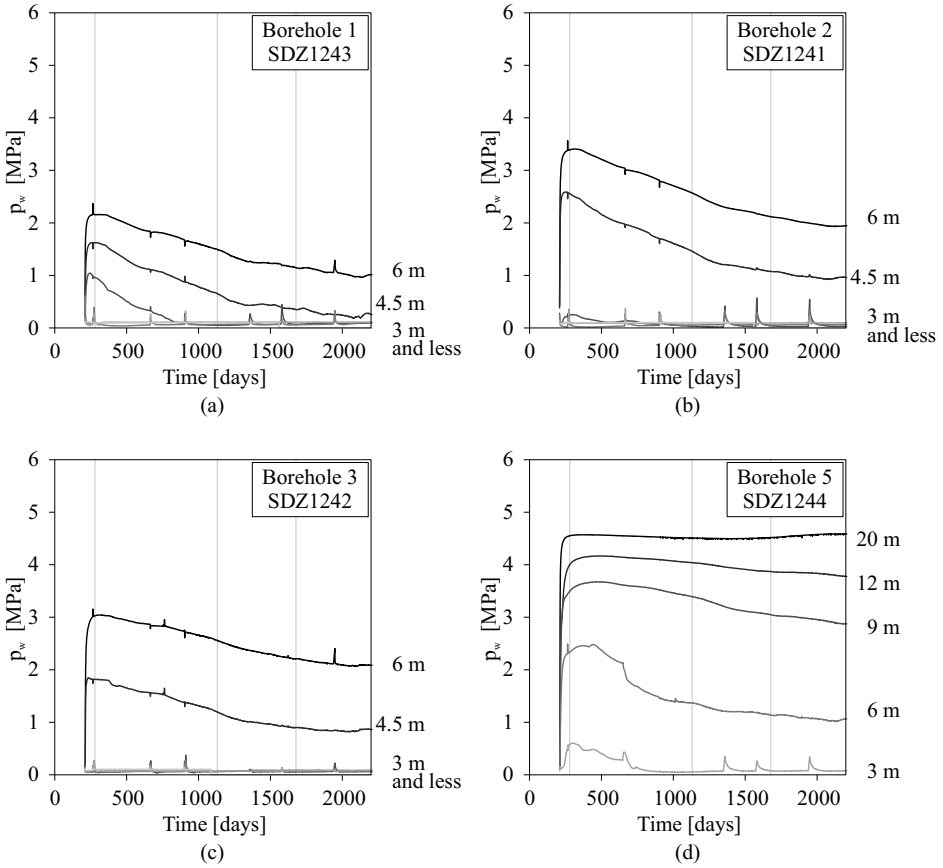

Fig. 2.14: Evolution of pore water pressure in boreholes drilled around the uncovered SDZ experimental zone for different distances from gallery wall: (a,d) horizontal, (b) oblique at 45°, and (c) vertical boreholes.

Moreover, the pore water pressures in the horizontal borehole located at the end of the gallery are higher than the initial pore water pressure of the rock (Fig. 2.15). This is characteristic of hydro-mechanical coupling engendered by the material anisotropy either of the initial stress state or of the mechanical behaviour. The analysis of the pore pressure temporal evolution around the uncovered zone is also performed for different sensors located at the same distance from the

gallery wall but in boreholes drilled with different orientations (Fig. 2.16). The results indicate that, at a depth of 4.5 m, pore water pressures are the highest when the dip of the borehole is 45° according to the horizontal plane. At 6 m depth, this is also observed in the short term but in the long term the pore water pressures in the vertical direction are slightly higher than the ones at 45° because the drainage is slower in the vertical borehole. On the other hand, the pore pressures are the lowest in the boreholes drilled in the horizontal plane, with a perpendicular orientation to the GED gallery. Such observations are characteristic of the material anisotropic permeability.

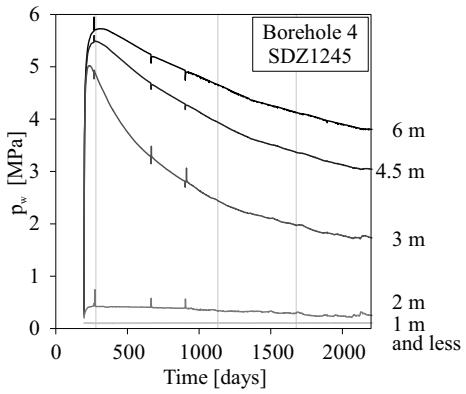

Fig. 2.15: Evolution of pore water pressure in the horizontal borehole drilled at the end of the GED drift for different distances from gallery wall.

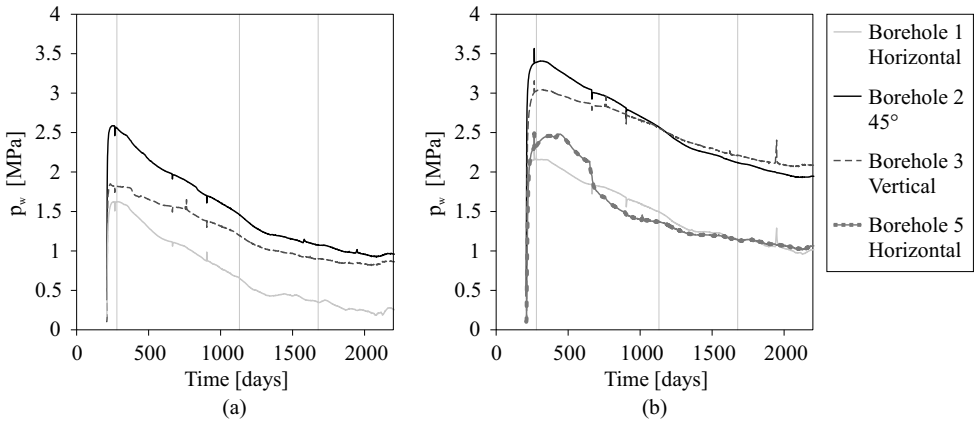

Fig. 2.16: Evolution of pore water pressure in sensors located at (a) 4.5 m and (b) 6 m from gallery wall for different boreholes orientations.

In the excavation damaged zone, it can be expected that the increase of permeability and the drainage lead to rock desaturation. Unfortunately, the sensors can not acquire negative measurements and can not characterise the desaturation. In the long term, the two controlled ventilation phases (phases (3) and (4) in Fig. 2.12) have only a minor effect on the measured pore water pressures. The decrease of the pore water pressure measurements in Figs. 2.14 and 2.16 is slightly reduced when the wetting phase with $RH = 60$ % is applied (phase (4) after 1680 days).

To characterise the desaturation, water content measurements have also been performed on core samples coming from horizontal boreholes, that were drilled in the experimental zone without covering. The water content w is a direct measurement of the degree of water saturation $S_{r,w}$ through the relations:

$$w = \frac{M_w}{M_s} \tag{2.1}$$

$$S_{r,w} = \frac{\rho_s}{\rho_w} \frac{1-\Phi}{\Phi} \, w \tag{2.2}$$

where M_s is the mass of the solid grains, M_w is the mass of the liquid water, ρ_s is the solid grain density, ρ_w is the water density, and Φ is the material porosity. These different material properties will be defined in the general framework for unsaturated porous media in section 2.4. The experimental results are illustrated in Fig. 2.17 (a). They indicate, firstly, a strong desaturation close to the gallery wall with 3 % $\leq w \leq$ 5 % that can extend up to 0.5 m depth, secondly, a moderated desaturation deeper in the rock, and thirdly, a limited desaturation or no desaturation deeper than 2 m with 6.7 % $\leq w \leq$ 8.2 % for the saturated claystone. The measurements in the URL show that the desaturation evolution occurs mainly during the excavation phase and the first interaction with the gallery air. In the long term, the desaturation propagation in the rock is limited which may be related to low vapour transfers at gallery wall, to fracture closure or to material sealing / healing. The evolution of the water content at gallery wall is also represented in Fig. 2.17 (b). The experimental values correspond to the measurements performed the closest to the gallery wall for each borehole. For three of them (SDZ1285 to 87) the first samples were taken at about 25 cm depth, and therefore the water content values have been corrected.

Furthermore, a geological survey of the fractured zone as well as measurements of the gallery convergence are also performed by the Andra in the SDZ experimental zone, after the gallery excavation.

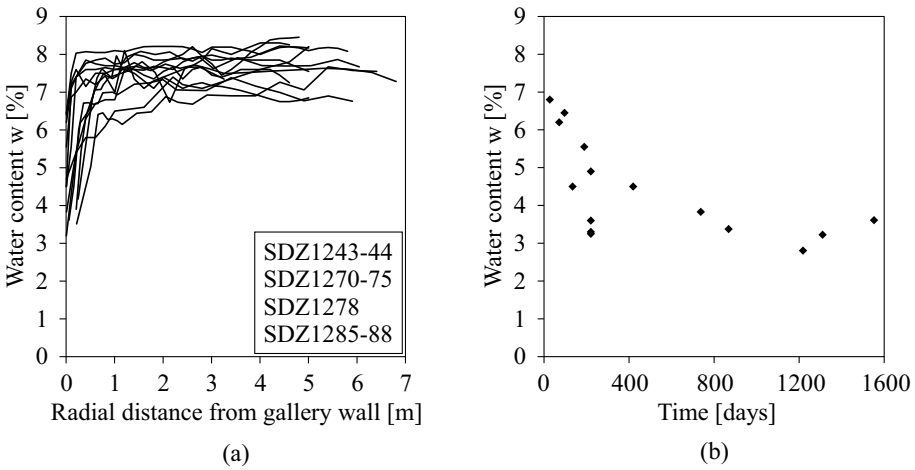

Fig. 2.17: Evolution of water content around the SDZ experimental zone in the horizontal direction: (a) in boreholes and (b) at gallery wall.

2.4 General framework for unsaturated porous media

The modelling of the excavation damaged zone and of the fluid transfers supposes the description of fractures and the use of a hydro-mechanical model for unsaturated porous media. An advanced hydro-mechanical framework should be ideally developed, as an anisotropic mechanical model or a model able to capture permeability evolution by hydro-mechanical coupling. Nevertheless, the large-scale ventilation experiment that will be reproduced highlights first and foremost fluid transfer processes in geomaterials. In a first modelling step, the focus is mainly on the reproduction of these fluid transfer processes in unsaturated porous media. This first approach permits to acquire a preliminary understanding of the transfer kinetics induced by gallery air ventilation around the galleries and in the damaged zone. Other aspects such as material desaturation and air-rock interactions at gallery wall can also be investigated with such approach. A more accurate

definition of the material behaviour and of the EDZ, with fractures description and permeability evolution, will be added in further developments.

To describe a general framework for geomaterials, it is commonly assumed that they exhibit a porous structure which, relying on a mixture theory, is considered as superimposed continua (Coussy, 1995, 2004). An assembly of solid grains forms the solid skeleton and fluids can fill the porous space between these grains (Fig. 2.18). Hereafter, the general framework is detailed for a binary fluid mixture composed of a wetting and a non-wetting fluid corresponding to a liquid and a gaseous phase, respectively. It is considered that the liquid phase is composed of liquid water and dissolved air, whilst the gaseous phase is an ideal mixture of dry air and water vapour.

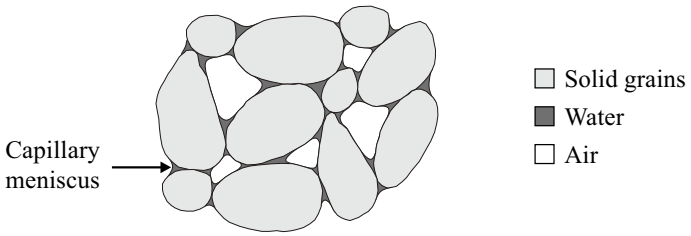

Fig. 2.18: Triphasic porous medium composed of a solid grain skeleton, water, and air.

Unsaturated conditions are considered, meaning that the liquid and gaseous phases partially occupy the pores (Fig. 2.18). Under these conditions, the fluids distribution is governed by interface phenomena (surface tensions) between the different phases that occur on a microscopic scale (Delage and Cui, 2000). These phenomena induce capillary forces which develop between the solid grains of the material. They are related to the liquid amount that fills the porous space with an increase of the capillary forces when the porous material desaturates. Such forces condition the material behaviour as well as the fluid transfers and must be taken into account.

Based on averaging theories (Hassanizadeh and Gray, 1979a,b), Lewis and Schrefler (2000) proposed the governing equations for the full dynamic behaviour of a partially saturated porous medium. Hereafter, the balance equations of the hydro-mechanical problem are recalled, then the constitutive equations of the fluid transfers and mechanical problems are described, with special emphasis on the different couplings existing between the mechanical and the hydraulic parts. These equations, valid at any time, are presented for a general framework where the liquid is water and the gas is air, with the gas pressure assumed non-constant. The balance equations and the constitutive relations can be nevertheless easily extended for other binary fluid mixtures of water and other gas species (nitrogen, hydrogen, helium, argon...).

2.4.1 Balance equations

The balance equations of the hydro-mechanical problem under unsaturated conditions are developed in usual differential local form. These equations consist of the balance of momentum of the mixture, the solid mass balance equation, and the fluids mass balance equations, both for the water and the air species. They are developed in updated Lagrangian configuration which corresponds to the current porous material configuration Ω (unit volume). Such formulation is typical of large deformation problems for which a distinction is realised between the deformed (current) and the initial configurations. The equations are restricted for quasi-static problem in unsaturated and isothermal conditions. The unknowns of the mechanical and flow problems are the displacements u_i, the pore water pressure p_w which is negative in unsaturated case corresponding to suction, and the gas pressure p_g (air).

Balance of momentum of the mixture

The mixture momentum balance equation corresponds to the equilibrium equation of the continuous medium (Malvern, 1969) composed of the three phases (solid, liquid, and gas). In this

equation, the interaction forces between fluid phases and grain skeleton cancels. It reads:

$$\frac{\partial \sigma_{ij}}{\partial x_j} + G_i = 0 \tag{2.3}$$

where x_i are the Cartesian coordinates, σ_{ij} is the total Cauchy stress field (symmetric tensor), and G_i is the gravity volume force. The latter is defined as:

$$G_i = \rho \; g_i \tag{2.4}$$

where ρ is the homogenised mass density of the mixture and g_i is the gravity acceleration vector of norm g. Developing the mixture homogenised density gives:

$$\rho = \rho_s \; (1 - \Phi) + S_{r,w} \; \rho_w \; \Phi + S_{r,g} \; \rho_g \; \Phi \tag{2.5}$$

where Φ is the porosity, ρ_s is the solid grain density, ρ_w is the water density ($\rho_w = 1000 \; kg/m^3$), ρ_g is the gas density, $S_{r,w}$ is the degree of water saturation (relative saturation), and $S_{r,g}$ is the gas degree of saturation. The porosity is defined as:

$$\Phi = \frac{\Omega_p}{\Omega} \tag{2.6}$$

where Ω_p is the current porous (voids) volume of the total volume Ω. The degrees of saturation correspond to the volumetric fractions of fluids occupying the porous space:

$$S_{r,w} = \frac{\Omega_w}{\Omega_p} \tag{2.7}$$

$$S_{r,g} = \frac{\Omega_g}{\Omega_p} = 1 - S_{r,w} \tag{2.8}$$

where Ω_w and Ω_g are the current water and gas volumes of Ω. The balance equation of mixture momentum becomes:

$$\frac{\partial \sigma_{ij}}{\partial x_j} + (\rho_s \; (1 - \Phi) + S_{r,w} \; \rho_w \; \Phi + S_{r,g} \; \rho_g \; \Phi) \; g_i = 0 \tag{2.9}$$

Solid mass balance equation

The used reference system follows the solid phase; therefore, the solid mass conservation is necessarily valid:

$$\dot{M}_s = \frac{\partial}{\partial t} \left(\rho_s \; (1 - \Phi) \; \Omega \right) = 0 \tag{2.10}$$

where M_s is the solid mass inside the current porous material configuration Ω. In this equation and in the following, the notation $\dot{a}$ corresponds to the time derivative of any quantity a:

$$\dot{a} = \frac{\partial a}{\partial t} \tag{2.11}$$

Fluids mass balance equations

Following the compositional approach of Panday and Corapcioglu (1989) and Olivella et al. (1994), the fluid mass balance equations are written for each chemical species, i.e. water and air, assuming the mass conservation of each one. In this way the terms related to the phase transfer cancel. The water and air mass balance equations read:

$$\underbrace{\frac{\partial f_{w,i}}{\partial x_i} + \dot{M}_w}_{Liquid \; water} + \underbrace{\frac{\partial f_{v,i}}{\partial x_i} + \dot{M}_v}_{Water \; vapour} - Q_w = 0 \tag{2.12}$$

$$\underbrace{\frac{\partial f_{a,i}}{\partial x_i} + \dot{M}_a}_{Dry\ air} + \underbrace{\frac{\partial f_{da,i}}{\partial x_i} + \dot{M}_{da}}_{Dissolved\ air} - Q_a = 0 \tag{2.13}$$

where $f_{w,i}$, $f_{v,i}$, $f_{a,i}$, and $f_{da,i}$ are the mass flows, respectively, of liquid water, water vapour, dry air, and dissolved air; Q_w and Q_a are the total sink mass terms of water and air; M_w, M_v, M_a, and M_{da} are the masses of liquid water, water vapour, dry air, and dissolved air inside the current porous material configuration Ω. The latter are expressed in rate forms (storage terms) as follows:

$$\dot{M}_w = \frac{\partial}{\partial t}\left(\rho_w\ \Phi\ S_{r,w}\ \Omega\right) \tag{2.14}$$

$$\dot{M}_v = \frac{\partial}{\partial t}\left(\rho_v\ \Phi\ S_{r,g}\ \Omega\right) \tag{2.15}$$

$$\dot{M}_a = \frac{\partial}{\partial t}\left(\rho_a\ \Phi\ S_{r,g}\ \Omega\right) \tag{2.16}$$

$$\dot{M}_{da} = \frac{\partial}{\partial t}\left(\rho_{da}\ \Phi\ S_{r,w}\ \Omega\right) \tag{2.17}$$

where ρ_v, ρ_a, and ρ_{da} are the densities of water vapour, dry air, and dissolved air, respectively. For a unit mixture volume, the above masses variations lead to:

$$\underbrace{\frac{\partial f_{w,i}}{\partial x_i} + \frac{\partial}{\partial t}\left(\rho_w\ \Phi\ S_{r,w}\right)}_{Liquid\ water} + \underbrace{\frac{\partial f_{v,i}}{\partial x_i} + \frac{\partial}{\partial t}\left(\rho_v\ \Phi\ S_{r,g}\right)}_{Water\ vapour} - Q_w = 0 \tag{2.18}$$

$$\underbrace{\frac{\partial f_{a,i}}{\partial x_i} + \frac{\partial}{\partial t}\left(\rho_a\ \Phi\ S_{r,g}\right)}_{Dry\ air} + \underbrace{\frac{\partial f_{da,i}}{\partial x_i} + \frac{\partial}{\partial t}\left(\rho_{da}\ \Phi\ S_{r,w}\right)}_{Dissolved\ air} - Q_a = 0 \tag{2.19}$$

The mass flows for the different phases and chemical species will be defined in the constitutive equations (section 2.4.3).

2.4.2 Effective stress definition

The characterisation of the stress state and of the hydro-mechanical coupling implied by the effect of fluid pressures on the Cauchy total stress field σ_{ij} must be defined. It is realised by considering the concept of effective stress (Nuth and Laloui, 2008b) that should represent only the stresses acting in the solid skeleton, between the solid grains. It constitutes an average stress over a representative elementary volume of the material that contains its different phases. For porous materials saturated with water, Terzaghi's postulate of effective stress reads (Terzaghi, 1936):

$$\sigma'_{ij} = \sigma_{ij} - p_w\ \delta_{ij} \tag{2.20}$$

where σ'_{ij} is the effective stress field, defined under soil mechanics convention in which compressive stress is positive, p_w is the pore water pressure, and δ_{ij} is the Kronecker symbol, i.e. the identity tensor. This expression is only representative of saturated soils with incompressible water and solid grains. For partially saturated porous materials, Bishop extended this postulate by defining the effective stress as a function of both liquid and gas pressures in the pores (Bishop, 1959):

$$\sigma'_{ij} = \sigma_{ij} - p_g\ \delta_{ij} + \chi\ s\ \delta_{ij} \tag{2.21}$$

where p_g is the gas pressure, $\sigma_{ij} - p_g\ \delta_{ij}$ is the net stress, χ is the effective Bishop's stress parameter, and s is the matric suction. The latter is related to the capillary effect and corresponds to the capillary pressure p_c:

$$s = p_c = p_g - p_w \tag{2.22}$$

The Bishop's parameter represents the saturation state and varies from 0 in dry state to 1 in fully saturated state, recovering Terzaghi's postulate (Eq. 2.20) for $\chi = 1$. Following experimental studies on unsaturated soils, various authors indicate that the effective stress parameter is linked to the degree of water saturation $\chi(S_{r,w})$ (Bishop and Donald, 1961; Jennings, 1960) but depends also on various factors as soil type, microstructure, and followed stress paths (Bishop and Blight, 1963; Jennings and Burland, 1962). An elementary relationship between them is proposed by Schrefler (1984) as:

$$\chi = S_{r,w} \tag{2.23}$$

although other expressions have been proposed in the literature. Under this most commonly used assumption, Eq. 2.21 can be rewritten in a simplified form:

$$\sigma_{ij}^{'} = \sigma_{ij} - (S_{r,w}\ p_w + S_{r,g}\ p_g)\,\delta_{ij} \tag{2.24}$$

which involves the average fluid pressure composed of the partial pressure of each fluid, with regard to their degree of saturation.

Another aspect to introduce in the effective stress definition is the material compressibility. For saturated materials, Biot proposed to scale down the effect of p_w in Eq. 2.20 as a function of the relative deformability of the solid structure (Biot, 1941; Biot and Willis, 1957; Skempton, 1960). The latter could be of importance for high stress level and when the solid grain compressibility is not negligible in comparison to the solid skeleton compressibility. The Biot's effective stress definition is expressed as:

$$\sigma_{ij}^{'} = \sigma_{ij} - b\ p_w\ \delta_{ij} \tag{2.25}$$

where the Biot's coefficient b represents the compressibility of the solid grains relative to the skeleton compressibility. It is defined as follows for isotropic materials:

$$b = 1 - \frac{K}{K_s} \tag{2.26}$$

where K is the drained bulk modulus of the material and K_s is the bulk modulus of the solid phase. If the bulk modulus of the porous material is low in comparison to the bulk modulus of the solid grains then b is close to 1. This may correspond, for instance, to unconsolidated materials having a high pore compressibility. In opposition, for consolidated rocks with a more rigid grain skeleton (a higher value of K), the pore compressibility and the effect of p_w on σ_{ij} are reduced by a value of $b < 1$. The compressibility of the porous material will be more largely detailed in section 2.4.4. Moreover, other approaches to scale down the effect of p_w in saturated compressible soils have also been proposed, such as considering change in porosity (Biot, 1955) or a scaling coefficient that is a combination of porosity and compressibility (Suklje, 1969).

Considering together partial saturation and compressibility effects can be realised presuming that the assumptions on compressibility hold under unsaturated conditions (Nuth and Laloui, 2008b). The Biot's stress definition can be formulated under unsaturated conditions by extension of Eq. 2.24:

$$\sigma_{ij}^{'} = \sigma_{ij} - b\,(S_{r,w}\ p_w + S_{r,g}\ p_g)\,\delta_{ij} \tag{2.27}$$

This expression is kept as the effective stress definition.

2.4.3 Constitutive equations for fluid transfers

The constitutive equations describe the porous media behaviour and are the basis of the hydro-mechanical model formulation. The equations of the fluid transfers are developed in this section with emphasis on hydro-mechanical couplings. The mechanical constitutive equations for the stress-strain behaviour will be described further, in section 2.4.5.

Biphasic fluid transfer model

For the fluid phases, a biphasic flow model is considered for the description of the fluid transport processes in partially saturated porous media. The mass flows take into account the advection of each phase using the generalised Darcy's law and the diffusion of the components within each phase by Fick's law. Due to the small amount of dissolved air in the liquid phase, the dissolved air influence on the liquid phase properties such as viscosity and density is neglected. For the same reason, the liquid water diffusion within the liquid phase is also neglected. The mass flows are expressed as:

$$f_{w,i} = \rho_w \; q_{l,i} \tag{2.28}$$

$$f_{v,i} = \rho_v \; q_{g,i} + i_{v,i} \tag{2.29}$$

$$f_{a,i} = \rho_a \; q_{g,i} + i_{a,i} \tag{2.30}$$

$$f_{da,i} = \rho_{da} \; q_{l,i} + i_{da,i} \tag{2.31}$$

where $q_{l,i}$ and $q_{g,i}$ are the advective fluxes (speed) of the liquid and the gaseous phases; $i_{v,i}$, $i_{a,i}$, and $i_{da,i}$ are the diffusion fluxes for the water vapour, the dry air, and the dissolved air.

The advection of each phase is described by the generalised Darcy's law for unsaturated cases. The permeability evolution with the saturation degree is taken into account by multiplying the intrinsic permeability by a relative permeability coefficient. Given the small amount of dissolved air, the liquid mixture advection is defined by the liquid water advection within the porous medium:

$$q_{l,i} = q_{w,i} = -\frac{k_{w,ij} \; k_{r,w}}{\mu_w} \left(\frac{\partial p_w}{\partial x_j} + \rho_w \; g_j \right) \tag{2.32}$$

This advective liquid flux corresponds to the average macroscopic speed of the liquid phase relative to the solid phase. The gaseous phase advection reads:

$$q_{g,i} = -\frac{k_{w,ij} \; k_{r,g}}{\mu_g} \left(\frac{\partial p_g}{\partial x_j} + \rho_g \; g_j \right) \tag{2.33}$$

In the two previous equations $k_{w,ij}$ is the water permeability tensor in saturated conditions, i.e. the intrinsic permeability tensor; $k_{r,w}$ and $k_{r,g}$ are the water and gas relative permeabilities; μ_w and μ_g are the water and gas dynamic viscosities ($\mu_w = 0.001 \; Pa \; s$).

For anisotropic materials, the general form of the intrinsic permeability tensor requires nine components for the description of the flow characteristics. This number reduces to six by the symmetric property of the tensor. Furthermore, geological media exhibiting a stratified structure are generally transversely isotropic materials. They have identical properties in the bedding planes which are perpendicular to an axis of symmetry and only two components are necessary for the description of the flow characteristics: one in the stratification direction and another perpendicular to the stratification. If the bedding planes are horizontal and the symmetry axis is vertical, as for numerous sedimentary materials including the Callovo-Oxfordian claystone, then the two parameters are the horizontal and vertical intrinsic hydraulic permeabilities, $k_{w,h}$

and $k_{w,v}$. For a vertical direction corresponding to the $x_2 = y$ coordinate, the anisotropic intrinsic water permeability tensor reduces to:

$$k_{w,ij} = \begin{bmatrix} k_{w,h} & 0 & 0 \\ 0 & k_{w,v} & 0 \\ 0 & 0 & k_{w,h} \end{bmatrix} \tag{2.34}$$

It is to mention that the intrinsic permeability tensor depends exclusively on the material and is independent of the considered fluid, in contrast to the hydraulic conductivity which depends on the fluid characteristics:

$$K_{w,ij} = \frac{k_{w,ij}\ \rho_w\ g}{\mu_w} \tag{2.35}$$

The properties of the gaseous phase in Eq. 2.33 remain to be defined. The gaseous phase being an ideal mixture of dry air and water vapour, its properties depend on both components. The dynamic viscosity corresponds to:

$$\mu_g = \left(\frac{\rho_a}{\rho_g\ \mu_a} + \frac{\rho_v}{\rho_g\ \mu_v} \right)^{-1} \tag{2.36}$$

where μ_a and μ_v are the dry air and water vapour dynamic viscosities. Similarly, the gaseous phase density is given by (Pollock, 1986; Gawin et al., 1996):

$$\rho_g = \rho_a + \rho_v \tag{2.37}$$

The diffusion of the components within each phase are defined by Fick's law. The diffusion in the gaseous mixture dry air-water vapour depends on the gradient of water vapour concentration, it reads:

$$i_{v,i} = -\Phi\ S_{r,g}\ \overline{\tau}\ D_{v-a}\ \rho_g\ \frac{\partial}{\partial x_i} \left(\frac{\rho_v}{\rho_g} \right) = -i_{a,i} \tag{2.38}$$

The diffusion of dissolved air in liquid water depends on the gradient of dissolved air concentration, it reads:

$$i_{da,i} = -\Phi\ S_{r,w}\ \overline{\tau}\ D_{da-w}\ \rho_w\ \frac{\partial}{\partial x_i} \left(\frac{\rho_{da}}{\rho_w} \right) \tag{2.39}$$

where D_{v-a} and D_{da-w} are the diffusion coefficients, respectively, in the gaseous mixture (dry air-water vapour) and for the dissolved air in liquid water; and $\overline{\tau}$ is the tortuosity of the porous medium, which characterises the path followed by the dissolved air particles between the solid grains. The diffusion coefficient of the gaseous phase is independent of the considered porous material but varies with the gas pressure and the absolute temperature T (Philip and de Vries, 1957):

$$D_{v-a} = 5.893 \times 10^{-6}\ \frac{T^{2.3}}{p_g} \tag{2.40}$$

and $D_{da-w} = 5.03 \times 10^{-9}\ m^2/s$ for a temperature of 20°C and atmospheric pressure (Gerard, 2011).

Variations of fluids densities

The fluids are assumed to be compressible which implies a variation of the liquid and gas densities. The compressible fluid is assumed to respect the following relationship (Lewis and Schrefler, 2000):

$$\frac{\dot{\rho}_w}{\rho_w} = \frac{\dot{p}_w}{\chi_w} \tag{2.41}$$

This predicts an increase of water density as a function of the pore water pressure, defining χ_w as the liquid water isotropic bulk modulus ($\chi_w^{-1} = 5 \times 10^{-10}\ Pa^{-1}$). For the gaseous ideal mixture

of dry air and water vapour, the ideal gas law is assumed. The state equations of perfect gas (Clapeyron's equation) and Dalton's law applied to dry air, water vapour, and moist air yield (Pollock, 1986; Gawin et al., 1996):

$$p_a = \frac{\rho_a \; R \; T}{m_a} \tag{2.42}$$

$$p_v = \frac{\rho_v \; R \; T}{m_v} \tag{2.43}$$

$$p_g = p_a + p_v \tag{2.44}$$

$$\rho_g = \rho_a + \rho_v \tag{2.45}$$

where p_v and p_a are the water vapour and dry air partial pressures, m_v and m_a are the molar masses of the water vapour and of the dry air ($m_v = 0.018 \; kg/mol$, $m_a = 0.029 \; kg/mol$), R is the universal gas constant ($R = 8.314 \; J/molK$), and T is the absolute temperature expressed in Kelvin. The above equations give the gaseous phase density variation in terms of the partial pressures of the gaseous components.

Equilibrium restrictions

An equilibrium equation for each chemical species is necessary for the partially saturated hydro-mechanical model. In porous media, if both gaseous and liquid phases are considered in the pores then both phases of the water species, the water vapour and the liquid water, should be in equilibrium. The equilibrium restriction equation corresponds to Kelvin's law which gives the concentration of water vapour in the gas phase as:

$$RH = \frac{p_v}{p_v^0} = \frac{\rho_v}{\rho_v^0} = exp\left(\frac{-s^{tot} \; m_v}{\rho_w \; R \; T}\right) \tag{2.46}$$

where RH is the relative humidity of the gaseous phase, p_v^0 is the pressure of saturated water vapour at the same temperature, p_v is the partial pressure of water vapour, ρ_v^0 is the density of saturated water vapour, ρ_v is the density of water vapour, and s^{tot} is the total suction which consists of the sum of matric and osmotic suctions. The matric suction depends on the capillary effect and corresponds to the capillary pressure (Eq. 2.22), whilst the osmotic suction is related to differences of solution concentrations and corresponds to the osmotic pressure. By taking into account only the capillary effects, the relative humidity takes the form:

$$RH = \frac{p_v}{p_v^0} = \frac{\rho_v}{\rho_v^0} = exp\left(\frac{-p_c \; m_v}{\rho_w \; R \; T}\right) \tag{2.47}$$

With this expression, the water vapour saturation pressure p_v^0 is defined as the vapour pressure in equilibrium with liquid water pressure if the capillary effects cancel. The saturated vapour concentration can be obtained by an empirical relationship proposed by Ewen and Thomas (1989):

$$\rho_v^0 = \left(194.4 \; exp\left(-0.06374(T - 273) + 0.1634 \times 10^{-3}(T - 273)^2\right)\right)^{-1} \tag{2.48}$$

for temperature range between 293 K and 331 K.

For the air species, the dissolved air in the liquid phase is assumed to be in equilibrium with the dry air of the gaseous phase by Henry's law (Weast, 1971). This law states that under partially saturated conditions, the amount of dissolved air is proportional to the dry air partial pressure by the relation:

$$p_a = K_{da}^{eq}(T) \; x_{da} \tag{2.49}$$

where K_{da}^{eq} is an equilibrium constant depending on the temperature and x_{da} is the mole fraction of dissolved air. By assuming the ideal gas law, the equilibrium equation can be rewritten in terms of the dry air and dissolved air densities. It specifies that the amount of dissolved air is proportional to the quantity of dry air as follows:

$$\rho_{da} = H_a(T)\ \rho_a \tag{2.50}$$

where H_a is Henry's coefficient for dissolved air (Gawin and Sanavia, 2009). This coefficient depends on temperature, although this influence is neglected under isothermal conditions and a constant value of $H_a = 0.0234$ is considered, for a reference temperature of 20°C and an atmospheric pressure.

Retention and relative permeability curves

Capillary forces develop between the material solid grains if it is partially saturated and affect the fluid transfers. These forces are related to the quantity of water filling the porous space; they increase when the porous material desaturates. The material retention behaviour is generally represented by a retention curve linking the capillary pressure to the degree of water saturation (or water content), as illustrated in Fig. 2.19. Moreover, this hydraulic constitutive behaviour plays an important role because retention curve and mechanical behaviour are coupled. Changes in degree of saturation produce mechanical effects whereas soil deformation modifies the degree of saturation.

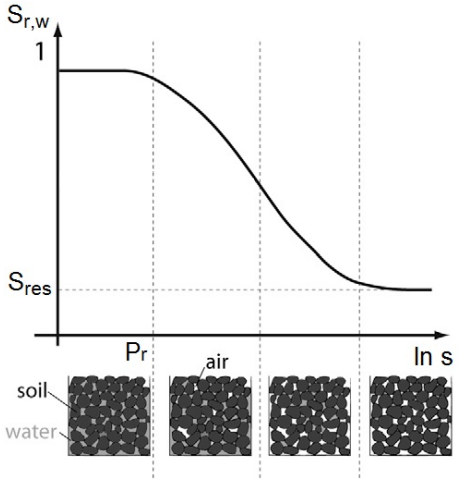

Fig. 2.19: Water retention curve and schematic representation of the saturation stages related to the matric suction (Nuth and Laloui, 2008a).

Among various analytical expressions available in the literature, the van Genuchten's model is used (van Genuchten, 1980):

$$S_{r,w} = S_{res} + (S_{max} - S_{res}) \left(1 + \left(\frac{p_c}{P_r}\right)^{\frac{1}{1-\mathcal{M}}}\right)^{-\mathcal{M}} \tag{2.51}$$

where P_r is the air entry pressure, S_{max} and S_{res} are the maximum and residual water degrees of saturation, and $\mathcal{M}$ is a measure of the pore-size distribution which controls the curve shape. The air entry pressure represents the minimal capillary pressure needed to desaturate the material pores and the residual saturation is a threshold value below which the water is discontinuously present in the pores and can only evaporate and diffuse as water vapour (Fig. 2.19).

On the other hand, the fluid flows are mainly controlled by flow parameters as the fluid permeabilities which are affected by the unsaturated conditions. In fact, the permeabilities

evolve with the degree of saturation by taking into account relative permeability coefficients in the generalised Darcy's law (Eqs. 2.32 and 2.33). A relative permeability curve defined by Mualem - van Genuchten's model (Mualem, 1976; van Genuchten, 1980) is used to link the permeability to the saturation degree. For the water relative permeability it reads:

$$k_{r,w} = \sqrt{S_{r,w}} \left(1 - \left(1 - S_{r,w}{}^{\frac{1}{\mathcal{M}}}\right)^{\mathcal{M}}\right)^2 \tag{2.52}$$

This expression reproduces the water permeability decrease during drying. On the other hand, the gas permeability would increase during drying, thereby a similar expression can be used (Mualem, 1976):

$$k_{r,g} = \sqrt{S_{r,g}} \left(1 - S_{r,w}{}^{\frac{1}{\mathcal{M}}}\right)^{2\mathcal{M}} \tag{2.53}$$

The gas relative permeability is also regularly expressed with a cubic relation as $k_{r,g} = S_{r,g}^3$ (Gerard, 2011).

The retention and relative permeability curves are available in Fig. 2.30 for the Callovo-Oxfordian claystone based on a calibration of experimental measurements. Moreover, a synthesis of the main hydraulic characteristics of the claystone will be presented in section 2.5.3.

2.4.4 Material compressibility

The compressibility of porous materials can influence the fluid flows and engenders hydro-mechanical couplings through the definitions of effective stress and porosity evolution. For porous materials, the compressibilities are of three types: the compressibility of the bulk material C (solid skeleton), the compressibility of the pores C_p, and the compressibility of the solid phase C_s.

Within the scope of poroelasticity (Detournay and Cheng, 1993), the bulk material compressibility corresponds to the relative change in volume Ω while subjected to a variation of mean stress σ under drained conditions: $\dot{p}_w = 0$ and $\dot{\sigma} = \dot{\sigma}^{'}$ from the Biot's effective stress definition of Eq. 2.25. The mean effective stress is defined as:

$$\sigma^{'} = \frac{\sigma_{ii}^{'}}{3} \tag{2.54}$$

and the bulk material compressibility reads:

$$C = \frac{1}{K} = -\frac{1}{\Omega}\frac{\partial \Omega}{\partial \sigma^{'}} \tag{2.55}$$

where K is the drained bulk modulus of the material. For isotropic materials it is given by:

$$K = \frac{E}{3(1-2\nu)} \tag{2.56}$$

where E is the isotropic drained Young's modulus and ν is the drained Poisson's ratio. Consequently, the volumetric strain variation of the medium depends linearly on the mean effective stress by the relation:

$$\dot{\sigma}^{'} = K\ \dot{\varepsilon}_v \tag{2.57}$$

The rate of the volumetric compaction deformation is given by:

$$\dot{\varepsilon}_v = -\frac{\dot{\Omega}}{\Omega} \tag{2.58}$$

and the volumetric strain reads:

$$\varepsilon_v = \varepsilon_{ij}\ \delta_{ij} = \varepsilon_{ii} \tag{2.59}$$

where ε_{ij} is the total strain tensor. Under the same conditions, the pore compressibility corresponds to the relative change in porous volume Ω_p:

$$C_p = \frac{1}{K_p} = -\frac{1}{\Omega_p}\frac{\partial \Omega_p}{\partial \sigma'} \tag{2.60}$$

where K_p is the bulk modulus of the pores. The solid grain compressibility is defined as:

$$C_s = \frac{1}{K_s} = C - \Phi\ C_p \tag{2.61}$$

where K_s is the bulk modulus of the solid phase. The Biot's coefficient used in the effective stress definition of Eq. 2.25 is defined with the above relations for isotropic materials as:

$$b = \frac{\Phi\ C_p}{C} = 1 - \frac{K}{K_s} \tag{2.62}$$

Because of the different types of compressibility, a porous material and its solid grains can behave differently. When the solid grain compressibility is neglected $C_s << C$, the variation of the total volume corresponds to the variation of the porous volume without deformation of the solid phase. However, the solid grain compressibility may not be negligible in comparison to the bulk material compressibility for consolidated materials and high stress environment. The magnitudes of deformation of the porous material and the solid grains may therefore be very different and the grains can remain in elastic state while the skeleton is possibly in a plastic regime because $K_s > K$.

Furthermore, the solid mass being constant inside a given material volume Ω by solid mass conservation (Eq. 2.10), the porosity time derivative is deduced:

$$\dot{\Phi} = (1 - \Phi)\left(\frac{\dot{\rho}_s}{\rho_s} + \frac{\dot{\Omega}}{\Omega}\right) \tag{2.63}$$

It depends on the evolution of the solid grain density and of the material volume. For the considered material and stress level around radioactive waste disposals, the solid grain deformability is not negligible and the general Biot framework (Biot, 1941) is used to model the hydro-mechanical coupling between the variations of pore fluid pressures and solid density. Following the ideas of Biot, Coussy (2004) proposed a thermodynamical framework of the problem for unsaturated poromechanics. The isotropic variation of solid density is linked to the variation of pore pressure and mean effective stress (Detournay and Cheng, 1993; Coussy, 2004):

$$\frac{\dot{\rho}_s}{\rho_s} = \frac{(b - \Phi)\,(S_{r,w}\ \dot{p}_w + S_{r,g}\ \dot{p}_g) + \dot{\sigma}'}{(1 - \Phi)\ K_s} \tag{2.64}$$

Using the definitions of Eqs. 2.57 and 2.62 leads to the following expression of the porosity time derivative:

$$\dot{\Phi} = (b - \Phi)\left(\frac{S_{r,w}}{K_s}\ \dot{p}_w + \frac{S_{r,g}}{K_s}\ \dot{p}_g + \frac{\dot{\Omega}}{\Omega}\right) \tag{2.65}$$

which is used in the computation of the storage terms of the fluid balance equations (Eqs. 2.18 and 2.19). It introduces a coupling term between the mechanical behaviour and the fluid transfers. Furthermore, it has to be mentioned that the Biot's theory has been developed only for elastic materials. Thus, the equations of poroelasticity and the porosity variation of Eq. 2.65 are valid solely under this hypothesis. An extension to poroplasticity, based on thermodynamic principles, has been proposed by Coussy (1995) who indicates that permanent plastic strain would engender permanent changes in porosity and in fluid mass content. Taking into account these permanent changes requires to include the plastic material behaviour, which is complex to implement and is not included in this work.

2.4.5 Mechanical constitutive equations

The mechanical behaviour of the Callovo-Oxfordian claystone is envisaged with a classical constitutive elastoplastic model. The objectives of the further numerical modelling are, in a first approach, to analyse if a classical model allows to reproduce the hydro-mechanical coupling that are observed experimentally in argillaceous rock, during gallery excavation and ventilation. The objective here is therefore not to develop a complex mechanical model, although different developments will be included in the next chapters.

An isotropic elastoplastic model is assumed to reproduce the mechanical behaviour of the porous media. The elastoplastic constitutive law expressing the relationship between the strain and effective stress field increments is defined as follows:

$$\tilde{\sigma}'_{ij} = C_{ijkl}\ \dot{\varepsilon}_{kl} \tag{2.66}$$

where C_{ijkl} is the elastoplastic constitutive tangent tensor for small strains and rotations, $\dot{\varepsilon}_{ij}$ is the Cauchy strain rate, and $\tilde{\sigma}'_{ij}$ is the Jaumann objective effective stress rate. The total strain rate is defined as:

$$\dot{\varepsilon}_{ij} = \frac{1}{2}\left(L_{ij} + L_{ji}\right) \tag{2.67}$$

It corresponds to the symmetric part of the velocity gradient field:

$$L_{ij} = \frac{\partial \dot{u}_i}{\partial x_j} \tag{2.68}$$

with $\dot{u}_i$ being the time derivative of the displacement field u_i:

$$u_i = x_i - x_{i,0} \tag{2.69}$$

which corresponds to the difference between current an initial positions. Furthermore, an objective derivative of the stress field, independent of rigid body rotation, is introduced through the Jaumann derivative (Jaumann, 1911) to describe large strains and rotations:

$$\tilde{\sigma}'_{ij} = \dot{\sigma}'_{ij} - \omega_{ij}\ \sigma'_{ij} + \sigma'_{ij}\ \omega_{ij} \tag{2.70}$$

where $\dot{\sigma}'_{ij}$ is the effective stress rate and ω_{ij} is the spin rate tensor corresponding to the antisymmetric part of the velocity gradient field L_{ij}:

$$\omega_{ij} = \frac{1}{2}\left(L_{ij} - L_{ji}\right) \tag{2.71}$$

In the context of elastoplasticity, the total strain rate $\dot{\varepsilon}_{ij}$ includes an elastic $\dot{\varepsilon}^e_{ij}$ and a plastic $\dot{\varepsilon}^p_{ij}$ components:

$$\dot{\varepsilon}_{ij} = \dot{\varepsilon}^e_{ij} + \dot{\varepsilon}^p_{ij} \tag{2.72}$$

The elastic and plastic theories are defined hereafter for isotropic materials.

Linear elasticity theory

By separating the elastic and plastic components of the strain tensor, a linear elastic relationship that links the elastic strain rate $\dot{\varepsilon}^e_{ij}$ to the Jaumann effective stress rate $\tilde{\sigma}'_{ij}$ through the Hooke's law is expressed:

$$\tilde{\sigma}'_{ij} = C^e_{ijkl}\ \dot{\varepsilon}^e_{kl} \tag{2.73}$$

$$\dot{\varepsilon}^e_{ij} = D^e_{ijkl}\ \tilde{\sigma}'_{kl} \tag{2.74}$$

where C^e_{ijkl} is the Hooke elastic constitutive tangent tensor that must be symmetric because of thermodynamic requirement (Love, 1927) and D^e_{ijkl} is the drained compliance elastic tensor

corresponding to the inverse of the Hooke elastic tensor C^e_{ijkl} (Love, 1927; Graham and Houlsby, 1983):

$$D^e_{ijkl} = \left[C^e_{ijkl}\right]^{-1} \tag{2.75}$$

For isotropic materials the relation is defined by two constants, E and ν or K and G:

$$\begin{bmatrix} \dot{\varepsilon}^e_{11} \\ \dot{\varepsilon}^e_{22} \\ \dot{\varepsilon}^e_{33} \\ \dot{\varepsilon}^e_{12} \\ \dot{\varepsilon}^e_{13} \\ \dot{\varepsilon}^e_{23} \end{bmatrix} = \frac{1}{E} \begin{bmatrix} 1 & -\nu & -\nu & 0 & 0 & 0 \\ -\nu & 1 & -\nu & 0 & 0 & 0 \\ -\nu & -\nu & 1 & 0 & 0 & 0 \\ 0 & 0 & 0 & 1+\nu & 0 & 0 \\ 0 & 0 & 0 & 0 & 1+\nu & 0 \\ 0 & 0 & 0 & 0 & 0 & 1+\nu \end{bmatrix} \begin{bmatrix} \tilde{\sigma}'_{11} \\ \tilde{\sigma}'_{22} \\ \tilde{\sigma}'_{33} \\ \tilde{\sigma}'_{12} \\ \tilde{\sigma}'_{13} \\ \tilde{\sigma}'_{23} \end{bmatrix} \tag{2.76}$$

with:

$$G = \frac{E}{2(1+\nu)} \tag{2.77}$$

$$K = \frac{C^e_{iijj}}{9} = \frac{E}{3(1-2\nu)} \tag{2.78}$$

where E is the isotropic drained Young's modulus, ν is the drained Poisson's ratio, G is the shear modulus, and K is the generalised drained bulk modulus of the poroelastic material.

Plasticity theory

An elastoplastic internal friction model with a Van Eekelen yield surface (Fig. 2.20) is used for the considered material (Van Eekelen, 1980). This model is broadly used in geomechanics for frictional materials and includes a dependence on the third stress invariant. The yield surface definition, under soil mechanics convention with positive compressive stress, is:

$$F^p \equiv II_{\hat{\sigma}'} - m\left(I_{\sigma'} + \frac{3\ c}{\tan\varphi_c}\right) = 0 \tag{2.79}$$

where $I_{\sigma'}$ is the first stress invariant, $II_{\hat{\sigma}'}$ is the second deviatoric stress invariant, m is a parameter of the yield surface, c is the cohesion, and φ_c is the compression friction angle. The first and second stress invariants are defined as follows:

$$I_{\sigma'} = \sigma'_{ij}\ \delta_{ij} = \sigma'_{ii} \tag{2.80}$$

$$II_{\hat{\sigma}'} = \sqrt{\frac{1}{2}\ \hat{\sigma}'_{ij}\ \hat{\sigma}'_{ij}} \tag{2.81}$$

where $\hat{\sigma}'_{ij}$ is the deviatoric part of the effective stress tensor given by:

$$\hat{\sigma}'_{ij} = \sigma'_{ij} - \frac{\sigma'_{kk}}{3}\ \delta_{ij} \tag{2.82}$$

The definition of the parameter m is:

$$m = d_1\ \ (1 + d_2\ sin(3\beta))^\eta \tag{2.83}$$

It depends on the Lode angle β (Fig. 2.21) which is given by:

$$sin(3\beta) = -\frac{3\sqrt{3}}{2}\frac{III_{\hat{\sigma}'}}{II^3_{\hat{\sigma}'}} \tag{2.84}$$

where $III_{\hat{\sigma}'}$ is the third deviatoric stress invariant:

$$III_{\hat{\sigma}'} = \frac{1}{3}\ \hat{\sigma}'_{ij}\ \hat{\sigma}'_{jk}\ \hat{\sigma}'_{ki} \tag{2.85}$$

The three parameters d_1, d_2, and η have to verify the conditions:

$$d_1 > 0 \tag{2.86}$$

$$d_2\ \eta > 0 \tag{2.87}$$

$$-1 < d_2 < 1 \tag{2.88}$$

The parameter η controls the yield surface convexity in the deviatoric plane (Fig. 2.20 (c)) and is generally chosen equal to -0.229 (default value) to ensure the convexity of the yield surface (Van Eekelen, 1980). The other coefficients d_1 and d_2 allow independent choice of the compression and extension friction angles, φ_c and φ_e:

$$d_1 = \frac{r_c}{(1+d_2)^{\eta}} \tag{2.89}$$

$$d_2 = \frac{\left(\frac{r_c}{r_e}\right)^{\frac{1}{\eta}} - 1}{\left(\frac{r_c}{r_e}\right)^{\frac{1}{\eta}} + 1} \tag{2.90}$$

where the reduced radii in compression r_c and in extension r_e read:

$$r_c = \frac{2\ sin(\varphi_c)}{\sqrt{3}\,(3 - sin(\varphi_c))} \tag{2.91}$$

$$r_e = \frac{2\ sin(\varphi_e)}{\sqrt{3}\,(3 + sin(\varphi_e))} \tag{2.92}$$

The yield surface is illustrated in Fig. 2.20 in the stress invariant plane, in the principal effective stress space, and in the deviatoric plane.

The Van Eekelen criterion is actually built from the Drucker-Prager criterion (for which $m = r_c = r_e$) by introducing a dependence on the Lode angle, with the purpose of matching more closely the Mohr-Coulomb criterion as illustrated in Fig. 2.21. This engenders a lower material resistance in extension compared to the resistance in compression ($r_c > r_e$ for $\varphi_c = \varphi_e$), which is characteristic of rock mechanical behaviour. In comparison to the Drucker-Prager criterion, the distinction introduced between the definition of compression and extension friction angles avoids an overestimation of the material extension resistance, especially in case of high value of the compression friction angle (Barnichon, 1998).

Furthermore, the material strength parameters can undergo hardening or softening. The friction angles and the cohesion are considered to evolve as a function of the Von Mises' equivalent deviatoric plastic strain $\dot{\varepsilon}^p_{eq}$ which rate form reads:

$$\dot{\varepsilon}^p_{eq} = \sqrt{\frac{2}{3}\ \dot{\varepsilon}^p_{ij}\ \dot{\varepsilon}^p_{ij}} \tag{2.93}$$

where $\dot{\varepsilon}^p_{ij}$ is the deviatoric part of the plastic strain rate tensor:

$$\dot{\varepsilon}^p_{ij} = \dot{\varepsilon}^p_{ij} - \frac{\dot{\varepsilon}^p_{kk}}{3}\ \delta_{ij} \tag{2.94}$$

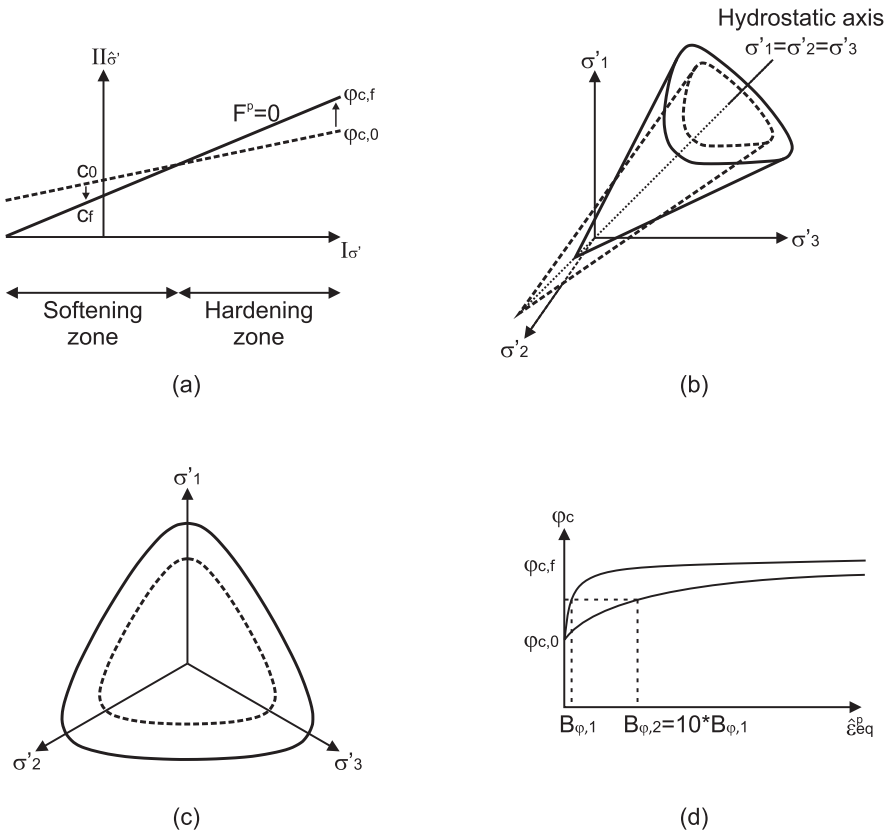

Fig. 2.20: Van Eekelen yield surface with isotropic φ_c hardening and c softening: (a) in the stress invariant plane, (b) in the principal effective stress space, (c) in the deviatoric plane, and (d) hyperbolic evolution of φ_c hardening for two values of coefficient B_φ.

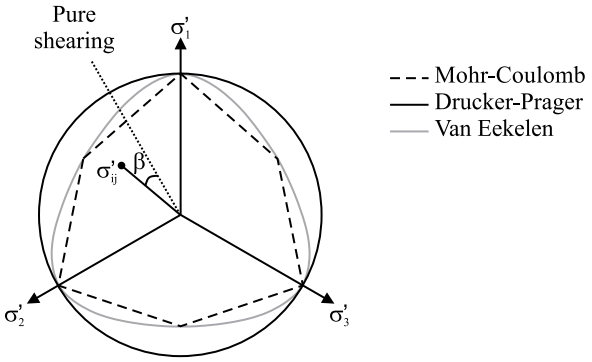

Fig. 2.21: Comparison of the yield surfaces of internal friction models in the deviatoric plane with influence of the Lode angle ($\varphi_c = 20°$).

Isotropic hardening/softening laws (Fig. 2.20 (d)) are introduced with hyperbolic functions (Barnichon, 1998):

$$c = c_0 + \frac{(c_f - c_0)\,\langle \hat{\varepsilon}^p_{eq} - dec_c \rangle}{B_c + \langle \hat{\varepsilon}^p_{eq} - dec_c \rangle} \tag{2.95}$$

$$\varphi_c = \varphi_{c,0} + \frac{(\varphi_{c,f} - \varphi_{c,0})\,\langle \hat{\varepsilon}^p_{eq} - dec_\varphi \rangle}{B_\varphi + \langle \hat{\varepsilon}^p_{eq} - dec_\varphi \rangle} \tag{2.96}$$

$$\varphi_e = \varphi_{e,0} + \frac{(\varphi_{e,f} - \varphi_{e,0})\,\langle \hat{\varepsilon}^p_{eq} - dec_\varphi \rangle}{B_\varphi + \langle \hat{\varepsilon}^p_{eq} - dec_\varphi \rangle} \tag{2.97}$$

where c_0 and c_f are the initial and final cohesions, $\varphi_{c,0}$ and $\varphi_{c,f}$ are the initial and final compression friction angles, $\varphi_{e,0}$ and $\varphi_{e,f}$ are the initial and final extension friction angles, dec_c and dec_φ are the equivalent deviatoric plastic strain values from which hardening/softening starts, the coefficients B_φ and B_c are the equivalent deviatoric plastic strain values for which half of the hardening/softening of friction angles and cohesion is attained, and $\langle\ \rangle$ are the Macaulay brackets with $\langle x \rangle = x$ if $x \geq 0$ and $\langle x \rangle = 0$ if $x < 0$. The evolution of the yield surface in case of friction angle hardening and cohesion softening is detailed in Fig. 2.20.

A non-associated plasticity framework is considered to define the plastic flow and to introduce the dilatancy of the material. The plastic strain rate is perpendicular to the plastic potential G^p and is defined as:

$$\dot{\varepsilon}^p_{ij} = \dot{\lambda}^p \frac{\partial G^p}{\partial \sigma'_{ij}} \tag{2.98}$$

where λ^p is the plastic multiplier. The non-associated plastic potential surface is defined similarly to the plastic loading surface F^p:

$$G^p \equiv II_{\hat{\sigma}'} - m_G\ I_{\sigma'} = 0 \tag{2.99}$$

where m_G is equivalent to m in Eq. 2.83 but introduces dilatancy angles ψ_c and ψ_e instead of φ_c and φ_e in the reduced radii of Eqs. 2.91 and 2.92:

$$r_{c,G} = \frac{2\ sin(\psi_c)}{\sqrt{3}\,(3 - sin(\psi_c))} \tag{2.100}$$

$$r_{e,G} = \frac{2\ sin(\psi_e)}{\sqrt{3}\,(3 + sin(\psi_e))} \tag{2.101}$$

The dilatancy which is introduced in the above expressions is the tendency of a granular material to dilate (volume increase) as it is sheared under plastic regime. If a material is neither dilatant, nor contractant, its volume and volumetric strain are constant under shearing $\dot{\varepsilon}_v = 0$ which implies only a deviatoric plastic flow (shearing). This is the case for the considered clayey rock which is not dilatant, or only very slightly dilatant, with $\psi = 0 - 0.5\ ^\circ$ as indicated in Table 2.1.

Moreover, the plastic multiplier amplitude is obtained from the coherence (i.e. consistency) condition stating that the stress state remains on the plastic limit surface during plastic flow: $\dot{F}^p = 0$. This leads to the definition of the elastoplastic constitutive tangent tensor (Eq. 2.66):

$$C_{ijkl} = C^e_{ijkl} - C^p_{ijkl} = C^e_{ijkl} - \frac{\dfrac{\partial F^p}{\partial \sigma'_{ab}}\ C^e_{abkl}\ C^e_{ijcd}\ \dfrac{\partial G^p}{\partial \sigma'_{cd}}}{\dfrac{\partial F^p}{\partial \sigma'_{mn}}\ C^e_{mnop}\ \dfrac{\partial G^p}{\partial \sigma'_{op}} - \dfrac{\partial F^p}{\partial \varkappa_q}\ \dfrac{d\varkappa_q}{d\lambda^p}} \tag{2.102}$$

where C^p_{ijkl} is the plastic constitutive tangent tensor and $\varkappa_i$ are the internal hardening/softening variables. It can be noted that C_{ijkl} is symmetric only in case of associated plasticity with $F^p = G^p$ and $\varphi = \psi$.

2.4.6 Boundary conditions

For the finite element formulation of the coupled problem, boundary conditions are required in addition to the balance equations. The balance equations represent the static equilibrium of a porous material elementary volume Ω, whilst the boundary conditions represent the equilibrium of the external surface Γ of the domain Ω (Fig. 2.22). These conditions are necessary to obtain a well-posed problem.

Mechanical and hydraulic equilibrium conditions have to be defined for any point on the boundary Γ. It requires to assume that the boundary is regular, which implies the existence and

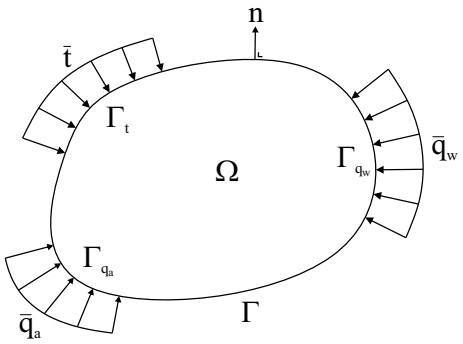

Fig. 2.22: Material system with current configuration Ω and boundary conditions.

uniqueness of the boundary normal vector for every point of the boundary. For the mechanical problem, classical conditions can be imposed displacements and imposed stresses. For these solicitations, the external traction force per unit area, in the normal direction to the boundary and acting on a part Γ_t of the boundary Γ, follows the condition:

$$\bar{t}_i = \sigma_{ij}\ n_j \tag{2.103}$$

where n_i is the normal unit vector to the boundary. For flows or coupled problems, classical hydraulic boundary conditions can be imposed pressures and imposed fluxes. The condition for prescribed water flux in the boundary normal direction, on a part Γ_{q_w} of Γ, reads:

$$\overline{q}_w + (f_{w,i} + f_{v,i})\ n_i = 0 \tag{2.104}$$

and the condition for prescribed normal air flux on a part Γ_{q_a} of Γ is defined as:

$$\overline{q}_a + (f_{a,i} + f_{da,i})\ n_i = 0 \tag{2.105}$$

where $\overline{q}_w$ and $\overline{q}_a$ are the input water and air masses (positive for inflow) per unit area on Γ_{q_w} and Γ_{q_a}, respectively. An impervious condition is assumed on the rest of the boundary where the components of the fluid fluxes in the boundary normal direction cancel.

2.5 Ventilation test modelling

In this section, the hydro-mechanical modelling of the *in situ* gallery air ventilation experiment SDZ (Saturation Damaged Zone experiment), performed in the underground laboratory of Bure (Andra), is presented. The modelling is performed in order to study the air-rock interaction as well as the effects it engenders on the host formation behaviour. A general description of the experiment and of the experimental measurements has been detailed in the section 2.3.2. The purpose of this section is not devoted to a full description of the numerical results, but rather on the emphasis on the main concepts that must be considered in the modelling of the hydro-mechanical unsaturated behaviour of claystone. Moreover the influence of some modelling choices on the numerical results is highlighted.

The general hydro-mechanical framework proposed in section 2.4 is considered, which allows adopting an anisotropic initial stress state and permeability in claystone. In a first modelling step, the reproduction of fluid transfer processes will be mainly investigated. The increase of the permeability induced by the hydro-mechanical coupling in the damaged zone is *a priori* imposed around the cavity, with a higher permeability than in the undisturbed claystone. A more complex definition of the EDZ will be investigated in the following chapters. First of all, the type of flow boundary condition imposed at the tunnel wall is addressed, then the boundary value problem and the claystone parameters are described, and finally the numerical results are presented.

In Charlier et al. (2013b), the detailed numerical modelling concerns two *in situ* experiments: the SDZ ventilation test and a gas injection test (PGZ1). The second experiment analyses the impact of gas migration on the rock mass behaviour through a gas injection test performed from an injection chamber set up in a small borehole. For this particular study, gas flows is of particular interest. However, for the SDZ ventilation experiment, the water transfers occurring around galleries are the dominant processes. Therefore, the gas flow problem is not solved hereafter meaning that the gas pressure and density variations are not considered. A constant pressure value that corresponds to the atmospheric pressure is assumed, $p_g = p_{atm} = 0.1\ MPa$, causing the cancellation of the gaseous phase advection $q_{g,i}$ (Eq. 2.33).

2.5.1 Hydraulic boundary condition at gallery wall

The air-rock interaction is a crucial issue which conditions the drainage kinetics in the rock formation. At the cavity wall, the pore pressures are first reduced by the drainage, before vapour exchanges occur. In a second stage, the pore pressures are progressively decreased to the value corresponding to the air relative humidity (according to Kelvin's law). To reproduce the vapour flows occurring at the gallery wall, a classical approach consists in assuming that the liquid water inside the rock is in equilibrium with the water vapour of the gallery air. This assumption corresponds to Kelvin's equilibrium equation (Eq. 2.47) and allows to impose the suction corresponding to the air relative humidity at the cavity wall (Jia et al., 2008). Such condition assumes an instantaneous equilibrium between the rock and the air which is probably too optimistic. The experimental measurements have indeed shown that the pore pressures in the different sensors remain high and decrease progressively, whereas the air relative humidity in the gallery is relatively low (section 2.3.2). In addition, the water content in the rock mass decreases progressively (Fig. 2.17 (b)) before reaching an equilibrium with the imposed atmospheric conditions in the gallery. These progressive drainage and desaturation seem to imply that the vapour transfer between the air and the rock is not so rapid. As a consequence, the use of a classical flow boundary condition inducing significant vapour exchanges would probably not allow the reproduction of the experimental data. Considering that a thermodynamic equilibrium is reached between the gallery wall rock and the gallery air in the long term seems to be more appropriated.

Non-classical condition

A better representation of the fluid exchanges at the gallery wall can be considered by taking into account the presence of a boundary layer where the rock-atmosphere vapour exchanges take place. It is proposed to reproduce the exchanges with a non-classical hydraulic boundary condition at gallery wall (Charlier et al., 2013b; Gerard et al., 2008). This condition implies that two modes of exchange can occur at the gallery wall of ventilated cavities (Ghezzehei et al., 2004): water vapour and liquid water exchanges. The total water flow corresponds to the sum of the two flows (Fig. 2.23):

$$\overline{q}_w = \bar{S} + \bar{E} \tag{2.106}$$

where $\bar{S}$ and $\bar{E}$ are the seepage flow (liquid water) and the evaporation flow (water vapour), respectively. The two flows at cavity wall are illustrated in Fig. 2.23 for a constant air ventilation. The expression of the hydraulic boundary condition for $\overline{q}_w$ is taken into account in the condition of Eq. 2.104, although the sign convention is opposite here with positive outflow for clarity. In fact, in case of gallery ventilation, the interaction with the gallery air causes a material drainage with water flow directed from the rock towards the gallery.

The liquid exchange is a unilateral seepage flow directed towards the gallery that occurs only when the material porous surface is fully saturated. It avoids unphysical liquid water flows from the gallery to the rock that are numerically observed in highly dilatant materials when the atmospheric pressure is imposed at the cavity wall (Gerard et al., 2008). Therefore, a seepage

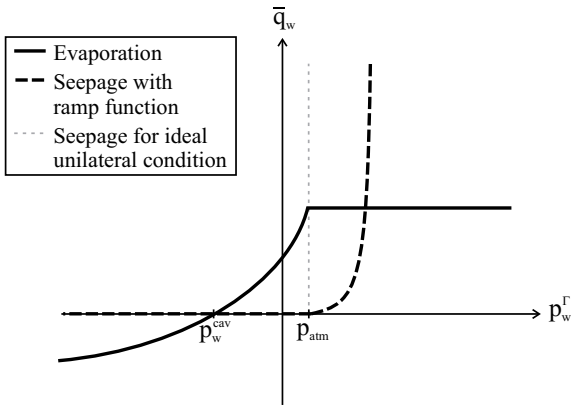

Fig. 2.23: Evaporation and seepage flows at gallery wall for a constant air ventilation (Gerard et al., 2008).

flow exists when the pore water pressure in the rock at gallery wall exceeds the water pressure in the cavity, $p_w^{\Gamma} \geq p_w^{cav}$, and exceeds the atmospheric pressure, $p_w^{\Gamma} \geq p_{atm}$. This flow is introduced by a unilateral boundary condition (Signorini's type) on the pore water pressure through a ramp function (Bardet and Tobita, 2002; Zheng et al., 2009):

$$\begin{cases} \bar{S} = K^{pen} \left(p_w^{\Gamma} - p_{atm} \right)^2 & if\ p_w^{\Gamma} \geq p_w^{cav}\ and\ p_w^{\Gamma} \geq p_{atm} \\ \bar{S} = 0 & if\ p_w^{\Gamma} < p_w^{cav}\ or\ p_w^{\Gamma} < p_{atm} \end{cases} \tag{2.107}$$

where K^{pen} is a numerical penalty coefficient for the seepage that must be as large as possible to respect the unilateral condition (Fig. 2.23). A value of $K^{pen} = 10^{-10}\ s^3/kg$ is assumed.

The vapour exchange mode between a porous medium and the air is based on desaturation kinetics at the interface. It can be considered that the exchanges occur in a boundary layer existing on the material porous surface (Ghezzehei et al., 2004; Pintado et al., 2009) and that they are not instantaneous. The boundary layer controls the exchanges and the external conditions are considered in the layer through a vapour mass transfer coefficient α_v. The exchange is therefore expressed as a function of this coefficient and of a transfer potential. Among different formulations proposed in the literature, the difference between the vapour density in the rock ρ_v^{Γ} and in the cavity air ρ_v^{cav} is considered (Nasrallah and Perre, 1988):

$$\bar{E} = \alpha_v \left(\rho_v^{\Gamma} - \rho_v^{cav} \right) \tag{2.108}$$

Moreover, the transfer coefficient involved in this expression depends on the external drying conditions and can be determined from drying flux curves deduced from laboratory drying experiments (Léonard et al., 2005). Nevertheless, in the following modelling, this parameter will be calibrated to match the experimental results.

Kinetics of drying process

During drying, a material progressively loses water and the drying kinetics can be quantified by measuring the water mass decrease in a sample subjected to a drying test. The progressive loss of water mass M_w and the evolution of the temperature at the surface of the sample are illustrated in Fig. 2.24 (a) and (c). The drying kinetics can also be analysed through the drying flux curve determined from the water mass loss as follows (Kowalski, 2003):

$$\bar{E} = -\frac{\dot{M}_w}{A_d} \tag{2.109}$$

where A_d is the external surface of the sample submitted to the drying, which could evolve because of material shrinkage (Léonard et al., 2002). The drying flux curve is represented in

Fig. 2.24 (b) as a function of the water content w which corresponds to the ratio of water mass versus solid mass by Eq. 2.1. Three periods of drying can be identified from the curves: (1) a preheating phase, (2) a constant flux phase, and (3) a decreasing flux phase.

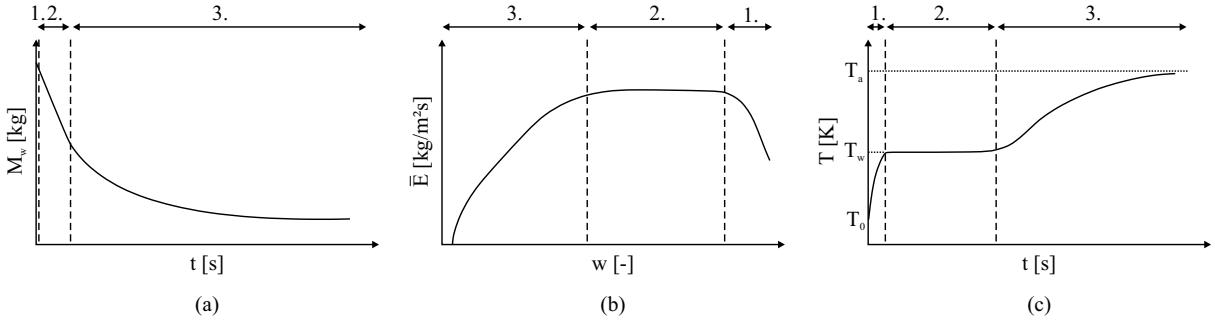

Fig. 2.24: Theoretical evolutions of (a) water mass, (b) water vapour flux, and (c) temperature during a drying test.

Firstly, the preheating phase is quite short but is apparent on the drying flux curve (Fig. 2.24 (b)) because of the water content decrease. It corresponds to an increase of the drying flux, which progressively reaches its maximum value, and to an increase of the surface temperature from its initial value T_0 to the wet-bulb temperature T_w. The latter is a characteristic of the moist air.

Secondly, during the constant flux phase (linear decrease of M_w), the totality of the heat supplied by the environment is used to evaporate the liquid water on the sample surface. It is assumed that the exchanges between the material and the atmosphere take place in a boundary layer existing at the surface of the material (Kowalski, 2003). They occur at constant temperature T_w and proceed as long as the water transfers from the inside of the sample towards its surface are sufficient to maintain the drying flux. It is therefore assumed that the boundary layer remains saturated with water during the phase of constant drying rate. Accordingly, the heat and vapour transfers are only affected and limited by external conditions. These conditions include the characteristics of the air, such as its relative humidity, temperature, and velocity, but also the characteristics of the surface (Geankoplis, 1993; Nadeau and Puiggali, 1995).

The water vapour exchange is therefore expressed as a function of a transfer coefficient representing the external conditions and of a transfer potential. Different formulations are proposed in the literature for the transfer potential between the atmosphere and the dried material. The vapour mass transfer coefficient α_v can be multiplied by a difference of vapour potential, vapour pressure, relative humidity, or vapour density (Gerard, 2011). Among these expressions, the difference between the vapour densities in the material ρ_v^Γ and in the air ρ_v^a (Nasrallah and Perre, 1988) is considered (Eq. 2.108). The transfer coefficient is assumed to depend only on the external conditions, which are the relative humidity, temperature, and velocity of the air. It is determined from the drying rate plateau of the experimental curve (Fig. 2.24 (b) and Eq. 2.109) under saturated conditions in the boundary layer:

$$\alpha_v = \frac{\bar{E}_{max}}{\rho_v^\Gamma - \rho_v^a} = \frac{max\left(-\dfrac{\dot{M}_w}{A_d}\right)}{\rho_v^{0,\Gamma}(T_w) - RH\ \rho_v^{0,a}(T_a)} \tag{2.110}$$

where $\rho_v^{0,\Gamma}$ and $\rho_v^{0,a}$ are the saturated water vapour densities of the sample surface and in the air obtained from Eq. 2.48, RH and T_a are the relative humidity and temperature of the air.

This method has been largely used in chemical engineering, on small-scale samples, and with severe drying conditions implying high temperature and low relative humidity. Unfortunately, very few experimental results are available for clay materials and for drying conditions similar

to the air ventilation of underground galleries. For clay material, Gerard (2011) performed convective drying tests on Boom clay samples and obtained a value of $\alpha_v = 0.022\ m/s$ for 50°C, a low air velocity of 1 m/s, and a relative humidity of 50 %.

Lastly, the constant exchange at the sample surface, i.e. the drying rate plateau, ends once internal resistances restrict the water outflow. Then, the drainage kinetics enter in the third phase of Fig. 2.24 with a desaturation of the boundary layer and a decrease of the transfer potential while drying proceeds up to completion. It results in a non-linear decrease of the mass of water towards its constant residual value (or dry state), a decrease of the evaporation flux, and an increase of the temperature towards an equilibrium with the air temperature T_a. In opposition to the constant drying phase during which the transfers are limited by external conditions, the transfers at the material surface are reduced by the internal limitations of water mass transfer during the decreasing flux phase. Moreover, the shrinkage has the effect of reducing the external surface subjected to drying A_d; consequently, the drying rate of Eq. 2.109 is affected by the combined effect of internal limitations and shrinkage. The latter can be evaluated by method such as X-ray microtomography coupled to image analysis (Léonard et al., 2003, 2004).

Boundary finite element

To introduce the flow boundary condition of Eq. 2.106 in a finite element code, classical quadrilateral two-dimensional finite elements are needed (Collin, 2003) and are associated with a new boundary finite element through which the hydraulic exchanges take place (Gerard et al., 2008). A reduced integration scheme is used in the 2D element in order to avoid shear locking. The special hydraulic boundary condition is defined by four nodes (Fig. 2.25). The first three nodes are located on the boundary (N1, N2, and N3). They allow a spatial discretisation of the water pressure distribution along the boundary. The fourth node (N4) is introduced to define the relative humidity of the surroundings (as far as they correspond to the d.o.f. of the fourth node). Its geometrical position does not influence the results. This fourth node is helpful for the modelling of the relative humidity evolution in the SDZ experimental zone. Two Gauss points are considered for the boundary finite element. The hydraulic flow is computed thanks to Eq. 2.106, where the vapour density of the surrounding air is computed at the fourth node and the vapour at the cavity wall is evaluated at the Gauss points. More details on the numerical formulation of the boundary finite element can be found in Gerard et al. (2008).

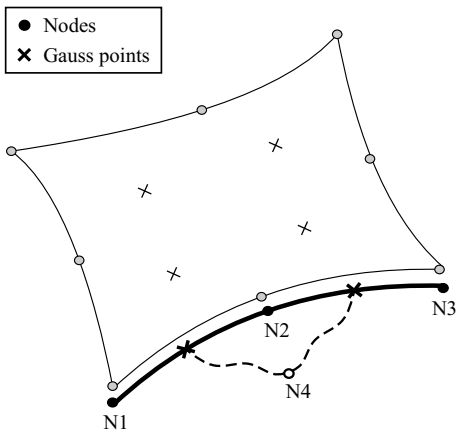

Fig. 2.25: Two-dimensional finite element and boundary element (Gerard et al., 2008).

This flow boundary condition has already been tested for the modelling of laboratory drying tests, performed on small-scale soil samples (Gerard et al., 2010), and for the modelling of a large-scale ventilated gallery with $p_w^{cav} = p_{atm} = 0.1\ MPa$ (Gerard et al., 2008). Hereafter, the relevance of such flow boundary condition is highlighted on a large scale with the modelling of an *in situ* ventilation experiment implying suction in the surrounding rock.

2.5.2 Boundary value problem

A two-dimensional plane strain state hydro-mechanical modelling of the SDZ experiment is performed. The section of the tunnel is chosen in the uncovered zone (Fig. 2.11), where most of the experimental data are available (Fig. 2.13). The geometry of the problem is given in Fig. 2.26 for the GED gallery, where only half of the gallery is considered for symmetry reason. The gallery has a radius of 2.3 m and an elliptic excavation damaged zone is considered with a higher intrinsic permeability than the undisturbed clayey rock (*a priori* defined). The outer limits of the model are located at 200 m from the centre of the gallery. An isotropic linear elastic-perfectly plastic model is used for the claystone (no hardening or softening of the strength parameters), whilst the mechanical behaviour of concrete slab is linear elastic.

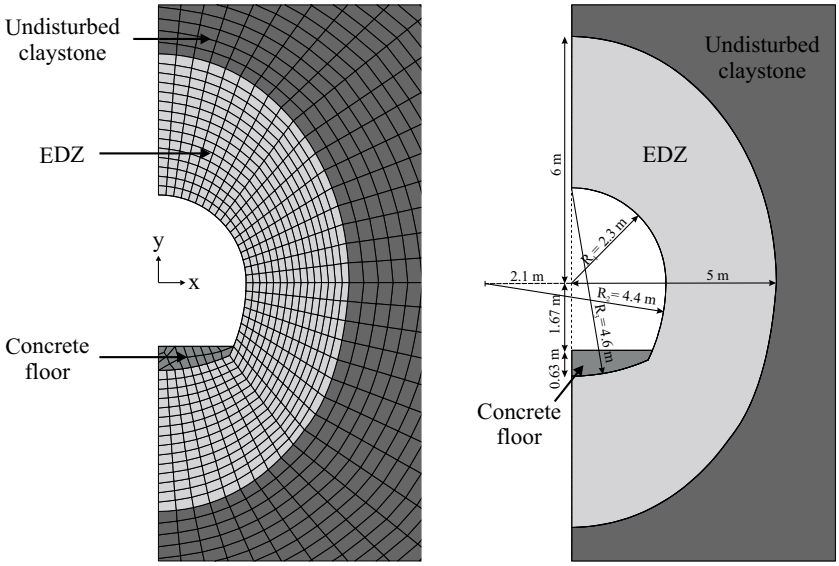

Fig. 2.26: Two-dimensional plane strain state model for the modelling of the gallery air ventilation test.

The initial conditions in the claystone are a homogeneous water pressure and an anisotropic initial stress state corresponding to the GED gallery which axis is oriented parallel to the minor horizontal principal total stress σ_h (section 2.1):

$$\sigma_{x,0} = \sigma_H = 1.3\ \sigma_h = 15.6\ MPa$$

$$\sigma_{y,0} = \sigma_v = 12\ MPa$$

$$\sigma_{z,0} = \sigma_h = 12\ MPa$$

$$p_{w,0} = 4.5\ MPa$$

where $p_{w,0}$ is the initial pore water pressure, $\sigma_{y,0}$ corresponds to the vertical principal total stress, $\sigma_{z,0}$ corresponds to the minor horizontal principal total stress, and $\sigma_{x,0}$ corresponds to the major horizontal principal total stress.

The normal total stresses and the pore water pressure are imposed constant at the mesh external boundary. To establish the symmetry, the normal displacements and water flows are blocked to a value of zero along the symmetry vertical y-axis, that is therefore impervious. In this problem, the gas pressure remains constant at the atmospheric pressure and isothermal conditions are considered (T = 293 K), because the temperatures remain relatively constant after the closure of the airlock. Moreover, the modelling takes into account the hydraulic permeability anisotropy and gravity is not considered $g_i = 0$.

Concerning the boundary conditions at the gallery wall, the gallery is first drilled then the ventilation is reproduced. During the excavation, the total radial stress at the cavity wall and the

water pressure at the environmental node p_w^{cav} (corresponding to the surroundings) are progressively decreased from their initial values to the atmospheric pressure. At the end of the drilling, the ventilation is applied and a constant total radial stress (atmospheric pressure) is imposed at gallery wall for the rest of the modelling. This stress imposition is representative of unsupported galleries. The claystone-atmosphere interactions are modelled by imposing at the environmental node the water pressure corresponding to the air relative humidity and temperature measured inside the gallery (Fig. 2.12). The water pressure in the gallery is obtained by Kelvin's law (Eq. 2.47) with $p_c = p_{atm} - p_w^{cav}$:

$$p_w^{cav} = \frac{\rho_w \; R \; T}{m_v} ln\,(RH) + p_{atm} \tag{2.111}$$

and its evolution is illustrated in Fig. 2.27 for the first 700 days of ventilation. The set up of the concrete floor is achieved 36 days after the end of the drilling. The closure of the airlock happens after 230 days, but it does not modify the boundary value problem because its influence on the gallery hygrometry remains imposed at gallery wall through the boundary condition.

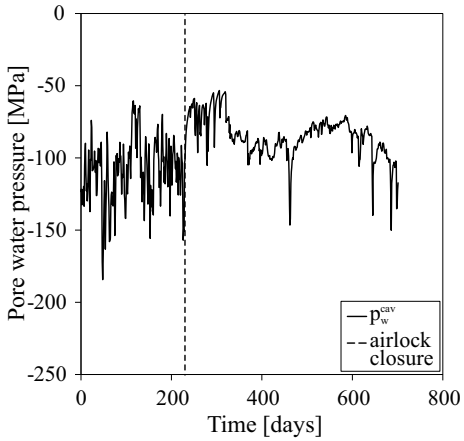

Fig. 2.27: Evolution of water pressure in the SDZ experimental zone.

For this preliminary modelling, the numerical reproduction of the experiment is realised up to 700 days of ventilation, with day 0 corresponding to the end of the drilling and the start of the ventilation. This period corresponds to the uncontrolled ventilation phase (phases (1) and (2) described in section 2.3.2); the controlled phase will be modelled afterwards with a more precise definition of the EDZ (see chapter 6).

2.5.3 Hydro-mechanical parameters

The determination of hydro-mechanical parameters of Callovo-Oxfordian claystone is needed for the modelling of the large-scale unsaturated experiment. The geological context met around the Andra's underground research laboratory has been described in section 2.1 together with a synthesis of typical geomechanical characteristics of the claystone. Hereafter, a synthesis of the main hydraulic characteristics available in the literature is presented as well. Then, the parameters chosen for the numerical modelling are exposed.

Mechanical parameters

The mechanical parameters of the different materials (undisturbed claystone, EDZ, and concrete) used in the constitutive equations are presented in Table 2.2. No differences between undisturbed claystone and excavation damaged zone are assumed from a mechanical point of view. This assumption is realised with the purpose of highlighting the hydraulic phenomena induced by gallery air ventilation, such as transfer kinetics and rock drainage. Another objective is to

evaluate if a "hydraulic" EDZ (with higher intrinsic permeability) and the hydraulic condition at gallery wall allow to reproduce the drainage kinetics, through the reproduction of the *in situ* pore water pressure measurements in the rock.

Symbol	Name	Undisturbed claystone	EDZ	Concrete	Unit
E	Young's modulus	4	4	30	GPa
ν	Poisson's ratio	0.3	0.3	0.3	$-$
c	Cohesion	3	3	$-$	MPa
$\varphi_c = \varphi_e$	Friction angles	20	20	$-$	$^\circ$
$\psi_c = \psi_e$	Dilatancy angles	0	0	$-$	$^\circ$
b	Biot's coefficient	0.6	0.6	1	$-$
ρ	Density	2300	2300	2300	kg/m^3

Table 2.2: Mechanical parameters.

Hydraulic parameters

Important relationships have to be precisely determined in order to obtain accurate numerical predictions of the hydro-mechanical behaviour of the rock mass: the retention curve and the water permeability evolution with the degree of saturation. Because gas pressure is assumed constant in the modelling, the gas permeability evolution with the degree of saturation is not detailed. For more details, please refer to Charlier et al. (2013b). Numerous experimental data exist in the literature concerning the determination of the retention and water relative permeability curves. A synthesis of these data is proposed for Callovo-Oxfordian claystone with an emphasis on the experimental scattering.

The main experimental studies that are used for the determination of the retention curve are based on the saline solutions methods (Delage et al., 1998). A synthesis of some experimental data available in literature is presented in Fig. 2.28 (a) where the degree of saturation is plotted against the suction. Although a lot of experimental data are available for the retention curve, few experimental studies investigate the behaviour close to the saturation (no data for suction lower than 2 MPa, which is the range of saline solutions technique), that corresponds to the conditions generally met around the disposal cavities of radioactive wastes. Moreover an important scattering of the experimental data is observed. It could be explained among other things by the hysteretic behaviour of the retention curves. Fig. 2.28 (b) shows indeed that a hysteresis can be introduced according to the hydraulic process imposed to the sample, which can be wetting or drying path. It is well known that the highest degrees of saturation are covered by a drying path, whilst the lowest ones are obtained on a wetting curve. It has to be added that most of the data are obtained on free volume sample. The effect of confining pressure on the retention curve is thus still not investigated in these experimental studies.

The relation between the water permeability and the degree of saturation is often deduced from the drying kinetics of samples submitted to evolutions of the surrounding air relative humidity (Fredlund and Rahardjo, 1993). Fig. 2.29 (a) presents the results of some experimental studies investigating the water permeability evolution of undisturbed Callovo-Oxfordian claystone, with $\overline{k}_w = k_w \; k_{r,w}$. The scattering of the experimental data is quite low but the permeability of saturated samples can vary between two orders of magnitude. It can be explained by anisotropy of the permeability as shown in Fig. 2.29 (b). The permeability in the direction parallel to the bedding planes (horizontal) is generally higher than the permeability along the perpendicular axis (vertical).

Thanks to this bibliographic analysis, a retention curve and a water permeability curve can be defined, even if the experimental review highlights some data dispersion. These relation-

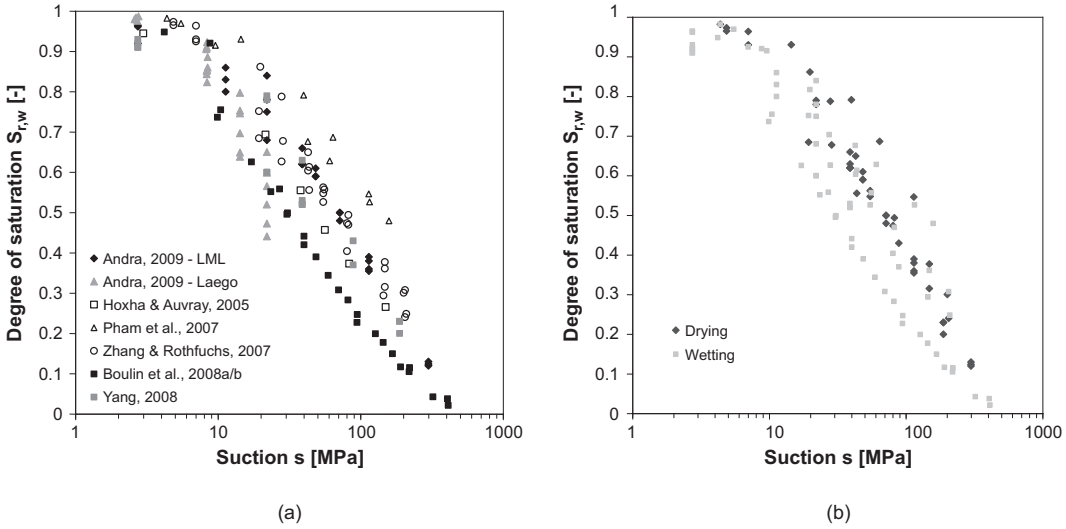

Fig. 2.28: Experimental data for the retention curve of Callovo-Oxfordian claystone classed by (a) authors and (b) drying or wetting path (Charlier et al., 2013b).

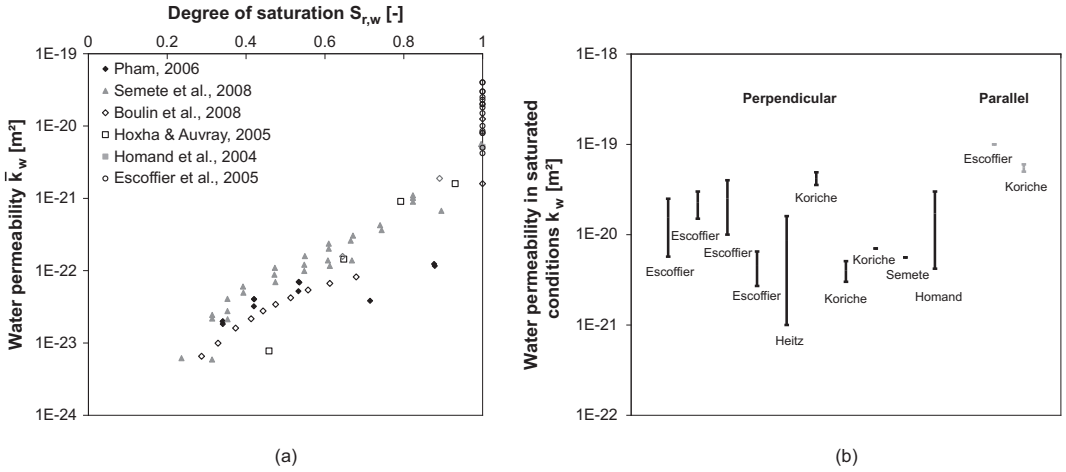

Fig. 2.29: Experimental data on Callovo-Oxfordian claystone for (a) the water permeability evolution with the degree of saturation and (b) the anisotropy effect on the water permeability in saturated conditions (Charlier et al., 2013b).

ships are based on the van Genuchten's equation (van Genuchten, 1980) detailed in Eqs. 2.51 and 2.52, with parameters calibrated in order to reproduce at best the available experimental data. The comparison between the experimental data and the relationships used in the modelling is illustrated in Fig. 2.30.

For the numerical modelling, the main hydraulic characteristics are defined in Table 2.3. It must be noted that the permeability anisotropy ratio $k_{w,h}/k_{w,v}$ is equal to 3, which corresponds to previous measurements from Andra. Moreover the permeability is strongly increased in the excavation damaged zone (Armand et al., 2007). Even if it is known that the principal directions of anisotropy in the damaged zone do not correspond to the principal directions of the initial anisotropy (Bossart et al., 2002), the same directions are considered. It could be justified by the large increase of permeability in the damaged zone and the low anisotropy ratio. The permeability in the damaged zone is almost homogeneous in comparison with the undisturbed claystone and the principal directions do not influence the numerical results.

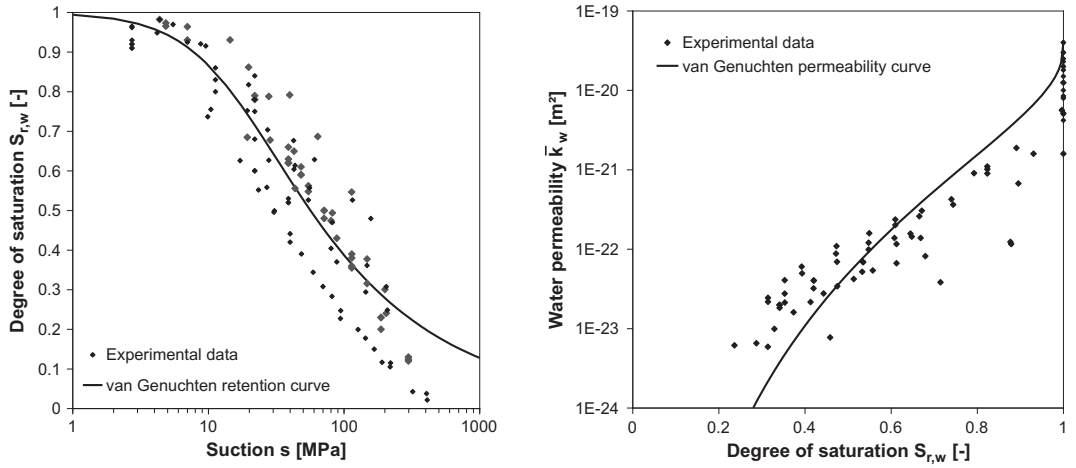

Fig. 2.30: (a) Retention curve and (b) water permeability curve of Callovo-Oxfordian claystone based on experimental data fitting of van Genuchten's model (Charlier et al., 2013b).

Symbol	Name	Undisturbed claystone	EDZ	Concrete	Unit
$k_{w,h}$	Horizontal intrinsic water permeability	4×10^{-20}	4×10^{-17}	1×10^{-18}	m^2
$k_{w,v}$	Vertical intrinsic water permeability	1.33×10^{-20}	1.33×10^{-17}	1×10^{-18}	m^2
Φ	Porosity	0.18	0.18	0.2	–
$\overline{\tau}$	Tortuosity	0.25	0.25	0.25	–
P_r	van Genuchten air entry pressure	15	15	2	MPa
$\mathcal{M}$	van Genuchten coefficient	0.33	0.33	0.35	–
S_{max}	Maximum water degree of saturation	1	1	1	–
S_{res}	Residual water degree of saturation	0.01	0.01	0.01	–

Table 2.3: Hydraulic parameters.

2.5.4 Numerical results and discussion

For the hydro-mechanical modelling of the SDZ ventilation test, the non-classical flow boundary condition reproducing seepage and vapour exchanges at the cavity wall is taken into account. With the chosen set of materials parameters and a calibration of the vapour mass transfer coefficient leading to $\alpha_v = 10^{-5}\ m/s$, good agreements between experimental measurements and numerical results are obtained in terms of water pressure kinetics, both in the further and in the nearest zones (Fig. 2.31). The anisotropic behaviour observed in the pore water pressure measurements is also well reproduced. Some discrepancies are nevertheless observed, especially in the horizontal and vertical boreholes (boreholes 1 and 3). It is to mention that in Fig. 2.31 and later in Fig. 2.32 the drilling phase is not illustrated; thus, the start of the ventilation corresponds to day 0, whilst it corresponds to day 50 in the experimental data detailed in section 2.3.2.

The discrepancies between the measured and predicted pore pressures can be also explained by some phenomena not currently reproduced in the modelling. For instance, a 2D plane strain state model does not allow the reproduction of the axial flows which play an important role in

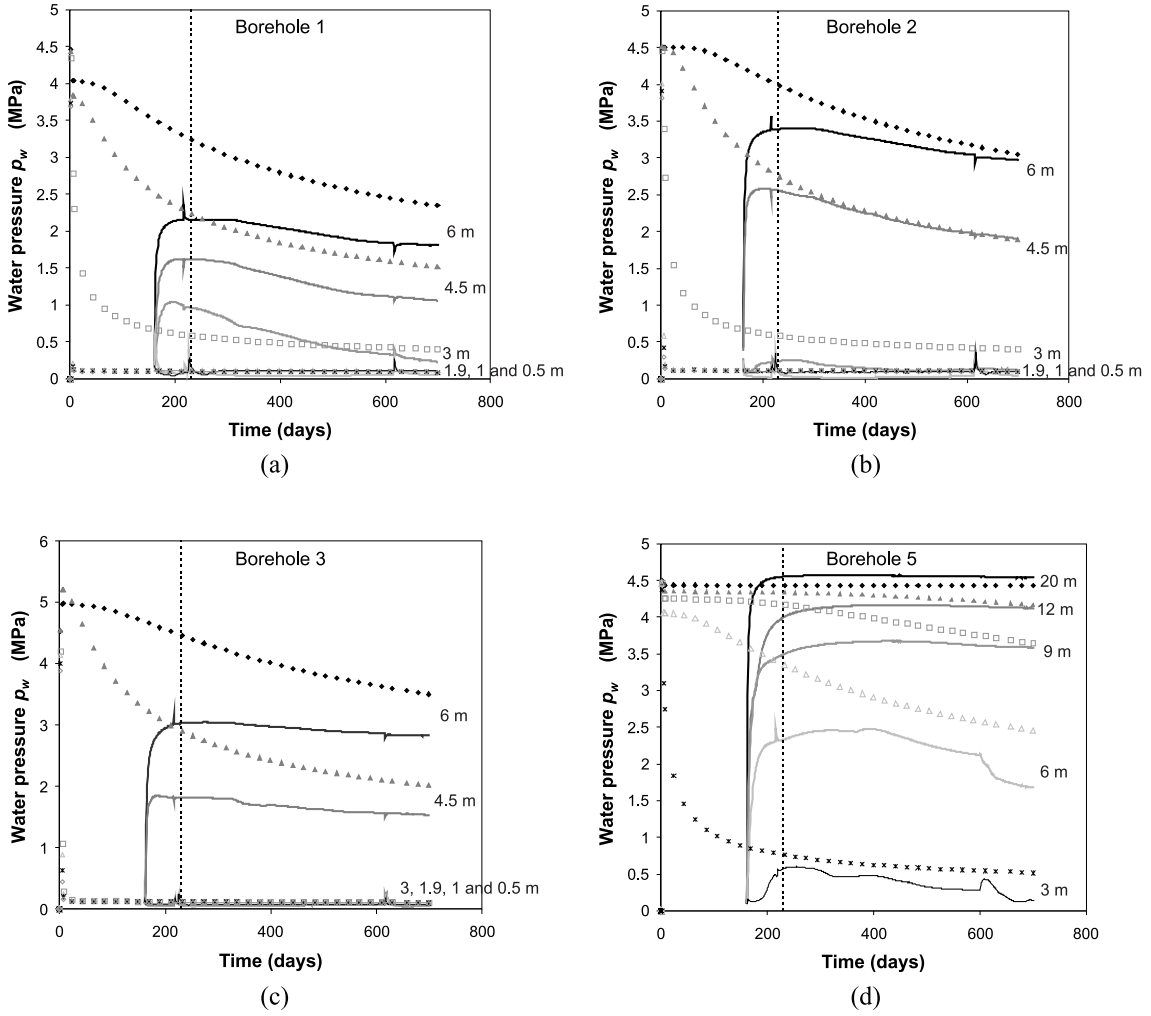

Fig. 2.31: Comparison between experimental (full lines) and numerical (symbols) pore water pressure around the uncovered SDZ experimental zone in (a,d) horizontal, (b) oblique at 45°, and (c) vertical boreholes (Charlier et al., 2013b).

the damaged zone when the airlock is closed. 2D axisymmetrical and 3D hydraulic modellings have also been performed in order to reproduce more accurately the fluid transfers and improve the numerical results. More details are available in Pardoen et al. (2012a,b) and Charlier et al. (2013a).

On the other hand, numerical water pressures higher than the initial value are observed along the vertical borehole (borehole 3 in Fig. 2.31 (c)). It can be explained by hydro-mechanical couplings induced by the anisotropy of the initial stress state, but these overpressures remain lower than the experimental values observed at the end of the GED gallery (Fig 2.15). These overpressures may also be characteristic of hydro-mechanical coupling induced by the anisotropy of the mechanical behaviour. An anisotropic mechanical model could be considered to reproduce the overpressures and improve the agreement between the measurements and the numerical results.

The influence of the vapour transfer at cavity wall can also be analysed to better understand the water transfers. The vapour mass transfer coefficient used in the boundary condition has a significant influence on the fluid transfers taking place around the gallery. In the modelling, a low value is used in comparison to coefficients determined on argillaceous material samples during drying tests (10^{-2} m/s) by Gerard et al. (2010). This low value implies low transfers and no desaturation of the claystone around the gallery. Thus, the water vapour exchange at

the gallery wall is not the predominant transport mechanism (the seepage is) and the ventilation has a small influence on the pore pressures distribution in the rock mass.

The low fluid transfers challenge the classical imposition at gallery wall. In fact, classical flow boundary condition, that imposes at the tunnel wall the suction corresponding to the relative humidity of the cavity air, does not allow a good reproduction of the pore water pressures in the undisturbed rock as shown in Fig. 2.32 (a). This modelling also illustrates the huge drainage and desaturation of the excavation damaged zone due to the classical imposition (Fig. 2.32 (b)). The variations of pore pressures on the curves correspond to the variations of pore pressures imposed at gallery wall, and therefore to the variations of gallery air relative humidity. Such variations rapidly influence the drainage kinetics of the EDZ because of the classical imposition at gallery wall and of the high damaged zone permeability.

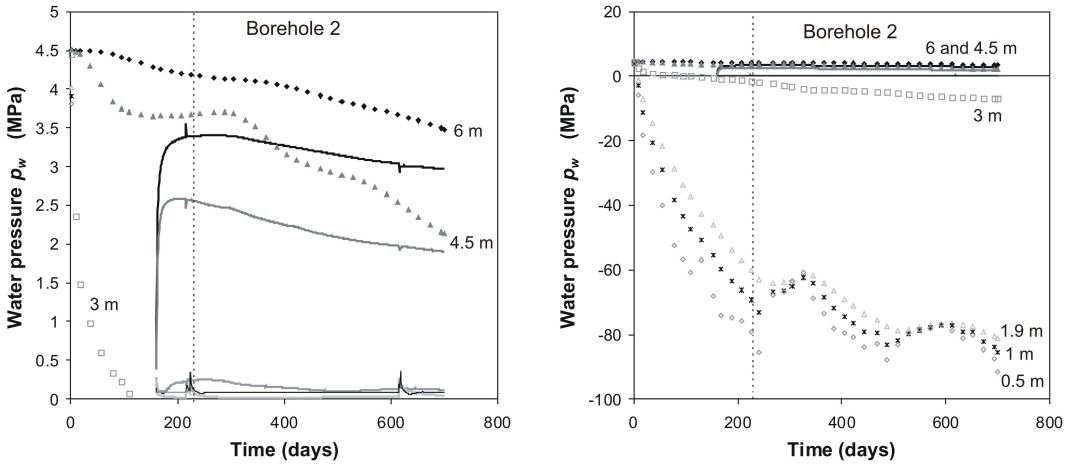

Fig. 2.32: Comparison between experimental (full lines) and numerical (symbols) pore water pressure with imposed suction at the cavity wall in the oblique borehole: (a) drainage in the rock mass and (b) desaturation of the EDZ (Charlier et al., 2013b).

Concerning the analysis of the rock desaturation process in the EDZ, the water content measures of Fig. 2.17 are used because the pore pressure sensors can not acquire negative measurements. The last numerical results have indicated that the classical imposition generates huge drainage, thenceforward an intermediate value of $\alpha_v = 10^{-2}\ m/s$ similar to the values determined experimentally (Gerard et al., 2010) is considered. This value leads to a desaturation of the rock at gallery wall and in the damaged zone as illustrated in Fig. 2.33 (a), which was not the case for the low value of $\alpha_v = 10^{-5}\ m/s$. Fig. 2.33 (b) shows that this desaturation is in better agreement with what is observed experimentally close to the gallery wall.

The issue about the reproduction of fluid flows around drifts is, as discussed here above, conditioned by the transfers at cavity wall but also by the definition of the EDZ behaviour. The latter needs to be improved with an accurate modelling of the hydro-mechanical coupling occurring in damaged and fractured zones, such as permeability evolution. The extent and the permeability of the damaged zone are indeed currently imposed at the beginning of the modelling, whereas the processes are more complex and can be coupled to rock damage and cracking (Arson and Gatmiri, 2012; Levasseur et al., 2009; Maleki and Poya, 2010; Shao et al., 2006b; Snow, 1969). Such improvement would allow to better represent the fluid transfers which conditions the progressive drainage in the far field as well as the desaturation close to the drift. Even though, the development of a non-classical flow boundary condition is still important to allow physical explanations of the vapour exchanges at the cavity wall and of the long-term equilibrium between the rock and the air.

Some mechanical results can also be discussed. Fig. 2.34 illustrates the yield index distribu-

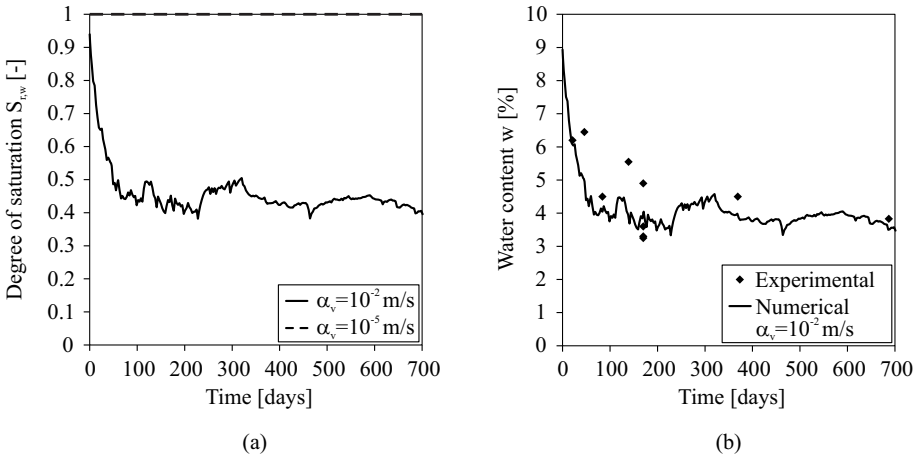

Fig. 2.33: Rock desaturation at gallery wall (a) for a high and a low values of the vapour mass transfer coefficient and (b) comparison to experimental measurements of water content.

tion around the gallery at the end of the modelling. The yield index corresponds to the reduced second deviatoric stress invariant:

$$YI = \frac{II_{\hat{\sigma}'}}{II^{p}_{\hat{\sigma}'}} \tag{2.112}$$

where $II^{p}_{\hat{\sigma}'}$ is the second deviatoric stress invariant value at plastic state (on the yield surface) for an identical value of $I_{\sigma'}$ (current value). The current state of the material is therefore elastic for $YI < 1$ and plastic for $YI = 1$. The evolution of the plastic zone extension occurs mainly during the excavation and its final dimensions are indicated in Fig. 2.34. Even if the damaged zone remains *a priori* defined in the model, the plastic zone obtained numerically can still be compared to the fractured or damaged zone measured *in situ* (Fig. 2.9). The numerical result shows that the anisotropy of the initial stress state is sufficient to obtain an elliptic plastic zone around the GED gallery, as observed experimentally. Moreover, the extent of this domain corresponds to the one where mixed fractures (tension and shear) are experimentally observed thanks to borehole core analysis (Table 2.4). Besides, if compared to the damaged zone extent based on permeability measurements, the plastic zone extent lies between the slightly disturbed and the highly disturbed zone extents. Considering only the plastic zone would underestimate the EDZ size, consequently a part of the elastic one should also be considered.

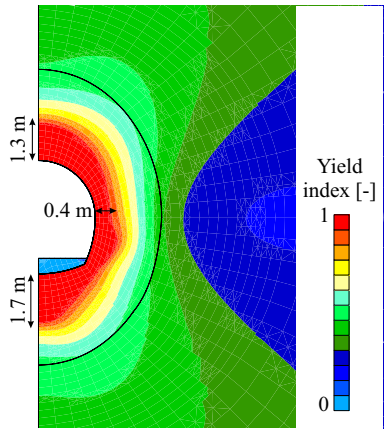

Fig. 2.34: Yield index and extension of the plastic zone at the end of the modelling.

Lastly, the diametrical convergence of the gallery (diameter variation) is illustrated in Fig. 2.35 where it is compared to experimental measurements from Armand et al. (2013), for both vertical and horizontal directions. One can observe that, even if the horizontal convergence is well

Zone	Horizontal [m]	Vertical upward [m] (gallery ceiling)	Vertical downward [m] (gallery floor)
Numerical plasticity	0.4	1.3	1.7
Mixed fractures	< 0.5	1.27	1.24
Shear fractures	< 0.5	2.75	3.70
Highly disturbed permeability	0.5	1.1	1.1
Slightly disturbed permeability	1.1	3.1	3.1

Table 2.4: Comparison between the thickness of the numerical plastic zone and of the measured fractured and permeability disturbed zones.

reproduced, the vertical one is underestimated and the convergence anisotropy is not captured. It is evident that the convergence prediction could be improved by taking into account the mechanical anisotropy of the rock (elastic modulus, strength parameters...) and by improving the description of the EDZ with the modelling of fractures.

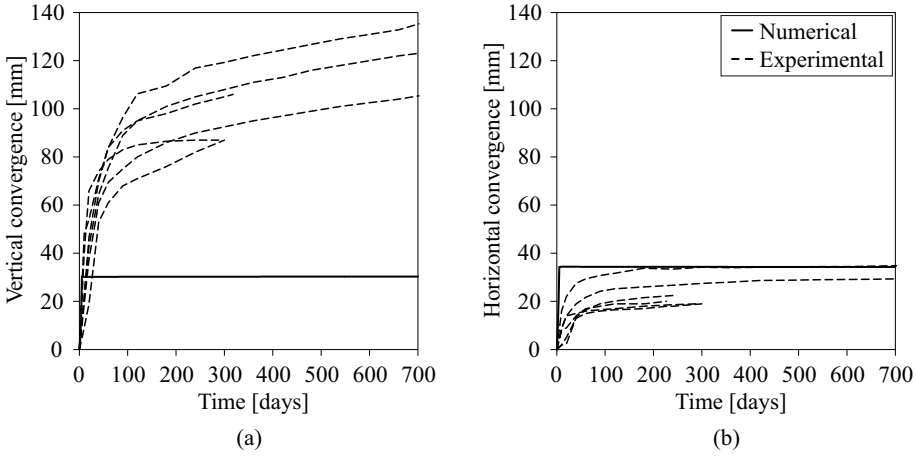

Fig. 2.35: Evolution of the (a) vertical and (b) horizontal convergences during and after gallery excavation, with comparison to experimental measurements in the GED drift.

2.6 Conclusions and outlooks

The hydro-mechanical unsaturated behaviour of Callovo-Oxfordian claystone and the fluid transfers around underground galleries have been investigated through the modelling of an *in situ* air ventilation experiment. The modelling mainly consists of a contribution in the understanding of the rock unsaturated behaviour, especially in the galleries vicinity and in the excavation damaged zone. It also constitutes an overview of the main aspects and future challenges to consider in the modelling of the EDZ and of its hydraulic behaviour.

The modelling of the SDZ ventilation test highlights the need of a more accurate reproduction of the damaged zone, of the hydro-mechanical coupling occurring in it and of the rock mechanical anisotropy. The major aspects to incorporate in the modelling are:

The fracturing. The actual modelling does not provide information about the rock state within the damaged zone. Nevertheless, the fracturing process induced by deconfinement must indubitably be taken into account to better represent the EDZ, including its structure and extension, as well as the gallery convergence. As far as material rupture is concerned, different

processes can lead to the failure. They include localised deformation, material damage with microcracks appearance, and the onset of fractures. An appropriate method for reproducing the fractures will be developed in chapter 3 with numerical validation in chapter 4.

The mechanical anisotropy. The anisotropic mechanical behaviour of the rock has not been included in the modelling yet. Besides, this anisotropy is certainly needed to explain the experimental observations of fracturing structure and extent with regard to the anisotropic stress state and gallery orientations. The introduction of anisotropy will be considered in chapter 5 with analyses of its influence on fracturing and damaged zone development.

The permeability variation. For now, the permeability inside the damaged zone is *a priori* and homogeneously defined, but in reality it is linked to the development and density of fractures which involve an inhomogeneous permeability distribution. The impact of fracturing on the transport properties will be addressed in chapter 6 by accounting for a hydraulic permeability evolution inside the damaged zone. A hydro-mechanical coupling that provides an increase of the permeability as a function of a mechanical aspect of the fractures (damage, deformation...) is certainly a way to better reproduce the EDZ and improve the transfer modelling.

The air-rock interaction. The preliminary numerical results show the relevance of a non-classical flow boundary condition for the reproduction of large-scale rock-atmosphere interaction problems. The tested condition allows to obtain an appropriate reproduction of the fluid transfers occurring between the air and the surrounding rock. This condition should be considered for later air ventilation analyses.

Chapter 3

Shear strain localisation modelling

Abstract Localised rupture is commonly observed in geomaterials and is frequently preceded by strain localisation in thin zones or bands. This strain localisation process is therefore a crucial issue when considering the material rupture and it has been widely investigated both theoretically and experimentally. This chapter summarises the different aspects related to shear strain localisation in shear band mode. Firstly, experimental evidences of localised phenomena are exposed. They are followed by theoretical and numerical tools required to allow a robust reproduction of the strain localisation. In particular, a regularisation method introducing microstructure enriched media (second gradient model) is presented for finite element methods. It takes into account the interactions occurring between the different phases of a biphasic porous media under saturated conditions. Finally, this method is applied to some typical problems engendering material failure to highlight its interest and limitations. The present chapter is part of a book about the finite element code Lagamine developed at the University of Liège and about its applications. The book is currently being drafted.

3.1 Strain localisation in geomaterials

3.1.1 Material rupture

Since the material behaviour and rupture are of importance regarding the design of geotechnical works for which material can be subjected to strong solicitations, the failure has been widely investigated in geomechanics. Experimental observations on geomaterial clearly indicate the appearance of localised ruptures (Desrues, 1984). Theoretically, the concept of rupture surface is one of the oldest case of material localised failure and was already used in the design of works and structures few centuries ago (Coulomb, 1773). In some cases, a diffuse mode of failure can also be observed and it corresponds to homogeneous failure in laboratory tests (Khoa et al., 2006). Nowadays, it is commonly assumed that localised deformation and damage can appear in materials prior to the rupture in many situations. In fact, the stress redistribution can engender damage that can firstly be diffused then localised. Once the damage threshold is reached, microcracks initiate, then grow, accumulate, and propagate within the material. If the microcracks coalesce, the distributed damage can further lead to strain localisation and to the initiation of interconnected fractures by the onset of macrocracks, which provokes a sudden material rupture (Diederichs, 2003).

The fracturing process instigates discontinuities in the material that can be represented theoretically and numerically by various approaches. Two mains categories exist: the continuous and discrete descriptions of the fractures. The continuous description includes material damage and strain localisation, while the discrete description actually represents the cracks. In fracture mechanics, the different fractures can be in tensile or opening mode (mode I), in sliding shear mode (mode II), in tearing shear mode (mode III), or in mixed-mode (mode I-II, Jenq and Shah (1988)), as illustrated in Fig. 3.1. In the context of underground waste repository, a particular attention is paid to the Callovo-Oxfordian claystone for which the fracturing due to the excavation process is dominated by shear fractures in mode II. Following this observation, it is proposed to consider shear strain localisation as a predictor of the fracturing process. The modelling of shear strain localisation is a continuous approach that does not explicitly reproduce the fractures and their discontinuities. Nevertheless, it generally induces the appearance of shear bands and non-uniform strain distribution that may engender a displacement discontinuity between the material located on the two sides of a shear band.

3.1.2 Experimental evidences of strain localisation

Strain localisation is frequently observed prior to the material rupture. Starting from a homogeneous deformation state, the strain localisation consists in a brutal accumulation of strain in a limited zone that can lead to cracks and failure (rupture lines). In geomaterials like soils

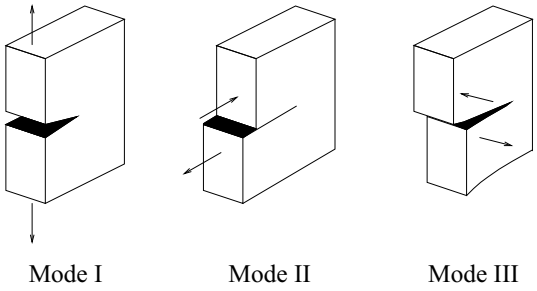

Fig. 3.1: Standard crack modes.

and rocks it is often considered as a shear strain accumulation in band mode (Desrues, 2005). Nevertheless, the type of localisation may be of different nature for other materials.

Geomaterials have low tensile strength, thus tensile rupture is arduous to characterise. On the other hand, plenty of small-scale compression laboratory tests are dedicated to strain localisation (Vardoulakis et al., 1978; Han and Drescher, 1993; Finno et al., 1996, 1997; Alshibli et al., 2003) and allow to characterise the compression material behaviour up to the rupture. They are generally realised on axisymmetric triaxial or plane-strain biaxial compression apparatus and involve special techniques, such as stereophotogrammetry (Desrues, 1984; Desrues and Viggiani, 2004), X-ray microtomography, and three dimensional digital image correlation (Lenoir et al., 2007), to study the evolution of the strain localisation process. The advantage of biaxial compression experiments is that the localisation process is clearly evidenced, whereas it can remain hidden inside the sample in triaxial compression tests.

Under compressive regime, the rupture is governed essentially by shear failure and these experimental studies generally highlight shear strain localisation in band mode (Desrues, 2005) as illustrated in Fig. 3.2. It is commonly accepted that the shear band establishment corresponds to a peak stress in the stress-strain global response curve of the specimen (Mokni and Desrues, 1999; Desrues, 2005).

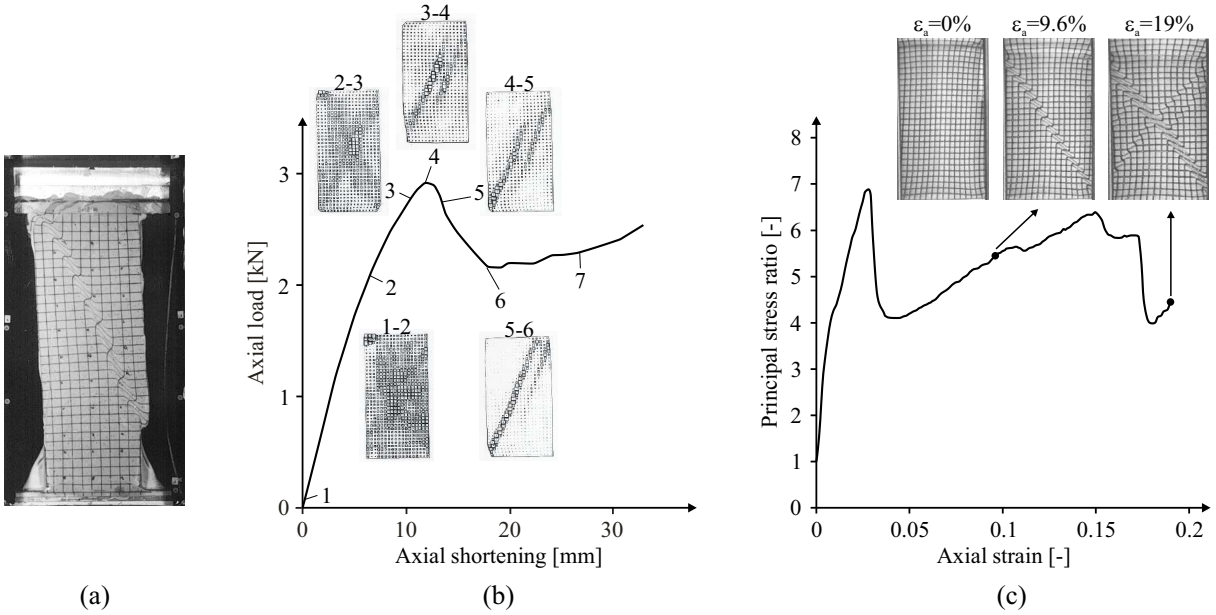

Fig. 3.2: Formation of shear bands during plane-strain biaxial compression test on sand: (a) specimen after shearing and (b,c) global response curves for one or two shear bands (according to Mokni and Desrues (1999) and Alshibli et al. (2003)).

The experimental localisation studies mostly analyse the behaviour of sand and only a few

are actually available on rocks (Bésuelle et al., 2000). Analysing the formation of fractures and strain localisation bands in rocks is quite challenging due to their high resistance and brittle behaviour (quasi-brittle material), thence the development of appropriate apparatus designed to test this type of material is necessary (Desrues and Viggiani, 2004).

Pre and post-peak behaviours

The localisation process has been deeply studied by Desrues and co-workers (Desrues, 1984; Desrues and Viggiani, 2004) for many biaxial compression tests. One example of shear band development in sand is represented in Fig. 3.2 (b) where the load-deformation curve and the incremental fields of shear strain intensity based on stereophotogrammetry are represented before and after the peak. The experimental results indicate that strain localisation initiates before the peak stress, generally at simultaneous multiple locations within a large part of the specimen. These multiple mechanisms of localised deformation are temporary because they are in competition as the deformation increases and finally one of them takes over the others at peak stress to complete a full formation of a shear band throughout the specimen.

However, for a perfect material, there is no reason that strain localisation initiates in the samples and it would deform homogeneously. In reality, the localisation process is generated because geomaterials exhibit some heterogeneities. The role of material imperfections, be it hard or weak inclusions, was investigated experimentally by Desrues (1984) and Desrues and Viggiani (2004). Two main observations were made. First, the inclusion does not affect neither the global stress-strain response of the specimen nor the peak stress and strain level for the same confining pressure. Second, the shear band position is dictated by the inclusion and passes through it if the imperfection is strong enough to act as a strain localisation attractor. In fact, the stress and strain fields are uniform for a homogeneous specimen, on the other hand an imperfection induces a non-uniformity of both fields in its vicinity which can be sufficient to act as a nucleation point for the strain localisation onset.

After the peak stress, the global reaction of the specimen generally exhibits a rapid decrease followed by whether a constant or a fluctuating reaction. This post-peak regime is dominated by the shear banding (or fracturing) process, including its structure and evolution. Moreover, several shear bands can even initiate in a specimen after the first peak (Fig. 3.2 (c)) and complex shear banding patterns may result of specific condition of the loading or geometry. The strain localisation as well as the post-localisation or post-peak material behaviour are therefore crucial and need to be understood and represented properly.

Concerning the thickness of the shear bands, it is governed by the solid grain size for granular materials (Roscoe, 1970; Vardoulakis and Sulem, 1995). For instance, it ranges generally between 10 to 20 times the average grain size (mean grain diameter) for sands and between 4 to 10 times for sandstone (El Bied et al., 2002). For fine-grained materials such as marls, clays, and clayey rocks, the shear bands can be very thin with a width smaller than 50 or 100 μm. Such thin shear bands are regularly referred as slip surfaces or displacement discontinuities, and extremely thin widths can even create a confusion between closed shear cracks in mode II (strong discontinuities) and shear bands (weak discontinuities) as mentioned by Lenoir (2006) and Viggiani et al. (2004). For the Callovo-Oxfordian claystone, Bésuelle et al. (2006b) performed compression tests on specimens and analysed the shear banding appearance with X-ray microtomography and three dimensional digital image correlation. The measurements indicate that the widths of the localised deformation zones are about 60 to 70 μm.

Hydro-mechanical processes

The strain localisation process has been investigated whether from a purely mechanical point of view or for hydro-mechanical coupled problems. The pure mechanical aspect is studied on dry or on globally drained samples at low strain rate whilst the coupled problem is analysed on globally

undrained or on globally drained samples at fast strain rate. The hydro-mechanical coupling introduces fluid (liquid water) flows that can have a potential impact on the strain localisation process (Collin et al., 2009b). This phenomenon is dependent of the problem boundary conditions and of the material characteristics, both mechanical and hydraulic.

The hydraulic boundary conditions on small-scale laboratory experiments are prescribed on the samples external faces meaning that the conditions are valid globally but not locally. Under globally drained conditions, fluid flows are possible and their impact on strain localisation can be low or non-existent in case of sufficiently high permeability in comparison to the loading velocity (low strain rate). If pore overpressures are not generated then the experimental observations correspond to dry conditions and purely mechanical aspect.

Under undrained conditions, overpressures appear in the sample and interactions with the localisation process are generated. Furthermore, fluid flows can still appear in the sample because of strain localisation effects, even if they are globally undrained. Among other experiments, the plane-strain undrained tests performed in Grenoble have highlighted some common features (Mokni and Desrues, 1999; Roger et al., 1998): strain localisation is observed on loose sand and is possible for dense (dilatant) sand only when cavitation develops. Before cavitation in the pore fluid, the localisation is inhibited by the liquid water transfers. This observation undoubtedly evidences the interaction between fluid and localisation process. Furthermore, the effect of cavitation on shear banding has been investigated numerically by Sieffert et al. (2014).

3.1.3 Modelling issues

The previous experimental results clearly evidence the necessity of a proper representation of the strain localisation process in shear band mode for geomaterials. The latter has to account for strain localisation onset, post-localisation (post-peak) material behaviour, as well as hydro-mechanical coupling. The shear band modelling has to be robustly addressed both theoretically and numerically.

3.2 Theoretical concepts

It has been highlighted that shear band formation can occur in geomaterials for many loading conditions. To reproduce such phenomenon, constitutive laws devoted to the modelling of the shear band behaviour have to be developed. The constitutive models must be able to predict a strain localisation in band mode and to reproduce it properly.

3.2.1 Bifurcation and shear banding theory

From a theoretical perspective, the appearance of strain localisation is considered as a bifurcation phenomenon which can be defined as the loss of uniqueness of a problem solution (Hill, 1958; Rice, 1976; Chambon and Caillerie, 1999). The bifurcation can be characterised by various modes such as surface wave (Triantafyllidis, 1980), necking (Hill and Hutchinson, 1975), diffuse loss of homogeneity (Vardoulakis, 1979, 1981), or shear banding (Rice, 1976). Among them, the focus is on the analysis of strain localisation in shear band mode.

Bifurcation phenomenon

To illustrate the bifurcation phenomenon, a one-dimensional problem of a bar under uniaxial tension is considered (Fig. 3.3 (a)). The bar has a length L, a constant section A, and the tension F is represented by an axial displacement of the bar's extremity $U = \Delta L$. The material behaviour depends on a quite simple constitutive law (Fig. 3.3 (b)) that exhibits a reduction of stress with increasing strain, resulting either of an elastic damage model or of a strain softening

elastoplastic model. Considering the latter, the first part of the curve constitutes the elastic behaviour, the second is the plastic behaviour, and σ_p is the yield stress.

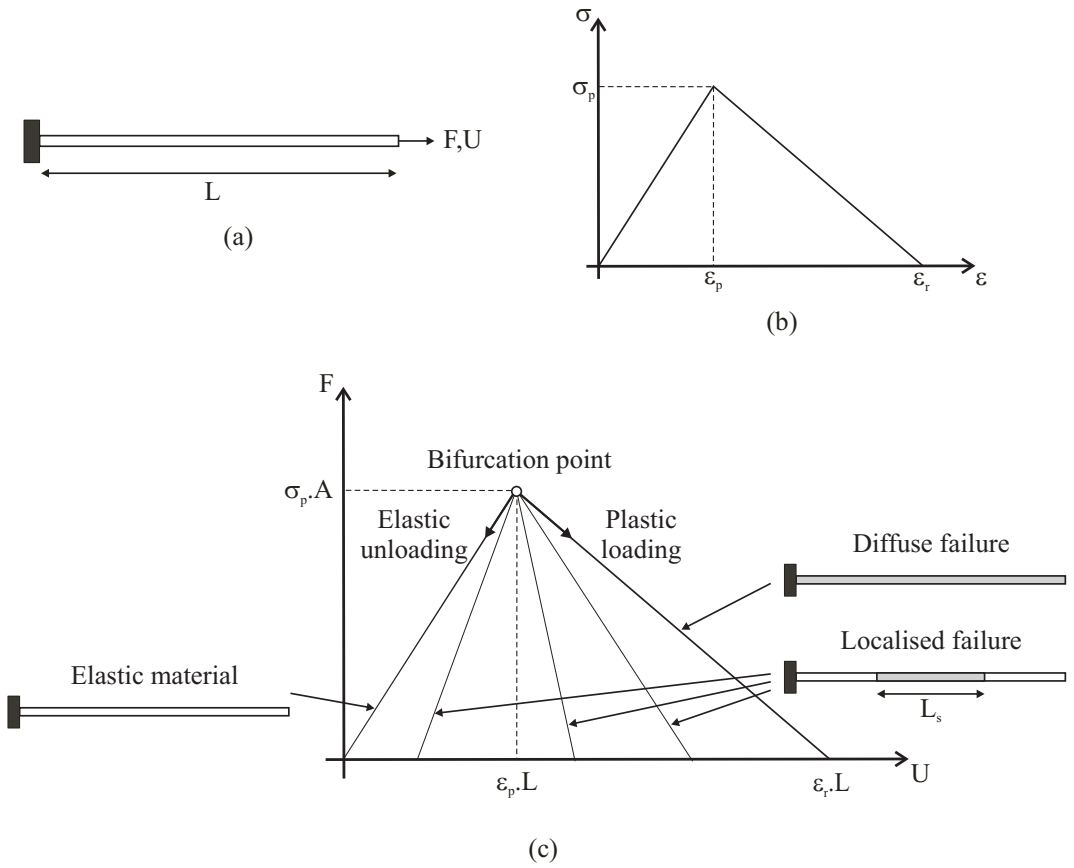

Fig. 3.3: One-dimensional bar under uniaxial tension: (a) schematic representation, (b) local constitutive behaviour law, and (c) global response.

During the elongation, the load-displacement curve of the global response of the bar (Fig. 3.3 (c)) firstly exhibits a linear behaviour up to σ_p. Under elastic regime, the response is unique and the strain distribution is uniform. In elastoplastic softening regime, the global axial force/stress decreases but, according to the static equilibrium condition, it must remain homogeneous all along the bar. As a consequence of the strain softening material behaviour, the solution at the peak stress is not unique and two possibilities can occur at any material point: softening plastic loading or elastic unloading. In fact, when the strength reduces beyond the peak strength, the material response can either continue along the plastic loading curve and undergo an increase of plastic strain, or it can also continue along the elastic unloading curve. Strain softening may therefore instigate an infinity of localised solutions with non-uniform strain distributions (Bazant et al., 1984; Benallal and Marigo, 2007; Jirásek and Rolshoven, 2009) and causes a loss of uniqueness of the post-peak solution.

The ratio of the length L_s under softening plastic loading versus the bar length L can be defined. $\frac{L_s}{L} = 1$ corresponds to a diffuse failure during which the bar load decreases linearly down to zero with a final elongation of $U_f = \varepsilon_r L$. For $0 < \frac{L_s}{L} < 1$, there exist an infinity of possible localised failures having a final elongation of $0 < U_f < \varepsilon_r L$ for $F = 0$. Some of these solutions exhibit an increase of axial deformation after the peak stress $\varepsilon_p L < U_f < \varepsilon_r L$, while others exhibit a decrease of axial deformation $0 < U_f < \varepsilon_p L$, such solutions are called snapback solutions and may cause computational instabilities. Lastly, $\frac{L_s}{L} = 0$ is a limit case for which the material becomes fully elastic after the peak stress. For this solution the load decreases linearly down to zero without final elongation $U_f = 0$ and without energy dissipation. Such solution is

not realistic and will be discussed later.

The previous discussion is also valid for a material under compression or shear, replacing the tension normal stress by compression normal stress or by shear stress. For compression experiments (as discussed in section 3.1.2), the loss of uniqueness might result in the development of shear bands among the different possible types of localised solutions. For such discontinuity, an elastic unloading is observed outside the shear band while the material remains under plastic loading inside with a concentration of the plastic strain. As illustrated in Fig. 3.4, the post-peak behaviour is governed by the degree of softening, i.e. the ratio of shear band thickness H_s versus the total height of the sample H, and strong discontinuities corresponding to very thin bands can appear.

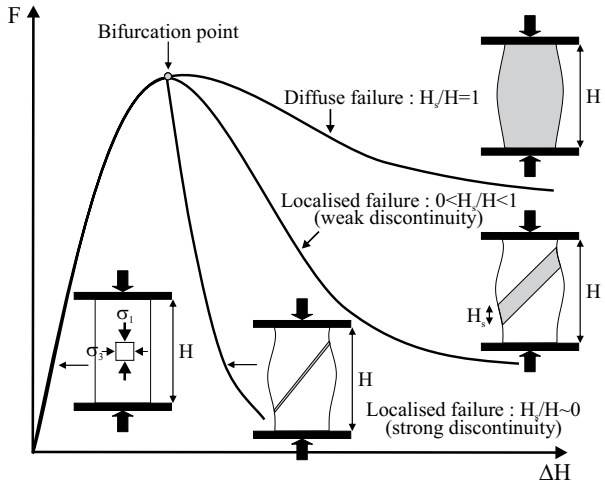

Fig. 3.4: Post-peak behaviour related to the shear band thickness for a specimen under uniaxial compression (Thakur, 2007).

Rice criterion

Following previous works (Hadamard, 1903; Hill, 1958; Mandel, 1966), a criterion was proposed by Rice and co-workers (Rudnicki and Rice, 1975; Rice, 1976) for strain localisation in shear band mode. It analyses the stress state and investigates the possibility of bifurcation appearance in the stress and strain paths. The shear band theoretical scheme is illustrated in Fig. 3.5 where the superscripts ^{0} and ^{1} denote quantities outside and inside the shear band, respectively. The following development are based on the hypothesis that shear bands are zero extension lines. The zero extension condition is a kinematic characteristic of the shear band implying that it has an indefinite length and no longitudinal deformation (Desrues, 1984, 1987). Moreover, additional quantities inside the band are independent of the longitudinal band direction.

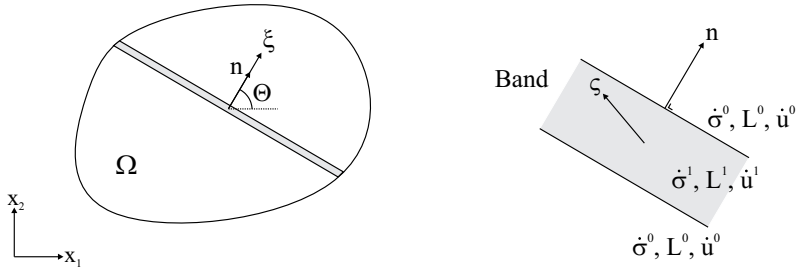

Fig. 3.5: Theoretical scheme of a shear band.

At the strain localisation appearance, the stress and strain fields are assumed to be continuous

on a solid body. The discontinuity appears on the shear band outer surfaces, that is to say on the interfaces between the shear band and the outer material, for the stress field rate $\dot{\sigma}_{ij}$ and for the corresponding velocity gradient field L_{ij}.

Two conditions are required to fulfil the Rice bifurcation criterion. Firstly, a kinematic condition specifies the discontinuity of the velocity gradient field L_{ij} across the shear band interfaces in its normal direction:

$$L^1_{ij} = L^0_{ij} + \varsigma_i \; n_j \tag{3.1}$$

which is equivalent to:

$$\varsigma_i \; n_j = \frac{\partial \left(\dot{u}^1_i - \dot{u}^0_i \right)}{\partial x_j} \tag{3.2}$$

where $n_i = \frac{\partial \xi}{\partial x_i}$ is the normal unit vector to the shear band, $\dot{u}_i$ is the velocity field, and ς_i is an additional velocity gradient field of the shear band that describes the band mode. It is defined as follows:

$$\varsigma_i = \frac{\partial \left(\dot{u}^1_i - \dot{u}^0_i \right)}{\partial \xi} \tag{3.3}$$

where ξ is the shear band normal coordinate axis. Secondly, a static condition specifies the surface equilibrium of the shear band interfaces with the outer material and the discontinuity of the stress field rate $\dot{\sigma}_{ij}$:

$$n_i \left(\dot{\sigma}^1_{ij} - \dot{\sigma}^0_{ij} \right) = 0 \tag{3.4}$$

It implies that the interface traction increments:

$$\dot{t}_i = \dot{\sigma}_{ij} \; n_j \tag{3.5}$$

imposed on both sides of the shear band are equal.

In addition to the two previous conditions, a material constitutive law expressing the relationship between the stress and strain field increments remains to be introduced in the Rice bifurcation criterion. Initially, the criterion was developed for classical material (associated plasticity) and incrementally linear behaviour. The assumption of linearity is quite strong and materials generally exhibit elastoplasticity with an incrementally non-linear relationship. The following constitutive law is considered:

$$\dot{\sigma}_{ij} = C_{ijkl} \; L_{kl} \tag{3.6}$$

A first possibility of bifurcation appearance is a continuous bifurcation with continuous constitutive tensor across the shear band:

$$C^0_{ijkl} = C^1_{ijkl} = C_{ijkl} \tag{3.7}$$

However, the bifurcation is often discontinuous (Rice and Rudnicki, 1980) which implies plastic loading inside the shear band and elastic unloading in the outer material. The constitutive tensor is therefore different outside and inside the shear strain localisation band:

$$C^0_{ijkl} = C^e_{ijkl} \quad , \quad C^1_{ijkl} = C_{ijkl} \tag{3.8}$$

Considering discontinuous bifurcation and introducing the expression of Eqs. 3.1 and 3.6 in Eq. 3.4 give:

$$n_i \left(C^1_{ijkl} \left(L^0_{kl} + \varsigma_k \; n_l \right) - C^0_{ijkl} \; L^0_{kl} \right) = 0 \tag{3.9}$$

which is a third order equation system where the unknown is the vector ς_i. The trivial solution $\varsigma_i = 0$ is always possible but implies that no shear band can appear with the unique solution $L^1_{ij} = L^0_{ij}$. Other non-trivial solutions implying bifurcation can be found for $\varsigma_i \neq 0$. Nonetheless, the difference between the constitutive tensors inside and outside the shear band complicates

the bifurcation analysis. Furthermore, it has been demonstrated that the continuous bifurcation always precedes the discontinuous bifurcation (Rice and Rudnicki, 1980; Simo et al., 1993) thus, by assuming continuous bifurcation, Eq. 3.9 becomes:

$$(n_i \; C_{ijkl} \; n_l) \; \varsigma_k = 0 \tag{3.10}$$

and non-trivial solutions $\varsigma_i \neq 0$ are found if the acoustic tensor determinant is less or equal to zero (Hill, 1958):

$$det\,(n_i \; C_{ijkl} \; n_l) \leq 0 \tag{3.11}$$

The solution of this equation gives n_i and the orientation of the shear band. This is a necessary bifurcation condition in shear band mode that corresponds to the first possible bifurcation, however, this is not a sufficient condition for the appearance of shear band. Furthermore, even if the continuous bifurcation assumption is a strong one, it has been proved that the previous criterion remains valid for a classical single-mechanism elastoplastic model to the condition that C_{ijkl} is the elastoplastic constitutive tensor (Chambon, 1986).

For two-dimensional plane state problems, the condition of Eq. 3.11 can be rewritten in a fourth order equation:

$$det(\wedge_{jk}) = n_1^4 \left(\ell_4 \; tan^4\Theta + \ell_3 \; tan^3\Theta + \ell_2 \; tan^2\Theta + \ell_1 \; tan\Theta + \ell_0\right) \leq 0 \tag{3.12}$$

where $tan\Theta = n_2/n_1$ with Θ being the orientation of the shear band normal with the x_1-axis, the parameters ℓ_i depend on the components of C_{ijkl} (Wang, 1993), and $\wedge_{jk}$ is the acoustic tensor:

$$\wedge_{jk} = n_i \; C_{ijkl} \; n_l \tag{3.13}$$

The orientation obtained by the bifurcation criterion is a double one which indicates that shear band can initiate in two conjugate bifurcation directions.

The criterion can be generalised to large strain problems. The elastoplastic constitutive law has been detailed for small strains and rotations in Eq. 3.6 and can be formulated as follows for large strains and rotations:

$$\dot{\sigma}_{ij} = \mathcal{A}_{ijkl} \; L_{kl} \tag{3.14}$$

where $\mathcal{A}_{ijkl}$ is the elastoplastic constitutive tangent tensor for large strains and rotations. This tensor can directly be used instead of C_{ijkl} in the bifurcation criterion. It is obtained by the modification of C_{ijkl} by the relation:

$$\mathcal{A}_{ijkl} = C_{ijmn} \; S_{mnkl} - A^J_{ijkl} \tag{3.15}$$

where S_{ijkl} and A^J_{ijkl} are Jaumann's corrections for large deformations (Wang, 1993).

Furthermore, similar developments can be extended to non-classical (non-associated) elastoplasticity. The discontinuous bifurcation condition (Eq. 3.9) remains valid, on the other hand, the continuous bifurcation assumption can not guarantee to obtain the first possible bifurcation for these materials. This assumption can nevertheless be generalised and leads to the definition of lower and upper bounds for the bifurcation criterion (Raniecki and Bruhns, 1981).

In addition to softening, materials can exhibit hardening of their plastic properties which corresponds to a non-linear elastoplastic behaviour before reaching the peak stress. For associated plasticity the bifurcation criterion is met only at peak stress or in softening regime while for non-associated plasticity it can be met for positive hardening (Rudnicki and Rice, 1975). It signifies that materials not satisfying the plastic normality rule are more inclined to strain localisation and instability. Nevertheless, elastic unloading occurs only for strain softening behaviour; therefore, the bifurcation can only be continuous in the hardening regime and discontinuous bifurcation can be observed after the peak stress.

It should also be pointed out that the previous developments are valid only for pure mechanical analyses, yet it has been shown that the localisation condition depends only on the material drained properties for hydro-mechanical coupled problems (Loret and Prevost, 1991).

Deformation band type

The nature of a strain localisation band depends on different factors as the material characteristics and the loading. Even if localisation bands are commonly called shear bands, they do not deform automatically in pure shearing. For instance, a shearing with dilatancy is generally observed in the shear bands for most geomaterials, loose materials can exhibit compacting shear bands and compaction bands because of their contractive behaviour (Issen and Rudnicki, 2000, 2001), and dilation bands can also appear for opening mode failure (Bésuelle, 2001; Du Bernard et al., 2002). Fig. 3.6 illustrates the main band types based on the predominant localised deformation.

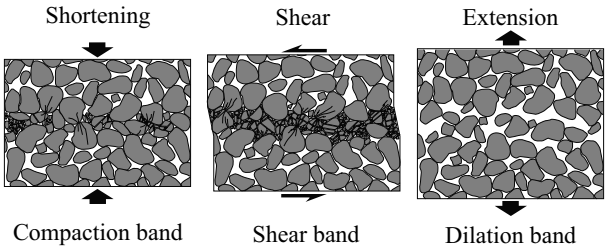

Fig. 3.6: Deformation band types in porous media depending on the predominant displacement gradient (Du Bernard et al., 2002).

The type of band can be described thanks to the Rice bifurcation criterion and to the additional velocity gradient field ς_i defined in the kinematic condition (Eq. 3.3). This vector is the non-trivial solution of Eq. 3.10 which depends on the acoustic tensor $\wedge_{jk}$. For two-dimensional cases it reads $\varsigma_i = (\wedge_{12}; -\wedge_{11})$ (see Wang (1993) for three-dimensional cases). The scalar product of the normalised (unit) vector of ς_i, also called band characteristic vector, and the normal unit vector n_i gives:

$$\underline{s} = \frac{\varsigma_i}{||\varsigma||}\, n_i = cos(\alpha_{\varsigma n}) \tag{3.16}$$

where $||\varsigma|| = \sqrt{\wedge_{11}^2 + \wedge_{12}^2}$ is the norm of the vector ς_i and $\alpha_{\varsigma n}$ is the angle between the vectors ς_i and n_i. The parameter $\underline{s}$ describes the discontinuity of the deformation nature and band mode according to the Table 3.1.

$\underline{s}$	$\alpha_{\varsigma n}$	Deformation nature	Band mode
-1	π	Pure closing	Compaction band
$]-1;0[$	$\left]\frac{\pi}{2};\pi\right[$	Contractive	Compacting shear band
0	$\frac{\pi}{2}$	Pure shear	Pure shear band
$]0;1[$	$\left]0;\frac{\pi}{2}\right[$	Dilative	Dilating shear band
1	0	Pure opening	Dilation band

Table 3.1: Characterisation of the type of deformation band.

Shear band orientation

Different theories exist about the shear band orientation based on plasticity or bifurcation theory; a summary is presented by Desrues (1984). A first theory is the maximal obliquity line of the stress vector (maximum shear stress at failure) stating that the shear band must be a line tangent at any point to the facets that satisfy the Coulomb criterion (Coulomb, 1773). This condition is a static characteristic of the shear band and, following Coulomb's theory, the orientation of the shear band is $\frac{\pi}{4} \pm \frac{\varphi}{2}$ with the principal directions of the total stresses.

Nonetheless, experimental measurements of shear band orientations disagree in many cases with this orientation. In a synthesis of many years of laboratory research results, Roscoe (1970) specifies that rupture lines, i.e. the sheared planes, have no reason to coincide with the maximal obliquity facets of the stress vector but are zero extension lines (Desrues, 1984, 1987). Following this condition, the shear band orientation is $\frac{\pi}{4} \pm \frac{\psi}{2}$ with the principal directions of the strain rate and introduces the influence of the dilatancy angle. This second theory is not accepted by all the authors in the literature and questions raise about the coincidence of maximal obliquity line with zero extension line, and therefore about the coincidence of the principal directions of the total stress and strain rate. This engenders the appearance of a concept of uncertainty about the principal axes directions of these tensors as well as a distinction between local and global directions and quantities.

Arthur et al. (1977b) and co-workers proposed that the orientation of the shear band can varies within a certain range defined by the two previous orientation values and that an intermediate value $\frac{\pi}{4} \pm \frac{\varphi+\psi}{4}$ can be assumed in some cases. Similar conclusions based on the bifurcation theory are formulated by other authors such as Vardoulakis (1980) who indicates that the previous orientation assumed by Arthur et al. (1977b) is valid with φ and ψ values at peak stress (bifurcation).

The definition of the two sets of conjugated shear band orientations Θ with respect to the minor principal stress can thus be summarised as follows:

$$|\Theta_R| \leq |\Theta| \leq |\Theta_C| \tag{3.17}$$

where Θ_C and Θ_R are Coulomb's and Roscoe's angle, respectively:

$$\Theta_C = \pm \left(\frac{\pi}{4} + \frac{\varphi_{bif}}{2} \right) \tag{3.18}$$

$$\Theta_R = \pm \left(\frac{\pi}{4} + \frac{\psi_{bif}}{2} \right) \tag{3.19}$$

These definitions are valid principally for perfectly-plastic models. In case of hardening non-associated plasticity, the strain localisation can initiate in the hardening phase before reaching the peak stress and a unique pair of shear bands exists for an intermediate orientation value of about (Mehrabadi and Cowin, 1980; Anand, 1983; Shuttle and Smith, 1988):

$$\Theta_A = \pm \left(\frac{\pi}{4} + \frac{\varphi_{bif} + \psi_{bif}}{4} \right) \tag{3.20}$$

These orientations depend on the local behaviour at the initiation of strain localisation which corresponds to the bifurcation state (Desrues, 1984). Once a shear band is initiated, it propagates mostly in a straight direction implying that the direction defined locally at initiation is preserved at the global scale (Desrues, 1984). The shear band orientations are therefore defined with φ_{bif} and ψ_{bif} which are the mobilised friction and the dilatancy angles at the bifurcation state.

3.2.2 Regularisation methods

The further step is to define an appropriate and robust method that allows to properly model the strain localisation and shear banding with finite element methods, leading finally to the rupture in localised mode. Local descriptions of the failure with classical finite element methods are not efficient in the reproduction of strain localisation because they suffer a mesh dependency (to mesh size and orientation) as indicated by Pietruszczak and Mróz (1981), Zervos et al. (2001b), Collin et al. (2009b), and Wu and Wang (2010). This pathological problem is due to the properties of the underlying mathematical problem.

To illustrate this deficiency, one can go back to the traction and compression examples illustrated in Figs. 3.3 and 3.4. With classical tools, the thicknesses L_s and H_s under softening

plastic loading are a priori undetermined and a mesh-dependency of the model response is observed as far as the problem is ill-posed. For strong discontinuity (most localised solution), L_s and H_s reduce to the size of the smallest element and may theoretically tend to cancel for an increasing number of elements (de Borst et al., 1993). Such numerical results can therefore predict physically inadmissible failure without any consummation of energy.

The evolution of the shear zone width has been studied for complete initial boundary value problem. For instance, Kotronis et al. (2008) indicate that the zone thickness in a one-dimensional layer problem remains constant or decreases while same structural behaviour can corresponds to different solutions (different elastic-plastic zones patterns). The latter also illustrates the deficiencies of classical models under softening regime for which the initial boundary value problem is not well posed mathematically.

The dependence to the finite element discretisation can be tackled by employing a proper regularisation technique. Such method has to introduce an internal length scale in the problem to model the post-localisation behaviour correctly. Two principal categories of enhanced models exist: one consists in the enrichment of the constitutive law with for instance non-local approaches (Bazant et al., 1984; Pijaudier-Cabot and Bazant, 1987; Peerlings et al., 1996b; Guy et al., 2012) or gradient plasticity (Aifantis, 1984; de Borst and Mühlhaus, 1992; Peerlings et al., 1996a), the other one consists in the enrichment of the continuum kinematics with microstructure effects. For this second category the microkinematics are characterised at microscale in addition to the classical macrokinematics (Cosserat and Cosserat, 1909; Toupin, 1962; Mindlin, 1964; Germain, 1973). Additionally, it is to mention that enhanced models restore mesh objectivity but not the uniqueness of the solution.

Enrichment of the constitutive law

For this theory, the internal length scale is introduced at the level of the constitutive model. Advanced analyses of localisation phenomena have indicated that constitutive equations with internal length are one solution to model strain localised pattern properly.

The internal length scale can be introduced by developing non-local definition of internal variables involved in the material behaviour. The non-local variable $\mathring{\mathrm{v}}$ at a material point x_i can be defined as an averaging value of the local variable v in a considered region Ω near that point (Pijaudier-Cabot and Bazant, 1987; Peerlings et al., 2001), as illustrated in Fig. 3.7.

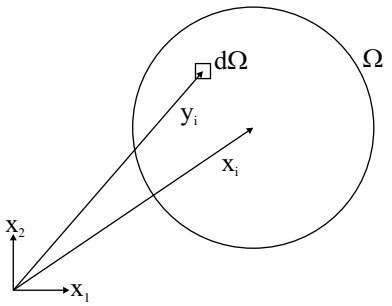

Fig. 3.7: Non-local approach on a representative material volume.

The non-local integral method gives:

$$\mathring{\mathrm{v}}(x_i) = \frac{1}{V} \int_{\Omega} \Psi \ \mathrm{v}(y_i) \ d\Omega \tag{3.21}$$

$$V = \int_{\Omega} \Psi \ d\Omega \tag{3.22}$$

where x_i is the coordinate vector of the material point where the non-local variable is considered, Ω is a representative volume centred in x_i, y_i is the coordinate vector of the infinitesimal volume $d\Omega$, and Ψ is a weight function scaling $\mathring{\mathrm{v}}$ to $\mathring{\mathrm{v}} = \mathrm{v}$ for a homogeneous distribution of the variable. It is generally defined with a Gaussian distribution:

$$\Psi = \frac{1}{(2\pi)^{3/2}\ l_c^3}\ exp\left(-\frac{||x_i - y_i||^2}{2\ l_c^2}\right) \tag{3.23}$$

which depends on the distance $||x_i - y_i||$ and on a characteristic length parameter l_c. This length parameter, or internal length scale, defines the material volume that significantly contributes to the non-local variable and is consequently related to the microstructure.

The regularised variable can also be defined explicitly from the local variable $\mathrm{v}(x_i)$ and its gradient. In his pioneering works, Aifantis (1984) introduced such gradient in constitutive equations. The explicit gradient formulation is:

$$\mathring{\mathrm{v}} = \mathrm{v} + \bar{l}\ \frac{\partial^2 \mathrm{v}}{\partial x_i \partial x_i} \tag{3.24}$$

where the dependence of v and $\mathring{\mathrm{v}}$ on the coordinate vector x_i is dropped for simplicity and $\bar{l}$ has the dimension of length squared so $\sqrt{\bar{l}}$ can be related to the internal length scale l_c introduced to regularise the model. Because the gradient term is a local quantity, the spatial interaction of the material points located in the vicinity of $\mathring{\mathrm{v}}$ is infinitesimal and the explicit gradient model is therefore local. This is a main difference with the non-local integral formulation of Eq. 3.21 where the interaction distance is finite and related to the weight function. Moreover, the explicit gradient formulation can be derived from the non-local integral formulation by introducing gradient of the internal variable, expanding the local variable $\mathrm{v}(y_i)$ into a Taylor series (Bazant et al., 1984; Lasry and Belytschko, 1988; Peerlings et al., 1996a), using the weight function definition of Eq. 3.23, and neglecting terms above second order (approximation).

The definition of Eq. 3.24 is less suitable in the context of numerical analyses, such as finite element formulation, because of the explicit dependence of $\mathring{\mathrm{v}}$ with its local (second) gradient. This dependence leads to continuity requirement for the internal variable which has to be a continuously differentiable function (class C^1 function whose derivative is continuous). To avoid this drawback, an alternative implicit gradient formulation, introducing an approximation of Eq. 3.21 similar to Eq. 3.24, can be expressed as follows (Peerlings et al., 1996a, 2001):

$$\mathring{\mathrm{v}} - \bar{l}\ \frac{\partial^2 \mathring{\mathrm{v}}}{\partial x_i \partial x_i} = \mathrm{v} \tag{3.25}$$

and enables a continuous definition of v (class C^0 function). For the implicit gradient model, the non-local internal variable is an additional unknown which is solution of the Helmoltz differential equation 3.25. Solution of this equation can only be found provided that additional boundary condition on $\mathring{\mathrm{v}}$ is specified. The following condition is usually assumed (Lasry and Belytschko, 1988):

$$\frac{\partial \mathring{\mathrm{v}}}{\partial x_i}\ n_i = 0 \tag{3.26}$$

where n_i is the normal unit vector to the external boundary. This condition enables $\mathring{\mathrm{v}} = \mathrm{v}$ for homogeneous distribution. In contrast to the explicit formulation, the non-local variable $\mathring{\mathrm{v}}$ is implicitly given as the solution of Eqs. 3.25 and 3.26, and the spatial interaction has a finite distance that implies a non-local character. The solution is of the same form of the non-local equation 3.21 with $\Psi = Gr$ and $V = 1$, Gr being the Green's function (Zauderer, 1989):

$$\mathring{\mathrm{v}}(x_i) = \int_{\Omega}\ Gr\ \mathrm{v}(y_i)\ d\Omega \tag{3.27}$$

$$Gr = \frac{1}{4\pi\ \bar{l}\,||x_i - y_i||}\ exp\left(-\frac{||x_i - y_i||}{\sqrt{\bar{l}}}\right) \tag{3.28}$$

The implicit gradient model is therefore a special case of the non-local model.

Non-local quantities as well as gradient of internal variables can finally be introduced in constitutive models. Among other authors, Bazant, Pijaudier-Cabot, and co-workers (Bazant et al., 1984; Pijaudier-Cabot and Bazant, 1987) proposed a family of constitutive models derived from non-local damage theory in which a non-local internal variable is used instead of the local one. For instance, a non-local damage energy release rate obtained by Eq. 3.21 is introduced in a loading function for damage. Other variables such as non-local equivalent strain are usually used in damage model (Peerlings et al., 2001).

Enrichment of the kinematics

The previous approaches with enrichment of the constitutive law introduce the effect of microstructure with non-local or gradient terms but the microstructure itself is not defined precisely. To this end, the classical kinematics of the continuous medium can be enriched with additional description of the microstructure kinematics, leading to microstructure continuum medium also called enriched medium.

For classical continuous medium, a material particle of volume Ω is defined at macroscopic scale by its (macro) displacement field u_i. The classical kinematic fields are the macro-deformation field:

$$F_{ij} = \frac{\partial u_i}{\partial x_j} \tag{3.29}$$

corresponding to the gradient of the displacement field, the macro-strain field:

$$\varepsilon_{ij} = \frac{1}{2}\left(F_{ij} + F_{ji}\right) \tag{3.30}$$

corresponding to the symmetric part of F_{ij}, and the macro-rotation field:

$$r_{ij} = \frac{1}{2}\left(F_{ij} - F_{ji}\right) \tag{3.31}$$

corresponding to the antisymmetric part of F_{ij}. Their rate forms are also commonly used; the velocity gradient field:

$$L_{ij} = \frac{\partial \dot{u}_i}{\partial x_j} \tag{3.32}$$

the strain rate field:

$$\dot{\varepsilon}_{ij} = \frac{1}{2}\left(L_{ij} + L_{ji}\right) \tag{3.33}$$

and the spin rate field:

$$\omega_{ij} = \frac{1}{2}\left(L_{ij} - L_{ji}\right) \tag{3.34}$$

The more ancient and famous enhanced model was developed by the Cosserat brothers (Cosserat and Cosserat, 1909) who introduced local rotation degrees of freedom r_i^c in addition to the displacements of classical continua u_i (Fig. 3.8). The Cosserat (or micropolar) elastic continuum theory is mostly suitable for the kinematic description of granular materials. Accordingly, additional kinematic fields are introduced (Vardoulakis and Sulem, 1995). The deformation due to the particle rotation, also called micro-rotation (antisymmetric tensor):

$$r_{ij}^c = e_{ijk}\ r_k^c \tag{3.35}$$

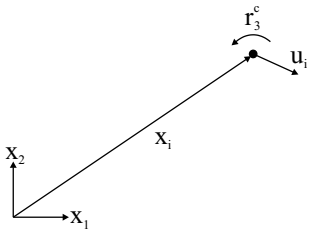

Fig. 3.8: Kinematic degrees of freedom of the Cosserat elastic continuum theory.

where e_{ijk} is the alternating tensor, and the gradient of the particle rotation, also called the curvature:

$$K_{ij}^c = \frac{\partial r_i^c}{\partial x_j} \tag{3.36}$$

A relative strain is deduced as the difference between macro-deformation and micro-rotation:

$$\overline{\varepsilon}_{ij} = F_{ij} - r_{ij}^c \tag{3.37}$$

whose symmetric part coincides with the macro-strain ε_{ij} and its antisymmetric part with the difference between the macro and micro-rotation $r_{ij} - r_{ij}^c$. The latter characterises the relative rotation of a material point with regard to the rotation of its neighbourhood. Additionally, a couple stress (torques) tensor associated to the rotations is also added and introduces bending and torsion at material point. This results in a moment equilibrium equation involving the couple stresses that comes in addition to the classical (local) momentum balance equation involving the stress field σ_{ij}. Moreover, supplementary elastic constants are added in the constitutive equations which consist of internal length scale parameters related to the microstructure (Vardoulakis and Sulem, 1995).

In the 1960's, Toupin (1962) and Mindlin (1964) defined materials with microstructure. A macro-volume Ω is composed of smaller microscale particles that can be represented by a micro-volume Ω^m, embedded in the material volume Ω (Fig. 3.9). A micro-displacement field u_i^m is defined independently of the macro-displacement u_i and its gradient leads to a micro-deformation field:

$$\upsilon_{ij} = \frac{\partial u_i^m}{\partial x_j} \tag{3.38}$$

which is homogeneous in the micro-volume Ω^m but non-homogeneous in the macro-volume Ω.

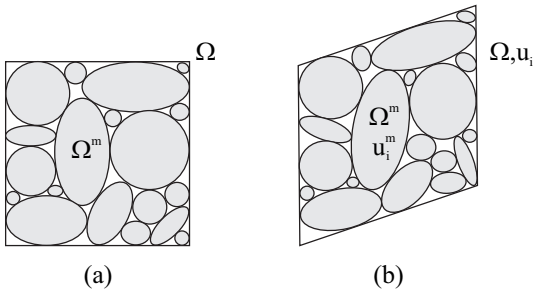

Fig. 3.9: Kinematics of microstructure continuum: (a) initial configuration and (b) configuration after external solicitation with relative displacement of the microstructure.

The symmetric and antisymmetric parts of υ_{ij} correspond to the micro-strain and micro-rotation:

$$\varepsilon_{ij}^m = \frac{1}{2}\left(\upsilon_{ij} + \upsilon_{ji}\right) \tag{3.39}$$

$$r_{ij}^m = \frac{1}{2}\left(\upsilon_{ij} - \upsilon_{ji}\right) \tag{3.40}$$

with the micro-rotation corresponding to the rotation components of the Cosserat model $r_{ij}^m = r_{ij}^c$ (Eq. 3.35). Cosserat model is in fact a particular case of microstructure medium. Moreover, the micro second gradient is defined as:

$$h_{ijk} = \frac{\partial \upsilon_{ij}}{\partial x_k} = \frac{\partial^2 u_i^m}{\partial x_j \partial x_k} \tag{3.41}$$

The relative deformation of the microstructure is defined as the difference between the macro and the micro-deformation fields:

$$\overline{\varepsilon}_{ij} = F_{ij} - \upsilon_{ij} \tag{3.42}$$

whose symmetric part coincides with the difference between the macro and the micro-strain $\varepsilon_{ij} - \varepsilon_{ij}^m$ and its antisymmetric part with the difference between the macro and micro-rotation $r_{ij} - r_{ij}^m$. Moreover, similarly to the Cosserat's continuum description, additional stresses are introduced: the microstress, which is an additive stress field associated to the microstructure, and the double stress.

Later, Germain (1973) introduced the virtual power principle to provide a global framework for the microstructure continuum formulation. This principle states that, by equilibrium, the virtual power of all forces acting on a mechanical system is null. In the following, materials with microstructure defined by Mindlin (1964) and Germain (1973) will be considered.

A large panel of models are developed by adding mathematical constraints to general microstructure materials. Among them, the second gradient model developed in Grenoble (Chambon et al., 1998, 2001a) will be most particularly used. Yet, the further conclusions could be generalised to other regularisation techniques.

3.3 Coupled local second gradient model for microstructure media

The coupled local second gradient model is developed for enriched continuum including microstructure effects (Chambon et al., 2001a). This model was extended from monophasic to biphasic porous medium (solid and fluid) by Collin et al. (2006) to highlight the possible interaction of the fluid (liquid water) with the strain localisation process and with the internal length introduced by the model. The developments proposed by Collin et al. (2006) are recalled in this section. They account for a medium with incompressible solid grains, under saturated and isothermal conditions. The solid and fluid phases are considered as immiscible and phase changes, like evaporation and dissolution, are not taken into account.

As for classical continuum, the material is considered as a porous medium and the balance equations are based on averaging theories. The unknowns of the coupled problem are the macro-displacement u_i, the micro-deformation field υ_{ij} (or the micro-displacement field u_i^m by Eq. 3.38), and the pore water pressure p_w. An additional unknown field of Lagrange multipliers λ_{ij} will be added for the finite element method implementation.

3.3.1 Balance equations for classical poromechanics

The governing equations of a classical multiphasic porous medium, composed of solid particles and liquid water under unsaturated conditions, are recalled firstly. These equations have already been developed in section 2.4 in usual differential local form; however, a weak form is required for finite element formulation. The balance equations can be written for both phases, or for the mixture and one of the phases. The second way is chosen in the following developments and the equations are written in updated Lagrangian configuration. The gas pressure variation is not considered and, therefore, the gas mass balance equation is not expressed.

Balance of momentum of the mixture

This equation is obtained in a weak form by the virtual work principle (Germain, 1973). Within the scope of this principle, the forces and stresses are introduced by the virtual work they produce for a given class of virtual kinematics. The forces acting on the mechanical system are the external and internal forces, and, by equilibrium, the principle of virtual work states that the virtual work of all forces acting on a mechanical system is null for a given time and for any considered virtual kinematic field.

For the classical kinematic theory of first gradient, the virtual motion is defined with a kinematically admissible virtual (macro) displacement field u_i^* on a system with current configuration Ω. The virtual work involves u_i^* and its first derivative F_{ij}^*. The general notations a^* corresponds to the virtual quantity of any quantity a. The virtual work of internal forces reads, for any virtual quantities:

$$W_{int}^* = \int_\Omega w_{int}^* \, d\Omega = \int_\Omega \sigma_{ij} \; F_{ij}^* \, d\Omega = \int_\Omega \sigma_{ij} \; \varepsilon_{ij}^* \, d\Omega \tag{3.43}$$

where w_{int}^* is the virtual volume work of internal forces and σ_{ij} is the Cauchy total stress field. Due to the symmetric property of σ_{ij}, only the symmetric part ε_{ij}^* of the gradient F_{ij}^* is involved in this equation. The external forces are composed of the gravity volume force $G_i = \rho \; g_i$, which act on the whole domain Ω, and of the traction force $\bar{t}_i$, acting on a part Γ_t of the boundary Γ of Ω (Fig. 3.10). Assuming that the boundary Ω is regular, the virtual works of external volume and contact forces are given by:

$$W_{ext,v}^* = \int_\Omega G_i \; u_i^* \, d\Omega \tag{3.44}$$

$$W_{ext,c}^* = \int_{\Gamma_t} \bar{t}_i \; u_i^* \, d\Gamma \tag{3.45}$$

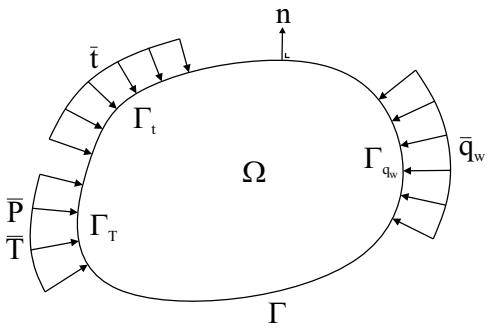

Fig. 3.10: Material system with current configuration Ω and boundary conditions for the second gradient model.

Applying the principle of virtual work leads to the weak form of the momentum balance equation:

$$W_{int}^* = W_{ext,v}^* + W_{ext,c}^* \tag{3.46}$$

$$\int_\Omega \sigma_{ij} \; \varepsilon_{ij}^* \, d\Omega = \int_\Omega \rho \; g_i \; u_i^* \, d\Omega + \int_{\Gamma_t} \bar{t}_i \; u_i^* \, d\Gamma \tag{3.47}$$

and because this principle holds for any u_i^*, the local equilibrium equations, i.e. the momentum balance equation and the boundary condition (Eqs. 2.3 and 2.103), are deduced inside the domain

Ω and for any point on the boundary Γ:

$$\frac{\partial \sigma_{ij}}{\partial x_j} + \rho \; g_i = 0 \tag{3.48}$$

$$\overline{t}_i = \sigma_{ij} \; n_j \tag{3.49}$$

The virtual work principle is thenceforward equivalent to the local equilibrium equations.

Furthermore, the mixture homogenised mass density is given by:

$$\rho = \rho_s \; (1 - \Phi) + \rho_w \; \Phi \tag{3.50}$$

and the effective stress is defined according to Terzaghi's postulate:

$$\sigma_{ij} = \sigma_{ij}^{'} + p_w \; \delta_{ij} \tag{3.51}$$

Water mass balance equation

The water mass balance equation is written, in a weak form, in a similar way as the momentum balance equation. A kinematically admissible virtual pore water pressure field p_w^* is considered and is involved, as well as its first derivative, in internal and external virtual quantities. The water mass balance equation reads:

$$\int\limits_{\Omega} \left(\dot{M}_w \; p_w^* - f_{w,i} \; \frac{\partial p_w^*}{\partial x_i} \right) d\Omega = \int\limits_{\Omega} Q_w \; p_w^* \; d\Omega - \int\limits_{\Gamma_{q_w}} \overline{q}_w \; p_w^* \; d\Gamma \tag{3.52}$$

where M_w is the water mass inside Ω, $f_{w,i}$ is the water mass flow, Q_w is a sink term of water mass, and $\overline{q}_w$ is the input water mass (positive for inflow) per unit area on a part Γ_{q_w} of Γ (Fig. 3.10). They are defined similarly to section 2.4 but for saturated conditions with $S_{r,w} = k_{r,w} = 1$ and for an isotropic intrinsic permeability:

$$M_w = \rho_w \; \Phi \; \Omega \tag{3.53}$$

$$f_{w,i} = -\rho_w \; \frac{k_w}{\mu_w} \; \left(\frac{\partial p_w}{\partial x_i} + \rho_w \; g_i \right) \tag{3.54}$$

The definitions of the phase density variations and of the porosity evolution are:

$$\frac{\dot{\rho}_w}{\rho_w} = \frac{\dot{p}_w}{\chi_w} \tag{3.55}$$

$$\dot{\rho}_s = 0 \tag{3.56}$$

$$\dot{\Phi} = (1 - \Phi) \, \frac{\dot{\Omega}}{\Omega} \tag{3.57}$$

The latter lead to the time derivative of the water mass per unit mixture volume:

$$\dot{M}_w = \rho_w \left(\frac{\dot{p}_w}{\chi_w} \; \Phi + \frac{\dot{\Omega}}{\Omega} \right) \tag{3.58}$$

Because Eq. 3.52 holds for any p_w^*, the local equilibrium equations, i.e. the liquid water mass balance equation and the hydraulic boundary condition, are deduced:

$$\dot{M}_w + \frac{\partial f_{w,i}}{\partial x_i} = Q_w \tag{3.59}$$

$$\overline{q}_w + f_{w,i} \; n_i = 0 \tag{3.60}$$

They correspond to Eqs. 2.12 and 2.104 but without considering the gaseous phase.

3.3.2 Balance equations for microstructure poromechanics

Local second gradient model for monophasic medium

The class of virtual kinematics introduced in the virtual work principle for classical kinematic theory can be extended in the framework of microstructure continuum theory, by adding a description of the microstructure kinematics to the classical displacement field. According to Eq. 3.38, the kinematics at microscale are described by a microkinematic gradient field υ_{ij}. With respect to classical continuum mechanics, additional terms are added in the internal virtual work of a given body (Germain, 1973). The following expression holds for any virtual quantities:

$$W^*_{int} = \int_\Omega \left(\sigma_{ij}\ F^*_{ij} - \tau_{ij}\ \overline{\varepsilon}^*_{ij} + \Sigma_{ijk}\ h^*_{ijk}\right) d\Omega \tag{3.61}$$

where $\overline{\varepsilon}^*_{ij}$ is the virtual relative deformation of the microstructure:

$$\overline{\varepsilon}^*_{ij} = F^*_{ij} - \upsilon^*_{ij} \tag{3.62}$$

τ_{ij} is an additional stress associated to the microstructure also called the microstress, $h^*_{ijk} = \frac{\partial \upsilon^*_{ij}}{\partial x_k}$ is the virtual micro second gradient, and Σ_{ijk} is the double stress dual of h^*_{ijk}, which needs an additional constitutive law introducing the internal length scale. The external virtual work can be defined as follows:

$$W^*_{ext} = \int_\Omega \rho\ g_i\ u^*_i\ d\Omega + \int_{\Gamma_\sigma} \left(\overline{t}_i\ u^*_i + \overline{P}_{ij}\ \upsilon^*_{ij}\right) d\Gamma \tag{3.63}$$

where $\overline{P}_{ij}$ is an additional external double surface traction acting on a part Γ_T of the boundary Γ (Fig. 3.10) and $\Gamma_\sigma = \{\Gamma_t \cup \Gamma_T\}$ regroups the classical and additional external solicitations. As previously, the virtual work principle assumes the equality between internal and external virtual works and leads to the weak form of the momentum balance equation:

$$\int_\Omega \left(\sigma_{ij}\ F^*_{ij} - \tau_{ij}\ \left(F^*_{ij} - \upsilon^*_{ij}\right) + \Sigma_{ijk}\ h^*_{ijk}\right) d\Omega = \int_\Omega \rho\ g_i\ u^*_i\ d\Omega + \int_{\Gamma_\sigma} \left(\overline{t}_i\ u^*_i + \overline{P}_{ij}\ \upsilon^*_{ij}\right) d\Gamma \tag{3.64}$$

The local equilibrium equations are formulated for the macro and the micro quantities; the local momentum balance equations are:

$$\frac{\partial \left(\sigma_{ij} - \tau_{ij}\right)}{\partial x_j} + \rho\ g_i = 0 \tag{3.65}$$

$$\frac{\partial \Sigma_{ijk}}{\partial x_k} - \tau_{ij} = 0 \tag{3.66}$$

and the boundary conditions are:

$$\overline{t}_i = \left(\sigma_{ij} - \tau_{ij}\right) n_j \tag{3.67}$$

$$\overline{P}_{ij} = \Sigma_{ijk}\ n_k \tag{3.68}$$

The boundary conditions for the mixture are also enriched with microstructure effects which leads to non-classical boundary conditions.

In the local second gradient model used in the following, a kinematic constraint is added in order to obtain a local second gradient continuum medium. No relative deformation of the microstructure is assumed $\overline{\varepsilon}_{ij} = 0$, meaning that the microkinematic gradient is equal to the macro-deformation:

$$\upsilon_{ij} = F_{ij} \tag{3.69}$$

As a consequence:

$$\upsilon_{ij}^{*} = F_{ij}^{*} \tag{3.70}$$

for the virtual fields. Finally, the principle of virtual work can be rewritten as follows:

$$\int_{\Omega} \left(\sigma_{ij} \ \frac{\partial u_i^*}{\partial x_j} + \Sigma_{ijk} \ \frac{\partial^2 u_i^*}{\partial x_j \partial x_k} \right) d\Omega = \int_{\Omega} \rho \ g_i \ u_i^* \ d\Omega + \int_{\Gamma_\sigma} \left(\bar{t}_i \ u_i^* + \overline{T}_i \ Du_i^* \right) d\Gamma \tag{3.71}$$

where $\overline{T}_i$ is the additional external double force per unit area on Γ_T (Fig. 3.10) and the notation Da denotes the normal derivative of any quantity a:

$$Da = \frac{\partial a}{\partial x_i} \ n_i \tag{3.72}$$

then:

$$Du_i^* = \frac{\partial u_i^*}{\partial x_j} \ n_j = F_{ij}^* \ n_j = \upsilon_{ij}^* \ n_j \tag{3.73}$$

The local momentum balance equation reads:

$$\frac{\partial \sigma_{ij}}{\partial x_j} - \frac{\partial^2 \Sigma_{ijk}}{\partial x_j \partial x_k} + \rho \ g_i = 0 \tag{3.74}$$

and the boundary conditions are:

$$\bar{t}_i = \sigma_{ij} \ n_j - n_k \ n_j \ D\Sigma_{ijk} - \frac{D\Sigma_{ijk}}{Dx_k} \ n_j - \frac{D\Sigma_{ijk}}{Dx_j} \ n_k + \frac{Dn_l}{Dx_l} \ \Sigma_{ijk} \ n_j \ n_k - \frac{Dn_j}{Dx_k} \ \Sigma_{ijk} \tag{3.75}$$

$$\overline{T}_i = \overline{P}_{ij} \ n_j = \Sigma_{ijk} \ n_j \ n_k \tag{3.76}$$

where $\frac{Da}{Dx_i}$ is the tangential derivative of any quantity a:

$$\frac{Da}{Dx_i} = \frac{\partial a}{\partial x_i} - \frac{\partial a}{\partial x_j} \ n_j \ n_i \tag{3.77}$$

The additional boundary condition on $\overline{T}_i$ allows to produce solutions with boundary layers (see section 3.4.2 and Collin et al. (2009a)).

The local second gradient possess the advantage that the constitutive equations remain local, with the stress fields σ_{ij} and Σ_{ijk} being local quantities. A second gradient extension can thenceforward be formulated for any classical model.

Coupled local second gradient model

The second gradient theory was extended from monophasic to biphasic medium by Collin et al. (2006). As for monophasic medium, microstructure effects have to be introduced in the balance equations of classical poromechanics. According to the previous assumptions, the momentum balance equation 3.71 remains valid provided ρ and $\sigma_{ij}^{'}$ are defined according to Eqs. 3.50 and 3.51.

Furthermore, it is assumed that the pore fluid does not have an influence at microscale; therefore, pore water pressure variations do not generate microkinematic gradient. Such additional hypothesis was formulated by Ehlers (Ehlers and Volk, 1998) on a Cosserat model for biphasic medium. Second gradient effects are only assumed for the solid phase and the water mass balance equation 3.52 of classical poromechanics is conserved. The governing equations of the coupled problem are therefore Eqs. 3.71 and 3.52.

As already mentioned for the classical poromechanics, the effect of water on the total stress is defined according to the effective stress postulate (Eq. 3.51) while on the contrary the double stress Σ_{ijk} is independent of the pore water pressure. The double stress is only related to the solid phase.

Second gradient constitutive equation

Similarly to classical media for which a constitutive equation linking $\tilde{\sigma}'_{ij}$ to the kinematic history has been defined (Eq. 2.66), an additional constitutive law has to be defined between the double stress and the microkinematics. The latter is assumed to be decoupled of the classical first gradient part and independent of the pore water pressure. However, only a little information is available on the relation existing between the double stress and the micro-deformation. A linear elastic mechanical law is chosen for simplicity reason with the purpose of introducing as few additional parameters as possible. It consists in an isotropic linear relationship involving five independent parameters derived by Mindlin (1965):

$$\tilde{\Sigma}_{ijk} = D_{ijklmn} \, \frac{\partial \dot{v}_{lm}}{\partial x_n} \tag{3.78}$$

giving the Jaumann double stress rate:

$$\tilde{\dot{\Sigma}}_{ijk} = \dot{\Sigma}_{ijk} + \Sigma_{ljk} \, \omega_{li} + \Sigma_{imk} \, \omega_{mj} + \Sigma_{ijp} \, \omega_{pk} \tag{3.79}$$

as a function of the micro second gradient rate $\dot{h}_{ijk}$. Because the physical meaning of the material parameters composing D_{ijklmn} is not well established, a simplified version introducing only one parameter has been proposed (Matsushima et al., 2002). For two-dimensional problems, it reads:

$$\begin{bmatrix} \tilde{\Sigma}_{111} \\ \tilde{\Sigma}_{112} \\ \tilde{\Sigma}_{121} \\ \tilde{\Sigma}_{122} \\ \tilde{\Sigma}_{211} \\ \tilde{\Sigma}_{212} \\ \tilde{\Sigma}_{221} \\ \tilde{\Sigma}_{222} \end{bmatrix} = D \begin{bmatrix} 1 & 0 & 0 & 0 & 0 & \frac{1}{2} & \frac{1}{2} & 0 \\ 0 & \frac{1}{2} & \frac{1}{2} & 0 & -\frac{1}{2} & 0 & 0 & \frac{1}{2} \\ 0 & \frac{1}{2} & \frac{1}{2} & 0 & -\frac{1}{2} & 0 & 0 & \frac{1}{2} \\ 0 & 0 & 0 & 1 & 0 & -\frac{1}{2} & -\frac{1}{2} & 0 \\ 0 & -\frac{1}{2} & -\frac{1}{2} & 0 & 1 & 0 & 0 & 0 \\ \frac{1}{2} & 0 & 0 & -\frac{1}{2} & 0 & \frac{1}{2} & \frac{1}{2} & 0 \\ \frac{1}{2} & 0 & 0 & -\frac{1}{2} & 0 & \frac{1}{2} & \frac{1}{2} & 0 \\ 0 & \frac{1}{2} & \frac{1}{2} & 0 & 0 & 0 & 0 & 1 \end{bmatrix} \begin{bmatrix} \frac{\partial \dot{v}_{11}}{\partial x_1} \\ \frac{\partial \dot{v}_{11}}{\partial x_2} \\ \frac{\partial \dot{v}_{12}}{\partial x_1} \\ \frac{\partial \dot{v}_{12}}{\partial x_2} \\ \frac{\partial \dot{v}_{21}}{\partial x_1} \\ \frac{\partial \dot{v}_{21}}{\partial x_2} \\ \frac{\partial \dot{v}_{22}}{\partial x_1} \\ \frac{\partial \dot{v}_{22}}{\partial x_2} \end{bmatrix} \tag{3.80}$$

The constitutive elastic parameter D represents the physical microstructure and the internal length scale relevant for the shear band width is related to this parameter (Chambon et al., 1998; Kotronis et al., 2007; Collin et al., 2009a).

For one-dimensional problems, the only components of v_{ij} and h_{ijk} different from zero are $v_{11} = \frac{\partial u_1}{\partial x_1}$ and $h_{111} = \frac{\partial^2 u_1}{\partial x_1^2}$. Similarly, σ_{11} and Σ_{111} are defined as the only components of the stress fields that dispose of non-zero space gradient. The previous relation simplifies in:

$$\tilde{\Sigma} = D \, \frac{\partial^2 \dot{u}}{\partial x^2} \tag{3.81}$$

Bifurcation criterion for second gradient model

A bifurcation analysis applied to the second gradient model is proposed by Bésuelle et al. (2006a). The authors indicate that the bifurcation criterion of the second gradient model is, as for classical model, a necessary but not sufficient condition for the localisation onset and that it is met after the bifurcation criterion of the classical model. Thus, the analysis of bifurcation reduces to an analysis on the classical part of the constitutive model.

3.3.3 Coupled finite element formulation

Numerical implementation

The virtual work formulation of second gradient models can be implemented in a finite element code. To implement the momentum balance equation of Eq. 3.71, the displacement field has to

be a continuously differentiable function because second order derivatives of the displacement field are involved (Zervos et al., 2001b). To fulfil this requirement and avoid such function, the kinematic restrictions $v_{ij} = F_{ij}$ and $v^*_{ij} = F^*_{ij}$ are introduced in the momentum balance equation through a field of Lagrange multipliers λ_{ij} related to a weak form of the constraint (Chambon et al., 1998). The field equations of the numerical coupled problem are:

$$\int_{\Omega^t} \left(\sigma^t_{ij} \, \frac{\partial u^*_i}{\partial x^t_j} + \Sigma^t_{ijk} \, \frac{\partial v^*_{ij}}{\partial x^t_k} \right) d\Omega^t - \int_{\Omega^t} \lambda^t_{ij} \left(\frac{\partial u^*_i}{\partial x^t_j} - v^*_{ij} \right) d\Omega^t = \int_{\Omega^t} \rho^t \, g_i \, u^*_i \, d\Omega^t + \int_{\Gamma^t_\sigma} \left(\overline{t}^t_i \, u^*_i + \overline{T}^t_i \, v^*_{ik} \, n^t_k \right) d\Gamma^t \tag{3.82}$$

$$\int_{\Omega^t} \lambda^*_{ij} \left(\frac{\partial u^t_i}{\partial x^t_j} - v^t_{ij} \right) d\Omega^t = 0 \tag{3.83}$$

$$\int_{\Omega^t} \left(\dot{M}^t_w \, p^*_w - f^t_{w,i} \, \frac{\partial p^*_w}{\partial x^t_i} \right) d\Omega^t = \int_{\Omega^t} Q^t_w \, p^*_w \, d\Omega^t - \int_{\Gamma^t_{q_w}} \overline{q}^t_w \, p^*_w \, d\Gamma^t \tag{3.84}$$

where the notation a^t corresponds to the current value of any quantity a for a given time t. For boundary conditions problems, the virtual quantities included in the above equations depend on the boundary conditions history. Thus, the governing equations and the constitutive equations have to hold at any time t.

Linearisation of the field equations

Solving the loading process of a boundary conditions problem consists in determining the unknown fields u_i, v_{ij}, λ_{ij}, and p_w for which the equilibrium equations 3.82, 3.83, and 3.84 are valid. Since this system of non-linear equations is *a priori* not verified for any instant t, the problem is numerically solved by iterative procedure. It involves a time discretisation over finite time steps Δt:

$$\tau = t + \Delta t \tag{3.85}$$

and an implicit scheme of finite differences for the rate of any quantity a:

$$\dot{a}^\tau = \frac{a^\tau - a^t}{\Delta t} \tag{3.86}$$

A full Newton-Raphson method is used to find a solution for the new fields u_i, v_{ij}, λ_{ij}, and p_w at the end of each time step which is in equilibrium with the boundary conditions.

Following the approach of Borja and Alarcón (1995), the method aims to define a linear auxiliary problem deriving from the continuum one. A first configuration Ω^t in equilibrium with the boundary conditions at a given time t is assumed to be known and another Ω^τ in equilibrium at the end of the time step $\tau = t + \Delta t$ has to be found. The aim of the iterative numerical procedure is to determine this new configuration at the end of the time step. Firstly, a configuration which is close to the solution but not at equilibrium is guessed and denoted as $\Omega^{\tau 1}$. Both configurations at time t and $\tau 1$ are assumed to be known and non-equilibrium forces for the three considered equations, i.e. the residuals $\Delta^{\tau 1}_1$, $\Delta^{\tau 1}_2$, and $\Delta^{\tau 1}_3$, are defined. The objective is to find another configuration $\Omega^{\tau 2}$ close to $\Omega^{\tau 1}$ for which the non-equilibrium forces vanish. To obtain the linear auxiliary problem, the field equations for $\Omega^{\tau 2}$ are subtracted from the field equations in configuration $\Omega^{\tau 1}$, after being rewritten in configuration $\Omega^{\tau 1}$ by using the Jacobian matrix of the transformation between the two configurations:

$$\overline{F}_{ij} = \frac{\partial x^{\tau 2}_i}{\partial x^{\tau 1}_j} \tag{3.87}$$

and its Jacobian determinant:

$$det(F) = \left| \frac{\partial x_i^{\tau 2}}{\partial x_j^{\tau 1}} \right| \tag{3.88}$$

Assuming that g_i, $\overline{t}_i$, $\overline{q}_w$, and Q_w are independent of the different unknown fields (displacement and pore water pressure), and that $\overline{T}_i$ vanishes give:

$$\begin{aligned}
&\int_{\Omega^{\tau 1}} \frac{\partial u_i^*}{\partial x_l^{\tau 1}} \left(\sigma_{ij}^{\tau 2} \, \frac{\partial x_l^{\tau 1}}{\partial x_j^{\tau 2}} \, det(F) - \sigma_{il}^{\tau 1} \right) + \frac{\partial \upsilon_{ij}^*}{\partial x_l^{\tau 1}} \left(\Sigma_{ijk}^{\tau 2} \, \frac{\partial x_l^{\tau 1}}{\partial x_k^{\tau 2}} \, det(F) - \Sigma_{ijl}^{\tau 1} \right) d\Omega^{\tau 1} \\
&- \int_{\Omega^{\tau 1}} \frac{\partial u_i^*}{\partial x_l^{\tau 1}} \left(\lambda_{ij}^{\tau 2} \, \frac{\partial x_l^{\tau 1}}{\partial x_j^{\tau 2}} \, det(F) - \lambda_{il}^{\tau 1} \right) - \upsilon_{ij}^* \left(\lambda_{ij}^{\tau 2} \, det(F) - \lambda_{ij}^{\tau 1} \right) d\Omega^{\tau 1} \\
&- \int_{\Omega^{\tau 1}} u_i^* \left(\rho^{\tau 2} \, det(F) - \rho^{\tau 1} \right) g_i \, d\Omega^{\tau 1} = -\Delta_1^{\tau 1}
\end{aligned} \tag{3.89}$$

$$\int_{\Omega^{\tau 1}} \lambda_{ij}^* \left(\left(\frac{\partial u_i^{\tau 2}}{\partial x_k^{\tau 1}} \, \frac{\partial x_k^{\tau 1}}{\partial x_j^{\tau 2}} \, det(F) - \frac{\partial u_i^{\tau 1}}{\partial x_j^{\tau 1}} \right) - \left(\upsilon_{ij}^{\tau 2} \, det(F) - \upsilon_{ij}^{\tau 1} \right) \right) d\Omega^{\tau 1} = -\Delta_2^{\tau 1} \tag{3.90}$$

$$\int_{\Omega^{\tau 1}} p_w^* \left(\dot{M}_w^{\tau 2} \, det(F) - \dot{M}_w^{\tau 1} \right) - \frac{\partial p_w^*}{\partial x_l^{\tau 1}} \left(f_{w,i}^{\tau 2} \, \frac{\partial x_l^{\tau 1}}{\partial x_i^{\tau 2}} \, det(F) - f_{w,l}^{\tau 1} \right) d\Omega^{\tau 1} = -\Delta_3^{\tau 1} \tag{3.91}$$

By making the two configurations tend towards each other, the variations between them can be defined for any quantity a as:

$$da^{\tau 1} = a^{\tau 2} - a^{\tau 1} \tag{3.92}$$

The balance equations can be rewritten by taking into account these variations. The complete development of the linearisation of the field equation system and of the resulting linear auxiliary problem is exposed by Collin et al. (2006).

Spatial discretisation

In finite element methods, each continuum body is discretised by finite elements and the above field equations are spatially discretised for each of them. For the second gradient model, the discretisation is realised by using two-dimensional plane-strain isoparametric finite elements. These elements are composed of eight nodes for the displacement field u_i and the pore water pressure p_w, four nodes for the microkinematic gradient field υ_{ij}, and one node for the Lagrange multiplier field λ_{ij} (Fig. 3.11). Quadratic serendipity shape functions (Zienkiewicz and Taylor, 2000) are used for u_i and p_w interpolations whereas linear shape functions are used for υ_{ij} and λ_{ij} is assumed constant.

The balance equations of the coupled finite element problem (linear auxiliary problem) have to be rewritten in matricial form to define the local stiffness matrix of an element:

$$\int_{\Omega^{\tau 1}} \left[U_{(x_1,x_2)}^{*,\tau 1} \right]^T \left[E^{\tau 1} \right] \left[dU_{(x_1,x_2)}^{\tau 1} \right] d\Omega^{\tau 1} = -\Delta_1^{\tau 1} - \Delta_2^{\tau 1} - \Delta_3^{\tau 1} \tag{3.93}$$

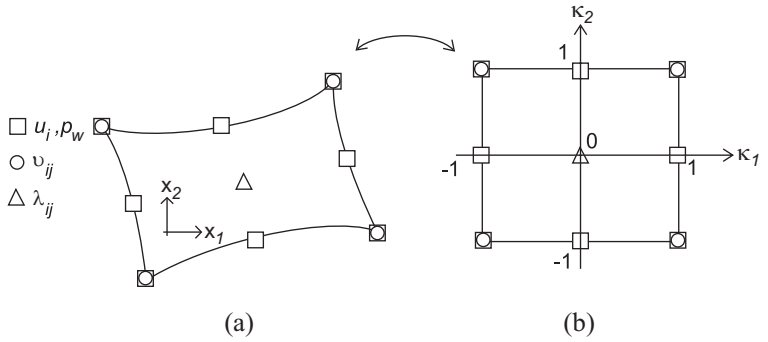

Fig. 3.11: Finite element used for the spatial discretisation of the coupled local second gradient model: (a) current quadrilateral element and (b) parent element (Collin et al., 2006).

where $\left[dU^{\tau 1}_{(x_1,x_2)}\right]$ is the vector of the unknown increments of nodal variables in the current element configuration:

$$\left[dU^{\tau 1}_{(x_1,x_2)}\right]_{25\times 1} = \left[\frac{\partial du_1^{\tau 1}}{\partial x_1^{\tau 1}}\ \frac{\partial du_1^{\tau 1}}{\partial x_2^{\tau 1}}\ \frac{\partial du_2^{\tau 1}}{\partial x_1^{\tau 1}}\ \frac{\partial du_2^{\tau 1}}{\partial x_2^{\tau 1}}\ du_1^{\tau 1}\ du_2^{\tau 1}\ \frac{\partial dp_w^{\tau 1}}{\partial x_1^{\tau 1}}\ \frac{\partial dp_w^{\tau 1}}{\partial x_2^{\tau 1}}\ dp_w^{\tau 1}\ \frac{\partial d\upsilon_{11}^{\tau 1}}{\partial x_1^{\tau 1}}\ \frac{\partial d\upsilon_{11}^{\tau 1}}{\partial x_2^{\tau 2}}\right.$$
$$\left.\frac{\partial d\upsilon_{12}^{\tau 1}}{\partial x_1^{\tau 1}}\ \ldots\ \frac{\partial d\upsilon_{22}^{\tau 1}}{\partial x_2^{\tau 1}}\ d\upsilon_{11}^{\tau 1}\ d\upsilon_{12}^{\tau 1}\ d\upsilon_{21}^{\tau 1}\ d\upsilon_{22}^{\tau 1}\ d\lambda_{11}^{\tau 1}\ d\lambda_{12}^{\tau 1}\ d\lambda_{21}^{\tau 1}\ d\lambda_{22}^{\tau 1}\right]^T \tag{3.94}$$

$\left[U^{*,\tau 1}_{(x_1,x_2)}\right]$ is a vector having the same structure with the corresponding virtual quantities:

$$\left[U^{*,\tau 1}_{(x_1,x_2)}\right]_{1\times 25} = \left[\frac{\partial u_1^*}{\partial x_1^{\tau 1}}\ \frac{\partial u_1^*}{\partial x_2^{\tau 1}}\ \frac{\partial u_2^*}{\partial x_1^{\tau 1}}\ \frac{\partial u_2^*}{\partial x_2^{\tau 1}}\ u_1^*\ u_2^*\ \frac{\partial p_w^*}{\partial x_1^{\tau 1}}\ \frac{\partial p_w^*}{\partial x_2^{\tau 1}}\ p_w^*\ \frac{\partial \upsilon_{11}^*}{\partial x_1^{\tau 1}}\ \frac{\partial \upsilon_{11}^*}{\partial x_2^{\tau 2}}\right.$$
$$\left.\frac{\partial \upsilon_{12}^*}{\partial x_1^{\tau 1}}\ \ldots\ \frac{\partial \upsilon_{22}^*}{\partial x_2^{\tau 1}}\ \upsilon_{11}^*\ \upsilon_{12}^*\ \upsilon_{21}^*\ \upsilon_{22}^*\ \lambda_{11}^*\ \lambda_{12}^*\ \lambda_{21}^*\ \lambda_{22}^*\right] \tag{3.95}$$

and $\left[E^{\tau 1}\right]$ is the current element stiffness (tangent) matrix defined as follows:

$$\left[E^{\tau 1}\right]_{25\times 25} = \begin{bmatrix} E^{\tau 1}_{1_{4\times 4}} & 0_{4\times 2} & K^{\tau 1}_{WM_{4\times 3}} & 0_{4\times 8} & 0_{4\times 4} & -I_{4\times 4} \\ G^{\tau 1}_{1_{2\times 4}} & 0_{2\times 2} & G^{\tau 1}_{2_{2\times 3}} & 0_{2\times 8} & 0_{2\times 4} & 0_{2\times 4} \\ K^{\tau 1}_{MW_{3\times 4}} & 0_{3\times 2} & K^{\tau 1}_{WW_{3\times 3}} & 0_{3\times 8} & 0_{3\times 4} & 0_{3\times 4} \\ E^{\tau 1}_{2_{8\times 4}} & 0_{8\times 2} & 0_{8\times 3} & D^{\tau 1}_{8\times 8} & 0_{8\times 4} & 0_{8\times 4} \\ E^{\tau 1}_{3_{4\times 4}} & 0_{4\times 2} & 0_{4\times 3} & 0_{4\times 8} & 0_{4\times 4} & I_{4\times 4} \\ E^{\tau 1}_{4_{4\times 4}} & 0_{4\times 2} & 0_{4\times 3} & 0_{4\times 8} & -I_{4\times 4} & 0_{4\times 4} \end{bmatrix} \tag{3.96}$$

The matrices $\left[E^{\tau 1}_1\right]$, $\left[E^{\tau 1}_2\right]$, $\left[E^{\tau 1}_3\right]$, $\left[E^{\tau 1}_4\right]$, and $\left[D^{\tau 1}\right]$ are the same as the ones used in the local second gradient model for monophasic medium by Chambon and Moullet (2004) ($\left[D^{\tau 1}\right] = D_{ijklmn}$ in Eqs. 3.78 and 3.80). $\left[K^{\tau 1}_{WW}\right]$ is the classical stiffness matrix of a flow problem, $\left[K^{\tau 1}_{MW}\right]$ and $\left[K^{\tau 1}_{WM}\right]$ are matrices of the coupling between the flow and the mechanical problems detailed by Collin et al. (2006). Moreover, $\left[G^{\tau 1}_1\right]$ and $\left[G^{\tau 1}_2\right]$ are related to the contribution of gravity volume force.

The finite element spatial discretisation of the linear auxiliary problem is introduced in Eq. 3.93 by using transformation matrices $\left[T^{\tau 1}\right]$ and $[B]$ that connect the current element vector

$\left[dU^{\tau 1}_{(x_1,x_2)}\right]$ to the parent element vector $\left[dU^{\tau 1}_{(\kappa_1,\kappa_2)}\right]$ and to the nodal variables $\left[dU^{\tau 1}_{Node}\right]$:

$$\left[dU^{\tau 1}_{(x_1,x_2)}\right] = \left[T^{\tau 1}\right]\left[dU^{\tau 1}_{(\kappa_1,\kappa_2)}\right] = \left[T^{\tau 1}\right][B]\left[dU^{\tau 1}_{Node}\right] \tag{3.97}$$

The matrices $[B]$ and $\left[T^{\tau 1}\right]$ contain the interpolation functions and their derivatives. Moreover, the vector $\left[U^{*,\tau 1}_{(x_1,x_2)}\right]$ is related to $\left[U^{*,\tau 1}_{Node}\right]$ in the same manner.

The integration in Eq. 3.93 can be expressed for each parent element as follows:

$$\int_{\Omega^{\tau 1}} \left[U^{*,\tau 1}_{(x_1,x_2)}\right]^T \left[E^{\tau 1}\right]\left[dU^{\tau 1}_{(x_1,x_2)}\right] d\Omega^{\tau 1} = \left[U^{*,\tau 1}_{Node}\right]^T \left[k^{\tau 1}\right]\left[dU^{\tau 1}_{Node}\right] \tag{3.98}$$

where $\left[k^{\tau 1}\right]$ is the local element stiffness matrix:

$$\left[k^{\tau 1}\right] = \int_{-1}^{1}\int_{-1}^{1} [B]^T \left[T^{\tau 1}\right]^T \left[E^{\tau 1}\right]\left[T^{\tau 1}\right][B]\, det(J^{\tau 1})\, d\kappa_1\, d\kappa_2 \tag{3.99}$$

with $det(J^{\tau 1})$ the determinant of the Jacobian matrix of the transformation between the parent (κ_1, κ_2) and the current (x_1, x_2) elements:

$$det(J^{\tau 1}) = \left|\frac{\partial x_i^{\tau 1}}{\partial \kappa_j}\right| \tag{3.100}$$

The residual terms are also computed locally for each element and define the elementary out of balance force vector $\left[f^{\tau 1}_{OB}\right]$:

$$-\Delta_1^{\tau 1} - \Delta_2^{\tau 1} - \Delta_3^{\tau 1} = \left[U^{*,\tau 1}_{Node}\right]^T \left[f^{\tau 1}_{OB}\right] \tag{3.101}$$

Global solution

Once the elementary stiffness matrices and out of balance force vectors are computed, they are assembled to obtain the global stiffness matrix $\left[K^{\tau 1}\right]$ and the global out of balance force vector $\left[F^{\tau 1}_{OB}\right]$ of the whole continuum. The linear auxiliary system is solved by computing:

$$\left[K^{\tau 1}\right]\left[\delta U^{\tau 1}_{Node}\right] = -\left[F^{\tau 1}_{OB}\right] \tag{3.102}$$

where $\left[\delta U^{\tau 1}_{Node}\right]$ is the global correction vector of the nodal degrees of freedom. The current configuration is actualised by adding the corrections to their respective current values. The new current configuration is closer to the well-balanced configuration and its equilibrium is checked, leading to a new iteration or to the end of the loading step of the iterative procedure.

3.4 Applications

The following examples demonstrate the interest of using the presented theoretical tools and point out their limitations. Three typical problems are studied: a one-dimensional bar in traction, a two-dimensional thick-walled cylinder under radial stress, and a two-dimensional small-scale material specimen subjected to plane-strain compression. These problems allow understanding how the internal length scale is introduced in second grade model. When a strain-softening constitutive law is used for the first gradient part, they also permit to analyse the regularisation properties of the coupled local second gradient model for the strain localisation process.

3.4.1 One-dimensional bar in traction

A simple example of a one-dimensional bar in traction was already discussed in section 3.2.1 for classical monophasic medium. It has been shown that the problem is ill-posed due to strain softening and that physically inadmissible failure could occur if elastic unloading is too important.

A second grade model is used hereafter to find analytical solutions of the boundary value problem corresponding to the uniaxial traction of a bar. A one-dimensional second grade elasto-plastic model is used by Chambon et al. (1998) and is illustrated in Fig. 3.12. It is composed of two parts, the first and second grade, defined with two internal stress fields σ and Σ being the usual normal stress in the bar and the second order stress, respectively. The model assumes no coupling between the first and second part.

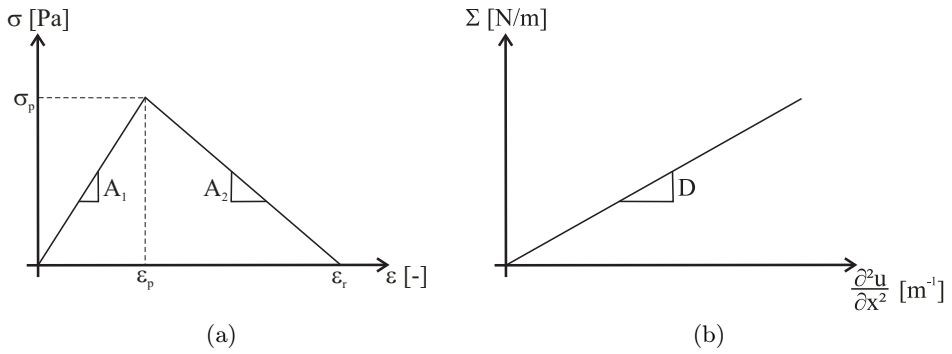

Fig. 3.12: Constitutive model for a bar in traction: (a) first grade and (b) second grade parts.

As previously (Fig. 3.3), the first grade constitutive equation is bilinear and involves first derivatives of the displacement field with respect to the space variable x, which corresponds to the strain under small strain assumption $\varepsilon = \frac{\partial u}{\partial x}$. The two linear parts are characterised by elastic and softening plastic domains, the latter allows strain localisation. It is given in incremental form under small strain assumption by:

$$\begin{array}{ll} \textit{Elastic}: & 0 < \varepsilon < \varepsilon_p \ , \quad \dot{\sigma} = A_1 \ \dot{\varepsilon} \\ \textit{Plastic}: & \varepsilon_p < \varepsilon < \varepsilon_r \ , \quad \dot{\sigma} = A_2 \ \dot{\varepsilon} \end{array} \tag{3.103}$$

where A_1 is the elastic slope, A_2 is the softening slope which is negative, ε_p is the limit between the elastic and the softening plastic domains, and ε_r reads:

$$\varepsilon_r = \varepsilon_p \ \left(1 - \frac{A_1}{A_2}\right) \tag{3.104}$$

The second grade constitutive equation is a linear elastic law involving second derivatives $\frac{\partial^2 u}{\partial x^2}$ and that is independent of the first grade term:

$$\dot{\Sigma} = D \ \frac{\partial^2 \dot{u}}{\partial x^2} \tag{3.105}$$

It corresponds to Eq. 3.81 for small strain assumption.

Based on the virtual power method (Germain, 1973), the balance equation of the one-dimensional second grade medium is:

$$\frac{\partial \sigma}{\partial x} - \frac{\partial^2 \Sigma}{\partial x^2} = 0 \tag{3.106}$$

It can also be obtained from Eq. 3.74 by neglecting the gravity volume force. Integrating this equilibrium equation and using Eqs. 3.103 and 3.105 lead to the general differential equation:

$$A_{1/2} \ u - D \ \frac{\partial^2 u}{\partial x^2} = N_{1/2} \ x + A_{1/2} \ \mathcal{K} \tag{3.107}$$

which gives the following analytical solutions by integration:

$$Elastic: \quad u = \underbrace{\frac{N_1}{A_1}\, x + \mathcal{K}}_{Classical} + \underbrace{\overline{\mathcal{K}}\; cosh(\varpi_1\, x) + \overline{\overline{\mathcal{K}}}\; sinh(\varpi_1\, x)}_{Microstructure}, \quad \varpi_1^2 = \tfrac{A_1}{D} > 0 \tag{3.108}$$

$$Plastic: \quad u = \underbrace{\frac{N_2}{A_2}\, x + \mathcal{K}}_{Classical} + \underbrace{\overline{\mathcal{K}}\; cos(\varpi_2\, x) + \overline{\overline{\mathcal{K}}}\; sin(\varpi_2\, x)}_{Microstructure}, \quad -\varpi_2^2 = \tfrac{A_2}{D} < 0 \tag{3.109}$$

where no solutions are considered for $\varepsilon > \varepsilon_r$; $\mathcal{K}$, $\overline{\mathcal{K}}$, and $\overline{\overline{\mathcal{K}}}$ are constants for a given part of the bar, i.e. for a given elastic or plastic solution; the normal stress N_1 is constant along the bar:

$$N_1 = \sigma - \frac{\partial \Sigma}{\partial x} \tag{3.110}$$

and N_2 corresponds to:

$$N_2 = N_1 + \varepsilon_p\,(A_2 - A_1) \tag{3.111}$$

Moreover, the classical solution and the contribution of the microstructure are clearly evidenced.

Particular solutions are studied by Chambon et al. (1998) for the considered problem. For the boundary conditions, a displacement is imposed at one end while the other end is fixed (Fig. 3.3 (a)) and additional limits conditions are necessary for the second grade part with the double stresses imposed equal to zero on both bar ends:

$$\begin{array}{ll} x = 0: & u = 0, \quad \Sigma = 0 \\ x = L: & u = U, \quad \Sigma = 0 \end{array} \tag{3.112}$$

As long as the loading implies an average strain in the bar U/L smaller than ε_p, the strain remains homogeneous all along the bar. If the average strain reaches ε_p (bifurcation point) and tends to exceed it, then softening plastic loading or elastic unloading are both possible, leading to non-unique solutions. For this case ($U/L > \varepsilon_p$), the bar can be divided in hard zones with $\varepsilon < \varepsilon_p$ corresponding to elastic unloading and soft zones with $\varepsilon > \varepsilon_p$ corresponding to localisation (dilation) bands under softening plastic loading. Each solution is given either by Eq. 3.108 or by Eq. 3.109 and the complete solution is an assembly of the unloading and loading parts. Different solutions that correspond to various number and positions of the localisation bands are possible. The finite number of solutions depends on the material parameters and on the bar length. For instance, a general case of $2n+1$ parts alternately hard and soft with whether both soft or both hard outer sides has a localisation bands length given by:

$$tanh\left(\varpi_1\left(\frac{L}{2n} - \frac{L_s}{2}\right)\right) = -\sqrt{-\frac{A_1}{A_2}}\; tan\left(\varpi_2 \frac{L_s}{2}\right) \tag{3.113}$$

where L is the length of the bar:

$$L = n\,(L_h + L_s) \tag{3.114}$$

L_s is the length of each inner soft part corresponding to the strain localisation band width, and L_h is the length of each inner hard part. The outer parts are half the size of the inner ones. An example of possible solutions is illustrated in Fig. 3.13 for a given set of material parameters. Four different post-peak solutions are available: a homogeneous one (solution 1) and three localised solutions (solutions 2, 3, and 4) having different patterns. The non-uniqueness of the solution to this second grade boundary value problem is clearly visible.

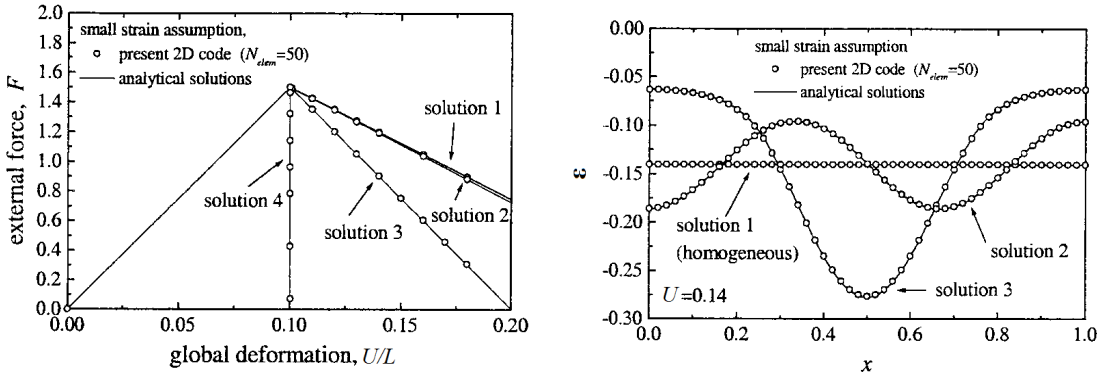

(a) (b)

Fig. 3.13: Global behaviour of a bar in traction: (a) global reaction F as a function of the global deformation U/L and (b) strain ε as a function of the coordinate x (Matsushima et al., 2002).

Furthermore, a wavelength is implicitly defined by the second gradient approach from Eq. 3.109 for a soft solution ($\varepsilon > \varepsilon_p$):

$$\overline{\lambda} = \frac{2\pi}{\varpi_2} = 2\pi \sqrt{-\frac{D}{A_2}} \tag{3.115}$$

where:

$$\varpi_2^{-1} = \sqrt{-\frac{D}{A_2}} \tag{3.116}$$

can be considered as the internal length scale of the softening loading regime. It is an indicator of the localisation band width but does not provide its exact value because it corresponds to the period of only the soft part (Kotronis et al., 2008). Similarly, a second internal length is implicitly defined from Eq. 3.108 for a hard solution ($\varepsilon < \varepsilon_p$):

$$\varpi_1^{-1} = \sqrt{\frac{D}{A_1}} \tag{3.117}$$

and corresponds to the unloading regime of the first gradient part. The solution L_s of Eq. 3.113 (and of other possible solutions) remains constant as long as the modulus ratios D/A_1 and D/A_2 remain constant. This implies that the strain localisation is correctly regularised for the considered one-dimensional problem.

Numerical solutions of this problem are also obtained with small or large strain finite elements analyses (Matsushima et al., 2000, 2002). As illustrated in Fig. 3.13, the results correspond to the above analytical solution. Moreover, the mesh size independence is proved provided that a sufficiently high number of elements is used.

3.4.2 Two-dimensional thick-walled cylinder under radial stress

Analytical axisymmetric solutions of a thick-walled cylinder problem (hollow cylinder) are proposed by Collin et al. (2009a) for a media enhanced with microstructure and involving second gradient model. The thick-walled cylinder is represented in Fig. 3.14 in Cartesian and cylindrical coordinates (r, θ, z) with orthonormal basis (e_r, e_θ, e_z). More details on strain gradient theory for orthogonal curvilinear coordinates are available in Zhao and Pedroso (2008). The material domain is comprised between two coaxial cylinders with radii R^{int} and R^{ext} and can be subjected to internal or external pressures. Only radial displacement u_r depending on r are considered for this boundary value problem.

Isotropic linear elastic laws are used for both the classical and the second gradient parts of the model (Eqs. 2.76 and 3.80). The second gradient law remains valid for any system of orthogonal

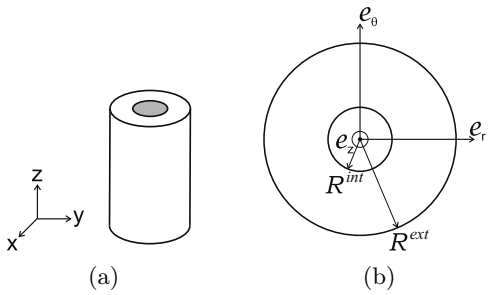

Fig. 3.14: Definition of the thick-walled cylinder problem in (a) Cartesian and (b) cylindrical coordinates (Collin et al., 2009a).

coordinates, including the cylindrical ones. It is noteworthy to mention that the use of a linear elastic law, without damage or strain softening, for the first gradient part of the model prevents strain localisation. Nonetheless, microstructure effects can still be generated in elastic solutions.

The balance equation of the problem is obtained by expressing Eq. 3.74 in cylindrical coordinates and by neglecting the gravity volume force:

$$\frac{\partial\left(r\ \sigma_{rr}\right)}{\partial r}-\sigma_{\theta\theta}+\frac{1}{r}\frac{\partial\left(r\ \left(\Sigma_{\theta\theta r}+\Sigma_{\theta r\theta}+\Sigma_{r\theta\theta}\right)\right)}{\partial r}-\frac{\partial^2\left(r\ \Sigma_{rrr}\right)}{\partial r^2}=0 \tag{3.118}$$

The constitutive equations of both stress fields can be included in this expression. It leads to the ordinary differential equation:

$$\frac{\partial}{\partial r}\left(\frac{1}{r}\frac{\partial\left(r\ u_r\right)}{\partial r}-\varpi_3^{-2}\frac{1}{r}\frac{\partial}{\partial r}\left(r\ \frac{\partial}{\partial r}\left(\frac{1}{r}\frac{\partial\left(r\ u_r\right)}{\partial r}\right)\right)\right)=0 \tag{3.119}$$

which is a fourth order equation for u_r where ϖ_3^{-1} is an internal length scale that governs the material behaviour for the thick-walled problem:

$$\varpi_3^{-1}=\sqrt{\frac{D}{M}} \tag{3.120}$$

The expression of Eq. 3.119 is general and involves only one elastic parameter for both first and second gradient parts, M and D, with:

$$M=\frac{E\ (1-\nu)}{(1+\nu)(1-2\nu)} \tag{3.121}$$

being the elastic P-wave modulus. The problem solution is obtained by integration:

$$u_r=\underbrace{c_1\ r+\frac{c_2}{r}}_{Classical}+\underbrace{c_3\ B^I\left(1,r\varpi_3\right)+c_4\ B^K\left(1,r\varpi_3\right)}_{Microstructure} \tag{3.122}$$

where $B^I(1,r\varpi_3)$ and $B^K(1,r\varpi_3)$ are the modified Bessel functions (Abramowitz and Stegun, 1972) and c_i are constants.

Particular solutions can be found for prescribed boundary conditions at the inner or outer boundaries. Collin et al. (2009a) mostly studied two cases to highlight the effect of boundary conditions for the double forces: firstly, a natural boundary condition without double forces, and secondly a non-zero condition. The first condition with $\overline{T}_r=0$ on both boundaries implies that the microstructure has no effect on the elastic solution because the constants c_3 and c_4 cancel. The solution therefore corresponds to a classical elastic medium. To exhibit effects of the microstructure, the more general isotropic linear relation for the second gradient law from

(Mindlin, 1965) must be used with the tensor D_{ijklmn} in Eq. 3.78 defined with five parameters. On the other hand, microstructure effects are generated for the second condition with $\overline{T}_r \neq 0$ and the solution depends on the internal length scale ϖ_3^{-1}. The imposed double stresses have an influence on the macrostresses that is more pronounced close to the boundary with an area of influence which decreases with decreasing internal length scale. This clearly exhibit a boundary layer effect.

Analytical solution for softening elastoplasticity is not developed by Collin et al. (2009a); thus, the analysis of strain localisation is not performed for the current problem. However, hollow cylinder tests have been numerically reproduced with finite element method and similar enhanced model to exhibit strain localisation pattern during the drilling (François et al., 2014). The mesh-independence and the non-uniqueness of the solution have also been investigated for borehole drilling by Sieffert et al. (2009) and Marinelli et al. (2014).

3.4.3 Two-dimensional specimen under compression

After the previous analytical solutions of simple problems, finite element modelling of two-dimensional plane-strain compression tests is considered. These tests have been widely reproduced on small-scale specimens to emphasise the strain localisation effects.

Among various authors, the results obtained by Collin et al. (2009b) for a uniaxial compression are principally developed hereafter. A sketch of the boundary value problem in plane-strain state is illustrated in Fig. 3.15. The vertical displacement u_a of the sample upper surface (smooth and rigid boundary) is progressively increased during the test with a constant loading strain rate to model the vertical compression. The vertical displacement of the bottom surface is blocked (rigid boundary) and the displacement of the central node is blocked in both directions to avoid rigid body displacement.

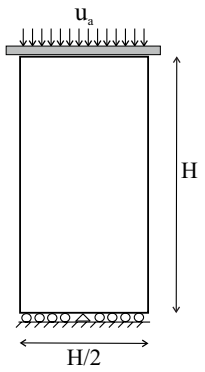

Fig. 3.15: Sketch of the plane-strain compression test.

Classical medium

Mechanical modelling are performed for classical medium without regularisation method. The used first gradient constitutive law is an elastoplastic strain-softening model similar to the one described in section 2.4.5. Some differences are nevertheless considered: an associated softening plasticity ($\varphi = \psi$, $F^p = G^p$), a Drucker-Prager yield criterion (without dependence on the Lode angle), no hardening of the friction angle, and a different cohesion softening function (Collin et al., 2009b).

A homogeneous response of the specimen is studied firstly. The global response is detailed in Fig. 3.16 (a) where one can observe a first linear elastic behaviour, then a non-linear plastic behaviour before peak stress including cohesion softening, and finally a plastic behaviour with decrease of the global load response. As discussed in section 3.2.1, the Rice criterion is relevant

for a single-mechanism classical elastoplastic model such as the studied one and the solution of Eq. 3.12 gives the orientation of the first possible shear band occurrence. The Rice criterion $det(\wedge_{jk})$ evolution is presented during the increasing loading history in Fig. 3.16 (b) as a function of $tan\Theta$, Θ being the orientation of the shear band normal with the loading vertical axis, i.e. the shear band orientation with the horizontal direction. The criterion is positive as long as the behaviour is elastic and even for elastoplastic loading until the bifurcation is predicted. For a certain load, the bifurcation criterion is met at every material point and two symmetric (conjugate) bifurcation directions are predicted with an orientation of $\Theta = \pm 60°$ close to $\Theta_C = \Theta_R = \Theta_A$. This bifurcation point corresponds to the peak stress on the global response curve and to the start of the load response reduction for associated plasticity. Further, a range of possible orientations is even predicted for an increasing load and corresponds to non-unique possible solutions.

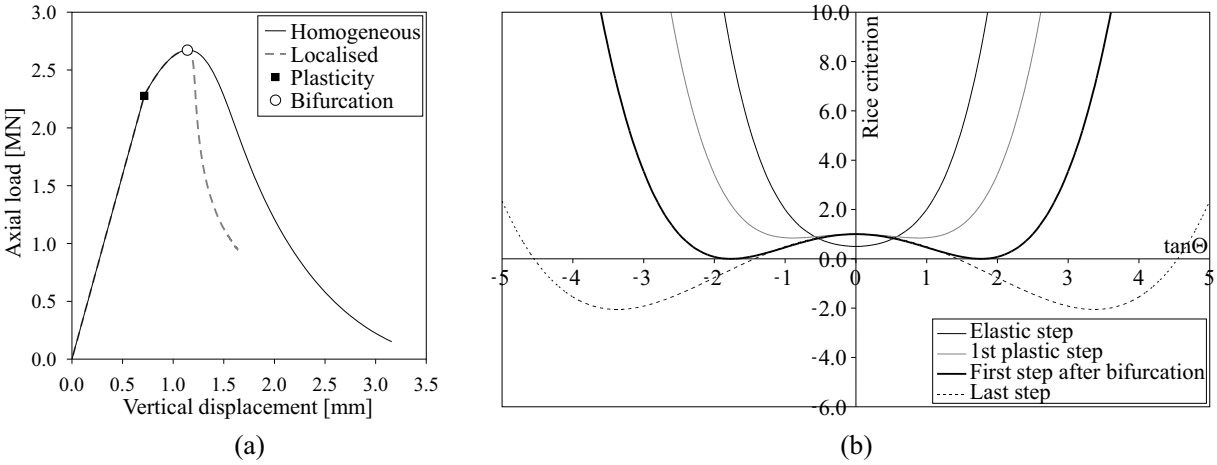

Fig. 3.16: Uniaxial compression: (a) global specimen response curves and (b) Rice criterion at several loading steps for the homogeneous solution (Collin et al., 2009b).

For a perfect sample, although softening plasticity is considered, the strain localisation is not triggered automatically and the numerical solution may remain homogeneous even after the bifurcation criterion is met. In reality, the localisation process is generated because geomaterials specimens exhibit some heterogeneities. Different numerical procedures are available to force the occurrence of strain localisation. The most used one is the introduction of an imperfection, such as disturbing force, material imperfection, or geometrical defect (Charlier et al., 1997; Matsushima et al., 2002; Zhang et al., 2001). The modification of numerical parameters, such as time step size and sequences can also be performed (Marinelli et al., 2014; Sieffert et al., 2009). A third method that will be discussed later is a random initialisation of characteristics (Chambon et al., 2001b).

Among these procedures, Collin et al. (2009b) introduced a material imperfection in the bottom left finite element of the sample under compression. Initially the strain field in the sample is homogeneous, and once the bifurcation criterion is met, the imperfection instigates the development of a shear band across the specimen. The strain localisation as well as its dependency to the mesh size is illustrated in Fig. 3.17 for classical finite element method. The localised solution is therefore non-homogeneous, with the shear band under plastic loading and the outer material under elastic unloading. The global sample response is detailed in Fig. 3.16 (a) where a rapid decrease of the global reaction is observed once the shear band establishes. The shear band appearance corresponds therefore to the curve peak load (or peak stress) as concluded from laboratory evidences in section 3.1.2. The latter also indicate that a material inclusion can act as a strain localisation attractor, which is confirmed by the numerical results. The non-uniqueness issue of the problem after the bifurcation point has consequently been addressed by the imperfection inclusion which leads to one post-bifurcation solution.

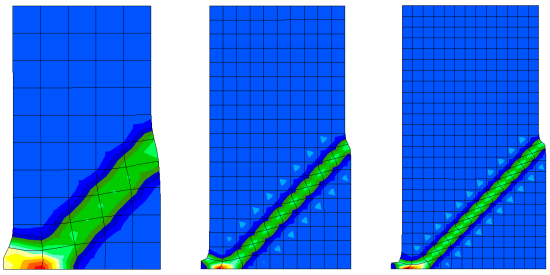

(a) (b) (c)

Fig. 3.17: Localised patterns represented by deviatoric deformation for classical material: meshes of (a) 50, (b) 190, and (c) 325 elements.

Microstructure enhanced medium

To fix the pathological mesh sensitivity, the local second gradient model is incorporated in the modelling with the second gradient constitutive law given by Eq. 3.80. The strain localisation pattern induced by the imperfection is illustrated in Fig. 3.18 with the Gauss integration points under softening plastic loading (red squares). This representation permits to measure the shear band width and to notice that it is constant no matter the element size, implying that the shear strain localisation is mesh-independent. Thus, the strain localisation is correctly regularised thanks to the internal length scale introduced by the second grade model. It is also the case for unstructured mesh (Bésuelle et al., 2006a) and for biphasic porous medium under saturated condition, using the coupled local second gradient model (Collin et al., 2006).

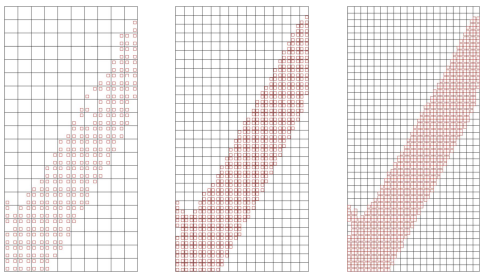

(a) (b) (c)

Fig. 3.18: Localised patterns represented by the plastic zone for microstructure material: meshes of (a) 200, (b) 450, and (c) 800 elements.

Nonetheless, the regularisation of the strain localisation process is obtained provided that the second gradient elastic modulus D is characterised to represent the shear bands properly. As already mentioned, the internal length scale inherent to the second gradient mechanical law is related to this constitutive parameter. The value of D should be evaluated based on experimental measurements of shear band thickness for the considered material. From a modelling point of view, a better numerical precision of the post-localisation plastic behaviour within the bands is obtained if a few elements (at least three) compose the shear band width (Bésuelle et al., 2006a). This remark is valid for any regularisation technique including second gradient model but also gradient plasticity and non-local formulation.

Non-uniqueness of the solution

The non-uniqueness of the post-peak solution of an initial boundary value problem can be studied using special techniques. In fact, instead of using a material imperfection, localised solutions can

be found for a perfect material by using random initialisation of the strain rate field (nodal velocity) or of material characteristics at the beginning of the iterative procedure. This technique has been mainly proposed by Chambon and co-workers (Chambon et al., 2001b) who developed an algorithm to search several eventual localised solutions by random initialisation. This algorithm has been adapted to second-gradient models by Chambon and Moullet (2004).

Numerical modelling of compression tests performed with the second gradient model illustrates the non-uniqueness of localised solutions of the same initial boundary value problem (Bésuelle et al., 2006a). The random initialisation is adopted for the increment of nodal quantities $\left[dU^{\tau 1}_{Node}\right]$ (Eq. 3.97) related to the values obtained at the end of the preceding time step. The obtained non-homogeneous solutions are detailed in Fig. 3.19 (a) where the different solutions exhibit one to three bands with a possible reflection on the top and bottom faces of the sample because of the imposed vertical displacement. The results indicate that the band thickness is reproducible even if the localisation pattern is different in terms of bands position and number.

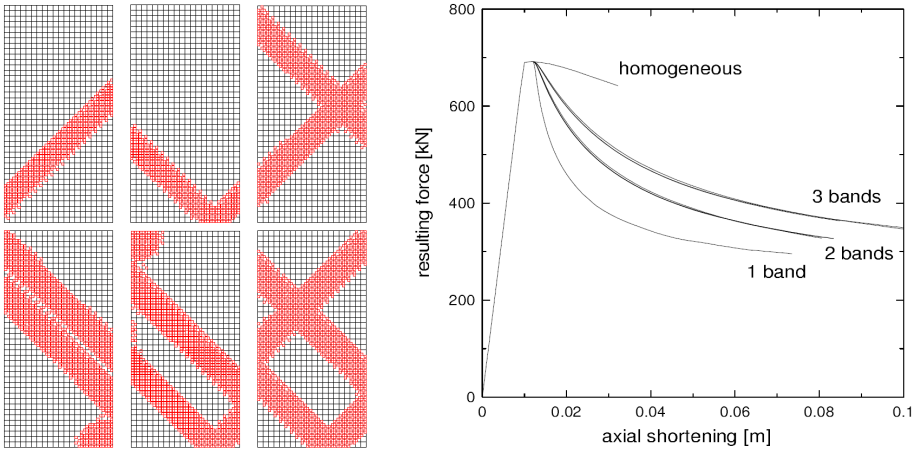

(a) (b)

Fig. 3.19: Example of localised solutions for compression test obtained after a random initialisation: (a) plastic zone and (b) global response curve (Bésuelle et al., 2006a).

As previously, the strain localisation occurring at bifurcation point is due to strain softening behaviour and possible elastic unloading. Fig. 3.19 (b) illustrates the global response curves that are different of those in Fig. 3.16 because a different first gradient law is used. These curves are grouped in packages characterised by the number of deformation bands. It is evident that the higher the band number, the closer the curves are to the homogeneous plastic case. A similar conclusion was drawn from the bar in traction studied by Chambon et al. (1998).

3.5 From strain localisation to rupture

When a material is subjected to strong solicitations, strain localisation is only one of the steps towards the material rupture. To properly reproduce the complete material rupture it would be necessary to take into account the different steps leading to rupture (section 3.1.1): first the material damage, then the strain localisation, the onset of fractures, and lastly the additional property modifications inside the fractures.

The material damage by microcracking is a continuous approach that corresponds to the degradation of the material elastic or plastic strength characteristics leading to a non-linear mechanical response. Different damage models exist in the context of continuum damage mechanics from purely macroscopic, continuous, and phenomenological approaches (Chaboche and Lemaitre, 1985; Kachanov, 1958; Krajcinovic, 1996) to multi-scale or micromechanical approaches.

For continuum micromechanics, microstructure effects on the material properties are included in the models (Budiansky and O'connell, 1976; Horii and Nemat-Nasser, 1983; Kachanov, 1993) and microcrack-induced damage can be developed (Levasseur et al., 2013; Zhu et al., 2008). All these damage models consist of one way of reproducing the complex process of microcracking by preserving the continuity of the description (continuous cracks). Moreover, the strain localisation phenomenon is a natural consequence of softening damage laws even if the strain softening behaviour is not a necessary condition for strain localisation appearance. Therefore, damage models can be introduced in continuous finite element methods involving strain localisation provided that the latter is represented properly.

The continuous approaches do not actually represent the cracks and a natural representation of a fracture is to consider it in a discrete manner. This type of discontinuity can even be considered in an undamaged material. The representation of such discontinuity can be traced back to the pioneering work of Griffith (1921) on linear elastic fracture mechanics developed for brittle materials and later to the works of Irwin (1948) and Orowan (1949) who included plastic consideration for material exhibiting ductility. If important yielding appears around the cracks as in ductile materials, linear elastic fracture mechanics is not applicable and elastic-plastic fracture mechanics has to be considered. In numerical approaches, the fractures can be modelled by various techniques. Some techniques that are regularly employed for discontinuous fracture modelling with finite element methods are the cohesive zone method (Barenblatt, 1962; Dugdale, 1960; Xu and Needleman, 1994), remeshing methods (Bouchard et al., 2003), discontinuous mesh, interface or contact elements (Zhong and Mackerle, 1992), and extended finite element methods (X-FEM, Moës et al. (1999)).

Besides the mechanical aspects discussed through continuous and discontinuous fracturing, the fracture behaviour is also dominated by hydro-mechanical property changes. In fact, the fracturing process induces important modifications in flow and transport properties. For instance, the water permeability can drastically increase of several orders of magnitude in fractured zones. This type of property modification can be introduced in finite element methods. Once more, different approaches exist to model the influence of the fracturing on permeability, from classical approaches based on fracture aperture (Snow, 1969; Witherspoon et al., 1980) to more complex theories based on hydraulic properties damage (Dormieux and Kondo, 2004; Barthélémy, 2009). Strain localisation effects can also be linked to hydraulic property modification in the shear strain localisation bands. A dependency of the permeability with a mechanical parameter, such as strain or plastic deformation for instance, can be investigated.

The material damage and discrete fracture descriptions will not be addressed and are mentioned only to give the general context of fracturing. However, strain localisation and its coupling with permeability evolution will be studied.

3.6 Conclusions and outlooks

Among the various methods for reproducing fracturing, shear strain localisation in band mode is considered. The displacement field is obviously discontinuous across fractures and shear banding modelling is able to reproduce this discontinuity in the sense that strain localisation induces non-uniform strain distribution. The elastic unloading outside the shear band and the concentration of the plastic strain inside result in a displacement jump between the outer material located on the two sides of a shear band even if the modelling remains continuous within the band. Consequently, such approach is mostly efficient for the reproduction of shear fractures in materials dominated by this type of failure, which is generally the case for high *in situ* stress environment (Diederichs, 2003), and for compressive regime. On the other hand, it is evident that additional mechanisms would be necessary for the reproduction of other type of fractures.

A regularisation technique based on the second gradient model has been detailed and employed to properly reproduce localised phenomena with finite element methods. The above

results point out that the method allows to numerically model the post-localisation behaviour of geomaterials. It leads to mesh-independence but do not restore the uniqueness of the solution to boundary value problems.

Furthermore, rocks and soils are porous materials for which the porous volume is not always totally filled with water and whose solid phase may be deformable under considerable stress. Additionally, sedimentary materials frequently exhibit anisotropic properties and, in case of rock fracturing, they can also undergo hydraulic property modifications as permeability increase in the fractures. For underground drilling in rocks, the challenge in term of strain localisation modelling is to be able to represent the impacts of these different aspects on the post-failure material behaviour and on the development of shear banding around galleries. The coupled local second gradient model has therefore to be extended in order to enlarge its application to unsaturated anisotropic rocks. Consequently, the unsaturated conditions will be added in the second gradient model together with the permeability anisotropy and the solid grain compressibility (with Biot's coefficient). Then, the constitutive laws have to be improved with mechanical anisotropy and intrinsic permeability evolution. The mechanical anisotropy will be added on both elastic and plastic mechanical behaviours and its effect on strain localisation will be highlighted. Lastly, the intrinsic water permeability variation will be related to strain localisation effects which is a crucial issue when considering the modelling of excavation damaged zone around galleries.

Chapter 4

Excavation fractured zone modelling with shear strain localisation

Abstract The prediction of the excavation damaged zone extent and fracturing structure remains a major issue especially in the context of underground nuclear waste storage. It is proposed to reproduce the excavation fractured zone in Callovo-Oxfordian claystone by considering the development of shear strain localisation bands with the coupled local second gradient model. Firstly, the model is extended to unsaturated conditions and the compressibility of the solid grains as well as the hydraulic permeability anisotropy are incorporated. Then, a gallery excavation is numerically modelled in order to reproduce the development of fractures at the scale of the nuclear waste repository. The gallery ventilation process is also reproduced to investigate the air-rock interaction and the desaturation of the rock. A particular attention is therefore paid to the prediction of the fractured zone extent, to the fracturing structure, and to the influence of the gallery ventilation. The main objectives are to model the fractures by considering shear strain localisation bands, and to investigate if an isotropic mechanical model reproduces the *in situ* measurements accurately. This type of modelling, especially at large repository scale and including solid grain compressibility as well as rock desaturation, has not been widely performed and constitutes a major novelty. The numerical modelling and its results are available in the scientific paper of Pardoen et al. (2015a).

Article Pardoen, B., Levasseur, S., and Collin, F. (2015). Using Local Second Gradient Model and Shear Strain Localisation to Model the Excavation Damaged Zone in Unsaturated Claystone. *Rock Mech Rock Eng*, 48(2):691-714. doi: 10.1007/s00603-014-0580-2.

4.1 Coupled local second gradient model for unsaturated medium with compressible solid grains

Until now, the modelling performed with the coupled second gradient model has been limited mainly to small-scale applications as biaxial compression tests. In term of strain localisation, a challenge consist in investigating if this numerical method is appropriate for the reproduction of shear bands on a large scale. The purpose, for the deep geological repository of nuclear wastes, is to examine if the method can accurately reproduce the fracturing pattern observed around underground structures with shear banding.

In the Callovo-Oxfordian claystone, the fractured structure around galleries develops preferentially in the horizontal or vertical direction depending on the anisotropy of both stress state and material properties (section 2.2.1). As a first large-scale approach including strain localisation, an isotropic mechanical model is used for the Callovo-Oxfordian claystone with the objective of analysing if the appearance of fractures during the drilling of galleries is governed by the anisotropy of the *in situ* stress state in the gallery section. The drilling of a gallery oriented parallel to the minor horizontal principal stresses with an anisotropic stress state in its section will therefore be modelled. So far, the numerical modelling of gallery drilling with the second gradient model has highlighted strain localisation but was essentially limited to mechanical analyses with isotropic initial stress state (Fernandes, 2009; Sieffert et al., 2009).

Moreover, during the operational phases (maintenance and repository) of underground repository that follow the excavation phase, an air ventilation is performed inside the galleries to control the air relative humidity and temperature. This ventilation induces fluid transfers and a desaturation of the rock that must be taken into account in the coupled second gradient model. Finally, for argillaceous rocks that are overconsolidated because of a high stress level, the compressibility of the solid grains must be considered. These aspects require to develop further the second gradient model.

The coupled local second gradient model developed by Collin et al. (2006) for biphasic porous medium can be extended to unsaturated materials with compressible solid grains. Hereafter, the unsaturated conditions are taken into account and the compressibility of the solid grains is introduced through the Biot's coefficient. Additionally, the permeability anisotropy is incorporated in

the model to better represent the water flows, even if the mechanical behaviour remains isotropic. These novelties are implemented in the non-linear finite element code Lagamine (University of Liège). The sign convention for the stress and strain fields is therefore chosen in accordance with the convention of the finite element code, which is the material mechanic convention with positive tensile stress and strain. This convention is only used for the numerical developments.

4.1.1 Balance equations

In order to properly model the shear strain localisation in geomaterials, classical poromechanics have been enriched with microstructure poromechanics. It permits to regularise the strain localisation problem by restoring the mesh-independence of the solution. The balance equations of the coupled local second gradient model for biphasic medium have been developed in the framework of microstructure continuum theory in section 3.3.2. The equations are obtained in usual differential local form and in a weak form by the virtual work principle (Germain, 1973). They include a description of the kinematics at microscale which leads to supplementary terms that come in addition to those of the classical continuum mechanics.

The momentum balance equation reads in a weak form:

$$\int_{\Omega} \left(\sigma_{ij} \, \frac{\partial u_i^*}{\partial x_j} + \Sigma_{ijk} \, \frac{\partial \upsilon_{ij}^*}{\partial x_k} \right) d\Omega = \int_{\Omega} \rho \; g_i \; u_i^* \; d\Omega + \int_{\Gamma_\sigma} \left(\bar{t}_i \; u_i^* + \overline{T}_i \; \upsilon_{ij}^* \; n_j \right) d\Gamma \tag{4.1}$$

In differential local form, it becomes:

$$\frac{\partial \sigma_{ij}}{\partial x_j} - \frac{\partial^2 \Sigma_{ijk}}{\partial x_j \partial x_k} + \rho \; g_i = 0 \tag{4.2}$$

and the boundary conditions are:

$$\bar{t}_i = \sigma_{ij} \; n_j - n_k \; n_j \; D\Sigma_{ijk} - \frac{D\Sigma_{ijk}}{Dx_k} \; n_j - \frac{D\Sigma_{ijk}}{Dx_j} \; n_k + \frac{Dn_l}{Dx_l} \; \Sigma_{ijk} \; n_j \; n_k - \frac{Dn_j}{Dx_k} \; \Sigma_{ijk} \tag{4.3}$$

$$\overline{T}_i = \overline{P}_{ij} \; n_j = \Sigma_{ijk} \; n_j \; n_k \tag{4.4}$$

In these equations the stress-strain relations are defined independently for the first and second gradient parts of the model. The first gradient constitutive law is an elastoplastic relationship defined as:

$$\tilde{\sigma}_{ij}^{'} = C_{ijkl} \; \dot{\varepsilon}_{kl} \tag{4.5}$$

and the second gradient constitutive law defined at microscale is a linear elastic relationship that links the double stress to the microkinematics (Mindlin, 1965):

$$\tilde{\Sigma}_{ijk} = D_{ijklmn} \; \frac{\partial \dot{\upsilon}_{lm}}{\partial x_n} \tag{4.6}$$

The momentum balance equation remains valid for unsaturated conditions and compressible solid grains provided that their influences are taken into account in the expression of the different terms. Among those terms the mixture homogenised mass density ρ and the total stress field σ_{ij} are influenced. In fact, ρ depends on the amount of water M_w inside the porous material configuration Ω and the total stress field is related to the effect of water through the effective stress definition. They will be defined in the material behaviour description of section 4.1.2.

However, the double stress Σ_{ijk} is not modified. It is assumed that the pore fluid does not have an influence at microscale; consequently, Σ_{ijk} is independent of the pore water pressure. Additionally, the second gradient constitutive equation is decoupled of the classical first gradient part of the model. Thus, neither the partial saturation nor the solid grain compressibility have an influence on the double stress.

Moreover, the classical and the second gradient boundary conditions on the external traction forces $\bar{t}_i$ and $\overline{T}_i$ defined in Eqs. 4.3 and 4.4 remain valid. $\bar{t}_i$ is related to the stress field σ_{ij} which is modified by the introduced aspects of the material behaviour; however, $\overline{T}_i$ is linked solely to Σ_{ijk} which is not affected.

The modification of the terms of the water mass balance equation must also be considered. The equation reads in a weak form:

$$\int_{\Omega} \left(\dot{M}_w \; p_w^* - f_{w,i} \; \frac{\partial p_w^*}{\partial x_i} \right) d\Omega = \int_{\Omega} Q_w \; p_w^* \; d\Omega - \int_{\Gamma_{q_w}} \overline{q}_w \; p_w^* \; d\Gamma \tag{4.7}$$

It corresponds to the balance equation for classical poromechanics because second gradient effects are assumed solely for the solid phase and the pore fluid does not have an influence at microscale. As a consequence, the variations of pore water pressure do not engender microkinematic gradient (Ehlers and Volk, 1998). In differential local form, the water mass balance equation and the hydraulic boundary condition are:

$$\dot{M}_w + \frac{\partial f_{w,i}}{\partial x_i} = Q_w \tag{4.8}$$

$$\overline{q}_w + f_{w,i} \; n_i = 0 \tag{4.9}$$

Once more, these equations are valid for compressible solid grains, partial saturation, and anisotropy of the intrinsic water permeability provided that their influences are taken into account. The time derivative of the water mass $\dot{M}_w$ inside Ω and the mass flow of water $f_{w,i}$ are affected and will be defined in section 4.1.2. $\dot{M}_w$ depends on the amount of water in Ω and on the porosity of the material, whilst $f_{w,i}$ depends both on the intrinsic and relative permeabilities through Darcy's law. The other terms, the sink term of water mass Q_w and the input water mass $\overline{q}_w$ on the porous material boundary, are linked to the other quantities through the equilibrium equation but do not need additional developments.

4.1.2 Material behaviour

The principal constitutive equations of the porous material behaviour, including partial saturation effect, solid grain compressibility, and anisotropic permeability are detailed hereafter.

Partial saturation

For unsaturated conditions the water mass inside a porous material volume Ω corresponds to:

$$M_w = \rho_w \; \Phi \; S_{r,w} \; \Omega \tag{4.10}$$

and its time derivative corresponds to:

$$\dot{M}_w = \dot{\rho}_w \; \Phi \; S_{r,w} \; \Omega + \rho_w \; \dot{\Phi} \; S_{r,w} \; \Omega + \rho_w \; \Phi \; \dot{S}_{r,w} \; \Omega + \rho_w \; \Phi \; S_{r,w} \; \dot{\Omega} \tag{4.11}$$

This amount of water, which depends on the degree of water saturation $S_{r,w}$, leads to the following mixture homogenised mass density:

$$\rho = \rho_s \; (1 - \Phi) + S_{r,w} \; \rho_w \; \Phi \tag{4.12}$$

The fluid isotropic compressibility follows the relation:

$$\frac{\dot{\rho}_w}{\rho_w} = \frac{\dot{p}_w}{\chi_w} \tag{4.13}$$

and the water advective flow for anisotropic hydraulic permeability is given by Darcy's law:

$$f_{w,i} = -\rho_w \ \frac{k_{w,ij} \ k_{r,w}}{\mu_w} \ \left(\frac{\partial p_w}{\partial x_j} + \rho_w \ g_j \right) \tag{4.14}$$

where $k_{r,w}$ is the water relative permeability.

The fluid mass and fluid flows are mostly governed by the water retention property of the material and by its hydraulic permeability. Both of them are related to the partial water saturation and a relative permeability coefficient is introduced in the generalised Darcy's law. Among various possible analytical expressions, the water retention and relative permeability curves are given by van Genuchten's and Mualem's models (Mualem, 1976; van Genuchten, 1980):

$$S_{r,w} = S_{res} + (S_{max} - S_{res}) \left(1 + \left(\frac{p_c}{P_r} \right)^{\frac{1}{1-\mathcal{M}}} \right)^{-\mathcal{M}} \tag{4.15}$$

$$k_{r,w} = \sqrt{S_{r,w}} \left(1 - \left(1 - S_{r,w}{}^{\frac{1}{\mathcal{M}}} \right)^{\mathcal{M}} \right)^2 \tag{4.16}$$

where P_r is the air entry pressure, S_{max} and S_{res} are the maximum and residual water degrees of saturation, $\mathcal{M}$ is a model coefficient, and p_c is the capillary pressure. In the absence of gaseous phase, it yields:

$$p_c = s = -p_w \tag{4.17}$$

The time derivative of the degree of water saturation is involved in the time derivative of the water mass (Eq. 4.11) and can be related to the pore water pressure by:

$$\dot{S}_{r,w} = \frac{\partial S_{r,w}}{\partial p_w} \ \dot{p}_w \tag{4.18}$$

The dependence of $S_{r,w}$ on p_w is obviously related to the considered model and gives, for the van Genuchten's expression:

$$\frac{\partial S_{r,w}}{\partial p_w} = \frac{(S_{max} - S_{res}) \ \mathcal{M}}{(1-\mathcal{M}) \, P_r^{\frac{1}{1-\mathcal{M}}} \left(1 + \left(\frac{-p_w}{P_r} \right)^{\frac{1}{1-\mathcal{M}}} \right)^{\mathcal{M}+1}} \ (-p_w)^{\frac{\mathcal{M}}{1-\mathcal{M}}} \tag{4.19}$$

The relative permeability being dependant on the saturation degree, its time derivative can be linked to $\dot{S}_{r,w}$ and to $\dot{p}_w$ as follows:

$$\dot{k}_{r,w} = \frac{\partial k_{r,w}}{\partial S_{r,w}} \ \dot{S}_{r,w} = \frac{\partial k_{r,w}}{\partial S_{r,w}} \ \frac{\partial S_{r,w}}{\partial p_w} \ \dot{p}_w \tag{4.20}$$

where:

$$\frac{\partial k_{r,w}}{\partial S_{r,w}} = \frac{1}{2\sqrt{S_{r,w}}} \left(1 - \left(1 - S_{r,w}^{\frac{1}{\mathcal{M}}} \right)^{\mathcal{M}} \right)^2 + 2\sqrt{S_{r,w}} \left(1 - \left(1 - S_{r,w}^{\frac{1}{\mathcal{M}}} \right)^{\mathcal{M}} \right) \ \left(1 - S_{r,w}^{\frac{1}{\mathcal{M}}} \right)^{\mathcal{M}-1} S_{r,w}^{\frac{1}{\mathcal{M}}-1} \tag{4.21}$$

for the considered model.

Anisotropy of the intrinsic permeability

The advective flow of water (Eq. 4.14) depends on the anisotropic characteristics of the material through the anisotropic intrinsic permeability. For anisotropic materials and by symmetry of the tensor, the intrinsic permeability tensor $k_{w,ij}$ requires six components to describe the flow characteristics. However, materials commonly exhibit limited forms of anisotropy and stratified

geomaterials require only two parameters for the description of the water flow. For horizontal layering in the plane (x_1,x_3), the intrinsic hydraulic permeability tensor is defined with the horizontal and vertical permeabilities, $k_{w,h}$ and $k_{w,v}$, as follows:

$$k_{w,ij} = \begin{bmatrix} k_{w,h} & 0 & 0 \\ 0 & k_{w,v} & 0 \\ 0 & 0 & k_{w,h} \end{bmatrix} \tag{4.22}$$

Compressibility of the solid grains

The material compressibility is defined within the scope of poroelasticity (Detournay and Cheng, 1993) and is based on the different compressibilities of a porous material (section 2.4.4). Those are: the compressibility of the bulk material C (solid skeleton), the compressibility of the pores C_p, and the compressibility of the solid phase C_s (rock matrix) with $C_s < C$. The different types of compressibility induce different behaviours of the rock matrix and of the porous material. They can deform differently and the porous material may enter plastic state while the solid grains remain elastic. In the general Biot framework (Biot, 1941), the Biot's coefficient is expressed by:

$$b = \frac{\Phi\ C_p}{C} = 1 - \frac{K}{K_s} \tag{4.23}$$

as a function of the drained bulk modulus of the material K and the bulk modulus of the solid phase K_s. This coefficient represents the relative deformability of the solid grains with regard to the solid skeleton (Biot, 1941; Biot and Willis, 1957; Skempton, 1960). Biot proposed for the effective stress definition to use b as a scaling factor that reduces the effect of p_w on σ_{ij} due to a reduction of pore compressibility. The Biot's stress definition can be formulated under unsaturated conditions presuming that the assumptions on compressibility hold under these conditions (Nuth and Laloui, 2008b):

$$\sigma_{ij} = \sigma_{ij}^{'} - b\ S_{r,w}\ p_w\ \delta_{ij} \tag{4.24}$$

The latter expression includes the effect of partial saturation on the effective stress field (tensile stress is positive).

For the solid phase behaviour, the isotropic solid density variation is linked to the variations of pore water pressure and mean effective stress by (Detournay and Cheng, 1993; Coussy, 2004):

$$\frac{\dot{\rho}_s}{\rho_s} = \frac{(b-\Phi)\, S_{r,w}\ \dot{p}_w - \dot{\sigma}^{'}}{(1-\Phi)\ K_s} \tag{4.25}$$

The time derivative of the porosity is obtained by solid mass conservation $\dot{M}_s = 0$ and reads:

$$\dot{\Phi} = (1-\Phi)\left(\frac{\dot{\rho}_s}{\rho_s} + \frac{\dot{\Omega}}{\Omega}\right) = (1-\Phi)\left(\frac{(b-\Phi)\, S_{r,w}\ \dot{p}_w - \dot{\sigma}^{'}}{(1-\Phi)\ K_s} + \frac{\dot{\Omega}}{\Omega}\right) \tag{4.26}$$

Furthermore, the time derivative of the water mass in Eq. 4.11 becomes by including the fluid compressibility, the porosity variation, and by considering a unit mixture volume:

$$\dot{M}_w = \rho_w \left(\frac{\dot{p}_w}{\chi_w}\ \Phi\ S_{r,w} + \frac{\dot{p}_w}{K_s}(b-\Phi)\ S_{r,w}^2 + \left(\frac{\dot{\Omega}}{\Omega} - \frac{\dot{\sigma}^{'}}{K_s}\right)\ S_{r,w} + \Phi\ \dot{S}_{r,w}\right) \tag{4.27}$$

The above expressions can be rewritten under poroelastic assumption:

$$\dot{\sigma}^{'} = K\ \dot{\varepsilon}_v = K\ \frac{\dot{\Omega}}{\Omega} \tag{4.28}$$

and using the Biot's coefficient expression of Eq. 4.23. The equations become:

$$\frac{\dot{\rho}_s}{\rho_s} = \frac{(b-\Phi)\, S_{r,w}\ \dot{p}_w - K\ \dfrac{\dot{\Omega}}{\Omega}}{(1-\Phi)\ K_s} \tag{4.29}$$

$$\dot{\Phi} = (b-\Phi)\left(\frac{S_{r,w}}{K_s}\ \dot{p}_w + \frac{\dot{\Omega}}{\Omega}\right) \tag{4.30}$$

$$\dot{M}_w = \rho_w \left(\frac{\dot{p}_w}{\chi_w}\ \Phi\ S_{r,w} + \frac{\dot{p}_w}{K_s}\,(b-\Phi)\ S_{r,w}^2 + b\ \frac{\dot{\Omega}}{\Omega}\ S_{r,w} + \Phi\ \dot{S}_{r,w}\right) \tag{4.31}$$

It is to recall that Biot's theory and the equations of poroelasticity are valid only for an elastic behaviour of the material. Extending these equations to poroplasticity (Coussy, 1995) with permanent changes in fluid mass content and in porosity requires to include the plastic material behaviour, which is complex to implement and is not included in this work.

Finally, the governing equations 4.1 and 4.7 of the coupled problem are valid provided ρ, σ_{ij}, $\dot{M}_w$, and $f_{w,i}$ are defined according to Eqs. 4.12, 4.24, 4.27 (or 4.31), and 4.14, respectively.

4.1.3 Coupled finite element formulation

Numerical implementation

For numerical application, the equilibrium equations 4.1 and 4.7 of the second gradient model are implemented in a finite element code. The non-linear field equations of the coupled problem that must hold at any time t read (see section 3.3.3):

$$\int_{\Omega^t} \left(\sigma_{ij}^t\ \frac{\partial u_i^*}{\partial x_j^t} + \Sigma_{ijk}^t\ \frac{\partial v_{ij}^*}{\partial x_k^t}\right) d\Omega^t - \int_{\Omega^t} \lambda_{ij}^t \left(\frac{\partial u_i^*}{\partial x_j^t} - v_{ij}^*\right) d\Omega^t = \int_{\Omega^t} \rho^t\ g_i\ u_i^*\ d\Omega^t + \int_{\Gamma_\sigma^t} \left(\overline{t}_i^t\ u_i^* + \overline{T}_i^t\ v_{ik}^*\ n_k^t\right) d\Gamma^t \tag{4.32}$$

$$\int_{\Omega^t} \lambda_{ij}^* \left(\frac{\partial u_i^t}{\partial x_j^t} - v_{ij}^t\right) d\Omega^t = 0 \tag{4.33}$$

$$\int_{\Omega^t} \left(\dot{M}_w^t\ p_w^* - f_{w,i}^t\ \frac{\partial p_w^*}{\partial x_i^t}\right) d\Omega^t = \int_{\Omega^t} Q_w^t\ p_w^*\ d\Omega^t - \int_{\Gamma_{q_w}^t} \overline{q}_w^t\ p_w^*\ d\Gamma^t \tag{4.34}$$

The kinematic restrictions of the second gradient model for the kinematic fields and their virtual quantities:

$$v_{ij} = F_{ij} \tag{4.35}$$

$$v_{ij}^* = F_{ij}^* \tag{4.36}$$

are introduced through a field of Lagrange multipliers λ_{ij} in Eqs. 4.32 and 4.33 (Chambon et al., 1998).

Linearisation of the field equations

Solving the equilibrium problem consists in determining the unknown fields u_i, v_{ij}, λ_{ij}, and p_w for which the non-linear field equations 4.32, 4.33, and 4.34 are valid. The numerical implementation of these equations for finite element method requires the linearisation of the equation system.

The field equations are *a priori* not verified for any instant t; consequently, the numerical resolution is realised by iterative procedure involving a time discretisation over finite time steps Δt:

$$\tau = t + \Delta t \tag{4.37}$$

and an implicit scheme (finite differences) for the rate of any quantity a:

$$\dot{a}^{\tau} = \frac{a^{\tau} - a^{t}}{\Delta t} \tag{4.38}$$

The iterative procedure uses a Newton-Raphson scheme to find a solution in equilibrium with the boundary conditions at the end of each time step. A configuration Ω^t in equilibrium with the boundary conditions at time t is assumed to be known and a second one Ω^{τ} in equilibrium at the end of the time step has to be found. Firstly, a configuration $\Omega^{\tau 1}$ not at equilibrium is guessed which leads to non-equilibrium forces ($\Delta_1^{\tau 1}$, $\Delta_2^{\tau 1}$, and $\Delta_3^{\tau 1}$) for the field equations. Another configuration at the end of the time step $\Omega^{\tau 2}$, close to $\Omega^{\tau 1}$ and for which the non-equilibrium forces cancel, has to be determined. Subtracting the balance equations of the two configurations, rewriting the equations for $\Omega^{\tau 2}$ in $\Omega^{\tau 1}$ configuration, assuming that g_i, $\overline{t}_i$, $\overline{q}_w$, and Q_w are independent of the different unknown fields, and assuming that $\overline{T}_i$ vanishes give:

$$\begin{aligned}
&\int_{\Omega^{\tau 1}} \frac{\partial u_i^*}{\partial x_l^{\tau 1}} \left(\sigma_{ij}^{\tau 2} \, \frac{\partial x_l^{\tau 1}}{\partial x_j^{\tau 2}} \, det(F) - \sigma_{il}^{\tau 1} \right) + \frac{\partial v_{ij}^*}{\partial x_l^{\tau 1}} \left(\Sigma_{ijk}^{\tau 2} \, \frac{\partial x_l^{\tau 1}}{\partial x_k^{\tau 2}} \, det(F) - \Sigma_{ijl}^{\tau 1} \right) d\Omega^{\tau 1} \\
&- \int_{\Omega^{\tau 1}} \frac{\partial u_i^*}{\partial x_l^{\tau 1}} \left(\lambda_{ij}^{\tau 2} \, \frac{\partial x_l^{\tau 1}}{\partial x_j^{\tau 2}} \, det(F) - \lambda_{il}^{\tau 1} \right) - v_{ij}^* \left(\lambda_{ij}^{\tau 2} \, det(F) - \lambda_{ij}^{\tau 1} \right) d\Omega^{\tau 1} \\
&- \int_{\Omega^{\tau 1}} u_i^* \left(\rho^{\tau 2} \, det(F) - \rho^{\tau 1} \right) g_i \, d\Omega^{\tau 1} = -\Delta_1^{\tau 1}
\end{aligned} \tag{4.39}$$

$$\int_{\Omega^{\tau 1}} \lambda_{ij}^* \left(\left(\frac{\partial u_i^{\tau 2}}{\partial x_k^{\tau 1}} \, \frac{\partial x_k^{\tau 1}}{\partial x_j^{\tau 2}} \, det(F) - \frac{\partial u_i^{\tau 1}}{\partial x_j^{\tau 1}} \right) - \left(v_{ij}^{\tau 2} \, det(F) - v_{ij}^{\tau 1} \right) \right) d\Omega^{\tau 1} = -\Delta_2^{\tau 1} \tag{4.40}$$

$$\int_{\Omega^{\tau 1}} p_w^* \left(\dot{M}_w^{\tau 2} \, det(F) - \dot{M}_w^{\tau 1} \right) - \frac{\partial p_w^*}{\partial x_l^{\tau 1}} \left(f_{w,i}^{\tau 2} \, \frac{\partial x_l^{\tau 1}}{\partial x_i^{\tau 2}} \, det(F) - f_{w,l}^{\tau 1} \right) d\Omega^{\tau 1} = -\Delta_3^{\tau 1} \tag{4.41}$$

where $det(F)$ is the Jacobian determinant of the transformation between the two configurations:

$$det(F) = \left| \frac{\partial x_i^{\tau 2}}{\partial x_j^{\tau 1}} \right| \tag{4.42}$$

By making the two configurations tend towards each other, the variations between them can be defined by finite differences for any quantity a as:

$$da^{\tau 1} = a^{\tau 2} - a^{\tau 1} \tag{4.43}$$

They read for the unknown fields:

$$du_i^{\tau 1} = dx_i^{\tau 1} = x_i^{\tau 2} - x_i^{\tau 1} \tag{4.44}$$

$$dv_{ij}^{\tau 1} = v_{ij}^{\tau 2} - v_{ij}^{\tau 1} \tag{4.45}$$

$$d\lambda_{ij}^{\tau 1} = \lambda_{ij}^{\tau 2} - \lambda_{ij}^{\tau 1} \tag{4.46}$$

$$dp_w^{\tau 1} = p_w^{\tau 2} - p_w^{\tau 1} \tag{4.47}$$

Including the Biot's effective stress definition for unsaturated materials of Eq. 4.24 and the stress-strain rates constitutive relations of Eqs. 4.5 and 4.6 gives:

$$d\sigma_{ij}^{\tau 1} = \sigma_{ij}^{\tau 2} - \sigma_{ij}^{\tau 1} = d\sigma_{ij}^{'\tau 1} - b\ S_{r,w}^{\tau 1}\ dp_w^{\tau 1}\delta_{ij} \tag{4.48}$$

$$d\sigma_{ij}^{'\tau 1} = \sigma_{ij}^{'\tau 2} - \sigma_{ij}^{'\tau 1} = C_{ijkl}\ \frac{\partial du_k^{\tau 1}}{\partial x_l^{\tau 1}} \tag{4.49}$$

$$d\Sigma_{ijk}^{\tau 1} = \Sigma_{ijk}^{\tau 2} - \Sigma_{ijk}^{\tau 1} = D_{ijklmn}\frac{\partial dv_{lm}^{\tau 1}}{\partial x_n^{\tau 1}} \tag{4.50}$$

The variations of the phase densities can be linearised from Eqs. 4.13 and 4.25:

$$d\rho_w^{\tau 1} = \rho_w^{\tau 2} - \rho_w^{\tau 1} = \rho_w^{\tau 1}\frac{dp_w^{\tau 1}}{\chi_w} \tag{4.51}$$

$$d\rho_s^{\tau 1} = \rho_s^{\tau 2} - \rho_s^{\tau 1} = \rho_s^{\tau 1}\frac{\left(b-\Phi^{\tau 1}\right)\ S_{r,w}^{\tau 1}\ dp_w^{\tau 1} - d\sigma^{'\tau 1}}{\left(1-\Phi^{\tau 1}\right)\ K_s} \tag{4.52}$$

and they lead to the variations of porosity and mixture density by Eqs. 4.26 and 4.12:

$$d\Phi^{\tau 1} = \Phi^{\tau 2} - \Phi^{\tau 1} = \left(1-\Phi^{\tau 1}\right)\left(\frac{\left(b-\Phi^{\tau 1}\right)\ S_{r,w}^{\tau 1}\ dp_w^{\tau 1} - d\sigma^{'\tau 1}}{\left(1-\Phi^{\tau 1}\right)\ K_s} + \frac{d\Omega^{\tau 1}}{\Omega^{\tau 1}}\right) \tag{4.53}$$

$$d\rho^{\tau 1} = \rho^{\tau 2} - \rho^{\tau 1} = d\rho_s^{\tau 1}\ \left(1-\Phi^{\tau 1}\right) - \rho_s^{\tau 1}\ d\Phi^{\tau 1} + dS_{r,w}^{\tau 1}\ \rho_w^{\tau 1}\ \Phi^{\tau 1} + S_{r,w}^{\tau 1}\ d\rho_w^{\tau 1}\ \Phi^{\tau 1} + S_{r,w}^{\tau 1}\ \rho_w^{\tau 1}\ d\Phi^{\tau 1} \tag{4.54}$$

with:

$$d\varepsilon_v^{\tau 1} = \frac{d\Omega^{\tau 1}}{\Omega^{\tau 1}} = \frac{\partial du_i^{\tau 1}}{\partial x_i^{\tau 1}} \tag{4.55}$$

The variations of the water mass storage term and of the water flow can also be linearised:

$$d\dot{M}_w^{\tau 1} = \dot{M}_w^{\tau 2} - \dot{M}_w^{\tau 1} \tag{4.56}$$

$$df_{w,i}^{\tau 1} = f_{w,i}^{\tau 2} - f_{w,i}^{\tau 1} \tag{4.57}$$

Their developments use Eqs. 4.27 and 4.14 and are available in the appendix A. Their final forms depend on the variations of water saturation $dS_{r,w}$ and relative permeability $dk_{r,w}$ that are obtained from Eqs. 4.18 and 4.20:

$$dS_{r,w}^{\tau 1} = S_{r,w}^{\tau 2} - S_{r,w}^{\tau 1} = \frac{\partial S_{r,w}^{\tau 1}}{\partial p_w^{\tau 1}}\ dp_w^{\tau 1} \tag{4.58}$$

$$dk_{r,w}^{\tau 1} = k_{r,w}^{\tau 2} - k_{r,w}^{\tau 1} = \frac{\partial k_{r,w}^{\tau 1}}{\partial S_{r,w}^{\tau 1}}\ dS_{r,w}^{\tau 1} = \frac{\partial k_{r,w}^{\tau 1}}{\partial S_{r,w}^{\tau 1}}\ \frac{\partial S_{r,w}^{\tau 1}}{\partial p_w^{\tau 1}}\ dp_w^{\tau 1} \tag{4.59}$$

and are related to the chosen retention and relative permeability curves.

Moreover, the Jacobian matrix $\overline{F}_{ij}$ of the transformation between the two configurations $\Omega^{\tau 1}$ and $\Omega^{\tau 2}$ is approximated by using a Taylor expansion and by retaining only the linear

approximation (Chambon and Moullet, 2004), meaning that the terms of degree greater than one are discarded:

$$\overline{F}_{ij} = \frac{\partial x_i^{\tau 2}}{\partial x_j^{\tau 1}} = \frac{\partial \left(x_i^{\tau 1} + du_i^{\tau 1} \right)}{\partial x_j^{\tau 1}} \approx \delta_{ij} + \frac{\partial du_i^{\tau 1}}{\partial x_j^{\tau 1}} \tag{4.60}$$

The Jacobian determinant becomes:

$$det(F) = \left| \frac{\partial x_i^{\tau 2}}{\partial x_j^{\tau 1}} \right| \approx 1 + \frac{\partial du_i^{\tau 1}}{\partial x_i^{\tau 1}} \tag{4.61}$$

Similarly and by applying the limit $\tau 2 = \tau 1$, the inverse relation yields:

$$\frac{\partial x_i^{\tau 1}}{\partial x_j^{\tau 2}} = \frac{\partial \left(x_i^{\tau 2} - du_i^{\tau 1} \right)}{\partial x_j^{\tau 2}} \approx \delta_{ij} - \frac{\partial du_i^{\tau 1}}{\partial x_j^{\tau 2}} \approx \delta_{ij} - \frac{\partial du_i^{\tau 1}}{\partial x_j^{\tau 1}} \tag{4.62}$$

The balance equations can be rewritten by taking into account the variations defined previously, by making the two configurations tend towards each other, which leads to the limit $\tau 2 = \tau 1$, and by neglecting terms of order higher than one. The complete algebraic developments of the linearisation of the field equation system and of the resulting linear auxiliary problem are available in the appendix A. The results are presented hereafter in a matricial form related to the spatial discretisation of the finite element method.

Element stiffness matrix

For the finite element method, continuum bodies are spatially discretised with finite elements. For the second gradient model, the type of two-dimensional finite element that is used has been detailed previously in section 3.3.3 and Fig. 3.11. Such discretisation implies that the balance equations are valid for each element. A convenient formulation of the coupled linear auxiliary problem is to write the equations in matricial form in order to define the local stiffness matrix of an element:

$$\int_{\Omega^{\tau 1}} \left[U^{*,\tau 1}_{(x_1,x_2)} \right]^T \left[E^{\tau 1} \right] \left[dU^{\tau 1}_{(x_1,x_2)} \right] d\Omega^{\tau 1} = -\Delta_1^{\tau 1} - \Delta_2^{\tau 1} - \Delta_3^{\tau 1} \tag{4.63}$$

where $\left[dU^{\tau 1}_{(x_1,x_2)} \right]$ is the vector of the unknown increments of nodal variables (Eq. 3.94), $\left[U^{*,\tau 1}_{(x_1,x_2)} \right]$ is the vector of the virtual quantities (Eq. 3.95), and $\left[E^{\tau 1} \right]$ is the element stiffness matrix defined as follows:

$$\left[E^{\tau 1} \right]_{25\times 25} = \begin{bmatrix} E^{\tau 1}_{1_{4\times 4}} & 0_{4\times 2} & K^{\tau 1}_{WM_{4\times 3}} & 0_{4\times 8} & 0_{4\times 4} & -I_{4\times 4} \\ G^{\tau 1}_{1_{2\times 4}} & 0_{2\times 2} & G^{\tau 1}_{2_{2\times 3}} & 0_{2\times 8} & 0_{2\times 4} & 0_{2\times 4} \\ K^{\tau 1}_{MW_{3\times 4}} & 0_{3\times 2} & K^{\tau 1}_{WW_{3\times 3}} & 0_{3\times 8} & 0_{3\times 4} & 0_{3\times 4} \\ E^{\tau 1}_{2_{8\times 4}} & 0_{8\times 2} & 0_{8\times 3} & D^{\tau 1}_{8\times 8} & 0_{8\times 4} & 0_{8\times 4} \\ E^{\tau 1}_{3_{4\times 4}} & 0_{4\times 2} & 0_{4\times 3} & 0_{4\times 8} & 0_{4\times 4} & I_{4\times 4} \\ E^{\tau 1}_{4_{4\times 4}} & 0_{4\times 2} & 0_{4\times 3} & 0_{4\times 8} & -I_{4\times 4} & 0_{4\times 4} \end{bmatrix} \tag{4.64}$$

Among the different submatrices composing $\left[E^{\tau 1} \right]$, the matrices $\left[E^{\tau 1}_1 \right]$, $\left[E^{\tau 1}_2 \right]$, $\left[E^{\tau 1}_3 \right]$, $\left[E^{\tau 1}_4 \right]$, and $\left[D^{\tau 1} \right]$ are identical to the ones used in the local second gradient model for monophasic medium by Chambon and Moullet (2004). In the present development, only the submatrices modified by the unsaturated conditions, by the compressibility of the solid grains, or by the anisotropy of the intrinsic water permeability are of interest. These submatrices are related to the flow problem, $\left[K^{\tau 1}_{WW} \right]$, to the coupling between the flow and the mechanical problems, $\left[K^{\tau 1}_{MW} \right]$ and $\left[K^{\tau 1}_{WM} \right]$,

and to the gravity volume force, $\left[G_1^{\tau 1}\right]$ and $\left[G_2^{\tau 1}\right]$. They are detailed below under poroelastic assumption.

The stiffness matrix of the flow problem is expressed as:

$$\left[K_{WW}^{\tau 1}\right]_{3\times 3} = \begin{bmatrix} \rho_w^{\tau 1}\dfrac{k_{w,11}^{\tau 1}k_{r,w}^{\tau 1}}{\mu_w} & \rho_w^{\tau 1}\dfrac{k_{w,12}^{\tau 1}k_{r,w}^{\tau 1}}{\mu_w} & K_{WW_{1,3}}^{\tau 1} \\ \rho_w^{\tau 1}\dfrac{k_{w,21}^{\tau 1}k_{r,w}^{\tau 1}}{\mu_w} & \rho_w^{\tau 1}\dfrac{k_{w,22}^{\tau 1}k_{r,w}^{\tau 1}}{\mu_w} & K_{WW_{2,3}}^{\tau 1} \\ 0 & 0 & K_{WW_{3,3}}^{\tau 1} \end{bmatrix} \tag{4.65}$$

where:

$$K_{WW_{1,3}}^{\tau 1} = \rho_w^{\tau 1}\frac{k_{w,1j}^{\tau 1}}{\mu_w}\frac{k_{r,w}^{\tau 1}}{\chi_w}\left(\frac{\partial p_w^{\tau 1}}{\partial x_j^{\tau 1}} + 2\rho_w^{\tau 1}g_j\right) + \rho_w^{\tau 1}\frac{k_{w,1j}^{\tau 1}}{\mu_w}\frac{\partial k_{r,w}^{\tau 1}}{\partial S_{r,w}^{\tau 1}}\frac{\partial S_{r,w}^{\tau 1}}{\partial p_w^{\tau 1}}\left(\frac{\partial p_w^{\tau 1}}{\partial x_j^{\tau 1}} + \rho_w^{\tau 1}g_j\right) \tag{4.66}$$

$$K_{WW_{2,3}}^{\tau 1} = \rho_w^{\tau 1}\frac{k_{w,2j}^{\tau 1}}{\mu_w}\frac{k_{r,w}^{\tau 1}}{\chi_w}\left(\frac{\partial p_w^{\tau 1}}{\partial x_j^{\tau 1}} + 2\rho_w^{\tau 1}g_j\right) + \rho_w^{\tau 1}\frac{k_{w,2j}^{\tau 1}}{\mu_w}\frac{\partial k_{r,w}^{\tau 1}}{\partial S_{r,w}^{\tau 1}}\frac{\partial S_{r,w}^{\tau 1}}{\partial p_w^{\tau 1}}\left(\frac{\partial p_w^{\tau 1}}{\partial x_j^{\tau 1}} + \rho_w^{\tau 1}g_j\right) \tag{4.67}$$

$$\begin{aligned} K_{WW_{3,3}}^{\tau 1} = {} & \frac{\rho_w^{\tau 1}}{\chi_w}\frac{\dot{p}_w^{\tau 1}}{\chi_w}\,\Phi^{\tau 1}\,S_{r,w}^{\tau 1} + \frac{\rho_w^{\tau 1}}{\chi_w\,\Delta t}\,\Phi^{\tau 1}\,S_{r,w}^{\tau 1} + 2\,\frac{\rho_w^{\tau 1}}{K_s}\frac{\dot{p}_w^{\tau 1}}{\chi_w}\left(b-\Phi^{\tau 1}\right)\left(S_{r,w}^{\tau 1}\right)^2 \\ & + \rho_w^{\tau 1}\frac{\dot{p}_w^{\tau 1}}{\chi_w}\,\Phi^{\tau 1}\frac{\partial S_{r,w}^{\tau 1}}{\partial p_w^{\tau 1}} - \frac{\rho_w^{\tau 1}}{K_s}\frac{\dot{p}_w^{\tau 1}}{K_s}\left(b-\Phi^{\tau 1}\right)\left(S_{r,w}^{\tau 1}\right)^3 \\ & + 2\,\rho_w^{\tau 1}\left(b-\Phi^{\tau 1}\right)\frac{\dot{p}_w^{\tau 1}}{K_s}\,S_{r,w}^{\tau 1}\frac{\partial S_{r,w}^{\tau 1}}{\partial p_w^{\tau 1}} + \frac{\rho_w^{\tau 1}}{K_s\,\Delta t}\left(b-\Phi^{\tau 1}\right)\left(S_{r,w}^{\tau 1}\right)^2 \\ & + \frac{\rho_w^{\tau 1}}{\chi_w}\,b\,\frac{\dot{\Omega}^{\tau 1}}{\Omega^{\tau 1}}\,S_{r,w}^{\tau 1} + \rho_w^{\tau 1}\,b\,\frac{\dot{\Omega}^{\tau 1}}{\Omega^{\tau 1}}\frac{\partial S_{r,w}^{\tau 1}}{\partial p_w^{\tau 1}} \\ & + \frac{\rho_w^{\tau 1}}{\chi_w}\,\Phi^{\tau 1}\,\dot{S}_{r,w}^{\tau 1} + \frac{\rho_w^{\tau 1}}{K_s}\left(b-\Phi^{\tau 1}\right)S_{r,w}^{\tau 1}\,\dot{S}_{r,w}^{\tau 1} + \frac{\rho_w^{\tau 1}}{\Delta t}\,\Phi^{\tau 1}\frac{\partial S_{r,w}^{\tau 1}}{\partial p_w^{\tau 1}} \end{aligned} \tag{4.68}$$

The stiffness matrices of the coupling between the flow and the mechanical problems are:

$$\left[K_{WM}^{\tau 1}\right]_{4\times 3} = \begin{bmatrix} 0 & 0 & -b\,S_{r,w}^{\tau 1} \\ 0 & 0 & 0 \\ 0 & 0 & 0 \\ 0 & 0 & -b\,S_{r,w}^{\tau 1} \end{bmatrix} \tag{4.69}$$

$$\left[K_{MW}^{\tau 1}\right]_{3\times 4} = \begin{bmatrix} A_{111}^{\tau 1} & f_{w,2}^{\tau 1} + A_{121}^{\tau 1} & A_{112}^{\tau 1} & -f_{w,1}^{\tau 1} + A_{122}^{\tau 1} \\ -f_{w,2}^{\tau 1} + A_{211}^{\tau 1} & A_{221}^{\tau 1} & f_{w,1}^{\tau 1} + A_{212}^{\tau 1} & A_{222}^{\tau 1} \\ C^{\tau 1} + \dot{M}^{\tau 1} & 0 & 0 & C^{\tau 1} + \dot{M}^{\tau 1} \end{bmatrix} \tag{4.70}$$

where:

$$A_{ijk}^{\tau 1} = -\rho_w^{\tau 1}\,\frac{k_{w,ij}\,k_{r,w}^{\tau 1}}{\mu_w}\,\frac{\partial p_w^{\tau 1}}{\partial x_k^{\tau 1}} \tag{4.71}$$

$$\begin{aligned} C^{\tau 1} = {} & \rho_w^{\tau 1}\,\frac{\dot{p}_w^{\tau 1}}{\chi_w}\left(b-\Phi^{\tau 1}\right)S_{r,w}^{\tau 1} - \rho_w^{\tau 1}\,\frac{\dot{p}_w^{\tau 1}}{K_s}\left(b-\Phi^{\tau 1}\right)\left(S_{r,w}^{\tau 1}\right)^2 \\ & + \rho_w^{\tau 1}\left(\frac{b}{\Delta t} - \frac{\dot{\Omega}^{\tau 1}}{\Omega^{\tau 1}}\right)S_{r,w}^{\tau 1} + \rho_w^{\tau 1}\,\left(b-\Phi^{\tau 1}\right)\dot{S}_{r,w}^{\tau 1} \end{aligned} \tag{4.72}$$

The matrices related to the contribution of gravity volume force are defined as follows:

$$\left[G_1^t\right]_{2\times 4} = \begin{bmatrix} -\rho_w^{\tau 1} S_{r,w}^{\tau 1} g_1 b & 0 & 0 & -\rho_w^{\tau 1} S_{r,w}^{\tau 1} g_1 b \\ -\rho_w^{\tau 1} S_{r,w}^{\tau 1} g_2 b & 0 & 0 & -\rho_w^{\tau 1} S_{r,w}^{\tau 1} g_2 b \end{bmatrix} \tag{4.73}$$

$$\left[G_2^{\tau 1}\right]_{2\times 3} = \begin{bmatrix} 0 & 0 & -\dfrac{\rho_w^{\tau 1}}{K_s}\left(b-\Phi^{\tau 1}\right)\left(S_{r,w}^{\tau 1}\right)^2 g_1 - \dfrac{\rho_w^{\tau 1}}{\chi_w}\Phi^{\tau 1} S_{r,w}^{\tau 1} g_1 - \rho_w^{\tau 1}\Phi^{\tau 1}\dfrac{\partial S_{r,w}^{\tau 1}}{\partial p_w^{\tau 1}} g_1 \\ 0 & 0 & -\dfrac{\rho_w^{\tau 1}}{K_s}\left(b-\Phi^{\tau 1}\right)\left(S_{r,w}^{\tau 1}\right)^2 g_2 - \dfrac{\rho_w^{\tau 1}}{\chi_w}\Phi^{\tau 1} S_{r,w}^{\tau 1} g_2 - \rho_w^{\tau 1}\Phi^{\tau 1}\dfrac{\partial S_{r,w}^{\tau 1}}{\partial p_w^{\tau 1}} g_2 \end{bmatrix} \tag{4.74}$$

If gravity is not taken into account, then they are null matrices and the terms including g_i also cancel in $K_{WW_{1,3}}^{\tau 1}$ and $K_{WW_{2,3}}^{\tau 1}$.

4.2 Constitutive models and parameters

The constitutive models and their parameters are required to study the numerical application of a gallery drilling in the Callovo-Oxfordian claystone. The hydro-mechanical description of the material behaviour includes a mechanical model for the classical first gradient part related to the macrostructure, a mechanical model for the second gradient part related to the microstructure, and a hydraulic model to reproduce the water flows in unsaturated porous media. A relatively simple isotropic mechanical law is used for the first gradient model to explore its aptitude to reproduce shear banding around galleries when coupled to a microstructure approach. It is calibrated based on experimental results of compression tests performed on the Callovo-Oxfordian claystone.

The convention of soil mechanics with positive compressive stress is used in the further modelling. The material mechanic convention was only used for the numerical developments added in the finite element formulation.

4.2.1 Hydraulic model

The hydraulic model for partially saturated porous media has already been described. It takes into account the water advection by Darcy's law (Eq. 4.14) as well as water retention and relative permeability evolutions (Eqs. 4.15 and 4.16). The hydro-mechanical parameters have been summarised in chapter 2 and the hydraulic parameters needed for the model are detailed in Table 4.1.

Symbol	Name	Value	Unit
$k_{w,h}$	Horizontal intrinsic water permeability	4×10^{-20}	m^2
$k_{w,v}$	Vertical intrinsic water permeability	1.33×10^{-20}	m^2
Φ	Porosity	0.18	–
P_r	van Genuchten air entry pressure	15	MPa
$\mathcal{M}$	van Genuchten coefficient	0.33	–
S_{max}	Maximum degree of water saturation	1	–
S_{res}	Residual degree of water saturation	0.01	–
μ_w	Water dynamic viscosity	0.001	$Pa\ s$
χ_w^{-1}	Water compressibility	0	Pa^{-1}

Table 4.1: Hydraulic parameters.

4.2.2 First gradient mechanical model

The mechanical model used for the clayey rock is an isotropic and non-associated elastoplastic internal friction model with linear elasticity and a Drucker-Prager yield criterion:

$$F^p \equiv II_{\hat{\sigma}'} - m\left(I_{\sigma'} + \frac{3\ c}{\tan\varphi_c}\right) = 0 \tag{4.75}$$

It is similar to the criterion described in section 2.4.5 without dependence on the Lode angle and it introduces hardening of the friction angle as well as softening of the cohesion. The elastic and plastic mechanical parameters are detailed in Table 4.2.

Symbol	Name	Value	Unit
E	Young's modulus	4	GPa
ν	Poisson's ratio	0.3	$-$
b	Biot's coefficient	0.6	$-$
ρ	Density	2300	kg/m^3
ψ_c	Dilatancy angles	0.5	$^\circ$
$\varphi_{c,0}$	Initial friction angle	10	$^\circ$
$\varphi_{c,f}$	Final friction angle	20	$^\circ$
B_φ	Friction angle hardening coefficient	0.002	$-$
dec_φ	Friction angle hardening shifting	0	$-$
c_0	Initial cohesion	3	MPa
c_f	Final cohesion	0.3	MPa
B_c	Cohesion softening coefficient	0.003	$-$
dec_c	Cohesion softening shifting	0.01	$-$

Table 4.2: Mechanical parameters.

The softening material behaviour has to be defined to allow the reproduction of shear banding. Small-scale compression laboratory experiments have been discussed in section 3.1.2. The results indicate the predominant role of shear bands and fractures in the post-peak regime.

A first approach is to consider the material as homogeneous, for which the peak stress and post-peak behaviour can be represented by the softening of strength parameters in the constitutive model. The friction angle and the cohesion define the plastic criterion; however, for granular materials, it can be assumed that the friction angle does not decrease significantly in the post-peak regime. On the other hand, the cohesion is affected and a lower residual value is generally observed. As a consequence, the residual strength is mostly affected by the cohesion which is therefore chosen as the softening variable, and no softening of the friction angle is assumed.

Experimental data on Callovo-Oxfordian claystone are required to calibrate the strength parameters. From a database provided by the Andra, it has been possible to realise a synthesis of compression tests results performed in the geomechanical unit C, located between -476 m and -515 m depth, which corresponds to the main level of the underground research laboratory. The synthesis of test results and their modelling are detailed in the report Pardoen et al. (2011). For a first calibration, five triaxial shear tests have been chosen. They were performed at a confining pressure close to $\sigma_3 = 10\ MPa$ (between 8.5 MPa and 11.5 MPa), perpendicular to the bedding planes, and in undrained conditions. The Table 4.3 details the selected triaxial compression tests. The results are illustrated in Fig. 4.1 where ε_1 is the axial strain, $\underline{q}$ is the deviatoric stress corresponding to the difference between the axial stress σ_1, and the confining stress σ_3:

$$\underline{q} = \sigma_1 - \sigma_3 \tag{4.76}$$

and $p^{'}$ is the mean effective stress:

$$p^{'} = \sigma^{'} = \frac{\sigma^{'}_{ii}}{3} = \frac{\sigma^{'}_1 + 2\sigma^{'}_3}{3} \tag{4.77}$$

Two of the tests, those with the smallest confinements, were performed with an initial pore water pressure of about 2 MPa, while the others were realised with an initial pore pressure of about 4.5 MPa that corresponds to the *in situ* pore pressure.

Symbol	Name	1	2	3	4	5	Unit
	Borehole	EST104	EST104	EST104	EST104	EST104	
	Sample number	EST02318	EST02336	EST02448	EST02318	EST02336	
	Laboratory	ANTEA	ANTEA	ANTEA	ANTEA	ANTEA	
	Average depth	476.2	479.0	499.5	476.2	479.0	m
	Diameter	40	40	40	40	40	mm
	Height	46	67	55	80	64	mm
	Test type[1]	ICUC	ICUC	ICUC	ICUC	ICUC	$-$
α	Orientation of the loading[2]	0	0	0	0	0	$^\circ$
σ_3	Confinement	8.6	8.7	9.2	11.3	11.5	MPa
$\dot{\varepsilon}$	Strain rate	0.001	0.001	0.001	0.001	0.001	$\%/min$
w	Water content	5.7	6.4	7	6.2	7.8	%
$S_{r,w}$	Water degree of saturation	94	86	97.1	100	97	%
$p_{w,0}$	Initial pore water pressure	1.8	2.1	4.5	4.8	4.5	MPa

[1]ICUC = isotropic consolidation, undrained compression.
[2]α is the angle between the compression direction and the normal to the bedding planes.

Table 4.3: Triaxial compression tests selected for a first calibration of the mechanical model.

On the curves, one can observe that the pre-peak behaviour is not linear which can be related to the damage of elastic properties or to the hardening of plastic properties. Damage of material characteristics is not taken into account in the model; then, the pre-peak behaviour can be captured by friction angle hardening. The peak stress appears at about $\varepsilon_1 \approx 1$ %, while the pore water pressure decrease starts slightly earlier. The post-peak behaviour highlights a material strength decrease that will be captured by cohesion softening. Moreover, the global decrease of pore water pressure as well as the engendered increase of effective stress can be related to a slightly dilatant behaviour.

Following these observations, the tests can be numerically reproduced by finite element method to calibrate the model. A hydro-mechanical modelling in two-dimensional axisymmetric state under undrained conditions is performed without the initial consolidation phase. The individual modellings are not discussed here and only one global modelling is presented for this first calibration, with $\sigma_3 = 10\ MPa$ and $p_{w,0} = 4.5\ MPa$. The numerical results, with and without cohesion softening, are compared to the experimental results in Fig. 4.1 where a satisfactory matching is obtained for the parameters detailed in Table 4.2. Achieving a good matching both on the stress global response and on the pore water pressure is not straightforward; thus, a particular attention is paid to the curve $q/p^{'}$ versus ε_1 that includes both aspects.

The main drawback of the homogeneous approach of the material behaviour is that it does not take into account any cracks or strain localisation effect. However, it is proposed to predict the fracturing process numerically with shear strain localisation. The global post-peak (post-localisation) response of the material therefore depends on the strain localisation process and its calibration requires information about the shear banding structure. More particularly, shear band pattern, orientations, number, thickness, and evolution would be necessary. Unfortunately, such information is rarely available, especially for rocks.

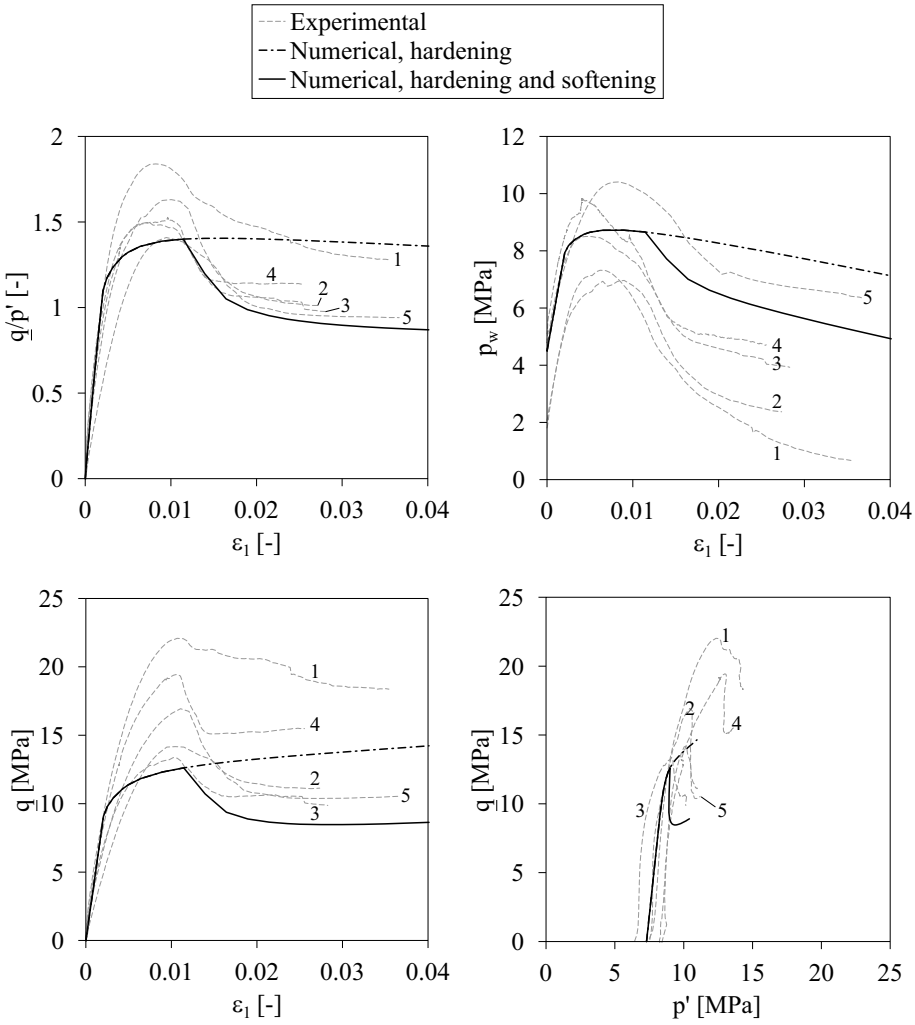

Fig. 4.1: Calibration of the mechanical parameters based on triaxial compression tests for a homogeneous material behaviour.

Nevertheless, the strain localisation has to be triggered to model shear banding. It is well known that a softening behaviour provides the conditions for strain localisation and may instigate an infinity of localised solutions (section 3.2.1; Benallal and Marigo (2007); Bésuelle et al. (2006a); Jirásek and Rolshoven (2009); Kotronis et al. (2008)). The softening parameters values (c_f, B_c, and dec_c) might therefore be adapted for that purpose. For the gallery excavation problem, preliminary calculations have indicated that the deformation around the gallery due to the drilling are globally lower than in compression laboratory tests. As a consequence, the introduction of a cohesion softening without delay (no shifting) is necessary to trigger the shear strain localisation. For the following modelling of gallery excavation, the same softening parameters c_f and B_c will be kept, however $dec_c = 0$.

4.2.3 Second gradient mechanical model

The second gradient mechanical law has been recalled in Eq. 4.6. It depends on one constitutive elastic modulus D (Eq. 3.80) that represents the microstructure and characterises the internal length scale of the second gradient model. Its value is chosen to represent the shear bands and the post-localisation behaviour properly. In fact, the strain localisation process for second gradient material is mesh-independent, but the post-localisation behaviour is better modelled if at least three elements compose the shear band width. The selected value is $D = 5\ kN$.

4.3 Modelling of gallery excavation

The processes of underground drilling and induced shear strain localisation in claystone are investigated at large scale. Papanastasiou and Vardoulakis (1992) were the first to present a numerical analysis of progressive localisation around excavated cavity in rock with Cosserat microstructure. Analogous two-dimensional hydro-mechanical modelling is performed with the coupled local second gradient model for a microstructure medium.

Many studies on claystone have been performed with two-dimensional isotropic mechanical models. Our purpose is to investigate if this type of model can reproduce the *in situ* observations and measurements by incorporating the fracture modelling with strain localisation. However, the coupling with permeability is not addressed in the fractures; therefore, the zone that develops around the gallery is called excavation fractured zone, the excavation damaged zone being related to irreversible hydro-mechanical property changes.

Furthermore, gallery air ventilation is also reproduced to highlight air-rock interaction, water drainage, and their effects on the shear banding structure. The reproduced ventilation is theoretical with constant air relative humidity inside the gallery and classical imposition at gallery wall.

It should be pointed out that regularisation techniques have already been used for this type of problem. They generate results that are mesh-independent but these theories do not restore the uniqueness of the solution for the gallery excavation problem (Fernandes, 2009; Sieffert et al., 2009). These remarks are valid for any application of regularisation methods.

4.3.1 Numerical model

A hydro-mechanical modelling of a gallery excavation is performed in two-dimensional plane strain state. The modelled gallery corresponds to the GED gallery of the Andra's URL oriented parallel to the minor horizontal principal total stress σ_h and having a radius of 2.3 m. The initial pore water pressure and anisotropic stress state are:

$$\sigma_{x,0} = \sigma_H = 1.3\ \sigma_h = 15.6\ MPa$$

$$\sigma_{y,0} = \sigma_v = 12\ MPa$$

$$\sigma_{z,0} = \sigma_h = 12\ MPa$$

$$p_{w,0} = 4.5\ MPa$$

A schematic representation of the models, the meshes, and the boundary conditions is detailed in Fig. 4.2. Two meshes are used: a full gallery and a quarter of a gallery. The mesh extension of the full gallery is 120 m, both horizontally and vertically, and the spatial discretisation is performed with a total of 29040 nodes and 7440 elements. Assuming symmetry along the x and y-axes, only one quarter of the gallery can be discretised. In this case, the mesh extension is 60 m, both horizontally and vertically, and the discretisation is performed with a total of 9801 nodes and 2480 elements. For both meshes, the initial stresses and pore water pressure are imposed at the mesh external boundary (drained boundary) and the meshes have a more refined discretisation close to the gallery. To establish the symmetry, the normal displacements and the normal water flows are blocked to a value of zero along the symmetry axes, which are therefore impervious. Nonetheless, as mentioned by Zervos et al. (2001a), a special care must be brought to the kinematic boundary conditions required to establish the symmetry. Due to the existence of gradient terms in the equilibrium equations, higher order constraints have to be characterised in addition to the classical boundary condition on the normal displacements. This second kinematic condition requires that the radial displacement u_r must be symmetric on both

sides of the symmetry axes. This implies that the normal derivative of u_r, with respect to the tangential (orthoradial) direction θ, has to cancel:

$$\frac{\partial u_r}{\partial \theta} = 0 \tag{4.78}$$

which is equivalent to:

$$x - axis : \qquad \frac{\partial u_x}{\partial y} = 0 \tag{4.79}$$

$$y - axis : \qquad \frac{\partial u_y}{\partial x} = 0 \tag{4.80}$$

Furthermore, natural boundary conditions for the double forces, $\overline{T}_i = 0$, are assumed on the different boundaries and gravity is not taken into account.

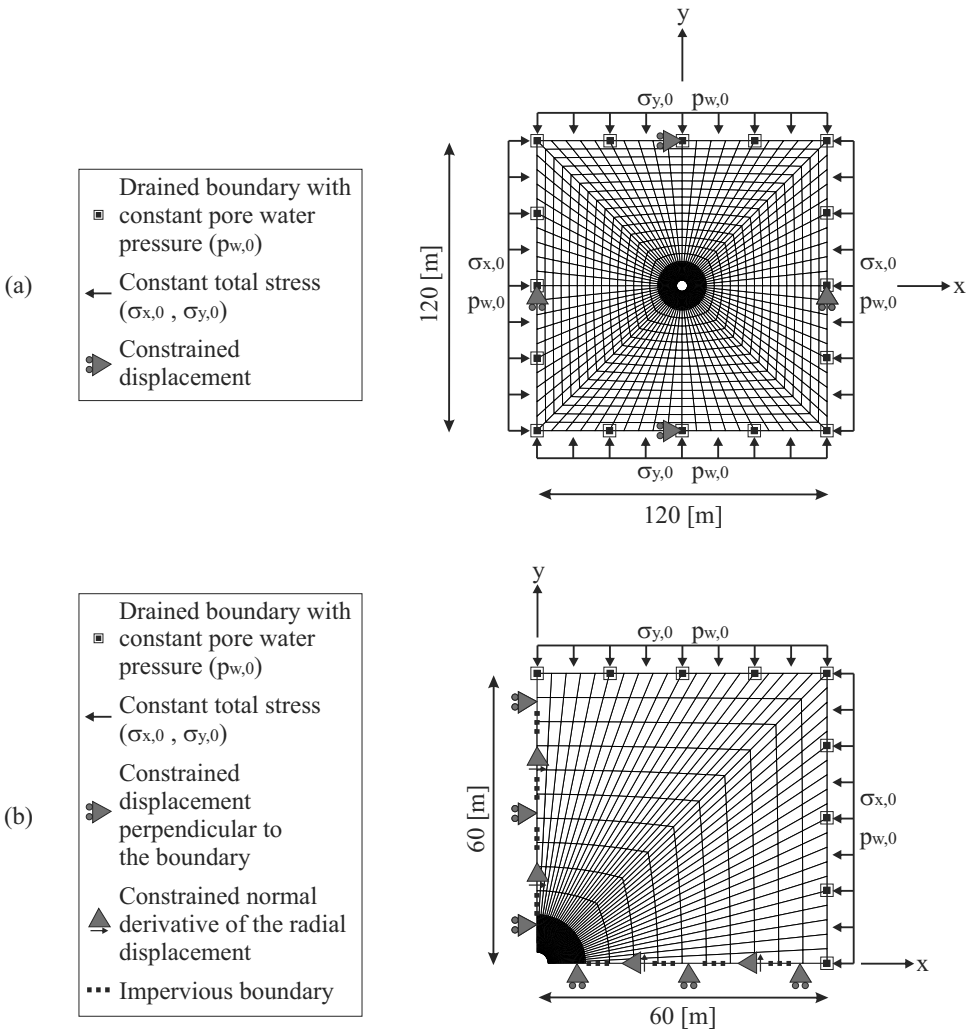

Fig. 4.2: Schematic representation of the models used for the modelling of a gallery excavation: (a) full gallery and (b) quarter of a gallery.

The gallery excavation can now be considered. It is modelled by decreasing during 5 days the total stresses and the pore water pressure at the gallery wall from their initial values to the atmospheric pressure of 100 kPa. After the excavation, the calculation is extended to 1000 days under constant total radial stress, to highlight possible long-term effects (Fig. 4.3). This stress imposition is representative of unsupported galleries. In the context of deep geological repository, different supports and coverings of the gallery walls are envisaged depending on the host material

properties. They can be rigid liner made of concrete slabs, flexible liner made of sliding arches with bolting and concrete covering, or the galleries can be unsupported for stiff materials. The two latter are envisaged for the galleries drilled in the Callovo-Oxfordian claystone. Furthermore, the geological surveys of fracturing as well as the gallery air ventilation experiment are performed in uncovered zones.

To model the air ventilation inside the gallery, a classical flow boundary condition is assumed and imposes the suction corresponding to the relative humidity of the cavity air at the tunnel wall. Two cases are considered for the air inside the gallery (Fig. 4.3). In the first case, there is no ventilation inside the gallery; thus, the air is saturated with water vapour and this maximum concentration corresponds to $RH = 100$ %. According to Kelvin's law (Eq. 2.47), the corresponding pore water pressure at the gallery wall is the atmospheric pressure $p_w = 100\ kPa$. The pore water pressure is then maintained constant after the end of the excavation and the claystone will remain almost saturated. In the second case, air ventilation is taken into account, since ventilation is usually realised in the galleries composing underground structures. It may drain the water from the rock, desaturate it, and modify the structure, the fracturing pattern, as well as the size of the fractured zone. Air ventilation can thus be modelled in order to observe its effects on the rock material. A theoretical ventilation, with constant air relative humidity, is envisaged to obtain a first outlook of the ventilation effect on shear banding. The air which is injected in the gallery is dryer than previously and a lower relative humidity of 80 % with a temperature of 25 $°C$ ($T = 298.15\ K$) are considered. Following Kelvin's law, this humidity corresponds to a pore water pressure at gallery wall of $p_w = -30.7\ MPa$. To reach this value, the decrease of p_w is performed in two steps: firstly, it decreases from its initial value to the atmospheric pressure during the excavation (5 days), and then an initiation phase of ventilation is considered (5 days) to reach the final value. After this initiation phase, a constant ventilation is maintained.

The imposed boundary conditions at gallery wall, for total stresses and pore water pressure evolutions, are presented in Fig. 4.3 for the two considered cases. It is worth mentioning that the ventilation effect on the shear banding is therefore represented by the hydro-mechanical model. In fact, the ventilation influences the pore water pressures and the effective stresses, which then influence the shear strain localisation structure and behaviour.

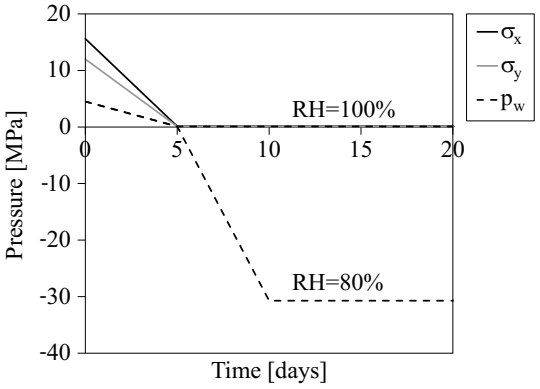

Fig. 4.3: Imposed total stresses and pore water pressure at the gallery wall for the modelling of a gallery excavation with and without air ventilation.

The main purpose of this numerical modelling is to represent the fractures with shear strain localisation and to reproduce, as well as possible, the *in situ* measurements and observations with an isotropic mechanical model.

4.3.2 Influence of *in situ* stress and permeability anisotropies

Creation and evolution of the fractured zone can be observed through the evolution of shear strain localisation. The latter is not *a priori* assured to be symmetric around the gallery and many solutions could emerge (Sieffert et al., 2009). To avoid any early symmetry assumption, the excavation of a full gallery is firstly modelled in isotropic conditions assuming $\sigma_{x,0} = \sigma_{y,0} = \sigma_{z,0} = 15.6\ MPa$ and $k_{w,h} = k_{w,v} = 4 \times 10^{-20}\ m^2$. The calculation is performed with incompressible solid grains $b = 1$ and no ventilation. With a circular gallery and such isotropic state, it is not possible to trigger the shear strain localisation and the deformation remains diffuse as shown in Fig. 4.4 (a). This figure presents the numerical results at the end of the excavation in terms of plastic zone, represented by the plastic loading integration points (red squares), and Von Mises' equivalent deviatoric total strain, i.e. total deviatoric strain:

$$\hat{\varepsilon}_{eq} = \sqrt{\frac{2}{3}\ \hat{\varepsilon}_{ij}\ \hat{\varepsilon}_{ij}} \tag{4.81}$$

where $\hat{\varepsilon}_{ij}$ is the deviatoric total strain field calculated from the total strain tensor ε_{ij}:

$$\hat{\varepsilon}_{ij} = \varepsilon_{ij} - \frac{\varepsilon_{kk}}{3}\ \delta_{ij} \tag{4.82}$$

Strain localisation can be triggered through the introduction of an imperfection in the material as illustrated in Fig. 4.4 (b). The imperfection consists of weaker elements with lower initial cohesion, $c_0 = 2\ MPa$, located at the gallery wall.

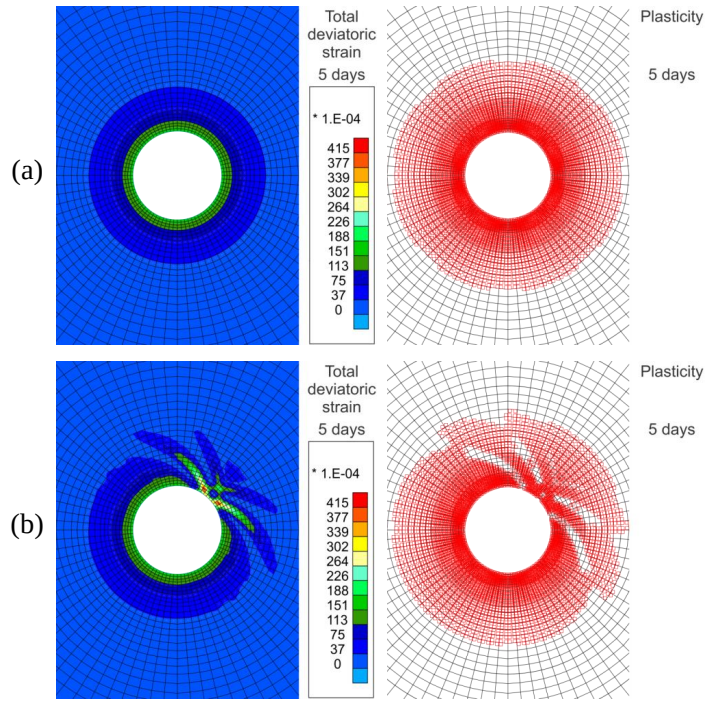

Fig. 4.4: Deformation and plasticity at the end of excavation for a full gallery and a full isotropic rock state: (a) without material imperfection and (b) with material imperfection.

However, in case of anisotropic stress state of the rock with $\sigma_{x,0} = 15.6\ MPa$ and $\sigma_{y,0} = \sigma_{z,0} = 12\ MPa$, the shear strain localisation appears without adding an imperfection in the rock. Fig. 4.5 illustrates the evolution of the strain localisation around the gallery, during and after the drilling. The numerical results that are presented are the total deviatoric strain, the plastic zone, and the deviatoric strain increment which represents the band activity:

$$\kappa_{eq} = \frac{\dot{\hat{\varepsilon}}_{eq}\ dt}{\int \dot{\hat{\varepsilon}}_{eq}\ dt} \tag{4.83}$$

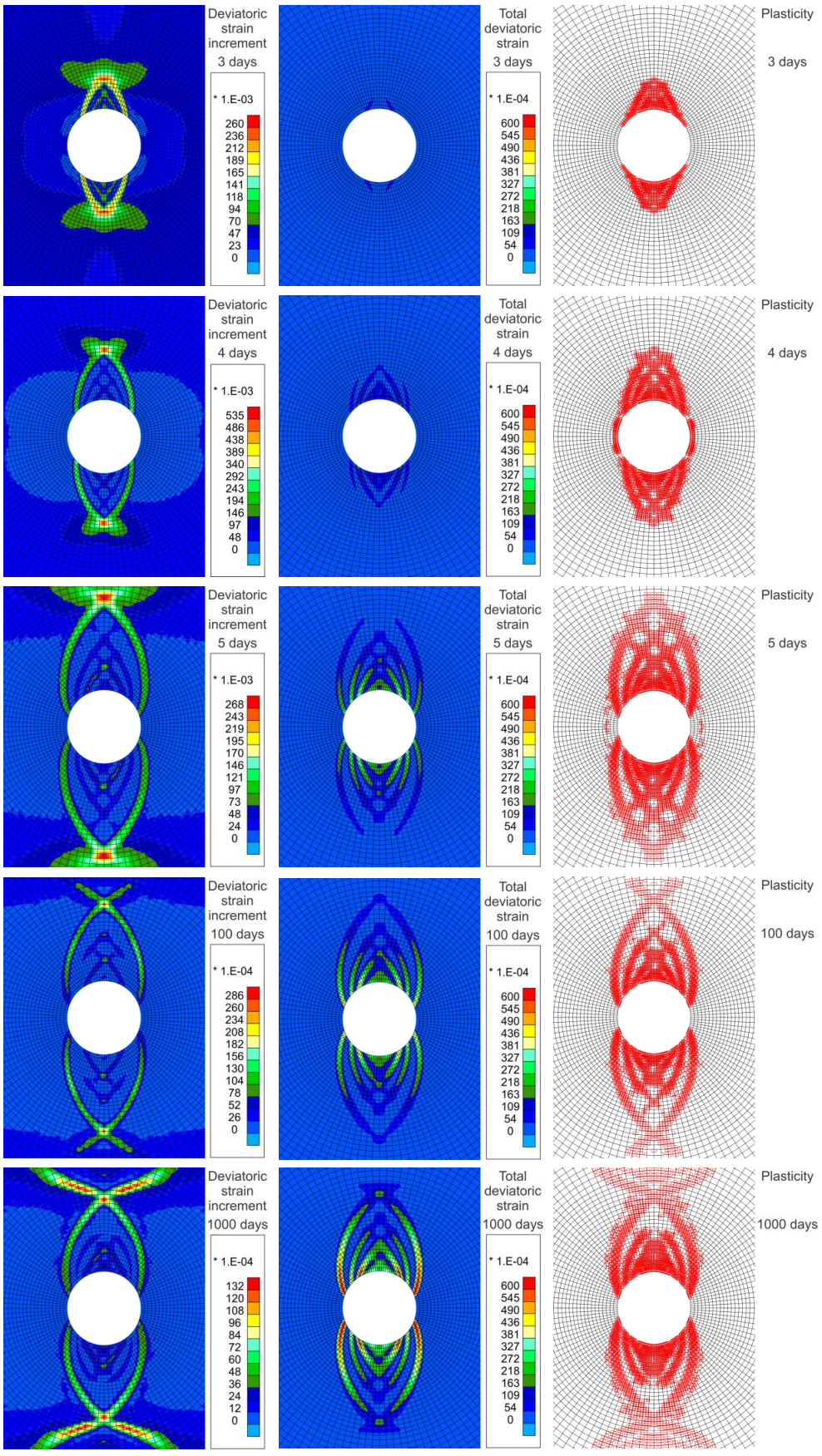

Fig. 4.5: Evolution of strain localisation during and after gallery excavation (5 days of excavation), for a full gallery and for a rock having anisotropic hydraulic permeability and anisotropic stress state.

The modelling exhibits a symmetric chevron fracture pattern around the gallery similar to *in situ* observations for galleries parallel to σ_h (see Fig. 2.6 (b)). The chevron fractures appear during the excavation and are mainly concentrated above the gallery because of the material anisotropic stress state. On the contrary, introducing only the anisotropy of the intrinsic water permeability with $k_{w,h} = 4 \times 10^{-20}\ m^2$ and $k_{w,v} = 1.33 \times 10^{-20}\ m^2$ does not lead to strain localisation unless an imperfection is introduced. It means that the appearance and shape of the strain localisation are mainly due to mechanical effects linked to the anisotropic stress state. The shear banding zone develops preferentially in the direction of the minor principal stress in the gallery section.

4.3.3 Influence of second gradient boundary condition

The previous modelling highlights that the anisotropic stress state of the Callovo-Oxfordian claystone is at the origin of a symmetry in the localisation pattern around the gallery. Then, it would be convenient, in the following, to consider only a quarter of a gallery. However, in the context of second gradient theory, a boundary condition of higher order should be considered in addition to the classical boundary condition of constrained displacement perpendicular to the boundary (Zervos et al., 2001a). This second kinematic condition specifies that the normal derivative of the radial displacement has to cancel on the symmetry axes.

To illustrate the necessity of this second gradient boundary condition, the strain localisation pattern of Fig. 4.5 is compared to the pattern obtained on a quarter of a gallery. The modelling on a quarter of a gallery is computed with the specific second gradient boundary condition, and with $b = 1$ and no ventilation as previously. In Fig. 4.6, one can observe that using the second gradient boundary condition produces a shear strain localisation pattern that is similar to the full-gallery results. Thus, it is confirmed that, for calculation simplicity and symmetry reasons, a quarter of a gallery can be adopted for future modelling, provided that the specific second gradient boundary condition is used.

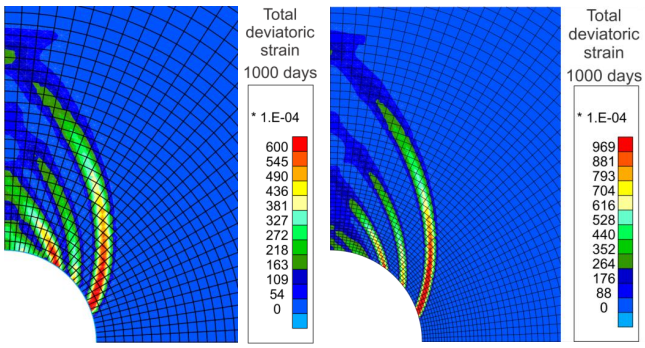

Fig. 4.6: Comparison of the strain localisation pattern at the end of the calculation for the modelling of: (a) a full gallery and (b) a quarter of a gallery with the second gradient boundary condition.

4.3.4 Influence of Biot's coefficient

Even if strain localisation seems to be mainly controlled by mechanical effects, hydraulic conditions can also impact the shear banding pattern. Here, the focus is on the influence of Biot's coefficient for the case without ventilation. In the first calculation, it is assumed that the solid grains are incompressible, which implies $b = 1$ (Fig. 4.7). In the second calculation, a value of $b = 0.6$ is used, which corresponds to the compressibility of solid grains commonly admitted for the Callovo-Oxfordian claystone (Fig. 4.8). Comparison of Figs. 4.7 and 4.8 indicates that the Biot's coefficient significantly influences the shear band pattern. With a value of 0.6, less bands

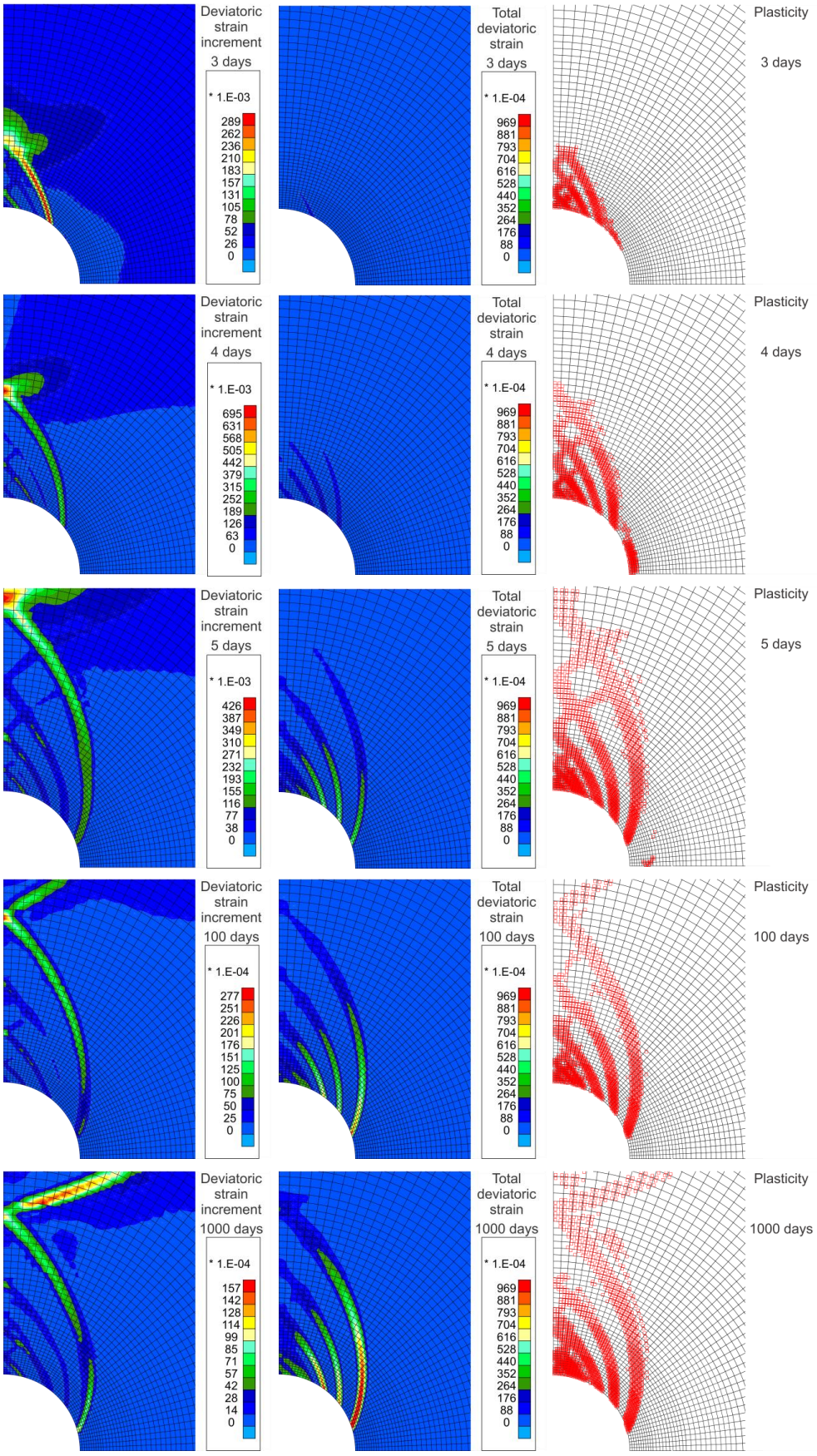

Fig. 4.7: Evolution of strain localisation during and after gallery excavation (5 days of excavation), without gallery ventilation and for a Biot's coefficient value of 1.

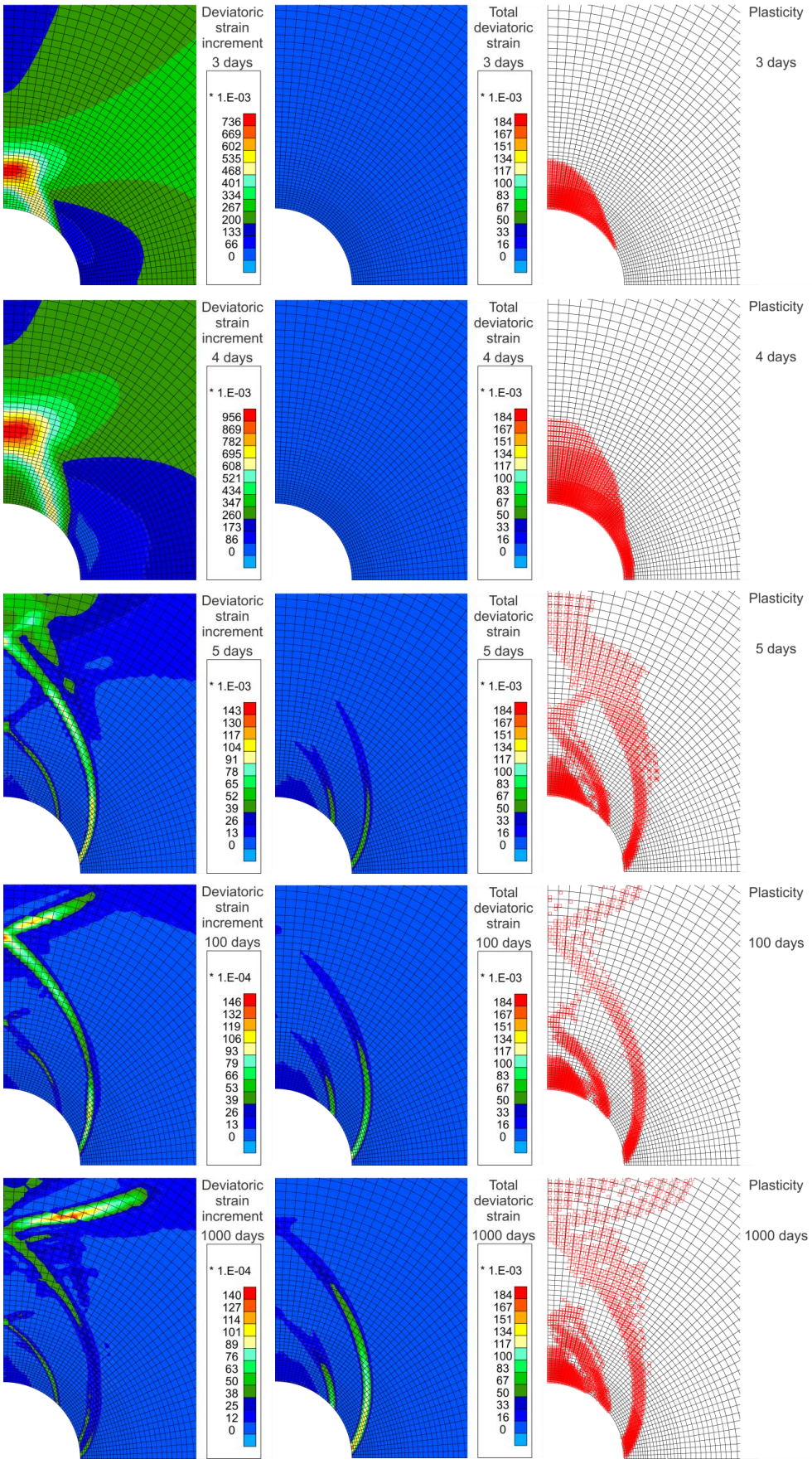

Fig. 4.8: Evolution of strain localisation during and after gallery excavation (5 days of excavation), without gallery ventilation and for a Biot's coefficient value of 0.6.

appear and the shear strain localisation is delayed. In fact, the strain remains diffuse until the fourth day of the excavation; nonetheless, the localisation appears before the end of the excavation. This can be explained by examining the stresses close to the gallery. At the gallery wall, the total stresses and the pore water pressure are imposed. Consequently, following the Biot's effective stress definition for unsaturated materials of Eq. 4.24, the lower the Biot's coefficient, the higher the effective compressive stress at the gallery wall. This implies that the rock close to the gallery wall is more resistant and that the shear strain localisation appears later.

For the last simulation with $b = 0.6$, the extent of the fractured zone in the rock, measured from the gallery wall up to the distance where strain localisation bands (total deviatoric strain) are observed, is detailed in Table 4.4. Comparing it to the measured values of Fig. 2.6 (b) provided by Armand et al. (2014) indicates an overestimation of the extent of the shear fracture zone. Nevertheless, these *in situ* experimental measurements are average values along the GED gallery, and maximal values of the fractured zone extent are also available in Armand et al. (2014) and in Cruchaudet et al. (2010b). The latter are detailed in Table 4.4, and the extent of the numerical shear banding zone is in a satisfactory agreement with the maximal extent of the shear fracture zone.

Zone	Horizontal [m]	Vertical upward [m] (gallery ceiling)	Vertical downward [m] (gallery floor)
Numerical shear banding	0.5	4.6	4.6
Mixed fractures	0.5	1.7	2.0
Shear fractures	0.8	3.9	5.1

Table 4.4: Comparison between the thickness of the numerical shear strain localisation zone and the maximal extents of the fractured zones around a gallery (GED) parallel to the minor horizontal principal stress.

Moreover, Fig. 4.9 illustrates the type of shear band obtained from the Rice bifurcation criterion (Table 3.1). At the end of excavation, the values of the parameter $\underline{s}$ inside the shear bands indicate that the strain localisation zones are whether compacting or dilating shear bands. The bands are in a dilative mode on the sides of the gallery and in a contractive mode above (and below) the gallery.

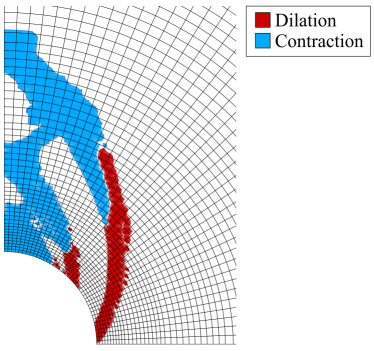

Fig. 4.9: Shear band type at the end of gallery excavation for a Biot's coefficient value of 0.6.

4.3.5 Influence of gallery ventilation

The modelling that is considered now includes the initial anisotropies, a Biot's coefficient value of 0.6, and the gallery ventilation. The drilling phase is not influenced by the ventilation, and the same results as in Fig. 4.8 are obtained until 5 days of computation. The results obtained after the excavation, displayed in Fig. 4.10, indicate that the suction imposed at the wall

strongly influences the results. Following the effective stress definition, the higher the suction, the higher the effective stress (Fig. 4.15). As noted before, this involves that the material is more resistant, and in this case, becomes elastic again close to the gallery. This inhibits the shear strain localisation around the gallery.

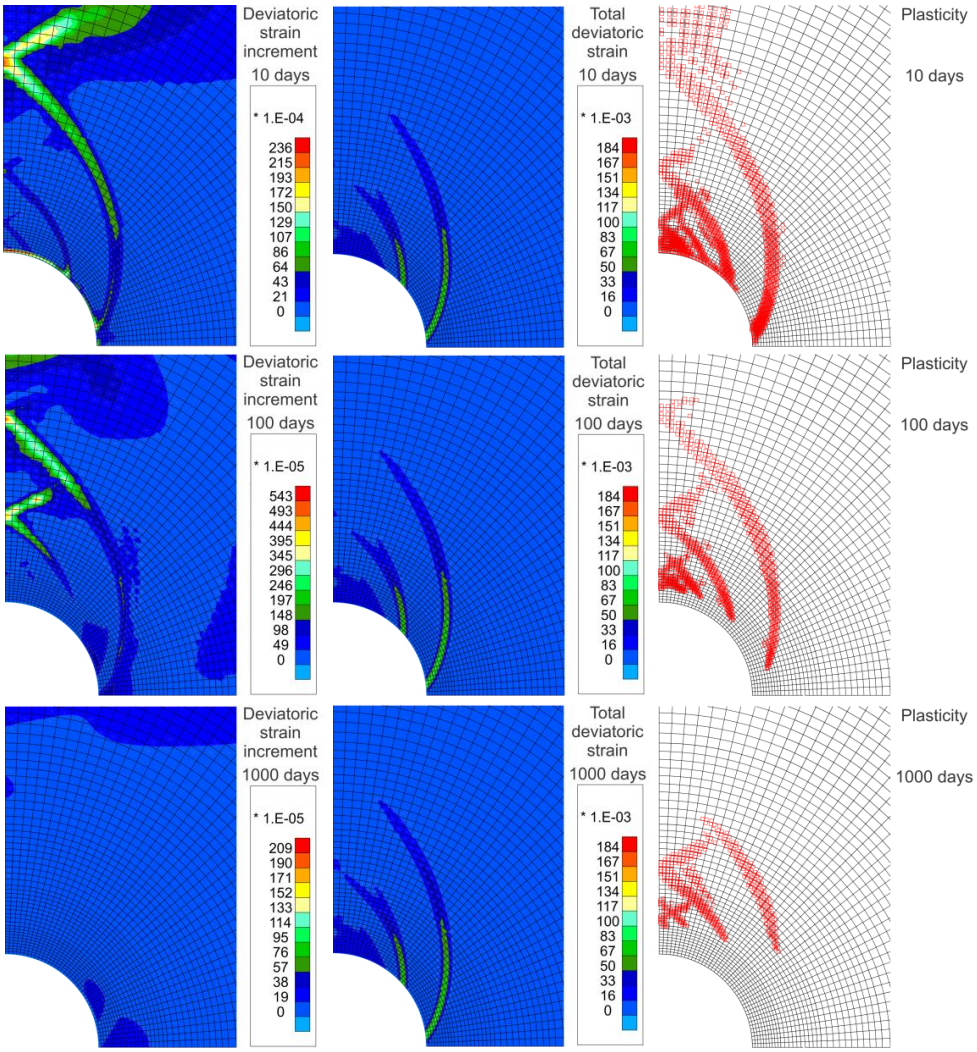

Fig. 4.10: Evolution of strain localisation after gallery excavation, with gallery ventilation and for a Biot's coefficient value of 0.6.

Various numerical results, coming from the gallery wall and the rock mass, are interpreted hereafter in order to emphasize the influence of the gallery air ventilation. The results come from the selected cross-sections and observation points on gallery wall that are presented in Fig. 4.11. The vertical cross-section goes through the shear bands and the results along it will highlight the effects of strain localisation, which is not the case for the horizontal cross-section. Furthermore, the results are compared for the cases considering (RH = 80 %) or not (RH = 100 %) the ventilation.

Firstly, the evolution of pore water pressure for the vertical and horizontal cross-sections is detailed in Fig. 4.12. In the rock mass, an increase of pressure is observed in the vertical direction and a decrease is observed in the horizontal direction up to a radial distance of about 30 m. These overpressures are related to hydro-mechanical coupling induced by the anisotropy of the initial stress state. The influence of the strain localisation bands is visible vertically but not horizontally. It is illustrated by the fluctuations of the pore water pressure in limited zones, with a decrease in the shear band. The influence of the shear band can be mostly observed during

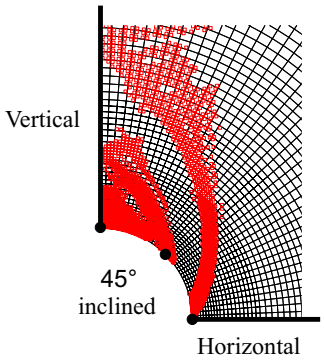

Fig. 4.11: Positions of cross-sections and gallery wall observation points.

the first 50 days of calculation then it tends to vanish. This is due to the strain increment inside the bands (band activity) and the hydro-mechanical coupling. As expected, the influence of the ventilation is marked close to the gallery wall, but tends to disappear deeper in the rock.

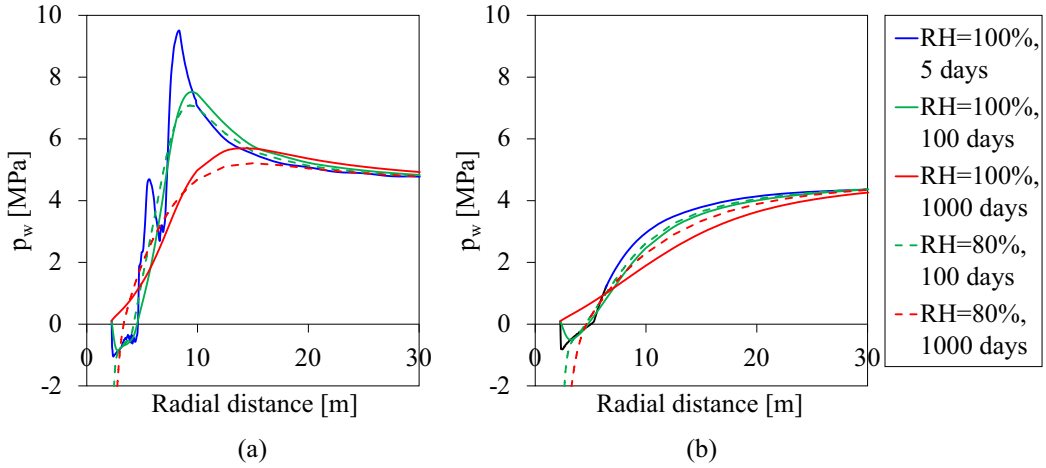

Fig. 4.12: Evolution of pore water pressure along (a) vertical and (b) horizontal cross-sections, after gallery excavation.

Secondly, the evolution of the degree of water saturation along the cross-sections is illustrated in Fig. 4.13. For the modelling without ventilation, the influence of the strain localisation bands activity is also visible in the vertical direction, in the short term. Nevertheless, the claystone remains almost saturated at the gallery wall and fully saturated after a distance of 3 m in the rock. For the modelling with ventilation, a strong desaturation is observed close to the wall. Fig. 4.14 illustrates the evolution of the degree of water saturation at the gallery wall and displays the desaturation more clearly.

Thirdly, the stress paths at the gallery wall are detailed in Fig. 4.15 where q is the deviatoric stress:

$$q = \sqrt{3}\ II_{\tilde{\sigma}'} \tag{4.84}$$

and p' is the mean effective stress. As mentioned before, in the case of ventilation, the effective stresses are much higher due to the suction. This explains the difference between the stress paths of the modelling with and without ventilation, after the end of the drilling phase.

Fourthly, Fig. 4.16 illustrates the displacements evolution along the vertical and horizontal cross-sections. In the vertical direction, a strong influence of the strain localisation bands is observed close to the gallery, until the end of the calculation, while it is not the case horizontally because the cross-section does not go through the localisation bands. For the modelling without ventilation, the displacements are important during the excavation and keep increasing

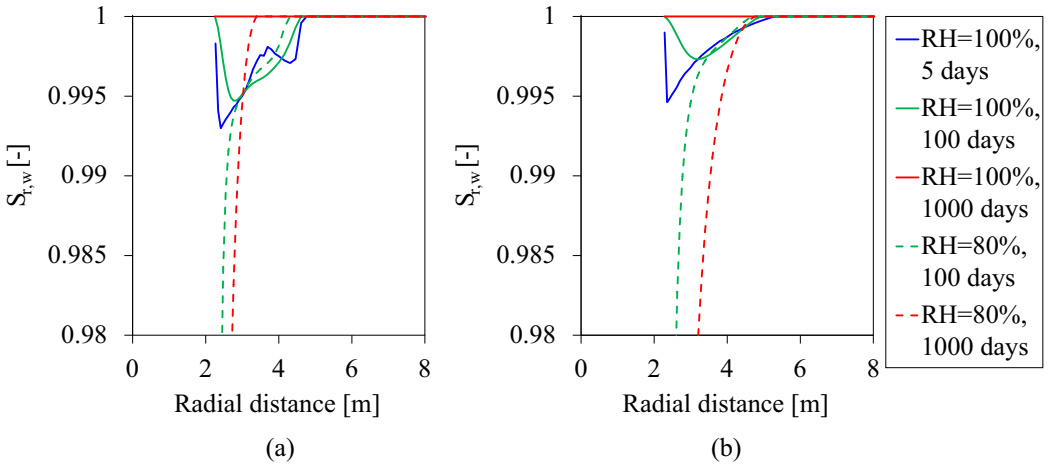

Fig. 4.13: Evolution of the degree of water saturation along (a) vertical and (b) horizontal cross-sections, after gallery excavation.

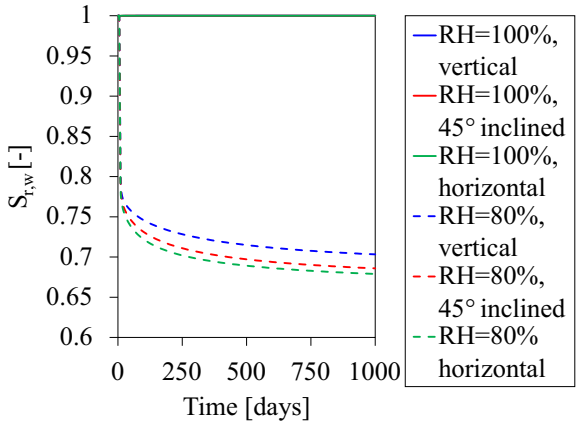

Fig. 4.14: Evolution of the degree of water saturation at the gallery wall, during and after gallery excavation.

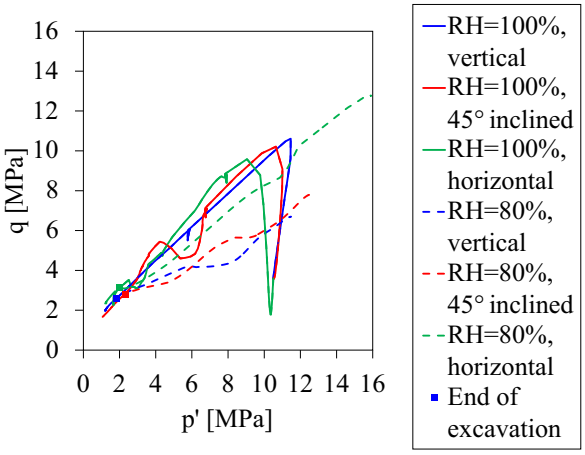

Fig. 4.15: Stress paths at the gallery wall, during and after gallery excavation.

afterwards, in both directions. When ventilation is applied, the displacements do not increase much after the excavation. This can also be observed in the evolution of the gallery convergence in Fig. 4.17 where a comparison with experimental results, from the same gallery of the Andra's URL, is presented. These results come from measurement sections named OHZ120 A, B, and

C that are performed in the GED gallery (Armand et al., 2013) and were already exposed in Fig. 2.7. One can observe that vertical convergence is captured by our model quite well; on the contrary, horizontal convergence is overestimated.

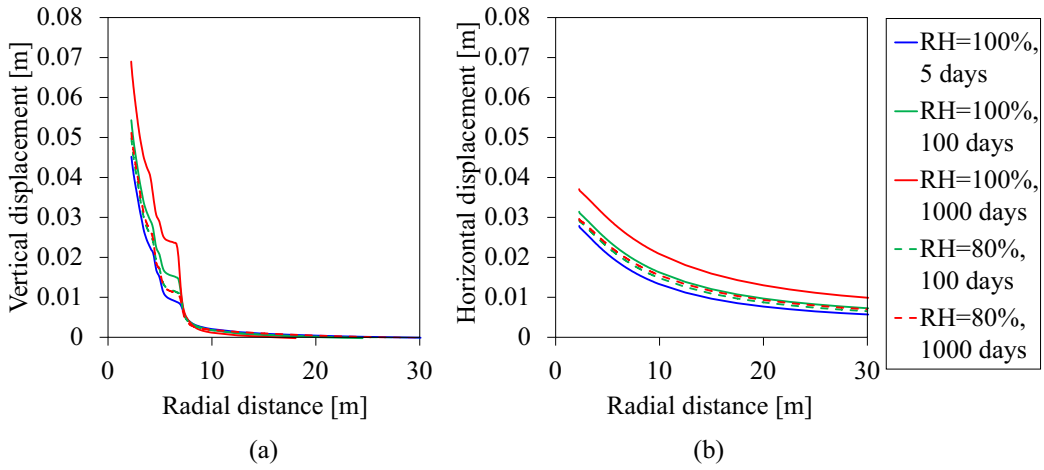

Fig. 4.16: Evolution of displacements along (a) vertical and (b) horizontal cross-sections, after gallery excavation.

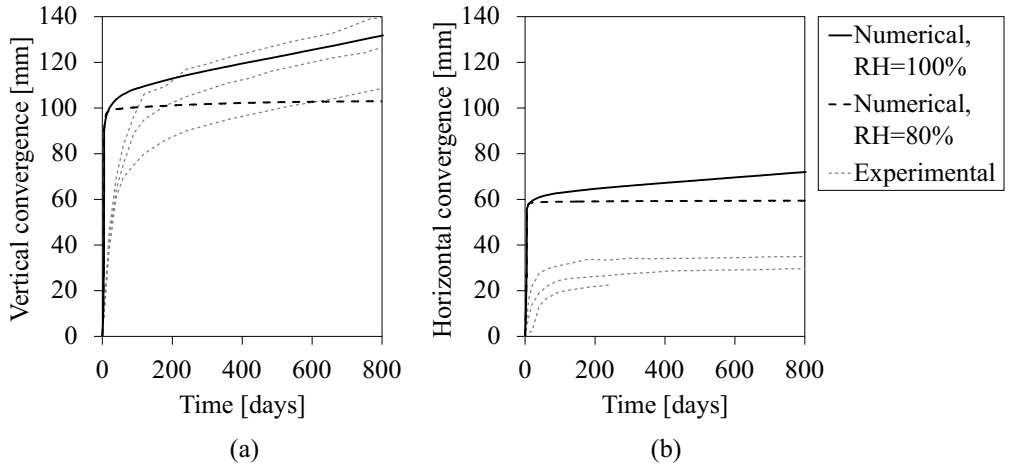

Fig. 4.17: Evolution of the (a) vertical and (b) horizontal convergences during and after gallery excavation, with comparison to experimental results.

All these results are evidences that noticeable differences exist whether ventilation is applied or not. For the modelling with ventilation, p_w remains negative close to the gallery (Fig. 4.12), the effective stresses increase after the excavation (Fig. 4.15) and the material becomes elastic again. Consequently, the desaturation of the rock close to the gallery inhibits the shear strain localisation (Fig. 4.10), which has the effect of restricting further deformation. On the contrary, without ventilation, p_w close to the gallery wall increases after the excavation (Fig. 4.12), the effective stresses reduce (Fig. 4.15) and the material remains partly plastic close to the gallery (Fig. 4.8). This increases the deformation and the gallery convergence (Fig. 4.17).

Concerning the prediction of convergence in the short term, an anisotropy in a ratio of three is observed on *in situ* measurements of horizontal and vertical convergences (Fig. 4.17). If the problem is studied with an isotropic model, without considering strain localisation but modelling the gallery ventilation, then the horizontal convergence is correctly reproduced but the vertical convergence is not (Fig. 4.18). Similar results are obtained by Plassart et al. (2013). Consequently, this type of approach fails to reproduce the *in situ* measurements, which indicates

that the fracturing and strain localisation processes permit to explain the convergence anisotropy. The creation of fractures, globally above the gallery due to the material anisotropic stress state, increases both the vertical and the horizontal convergences (Fig. 4.17). A good prediction of the vertical convergence is obtained but the horizontal convergence is overestimated. In that direction, the proximity of the shear bands induces excessive deformations. In the long term, the delayed deformations that are observed *in situ* might be explained by consolidation or creep effects. In contrast to this, when gallery ventilation is reproduced, the material close to the gallery wall becomes elastic again which restricts the plastic deformation and convergence in the long term.

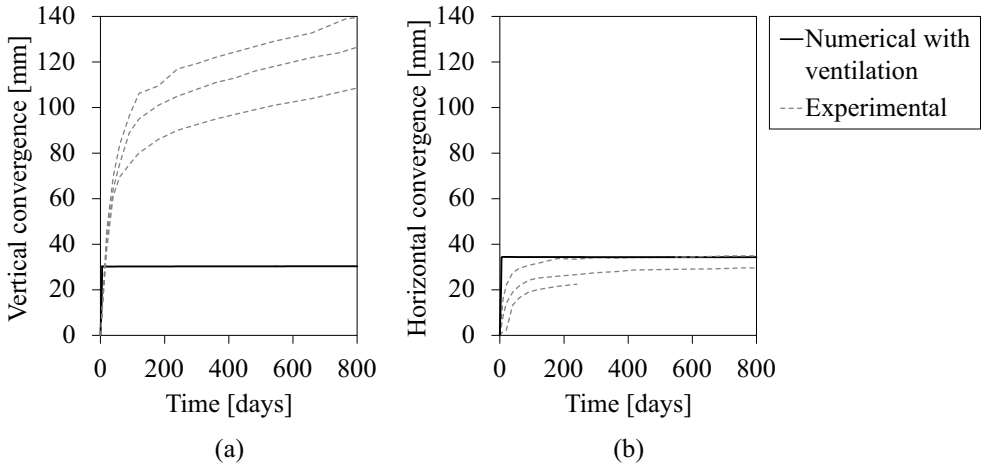

Fig. 4.18: Evolution of the (a) vertical and (b) horizontal convergences during and after gallery excavation, with comparison to experimental results, for a modelling without strain localisation and including gallery ventilation.

Moreover, it is well known that the fracturing structure varies when considering another initial stress state or another gallery direction for the considered host material (Armand et al., 2014). The modelled gallery, drilled in the Callovo-Oxfordian claystone, is oriented in the direction of the minor horizontal principal stress, which leads to an anisotropic initial stress state in the gallery section. Since no other mechanical anisotropy is considered, this anisotropic initial stress state permits the appearance of shear strain localisation. Considering a gallery oriented parallel to the major horizontal principal stress would lead to a quasi-isotropic initial stress state (very low anisotropy) in the gallery section. Unfortunately, this type of initial stress state does not permit the strain localisation appearance for an isotropic mechanical behaviour. In this case, the anisotropic rock behaviour should also be considered to model the fractures with shear bands.

4.4 Conclusions and outlooks

Following evidences of shear fractures, the second gradient theory is used to properly model the fractures around galleries with strain localisation in shear band mode. The theory is successfully extended to biphasic porous media under unsaturated conditions, and the solid grain compressibility is taken into account through the Biot's coefficient.

By using the second gradient model, the excavation fractured zone around a gallery in claystone is fairly well reproduced. Within this zone, the modelling provides information about the fracturing structure and its evolution that are in good agreement with *in situ* observations and measurements. In fact, fracturing represented by strain localisation bands develops during the gallery excavation and the modelling exhibits a chevron fracture pattern around the gallery. This pattern and the extent of the shear strain localisation zone correspond fairly well to fracture observations and measurements, with a significantly larger extent in the direction of the minor

principal stress in the gallery section. The anisotropy of the convergence and the differences between results in the horizontal and vertical directions can be well explained by the material anisotropic stress state as well as by the strain localisation bands. Furthermore, even if important changes occur during the drilling, transient and long-term effects are observed after it.

The impacts of shear strain localisation bands and gallery ventilation on pore water pressures, degree of saturation, and displacements are highlighted. Regarding the influence of the gallery ventilation, a desaturation is observed close to the gallery wall and tends to disappear deeper in the rock mass where the claystone remains fully saturated. Moreover, the gallery convergence is reproduced with its anisotropy, its long-term evolution, and the influence of the rock desaturation. The anisotropic convergence is related to the strain localisation bands whose pattern is mostly dictated by the material anisotropic stress state. Despite the good reproduction of the vertical convergence, the horizontal convergence has still to be improved.

To further enhance the modelling, the rock behaviour and its properties changes still need to be better addressed. From a mechanical point of view, the anisotropic and viscoplastic behaviours of the material should be taken into account. The anisotropic behaviour may permit the development of strain localisation for a gallery having a quasi-isotropic initial stress state in its section. Time-dependent effects, such as viscoplasticity and creep deformations, may allow to improve the long-term behaviour of the material and the reproduction of the convergence increase when gallery ventilation is performed. On the other hand, characterising the influence of the rock fracturing or damage on the hydraulic properties remains a major issue. More precisely, it is necessary to develop a more accurate modelling of the hydro-mechanical coupling that occurs in the excavation damaged zone.

Chapter 5

Shear banding in cross-anisotropic rock

Abstract Sedimentary geomaterials such as rocks frequently exhibit cross-anisotropic properties and their behaviour depends on the direction of loading with respect to their microstructure. As far as material rupture is concerned, localised deformation in shear band mode appears generally before cracks and material failure. The influence of cross-anisotropy on the shear strain localisation remains an important issue that needs to be investigated. To do so, a constitutive elasto-viscoplastic cross-anisotropic model, that includes anisotropy of both elastic and plastic characteristics, is defined. For the plastic part of the model, the anisotropy of a strength parameter is introduced with a microstructure fabric tensor. Then, the fractures are modelled in Callovo-Oxfordian claystone with finite element method by considering the development of shear strain localisation bands, and by using an enriched model to reproduce the shear banding properly. The cross-anisotropy influence on shear banding is studied through numerical applications of small and large-scale geotechnical problems that engender fractures. The two considered applications are a plane-strain biaxial compression test and an underground gallery excavation. The numerical results provide information about the influence of cross-anisotropy on the appearance and development of shear bands. It has been noticed, among other observations, that the material strength vary with the loading direction and that the development and shape of the excavation fractured zone developing around a gallery is strongly influenced by the anisotropic characteristics. Furthermore, rock materials may exhibit time-dependent or delayed plastic deformation that could be of importance for the long-term behaviour of underground structures. The material viscosity is consequently included in the modelling to reproduce the increase of deformation and gallery convergence in the long term. The details of the shear banding modelling in cross-anisotropic rocks are available in the research articles of Pardoen et al. (2015c) and Pardoen and Collin (2016).

Articles

Pardoen, B., Seyedi, D. M., and Collin, F. (2015). Shear banding modelling in cross-anisotropic rocks. *Int J Solids Struct*, 72:63-87. doi: 10.1016/j.ijsolstr.2015.07.012.

Pardoen, B. and Collin, F. (2016). Modelling the influence of strain localisation and viscosity on the behaviour of underground drifts drilled in claystone. *Comput Geotech*, in press, doi: 10.1016/j.compgeo.2016.05.017.

5.1 Anisotropy features and influence on fractures

Various geomaterials, like soils and rocks, are sedimentary materials that feature an anisotropic behaviour and different responses depending on the loading direction. The first type of anisotropy is the inherent anisotropy that is related to the initial fabric of the particles assembly (Casagrande and Carillo, 1944; Arthur and Menzies, 1972; Ochiai and Lade, 1983). For sedimentary materials, a layered structure is observed because they were usually deposited vertically in a succession of layers and were subjected to stress. Over time, this structure can lead to the creation of weakness planes called bedding planes due to metamorphism or diagenetic processes (Blümling et al., 2007). From a theoretical point of view and due to this structural arrangement, the anisotropic properties of such materials exhibit a certain type of symmetry with a symmetry axis and isotropic properties in the (bedding) planes perpendicular to this axis (Abelev and Lade, 2004). This type of material is said to be transversely isotropic or cross-anisotropic (Amadei, 1983), and their behaviour and response to external solicitations depend on the loading direction with respect to their microstructure. A second possible type of anisotropy is an induced anisotropy that results of the loading and deformation following the material deposition (Arthur et al., 1977a; Abelev and Lade, 2004). During material loading, applied stresses may in fact engender a modification of the solid particles spatial arrangement which can lead to anisotropic material behaviour (Oda et al., 1985). Induced anisotropy was firstly observed by Casagrande and Carillo (1944) in relation to soils shear failure and it can develop in materials having pre-existing inherent anisotropic

features as well as in inherent isotropic materials.

Since the material behaviour and failure constitute crucial issues in many geotechnical problems, various theories and failure criteria have been developed for these anisotropic materials (Graham and Houlsby, 1983; Duveau et al., 1998; Abelev and Lade, 2004; Lade, 2007). The influence of cross-anisotropy on the material behaviour, on the shear strain localisation, and on the fractures has been investigated by different authors whether on a small or on a large scale. At small scale, Abelev and Lade (2003) and Lade et al. (2008) performed different tests on sand with rotation of principal stress axes with regard to the isotropic planes of the material. They concluded that the material strength (peak stress value) as well as the shear band inclination and pattern may vary with the direction of loading (Fig. 5.1). Among other authors, Tejchman et al. (2007) analysed the effect of fabric anisotropy on the shear strain localisation and on the stress-strain behaviour, during plane-strain compression tests performed on cohesionless granular materials. They concluded that the peak stress amplitude varies with the direction of the bedding planes, while it has only a minor influence on the shear zone thickness and inclination. However, most of the laboratory experiments on strain localisation analyse sandy materials and only a few are realised on rocks. At large scale, the material cross-anisotropy may also influence the development of fractures around underground galleries as indicated by Armand et al. (2014) and Marschall et al. (2008). This influence has been discussed previously in section 2.2.1. It is to recall that the fracturing pattern and its extension in Callovo-Oxfordian claystone depend on the stress state anisotropy, and that fractures even develop for galleries having a quasi-isotropic stress state in their sections. It suggests that the anisotropic characteristics of the material may play a paramount role in the onset of fractures.

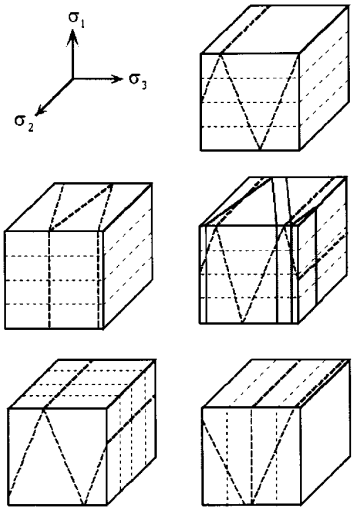

Fig. 5.1: Shear banding patterns observed on true triaxial tests performed on Santa Monica beach sand for various material orientations (Abelev and Lade, 2003).

In the following, the influence of the material cross-anisotropic features on the fracturing, modelled with shear strain localisation bands, will be principally analysed. It will be investigated with finite element method for a cross-anisotropic rock, both on a small and on a large scales. Firstly, the constitutive elasto-viscoplastic and cross-anisotropic model is detailed in section 5.2. The anisotropy is taken into account in the model both in the elastic and plastic behaviours. For the plasticity, the anisotropy of a strength parameter (the material cohesion) is introduced with a second order microstructure fabric tensor, which is a measure of the material fabric that describes the spatial distribution of the considered strength parameter (Pietruszczak and Mroz, 2000; Pietruszczak et al., 2002). The cohesion therefore specifies the effect of the loading orientation relative to the material microstructure directions. Then, once the model is described, the different parameters are calibrated based on experimental data (section 5.3).

Finally, the influence of cross-anisotropy on shear strain localisation is investigated in rock with hydro-mechanical numerical applications. A plane-strain biaxial compression test and the excavation of an underground gallery are considered among various geotechnical problems generating fractures. Concerning the biaxial compression, the appearance of shear banding and its orientation will be investigated, as well as the effect of bedding planes rotation. For the gallery excavation modelling, a particular attention is paid to the development of an excavation fractured zone around the gallery due to material anisotropy. This development is analysed firstly in case of initial isotropic stress state, then for a major stress in the gallery axial direction.

The main novelties consist firstly in the introduction of the material inherent anisotropy and viscosity in finite element method involving coupled second gradient approach, and secondly in the reproduction of strain localisation with rock anisotropy influence on a large scale, around a gallery.

5.2 Cross-anisotropic elasto-viscoplastic constitutive model

The mechanical constitutive model is defined by an elasto-viscoplastic model taking into account the transversely isotropic behaviour of the material, in both elastic and plastic behaviours. For the first gradient part, an anisotropic mechanical model is developed from the isotropic one described in section 2.4.5. In addition, viscosity effects are introduced in the model with time-dependent plastic strain. For the second gradient part of the model, the constitutive law remains isotropic but the influence of the anisotropy of the first gradient part on the linearisation of the balance equations is exposed. Lastly, for the hydraulic model, the anisotropy of hydraulic properties that has already been included in Darcy's equation is recalled.

5.2.1 First gradient mechanical model

The elasto-viscoplastic relation for the stress-strain relationship is expressed in rate (incremental) form as follows:

$$\tilde{\sigma}'_{ij} = C_{ijkl}\ \dot{\varepsilon}_{kl} \tag{5.1}$$

where $\dot{\varepsilon}_{ij}$ is the strain rate, C_{ijkl} is the constitutive tensor, and $\tilde{\sigma}'_{ij}$ is the Jaumann objective effective stress rate. The pore fluid pressure effect on the Cauchy total stress field σ_{ij} is characterised by taking into account the anisotropy of Biot's coefficients and the partial saturation effect. The Biot's stress definition for unsaturated and anisotropic materials yields:

$$\sigma_{ij} = \sigma'_{ij} + b_{ij}\ S_{r,w}\ p_w \tag{5.2}$$

where σ'_{ij} is the effective stress field, $S_{r,w}$ is the degree of water saturation, p_w is the pore water pressure, and b_{ij} is the Biot's anisotropic tensor (see Eqs. 5.22 and 5.42).

Viscosity is taken into account by assuming that the plastic strain is composed of a time-independent instantaneous strain ε^p_{ij} but also of a time-dependent creep strain ε^{vp}_{ij}. Consequently, the total strain rate is partitioned in an elastic $\dot{\varepsilon}^e_{ij}$, a plastic $\dot{\varepsilon}^p_{ij}$, and a viscoplastic $\dot{\varepsilon}^{vp}_{ij}$ components:

$$\dot{\varepsilon}_{ij} = \dot{\varepsilon}^e_{ij} + \dot{\varepsilon}^p_{ij} + \dot{\varepsilon}^{vp}_{ij} \tag{5.3}$$

The elastic and plastic behaviours are defined in the following for anisotropic materials, which means that the elastoplastic properties depend on the coordinate axes to which the properties are referred and therefore depend on the orientation. Furthermore, as the plastic strain, the viscoplastic strain is described by a loading function, a viscoplastic potential, and a hardening law.

Linear elasticity theory

The linear elastic theory is based on the Hooke's law:

$$\tilde{\sigma}'_{ij} = C^e_{ijkl}\ \dot{\varepsilon}^e_{kl} \tag{5.4}$$

where $\dot{\varepsilon}^e_{ij}$ is the elastic strain rate and C^e_{ijkl} is the elastic stiffness tensor of the drained material, which is anisotropic for anisotropic materials (Graham and Houlsby, 1983). This tensor is composed of 36 components that reduce, because of symmetry, to 21 independent parameters that are necessary to fully describe the material anisotropic elasticity. Generally, materials show limited forms of anisotropy. For instance, an orthotropic elastic material has three mutually orthogonal symmetry planes and a cross-anisotropic material exhibits parallel isotropic planes with a vertical axis of symmetry (Lekhnitskii, 1963). The planes of material symmetry are described in Fig. 5.2 for these two types of anisotropic materials.

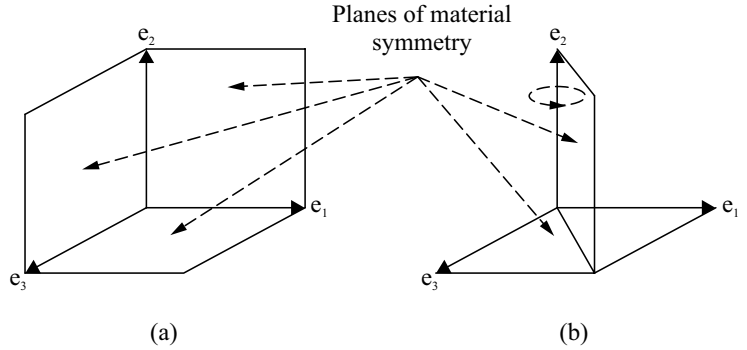

Fig. 5.2: Anisotropic materials: (a) orthotropic anisotropy and (b) transverse isotropy.

In case of orthotropy and cross-anisotropy, the properties are related to the orthotropic (and orthogonal) coordinate axes e_1, e_2, and e_3, and the (e_1,e_2,e_3) space represents the orthotropic configuration (Amadei, 1983) as illustrated in Fig. 5.3. These orthotropic coordinate axes may not correspond to the global coordinate axes (x,y,z) and the change of reference system is characterised by the rotations around the orthotropic axes. In Fig. 5.3, only one rotation around the e_3 axis is illustrated since this isotropic planes rotation will be analysed in numerical applications. However, rotations around the other orthotropic axes can be envisaged in three-dimensional problems.

The Hooke's stress-strain relation is formulated in the orthotropic axes as follows:

$${}^\sharp\tilde{\sigma}'_{ij} = C^e_{ijkl}\ {}^\sharp\dot{\varepsilon}^e_{kl} \tag{5.5}$$

$${}^\sharp\dot{\varepsilon}^e_{ij} = D^e_{ijkl}\ {}^\sharp\tilde{\sigma}'_{kl} \tag{5.6}$$

where the notation $^\sharp$ denotes a quantity in the orthotropic axes and D^e_{ijkl} is the elastic compliance tensor corresponding to the inverse of the matrix C^e_{ijkl}. For orthotropy, the behaviour of the material is described by 9 independent parameters: E_1, E_2, E_3, ν_{12}, ν_{13}, ν_{23}, G_{12}, G_{13}, G_{23}. The

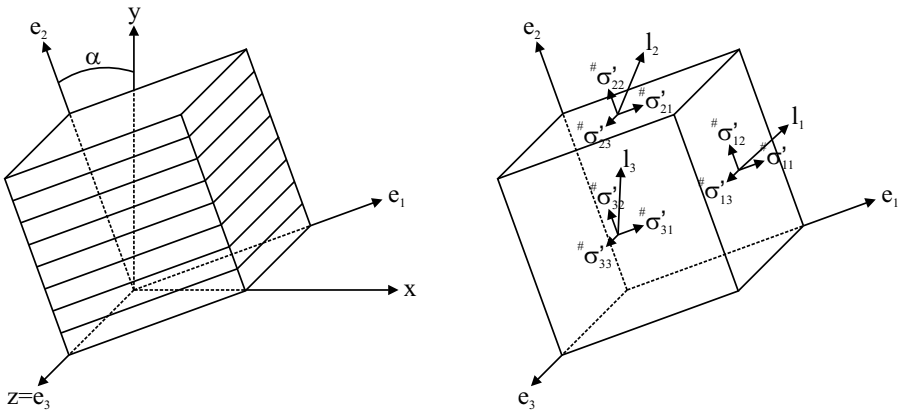

Fig. 5.3: Principal and orthotropic axes for a representative elementary volume exhibiting cross-anisotropy: (a) rotation of the isotropic planes, (b) stress state in the orthotropic configuration and generalised loading vector.

elastic relation is defined as follows:

$$\begin{bmatrix} {}^{\sharp}\dot{\varepsilon}^{e}_{11} \\ {}^{\sharp}\dot{\varepsilon}^{e}_{22} \\ {}^{\sharp}\dot{\varepsilon}^{e}_{33} \\ {}^{\sharp}\dot{\varepsilon}^{e}_{12} \\ {}^{\sharp}\dot{\varepsilon}^{e}_{13} \\ {}^{\sharp}\dot{\varepsilon}^{e}_{23} \end{bmatrix} = \begin{bmatrix} \frac{1}{E_1} & -\frac{\nu_{21}}{E_2} & -\frac{\nu_{31}}{E_3} & 0 & 0 & 0 \\ -\frac{\nu_{12}}{E_1} & \frac{1}{E_2} & -\frac{\nu_{32}}{E_3} & 0 & 0 & 0 \\ -\frac{\nu_{13}}{E_1} & -\frac{\nu_{23}}{E_2} & \frac{1}{E_3} & 0 & 0 & 0 \\ 0 & 0 & 0 & \frac{1}{2\,G_{12}} & 0 & 0 \\ 0 & 0 & 0 & 0 & \frac{1}{2\,G_{13}} & 0 \\ 0 & 0 & 0 & 0 & 0 & \frac{1}{2\,G_{23}} \end{bmatrix} \begin{bmatrix} {}^{\sharp}\tilde{\sigma}'_{11} \\ {}^{\sharp}\tilde{\sigma}'_{22} \\ {}^{\sharp}\tilde{\sigma}'_{33} \\ {}^{\sharp}\tilde{\sigma}'_{12} \\ {}^{\sharp}\tilde{\sigma}'_{13} \\ {}^{\sharp}\tilde{\sigma}'_{23} \end{bmatrix} \tag{5.7}$$

and the equality below must be satisfied due to the symmetry of the tensor:

$$\frac{\nu_{ij}}{E_i} = \frac{\nu_{ji}}{E_j} \tag{5.8}$$

which corresponds to:

$$\frac{\nu_{12}}{E_1} = \frac{\nu_{21}}{E_2} \quad , \quad \frac{\nu_{13}}{E_1} = \frac{\nu_{31}}{E_3} \quad , \quad \frac{\nu_{23}}{E_2} = \frac{\nu_{32}}{E_3} \tag{5.9}$$

Moreover, thermodynamic considerations require that the energy stored in a material configuration Ω undergoing deformation must be positive for elastic materials (Lekhnitskii, 1963). The strain energy per unit volume reads:

$$\frac{1}{2}\,{}^{\sharp}\dot{\varepsilon}^{e}_{ij}\,{}^{\sharp}\tilde{\sigma}'_{ij} = \frac{1}{2}\,{}^{\sharp}\dot{\varepsilon}^{e}_{ij}\,{}^{\sharp}\dot{\varepsilon}^{e}_{kl}\,C^{e}_{ijkl} = \frac{1}{2}\,{}^{\sharp}\tilde{\sigma}'_{ij}\,{}^{\sharp}\tilde{\sigma}'_{kl}\,D^{e}_{ijkl} > 0 \tag{5.10}$$

This quadratic form of the strain energy function is positive definite if the conditions below are satisfied:

$$1 - \nu_{12}\,\nu_{21} > 0 \quad , \quad 1 - \nu_{13}\,\nu_{31} > 0 \quad , \quad 1 - \nu_{23}\,\nu_{32} > 0 \tag{5.11}$$

$$1 - \nu_{12}\,\nu_{23}\,\nu_{31} - \nu_{21}\,\nu_{13}\,\nu_{32} - \nu_{12}\,\nu_{21} - \nu_{13}\,\nu_{31} - \nu_{23}\,\nu_{32} > 0 \tag{5.12}$$

$$E_1 > 0 \quad , \quad E_2 > 0 \quad , \quad E_3 > 0 \tag{5.13}$$

$$G_{12} > 0 \quad , \quad G_{13} > 0 \quad , \quad G_{23} > 0 \tag{5.14}$$

By inverting the compliance matrix:

$$C^e_{ijkl} = \left[D^e_{ijkl}\right]^{-1} \tag{5.15}$$

the elastic stiffness tensor and the Hooke's law read:

$$\begin{bmatrix} {}^{\sharp}\tilde{\sigma}'_{11} \\ {}^{\sharp}\tilde{\sigma}'_{22} \\ {}^{\sharp}\tilde{\sigma}'_{33} \\ {}^{\sharp}\tilde{\sigma}'_{12} \\ {}^{\sharp}\tilde{\sigma}'_{13} \\ {}^{\sharp}\tilde{\sigma}'_{23} \end{bmatrix} = \begin{bmatrix} \frac{1-\nu_{23}\,\nu_{32}}{E_2\,E_3\,\Upsilon} & \frac{\nu_{21}+\nu_{31}\,\nu_{23}}{E_2\,E_3\,\Upsilon} & \frac{\nu_{31}+\nu_{21}\,\nu_{32}}{E_2\,E_3\,\Upsilon} & 0 & 0 & 0 \\ \frac{\nu_{12}+\nu_{13}\,\nu_{32}}{E_1\,E_3\,\Upsilon} & \frac{1-\nu_{13}\,\nu_{31}}{E_1\,E_3\,\Upsilon} & \frac{\nu_{32}+\nu_{12}\,\nu_{31}}{E_1\,E_3\,\Upsilon} & 0 & 0 & 0 \\ \frac{\nu_{13}+\nu_{12}\,\nu_{23}}{E_1\,E_2\,\Upsilon} & \frac{\nu_{23}+\nu_{21}\,\nu_{13}}{E_1\,E_2\,\Upsilon} & \frac{1-\nu_{12}\,\nu_{21}}{E_1\,E_2\,\Upsilon} & 0 & 0 & 0 \\ 0 & 0 & 0 & 2\,G_{12} & 0 & 0 \\ 0 & 0 & 0 & 0 & 2\,G_{13} & 0 \\ 0 & 0 & 0 & 0 & 0 & 2\,G_{23} \end{bmatrix} \begin{bmatrix} {}^{\sharp}\dot{\varepsilon}^e_{11} \\ {}^{\sharp}\dot{\varepsilon}^e_{22} \\ {}^{\sharp}\dot{\varepsilon}^e_{33} \\ {}^{\sharp}\dot{\varepsilon}^e_{12} \\ {}^{\sharp}\dot{\varepsilon}^e_{13} \\ {}^{\sharp}\dot{\varepsilon}^e_{23} \end{bmatrix} \tag{5.16}$$

with:

$$\Upsilon = \frac{1-\nu_{12}\,\nu_{21}-\nu_{13}\,\nu_{31}-\nu_{23}\,\nu_{32}-2\,\nu_{12}\,\nu_{23}\,\nu_{31}}{E_1\,E_2\,E_3} \tag{5.17}$$

For cross-anisotropy, the number of independent parameters needed to describe the material elasticity decreases to 5: $E_\parallel$, $E_\perp$, $\nu_{\parallel\parallel}$, $\nu_{\parallel\perp}$, $G_{\parallel\perp}$, where the subscripts $\parallel$ and $\perp$ indicate, respectively, the directions parallel and perpendicular to the isotropic planes. Considering (e_1,e_3) as the orientation of the isotropic planes (bedding planes for sedimentary materials) and e_2 as the normal to these planes lead to the following definition of the elastic compliance matrix:

$$\begin{bmatrix} {}^{\sharp}\dot{\varepsilon}^e_{11} \\ {}^{\sharp}\dot{\varepsilon}^e_{22} \\ {}^{\sharp}\dot{\varepsilon}^e_{33} \\ {}^{\sharp}\dot{\varepsilon}^e_{12} \\ {}^{\sharp}\dot{\varepsilon}^e_{13} \\ {}^{\sharp}\dot{\varepsilon}^e_{23} \end{bmatrix} = \begin{bmatrix} \frac{1}{E_\parallel} & -\frac{\nu_{\perp\parallel}}{E_\perp} & -\frac{\nu_{\parallel\parallel}}{E_\parallel} & 0 & 0 & 0 \\ -\frac{\nu_{\parallel\perp}}{E_\parallel} & \frac{1}{E_\perp} & -\frac{\nu_{\parallel\perp}}{E_\parallel} & 0 & 0 & 0 \\ -\frac{\nu_{\parallel\parallel}}{E_\parallel} & -\frac{\nu_{\perp\parallel}}{E_\perp} & \frac{1}{E_\parallel} & 0 & 0 & 0 \\ 0 & 0 & 0 & \frac{1}{2G_{\parallel\perp}} & 0 & 0 \\ 0 & 0 & 0 & 0 & \frac{1}{2G_{\parallel\parallel}} & 0 \\ 0 & 0 & 0 & 0 & 0 & \frac{1}{2G_{\perp\parallel}} \end{bmatrix} \begin{bmatrix} {}^{\sharp}\tilde{\sigma}'_{11} \\ {}^{\sharp}\tilde{\sigma}'_{22} \\ {}^{\sharp}\tilde{\sigma}'_{33} \\ {}^{\sharp}\tilde{\sigma}'_{12} \\ {}^{\sharp}\tilde{\sigma}'_{13} \\ {}^{\sharp}\tilde{\sigma}'_{23} \end{bmatrix} \tag{5.18}$$

The symmetry of the tensor imposes:

$$\frac{\nu_{\perp\parallel}}{E_\perp} = \frac{\nu_{\parallel\perp}}{E_\parallel} \tag{5.19}$$

The shear modulus in the isotropic planes is obtained as follows:

$$G_{\parallel\parallel} = \frac{E_\parallel}{2(1+\nu_{\parallel\parallel})} \tag{5.20}$$

and the other shear moduli are equal because of the symmetry of the stress and strain tensors:

$$G_{\parallel\perp} = G_{\perp\parallel} \tag{5.21}$$

As previously, the elastic stiffness tensor can be obtained by inverting the matrix of Eq. 5.18 or by replacing the subscripts 1, 2, and 3 by $\parallel$, $\perp$, and $\parallel$ in Eqs. 5.16 and 5.17. Lastly, for isotropic materials, the elastic properties are independent of the direction and the previous relations reduces to those of Eqs. 2.76 to 2.78.

Another important aspect of the anisotropic elasticity is the compressibility of the solid grains. It is expressed through Biot's symmetric tensor which is defined for anisotropic material as follows (Cheng, 1997):

$$^\sharp b_{ij} = \delta_{ij} - \frac{C^e_{ijkk}}{3\ K_s} \tag{5.22}$$

where δ_{ij} is the Kronecker symbol and K_s is the bulk modulus of the solid phase. This expression adopts the micro-homogeneity and micro-isotropy assumptions (Cheng, 1997) for which K_s is homogeneous and isotropic at grain scale. The generalised Biot's coefficient reads:

$$b = \frac{b_{ii}}{3} = \frac{^\sharp b_{ii}}{3} = 1 - \frac{K}{K_s} \tag{5.23}$$

where K is the generalised drained bulk modulus of the poroelastic material:

$$K = \frac{C^e_{iijj}}{9} \tag{5.24}$$

For orthotropic materials, the definition of Eq. 5.22 is valid in the orthotropic axes and reduces to a diagonal matrix expressed as follows:

$$^\sharp b_{ij} = \begin{bmatrix} ^\sharp b_{11} & 0 & 0 \\ 0 & ^\sharp b_{22} & 0 \\ 0 & 0 & ^\sharp b_{33} \end{bmatrix} \tag{5.25}$$

Following the Biot's tensor definition of Eq. 5.22, the Biot's coefficients can be expressed as:

$$^\sharp b_{11} = 1 - \frac{C^e_{1111} + C^e_{1122} + C^e_{1133}}{3\ K_s} = 1 - \frac{1 - \nu_{23}\ \nu_{32} + \nu_{21} + \nu_{31}\ \nu_{23} + \nu_{31} + \nu_{21}\ \nu_{32}}{3\ E_2\ E_3\ \Upsilon\ K_s} \tag{5.26}$$

$$^\sharp b_{22} = 1 - \frac{C^e_{2211} + C^e_{2222} + C^e_{2233}}{3\ K_s} = 1 - \frac{\nu_{12} + \nu_{13}\ \nu_{32} + 1 - \nu_{13}\ \nu_{31} + \nu_{32} + \nu_{12}\ \nu_{31}}{3\ E_1\ E_3\ \Upsilon\ K_s} \tag{5.27}$$

$$^\sharp b_{33} = 1 - \frac{C^e_{3311} + C^e_{3322} + C^e_{3333}}{3\ K_s} = 1 - \frac{\nu_{13} + \nu_{12}\ \nu_{23} + \nu_{23} + \nu_{21}\ \nu_{13} + 1 - \nu_{12}\ \nu_{21}}{3\ E_1\ E_2\ \Upsilon\ K_s} \tag{5.28}$$

with Υ defined in Eq. 5.17. For cross-anisotropic materials with isotropic planes oriented parallel to (e_1,e_3), it becomes:

$$^\sharp b_{ij} = \begin{bmatrix} b_\parallel & 0 & 0 \\ 0 & b_\perp & 0 \\ 0 & 0 & b_\parallel \end{bmatrix} \tag{5.29}$$

$$b_\parallel = 1 - \frac{2\ C^e_{\parallel\parallel\parallel\parallel} + C^e_{\parallel\parallel\perp\perp}}{3\ K_s} = 1 - \frac{1 + \nu_{\parallel\parallel} + \nu_{\parallel\parallel}\ \nu_{\perp\parallel} + \nu_{\perp\parallel}}{3\ E_\parallel\ E_\perp\ \Upsilon\ K_s} \tag{5.30}$$

$$b_\perp = 1 - \frac{2\ C^e_{\perp\perp\parallel\parallel} + C^e_{\perp\perp\perp\perp}}{3\ K_s} = 1 - \frac{1 - \nu^2_{\parallel\parallel} + 2\ \nu_{\parallel\perp} + 2\ \nu_{\parallel\perp}\ \nu_{\parallel\parallel}}{3\ E_\parallel\ E_\parallel\ \Upsilon\ K_s} \tag{5.31}$$

$$\Upsilon = \frac{1 - \nu_{|||}^2 - 2\ \nu_{\perp\|}\ \nu_{\|\perp}\left(1 + \nu_{|||}\right)}{E_{\|}^2\ E_{\perp}} \tag{5.32}$$

with identical coefficients values in the isotropic planes direction. For isotropic materials, the Biot's coefficients reduce to:

$$b_{ij} = b\ \delta_{ij} \tag{5.33}$$

with:

$$b = 1 - \frac{K}{K_s} \tag{5.34}$$

$$K = \frac{E}{3(1 - 2\nu)} \tag{5.35}$$

Because the Hooke's law is formulated in the orthotropic axes (Eqs. 5.5 and 5.6) and the stress field is formulated in the global axes (Eq. 5.2), a change of coordinate reference system has to be computed. It is characterised by the three Euler's angles α_i corresponding to rotations around the three orthotropic axes e_i. The matrix of rotation is defined as:

$$R_{ij} = \begin{bmatrix} cos\alpha_2\ cos\alpha_3 & -cos\alpha_2\ sin\alpha_3 & sin\alpha_2 \\ cos\alpha_1\ sin\alpha_3 + sin\alpha_1\ sin\alpha_2\ cos\alpha_3 & cos\alpha_1\ cos\alpha_3 - sin\alpha_1\ sin\alpha_2\ sin\alpha_3 & -sin\alpha_1\ cos\alpha_2 \\ sin\alpha_1\ sin\alpha_3 - cos\alpha_1\ sin\alpha_2\ cos\alpha_3 & sin\alpha_1\ cos\alpha_3 + cos\alpha_1\ sin\alpha_2\ sin\alpha_3 & cos\alpha_1\ cos\alpha_2 \end{bmatrix} \tag{5.36}$$

If only a rotation α around e_3 is considered (Fig. 5.3), as in two-dimensional problems for instance, the rotation matrix reduces to:

$$R_{ij} = \begin{bmatrix} cos\alpha & -sin\alpha & 0 \\ sin\alpha & cos\alpha & 0 \\ 0 & 0 & 1 \end{bmatrix} \tag{5.37}$$

To obtain the elastic strain tensor rate in the orthotropic axes from the one expressed in the global axes, the change of reference system is defined as:

$${}^{\sharp}\dot{\varepsilon}_{ij}^{e} = R_{ik}\ R_{jl}\ \dot{\varepsilon}_{kl}^{e} \tag{5.38}$$

Once the stress state is calculated in the orthotropic axes with Hooke's law (Eq. 5.5) it can be reformulated in the global axes by reversing the rotation:

$$\tilde{\sigma}_{ij}^{'} = R_{ki}\ R_{lj}\ {}^{\sharp}\tilde{\sigma}_{kl}^{'} \tag{5.39}$$

With the above transformations, the stress state can be expressed in both systems:

$$\sigma_{ij} = \sigma_{ij}^{'} + b_{ij}\ S_{r,w}\ p_w \tag{5.40}$$

$${}^{\sharp}\sigma_{ij} = {}^{\sharp}\sigma_{ij}^{'} + {}^{\sharp}b_{ij}\ S_{r,w}\ p_w \tag{5.41}$$

provided that an identical transformation is realised for the Biot's tensor:

$$b_{ij} = R_{ki}\ R_{lj}\ {}^{\sharp}b_{kl} \tag{5.42}$$

Plasticity theory

The plasticity theory is equivalent to the one detailed in section 2.4.5. For the considered material, it consists of a non-associated elastoplastic internal friction model with a Van Eekelen yield surface. In addition to the anisotropic elastic behaviour detailed in the previous section, the plastic behaviour and the strength parameters of the material can also be anisotropic and therefore depend on loading direction and material structure orientation. Various failure criteria for anisotropic materials have been developed and different ways are possible to introduce the structural inherent rock anisotropy in the mechanical constitutive model, and to couple it to strain localisation approach.

Duveau et al. (1998) classified these failure criteria in two main categories: the continuous and the discontinuous criteria. For the continuous approaches (Hill, 1950; Boehler and Sawczuk, 1977), the mathematical description of the inherent anisotropy can be realised with strength variation related to strength tensors, to the type of material symmetries (axes of symmetry), and including stress dependency. To describe the material fabric, the anisotropy has also been formulated by invoking the notion of microstructure fabric tensor (Pietruszczak and Mroz, 2000; Lade, 2007). Moreover, the strength anisotropy can be described in an empirical manner by the determination of evolution laws, as a function of loading orientation, for the strength parameters of isotropic criteria (Jaeger, 1971). For the discontinuous approaches, the emphasis is put on the description of the failure process and on the related physical mechanisms. These theories envisage discontinuous weakness planes (Jaeger, 1960) and assume, for cross-anisotropic rocks, that fracture of the bedding planes or of the rock matrix can occur and are defined by different failure criteria. Other criteria postulate the existence of a critical plane (weakest orientation) along which the failure criterion reaches a maximum (Walsh and Brace, 1964; Hoek and Brown, 1980).

Among the different manners of introducing the anisotropy, the fabric tensor concept is considered. It introduces a second order microstructure tensor which is a measure of the material fabric. This tensor can characterise the arrangement of intergranular contacts (particles assembly), or can describe the spatial distribution of voids, cracks, and material strength parameters, as proposed in homogeneous problems by Chen (2009), Chen et al. (2010), Pietruszczak and Pande (2001), and Pietruszczak et al. (2002).

For anisotropic cohesive-frictional materials and the considered plastic criterion, both cohesive and frictional characteristics could depend on the orientation as considered by Pietruszczak and Mroz (2001) for instance. In the stress invariant plane (Fig. 2.20 (a)), a modification of the cohesion engenders a shifting of the yield surface parallel to the initial surface which means that the strength variation does not evolve with the mean effective stress. A modification of the friction angle engenders an increase of the slope of the yield surface meaning that the strength variation depends on the mean effective stress. To clarify if the strength dependence on the loading orientation evolves with increasing mean stress, the material resistance should be analysed from laboratory compression tests for various orientations and various confining pressures. However, such results are not always available in a sufficient number to precisely define the strength evolution of a given material. In the following, uniaxial compression tests on Callovo-Oxfordian claystone are mainly used to calibrate the anisotropy of the plastic material behaviour and it is assumed that the strength variation depends mainly on the orientation, not on the mean stress. As a consequence, only the cohesion anisotropy is envisaged.

Hereafter, the material cohesion anisotropy is defined with a second order microstructure fabric tensor a_{ij} describing the cohesion spatial distribution. It characterises the initial fabric of the material and its eigenvectors correspond to the principal material microstructure axes, i.e. the orthotropic axes e_i. The cohesion corresponds to the projection of this tensor on a generalised unit loading vector l_i that characterises the loading direction relative to the material microstructure orientations (Pietruszczak and Mroz, 2000, 2001; Chen et al., 2010). As detailed in Fig. 5.3, each component of l_i corresponds to the stress resultant acting on facets of normal

e_i and is defined as follows:

$$l_i = \sqrt{\frac{\sharp\sigma_{i1}'^2 + \sharp\sigma_{i2}'^2 + \sharp\sigma_{i3}'^2}{\sharp\sigma_{jk}' \, \sharp\sigma_{jk}'}} \tag{5.43}$$

where $\sharp\sigma_{ij}'$ is expressed in reference to the material orthotropic axes. Therefore, the cohesion specifies the effect of the load orientation relative to the material axes (Pietruszczak et al., 2002; Pietruszczak, 2010):

$$c_0 = a_{ij} \; l_i \; l_j \tag{5.44}$$

where c_0 is the initial cohesion before softening. It can also be expressed by employing the deviatoric part of the microstructure fabric tensor (Kanatani, 1984):

$$c_0 = \bar{c}\,(1 + A_{ij} \; l_i \; l_j) \tag{5.45}$$

$$A_{ij} = \frac{\hat{a}_{ij}}{\bar{c}} = \frac{a_{ij}}{\bar{c}} - \delta_{ij} \tag{5.46}$$

$$\bar{c} = \frac{a_{ii}}{3} \tag{5.47}$$

where $\bar{c}$ is a microstructure parameter, A_{ij} is a traceless symmetric tensor, $A_{ii} = 0$, and $\hat{a}_{ij}$ is the deviatoric part of the microstructure tensor a_{ij}:

$$\hat{a}_{ij} = a_{ij} - \frac{a_{kk}}{3} \; \delta_{ij} \tag{5.48}$$

The above expression of Eq. 5.45 can be generalised by considering higher order tensors:

$$c_0 = \bar{c}\left(1 + A_{ij} \; l_i \; l_j + b_1 \left(A_{ij} \; l_i \; l_j\right)^2 + b_2 \left(A_{ij} \; l_i \; l_j\right)^3 + ...\right) \tag{5.49}$$

where b_1, b_2... are constants.

Considering orthotropy and referring the problem to the material axes imply $A_{ij} = 0$ for $i \neq j$ with $A_{ii} = A_{11} + A_{22} + A_{33} = 0$ and the projection of A_{ij} on the loading vector is:

$$A_{ij} \; l_i \; l_j = A_{11} \; l_1^2 + A_{22} \; l_2^2 + A_{33} \; l_3^2 \tag{5.50}$$

Moreover, for an isotropic stress state $l_1 = l_2 = l_3 = \sqrt{1/3}$ by Eq. 5.43 which leads to $A_{ij} \; l_i \; l_j = A_{ii}/3 = 0$ by Eq. 5.50 and to $c_0 = \bar{c}$ by Eq. 5.49. Consequently, $\bar{c}$ is the cohesion of the orthotropic material subjected to an isotropic loading. Considering cross-anisotropy implies $A_{11} = A_{33} = A_{\parallel}$ and $A_{22} = -A_{11} - A_{33} = -2A_{\parallel}$ if the isotropic planes are parallel to (e_1,e_3), with $A_{\parallel}$ being the component of the microstructure operator A_{ij} in the isotropic planes. This yields:

$$A_{ij} \; l_i \; l_j = A_{\parallel}\left(1 - 3 \; l_2^2\right) \tag{5.51}$$

where l_2 is the component of l_i acting on a facet parallel to the isotropic planes. The late expression for cohesion of Eq. 5.49 becomes:

$$c_0 = \bar{c}\left(1 + A_{\parallel}\left(1 - 3 \; l_2^2\right) + b_1 \; A_{\parallel}^2\left(1 - 3 \; l_2^2\right)^2 + b_2 \; A_{\parallel}^3\left(1 - 3 \; l_2^2\right)^3 + ...\right) \tag{5.52}$$

where the constants $\bar{c}$, $A_{\parallel}$, b_1, b_2... can be obtained from experimental data and laboratory tests.

The above definition of the cohesion is related to the initial material cohesion, before softening. The cohesion softening is given by:

$$c = c_0 + \frac{(c_f - c_0)\,\langle \hat{\varepsilon}_{eq}^p - dec_c \rangle}{B_c + \langle \hat{\varepsilon}_{eq}^p - dec_c \rangle} \tag{5.53}$$

and has already been described in Eq. 2.95. More information about the different softening parameters is available in the section 2.4.5. Because c_0 evolves due to the material fabric and to the loading, it is more appropriate for the cohesion softening to define a final cohesion that evolves in the same manner by:

$$c_f = \frac{c_0}{\xi_c} \tag{5.54}$$

where ξ_c is the ratio of the cohesion softening.

Viscoplasticity theory

Creep deformations may be important to take into account for the long-term feasibility analysis of deep geological repository of nuclear radioactive wastes. Such deformations are introduced with the objective of analysing if a viscoplastic mechanism could improve the reproduction of the increase of gallery convergence in the long term. The approach is basic and involves one simple mechanism for the creep behaviour which is defined independently of the plastic behaviour. It is based on the development proposed by Jia et al. (2008) and Zhou et al. (2008) who analysed the viscoplastic behaviour of the Callovo-Oxfordian claystone.

Viscoplasticity is introduced by considering that the material viscosity implies a time-dependent plastic strain ε_{ij}^{vp} corresponding to a delayed plastic deformation (Perzyna, 1966). The time development of deformation can be related to the progressive evolution of the material microstructure or to mechanical properties degradation (damage) that are due to diverse chemical and physical processes (Shao et al., 2003, 2006a). Different processes with different time scales may exist and lead to different viscoplastic flow mechanisms; nevertheless, only one isotropic mechanism is considered hereafter.

Based on the work of Jia et al. (2008) and Zhou et al. (2008), a viscoplastic flow mechanism is introduced with a yield function F^{vp} and a potential G^{vp}. The viscoplastic loading surface and potential surface are given by:

$$F^{vp} \equiv \sqrt{3}\ II_{\hat{\sigma}'} - \alpha^{vp}\ g\left(\beta\right) \bar{R} \sqrt{A^{vp}\left(C^{vp} + \frac{I_{\sigma'}}{3\bar{R}}\right)} = 0 \tag{5.55}$$

$$G^{vp} \equiv \sqrt{3}\ II_{\hat{\sigma}'} - \left(\alpha^{vp} - \beta^{vp}\right) g\left(\beta\right) \bar{R} \left(C^{vp} + \frac{I_{\sigma'}}{3\bar{R}}\right) = 0 \tag{5.56}$$

where $I_{\sigma'}$ is the first stress invariant, $II_{\hat{\sigma}'}$ is the second deviatoric stress invariant, $\bar{R}$ is a normalising parameter taken as equal to the uniaxial compressive strength $\bar{R} = R_c$, A^{vp} is an internal friction coefficient defining the curvature of the viscoplastic loading surface, C^{vp} is a constant cohesion coefficient that denotes the material cohesion in saturated condition, β^{vp} is a viscoplastic potential parameter, and $g\left(\beta\right)$ is a function allowing to take into account the influence of the Lode angle on the viscoplastic loading surface ($g\left(\beta\right) = 1$ for simplicity reason). Moreover, the consistency condition does not hold for viscoplasticity; thus, the yield function can be positive $F^{vp} \geq 0$.

Both the yield and potential functions are controlled by a delayed viscoplastic hardening function α^{vp} which generates isotropic hardening and describes the increase of the internal friction coefficient related to the viscoplastic loading surface. It is defined as:

$$\alpha^{vp} = \alpha_0^{vp} + \left(1 - \alpha_0^{vp}\right) \frac{\varepsilon_{eq}^{vp}}{B^{vp} + \varepsilon_{eq}^{vp}} \tag{5.57}$$

where α_0^{vp} is the initial threshold for the viscoplastic flow, B^{vp} is a parameter controlling the evolution of α^{vp}, and ε_{eq}^{vp} is the equivalent viscoplastic strain, i.e. the generalised viscoplastic distortion. The rate of the equivalent viscoplastic strain is given by:

$$\dot{\varepsilon}_{eq}^{vp} = \sqrt{\frac{2}{3}\ \dot{\bar{\varepsilon}}_{ij}^{vp}\ \dot{\bar{\varepsilon}}_{ij}^{vp}} \tag{5.58}$$

where the viscoplastic distortion reads (Jia et al., 2008):

$$\dot{\varepsilon}_{ij}^{vp} = \dot{\varepsilon}_{ij}^{vp} - \dot{\varepsilon}_{kk}^{vp}\ \delta_{ij} \tag{5.59}$$

The viscoplastic flow rule is defined as follows (Perzyna, 1966):

$$\dot{\varepsilon}_{ij}^{vp} = \gamma\ \left\langle \frac{F^{vp}}{\bar{R}} \right\rangle^{\mathcal{N}}\ \frac{\partial G^{vp}}{\partial \sigma'_{ij}} \tag{5.60}$$

where γ is the fluidity coefficient that depends generally on the temperature T, $\mathcal{N}$ is a parameter which describes the creep curve shape, and $\langle\ \rangle$ are the Macaulay brackets with $\langle x \rangle = x$ if $x \geq 0$ and $\langle x \rangle = 0$ if $x < 0$. The following function is used for the fluidity:

$$\gamma = \gamma_0\ exp\left(-\frac{\gamma_1}{R\ T}\right) \tag{5.61}$$

where γ_0 is the fluidity value at a reference temperature, R is the gas constant, T is the absolute temperature expressed in Kelvin, and γ_1 is a parameter controlling the influence of temperature on the material viscosity. However, the temperature is assumed constant and a value of $T = 293\ K\ (20\ ^\circ C)$ is adopted.

It has to be mentioned that, in the proposed approach, the plastic and creep deformations are separately treated and two different models are used to describe the deformation mechanisms. The plastic and viscoplastic loading surfaces are not defined with an identical mathematical expression and similar internal variables. Yet, the plastic and viscoplastic strains are both related to the plastic behaviour of the material and differ by the time scales at which they develop. Consequently, for this type of approach, the physical explanation of the creep mechanism is not clearly established. In contrast to this classical approach exist unified approaches for which the plastic and viscoplastic deformations are treated in a similar manner (Zhou et al., 2008). Nonetheless, a classical approach is valid as long as the viscoplastic loading surface remains inside the plastic one.

The two surfaces are illustrated in the stress invariants plane in Fig. 5.4 for different values of the hardening function α^{vp}. It is observed for $\alpha^{vp} = 0$ that the viscoplastic loading surface corresponds to a second deviatoric stress invariant equal to zero, $II_{\hat{\sigma}'} = 0$. Such case is possible only if instantaneous viscoplastic mechanism is envisaged at very low deviatoric stress, without initial threshold for the viscoplastic flow, $\alpha_0^{vp} = 0$. It generates viscoplastic flow $F^{vp} > 0$ and deformation $\dot{\varepsilon}_{ij}^{vp} > 0$ as soon as the deviatoric stress is not equal to zero. For $\alpha^{vp} > 0$, viscoplastic deformations are generated if the current stress state is located outside the viscoplastic loading surface (no consistency condition for viscoplasticity), which causes an increase of α^{vp} and the hardening of the surface. The viscoplastic flow reduces and stops if the current stress state is located inside the surface, which can be achieved by hardening or modification of the stress state.

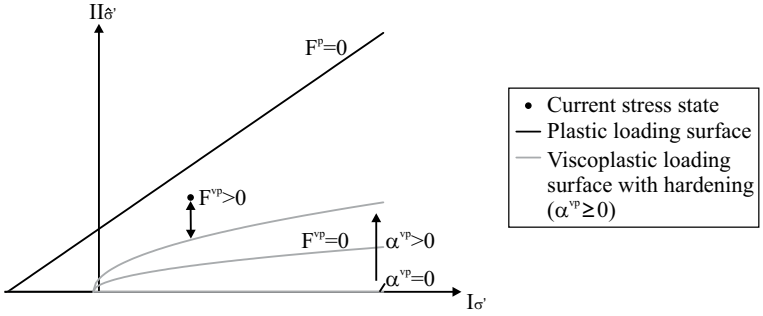

Fig. 5.4: Viscoplastic surface hardening.

5.2.2 Second gradient mechanical model

As already mentioned in section 3.3.2, only a little information is available on the second gradient constitutive equation (Eq. 3.78); thus, the linear elastic law remains isotropic. However, the anisotropy of the first gradient model may have an influence on the balance equations and on their linearisation.

The constitutive tensor C_{ijkl} is involved in the definition of the first gradient constitutive law (Eq. 5.1) and in the matrix $\left[E_1^{\tau 1}\right]$ composing the element stiffness matrix $\left[E^{\tau 1}\right]$ (Eq. 4.64). Nevertheless, the expression of $\left[E_1^{\tau 1}\right]$ remains unchanged (no additional terms) even if C_{ijkl} is anisotropic (Chambon and Moullet, 2004). The Biot's tensor is also anisotropic and the poroelastic relation:

$$\dot{\sigma}' = K\dot{\varepsilon}_v \tag{5.62}$$

assumed in the field equation linearisation of the second gradient model (section 4.1.3), remains valid by considering the relations of Eqs. 5.22 to 5.24. Moreover, the time derivative of the solid density is related to the variations of pore water pressure as well as of mean effective stress, and involves the Biot's coefficient. Nonetheless, the relation:

$$\frac{\dot{\rho}_s}{\rho_s} = \frac{(b-\Phi)\, S_{r,w}\ \dot{p}_w + \dot{\sigma}'}{(1-\Phi)\ K_s} \tag{5.63}$$

remains valid provided that b is the generalised Biot's coefficient (Eq. 5.23). It is also the case for related relationships as the porosity time derivative for instance. Therefore, the different matrices composing $\left[E^{\tau 1}\right]$ remain identical except $\left[K_{WM}^{\tau 1}\right]$ which becomes:

$$\left[K_{WM}^{\tau 1}\right]_{4\times 3} = \begin{bmatrix} 0 & 0 & -b_{11}\ S_{r,w}^{\tau 1} \\ 0 & 0 & 0 \\ 0 & 0 & 0 \\ 0 & 0 & -b_{22}\ S_{r,w}^{\tau 1} \end{bmatrix} \tag{5.64}$$

due to the effective stress definition of Eq. 5.2.

5.2.3 Hydraulic model

The anisotropy of hydraulic properties has already been included in Darcy's equation with the anisotropic intrinsic water permeability tensor $k_{w,ij}$ (Eq. 4.14). For anisotropic materials, the general form of the intrinsic permeability tensor requires nine components to describe the flow characteristics, which reduce to six by symmetry of the tensor. For orthotropic materials, the tensor reduces to a diagonal matrix with three independent parameters that refer to the orthotropic axes:

$${}^\sharp k_{w,ij} = \begin{bmatrix} {}^\sharp k_{w,11} & 0 & 0 \\ 0 & {}^\sharp k_{w,22} & 0 \\ 0 & 0 & {}^\sharp k_{w,33} \end{bmatrix} \tag{5.65}$$

For cross-anisotropic materials, it is defined by two parameters in the directions parallel and perpendicular to the isotropic planes:

$${}^\sharp k_{w,ij} = \begin{bmatrix} k_{w,\parallel} & 0 & 0 \\ 0 & k_{w,\perp} & 0 \\ 0 & 0 & k_{w,\parallel} \end{bmatrix} \tag{5.66}$$

Since the above permeability tensor is related to the orthotropic axes, a change of reference system gives it in the global axes:

$$k_{w,ij} = R_{ki}\ R_{lj}\ {}^\sharp k_{w,ij} \tag{5.67}$$

If the isotropic planes are horizontal, as for various sedimentary geomaterials with stratified structure, then the permeabilities correspond to the horizontal and vertical ones: $k_{w,\parallel} = k_{w,h}$ and $k_{w,\perp} = k_{w,v}$ as in Eq. 4.22.

5.3 Calibration of model parameters

The Callovo-Oxfordian claystone is a sedimentary material that exhibits horizontal or quasi-horizontal bedding planes; thus, the main orientations of anisotropy are located in the horizontal isotropic planes and along the vertical direction. It goes without saying that the calibration of the claystone parameters has to take into account these preferential material directions. In this section, the anisotropic and elasto-viscoplastic mechanical parameters are calibrated by assuming a homogeneous material without strain localisation as in previous calibration (section 4.2). Localised solutions with shear banding will be interpreted in the numerical modelling of section 5.4. The anisotropic hydraulic parameters have already been defined for the considered claystone with $k_{w,\parallel} = k_{w,h}$ and $k_{w,\perp} = k_{w,v}$, and will only be summarised without further investigations.

5.3.1 Elastic parameters

To evaluate the anisotropic elastic parameters, compression experiments have been realised on samples for different loading directions with regard to the orientation of the isotropic planes (Fig. 5.5). The loading direction is defined by the angle α between the normal to the bedding planes and the axial (vertical) direction of loading. For a loading with stress acting in the i direction, the Young's modulus is the ratio of the stress to the strain in the i direction:

$$E_i = \frac{\sigma_i}{\varepsilon_i} \tag{5.68}$$

whilst the Poisson's ratio is the ratio of strain in the j direction to the strain in the i direction:

$$\nu_{ij} = -\frac{\varepsilon_j}{\varepsilon_i} \tag{5.69}$$

The indexes i and j are not doubled in the latter expressions to avoid confusion with summation index. By adequately placing strain gauges on the samples, a loading perpendicular to the bedding planes ($\alpha = 0°$) allows to determine $E_\perp$ and $\nu_{\perp\parallel}$, a parallel loading ($\alpha = 90°$) provides $E_\parallel$ and $\nu_{\parallel\parallel}$, and an inclined loading provides $G_{\parallel\perp}$ (Amadei, 1983). Such determination requires that the anisotropic directions are clearly apparent and known beforehand.

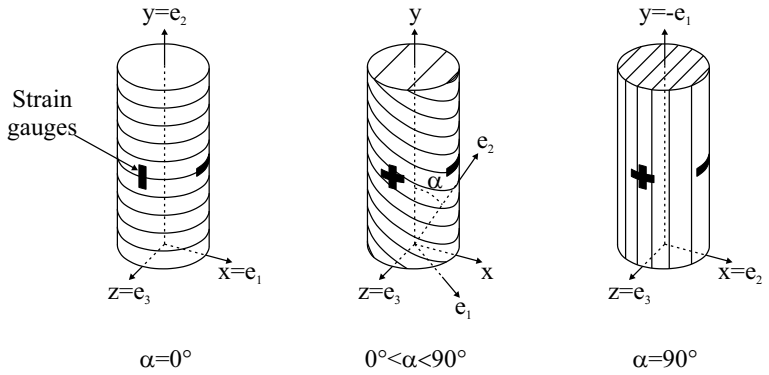

Fig. 5.5: Samples under axial compression with different orientations of the isotropic planes.

Following the reference document of Andra (2005b) and the technical report of Charlier et al. (2008) that detail the behaviour of the Callovo-Oxfordian claystone, the ratio of Young's modulus parallel and perpendicular to the bedding planes ranges from 1.05 to 1.4, with average values of about $E_\perp = 4\ GPa$, $E_\parallel = 5\ GPa$, and $E_\parallel/E_\perp = 1.25$. For the other anisotropic elastic parameters, a certain dispersion is observed and a clear tendency is not straightforward. The values that are finally chosen are detailed in Table 5.1. Moreover, the Biot's coefficient in the orientation of the bedding planes corresponds to the isotropic value used previously $b_\parallel = 0.6$ which gives $K_s = 8.88\ GPa$ and $b_\perp = 0.64$ by Eqs. 5.30 and 5.31.

Symbol	Name	Value	Unit
$E_{\parallel}$	Parallel Young's modulus	5	GPa
$E_{\perp}$	Perpendicular Young's modulus	4	GPa
$G_{\parallel\perp}$	Shear modulus	1.63	GPa
$\nu_{\parallel\parallel}$	Poisson's ratio	0.24	–
$\nu_{\parallel\perp}$	Poisson's ratio	0.33	–
$b_{\parallel}$	Parallel Biot's coefficient	0.60	–
$b_{\perp}$	Perpendicular Biot's coefficient	0.64	–
ρ_s	Solid grain density	2750	kg/m^3

Table 5.1: Anisotropic elastic mechanical parameters.

5.3.2 Plastic parameters

The calibration of the plastic parameters is realised based on experimental data provided by the Andra in the context of the benchmark named "Transversal action - Models" (Seyedi et al., 2012, 2013) and on additional compression tests (Andra, 2005b; Charlier et al., 2008; Yang et al., 2013). The different experimental results are detailed in this section together with the calibration of the numerical model.

Hardening and softening

The hardening and softening plastic behaviour of the Callovo-Oxfordian claystone is calibrated based on triaxial compression tests. The reference tests are performed at different confining pressures, under a relative humidity of 90 %, and are assumed to be realised under undrained conditions. Their characteristics and results are available in Table 5.2 and Fig. 5.6, where ε_1 is the axial strain, ε_3 is the lateral strain, and $\underline{q}$ is the deviatoric stress corresponding to the difference between the axial stress σ_1 and the confining stress σ_3:

$$\underline{q} = \sigma_1 - \sigma_3 \tag{5.70}$$

The tests are numerically reproduced by finite element method, with a hydro-mechanical modelling in two-dimensional axisymmetric state. The value $RH = 90$ % corresponds to $p_w = -14.2\ MPa$ by Kelvin's law and to $S_{r,w} = 81$ % by the retention curve of the material. As previously (section 4.2), the material is considered with an isotropic plasticity (no cohesion anisotropy) and as homogeneous in a first approach. The pre-peak non-linear behaviour is controlled by friction angle hardening and the post-peak behaviour is represented by cohesion softening. Because the material is subjected to compression, either a Drucker-Prager or a Van Eekelen yield criterion can be used without affecting the results and only the compressive resistance is calibrated. The calibration results for each individual triaxial compression test are available in Fig. 5.6 and Table 5.2 where one can observe that the values of c_f are widely scattered. Therefore, only the friction angle hardening will be included in the following calibrations for homogeneous material; the cohesion softening will be introduced later to model shear banding (section 5.4). Nevertheless, the average values are kept at this stage and a global calibration with this set of parameters is illustrated in Fig. 5.6 without softening. In that figure are also detailed the results for an anisotropic plasticity which will be discussed further.

Extensional properties

The extensional material properties are evaluated from triaxial extension tests that are performed at constant mean stress:

$$\sigma = \frac{\sigma_{ii}}{3} \tag{5.71}$$

Symbol	Name	Triax 01	Triax 02	Triax 03	Triax 04	Triax 05	Average	Unit
	Laboratory	LML	LML	LML	LAEGO	LAEGO		
RH	Relative humidity	90	90	90				%
$\dot{\varepsilon}$	Strain rate	1×10^{-6}	1×10^{-6}	1×10^{-6}	20×10^{-6}	3.5×10^{-6}		s^{-1}
σ_3	Confining pressure	12	12	6	2	12		MPa
α	Orientation of the loading	0	90	0	0	0		°
ψ_c	Dilatancy angle	0.5	0.5	0.5	0.5	0.5	0.5	°
$\varphi_{c,0}$	Initial compression friction angle	10	10	10	10	6	10	°
$\varphi_{c,f}$	Final compression friction angle	23	22	24	23	24	23	°
B_φ	Friction angle hardening coefficient	0.0010	0.0015	0.0007	0.0005	0.0015	0.0010	–
dec_φ	Friction angle hardening shifting	0	0	0	0	0	0	–
c_0	Initial cohesion	4	4	4	4.5	5	4.2	MPa
c_f	Final cohesion	1	0.04	0.04	1	2.5	$0.04 - 2$	MPa
B_c	Cohesion softening coefficient	0.001	0.0005	0.002	0.002	0.001	0.001	–
dec_c	Cohesion softening shifting	0.016	0.014	0.007	0.004	0.015	0.011	–

Table 5.2: Triaxial compression tests and calibration of plastic parameters for elastoplastic mechanical model.

Two test results are analysed, one with $\sigma = 12\ MPa$ and another with $\sigma = 13\ MPa$, for an axial load perpendicular to the bedding planes and assuming a relative humidity of $RH = 90\%$ as well as undrained conditions (as for the triaxial compression tests). During these tests, the axial load decreases and the confining pressure increases; therefore, the extension is in the axial direction. The modelling is performed with both the Drucker-Prager and the Van Eekelen plastic criteria, for an isotropic plasticity, and with the average parameters of Table 5.2. The numerical results without cohesion softening are illustrated in Fig. 5.7 where they are compared to the experimental results. Using the Van Eekelen model instead of the Drucker-Prager model improves the fitting by avoiding an overestimation of the material resistance. In fact, the resistance in extension is lower than in compression with the Van Eekelen model, which is not the case for the Drucker-Prager criterion. This validates the use of the Van Eekelen criterion for the following numerical applications. The final friction angles in compression and extension are equal but the initial friction angle in extension is decreased to better match the experimental curves: $\varphi_{e,f} = \varphi_{c,f} = 23°$, $\varphi_{e,0} = 7°$, and $\varphi_{c,0} = 10°$. The dilatancy angles in compression and extension are also equal $\psi_c = \psi_e = 0.5°$.

Anisotropy of cohesion

The anisotropic plastic parameters for the cohesion in Eq. 5.52 are determined from compression tests (Andra, 2005b; Charlier et al., 2008; Yang et al., 2013) which results indicate that the material strength varies upon the loading orientation α. For a triaxial compression, this orientation is linked to the loading vector component l_2 by the relation:

$$l_2 = \sqrt{\frac{\sigma_3^2\ sin^2\alpha + \sigma_1^2\ cos^2\alpha}{2\ \sigma_3^2 + \sigma_1^2}} \tag{5.72}$$

which reduces to:

$$l_2 = cos\alpha \tag{5.73}$$

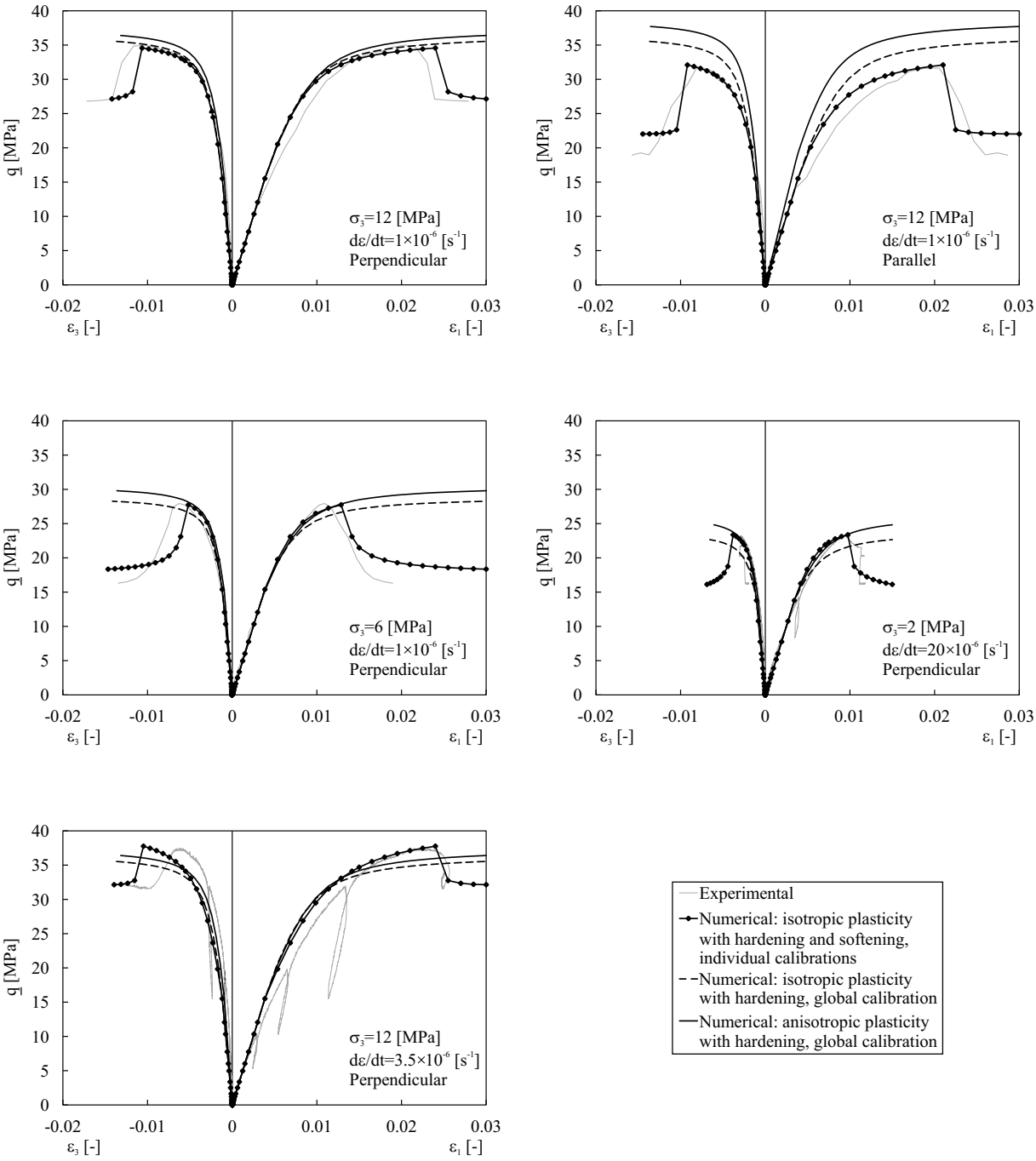

Fig. 5.6: Fitting of triaxial compression tests for elastoplastic mechanical model.

for a uniaxial compression. For this type of compression, the cohesion and the uniaxial compressive strength R_c are linked by:

$$c = \frac{1 - sin\varphi_{c,f}}{2\ cos\varphi_{c,f}}\ R_c + b\ S_{r,w}\ p_w\ tan\varphi_{c,f} \tag{5.74}$$

based on a Drucker-Prager criterion and on the effective stress definition. The cohesion values for different orientations can be obtained from mean uniaxial compressive strengths detailed by Charlier et al. (2008): $R_{c,0^\circ} = R_{c,\perp} = 23.5\ MPa$, $R_{c,30^\circ} = 18.7\ MPa$, $R_{c,90^\circ} = R_{c,\parallel} = 20.6\ MPa$. It is assumed that the samples are slightly desaturated ($S_{r,w} = 95\%$ from Charlier et al. (2008)), $\varphi_{c,f} = 23^\circ$ (Table 5.2), the generalised Biot's coefficient value is $b = 0.61$, and p_w is obtained from the retention curve of the material. This leads to $c_{0^\circ} = c_\perp = 6.3\ MPa$, $c_{30^\circ} = 4.8\ MPa$,

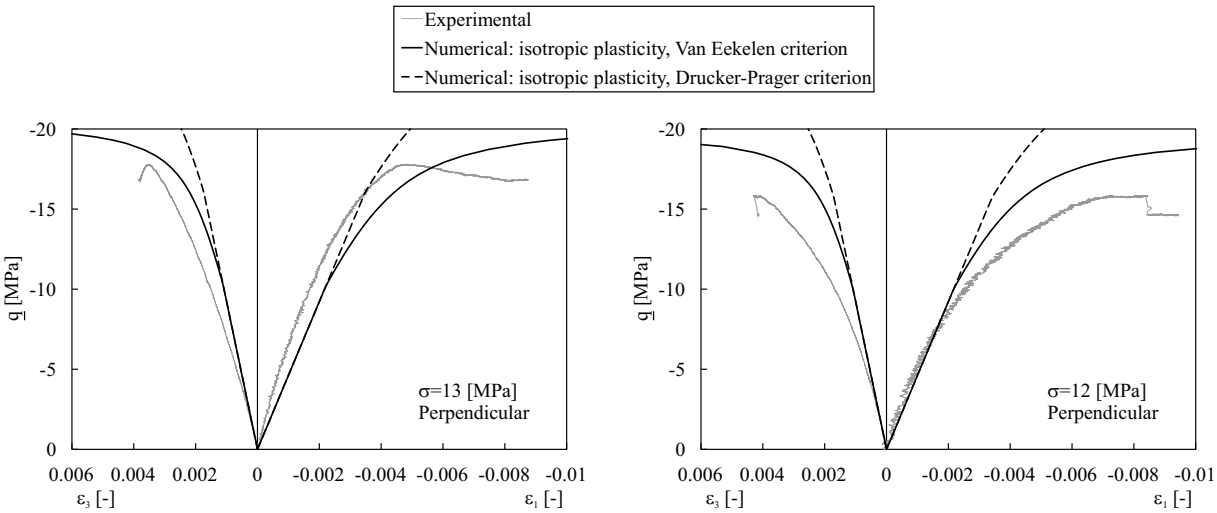

Fig. 5.7: Fitting of triaxial extension tests for elastoplastic mechanical model.

$c_{90^\circ} = c_{\parallel} = 5.4\ MPa$. The constants of the second order microstructure fabric tensor can therefore be calculated: $\bar{c} = 4.1 MPa$, $A_{\parallel} = 0.117$, $b_1 = 14.24$, and $b_2 = 0$ as well as higher order terms. For these parameters, the evolution of the cohesion with orientation is illustrated in Fig. 5.8 with a minimum value about $\alpha = 45^\circ$ which is consistent with experimental observations on other cross-anisotropic argillaceous rock (Niandou et al., 1997; Valès et al., 2004). Moreover, the influence of the cohesion anisotropy amplitude on the shear banding appearance will be discussed in the numerical modelling.

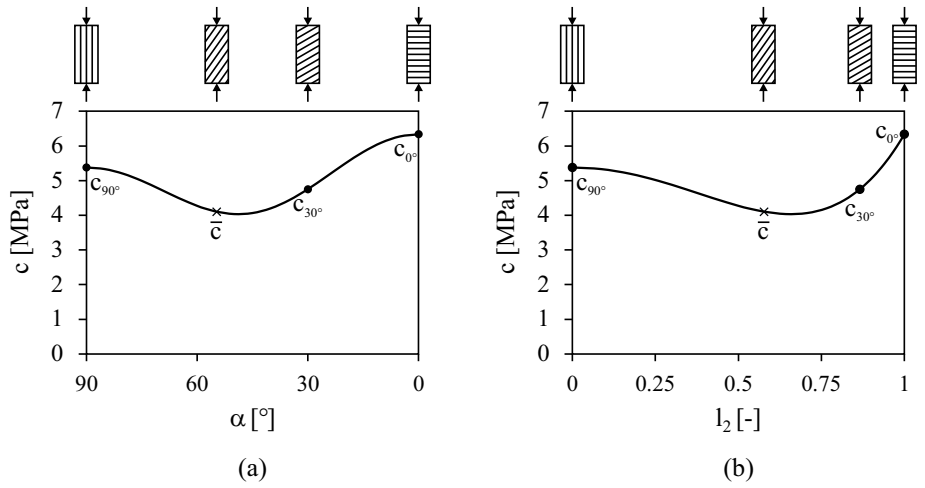

Fig. 5.8: Evolution of the cohesion (a) as a function of the angle between the normal to the bedding planes and the direction of loading and (b) as a function of the loading vector.

To validate these anisotropic parameters, the triaxial compression tests used to determine the hardening and softening parameters can be modelled with the anisotropic model. Only one global fitting is performed with the Van Eekelen criterion and without softening; the results are available in Fig. 5.6. Among the five triaxial compression tests, the resistance is overestimated only for the compression test performed parallel to the bedding planes. To improve this, the value of the cohesion parallel to the bedding planes c_{90° can be decreased without altering the reproduction of the compression tests performed perpendicularly to the bedding. Nevertheless, the reduction of the cohesion c_{90° leads to a cohesion evolution that does not correspond to classical measured values for the considered material because it does not exhibit a lower value around $\alpha = 45^\circ$ anymore. Besides, only one compression test performed parallel to the stratification is

modelled here which does not capture the dispersion of laboratory results. On the other hand, the anisotropic cohesion parameters determined from the uniaxial compression tests come from a large number of laboratory tests. Consequently, the first set of parameters seems to better suit for the material and is kept.

5.3.3 Viscoplastic parameters

As for the plastic parameters, the viscoplastic parameters are determined based on experimental data provided by the Andra in the context of the benchmark "Transversal action - Models". Additionally, typical values of viscoplastic parameters for the Callovo-Oxfordian claystone under -450 m depth are available in Jia et al. 2008. Those parameters come from a particular fitting procedure and are therefore adjusted based on the provided reference creep tests. These creep tests are performed at a confining pressure of 12 MPa and at different constant stress deviators to highlight creep deformation in the long term. The stress deviators $\underline{q} = \sigma_1 - \sigma_3$ correspond to 50 %, 75 %, and 90 % of a considered deviatoric peak stress of 34 MPa, which gives 17, 25.5, and 30.6 MPa. Once again, a relative humidity of 90 % is considered however drained conditions are assumed due to the long-term testing procedure. To reproduce the constant stresses in the different directions, the tests are numerically modelled at small scale with a three-dimensional structure corresponding to one cubic finite element. A hydro-mechanical modelling is realised, with the average values of Table 5.2 for the friction angle hardening parameters and no cohesion softening.

To calibrate the different parameters, the value of the initial threshold for the creep deformation α_0^{vp} has to be identified firstly. It should be determined at the onset of irreversible creep strains during compression tests but, in practice, it is not simple to define such point precisely. It is therefore assumed that creep strains start at low deviatoric stress for hard clay (Zhou et al., 2008) and two types of fitting are analysed. First, in agreement with instantaneous viscoplastic deformation mechanism, a value of $\alpha_0^{vp} = 0$ is chosen and leads to an initial viscoplastic flow $F_0^{vp} = \sqrt{3}\ II_{\hat{\sigma}',0}$ by Eq. 5.55. The initial second deviatoric stress invariant and viscoplastic flow cancel only in case of initial isotropic effective stress state. Second, anticipating the further modelling of a gallery excavation in Callovo-Oxfordian claystone, its initial anisotropic stresses and pore water pressure are considered. In order to avoid an initial viscoplastic flow in the rock mass, $F_0^{vp} = 0$, the value of α_0^{vp} is chosen as (Eq. 5.55):

$$\alpha_0^{vp} = \frac{\sqrt{3}\ II_{\hat{\sigma}',0}}{g\left(\beta\right) R_c \sqrt{A^{vp}\left(C^{vp} + \dfrac{I_{\sigma',0}}{3R_c}\right)}} \tag{5.75}$$

where the values of the parameters come from Jia et al. (2008): $g(\beta) = 1$, $R_c = 21\ MPa$, $A^{vp} = 2.62$, $C^{vp} = 0.03$; and the initial stress invariants, $I_{\sigma',0}$ and $II_{\hat{\sigma}',0}$, are determined from the initial *in situ* effective stress state of the argillaceous rock. In the context of the Andra's benchmark, the recommended anisotropic total stress state and pore water pressure are:

$$\sigma_v = 12.7\ MPa$$

$$\sigma_h = 12.4\ MPa$$

$$\sigma_H = 1.3\ \sigma_h = 16.12\ MPa$$

$$p_w = 4.7\ MPa$$

where σ_v is the vertical principal total stress, σ_h is the minor horizontal principal total stress, and σ_H is the major horizontal principal total stress. In that case, the initial threshold for the viscoplastic flow is $\alpha_0^{vp} = 0.142$. Finally, global calibrations are realised for the two cases for which the final values of the viscoplastic parameters are available in Table 5.3 and the correspondences with the experimental data are illustrated in Fig. 5.9.

	Symbol	Name	Value	Unit
Tests		Laboratory	LAEGO	
description	RH	Relative humidity	90	%
	σ_3	Confining pressure	12	MPa
	$\underline{q}$	Stress deviator	$17, 25.5, 30.6$	MPa
Global	R_c	Uniaxial compressive strength	21	MPa
parameters	A^{vp}	Internal friction coefficient	2.62	–
	C^{vp}	Cohesion coefficient	0.03	–
	β^{vp}	Viscoplastic potential parameter	1.1	–
	$g(\beta)$	Influence of the Lode angle	1	–
Parameters for	α_0^{vp}	Initial threshold for the viscoplastic flow	0	–
$F_0^{vp} = II_{\hat{\sigma}',0}$	γ_0	Reference fluidity	500	s^{-1}
	γ_1	Temperature parameter	63×10^3	J/mol
	$\mathcal{N}$	Creep curve shape parameter	6.6	–
	B^{vp}	Viscoplastic hardening function parameter	11.0×10^{-3}	–
Parameters for	α_0^{vp}	Initial threshold for the viscoplastic flow	0.142	–
$F_0^{vp} = 0$	γ_0	Reference fluidity	700	s^{-1}
(*in situ*)	γ_1	Temperature parameter	57×10^3	J/mol
	$\mathcal{N}$	Creep curve shape parameter	5.0	–
	B^{vp}	Viscoplastic hardening function parameter	7.5×10^{-3}	–

Table 5.3: Calibration of viscoplastic parameters for elasto-viscoplastic mechanical model.

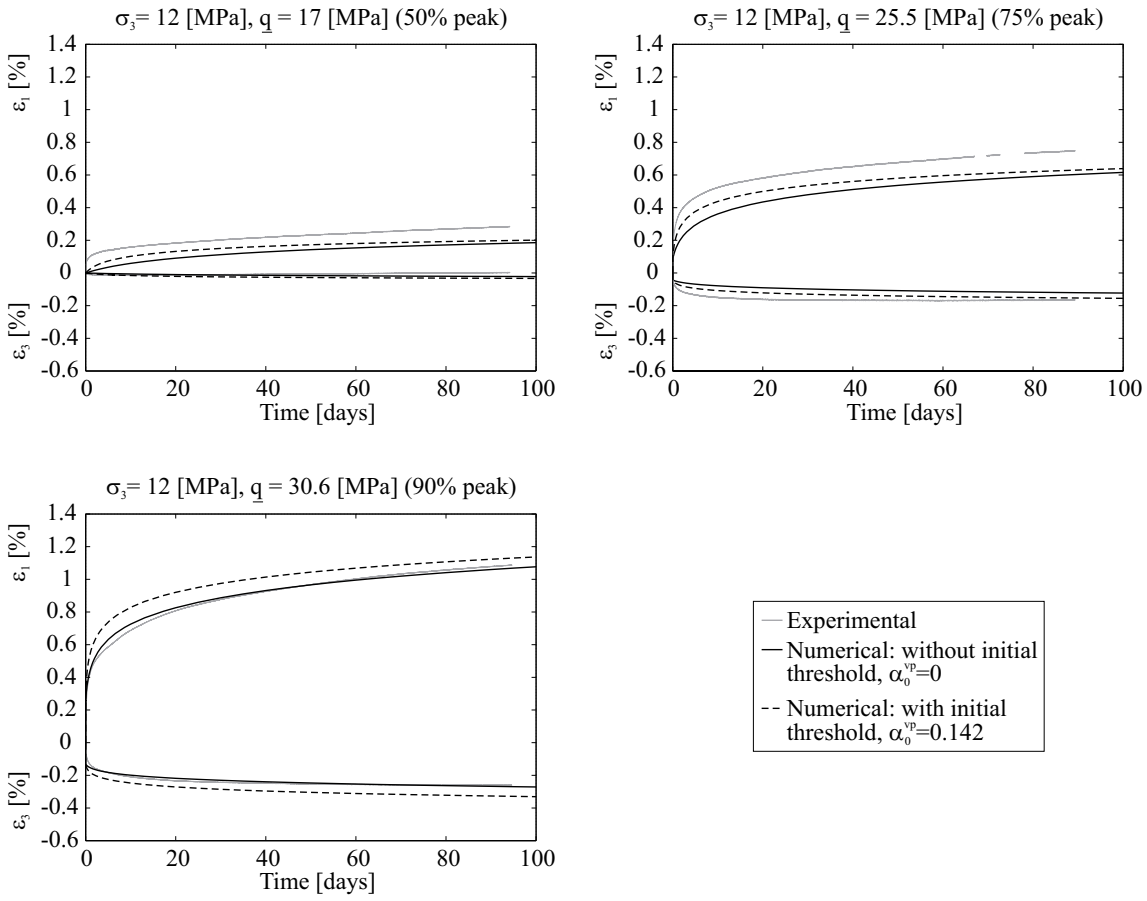

Fig. 5.9: Fitting of creep tests for elasto-viscoplastic mechanical model.

5.3.4 Final parameters

The final parameters are detailed in Table 5.4 for the elasto-viscoplastic model with the Van Eekelen yield criterion. The values of the softening parameters ($\xi_c = c_0/c_f$, B_c, and dec_c) will be defined later for the numerical applications with the purpose of triggering strain localisation. For the viscoplasticity, the set of parameters with initial threshold for the viscoplastic flow ($\alpha_0^{vp} = 0.142$) and avoiding initial *in situ* creep deformations in the claystone ($F_0^{vp} = 0$) is kept.

	Symbol	Name	Value	Unit
Hydraulic parameters	$k_{w,\parallel}$	Parallel intrinsic water permeability	4×10^{-20}	m^2
	$k_{w,\perp}$	Perpendicular intrinsic water permeability	1.33×10^{-20}	m^2
	Φ	Porosity	0.173	–
	P_r	van Genuchten air entry pressure	15	MPa
	$\mathcal{M}$	van Genuchten coefficient	0.33	–
	S_{max}	Maximum degree of water saturation	1	–
	S_{res}	Residual degree of water saturation	0.01	–
	μ_w	Water dynamic viscosity	0.001	$Pa\ s$
	χ_w^{-1}	Water compressibility	5×10^{-10}	Pa^{-1}
Elastic parameters	$E_\parallel$	Parallel Young's modulus	5	GPa
	$E_\perp$	Perpendicular Young's modulus	4	GPa
	$G_{\parallel\perp}$	Shear modulus	1.63	GPa
	$\nu_{\parallel\parallel}$	Poisson's ratio	0.24	–
	$\nu_{\parallel\perp}$	Poisson's ratio	0.33	–
	$b_\parallel$	Parallel Biot's coefficient	0.60	–
	$b_\perp$	Perpendicular Biot's coefficient	0.64	–
	ρ_s	Solid grain density	2750	kg/m^3
Plastic parameters	η	Van Eekelen yield surface convexity parameter	-0.229	–
	$\psi_c = \psi_e$	Dilatancy angles	0.5	°
	$\varphi_{c,0}$	Initial compression friction angle	10	°
	$\varphi_{c,f}$	Final compression friction angle	23	°
	$\varphi_{e,0}$	Initial extension friction angle	7	°
	$\varphi_{e,f}$	Final extension friction angle	23	°
	B_φ	Friction angle hardening coefficient	0.001	–
	dec_φ	Friction angle hardening shifting	0	–
	$\bar{c}$	Cohesion for isotropic loading	4.1	MPa
	$A_\parallel$	Cohesion parameter	0.117	–
	b_1	Cohesion parameter	14.24	–
Viscoplastic parameters	R_c	Uniaxial compressive strength	21	MPa
	A^{vp}	Internal friction coefficient	2.62	–
	C^{vp}	Cohesion coefficient	0.03	–
	β^{vp}	Viscoplastic potential parameter	1.1	–
	$g(\beta)$	Influence of the Lode angle	1	–
	α_0^{vp}	Initial threshold for the viscoplastic flow	0.142	–
	γ_0	Reference fluidity	700	s^{-1}
	γ_1	Temperature parameter	57×10^3	J/mol
	$\mathcal{N}$	Creep curve shape parameter	5.0	–
	B^{vp}	Viscoplastic hardening function parameter	7.5×10^{-3}	–

Table 5.4: Elasto-viscoplastic parameters for the Callovo-Oxfordian claystone.

5.4 Numerical applications

Two numerical applications are modelled for a cross-anisotropic rock, namely the Callovo-Oxfordian claystone, in order to highlight the effect of properties' anisotropy on shear banding appearance. The shear strain localisation is properly reproduced thanks to the coupled local second gradient model defined in the preceding chapters (sections 3.3 and 4.1). Firstly, a plane-strain biaxial compression test is modelled on a small-scale material specimen, and secondly, an underground gallery drilling is reproduced on a large scale. Two values of 0.5 N and 5 kN are used for the second gradient elastic modulus D, for the compression test and for the gallery excavation, respectively. These values allow to properly represent shear banding with a good numerical precision of the post-localisation behaviour within the shear bands.

5.4.1 Modelling of biaxial compression test

A plane-strain biaxial compression test under undrained conditions is reproduced numerically. Various studies have already been performed for this type of loading, from laboratory testing to numerical modelling (Han and Drescher, 1993; Finno et al., 1997; Collin et al., 2006; Bésuelle et al., 2006a; Tejchman et al., 2007). In the following, the objective is to highlight the effects of anisotropy and understand the appearance of shear strain localisation in a small material specimen. Only saturated conditions are considered, meaning that the liquid phase (water) fully occupies the pores, and the material viscosity is not taken into account because of the relatively short duration of the compression test.

Numerical model

The representation of the hydro-mechanical model with its boundary conditions is detailed in Fig. 5.10. The considered sample has a height of 50 mm and a width of 20 mm with a zero initial pore water pressure, the normal water flows are blocked to a value of zero along the sample boundaries which makes them impervious (globally undrained sample), and a constant confining pressure is applied. Experimental studies indicate that a high confinement delays the appearance of strain localisation and therefore implies a larger vertical deformation and a higher peak stress to reach the localisation appearance (Mokni and Desrues, 1999). Nonetheless, the investigation of different confinements is not treated and only one confining pressure of $\sigma_x = 6\ MPa$ is considered.

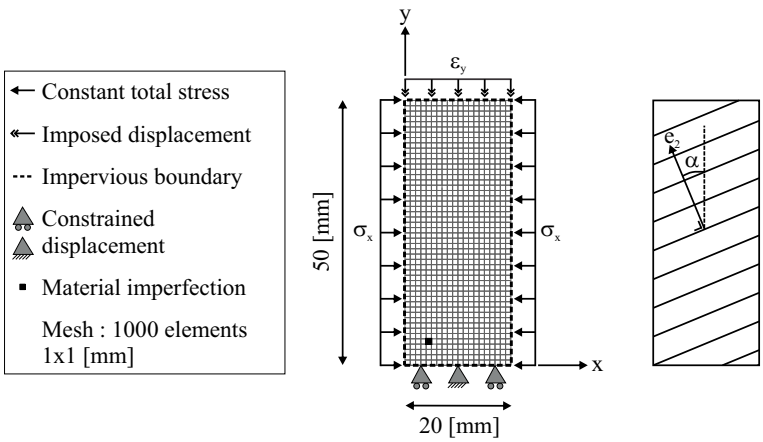

Fig. 5.10: Numerical model used for the modelling of a plane-strain biaxial compression test performed on a cross-anisotropic rock.

To model the vertical compression, the vertical displacement of all nodes of the sample's upper surface is progressively increased during the test with a constant loading strain rate of

$1 \times 10^{-6}\ s^{-1}$ up to 1.5 mm, which corresponds to a total vertical strain of $\varepsilon_y = 0.03$. The vertical displacement of all nodes of the bottom surface is blocked and the displacement of the central node is blocked both in the vertical and horizontal directions to avoid rigid body displacement. Such boundary conditions correspond to top and bottom smooth boundaries. When cross-anisotropy is considered, the orientation of the material isotropic planes is defined by the angle α between the vertical loading direction and the normal to the isotropic planes. This angle corresponds to the Euler's angle in the rotation matrix of Eq. 5.37.

The parameters of the cohesion softening are defined to trigger the strain localisation and are a ratio of cohesion softening of $\xi_c = 2$, a cohesion softening coefficient of $B_c = 0.03$, and a cohesion softening shifting of $dec_c = 0.011$. This shifting permits to delay the appearance of strain localisation and of the peak stress in the global stress-strain response curve of the specimen. Although cohesion softening is considered, strain localisation is not automatically triggered in a small material sample subjected to a biaxial compression. To ease the localisation onset, a material imperfection is included in the specimen and consists of an element (Fig. 5.10) having a constant cohesion of $\bar{c} = 4.1\ MPa$ (Table 5.4). It is to recall that a material imperfection does not affect the global stress-strain responses of the specimen during a biaxial plane-strain compression for the same confining pressure (Desrues, 1984; Desrues and Viggiani, 2004).

Anisotropy effect and strain localisation

Because a low elastic anisotropy is considered, it has only a small influence on the global reaction of a specimen biaxially loaded. Therefore, a cross-anisotropic elasticity with horizontal isotropic planes ($\alpha = 0°$) is taken into account and the effect of plastic anisotropy is investigated. The evolution of the global deviatoric stress:

$$\underline{q} = \sigma_y - \sigma_x \tag{5.76}$$

with the vertical strain ε_y is detailed in Fig. 5.11 for an isotropic ($c_0 = \bar{c} = 4.1\ MPa$, $A_{\parallel} = b_1 = 0$) and an anisotropic plasticity ($\bar{c} = 4.1\ MPa$, $A_{\parallel} = 0.117$, and $b_1 = 14.24$ from Table 5.4). The homogeneous solution without cohesion softening ($\xi_c = 1$) and the localised solution are detailed for both cases.

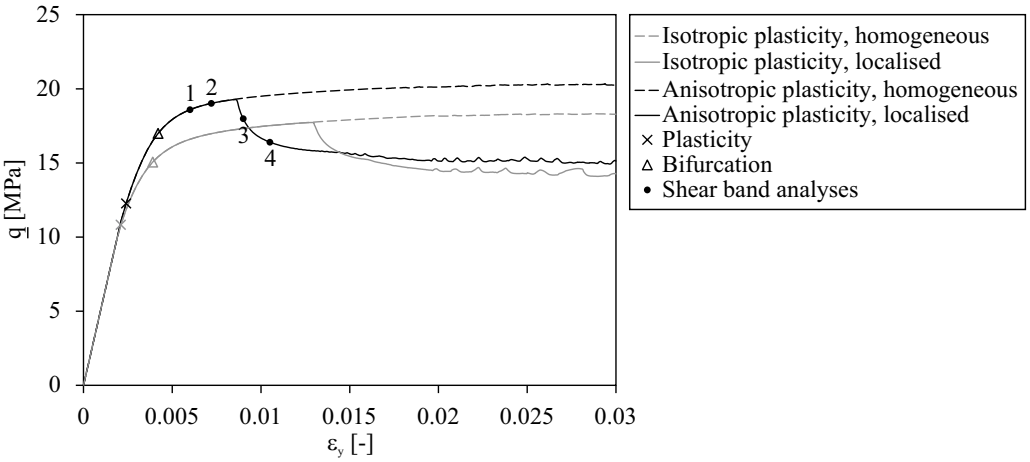

Fig. 5.11: Stress-strain curves for isotropic and cross-anisotropic plasticity with horizontal isotropic planes.

For the homogeneous solutions, the material is initially in an elastic state up to a deformation where plasticity is observed all over the specimen, which corresponds to the crosses on the stress-strain curves. In the plastic domain, the increase of the deviatoric stress is due to the friction angles hardening. If the isotropic and anisotropic homogeneous solutions are compared, one can observe an increase of the material global resistance due to the anisotropy of the cohesion

and its evolution during the loading. When the isotropic planes are horizontal and an isotropic confinement followed by a vertical loading is applied, the global loading tends to be more and more perpendicular to the bedding. In this case the cohesion evolves from its original value $\bar{c}$, corresponding to an isotropic loading with loading vector component $l_2 = \sqrt{1/3} = 0.58$, towards the right hand side of the curve detailed in Fig. 5.8. The evolution of the cohesion in the specimen can be described more accurately by studying one element (element 1 in Fig. 5.14). Only one element needs to be analysed so far because the considered solutions are homogeneous and the evolutions of its cohesion, loading vector, and yield index are represented in Fig. 5.15. The increase of cohesion is clearly noticeable in Fig. 5.15 (a) when anisotropy is taken into account because the loading vector component l_2 increases from 0.58 to 0.88 during the loading (Fig. 5.15 (b)), which affects the cohesion value (Eq. 5.52). The yield index is defined as the reduced second deviatoric stress invariant:

$$YI = \frac{II_{\hat{\sigma}'}}{II^p_{\hat{\sigma}'}} \tag{5.77}$$

where $II_{\hat{\sigma}'}$ is the current second deviatoric stress invariant and $II^p_{\hat{\sigma}'}$ corresponds to the value for which the material enters plastic state for an identical value of the current first stress invariant $I_{\sigma'}$. The current state of the material is therefore elastic for $YI < 1$ and plastic for $YI = 1$. One can observe in Fig. 5.15 (c) for the homogeneous solutions that the material becomes rapidly plastic and remains plastic up to the end of the loading whether cross-anisotropic plasticity is taken into account or not.

To trigger strain localisation the cohesion softening ($\xi_c = 2$, $B_c = 0.03$, and $dec_c = 0.011$) and the material imperfection are added to the previous modelling. The evolution of the global deviatoric stress with the vertical strain (Fig. 5.11) exhibits different zones: an elastic zone, a pre-peak plastic zone without reaching the bifurcation criterion, a pre-peak plastic zone where the bifurcation criterion is reached, and a post-peak plastic zone. In homogeneous plastic state, the friction angle increases due to hardening before the peak stress is reached. The possibility of localisation occurrence is then derived from the solutions of the characteristic equation of the bifurcation criterion (Eq. 3.11). For associated plasticity the bifurcation criterion is met only at peak stress but for non-associated plasticity, which is assumed here, it can be met for positive hardening and shear banding can occurs in the hardening regime (Rudnicki and Rice, 1975). The pre-peak hardening plastic regime can thus be divided in two parts: one in which the bifurcation criterion is not reached and another where it is reached all over the specimen (after the triangles on the stress-strain curves) and where strain localisation can initiate even if the specimen still remains homogeneously plastic. The latter corresponds to continuous bifurcation as described in the Rice criterion development in section 3.2.1.

In order to understand the evolution of the shear band activity during the biaxial loading, different shear band analyses are performed for the anisotopic case. Theses analyses are indicated with dots on the stress-strain curve of Fig. 5.11 and are detailed in Fig. 5.12 where the deviatoric strain increment, the plastic zone, the nodal velocity norm, and the pore water pressure are illustrated. The deviatoric strain increment κ_{eq} represents the band activity:

$$\kappa_{eq} = \frac{\dot{\hat{\varepsilon}}_{eq}\, dt}{\int \dot{\hat{\varepsilon}}_{eq}\, dt} \tag{5.78}$$

with $\hat{\varepsilon}_{eq}$ being the equivalent total deviatoric strain:

$$\hat{\varepsilon}_{eq} = \sqrt{\frac{2}{3}\, \hat{\varepsilon}_{ij}\, \hat{\varepsilon}_{ij}} \tag{5.79}$$

The plastic zone represents the plastic loading integration points, and the nodal velocity norm corresponds to the norm of the nodal displacement rates:

$$||v|| = \sqrt{\dot{u}_x^2 + \dot{u}_y^2} \tag{5.80}$$

The velocity is represented on the deformed mesh and the global movements in the specimen are indicated with arrows.

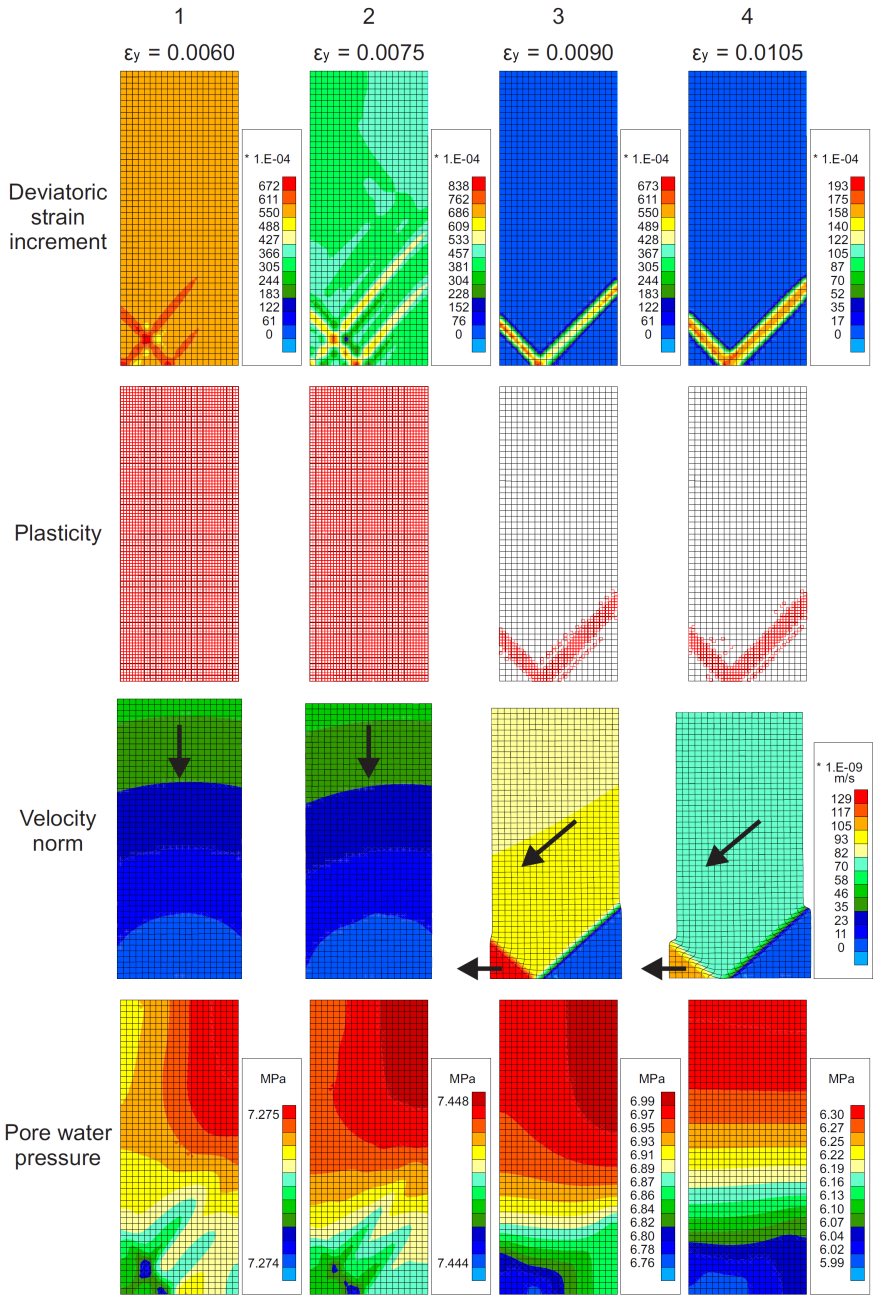

Fig. 5.12: Appearance of strain localisation before peak stress and complete formation of a shear band after peak stress for cross-anisotropic material with horizontal isotropic planes.

The analyses of shear band once the bifurcation is reached but before the peak stress can be observed for $\varepsilon_y = 0.0060$ (1) and $\varepsilon_y = 0.0075$ (2) in Fig. 5.12. The results in terms of deviatoric strain increment indicate clearly that different shear bands appear and are in competition at this stage. Still, the plasticity remains homogeneous and the velocity norms are globally directed downwards which indicate that these shear bands are not fully formed yet. Furthermore, the material imperfection dictates the shear band position which passes through it. In fact, the stress field is uniform for a uniform specimen and the bifurcation criterion is reached simultaneously in the whole specimen. On the other hand, an imperfection induces a non-uniformity of the stress field in its vicinity which can be sufficient to reach first the bifurcation criterion (only in

the imperfection), and then the material imperfection acts as a nucleation point for the strain localisation onset.

Once the cohesion softening starts, one of the shear bands outweighs the others and fully develops. The peak stress corresponds then to the appearance of a fully formed shear band throughout the specimen. The full formation of the shear band can be observed in Fig. 5.12 for $\varepsilon_y = 0.0090$ (3) and $\varepsilon_y = 0.0105$ (4) by the concentration of deviatoric strain and plasticity inside the shear band. After the peak, a rapid drop of the deviatoric stress is observed (Fig. 5.11) due to the cohesion softening and to the elastic unloading of the elements located outside the shear band, the elements inside the band remain plastic. As already mentioned in previous chapters, the strain softening behaviour (reduction of deviatoric stress with increase of plastic strain) causes a loss of uniqueness of the post-peak solution due to the possible elastic unloading. An infinity of localised solutions with non-uniform strain distributions may occur at the peak stress bifurcation point and even if a material imperfection might act as a strain localisation attractor, it does not restore the uniqueness of the solution. Further, the strong decrease of the specimen global reaction is followed by a plateau with a quasi-constant deviatoric stress value.

The same type of shear strain localisation results have been obtained experimentally by Desrues (1984) and Desrues and Viggiani (2004) for many biaxial compression tests. Their results have been discussed in section 3.1.2 and Fig. 5.13 illustrates a supplementary example of shear banding development in sand, with stress-strain curve and incremental fields of shear strain intensity. The experimental results highlight multiple initiations of strain localisation before the peak stress, with temporary localisation mechanisms being in competition, and a complete formation of a shear band at peak stress, which passes through the material inclusion if the imperfection is strong enough. The latter observations are confirmed by the numerical results. Unfortunately, as mentioned in section 3.1.2, only a few experimental analyses of shear strain localisation are available for rocks like the Callovo-Oxfordian claystone. Besides, the resaturation conditions are generally not the same as the ones of the developed modelling; consequently, comparison is not straightforward and only qualitative comparisons are proposed.

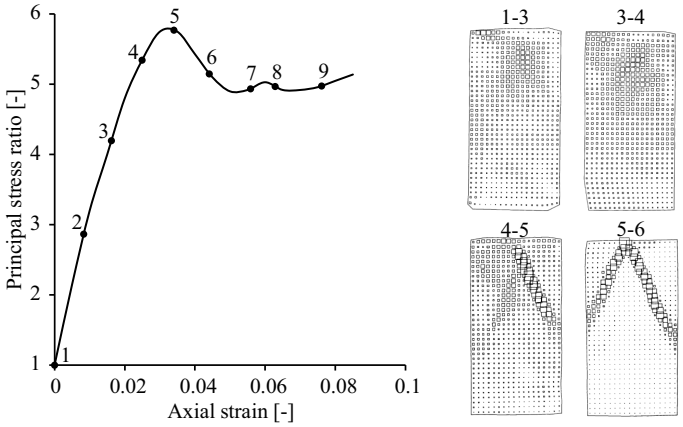

Fig. 5.13: Stress-strain curve and incremental fields of shear strain intensity based on stereophotogrammetry in sand (according to Desrues and Viggiani (2004)).

Going back to the numerical results, the shear strain localisation band exhibits a reflexion on the bottom surface of the sample; consequently, the material is divided in three zones or blocks with different types of movements (see the nodal velocity norm in Fig. 5.12). Firstly, the bottom right zone is blocked due to the constrained displacements in both directions imposed on the central node of the bottom surface. Secondly, the major central zone is pushed downwards and slides along the bottom right zone in the bottom left direction. Lastly, the bottom left zone can move only in the left direction because it is blocked in the vertical direction. The same types of block displacements along the shear bands are observed on experimental results (Desrues, 1984; Desrues and Viggiani, 2004).

Fig. 5.12 also illustrates the evolution of the pore water pressure during the localisation process. Initially, the pore pressure is nil in the sample, then it evolves during the loading and a uniform variation is expected under undrained conditions. As long as the deformation is uniform within the sample, the pore pressure remains uniform as well. Once strain localisation and non-uniformity appear, one can observe a slight variation of the pore pressure across the sample. Before the peak stress ($\varepsilon_y < 0.0086$), the pressure remains quasi-uniform and globally increases. After the peak stress, a vertical gradient tends to appear with lower values in the localised zone that may be due to dilatancy effect. The material dilatancy angle is very low ($\psi = \psi_c = \psi_e = 0.5°$ in Table 5.4) so such phenomenon should be limited; nevertheless, it can also be due to the kinematics related to localisation process. Nonetheless, the pore pressure variations remain low across the whole sample.

Moreover, as the results of Fig. 5.11 indicate, the peak stress amplitude $\underline{q}$ and position ε_y of the localised solutions are different when plastic anisotropy is taken into account. The peak resistance of the specimen is higher when considering cohesion anisotropy and the global vertical deformation required to reach this peak is lower. This is due to the homogeneous evolution of the specimen cohesion before the peak stress (Fig. 5.15 (a)). After the peak stress ($\varepsilon_y > 0.0086$), the evolution of cohesion is not homogeneous anymore and, consequently, different elements in the specimen have to be analysed to capture this non-homogeneous evolution. The three elements of Fig. 5.14 have been chosen: element 1 is the same central element as considered for the homogeneous solutions and is located outside the shear band, element 2 is located inside the shear band, and element 3 is located on the interface between the shear band and the outer material. The evolution of cohesion, loading vector, and yield index of those three elements are detailed in Fig. 5.15.

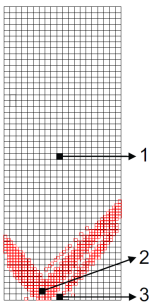

Fig. 5.14: Elements chosen for the analysis of cohesion evolution during biaxial compression test.

The element 1 is located outside the shear band and does not remain plastic after it fully develops. Plastic deformation is not accumulated after the peak stress because of this elastic unloading, and the cohesion decreases only a little regarding the homogeneous solution due to the modification of loading orientation (l_2 slightly decreases after the peak) and to the cohesion anisotropy. The element 2 is located inside the shear band and remains plastic which engenders an accumulation of plastic deformation and a strong cohesion decrease due to softening. A slight part of the cohesion decrease is still due to the cohesion anisotropy; thenceforward, the cohesion is affected by material softening as well as anisotropic characteristics. For the element 3, the cohesion evolves quite differently than for the two other elements. In fact, this element is located at the interface between the shear band and the outer material but the position of this interface is not fixed during the loading, it slightly evolves due to the band activity. Then, the element 3 can be located inside or outside the shear band which implies plastic or elastic state and an intermittent accumulation of plastic strain causing cohesion softening. Besides this, the stress state and the loading vector component l_2 evolve in element 3 after the full development of the shear band which modifies the cohesion due to its anisotropy. As for element 2, both material softening and anisotropy contribute to the cohesion evolution.

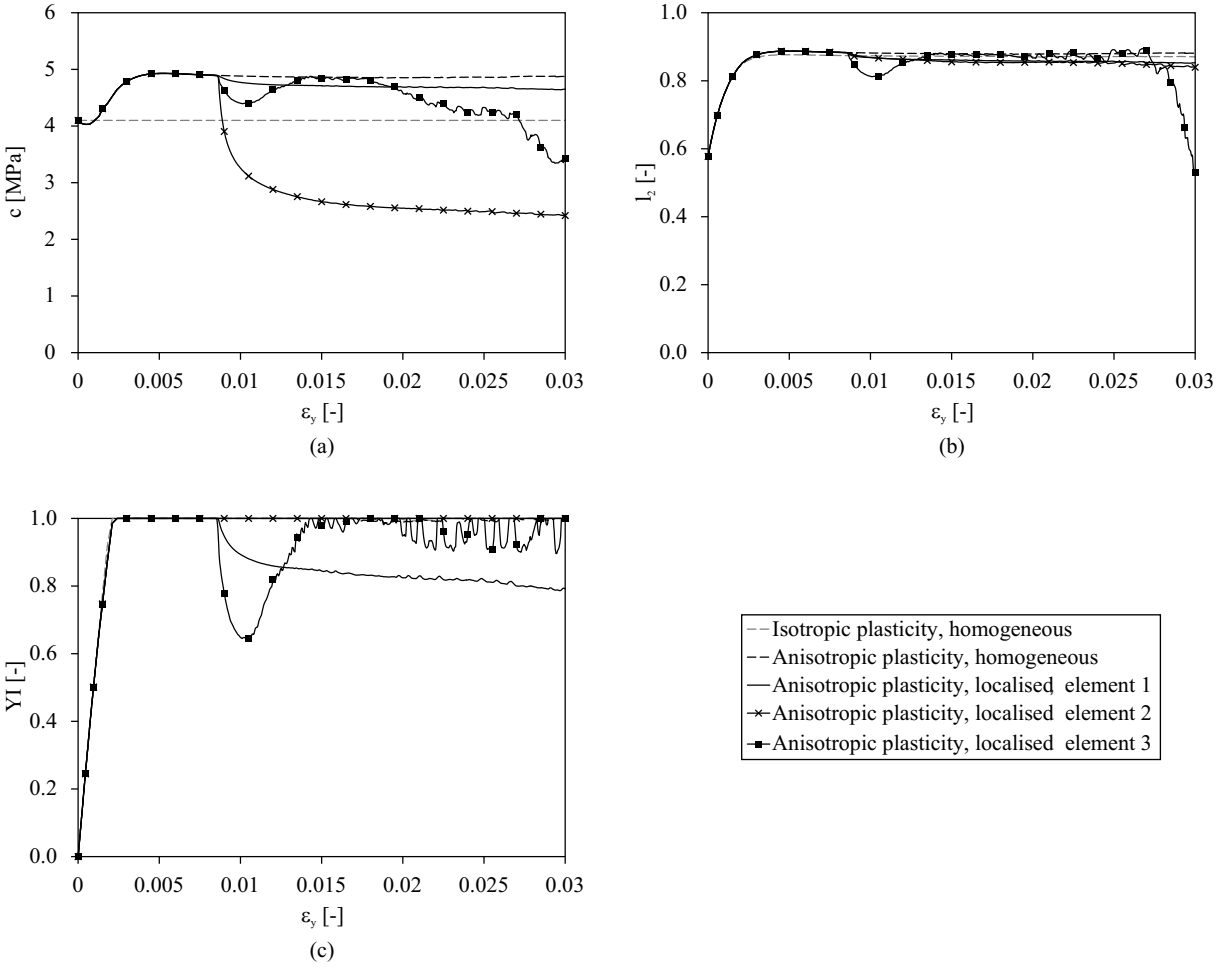

Fig. 5.15: Evolutions of (a) cohesion, (b) loading vector, and (c) yield index for isotropic and cross-anisotropic plasticity with horizontal isotropic planes.

Isotropic planes rotation

To highlight the effect of cross-anisotropy, the biaxial compression can be performed for different orientations of the isotropic planes. For $\alpha = 45°$, the obtained stress-strain curve and the evolution of the shear band pattern are detailed in Fig. 5.16 and Fig. 5.17, respectively. Different shear band analyses are again realised for different vertical deformations during the biaxial loading. They are indicated with dots on the stress-strain curve. As observed previously, strain localisation appears before the peak stress when the bifurcation criterion is met ($\varepsilon_y = 0.0075$ (1)) and one shear band fully develops once the peak stress is reached ($\varepsilon_y = 0.0090$ (2)). In comparison with the loading of a specimen having horizontal isotropic planes, the results are globally the same except that the pattern of strain localisation at its onset varies, the peak stress value is lower, and the post-peak behaviour exhibits variations of the deviatoric stress.

The two first differences are once more due to the anisotropy of the cohesion and its evolution during the loading (Fig. 5.8). In fact, when the isotropic planes are not horizontal and the vertical loading is performed, the cohesion evolves from $\bar{c}$ towards c_α and in this case $c_{45°}$ is about the lowest cohesion value, which leads to a lower peak stress value. $c_{45°}$ is also very close to the initial cohesion value $\bar{c}$ thenceforward the modification of cohesion in the specimen during the loading is very low and the imperfection, with its constant cohesion value of $\bar{c}$, is of minor importance. This minor imperfection is not strong enough to act as a strain localisation attractor and more multiple mechanisms of localised deformation appear at the onset of localisation ($\varepsilon_y = 0.0075$ (1) in Fig. 5.17). After the competition process among the different localised structures, the shear

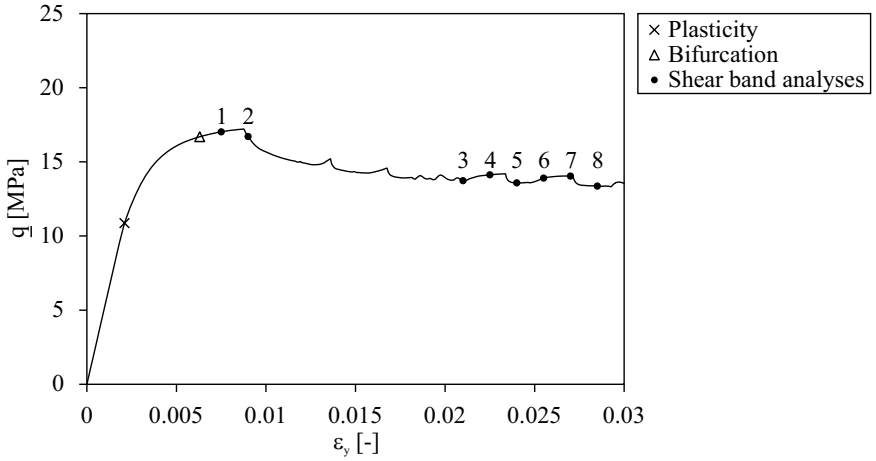

Fig. 5.16: Stress-strain curve for cross-anisotropic plasticity with isotropic plane orientation of $\alpha = 45°$.

band that outweighs the others does not pass by the imperfection. It suggests that a material imperfection has to be strong enough to act as a localisation attractor, and in case of strong imperfection only one well-defined shear band passing by the imperfection could be triggered without any competition process. The same conclusions were drawn by Desrues and Viggiani (2004) based on experimental results.

The variation of the deviatoric stress in the post-peak behaviour is due to the plastic loading of the elements located inside the shear band and to the elastic unloading of the elements located outside. An increase of the global response force corresponds to an increase of the shear band activity. From $\varepsilon_y = 0.0210$ (3) to $\varepsilon_y = 0.0225$ (4) it is observed that a second shear band appears next to the principal one causing a slight increase of the plastic zone size and of the specimen response. Then, a decrease of the global response force is observed and corresponds to a decrease of the shear band activity. For $\varepsilon_y = 0.0240$ (5) only one shear band and a slight decrease of the plastic zone size are observed with elastic unloading of the elements outside the shear band. The same behaviour is observed for the other increases and decreases of the deviatoric stress (see $\varepsilon_y = 0.0255$ (6), 0.0270 (7), and 0.0285 (8) in Fig. 5.17). Experimentally, a consequent drop of the global stress response in the post-peak regime corresponds to the emergence of a new shear band across the whole specimen (Fig. 3.2 (c)) which is not observed on the numerical result for the considered material and the smooth boundary conditions. Nonetheless, experimental techniques, such as digital image correlation, have revealed the evolution of strain localisation during the entire duration of the tests and point out that variations of band activity as well as competition between the emerging shear bands are observed for diverse materials (Viggiani and Desrues, 2004; Thakur, 2007).

Various orientations of the isotropic planes ranging from 0° to 90° are also considered in order to deeper analyse the isotropic planes rotation effect and the obtained stress-strain curves are detailed in Fig. 5.18. One can observe that the elastic response varies in function of the elastic modulus anisotropy; $E_{\parallel}$ being larger than $E_{\perp}$ in a ratio of 1.25 (see Table 5.4) leads to a steeper slope as α increases. Concerning the plastic response, the peak stress values evolve with the cohesion which is the lowest around 45° (Fig. 5.8) and the post-peak regime is similar to what has already been observed, with or without variations of the deviatoric stress. The final shear band patterns at $\varepsilon_y = 0.03$ are detailed in Fig. 5.19 in terms of total deviatoric strain $\hat{\varepsilon}_{eq}$ (Eq. 5.79). A reflexive shear band is observed on the bottom surface of the specimen for 0° and 90°, and only one band is observed in the middle of the specimen for the other intermediate orientations. The rupture and deformation of the specimen have already been discussed through the movements of material blocks in case of a reflexive shear band. For a shear band going across the specimen, the bottom zone is blocked because of the constrained displacements and the top

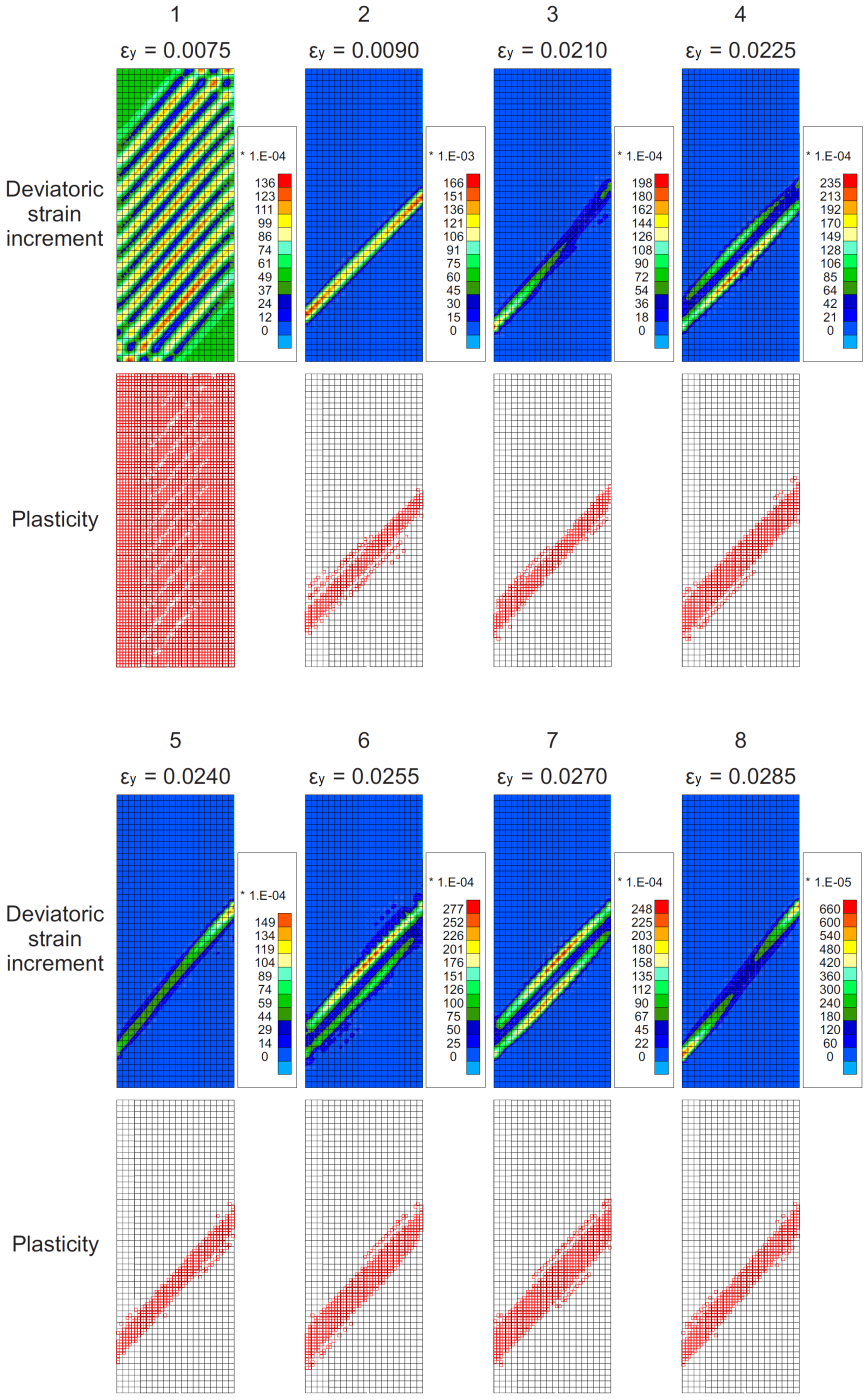

Fig. 5.17: Characterisation of the post-localisation regime by shear band activity for cross-anisotropic material with isotropic plane orientation of $\alpha = 45°$.

block slides on it in the bottom right or left direction depending on the orientation of the shear band. It can also be observed that the position of the shear band varies with the isotropic plane orientation but not the number of bands, neither their orientations with the horizontal direction.

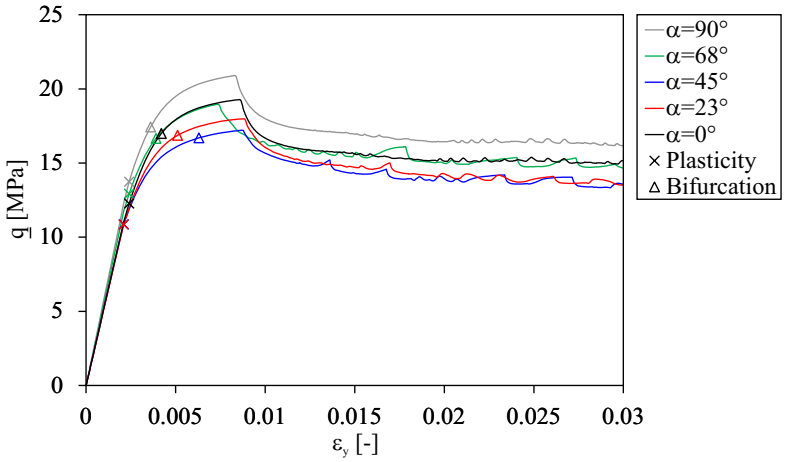

Fig. 5.18: Stress-strain curves for cross-anisotropic material with isotropic plane orientations ranging from $\alpha = 0°$ to 90°.

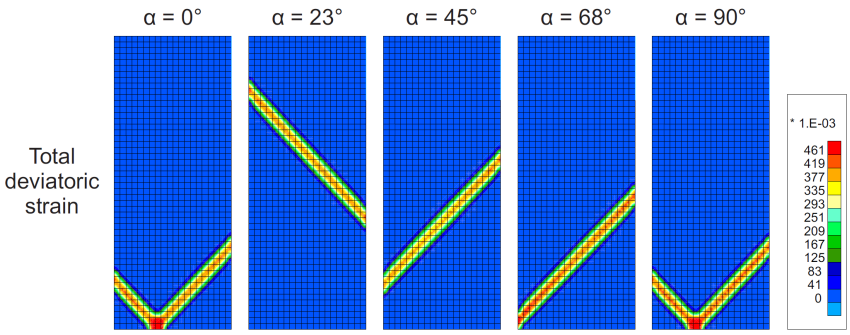

Fig. 5.19: Shear band patterns for cross-anisotropic material with isotropic plane orientations ranging from $\alpha = 0°$ to 90°.

The shear band pattern is also affected by the boundary conditions and the different patterns that are observed are characteristic of smooth boundary conditions, on the top and bottom surfaces of the sample. For frictional and rough boundaries, respectively, with friction or blocked horizontal displacement, a compression cone generally appears in the sample which undergoes barrel distortion before strain localisation and fractures appear. The influence of smooth and rough boundary conditions on the development of shear bands has been numerically studied for biaxial compression tests in a recent study by Gao and Zhao (2013). The results indicate that a single shear band is generally observed for smooth boundary conditions, as in the results of Fig. 5.19, whilst cross shear band appears for rough boundary conditions.

Shear band orientation

The shear band orientation theories have been detailed in section 3.2.1 with three possible orientations with respect to the minor principal stress:

$$\Theta_C = \pm\left(\frac{\pi}{4} + \frac{\varphi_{bif}}{2}\right) \tag{5.81}$$

$$\Theta_A = \pm\left(\frac{\pi}{4} + \frac{\varphi_{bif} + \psi_{bif}}{4}\right) \tag{5.82}$$

$$\Theta_R = \pm\left(\frac{\pi}{4} + \frac{\psi_{bif}}{2}\right) \tag{5.83}$$

These orientations are Coulomb's, Arthur's, and Roscoe's angles, and the orientation of the shear band Θ provided by the numerical results can be related to these orientations. The angles are defined with respect to the minor principal stress direction which is oriented horizontally during the biaxial compression. The observed orientation for the localised results with horizontal isotropic planes ($\alpha = 0°$) is about $\Theta = 47°$ and, even if anisotropic parameters are included in the model, this orientation does not depend on them. At bifurcation state, $\varphi_{bif} = 17.5°$ (inside the shear band when it is initiated) and $\psi_{bif} = 0.5°$ which give $\Theta_R = 45.3°$, $\Theta_A = 49.5°$, and $\Theta_C = 53.8°$. The numerical result lies between the lower bound of Roscoe's angle Θ_R and the intermediate value Θ_A. Other values of dilatancy angle ($\psi = \psi_c = \psi_e$) are investigated and lead to a modification of the shear band orientation as illustrated in Fig. 5.20. The evolution of φ_{bif}, Θ_R, Θ_A, Θ_C, as well as the evolution of the shear band orientation obtained numerically Θ is detailed in Fig. 5.21 for the considered dilatancy angles. The numerical results highlight that the shear band orientation increases with the dilatancy angle and that it is close to Θ_R for low values of ψ and close to Θ_A for higher values.

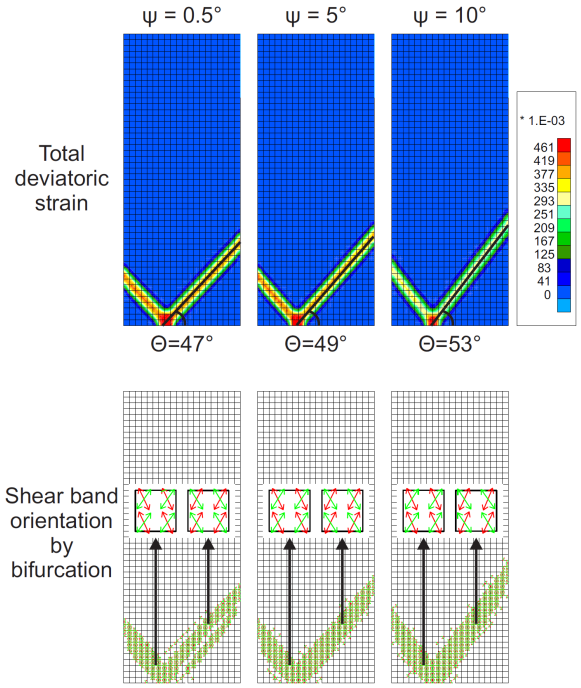

Fig. 5.20: Evolution of shear band patterns and orientations with dilatancy angle at the end of the compression test for cross-anisotropic material with horizontal isotropic planes.

The orientation obtained by considering bifurcation theory can also be investigated. The solution of Eq. 3.11 gives the components of the normal vector to the shear band and its orientation with the isotropic planes, which are horizontal in this case. The shear band directions at the end of the compression test are detailed in Fig. 5.20 with an enlargement for two elements located on different parts of the band. The orientations obtained by the bifurcation criterion indicate that shear band can initiate in two conjugate directions at every material point but only one shear band fully develops at the global specimen scale. Moreover, these orientations on each element correspond to the global shear band direction.

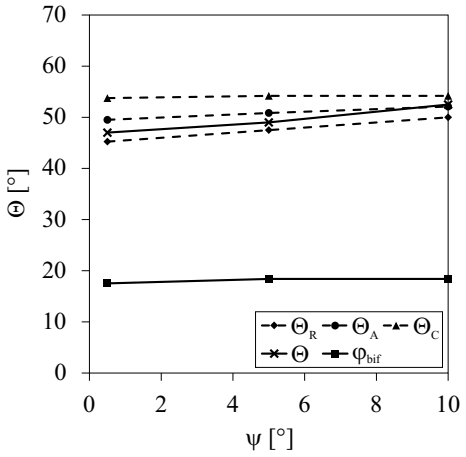

Fig. 5.21: Evolution of shear band orientation with dilatancy angle for cross-anisotropic material with horizontal isotropic planes.

5.4.2 Modelling of gallery drilling for isotropic initial stress state

The modelling of a gallery drilling in rock is performed in two-dimensional plane-strain state with hydro-mechanical coupling. The main objective is to highlight the effects of material anisotropy on the appearance of shear strain localisation at large scale, around an underground gallery. A particular attention is paid to the development of the excavation fractured zone due to material anisotropy with initial isotropic stress state. The excavation phase is mainly studied so long-term effects through material viscosity are not included in the modelling and saturated conditions are assumed.

Numerical model

The claystone cross-anisotropy with horizontal bedding planes ($\alpha = 0°$) is considered; however, an initial isotropic stress state is firstly envisaged to highlight only the effect of material anisotropy on the development of shear bands around the gallery:

$$\sigma_{x,0} = \sigma_{y,0} = \sigma_{z,0} = 12\ MPa$$

$$p_{w,0} = 4.7\ MPa$$

where $\sigma_{x,0}$, $\sigma_{y,0}$, $\sigma_{z,0}$ are the initial total stresses and $p_{w,0}$ is the initial pore water pressure. The numerical model of a 2.6 m radius gallery is represented schematically in Fig. 5.22 with the mesh structure and the boundary conditions. Only one gallery quarter is discretised by assuming symmetry along the x and y-axes with a mesh extension of 50 m in both directions. The discretisation is realised with a total of 4880 elements, 19521 nodes, and a more refined discretisation close to the gallery. Concerning the boundary conditions, the initial pore water pressure and total stresses are imposed constant at the mesh external boundaries. To establish the symmetry, the normal displacements and the normal water flows are blocked to zero along the symmetry axes (impervious axes), and the second gradient boundary condition of Eqs. 4.78 to 4.80 is taken into account.

Now that the initial state, the geometry and the boundary conditions are defined, the gallery excavation can be characterised. It is performed with the convergence-confinement method which is an approximation method for tunnelling that allows to transform a whole three dimensional study of tunnel excavation in a two dimensional study in plane-strain state (Bernaud and Rousset, 1992), based on an identical gallery convergence assumption. The effect of the excavation front progress is taken into account by applying a fictive pressure σ_r^Γ (total radial stress) on the gallery wall that depends on the proximity of the excavation front to the studied gallery section,

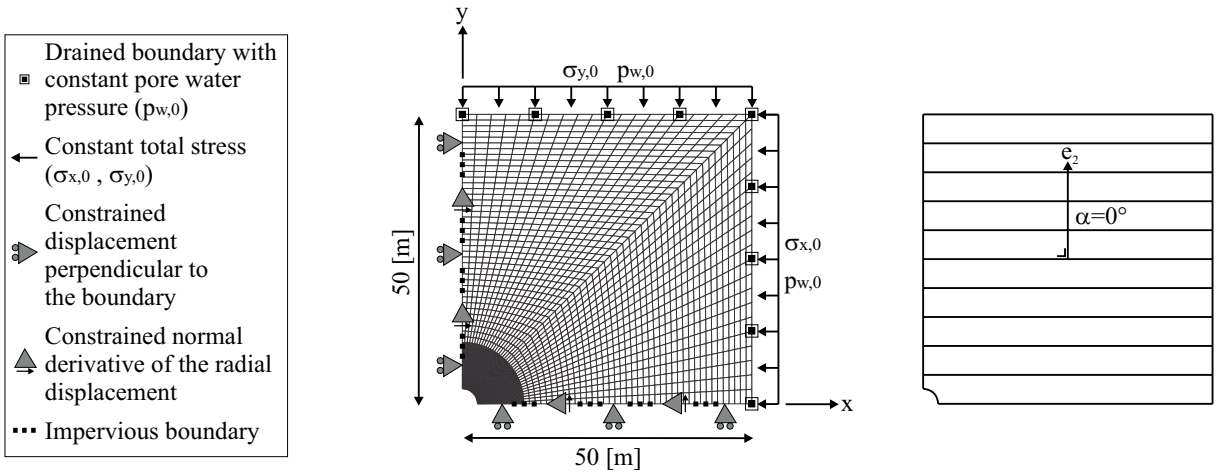

Fig. 5.22: Numerical model used for the modelling of a gallery excavation in cross-anisotropic rock with horizontal bedding planes.

as detailed in Fig. 5.23. A deconfinement rate ζ ranging from 0 to 1 is defined by Panet and Guellec (1974):

$$\sigma_r^\Gamma = (1-\zeta)\,\sigma_{r,0} \tag{5.84}$$

where $\sigma_{r,0}$ is the initial pressure on the gallery wall that corresponds to the initial isotropic stress in the material.

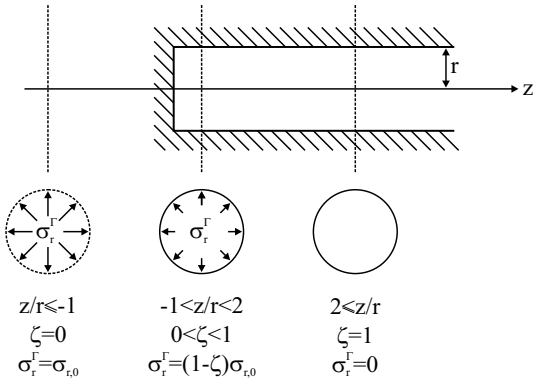

Fig. 5.23: Deconfinement rate during gallery excavation (Panet and Guenot, 1982).

The deconfinement rate depends on various parameters and its analytical determination is beyond the scope of the present modelling. Among different theories (Bernaud and Rousset, 1992; Carranza-Torres and Fairhurst, 2000), the deconfinement curve given by Panet and Guenot (1982) is used and is detailed in Fig. 5.24 where $1-\zeta$ depends on the ratio of the distance between the excavation front and the studied section z by the gallery radius r. The deconfinement rate can also be expressed as a function of time if the rate of excavation is known. Hereafter, a rate of one gallery radius (2.6 m) per week is considered implying that the excavation front crosses the studied section after one week (7 days) and that the excavation is fully completed after three weeks (21 days). The evolution of the deconfinement rate with time is detailed in Fig. 5.24.

The decrease of pore water pressure at gallery wall p_w^Γ during the drilling has to be considered as well because a hydro-mechanical modelling is performed. A deconfinement rate ζ_w ranging from 0 to 1 can be defined in the same manner as for the total radial stress:

$$p_w^\Gamma = (1-\zeta_w)\,p_{w,0} \tag{5.85}$$

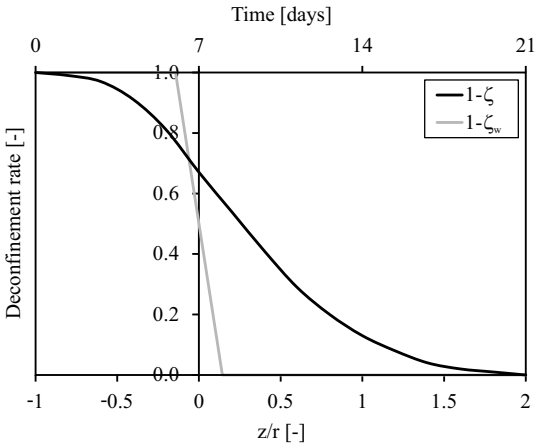

Fig. 5.24: Deconfinement curves for the total radial stress and for the pore water pressure during gallery excavation.

where $p_{w,0}$ is the initial pore water pressure on the gallery wall that corresponds to the initial pore water pressure in the material.

The approach of Panet and Guellec (1974) was originally validated for dry isotropic materials and its generalisation to anisotropic rock under saturated conditions is not straightforward. During the drilling, pore overpressures are usually observed in the rock ahead of the excavation front and are characteristic of hydro-mechanical coupling induced by the anisotropy, whether of the stress state or of the rock mechanical behaviour. Nonetheless, for the sake of simplicity, a linear decrease of pore water pressure is assumed during the excavation (no overpressures) and a uniform deconfinement rate is considered for the total radial stress (Eq. 5.84). The pore water pressure is assumed to decrease rapidly when the excavation front crosses the studied section, from one day before the front up to one day after (Fig. 5.24) with a final value of zero. More accurate definitions of the deconfinement rates would need to be validated with three-dimensional excavation computations; nevertheless, these developments are beyond the objectives of this modelling.

As in previous modelling of gallery excavation, the deformation around the gallery are lower than in compression tests and the introduction of a stronger cohesion softening without shifting is necessary for the onset of shear banding. The softening parameters are $\xi_c = 5$, $B_c = 0.003$, and $dec_c = 0$.

Anisotropy effect and strain localisation

The onset of fractures and strain localisation around galleries depend on the material anisotropy. The previous numerical modelling of section 4.3.2 indicates that for an isotropic material with an isotropic initial stress state, shear strain localisation is not triggered during the drilling unless a material imperfection is used (Fig. 4.4). The numerical results also indicate that, an anisotropic stress state in the plane perpendicular to the gallery axis (gallery section) is a predominant factor that leads to the triggering of strain localisation and to the creation of the excavation fractured zone during the drilling (Collin and Pardoen, 2013; Pardoen et al., 2015a; Salehnia et al., 2015). The fractured zone has an elliptical shape with a significantly larger extent in one direction, depending on the stress anisotropy. This direction coincides with the minor principal stress in the gallery section

Nevertheless, the development of a fractured zone has been observed in some materials, such as the Callovo-Oxfordian claystone, even for isotropic or quasi-isotropic stress state in the gallery section (Armand et al., 2014). In this case, it seems necessary to consider the material anisotropy. To do so, the elastic cross-anisotropy is taken into account (Table 5.4) and, since the

bifurcation criterion as well as the strain localisation can be reached only when the material is in plastic state, the plastic anisotropy is analysed through the cohesion anisotropy. Different cases are considered from an isotropic cohesion of 4.1 MPa to the anisotropic parameters detailed in Table 5.4. Two other cohesion anisotropies are considered between those two cases which leads to a total of four sets of anisotropic cohesion parameters detailed in Table 5.5. The evolutions of the cohesion with the loading vector component l_2 are detailed in Fig. 5.25.

Symbol	Name	Isotropy	Anisotropy set 1	Anisotropy set 2	Anisotropy set 3	Unit
$\bar{c}$	Cohesion for isotropic loading	4.1	4.1	4.1	4.1	MPa
$A_{\parallel}$	Cohesion parameter	0	-0.007	0.049	0.117	–
b_1	Cohesion parameter	0	1105	50.93	14.24	–

Table 5.5: Various sets of anisotropic cohesion parameters for gallery excavation.

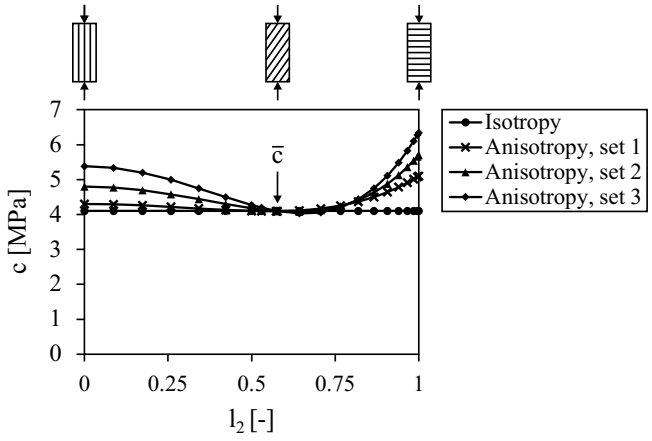

Fig. 5.25: Various evolutions of the cohesion as a function of the loading vector.

The shear band patterns obtained at the end of the excavation in case of horizontal bedding are detailed in Fig. 5.26 for the different sets of cohesion parameters. The illustrated results are the total deviatoric strain, the plastic zone, and the cohesion. For the isotropic cohesion, one can observe that the deformation and the plastic zone are diffuse around the gallery with a quasi-circular extension of about one gallery radius (2.6 m) in the rock. Actually, it is slightly wider in the horizontal direction due to the elastic anisotropic properties. The plasticity engenders cohesion softening around the gallery which is also diffuse. For the set 1 of anisotropic cohesion parameters, the plastic zone remains almost circular around the gallery with the same extent and the total deviatoric strain as well as the cohesion softening concentrate in an inclined direction at about 45° with the horizontal. For the set 2 of anisotropic cohesion parameters, the strain localisation is triggered during the excavation in an inclined direction and shear bands in chevron pattern develop with elastic unloading outside the bands. The plasticity, the total deviatoric strain, and the cohesion softening concentrate within the shear bands. For the set 3 of anisotropic cohesion parameters, the strain localisation starts earlier with the same type of shear banding pattern but with a larger number of bands, located preferentially in the horizontal direction, and a larger concentration of deformation.

Looking at all the results indicates that, in case of isotropic stress state, the material plastic anisotropy is a predominant factor leading to the appearance of strain localisation in shear band mode around a gallery during its excavation. In fact, the excavation process does not lead to strain localisation unless a sufficient material anisotropy is considered.

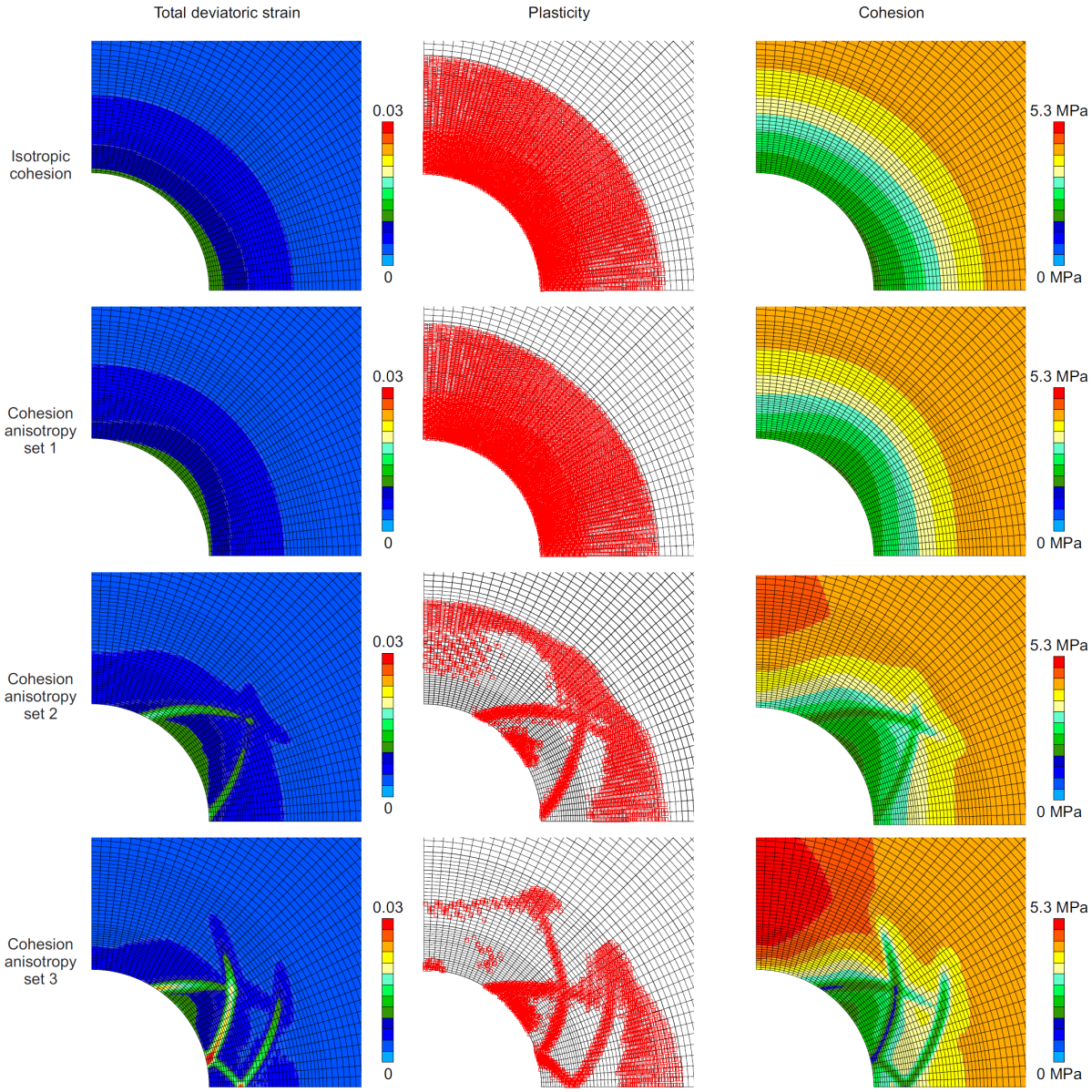

Fig. 5.26: Shear strain localisation at the end of excavation for the different sets of anisotropic cohesion parameters.

The preferential development of shear bands in the inclined and horizontal directions can be explained by the evolution of the cohesion. To better illustrate this cohesion evolution, three elements on gallery wall have been considered and are illustrated in Fig. 5.27. For the anisotropic cohesion parameters of set 3, the evolutions of cohesion, loading vector, and yield index of those elements are detailed in Fig. 5.28. The cohesion evolution depends only on anisotropic effect when the element is in elastic state, and it depends on both anisotropic and softening effects when the element is in plastic state.

While the radial stress decreases and vanishes at gallery wall during the excavation, the orthoradial stress increases. This implies that the loading tends to be horizontal above and below the gallery which corresponds to a loading parallel to the horizontal isotropic planes. Then, the loading vector component l_2 decreases and the cohesion increases by evolving from its original value $\bar{c}$ towards the left hand side of the cohesion curve in Fig. 5.25. It is in fact observed in Fig. 5.28 (b) that l_2 decreases towards a value of zero above the gallery (vertical direction) which leads to an increase of the cohesion before plasticity is reached, then softening engenders the

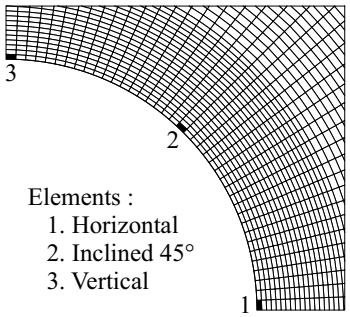

Fig. 5.27: Elements on gallery wall chosen for the analysis of cohesion evolution during excavation.

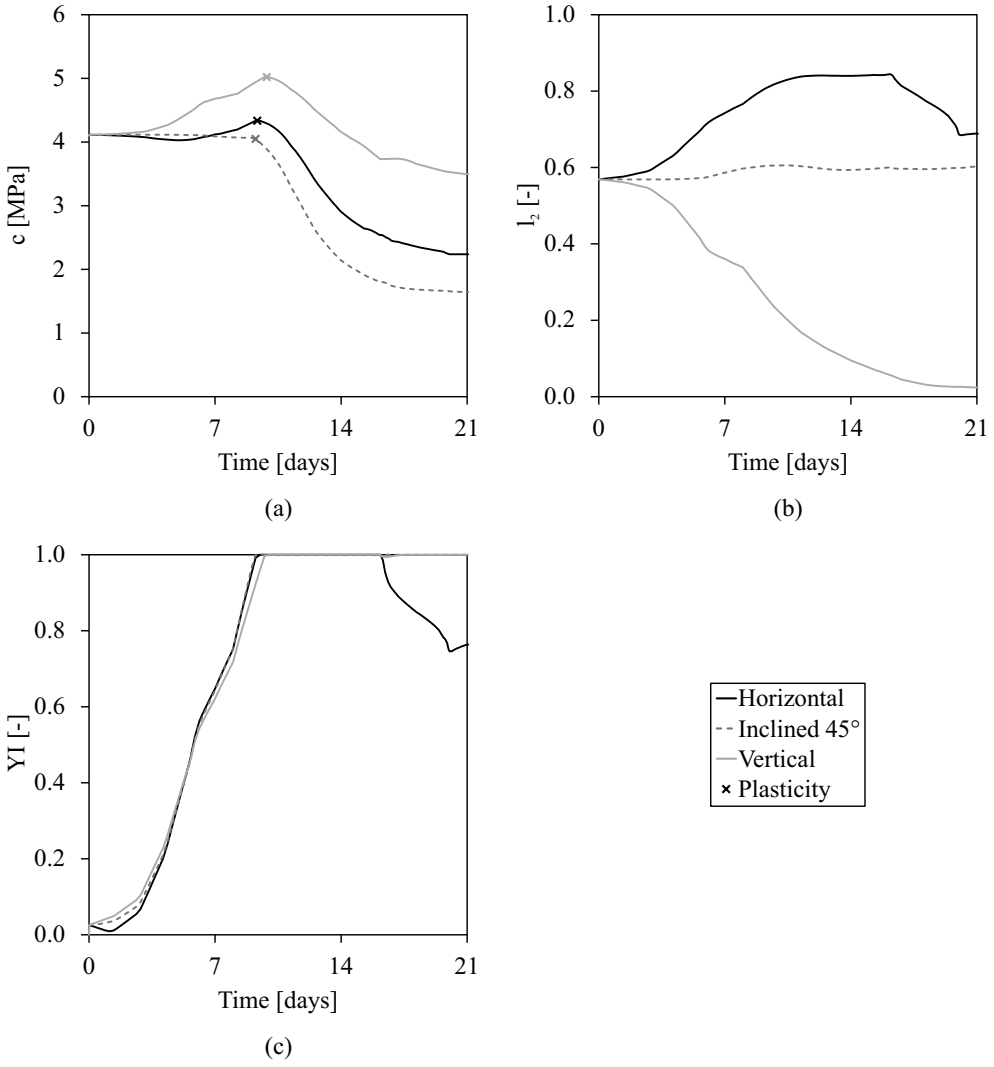

Fig. 5.28: Evolutions of (a) cohesion, (b) loading vector, and (c) yield index during the excavation for the set 3 of anisotropic cohesion parameters.

following cohesion decrease. On the contrary, the loading tends to be vertical or perpendicular to the horizontal isotropic planes on both left and right sides of the gallery, causing an increase of l_2 and an evolution of the cohesion from $\bar{c}$ towards the right hand side of the cohesion curve. On this side of the curve, the cohesion decreases slightly before reaching its lowest value and may finally increase for an important increase of l_2. This can be observed in Fig. 5.28 (a) for the element located on the side of the gallery (horizontal direction). Nevertheless, the increase of l_2 is limited because the stress in the gallery axial direction does not cancel during the excavation

(Eq. 5.43); thus, the increase of cohesion before reaching plasticity and softening is lower than above the gallery. Concerning the element in the inclined direction (at 45° with the horizontal), l_2 remains almost constant, the cohesion remains low in the elastic regime and decreases rapidly in plastic regime due to softening.

This analysis of the cohesion indicates that the material is weaker in the inclined direction and the strain localisation is therefore initiated in that direction (Fig. 5.26). Furthermore, the material strengthening above and below the gallery leads to a preferential development of plasticity as well as strain localisation in the horizontal direction. The material plastic anisotropy is thus the cause of the excavation fractured zone shape and extent.

The development of the shear bands during the excavation can be considered more thoroughly for the anisotropic cohesion parameters of set 3. The evolution of the deviatoric strain increment, the total deviatoric strain, the plastic zone, the nodal velocity norm (with the global movements in the rock indicated with arrows), and the pore water pressure are illustrated in Figs. 5.29 and 5.30, for different instants during the excavation. One can observe that the strain localisation is initiated before $1 - \zeta = 0.08$ (15.4 days) with different shear bands that are in competition (see the deviatoric strain increment in Fig. 5.29) but not fully developed (see the total deviatoric strain and the plastic zone in Fig. 5.29). At this stage, the deformation slightly concentrates around the gallery in an inclined direction and it is observed that the velocity norms are greater for a direction lying between 25° and 45° with the horizontal direction (Fig. 5.30). Later, two shear bands fully develop before $1 - \zeta = 0.04$ (16.8 days) with elastic unloading in the outer material (Fig. 5.29). The elastic unloading appears at $1 - \zeta = 0.057$ or 16.2 days in Fig. 5.28. The position and shape of the shear bands create a block of rock between them that tends to "unhook" from the gallery wall and to converge rapidly towards the gallery center (see the velocity and the global movements in Fig. 5.30). Finally, a supplementary shear band propagates with a reflection on the symmetry x-axis before the end of the excavation $1 - \zeta = 0$ (21 days). It creates a second block that converges rapidly towards the gallery center. These different stages of the unloading with the initiation of strain localisation, the full development of some shear bands, and the varying shear band activity are similar to what has been observed in the biaxial compression test results.

Fig. 5.30 also illustrates the pore water pressure evolution during the excavation and the strain localisation process. A drainage progressively develops in the vicinity of the gallery due to the imposed hydraulic boundary condition at gallery wall. Negative pore pressures and pore pressures higher than the initial value are observed as a result of hydro-mechanical coupling and shear bands activity. The pore pressure variations in the rock remain low due to the low value of dilatancy angle.

Furthermore, the shear band mode is presented in Fig. 5.31 at the end of the excavation. The type of localisation band is described thanks to the Rice bifurcation criterion and to an additional velocity gradient field of the shear band ς_i (Eq. 3.3), which characterises the discontinuity of the velocity between the band and the outer material (Rice, 1976; Rudnicki and Rice, 1975). The discontinuity band nature is defined by the parameter $\underline{s}$ (Eq. 3.16) according to the Table 3.1. Globally, dilating shear bands are observed in Fig. 5.31.

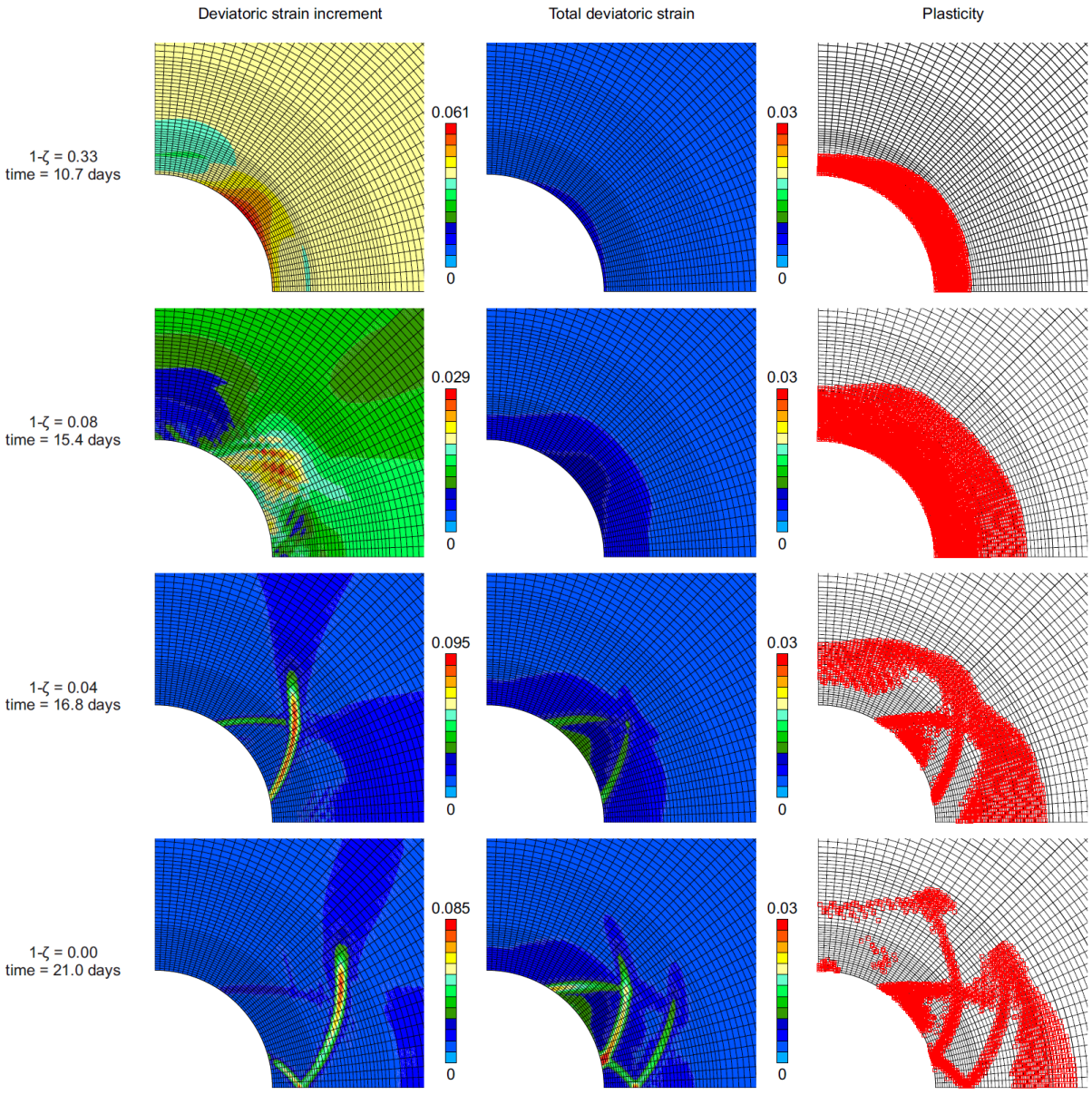

Fig. 5.29: Development of shear strain localisation during the excavation for the set 3 of anisotropic cohesion parameters: deviatoric strain increment, total deviatoric strain, and plastic zone.

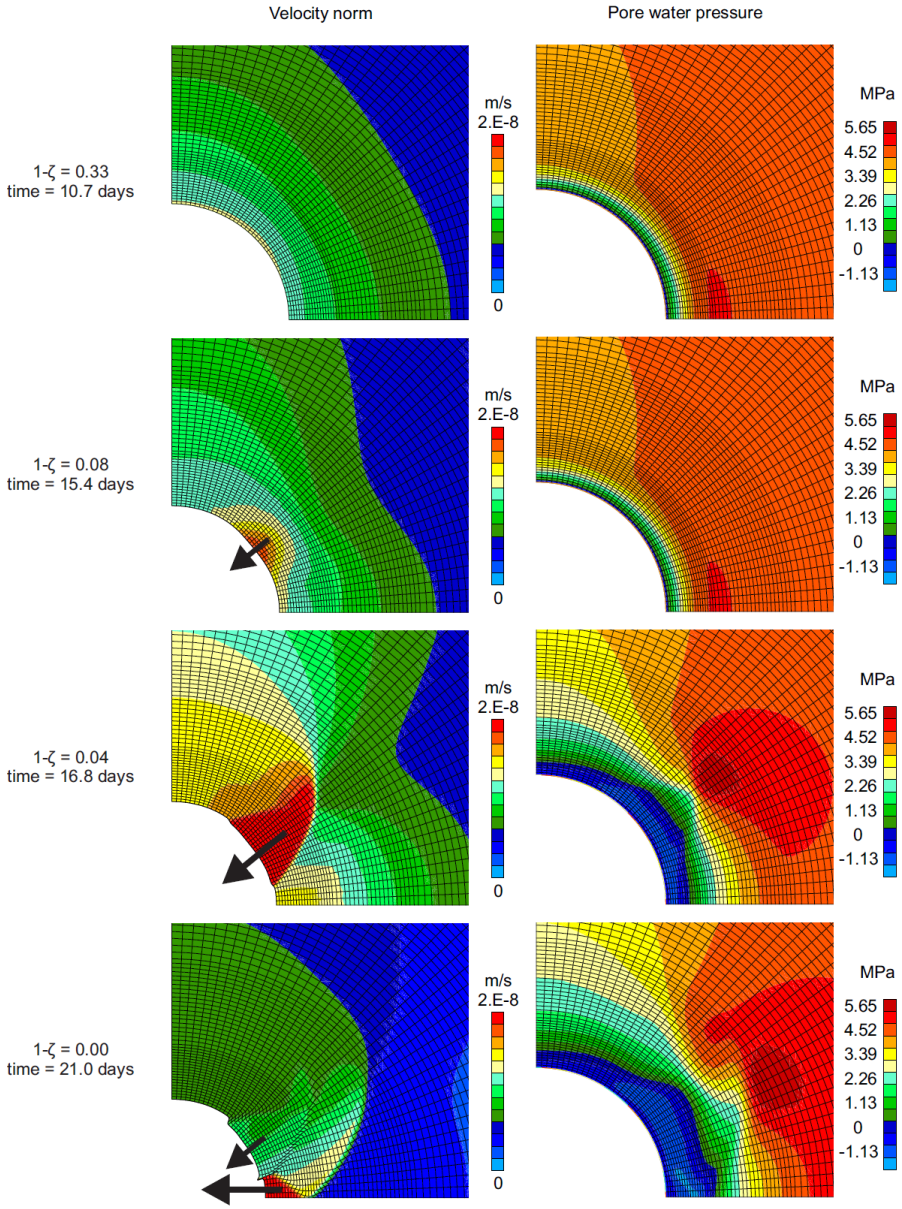

Fig. 5.30: Development of shear strain localisation during the excavation for the set 3 of anisotropic cohesion parameters: velocity norm and pore water pressure.

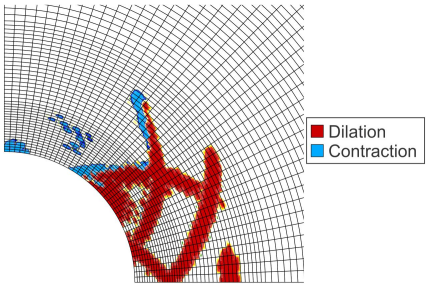

Fig. 5.31: Shear band type at the end of gallery excavation for the set 3 of anisotropic cohesion parameters.

Gallery convergence

The shear band development inevitably influences the convergence of the gallery. The convergence is defined by the variation of the gallery diameter and is investigated in three directions: the horizontal, the vertical, and the inclined direction at 45°. It is illustrated in Fig. 5.32 for the anisotropic cohesion parameters of set 3, both for localised and homogeneous solutions, and for different time scales.

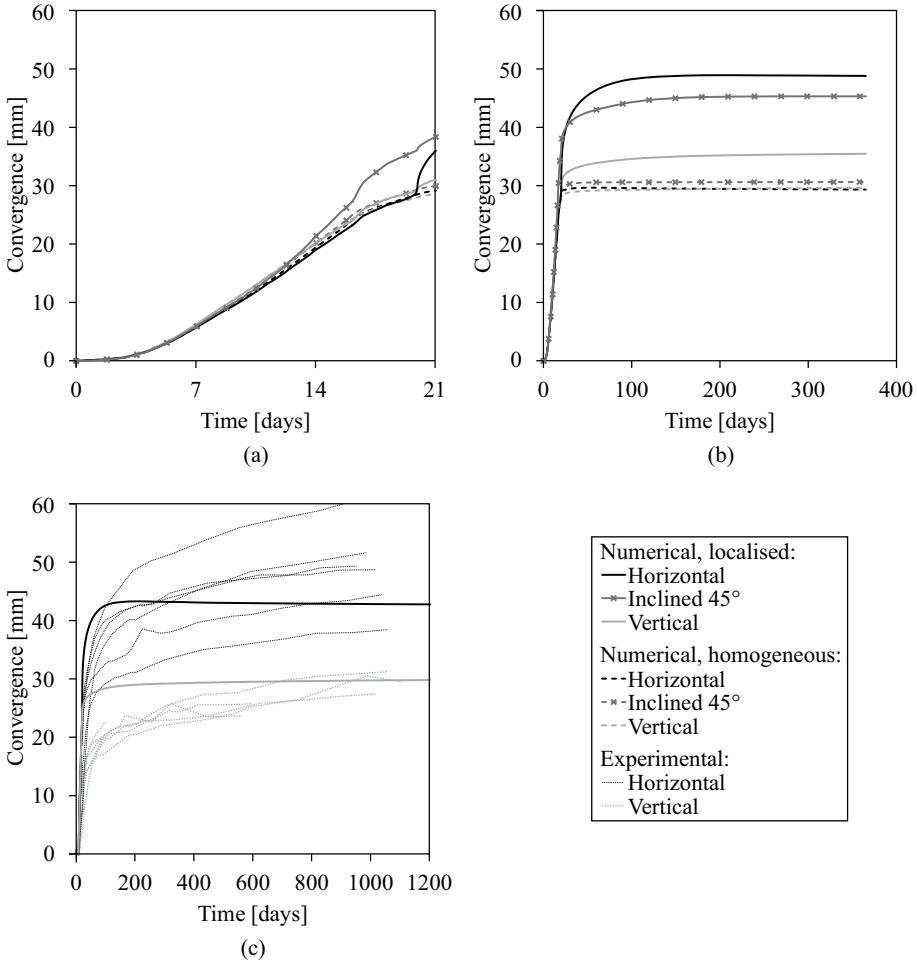

Fig. 5.32: Evolution of gallery convergence (a) during excavation, (b) after excavation, and (c) comparison to experimental measurements in the long term.

The homogeneous solution is obtained if the appearance of strain localisation is avoided which can be done by increasing the second gradient elastic modulus D. This solution exhibits therefore a diffuse plastic zone and a quasi-isotropic convergence. In contrast, an anisotropic convergence is obtained for the localised solution that reproduces the development of shear bands. This anisotropy can be explained by relating the strain localisation results of Figs. 5.29 and 5.30 to the convergence of Fig. 5.32 (a) during the excavation period. In fact, it is observed that the convergence at 45° increases more rapidly than the other convergences from 12.5 days. This increase can be related to the appearance of strain localisation and to the increase of nodal velocities towards the gallery center in the inclined direction (visible at 15.4 days in Fig. 5.30). Around 16.5 days, a slight fluctuation in the convergence curves is observed especially in the 45° direction. It corresponds to the complete development of the shear bands and to the movement towards the gallery center of the block located between them (visible at 16.8 days in Fig. 5.30). Around 20 days, a strong variation of the horizontal convergence is observed which corresponds to the appearance of the supplementary shear band and supplementary block that converges

rapidly (visible at 21 days in Fig. 5.30).

At the end of excavation, the convergence at 45° is still greater than the two other convergences but they can evolve afterwards because of hydro-mechanical coupling and shear band activity that influence the different block movements. The modelling has then been extended under constant zero total radial stress and zero pore water pressure at gallery wall. The resulting convergences (Fig. 5.32 (b)) are greater than for the homogeneous case and highlight a strong anisotropy with an important horizontal convergence. This indicates that the block at gallery wall located in the horizontal direction continues to move significantly towards the gallery center after the end of excavation, which is due to the progressive drainage of the rock around the gallery and to hydro-mechanical coupling. An increase of convergence after the end of excavation has also been observed in Fig. 4.17 for a gallery oriented parallel to the minor horizontal principal stress in Callovo-Oxfordian claystone, but the increase is much greater in that case.

The convergences can be compared to *in situ* experimental measurements that are performed in the French underground research laboratory (Armand et al., 2013; Guayacan-Carrillo et al., 2015). A drift (GCS) oriented parallel to the major horizontal principal stress and having a quasi-isotropic stress state of 12 MPa in its section is considered. For the different convergence measurement sections (GCS-OHZ170B to G, see Fig. 2.7 (a)), the experimental results indicate that the convergence is anisotropic and that it increases in the long term (Fig. 5.32 (c)). The major convergence is measured in the horizontal direction which corresponds to the location of the fractures around this gallery (Fig. 2.6 (a)). The convergence measurement sections are installed inside the gallery just after the excavation front which implies that the beginning of the measurements corresponds to the seventh day of the numerical modelling. Thus, the numerical convergences in Fig. 5.32 (c) are detailed only from that time, excluding the rock deformation that develops before. One can observe that both horizontal and vertical convergences are well reproduced, with a small overestimation of the vertical convergence in the short term. For reproducing the convergence increase in the long term the viscosity effect and creep deformations must be taken into account. It has to be added that the comparison between the numerical and experimental results should be regarded with some reserve because the modelling is performed for an initial isotropic stress state, without the major principal stress in the gallery longitudinal direction. The anisotropic stress state will be included in section 5.4.3 where the gallery convergence will be analysed as well.

Isotropic plane rotation

The gallery excavation is also modelled with isotropic planes oriented in another direction than the horizontal. Such bedding plane orientation does not correspond to the Callovo-Oxfordian claystone; nevertheless, this modelling is realised in order to investigate the influence of isotropic planes rotation on shear banding. An inclination of 45° is chosen. It corresponds for instance to the stratification orientation of the Opalinus clay, which is another low-permeability geological formation envisaged for nuclear waste repository in Switzerland on the Mont Terri site. The characteristics of the Callovo-Oxfordian claystone remain nonetheless used.

The symmetry assumed with a quarter of a gallery is not valid anymore for other orientations than horizontal ($\alpha = 0°$) and vertical ($\alpha = 90°$). A full gallery has to be modelled and is represented schematically in Fig. 5.33 with the bedding planes oriented at $\alpha = 45°$. The mesh extension is 100 m, the discretisation is realised with a total of 7440 elements and 29040 nodes, and a more refined discretisation close to the gallery. The initial stresses and pore water pressure are imposed at the mesh external boundary.

For the considered bedding plane orientation, the deviatoric strain increments obtained when strain localisation appears are represented in Fig. 5.34. The strain localisation in band mode appears between the deconfinement rate values of $1 - \zeta = 0.04$ and $1 - \zeta = 0.02$, just before the end of the excavation. At $1 - \zeta = 0.04$, the deformation is not homogeneous but remains quite diffuse. At $1 - \zeta = 0.02$, the shear bands have developed and a chevron pattern is once

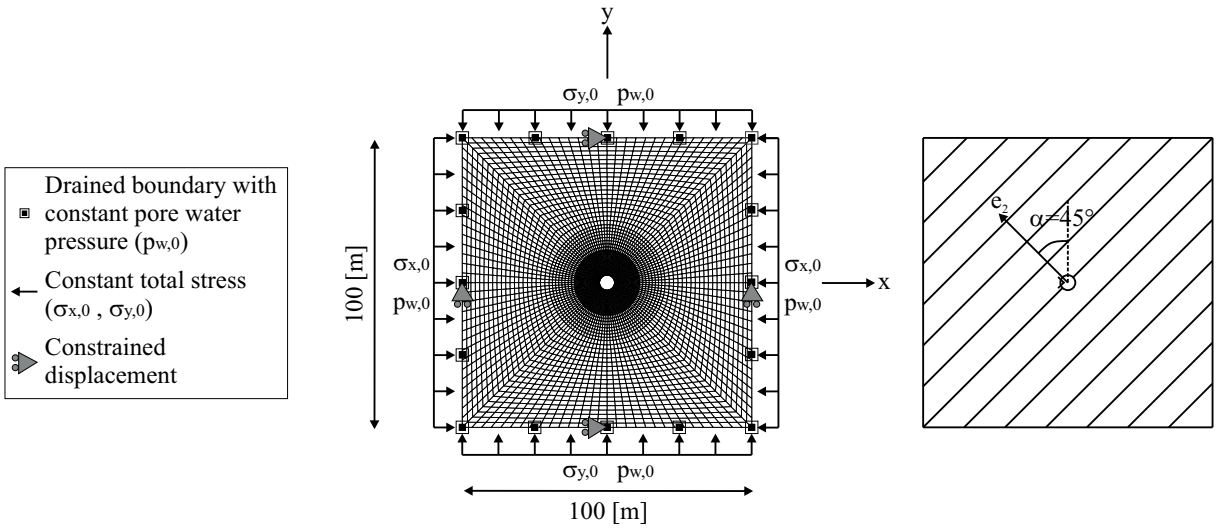

Fig. 5.33: Numerical model used for the modelling of a gallery excavation in cross-anisotropic rock with bedding planes inclined at $\alpha = 45°$.

more observed. The influence of cross-anisotropy and bedding planes rotation is clearly visible on these results with a localised pattern that develops symmetrically around the bedding planes direction at 45°.

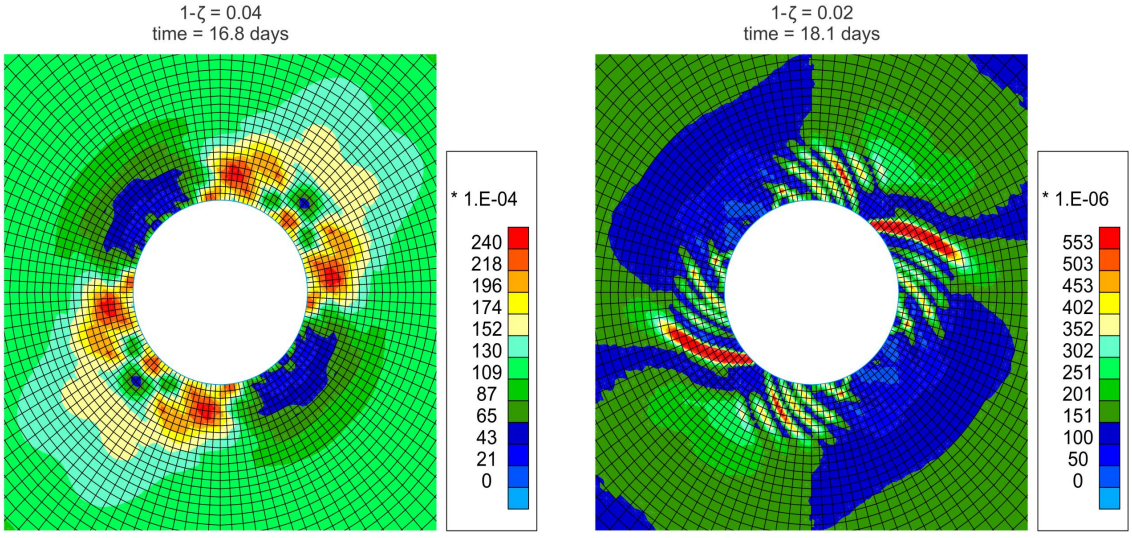

Fig. 5.34: Development of shear strain localisation illustrated with deviatoric strain increment, during the excavation and with bedding planes inclined at $\alpha = 45°$.

The solution of Fig. 5.34 is obtained for a chosen set of computational numerical parameters. Restarting the computation from $1 - \zeta = 0.04$ but with a modification of the numerical parameters, such as increasing the time step size and decreasing the precision of equilibrium parameters for the iterative procedures, provides the solution of Fig. 5.35 at $1 - \zeta = 0.02$. The strain localisation pattern is quite different than the previous one thence such numerical procedure highlights the non-uniqueness of the solution for the gallery excavation problem. In fact, as discussed in chapter 3, regularisation methods based on the second gradient model do not restore the uniqueness of the solution to boundary value problems. Other solutions can be obtained with different numerical procedures to force the occurrence of strain localisation, such as including material imperfections. Actually, among the different possible solutions, some modes are more frequent than others (Marinelli et al., 2014; Sieffert et al., 2009). A study on this particular point

would be interesting to realise.

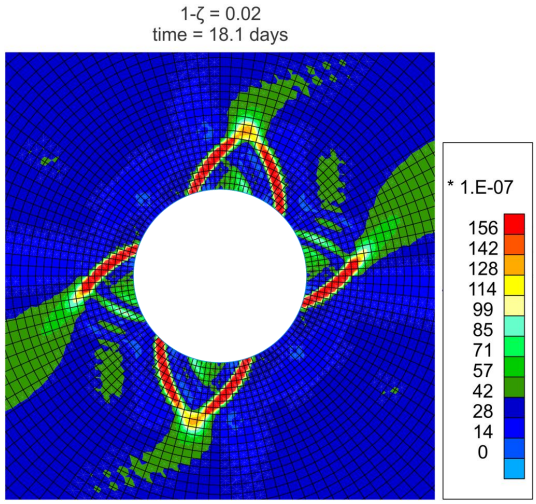

Fig. 5.35: Development of shear strain localisation illustrated with deviatoric strain increment, during the excavation, with bedding planes inclined at $\alpha = 45°$, and with a modification of the numerical parameters.

5.4.3 Modelling of gallery drilling with major stress in the axial direction

The previous modelling of a gallery excavation highlights how the material anisotropy influences the strain localisation appearance in case of an isotropic initial stress state. When considering the Callovo-Oxfordian claystone, its anisotropic stress state must also be taken into account because it influences the fracturing structure. This stress anisotropy has already been considered for a gallery oriented parallel to the minor horizontal principal stress σ_h but not for a gallery parallel to the major horizontal principal stress σ_H. For a gallery parallel to σ_h, the results of section 4.3 indicate that the initial stress state anisotropy in the gallery section controls the fracturing appearance and pattern, for an isotropic mechanical behaviour of the rock. For a gallery parallel to σ_H, the major stress is in the axial direction and the stress state is quasi-isotropic in the gallery section, which requires an anisotropic mechanical behaviour of the material to exhibit strain localisation during the excavation. The results may be similar to those obtained for a full isotropic initial stress state but the major horizontal (axial) stress may still influence the shear banding.

The following modelling has been performed in the context of the Andra's benchmark "Transversal action - Models". Additional informations are available in the reference document of Seyedi et al. (2013) and in the technical report of Pardoen et al. (2014a).

Numerical model

A hydro-mechanical modelling of the gallery drilling is performed in two-dimensional plane strain state with the numerical model of Fig. 5.22 and horizontal isotropic bedding planes. The gallery that is considered is the GCS gallery of the Andra's URL (Fig. 2.2) oriented parallel to σ_H and having a radius of 2.6 m. Following the Andra's recommendations, the initial anisotropic total stress state and pore water pressure are:

$$\sigma_{x,0} = \sigma_h = 12.4\ MPa$$

$$\sigma_{y,0} = \sigma_v = 12.7\ MPa$$

$$\sigma_{z,0} = \sigma_H = 1.3\ \sigma_h = 16.12\ MPa$$

$$p_{w,0} = 4.7\ MPa$$

The boundary conditions at gallery wall, recommended by the Andra, are illustrated in Fig. 5.36. The excavation is performed in a total of 28 days, with the excavation front crossing the studied section after 14 days. The average rate of the excavation is about 2 m per week. The total radial stress follows a uniform deconfinement curve adapted from the convergence-confinement method and considers a flexible liner at gallery wall after the excavation. The latter is modelled by maintaining a total radial stress of 0.3 MPa at gallery wall after the drilling. A linear decrease of the pore water pressure without overpressures is again assumed during the drilling, with a rapid decrease from its original value to zero when the drilling front crosses the studied section (from one day before the front up to one day after). Then, after the excavation, a zero constant pore water pressure is maintained on the gallery wall. It means that the air inside the gallery remains fully saturated with water vapour after the excavation, which corresponds to an air relative humidity of $RH = 100$ % by Kelvin's law (Eq. 2.47). This consists of a classical flow boundary condition assuming an instantaneous hydraulic equilibrium between the liquid water inside the rock and the water vapour of the cavity air.

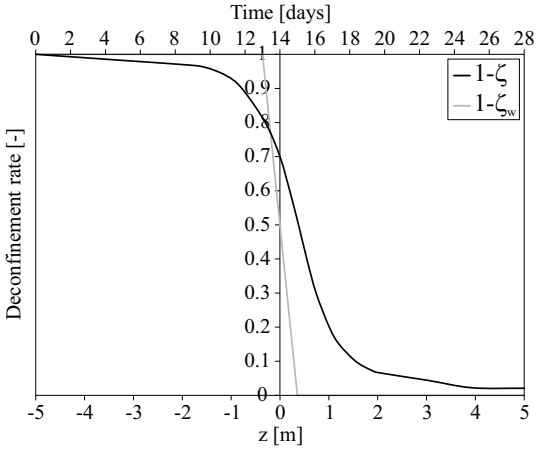

Fig. 5.36: Deconfinement curves for the total radial stress and for the pore water pressure during the excavation of a gallery parallel to the major horizontal principal stress.

Concerning the material behaviour, the anisotropic mechanical model is used with horizontal bedding planes, and the softening parameters allowing shear strain localisation appearance are $\xi_c = 10$, $B_c = 0.003$, and $dec_c = 0$. In addition to the previous modelling, the material viscosity is introduced with the elasto-viscoplastic model to account for long-term deformation of the rock. To avoid an initial viscoplastic flow in the rock mass caused by its initial anisotropic effective stress state, the set of viscoplastic parameters of Table 5.4 is used, with $F_0^{vp} = 0$ and $\alpha_0^{vp} = 0.142$. The viscosity effects are mainly apparent in the long term, after the gallery excavation, and the elasto-viscoplastic model will be tested for different sets of viscoplastic parameters to highlight their influences on deformation and gallery convergence.

Furthermore, unsaturated conditions are also considered but their impact is very limited because the claystone remains almost saturated in the absence of gallery air ventilation. The claystone desaturation around a gallery has been analysed in previous modelling (see section 4.3.5). The results indicate that a slight desaturation can appear close to the drift wall due to hydro-mechanical coupling and to the influence of the strain localisation process (Fig. 4.13). The rock desaturation will not be discussed hereafter, but the pore water pressure evolution will.

Shear banding pattern

As for the full isotropic stress state, the anisotropic model allows the appearance of shear strain localisation around the gallery. The plastic zone and total deviatoric strain evolutions are il-

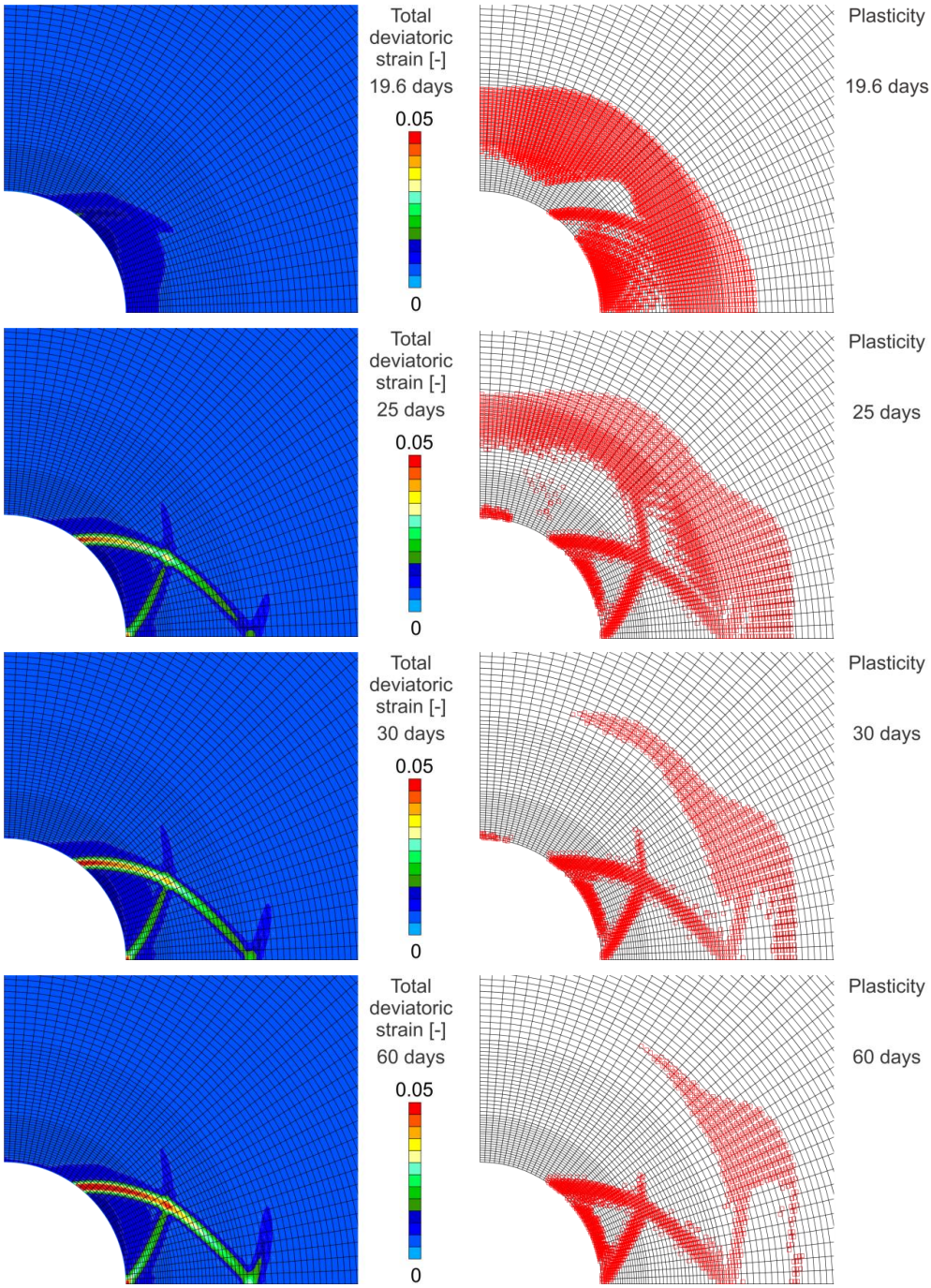

Fig. 5.37: Development of shear banding around a gallery parallel to the major horizontal principal stress: total deviatoric strain and plastic zone.

lustrated in Fig. 5.37 where one can observe the appearance and the development of the shear bands before the end of the excavation (28 days). The complete formation of shear bands occurs between 19.6 and 25 days that correspond to $1-\zeta = 0.067$ and $1-\zeta = 0.024$, respectively. The shear band pattern is similar to the one of Fig. 5.29 with a development even more pronounced in the horizontal direction due to the initial anisotropic stress state, and to the major stress in the gallery axial direction. The full shear band pattern is recomposed by symmetry in Fig. 5.38 and the observed shape is in good agreement with the experimental measurements of the shear fracture pattern and extent around the gallery, as illustrated in Fig. 2.6 (a). The extent of the numerical shear banding zone is compared to the *in situ* measurements in Table 5.6 which in-

dicates a satisfactory agreement. The shear banding zone extent lies between the mixed (shear and tensile) fracture zone and the shear fracture zone.

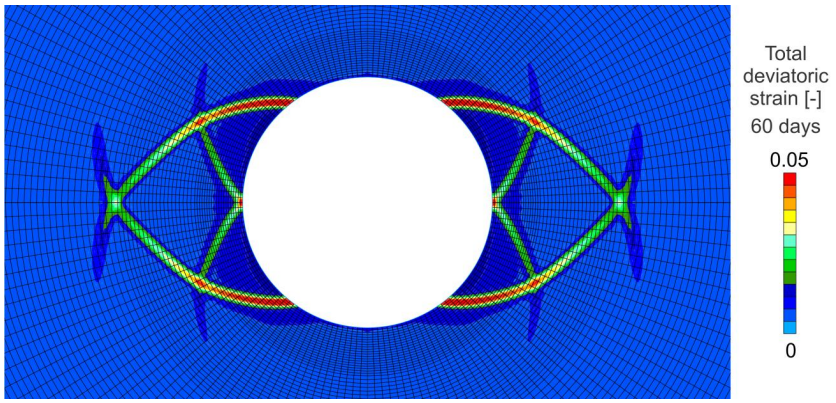

Fig. 5.38: Shear banding around a gallery parallel to the major horizontal principal stress.

Zone	Horizontal left [m]	Horizontal right [m]	Vertical [m]
Numerical shear banding	3	3	0
Mixed fractures	1.4	1.4	< 0.5
Shear fractures	4.7	4.5	< 0.5

Table 5.6: Comparison between the thickness of the numerical shear strain localisation zone and the extents of the fractured zones around a gallery (GCS) parallel to the major horizontal principal stress.

Gallery convergence

The diametrical convergence of the gallery is illustrated in Fig. 5.39 and compared to experimental measurements of the GCS gallery convergence (Armand et al., 2013). Because the convergence measurement sections are installed after the excavation front, the beginning of the measurements corresponds to the 14th day of the numerical modelling. Two numerical convergences are detailed in Fig. 5.39: one from the beginning of the calculation (day 0) that includes the rock deformation developing before the excavation front crosses the studied section, and another from the excavation front (day 14) that corresponds only to the gallery convergence. The numerical modelling captures correctly the convergences for both directions; nonetheless, the viscosity effects seems to remain limited in the long term.

In the Andra's URL, displacement measurements in the rock mass around galleries are also realised in addition to diametrical convergence measurements. They are performed with borehole extensometers drilled from the considered gallery or from a pre-existing gallery. These extensometers record the radial displacements between the gallery rock wall (tip of the extensometer) and the anchors located at different depths in the rock formation. These measurements permit to quantify the displacement and the deformation of the rock.

The first borehole extensometer that is studied was drilled in the context of a mine-by experiment. The latter is a state-of-the-art project that aims to characterise the various impacts of underground drilling on the rock (Armand et al., 2013). Before the GCS drift was excavated, different instrumented boreholes were drilled from surrounding galleries towards the location of the future drift, as illustrated in the set up of the GCS mine-by test in Fig. 5.40. These boreholes contain extensometers, pore pressure sensors, and inclinometers. Among them, the borehole extensometer OHZ1501 was drilled horizontally from the GAT gallery, located 30 m away from

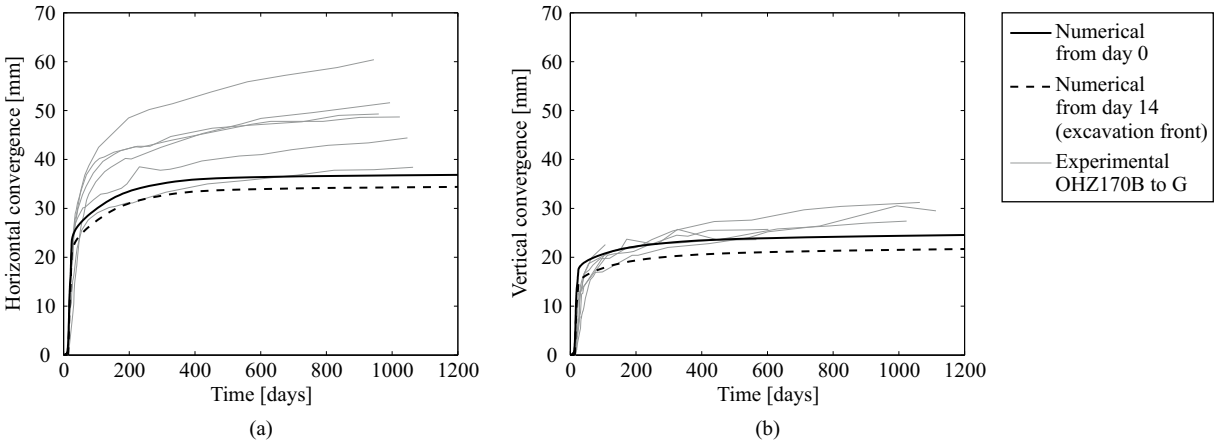

Fig. 5.39: Evolution of the convergence of a gallery parallel to the major horizontal principal stress in (a) horizontal and (b) vertical directions.

the GCS location, and the different anchors are set up from the GAT drift wall up to 30 m in the rock as illustrated in Fig. 5.41. The measurements of radial displacements between the GAT drift wall and the anchors are available in (Armand et al., 2013). They can be easily transformed in radial displacements between the GED drift wall and the anchors by assuming that the anchor located at 30 m depth from the GAT drift wall corresponds to the GED drift wall. The second borehole extensometer that is considered is the OHZ1707. It is drilled vertically upward from a gallery measurement section that is installed inside the GCS gallery during its drilling progress, which means just after the excavation front. The different anchors are set up from the GCS drift wall up to a depth of about 30 m in the claystone (Fig. 5.41 (b)).

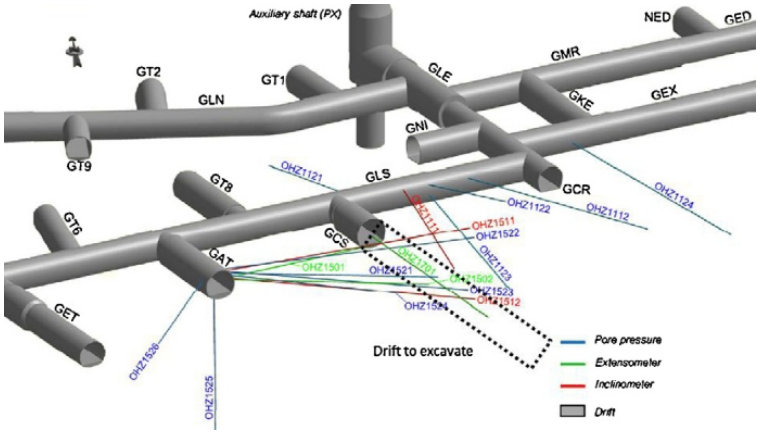

Fig. 5.40: Set up of the mine-by experiment around the GCS gallery in Andra's URL with pore pressure measurements in blue, extensometers in green, and inclinometers in red (Armand et al., 2013).

In the numerical modelling, the relative radial displacement between any location and the gallery wall corresponds to:

$$\Delta u_r = u_r - u_r^{\Gamma} \tag{5.86}$$

where u_r and u_r^{Γ} are the current radial displacements of a considered material point and of the gallery wall for the same orientation. The relative radial displacements are compared to the experimental measurements for both boreholes in Fig. 5.42 where:

$$\Delta u_x = u_x - u_x^{\Gamma} \tag{5.87}$$

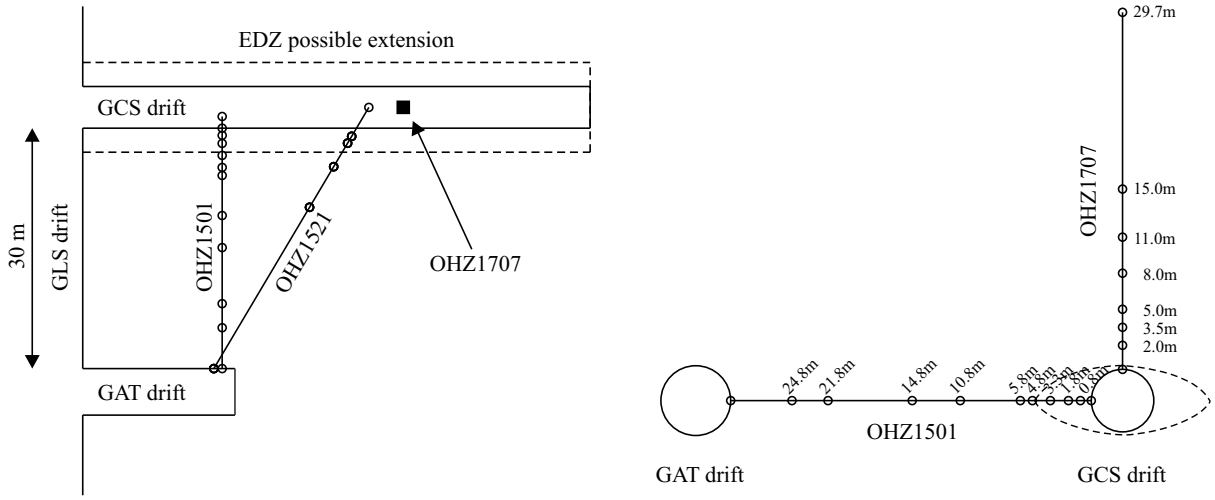

Fig. 5.41: Positions of the boreholes around the GCS drift: (a) in a horizontal plane and (b) in the cross section of the drift with the extensometers and the radial distances of the anchors to the gallery wall.

$$\Delta u_y = u_y - u_y^{\Gamma} \tag{5.88}$$

and the different distances from the gallery wall correspond to the anchors of the extensometers. The numerical results are detailed only after the excavation front crosses the studied gallery section: from 14 days in Fig. 5.42 (a) and from 17.4 days in Fig. 5.42 (b). The latter time corresponds to the position of the second borehole, in fact it was drilled 1.2 m behind the gallery front, which corresponds to 17.4 days in the convergence confinement curve of Fig. 5.36. As for the gallery convergence, the displacements are satisfactorily reproduced unless for the long-term horizontal displacements.

The increases of convergence and relative displacements in the long term can be reproduced by adjusting the viscoplastic parameters of Table 5.4. In fact, these parameters come from experimental data fitting based on laboratory creep tests (section 5.3.3) that last a hundred days, not a thousand days like the *in situ* experimental measurements around the underground gallery. Different sets of viscoplastic parameters are tested and their results in terms of gallery convergence are illustrated in Fig. 5.43. They are compared to experimental measurements from the 14th day of the numerical excavation. Firstly, comparing the results with the viscoplastic parameters based on the creep tests to the results without taking into account material viscosity indicates that these parameters generate only a limited long-term deformation. In fact, the numerical curves for both convergences are relatively close in the long term. The viscoplastic parameters must be adapted to increase the long-term deformation and have a better reproduction of the gallery convergence. Increasing the parameter B^{vp} will slow down the evolution of the function α^{vp} (Eq. 5.57) as well as the hardening of the viscoplastic loading surface (Fig. 5.55). This will have the effect of increasing the viscoplastic flow and deformation (Eq. 5.60). Multiplying by ten this parameter ($B^{vp} = 7.5 \times 10^{-2}$) leads to larger long-term deformations and to a better match with the *in situ* measurements of convergences, in both horizontal and vertical directions (Fig. 5.43). The convergences from the beginning of the calculation (day 0) are also displayed in Fig. 5.43 for this last set of viscoplastic parameters.

The relative radial displacements for the two borehole extensometers are reproduced with this new set of viscoplastic parameters. Fig. 5.44 illustrates that the prediction of the horizontal displacements is improved, but the prediction of the vertical displacements is deteriorated. The

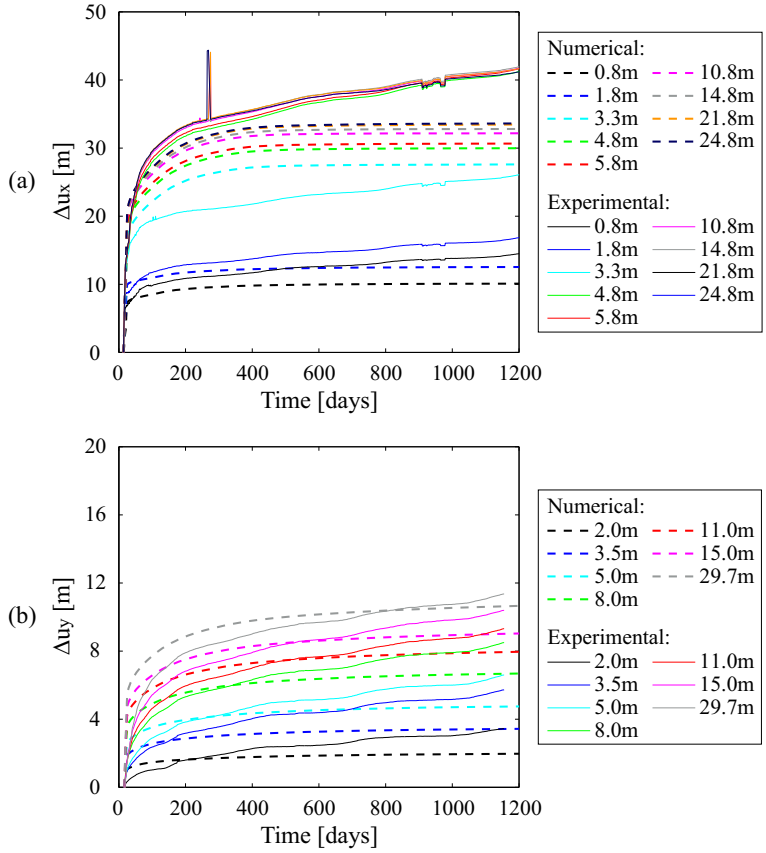

Fig. 5.42: Evolution of relative radial displacements to gallery wall for two borehole extensometers: (a) OHZ1501 horizontal and (b) OHZ1707 vertical upward.

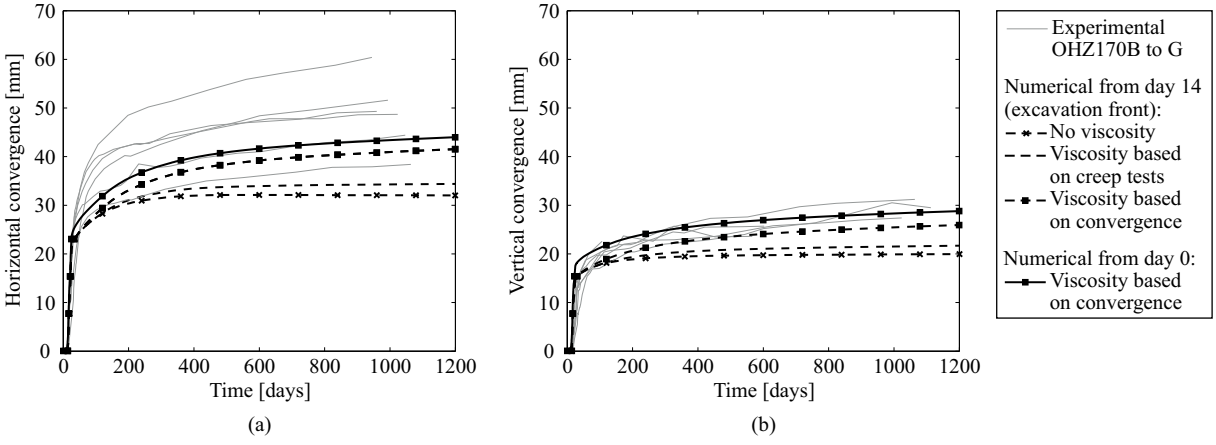

Fig. 5.43: Evolution of the convergence of a gallery parallel to the major horizontal principal stress for different sets of viscoplastic parameters in (a) horizontal and (b) vertical directions.

latter were already well reproduced in Fig. 5.42 (b) so increasing the viscosity can only deteriorate the agreement with the experimental measurements of the vertical borehole. Nevertheless, this borehole extensometer concerns only one measurement section in the GCS gallery while the convergence measurements in Fig. 5.43 are related to several measurement sections, which make them more reliable in a general sense.

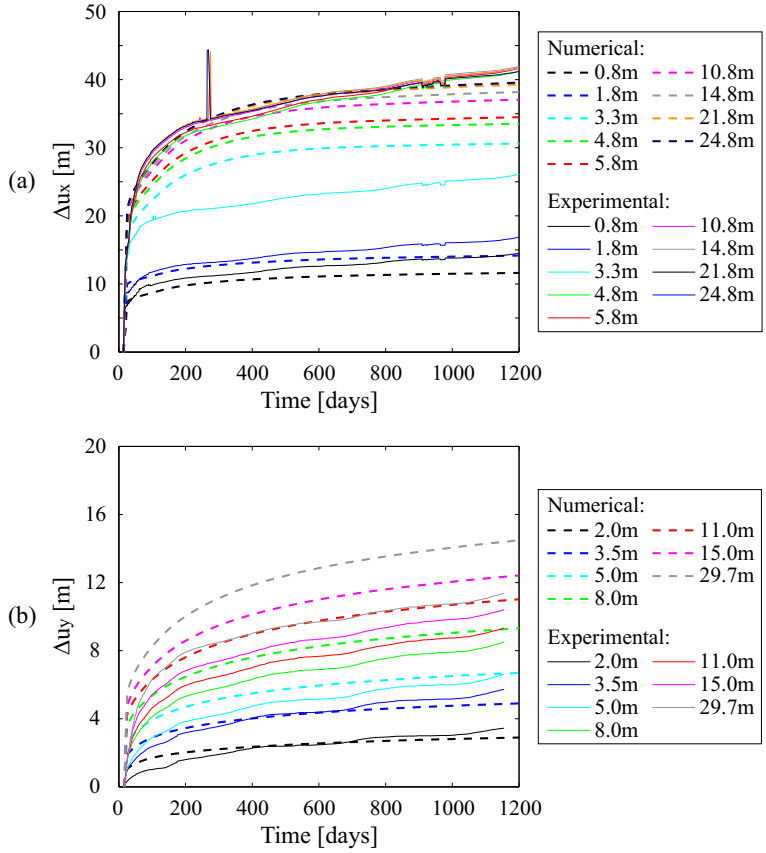

Fig. 5.44: Evolution of relative radial displacements to gallery wall with improvement of the viscoplastic parameters, for two borehole extensometers: (a) OHZ1501 horizontal and (b) OHZ1707 vertical upward.

Pore water pressure

The pore water pressure in the rock is measured in the context of the mine-by experiment of the GCS gallery (Fig. 5.40). Among the different boreholes dedicated to pore water pressure measurements the OHZ1521 and OHZ1522 are analysed. These boreholes were drilled from the GAT gallery in inclined orientations (not perpendicular to the gallery axis): the borehole OHZ1521 is located in a horizontal plane (Fig. 5.41 (a)) and the borehole OHZ1522 is inclined also in the vertical direction. The positions of the different sensors projected in the drift cross-section plane are illustrated in Fig. 5.45. For all these sensors, the experimental measurements and the numerical results obtained with the viscoplastic parameters of Table 5.4 are compared in Figs. 5.46 and 5.47, for different time scales. It is to recall that, after the excavation, the numerical computation is performed with a zero constant pore water pressure at drift wall ($RH = 100$ %).

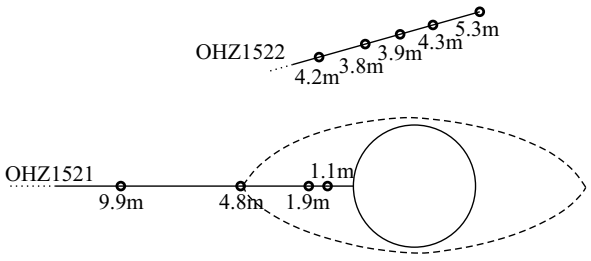

Fig. 5.45: Projection in the GCS drift section of the positions of the pore water pressure sensors around the drift, with radial distances to the gallery wall.

The experimental measurements in the horizontal direction (Fig. 5.46 (a) and (b)) indicate an increase of the pore water pressure as the excavation front get closer to the sensors, then pore pressure dissipation is observed in the rock once the excavation front crosses the sensors positions. These pore overpressures in the rock ahead of the excavation front result of hydro-mechanical coupling linked to the material anisotropy, principally of the stress state but also of the material characteristics. The pore pressure dissipation and stabilisation with the gallery hygrometry is more rapid close to the gallery, especially in the damaged zone where the permeability is important because of the interconnected extensional fracture network. Unfortunately, the measurements can not capture the possible desaturation of the excavation damaged zone because the sensors can acquire only positive measurements. In the far distance, the dissipation is delayed and restricted by the low material permeability as well as by the distance to the gallery.

The numerical results exhibit overpressures in the short term as well (Fig. 5.46 (a)) but the increase starts later than for the experimental measurements and its amplitude is smaller. It is related to the hydraulic boundary condition applied at gallery wall (Fig. 5.36) which consists of a linear decrease without overpressures from day 13 to day 15. The decrease of pore pressure after the excavation is also reproduced but is underestimated (Fig. 5.46 (a) and (b)). An increase of the pore water pressure even appears close to the gallery because of hydro-mechanical coupling, before the long-term drainage of the rock (Fig. 5.46 (c)).

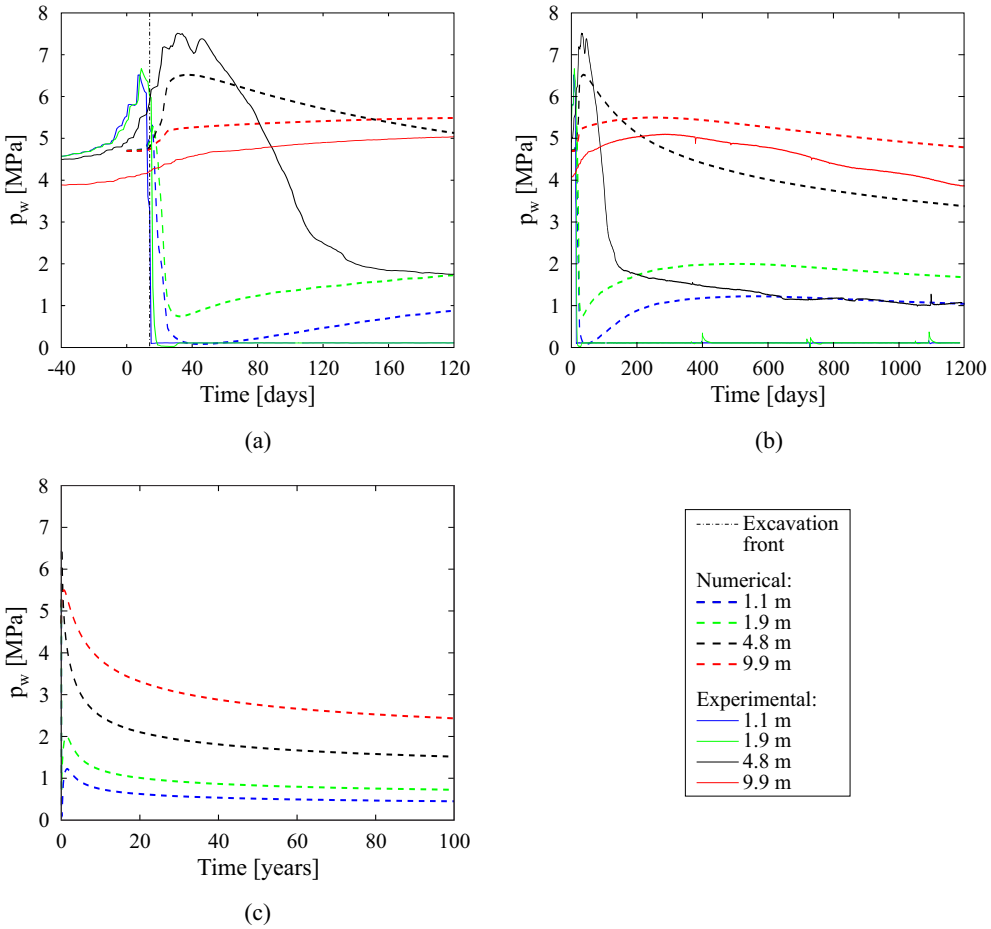

Fig. 5.46: Evolution of the pore water pressure around the gallery for the horizontal borehole OHZ1521: (a) short, (b) medium, and (c) long term.

For the other borehole located above the gallery, there are almost no overpressures before the pore pressure dissipation, as illustrated in the experimental measurements of Fig. 5.47 (a) and (b). When compared to the measurements in the horizontal borehole, this clearly evidences the hydro-mechanical coupling effects linked to the material anisotropy. Fig. 5.47 (c) shows that

a slight decrease of the pore pressure is reproduced by the numerical modelling but it is again underestimated after the excavation, even if a long-term drainage appears in the rock.

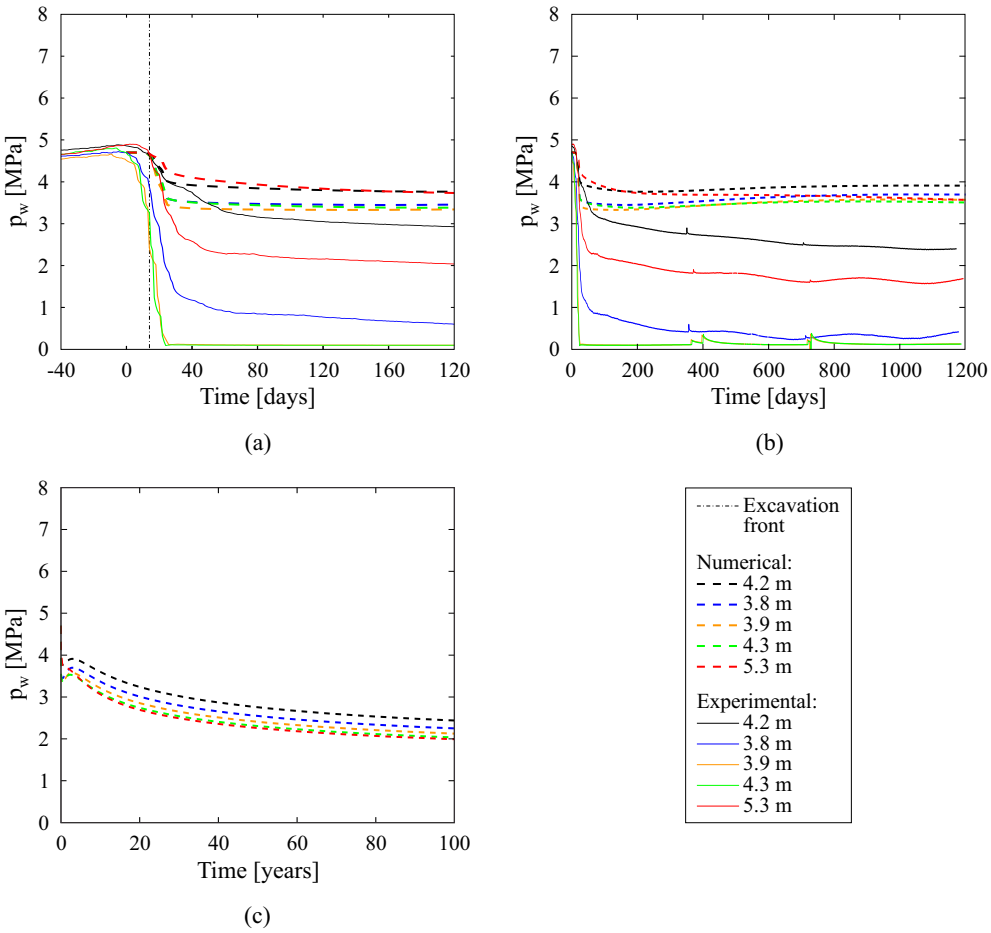

Fig. 5.47: Evolution of the pore water pressure around the gallery for the inclined borehole OHZ1522: (a) short, (b) medium, and (c) long term.

To better reproduce the pore pressure decrease and accentuate the drainage in the rock, the increase of permeability in the damaged zone must be modelled. Indeed, the flow kinetics in the rock are mainly controlled by the hydraulic permeability of the material. Consequently, a higher permeability in the excavation damaged zone will engender a stronger drainage of the rock. Among different possibilities, and because the fractures are represented with shear bands, strain localisation effects on the intrinsic permeability evolution can be considered. Linking the intrinsic permeability to a mechanical parameter, such as strain or plastic deformation, will generate modifications of the hydraulic properties in the damaged zone and especially in the shear strain localisation bands. Another possibility to accentuate the drainage is to consider the hygrometry of the gallery air. In fact, an air saturated with water vapour can not generate a desaturation of the rock surrounding the gallery. If the air is dryer ($RH < 100\%$) after the excavation, it induces a stronger drainage and a possible desaturation of the excavation damaged zone. Such aspects have been discussed in chapter 2 through the effect of a ventilation experiment performed inside an experimental gallery (GED) of the Andra's underground research laboratory. The modelling of the air-rock interaction at gallery wall is also relevant because an instantaneous equilibrium between the water vapour of the cavity air and the liquid water inside the rock may not be assumed beforehand. Therefore, the pore water pressure corresponding to the relative humidity of the gallery air may not be imposed directly on the drift wall (classical imposition).

The aspects of permeability modification, gallery air hygrometry, and air-rock interaction must be considered simultaneously to accurately reproduce the drainage as well as the possible

material desaturation, during gallery excavation and maintenance phases.

5.5 Conclusions and outlooks

The influence of cross-anisotropic properties on the development of shear banding has been highlighted for geomechanical applications on rock. A cross-anisotropic model including anisotropy of the elastic and plastic behaviours is used together with an enriched model, the coupled local second gradient model, that allows to reproduce the shear strain localisation correctly.

The shear banding appearance and development are well reproduced on small rock specimens subjected to plane-strain biaxial compression. The material strength (peak stress amplitude) as well as the shear banding pattern vary according to the loading direction with respect to the microstructure (bedding planes) orientation. The post-peak behaviour is also investigated and an evolution of the shear banding activity is observed.

On a large scale, the development of an excavation fractured zone composed of shear bands around an underground gallery is also controlled by the material anisotropy. Previously, it has been shown that the anisotropy of the stress state in the gallery section is a predominant factor leading to shear bands onset and to the elliptical shape of the excavation damaged zone, with a significantly larger extent in the direction of the minor principal stress. In case of initial isotropic stress state, the anisotropy of the plastic material behaviour is the prevailing factor that governs the strain localisation onset and the banding pattern (shape, location, and orientation). Different amplitudes of anisotropy have been considered for the material cohesion and strain localisation in shear bands appears around the gallery only if a sufficient anisotropy amplitude is considered. This anisotropy is also the origin of the anisotropic shape of the excavation fractured zone that displays a larger extent in the direction of the lower material resistance. Furthermore, the numerical results also indicate that the shear bands appearance and pattern are the cause of the convergence anisotropy. Lastly, the viscosity effects have been analysed and they permit to reproduce the convergence and deformation increases in the long term. Such creep deformations have been studied because they may also be important to take into account for the long-term feasibility analysis of deep geological repository of nuclear radioactive wastes.

Nonetheless, the change of the rock properties in the fractured zone still need to be improved with a more accurate description of the hydro-mechanical coupling. An evolution of the hydraulic permeability around the gallery can be added in the model by considering strain localisation effect and a dependency with a mechanical parameter.

Chapter 6

Permeability evolution and water transfer

Abstract The flow transfers occurring around underground galleries are of paramount importance when envisaging the long-term sustainability of underground structures for nuclear waste disposal. These transfers are mainly conditioned by the behaviour of the surrounding material and by its interaction with the gallery air. The hydro-mechanical behaviour of the excavation damaged zone, which develops around galleries due to the drilling process, is thenceforward critical because it is composed of fractures having a significant irreversible impact on flow characteristics and transfer kinetics. Besides, the material interaction with the gallery air may engender water drainage and desaturation. Thus, a gallery air ventilation experiment, preceded by its excavation, is numerically modelled in an unsaturated argillaceous rock to study its influence on the hydraulic transfers. The fractures are numerically represented with shear strain localisation bands by means of a microstructure enriched model including a regularisation method. The impact of fracturing on the transport properties is addressed by associating the intrinsic permeability increase with mechanical deformation, which is amplified in the strain localisation discontinuities. Such dependence permits to reproduce a significant permeability increase of several orders of magnitude in the excavation damaged zone, in agreement with available experimental measurements. After the excavation, the hydraulic transfers are studied through the reproduction of a gallery air ventilation experiment (SDZ) that implies drainage and desaturation of the surrounding material. These transfers depend on liquid water and water vapour exchanges at gallery wall that are introduced through a non-classical boundary condition. The model prediction successfully captures the drainage and desaturation kinetics of the undisturbed and damaged rock. The numerical modelling and results are available in the research article of Pardoen et al. (2016).

Article Pardoen, B., Talandier, J., and Collin, F. Permeability evolution and water transfer in the excavation damaged zone of a ventilated gallery. *Int J Rock Mech Min Sci.* under review.

6.1 Hydro-mechanical behaviour of the excavation damaged zone

In the context of long-term nuclear waste management, the deep underground repository of high-level radioactive waste is envisaged in geological media having good confining characteristics. The behaviour of the surrounding material has to be precisely characterised in order to assess the long-term sustainability of the underground structures. It is significantly influenced by the drilling process and by the interaction between the material and the gallery air. On one hand, the drilling leads to the appearance of cracks or fractures concentrated in an Excavation Damaged Zone (EDZ) that develops around galleries. On the other hand, the interaction with air may engender drainage and desaturation. Both of these aspects modify the transport properties of the underground material.

As previously, the behaviour of the Callovo-Oxfordian claystone is envisaged. It is a low permeability rock exhibiting a transversely isotropic behaviour and which is envisaged for deep underground repository of nuclear wastes in France (Andra, 2005a).

6.1.1 Increase of permeability

Nowadays, it is commonly assumed that underground drilling process engenders cracks and eventually fractures (Diederichs, 2003) that deteriorate the hydro-mechanical properties of the surrounding host material. These property deteriorations take place in the EDZ located around the galleries which is affected by important modifications of the material flow characteristics, such as permeability increase as illustrated in Fig. 6.1 (Armand et al., 2007; Bossart et al., 2002; Emsley et al., 1997; Tsang and Bernier, 2004; Tsang et al., 2005).

Since a low hydraulic conductivity is required to ensure a safe long-term disposal, the hydro-mechanical behaviour of the EDZ is a major issue because it may constitute a preferential flow

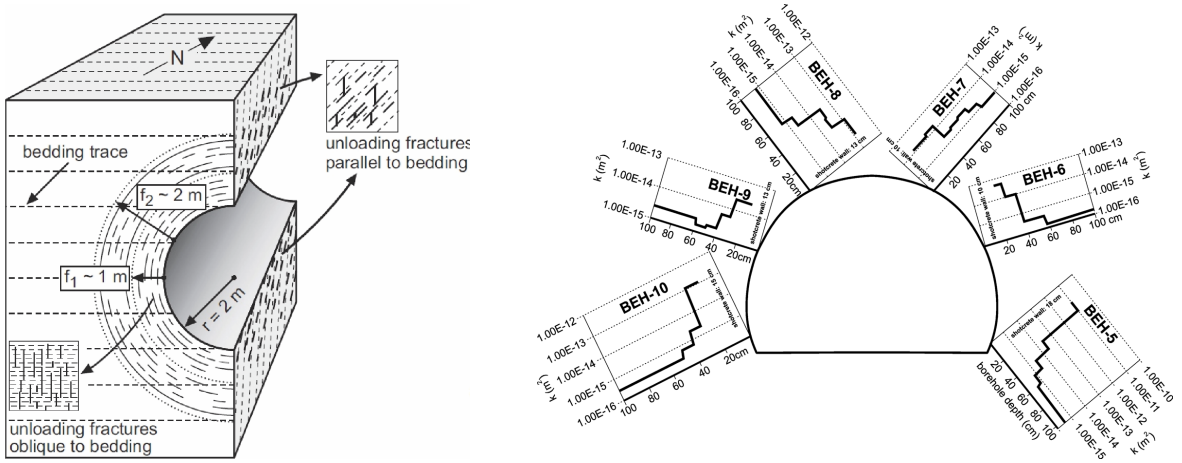

(a) (b)

Fig. 6.1: Excavation damaged zone around a gallery in Opalinus clay: (a) mechanical fracturing and (b) permeability change (Bossart et al., 2002).

path for radionuclide migration (Blümling et al., 2007). Consequently, the characterisation of the material transport properties and of the transfer kinetics that occur around galleries still need to be investigated. These properties depend mainly on the fracturing process and on the hydraulic permeability increase it engenders. The hydro-mechanical characteristics of the surrounding geological formation are evaluated thanks to experimental measurements performed in the Underground Research Laboratories (URL). These laboratories have been developed to investigate the suitability of host formations for nuclear waste disposal and to evaluate the repository feasibility (Delay et al., 2007, 2010).

For the Callovo-Oxfordian claystone, the EDZ, the development of fractures, and the evolution of permeability around underground cavities have been detailed in section 2.2. The experimental measurements indicate that induced extension and shear fractures are detected in the proximity of the galleries composing the Andra's URL, with a severe increase of hydraulic permeability in the fractured zones. Furthermore, the damaged zone shape differs depending on the induced fracture network which is related to the orientations of the galleries and to the stress state anisotropy (Armand et al., 2014) as illustrated in Fig. 6.2.

Around the experimental gallery named GED, which is oriented parallel to the minor horizontal principal stress σ_h, the permeability increase has been highlighted by measurements (Fig. 6.3) performed under saturated conditions in boreholes that are drilled in different orientations (Armand et al., 2014). Three zones have been be defined: an undisturbed zone with $k_w < 10^{-19}\ m^2$ far from the gallery, a slightly disturbed zone with $10^{-19}\ m^2 < k_w < 10^{-17}\ m^2$, and a highly disturbed zone close to the gallery with $k_w > 10^{-17}\ m^2$. The extents of the zones are detailed in Fig. 6.3 and in Fig. 6.4 with a parallelism between hydraulic and fracture measurements. Moreover, the permeability is not homogeneous in the damaged zone and the measurements in the fractured zone are representative of the fracture permeability, not of the permeability of the continuous rock matrix.

6.1.2 Gallery air ventilation

The flow transfers are also conditioned by the interaction with the gallery air. At the scale of nuclear waste repository, air ventilation is usually realised in the underground galleries during the excavation and the maintenance phases. This ventilation can affect the behaviour of the surrounding material and of the underground structures by draining the water from the rock. If the drainage is important, it can even engender rock desaturation, stress modification, and a

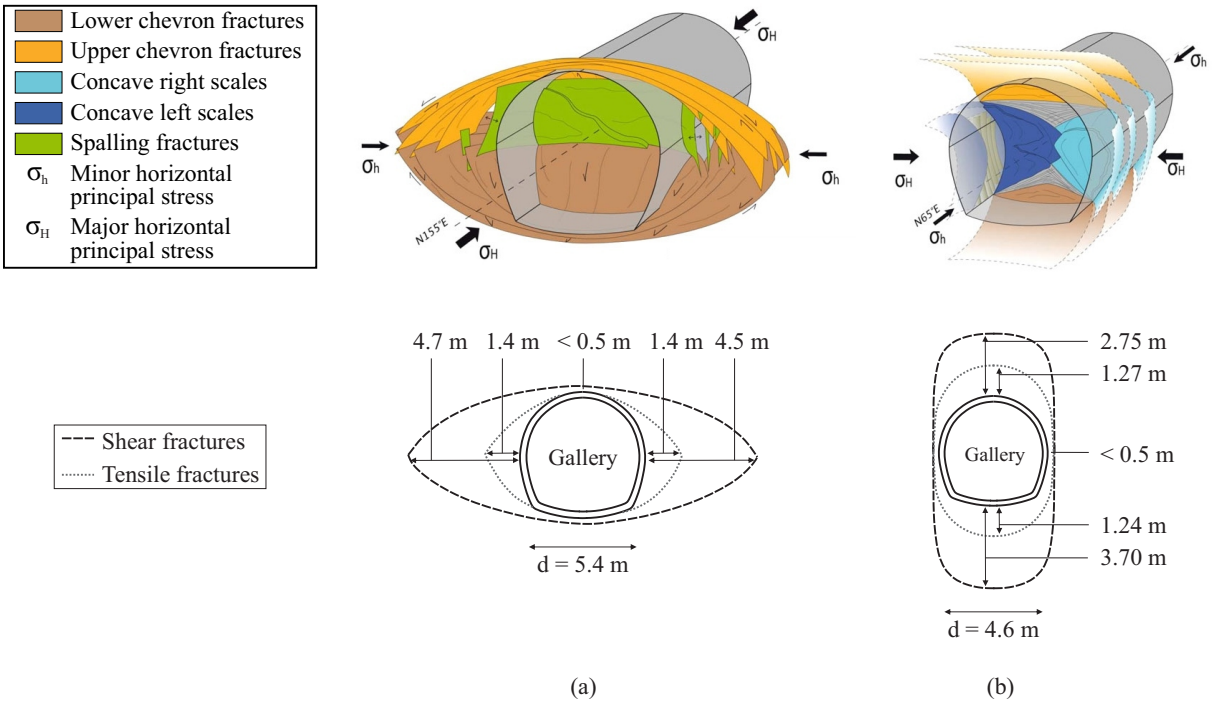

Fig. 6.2: Conceptual model of the induced fractures in Callovo-Oxfordian claystone around drifts parallel to the (a) major and (b) minor horizontal principal stresses (according to Armand et al. (2014)).

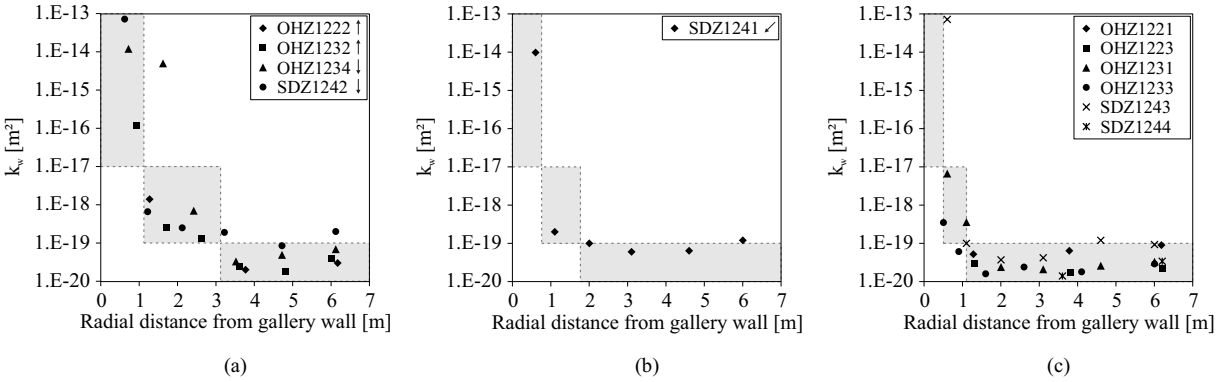

Fig. 6.3: Evolutions of hydraulic permeability along (a) vertical, (b) oblique at 45°, and (c) horizontal boreholes drilled around a gallery (GED) parallel the minor horizontal principal stress in Callovo-Oxfordian claystone.

modification of the fracturing structure close to the galleries. As a consequence, the behaviour of the damaged zone could be impacted (Matray et al., 2007).

Large-scale experiments of gallery air ventilation are realised in the URL to characterise the air-rock interaction. Among them, the Saturation Damaged Zone experiment (SDZ) is conducted in the GED gallery of the Andra's URL (Charlier et al., 2013b; Guillon, 2011; Pardoen et al., 2012a) to analyse the influence of a controlled ventilation on the Callovo-Oxfordian claystone. During the experiment, the hydro-mechanical behaviour and the hydraulic transfers of the rock, including the drainage and desaturation processes, are studied. The ventilation experiment has been detailed in section 2.3.2. It is performed at the end of the GED gallery, in an experimental zone isolated from the rest of the laboratory (Fig. 2.11). A part of this zone is uncovered to allow direct exchanges between the air and the rock. The controlled ventilation consists of different levels of constant hygrometry with the purpose of exhibiting the effects of drainage and wetting,

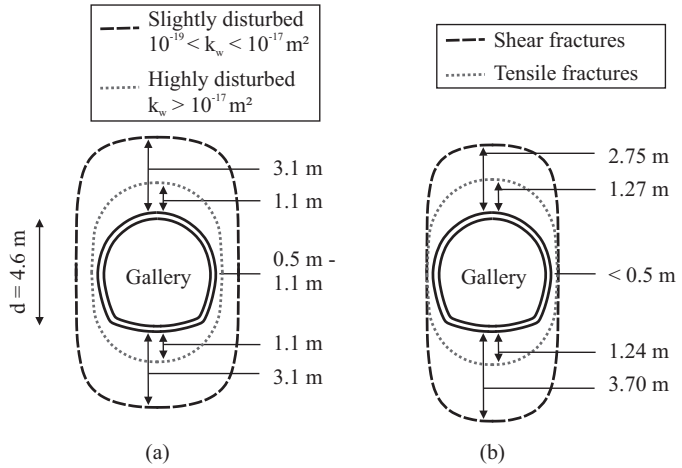

Fig. 6.4: Extensions of (a) hydraulic permeability and (b) fracture zones measured around a gallery (GED) parallel to the minor horizontal principal stress in Callovo-Oxfordian claystone.

or of desaturation and possible resaturation. The different ventilation phases are (Fig. 6.5): (1) a global laboratory ventilation before the insulation of the experimental zone, (2) no ventilation with exchanges between the GED gallery and the SDZ zone occurring through the EDZ, (3) a controlled ventilation with an air relative humidity of $RH = 30$ %, and (4) of $RH = 60$ %. The air temperature T and relative humidity RH evolutions are monitored in the experimental zone in different gallery sections. The measurements are illustrated in Fig. 6.5 with the four different ventilation phases.

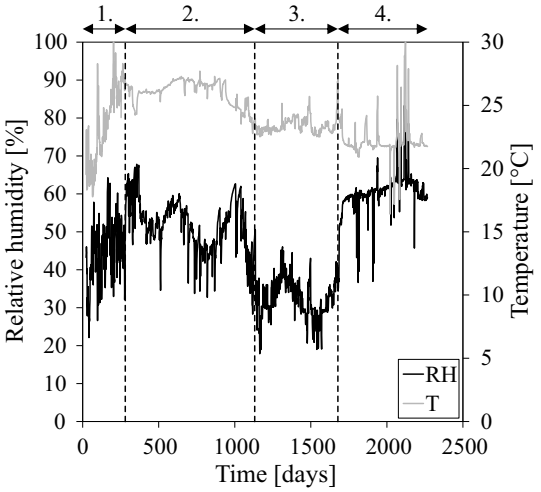

Fig. 6.5: Evolutions of temperature and relative humidity in the SDZ experimental zone.

Various experimental measurements are realised during the test, around the uncovered experimental zone (Fig. 6.6). They consist mainly of pore water pressure (Fig. 6.18) and water content (Fig. 6.19) measurements. They allow to quantify the progressive drainage and the desaturation of the rock which are limited in the far field and increase close to the gallery. Furthermore, fractures and gallery convergence measurements are performed after the gallery excavation (Figs. 6.2 (b) and 2.7 (b)).

6.1.3 Modelling issues

The observations mentioned here above clearly indicate the need for a modelling of the excavation damaged zone and of its interaction with the gallery air. The first step is to consider the exca-

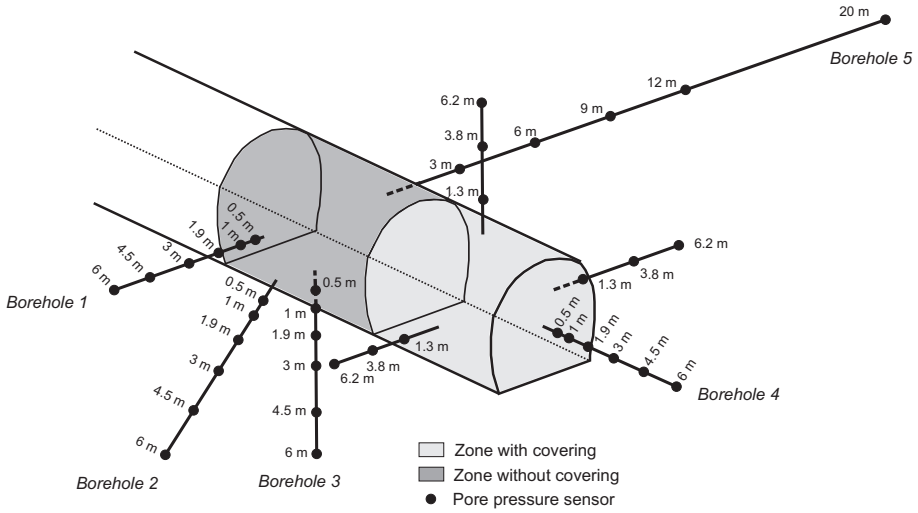

Fig. 6.6: Position of the pore water pressure sensors around the SDZ experimental zone with depths measured from the gallery wall (Charlier et al., 2013b).

vation process and the development of the EDZ with fractures induced by rock deconfinement. Considering the modelling of the fracturing process, shear strain localisation is considered as a precursor to fractures. In fact, material rupture is generally preceded by localised deformation in shear band mode (Desrues, 2005) that can lead to material damage, microcracks, and fractures. Moreover, shearing is the principal failure mechanism for the Callovo-Oxfordian claystone; thus, shear bands are used to predict the appearance of fractures numerically. In the previous chapters, the excavation fractured zone around galleries has been modelled with shear banding. However, the irreversible impact of the fracturing on flow characteristics has not been addressed in the EDZ yet.

The second modelling step concerns the reproduction of the hydraulic property evolutions and inhomogeneity inside the damaged zone. In fact, the definition of the EDZ behaviour needs to be improved with an accurate modelling of the hydro-mechanical coupling occurring in the damaged and fractured zones. The evolution of permeability within the EDZ can be associated to the macroscopic description of the strain localisation discontinuities. It will be addressed with a hydro-mechanical coupling which involves a strain-dependent evolution of the material intrinsic permeability. Considering the fractured rock as a continuous medium at the macroscale, the intrinsic hydraulic permeability evolution will be reproduced through a dependence to the mechanical deformation. Such evolution will engender a more pronounced increase of permeability inside the fractures (shear bands) due to strain localisation effect.

Another aspect that can be influenced by the cracking and the material damage is the water retention property. The damage process in porous materials can modify the pore network morphology, the permeability, the water retention curve, and the gas breakthrough pressure (Arson and Pereira, 2013; M'Jahad et al., 2015; Pereira and Arson, 2013). An additional hydro-mechanical coupling could therefore be introduced by considering an evolution of the retention curve with the deformations (Gerard, 2011; Olivella and Alonso, 2008). For such approach, it is assumed that the increase of the pore size generates a decrease of the air entry pressure, i.e. the minimal capillary force needed to desaturate the material. It results in an amplification of the desaturation in fractured zones for a given capillary pressure (matric suction).

The third step is the modelling of the ventilation of the gallery air. The SDZ experiment in the experimental zone without covering is reproduced after the gallery excavation. Firstly, the air-rock interaction is characterised with a non-classical hydraulic boundary condition at gallery wall, taking into account liquid water and water vapour transfers (Gerard et al., 2008). Secondly, the air ventilation is reproduced with a particular focus on the analysis of the rock drainage and

desaturation. This ventilation experiment has already been studied in section 2.5 (Charlier et al., 2013b) but with a basic definition of the EDZ and only for the uncontrolled ventilation phase (phases (1) and (2)). The previous definition of the EDZ did not take into account neither the description of the fractures nor the hydro-mechanical coupling involved in the evolution of permeability. The EDZ and its extent were *a priori* defined in the numerical model with a higher homogeneous intrinsic permeability than in the undisturbed claystone, whereas the processes are more complex and can be coupled to rock damage and cracking. The focus was principally on a first understanding of the fluid transfer processes. Hereafter, the permeability evolution will be investigated with a more elaborate description of hydro-mechanical coupling, especially within the EDZ. In fact, the coupling between mechanical deformation, permeability, and hydraulic flow, which was not taken into account in earlier modelling, is indubitably of paramount importance to obtain an adequate representation of the hydro-mechanical behaviour of the EDZ.

6.2 Constitutive models

The modelling of underground drilling and ventilation requires a hydro-mechanical model describing the constitutive equations of the coupled problem for an unsaturated porous media. This model is composed of a first gradient mechanical part (macrostructure), including viscosity and the transversely isotropic properties of the rock, a second gradient mechanical part (microstructure), introducing an internal length scale for the description of the shear bands, and a hydraulic part, which defines the liquid phase transfers under unsaturated condition. The constitutive models are the same as those used in the precedent chapters and are recalled succinctly.

A proper reproduction of the shear bands is still realised by using the coupled local second gradient model for microstructure media (enriched model with regularisation method). The development of the balance equations of this model have been detailed previously in section 3.3.2 and are not recalled. The non-linear field equations are available in Eqs. 4.32, 4.33, and 4.34.

As mentioned in section 6.1, the hydraulic flow kinetics around the galleries are conditioned by permeability evolution and air-rock interaction. The modification of the permeability in the damaged zone as well as the fluid transfer at gallery wall must still be taken into account. They will be described later in the numerical sections 6.3 and 6.4. Furthermore, the influence of the variation of the intrinsic water permeability on the coupled finite element formulation is developed.

6.2.1 First gradient mechanical model

The elasto-viscoplastic relation between the stress and strain fields is defined as:

$$\tilde{\sigma}'_{ij} = C_{ijkl}\ \dot{\varepsilon}_{kl} \tag{6.1}$$

The stress field is defined for unsaturated anisotropic materials with compressible solid grains by:

$$\sigma_{ij} = \sigma'_{ij} + b_{ij}\ S_{r,w}\ p_w \tag{6.2}$$

The viscosity is taken into account by assuming that the total strain rate is partitioned in an elastic, a plastic, and a viscoplastic components:

$$\dot{\varepsilon}_{ij} = \dot{\varepsilon}^e_{ij} + \dot{\varepsilon}^p_{ij} + \dot{\varepsilon}^{vp}_{ij} \tag{6.3}$$

The elastic and plastic behaviours are defined in the following for transversely isotropic materials, which properties are related to the material axes and depend on the orientation. Both plastic and viscoplastic strains are described by loading functions, potentials, and hardening laws.

Linear elasticity theory

Anisotropic geomaterials often exhibit limited forms of anisotropy such as orthotropy or transverse isotropy, i.e. cross-anisotropy (Lekhnitskii, 1963). For these types of anisotropy, the material characteristics are associated to the orthotropic axes (e_1,e_2,e_3) (Amadei, 1983). The Callovo-Oxfordian claystone exhibits a transverse isotropy with horizontal bedding planes as detailed in Fig. 6.7, and only this material configuration is modelled numerically hereafter. For this orientation, the orthotropic axes correspond to the global coordinate axes $e_i = x_i$; thus, a change of coordinate reference system is not required. The notation $^\sharp$ used in chapter 5 to denote a quantity in the orthotropic axes is omitted for simplicity.

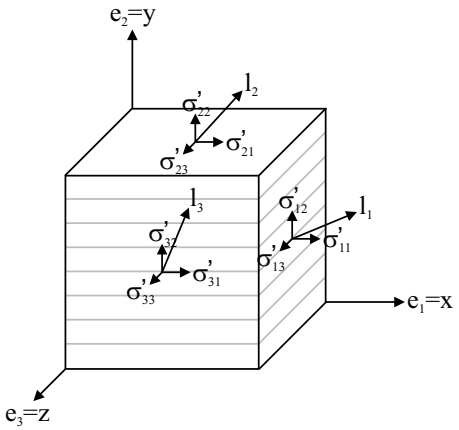

Fig. 6.7: Material axes, stress state, and generalised loading vector l_i for a representative elementary volume of a transversely isotropic material with horizontal isotropic planes.

For transversely isotropic materials with isotropic planes oriented along (e_1,e_3), the effective stress and the elastic strain rates are linked by the Hooke's law as follows:

$$\begin{bmatrix} \dot{\varepsilon}^e_{11} \\ \dot{\varepsilon}^e_{22} \\ \dot{\varepsilon}^e_{33} \\ \dot{\varepsilon}^e_{12} \\ \dot{\varepsilon}^e_{13} \\ \dot{\varepsilon}^e_{23} \end{bmatrix} = \begin{bmatrix} \frac{1}{E_\parallel} & -\frac{\nu_{\perp\parallel}}{E_\perp} & -\frac{\nu_{\parallel\parallel}}{E_\parallel} & 0 & 0 & 0 \\ -\frac{\nu_{\parallel\perp}}{E_\parallel} & \frac{1}{E_\perp} & -\frac{\nu_{\parallel\perp}}{E_\parallel} & 0 & 0 & 0 \\ -\frac{\nu_{\parallel\parallel}}{E_\parallel} & -\frac{\nu_{\perp\parallel}}{E_\perp} & \frac{1}{E_\parallel} & 0 & 0 & 0 \\ 0 & 0 & 0 & \frac{1}{2G_{\parallel\perp}} & 0 & 0 \\ 0 & 0 & 0 & 0 & \frac{1}{2G_{\parallel\parallel}} & 0 \\ 0 & 0 & 0 & 0 & 0 & \frac{1}{2G_{\perp\parallel}} \end{bmatrix} \begin{bmatrix} \tilde{\sigma}'_{11} \\ \tilde{\sigma}'_{22} \\ \tilde{\sigma}'_{33} \\ \tilde{\sigma}'_{12} \\ \tilde{\sigma}'_{13} \\ \tilde{\sigma}'_{23} \end{bmatrix} \tag{6.4}$$

where:

$$\frac{\nu_{\perp\parallel}}{E_\perp} = \frac{\nu_{\parallel\perp}}{E_\parallel} \tag{6.5}$$

$$G_{\parallel\parallel} = \frac{E_\parallel}{2(1+\nu_{\parallel\parallel})} \tag{6.6}$$

$$G_{\parallel\perp} = G_{\perp\parallel} \tag{6.7}$$

The elasticity is characterised by 5 independent parameters describing the material behaviour in the directions perpendicular $\perp$ and parallel $\parallel$ to the isotropic planes: $E_\parallel$, $E_\perp$, $\nu_{\parallel\parallel}$, $\nu_{\parallel\perp}$, $G_{\parallel\perp}$.

The compressibility of the solid grains is described by the symmetric Biot's tensor as follows (Cheng, 1997):

$$b_{ij} = \delta_{ij} - \frac{C^e_{ijkk}}{3\ K_s} = \begin{bmatrix} b_{\parallel} & 0 & 0 \\ 0 & b_{\perp} & 0 \\ 0 & 0 & b_{\parallel} \end{bmatrix} \tag{6.8}$$

Plasticity theory

The plastic model is an internal friction model with a Van Eekelen yield surface (Van Eekelen, 1980) and a non-associated plasticity. The plastic loading surface, plastic potential surface, and plastic flow (plastic strain rate) are given by:

$$F^p \equiv II_{\hat{\sigma}'} - m\left(I_{\sigma'} + \frac{3\ c}{\tan\varphi_c}\right) = 0 \tag{6.9}$$

$$G^p \equiv II_{\hat{\sigma}'} - m_G\ I_{\sigma'} = 0 \tag{6.10}$$

$$\dot{\varepsilon}^p_{ij} = \dot{\lambda}^p\ \frac{\partial G^p}{\partial \sigma^{'}_{ij}} \tag{6.11}$$

The friction angles and the cohesion can undergo an isotropic softening or hardening introduced with hyperbolic functions (Barnichon, 1998):

$$c = c_0 + \frac{(c_f - c_0)\ \langle \hat{\varepsilon}^p_{eq} - dec_c \rangle}{B_c + \langle \hat{\varepsilon}^p_{eq} - dec_c \rangle} \tag{6.12}$$

$$\varphi_c = \varphi_{c,0} + \frac{(\varphi_{c,f} - \varphi_{c,0})\ \langle \hat{\varepsilon}^p_{eq} - dec_\varphi \rangle}{B_\varphi + \langle \hat{\varepsilon}^p_{eq} - dec_\varphi \rangle} \tag{6.13}$$

$$\varphi_e = \varphi_{e,0} + \frac{(\varphi_{e,f} - \varphi_{e,0})\ \langle \hat{\varepsilon}^p_{eq} - dec_\varphi \rangle}{B_\varphi + \langle \hat{\varepsilon}^p_{eq} - dec_\varphi \rangle} \tag{6.14}$$

The plastic behaviour anisotropy is defined for the cohesion by means of a second order microstructure fabric tensor A_{ij}. The latter represents the material fabric and describes the spatial distribution of the strength parameter. Besides, the cohesion also depends on the loading direction with regard to the material microstructure orientation (Pietruszczak et al., 2002; Pietruszczak, 2010). For transversely isotropic materials with isotropic planes parallel to (e_1,e_3), it is given by:

$$c_0 = \bar{c}\left(1 + A_{\parallel}\left(1 - 3\ l_2^2\right) + b_1\ A_{\parallel}^2\left(1 - 3\ l_2^2\right)^2\right) \tag{6.15}$$

where l_2 is the component of the generalised unit loading vector l_i acting on a facet parallel to the isotropic planes as illustrated in Fig. 6.7. The vector l_i corresponds to the stress resultant on the material facets (Pietruszczak and Mroz, 2000, 2001; Chen et al., 2010) and is defined by:

$$l_i = \sqrt{\frac{\sigma^{'2}_{i1} + \sigma^{'2}_{i2} + \sigma^{'2}_{i3}}{\sigma^{'}_{jk}\ \sigma^{'}_{jk}}} \tag{6.16}$$

Viscoplasticity theory

The viscoplastic flow mechanism is introduced with the following loading surface, potential surface, and viscoplastic flow (viscoplastic strain rate):

$$F^{vp} \equiv \sqrt{3}\ II_{\hat{\sigma}'} - \alpha^{vp}\ g\left(\beta\right)\bar{R}\ \sqrt{A^{vp}\left(C^{vp} + \frac{I_{\sigma'}}{3\bar{R}}\right)} = 0 \tag{6.17}$$

$$G^{vp} \equiv \sqrt{3}\ II_{\hat{\sigma}'} - \left(\alpha^{vp} - \beta^{vp}\right) g\left(\beta\right) \bar{R} \left(C^{vp} + \frac{I_{\sigma'}}{3\bar{R}}\right) = 0 \tag{6.18}$$

$$\dot{\varepsilon}_{ij}^{vp} = \gamma \left\langle \frac{F^{vp}}{\bar{R}} \right\rangle^{\mathcal{N}} \frac{\partial G^{vp}}{\partial \sigma'_{ij}} \tag{6.19}$$

where A^{vp} is an internal friction coefficient, C^{vp} is a constant cohesion coefficient, $\bar{R} = R_c$ is a normalising parameter taken as equal to the uniaxial compressive strength, $g\left(\beta\right)$ is a function allowing to take into account the influence of the Lode angle ($g\left(\beta\right) = 1$ for simplicity), β^{vp} is a viscoplastic potential parameter, γ is the fluidity coefficient (Eq. 5.61), and $\mathcal{N}$ is a creep parameter. The surfaces F^{vp} and G^{vp} are both controlled by a delayed viscoplastic hardening function α^{vp} (Jia et al., 2008; Zhou et al., 2008) which takes the form:

$$\alpha^{vp} = \alpha_0^{vp} + \left(1 - \alpha_0^{vp}\right) \frac{\varepsilon_{eq}^{vp}}{B^{vp} + \varepsilon_{eq}^{vp}} \tag{6.20}$$

where α_0^{vp} is the initial threshold for the viscoplastic flow, B^{vp} is a parameter controlling the evolution of α^{vp}, and ε_{eq}^{vp} is the equivalent viscoplastic strain (Eq. 5.58).

6.2.2 Second gradient mechanical model and coupled finite element formulation

The second gradient constitutive law is related to the microkinematics and links the double stress rate to the micro second gradient rate (section 3.3.2):

$$\tilde{\Sigma}_{ijk} = D_{ijklmn} \frac{\partial \dot{v}_{lm}}{\partial x_n} \tag{6.21}$$

It depends on an elastic modulus D (Eq. 3.80) which characterises the internal length scale of the second gradient model.

In addition to the developments of the second gradient model realised in the previous chapters, the variation of the intrinsic water permeability will be added in section 6.3.3. The latter has an influence on some terms of the balance equations of the coupled local second gradient model (Eqs. 4.32, 4.33, and 4.34) and on their linearisation for the finite element formulation (see section 3.3.3, section 4.1.3, and appendix A for the complete details). The time derivative of the intrinsic permeability obviously depends on the chosen evolution law and on the considered evolution parameters. If it varies according to a set of parameters $\overline{m}_i$ and with the pore water pressure, the time derivative of the intrinsic water permeability reads:

$$\dot{k}_{w,ij} = \frac{\partial k_{w,ij}}{\partial \overline{m}_k} \dot{\overline{m}}_k + \frac{\partial k_{w,ij}}{\partial p_w} \dot{p}_w \tag{6.22}$$

The dependence on the pore water pressure can for instance be linked to the effect of porosity variation if the Biot's coefficient is lower than 1 (Eq. 4.26). The variation form of Eq. 6.22 for the linearisation of the field equations reads:

$$dk_{w,ij}^{\tau 1} = k_{w,ij}^{\tau 2} - k_{w,ij}^{\tau 1} = \frac{\partial k_{w,ij}^{\tau 1}}{\partial \overline{m}_k^{\tau 1}} d\overline{m}_k^{\tau 1} + \frac{\partial k_{w,ij}^{\tau 1}}{\partial p_w^{\tau 1}} dp_w^{\tau 1} \tag{6.23}$$

The local stiffness matrix of an element $\left[E^{\tau 1}\right]$ (Eq. 4.64), which is involved in the linear auxiliary problem (Eq. 4.63) of the finite element formulation, is modified by the evolution of the intrinsic permeability. If it depends on the pore water pressure then $\frac{\partial k_{w,ij}^{\tau 1}}{\partial p_w^{\tau 1}} \neq 0$ and the

terms $K^{\tau 1}_{WW_{1,3}}$ and $K^{\tau 1}_{WW_{2,3}}$ (Eqs. 4.66 and 4.67) of the submatrix of the flow problem $\left[K^{\tau 1}_{WW}\right]$ (Eq. 4.65) take the forms:

$$\begin{aligned} K^{\tau 1}_{WW_{1,3}} = {} & \rho^{\tau 1}_w \frac{k^{\tau 1}_{w,1j}}{\mu_w} \frac{k^{\tau 1}_{r,w}}{\chi_w} \left(\frac{\partial p^{\tau 1}_w}{\partial x^{\tau 1}_j} + 2\rho^{\tau 1}_w g_j \right) + \rho^{\tau 1}_w \frac{k^{\tau 1}_{w,1j}}{\mu_w} \frac{\partial k^{\tau 1}_{r,w}}{\partial S^{\tau 1}_{r,w}} \frac{\partial S^{\tau 1}_{r,w}}{\partial p^{\tau 1}_w} \left(\frac{\partial p^{\tau 1}_w}{\partial x^{\tau 1}_j} + \rho^{\tau 1}_w g_j \right) \\ & + \rho^{\tau 1}_w \frac{k^{\tau 1}_{r,w}}{\mu_w} \frac{\partial k^{\tau 1}_{w,1j}}{\partial p^{\tau 1}_w} \left(\frac{\partial p^{\tau 1}_w}{\partial x^{\tau 1}_j} + \rho^{\tau 1}_w g_j \right) \end{aligned} \tag{6.24}$$

$$\begin{aligned} K^{\tau 1}_{WW_{2,3}} = {} & \rho^{\tau 1}_w \frac{k^{\tau 1}_{w,2j}}{\mu_w} \frac{k^{\tau 1}_{r,w}}{\chi_w} \left(\frac{\partial p^{\tau 1}_w}{\partial x^{\tau 1}_j} + 2\rho^{\tau 1}_w g_j \right) + \rho^{\tau 1}_w \frac{k^{\tau 1}_{w,2j}}{\mu_w} \frac{\partial k^{\tau 1}_{r,w}}{\partial S^{\tau 1}_{r,w}} \frac{\partial S^{\tau 1}_{r,w}}{\partial p^{\tau 1}_w} \left(\frac{\partial p^{\tau 1}_w}{\partial x^{\tau 1}_j} + \rho^{\tau 1}_w g_j \right) \\ & + \rho^{\tau 1}_w \frac{k^{\tau 1}_{r,w}}{\mu_w} \frac{\partial k^{\tau 1}_{w,2j}}{\partial p^{\tau 1}_w} \left(\frac{\partial p^{\tau 1}_w}{\partial x^{\tau 1}_j} + \rho^{\tau 1}_w g_j \right) \end{aligned} \tag{6.25}$$

The other terms of the stiffness matrix of the flow problem are not affected.

If the intrinsic permeability evolution depends on parameters linked to the displacement field $\dot{u}_i$, as the strain field for instance, therefore the first part of Eq. 6.22 becomes for each parameter $\overline{m}$:

$$\frac{\partial k_{w,ij}}{\partial \overline{m}} \ \dot{\overline{m}} = \frac{\partial k_{w,ij}}{\partial \overline{m}} \ \frac{\partial \overline{m}}{\partial \varepsilon_{kl}} \ \dot{\varepsilon}_{kl} = \frac{\partial k_{w,ij}}{\partial \varepsilon_{kl}} \ \frac{\partial \dot{u}_k}{\partial x_l} \tag{6.26}$$

It can be rewritten in variation form as:

$$\frac{\partial k^{\tau 1}_{w,ij}}{\partial \overline{m}^{\tau 1}} \ d\overline{m}^{\tau 1} = \frac{\partial k^{\tau 1}_{w,ij}}{\partial \varepsilon^{\tau 1}_{kl}} \ \frac{\partial du^{\tau 1}_k}{\partial x^{\tau 1}_l} \tag{6.27}$$

where $\frac{\partial k^{\tau 1}_{w,ij}}{\partial \varepsilon^{\tau 1}_{kl}} \neq 0$ depends on the evolution law for $k_{w,ij}$ and on the link between the evolution parameters and the strain field. The matrix of the mechanic influence on the fluid (Eq. 4.70) becomes:

$$\left[K^{\tau 1}_{MW}\right]_{3\times 4} = \begin{bmatrix} A^{\tau 1}_{111} & f^{\tau 1}_{w,2} + A^{\tau 1}_{121} & A^{\tau 1}_{112} & -f^{\tau 1}_{w,1} + A^{\tau 1}_{122} \\ -f^{\tau 1}_{w,2} + A^{\tau 1}_{211} & A^{\tau 1}_{221} & f^{\tau 1}_{w,1} + A^{\tau 1}_{212} & A^{\tau 1}_{222} \\ C^{\tau 1} + \dot{M}^{\tau 1} & 0 & 0 & C^{\tau 1} + \dot{M}^{\tau 1} \end{bmatrix} + \left[K^{\tau 1}_k\right] \tag{6.28}$$

where $A^{\tau 1}_{ijk}$ and $C^{\tau 1}$ are defined in Eqs. 4.71 and 4.72, and $\left[K^{\tau 1}_k\right]$ is a matrix that considers the evolution of the intrinsic permeability. The terms of this matrix differ depending on the intrinsic permeability evolution. By considering an evolution with the strain tensor as described in Eq. 6.27, the matrix is defined as follows:

$$\left[K^{\tau 1}_k\right]_{3\times 4} = \rho^{\tau 1}_w \ \frac{k^{\tau 1}_{r,w}}{\mu_w} \left(\frac{\partial p^{\tau 1}_w}{\partial x^{\tau 1}_j} + \rho^{\tau 1}_w \ g_j \right) \begin{bmatrix} \frac{\partial k^{\tau 1}_{w,1j}}{\partial \varepsilon^{\tau 1}_{11}} & \frac{\partial k^{\tau 1}_{w,1j}}{\partial \varepsilon^{\tau 1}_{12}} & \frac{\partial k^{\tau 1}_{w,1j}}{\partial \varepsilon^{\tau 1}_{21}} & \frac{\partial k^{\tau 1}_{w,1j}}{\partial \varepsilon^{\tau 1}_{22}} \\ \frac{\partial k^{\tau 1}_{w,2j}}{\partial \varepsilon^{\tau 1}_{11}} & \frac{\partial k^{\tau 1}_{w,2j}}{\partial \varepsilon^{\tau 1}_{12}} & \frac{\partial k^{\tau 1}_{w,2j}}{\partial \varepsilon^{\tau 1}_{21}} & \frac{\partial k^{\tau 1}_{w,2j}}{\partial \varepsilon^{\tau 1}_{22}} \\ 0 & 0 & 0 & 0 \end{bmatrix} \tag{6.29}$$

where j is a summation index. The other submatrices that composes the element stiffness matrix $\left[E^{\tau 1}\right]$ of Eq. 4.64 are not modified.

6.2.3 Hydraulic model

The liquid phase transfer by advection in anisotropic porous media is defined by Darcy's law:

$$f_{w,i} = -\rho_w \, \frac{k_{w,ij} \, k_{r,w}}{\mu_w} \, \left(\frac{\partial p_w}{\partial x_j} + \rho_w \, g_j \right) \tag{6.30}$$

For transversely isotropic materials with horizontal bedding planes, the anisotropic tensor of intrinsic water permeability $k_{w,ij}$ is defined by two values in the horizontal and vertical directions: $k_{w,\parallel} = k_{w,h}$ and $k_{w,\perp} = k_{w,v}$ (Eqs. 5.66 and 4.22).

The unsaturated behaviour of the material is reproduced by defining a water retention and a relative permeability curves from van Genuchten's and Mualem's models (Mualem, 1976; van Genuchten, 1980) as in Eqs. 4.15 and 4.16.

6.2.4 Parameters

The parameters for the Callovo-Oxfordian claystone are detailed in Table 6.1. The evolution of the anisotropic cohesion with the loading orientation is represented in Fig. 6.8 (Pardoen et al., 2015c). The parameters for the cohesion softening and for the viscosity correspond to those used for the gallery drilling in chapter 5. The viscoplastic parameters were calibrated to reproduce the long-term convergence of a gallery (GCS) parallel to the major horizontal principal stress σ_H (see section 5.4.3).

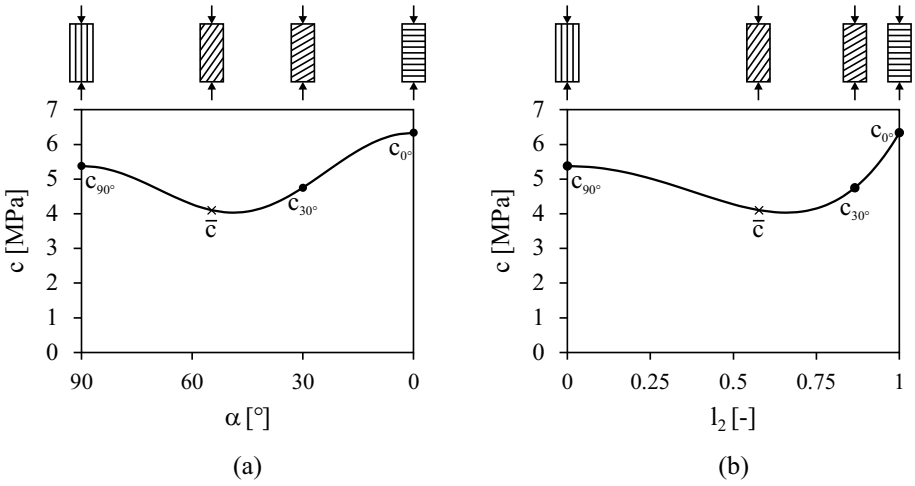

Fig. 6.8: Evolution of the cohesion (a) as a function of the angle between the normal to bedding planes and the direction of loading and (b) as a function of the loading vector.

6.3 Excavation and permeability evolution

As mentioned previously, when considering deep underground repository of nuclear wastes, there is a need for a more accurate modelling of the EDZ and the gallery air ventilation effect on the flow transfers that take place around the galleries. Consequently, a hydro-mechanical modelling of the SDZ ventilation test, preceded by the gallery excavation, is realised in two-dimensional plane-strain state. As a first step, the drilling process and the EDZ development are modelled. During the excavation, the major objectives are to characterise the development of fractures induced by rock deconfinement and the modification of the hydraulic properties. The fractures are represented with shear banding and the permeability evolution is addressed with a strain-dependent relation. The SDZ experiment will be reproduced in the second part of the numerical modelling, in section 6.4.

	Symbol	Name	Value	Unit
Hydraulic parameters	$k_{w,\parallel,0}$	Initial parallel intrinsic water permeability	4×10^{-20}	m^2
	$k_{w,\perp,0}$	Initial perpendicular intrinsic water permeability	1.33×10^{-20}	m^2
	Φ	Porosity	0.173	–
	P_r	van Genuchten air entry pressure	15	MPa
	$\mathcal{M}$	van Genuchten coefficient	0.33	–
	S_{max}	Maximum degree of water saturation	1	–
	S_{res}	Residual degree of water saturation	0.01	–
	μ_w	Water dynamic viscosity	0.001	$Pa\ s$
	χ_w^{-1}	Water compressibility	5×10^{-10}	Pa^{-1}
Elastic parameters	$E_\parallel$	Parallel Young's modulus	5	GPa
	$E_\perp$	Perpendicular Young's modulus	4	GPa
	$G_{\parallel\perp}$	Shear modulus	1.63	GPa
	$\nu_{\parallel\parallel}$	Poisson's ratio	0.24	–
	$\nu_{\parallel\perp}$	Poisson's ratio	0.33	–
	$b_\parallel$	Parallel Biot's coefficient	0.60	–
	$b_\perp$	Perpendicular Biot's coefficient	0.64	–
	ρ_s	Solid grain density	2750	kg/m^3
	D	Second gradient elastic modulus	5	kN
Plastic parameters	η	Van Eekelen yield surface convexity parameter	-0.229	–
	$\psi_c = \psi_e$	Dilatancy angles	0.5	$^\circ$
	$\varphi_{c,0}$	Initial compression friction angle	10	$^\circ$
	$\varphi_{c,f}$	Final compression friction angle	23	$^\circ$
	$\varphi_{e,0}$	Initial extension friction angle	7	$^\circ$
	$\varphi_{e,f}$	Final extension friction angle	23	$^\circ$
	B_φ	Friction angle hardening coefficient	0.001	–
	dec_φ	Friction angle hardening shifting	0	–
	$\bar{c}$	Cohesion for isotropic loading	4.1	MPa
	$A_\parallel$	Cohesion parameter	0.117	–
	b_1	Cohesion parameter	14.24	–
	ξ_c	Ratio of cohesion softening	5	–
	B_c	Cohesion softening coefficient	0.003	–
	dec_c	Cohesion softening shifting	0	–
Viscoplastic parameters	R_c	Uniaxial compressive strength	21	MPa
	A^{vp}	Internal friction coefficient	2.62	–
	C^{vp}	Cohesion coefficient	0.03	–
	β^{vp}	Viscoplastic potential parameter	1.1	–
	$g(\beta)$	Influence of the Lode angle	1	–
	α_0^{vp}	Initial threshold for the viscoplastic flow	0.142	–
	γ_0	Reference fluidity	700	s^{-1}
	γ_1	Temperature parameter	57×10^3	J/mol
	$\mathcal{N}$	Creep curve shape parameter	5.0	–
	B^{vp}	Viscoplastic hardening function parameter	7.5×10^{-2}	–

Table 6.1: Elasto-viscoplastic parameters for the Callovo-Oxfordian claystone.

6.3.1 Numerical model

The considered rock is the Callovo-Oxfordian claystone which is a transversely isotropic material with horizontal bedding planes and an initial anisotropic stress state. The hydraulic transfers are studied through the SDZ experiment; consequently, the considered gallery is the GED drift where the experiment is performed and which is oriented parallel to the minor horizontal principal stress σ_h. For this drift, the initial anisotropic stress state and pore water pressure are:

$$\sigma_{x,0} = \sigma_H = 1.3\ \sigma_h = 15.6\ MPa$$

$$\sigma_{y,0} = \sigma_v = 12\ MPa$$

$$\sigma_{z,0} = \sigma_h = 12\ MPa$$

$$p_{w,0} = 4.5\ MPa$$

where $p_{w,0}$ is the initial pore water pressure and $\sigma_{x,0}$, $\sigma_{y,0}$, $\sigma_{z,0}$ are the initial total stresses. The stress state in the gallery section is anisotropic for this gallery orientation.

The modelling considers the SDZ experimental zone without covering and only one gallery quarter by symmetry. The mesh geometry and boundary conditions are illustrated in Fig. 6.9. To establish the symmetry, the symmetry x and y-axes are considered as impervious (no normal water flow) and the normal displacement as well as the normal derivative of the radial displacement cancel along these axes. At the mesh external boundaries, the normal total stress and the pore water pressure are imposed constant. Furthermore, natural boundary conditions for the double forces, $\overline{T}_i = 0$, are assumed on the different boundaries and gravity is not taken into account.

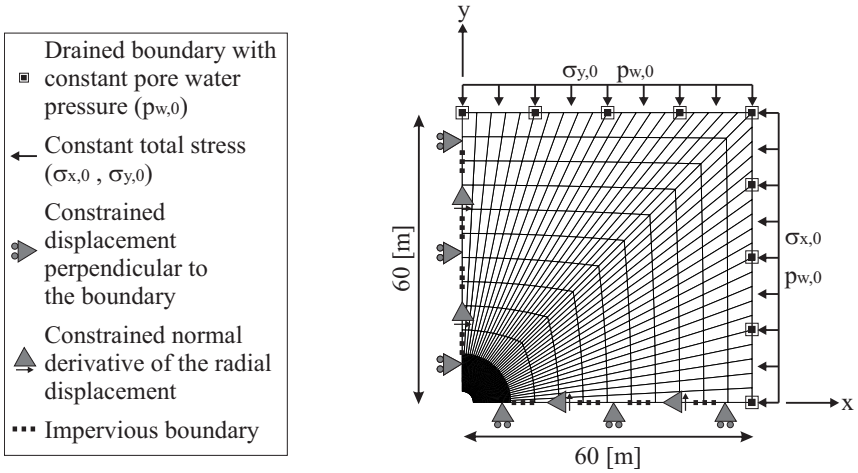

Fig. 6.9: Numerical model and boundary conditions used for the modelling of a gallery excavation and ventilation.

The gallery excavation is performed with a convergence-confinement method (Panet and Guenot, 1982) that implies decreasing stresses at gallery wall, with the excavation front crossing the studied section after one week (Fig. 6.10). The pore water pressure in the gallery is assumed to decrease rapidly to the atmospheric pressure of $p_{atm} = 0.1\ MPa$ when the excavation front crosses the studied section.

6.3.2 Gallery excavation

The appearance of strain localisation during the excavation has been studied for the same gallery and stress state in section 4.3. The results indicate that, for an isotropic material, the appearance and shape of the strain localisation are mainly controlled by the anisotropy of the stress state.

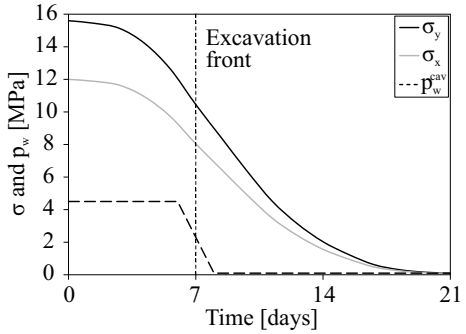

Fig. 6.10: Deconfinement curves for the total stresses and for the pore water pressure during gallery excavation.

The shear banding zone develops preferentially in the direction of the minor principal stress in the gallery section σ_v, which corresponds to the vertical direction. On the other hand, the influence of the anisotropy of the material behaviour on the development of shear banding around galleries has also been studied but for an isotropic stress state in the gallery section. The results presented in the sections 5.4.2 and 5.4.3 indicate that, for such stress state, the strain localisation pattern strongly depends on the anisotropic plastic properties of the rock. The shear banding zone develops preferentially in the direction of lower material resistance, which corresponds to the 45° and the horizontal orientations. As a consequence, if both anisotropic characteristics of the rock are considered for the drilling of the GED gallery, the shape of the shear banding zone is governed by two antagonistic effects related to the material anisotropy. In fact, the anisotropy of the stress state favours a development of the shear bands in the vertical direction, while the anisotropy of the material behaviour favours a development in the horizontal direction.

A first modelling of the excavation phase that takes into account both material and stress anisotropies is realised. The result at the end of the drilling is illustrated in Fig. 6.11 with the shear strain localisation bands around the gallery in terms of plastic zone, represented by the plastic loading integration points, and of Von Mises' equivalent deviatoric total strain. The latter is defined as:

$$\hat{\varepsilon}_{eq} = \sqrt{\frac{2}{3}\ \hat{\varepsilon}_{ij}\ \hat{\varepsilon}_{ij}} \tag{6.31}$$

where $\hat{\varepsilon}_{ij}$ is the deviatoric part of the total strain tensor:

$$\hat{\varepsilon}_{ij} = \varepsilon_{ij} - \frac{\varepsilon_{kk}}{3}\ \delta_{ij} \tag{6.32}$$

During the drilling the deformation and the plastic zone develop firstly in a diffuse manner around the gallery. Then, before the end of the excavation, strain localisation appears in the vicinity of the gallery with the material under plastic loading in the shear bands (concentration of plastic strain) and an elastic unloading in the outer material. One can observe that the shear band pattern develops in the vertical direction which still corresponds to the shape of the excavation damaged zone determined around the GED gallery with *in situ* experimental measurements (Figs. 6.2 (b) and 6.4). This demonstrates that, for a gallery having an initial anisotropic stress state in its section, the effect of the stress state anisotropy is the predominant factor that leads to the directional development of the fractured zone during the drilling. The influence of the anisotropy of the material behaviour seems secondary.

The solution of Fig. 6.11 is the "natural" solution that is obtained due to the different material anisotropies. However, regularisation methods such as the second gradient model do not restore the uniqueness of the solution to a boundary value problem. Different numerical procedures can be employed to force the occurrence of strain localisation and to create various solutions for the gallery excavation problem. A first procedure consists in introducing an imperfection,

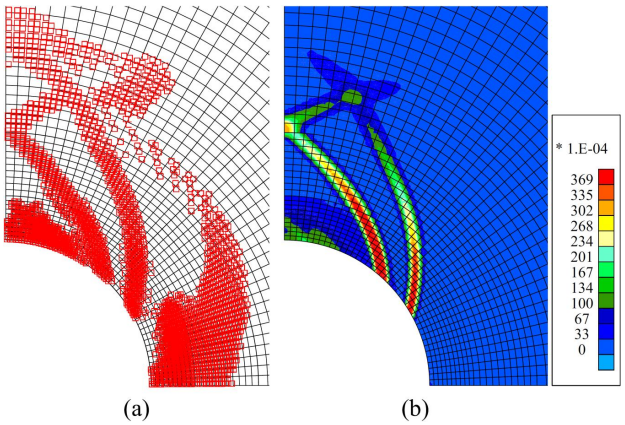

Fig. 6.11: Localisation zone at the end of excavation: (a) plastic zone and (b) total deviatoric strain.

which can be a disturbing force, a material imperfection, or a geometrical defect (Charlier et al., 1997; Matsushima et al., 2002; Zhang et al., 2001). Other methods consider the modification of numerical parameters (Marinelli et al., 2014; Sieffert et al., 2009) or a random initialisation of characteristics (Chambon et al., 2001b).

In reality, the strain localisation and fracturing processes are generated because geomaterials are not homogeneous and exhibit heterogeneities. Therefore, the procedure which is the most used to trigger the strain localisation consists in introducing material imperfections. As discussed in the previous chapters, it has been shown both experimentally (Desrues, 1984; Desrues and Viggiani, 2004) and numerically (Collin et al., 2009b; Pardoen et al., 2015a,c) that a material inclusion may dictate the shear band position (which passes through it) if it is strong enough to act as a strain localisation attractor. In fact, the imperfection generates a non-uniformity of the stress and strain fields in its vicinity which can be sufficient to reach first the bifurcation criterion in the imperfection. Then, the material imperfection acts as a nucleation point for the strain localisation onset. Yet, if the material imperfection is not strong enough or if it does not enter plastic state, then it will not behave as a strain localisation attractor.

For underground excavations, the drilling process inevitably generates supplementary defects in the rock at gallery wall, in addition to the pre-existing material imperfections. These defects may obviously have an important impact on the location of the fracture appearance. To reproduce this random scattering of rock defects, some defects are placed at gallery wall and are scattered all around the gallery as illustrated in Fig. 6.12 (a). They consist of weaker elements that have a constant cohesion of $\bar{c} = 4.1\ MPa$ (Table 6.1). The numerical results in Fig. 6.12 (b) and (c) present the pattern of shear strain localisation bands around the gallery at the end of drilling. The strain localisation remains concentrated above the gallery but the pattern is quite different than the one in Fig. 6.11 which illustrates the non-uniqueness of the solution.

The reproduction of both mechanical and hydraulic experimental measurements (realised around the gallery) with strain localisation in shear bands is quite complex because the two aspects are coupled and influence each other. Different configurations of defects have been tested and the mechanical and hydraulic data have been analysed simultaneously. The configuration of Fig. 6.12 (a) allows a good reproduction of both mechanical and hydraulic measurements; consequently, the results that are exposed in the following concern only this configuration of material defects.

6.3.3 Evolution of the intrinsic hydraulic permeability

Modelling the hydraulic property evolution and inhomogeneity inside the damaged zone is a crucial issue when considering rock drainage and desaturation. Different approaches exist to

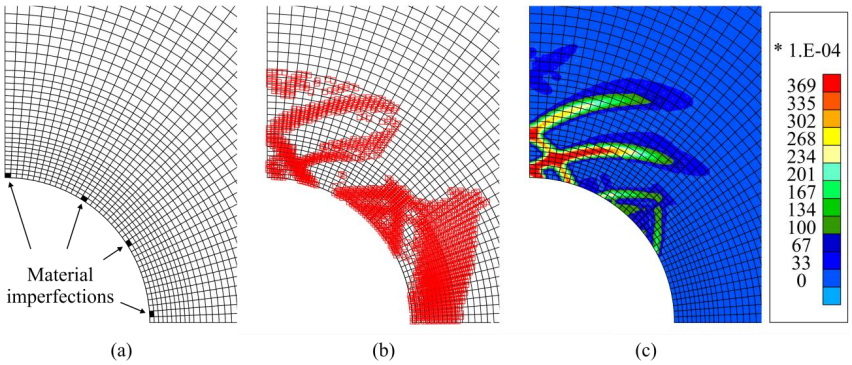

Fig. 6.12: Localisation zone at the end of excavation for a gallery with defects on its wall: (a) material imperfections, (b) plastic zone, and (c) total deviatoric strain.

take into account the influence of deformation or fracturing on the hydraulic permeability.

For porous materials, a first well-known approach is the Kozeny-Carman relationship that links the intrinsic hydraulic permeability to the porosity (Chapuis and Aubertin, 2003). However, it is commonly assumed in soil mechanics that this relation is approximately valid for sands but not for clay materials; thus, this relation is not commonly used (Chapuis and Aubertin, 2003). Other relations linked to the porosity can be studied; nevertheless, using a variation with the porosity highlights volumetric deformation effects which remain low for slightly dilatant material such as the studied claystone.

Another possible approach is to consider rock damage and the appearance of microcracks in the material with a coupling between microcracking and permeability (Arson and Gatmiri, 2012; Maleki and Poya, 2010). In fact, damage in rock is related to the formation of a network of cracks that can constitute preferential flow paths in the material. The damage by microcracking process (initiation, growth, accumulation, propagation, and coalescence of microcracks) is represented in damage models by the degradation of the material characteristics, either mechanical or hydraulic. Different damage models exist in the context of continuum damage mechanics from purely macroscopic (phenomenological) and continuous approaches to multi-scale (micromechanical) approaches. For instance, models with multi-scale and homogenisation approaches of permeability evolution are developed (Barthélémy, 2009; Dormieux and Kondo, 2004) and applied to the excavation damaged zone in rock (Levasseur et al., 2013). The macroscopic homogenised permeability of a heterogeneous material depends on the permeability of the solid matrix as well as on the permeability and shape of the microcracks. Numerical results indicate that a significant permeability increase of several orders of magnitude can be obtained in the EDZ that develops around boreholes. Nonetheless, rock damage is not incorporated in the present study and another type of permeability evolution must be computed.

Microcracking process can lead to the coalescence of microcracks. When this happens, the distributed damage becomes localised which engenders strain localisation and later the onset of interconnected fractures. The latter are also called macrocracks and can be of different types such as tensile or shear. For tensile fractures, it can be assumed that the fracture opening leads to a permeability increase in the fractures direction (anisotropic permeability increase) and therefore that the traction is an important factor leading to preferential flow paths. The evolution of permeability can be described as a function of the crack normal stress or as a function of the crack aperture (Olsson and Barton, 2001) and density. Traditionally, the hydraulic flows in rock joints have been expressed with a cubic law under the parallel plates approach (Witherspoon et al., 1980). Macroscopic (Snow, 1969) and, more recently, multi-scale (Dormieux and Kondo, 2004) approaches have also been used. For macroscopic approaches, the evolution of the fracture opening can be linked to the tensile strain in the normal direction to the crack (Chen et al., 2007; Liu et al., 1999; Olivella and Alonso, 2008; Shao et al., 2006b). Such method has been

applied to underground borehole drilling for an indurated clay (Levasseur et al., 2010), namely the Opalinus clay, with anisotropic permeability and which prevailing mechanism of fracture in the excavation damaged zone is extension (Marschall et al., 2008). The numerical results indicate that the size of the EDZ, based on the predicted permeability increase, is overestimated if the tensile strain includes both plastic and elastic parts. However, considering only the plastic zone underestimates the size of the EDZ (Levasseur et al., 2010; Tsang et al., 2005); thus, it seems necessary to consider the plastic zone and a part of the elastic one to better reproduce the EDZ extent.

For the Callovo-Oxfordian claystone, shearing is the principal failure mechanism around the galleries at the underground laboratory level because of the high *in situ* stress (Armand et al., 2014). In the developed numerical approach, the shear fractures are represented at macroscale by shear strain localisation in band mode. Thus, because the permeability is not homogeneous in fractured zones, one way to model its increase is to introduce a permeability modification that considers a dependency with the deformation. This type of hydro-mechanical coupling takes into account the effects of strain localisation and will engender a permeability increase that is more pronounced inside the shear bands.

Considering the fractured rock at macroscale as a continuous medium, a strain-dependent isotropic evolution of the hydraulic permeability tensor is taken into account based on a power (cubic) formulation:

$$k_{w,ij} = k_{w,ij,0} \left(1 + \beta_{per} \ \langle \gamma_{per} \rangle^3\right) \tag{6.33}$$

where $k_{w,ij,0}$ is the initial intrinsic water permeability tensor, β_{per} is an evolution parameter, $\langle \ \rangle$ are the Macaulay brackets, and γ_{per} is a deformation parameter for which different expressions are envisaged hereafter. For such evolution the time derivative of the permeability reads:

$$\dot{k}_{w,ij} = \frac{\partial k_{w,ij}}{\partial \varepsilon_{kl}} \ \dot{\varepsilon}_{kl} = \frac{\partial k_{w,ij}}{\partial \varepsilon_{kl}} \ \frac{\partial \dot{u}_k}{\partial x_l} \tag{6.34}$$

where:

$$\frac{\partial k_{w,ij}}{\partial \varepsilon_{kl}} = \frac{\partial k_{w,ij}}{\partial \gamma_{per}} \ \frac{\partial \gamma_{per}}{\partial \varepsilon_{kl}} = k_{w,ij,0} \ 3 \ \beta_{per} \ \gamma_{per}^2 \ \frac{\partial \gamma_{per}}{\partial \varepsilon_{kl}} \tag{6.35}$$

with $\frac{\partial \gamma_{per}}{\partial \varepsilon_{kl}}$ depending on the expression of γ_{per}. The expression of Eq. 6.35 can be used in Eqs. 6.26 to 6.29.

For the different expressions of γ_{per} that are considered, the evolutions of the intrinsic permeability tensor are illustrated in Fig. 6.13 along the horizontal axis (x-axis), the vertical axis (y-axis), and a 45° inclined direction (oblique cross-section). The permeability variation is analysed at the end of the excavation because the main part of the material deformation around a gallery appears during the excavation.

Firstly, the volumetric deformation is used:

$$\gamma_{per} = \epsilon_v = \frac{\epsilon_{ii}}{3} \tag{6.36}$$

The results in Fig. 6.13 (a) are detailed for $\beta_{per} = 10^{14}$. One can observe that the permeability increases of several orders of magnitude around the gallery, especially in the shear bands where the deformation is concentrated. In the horizontal direction, no shear bands are crossed by the x-axis (see Fig. 6.12); then, the increase remains quite diffuse and expands too deeply in the rock formation, in comparison with the experimental data of Figs. 6.3 and 6.4. The volumetric deformation remains low for a slightly dilatant material and an important value of β_{per} has been used to reproduce a permeability increase of several orders of magnitude.

Secondly, to emphasize shear strain effect, the deformation parameter can be taken as equal to the equivalent deviatoric total strain (Eq. 6.31):

$$\gamma_{per} = \hat{\varepsilon}_{eq} \tag{6.37}$$

The results for $\beta_{per} = 10^{10}$ in Fig. 6.13 (b) show a more important increase of the permeability in the shear bands but it increases too deeply in the rock in all directions.

Thirdly, to consider only the plastic deformation in the permeability evolution, γ_{per} in Eq. 6.33 can be taken as the Von Mises' equivalent deviatoric plastic strain:

$$\gamma_{per} = \hat{\varepsilon}^p_{eq} \tag{6.38}$$

which rate form reads:

$$\dot{\hat{\varepsilon}}^p_{eq} = \sqrt{\frac{2}{3}\ \dot{\hat{\varepsilon}}^p_{ij}\ \dot{\hat{\varepsilon}}^p_{ij}} \tag{6.39}$$

where $\dot{\hat{\varepsilon}}^p_{ij}$ is the deviatoric part of the plastic strain rate tensor:

$$\dot{\hat{\varepsilon}}^p_{ij} = \dot{\varepsilon}^p_{ij} - \frac{\dot{\varepsilon}^p_{kk}}{3}\ \delta_{ij} \tag{6.40}$$

The results for $\beta_{per} = 10^{10}$ are illustrated in Fig. 6.13 (c). The expand of the permeability increase is satisfactory in the vertical and the oblique directions but it does not increase sufficiently in the horizontal direction in comparison to the experimental measurements of Fig. 6.3 (c). This would lead to an underestimation of the drainage in that direction. Moreover, if the permeability increase is too much concentrated inside the shear bands then the EDZ does not expand sufficiently and the drainage in the claystone would be underestimated, because the rock mass outside the shear bands is not be affected (Pardoen et al., 2014a,b).

An appropriate solution may be an intermediate case between considering all the deformation and only the plastic one. To consider the plastic deformation and a part of the elastic one, the Eq. 6.33 is adapted as follows:

$$k_{w,ij} = k_{w,ij,0}\left(1 + \beta_{per}\ \langle YI - YI^{thr}\rangle\ \hat{\varepsilon}_{eq}{}^3\right) \tag{6.41}$$

where YI is the yield index and YI^{thr} is a threshold value below which the intrinsic permeability variation is not considered. The yield index is defined as the reduced second deviatoric stress invariant:

$$YI = \frac{II_{\hat{\sigma}'}}{II^p_{\hat{\sigma}'}} \tag{6.42}$$

with $YI < 1$ if the current state of the material is elastic and $YI = 1$ for plastic state (on the yield surface). Furthermore, following Eq. 6.41, the intrinsic permeability could decrease if the yield index or the equivalent deviatoric strain decreases by elastic unloading. Such phenomenon could be related to fracture closure or to material sealing / healing but it is not treated in the present development. Thus, to avoid a decrease of the permeability, the latter is the maximal value between the current and the last computed permeabilities, for every computation step of the resolution of the finite element method with $\tau = t + \Delta t$:

$$k^\tau_{w,ij} = max(k^t_{w,ij}, k^\tau_{w,ij}) \tag{6.43}$$

The results for $\beta_{per} = 10^{10}$ and $YI^{thr} = 0.95$ illustrated in Fig. 6.13 (d) show a permeability increase in a quite good agreement with the experimental measurements for all the directions (Figs. 6.3 and 6.4). The permeability evolution during the excavation and the comparison to experimental data are illustrated in Fig. 6.14 where a good match is observed. As a consequence, plastic deformation and a limited part of the elastic one allow a good reproduction of the EDZ extent. The relations of Eqs. 6.41 and 6.43 with $\beta_{per} = 10^{10}$ and $YI^{thr} = 0.95$ will consequently be kept for the following modelling. For this permeability evolution, the permeability distribution of the ratio $k_{w,ij}/k_{w,ij,0}$ around the gallery is represented at the end of excavation in Fig. 6.15 (logarithmic scale). An increase of at least 2 orders of magnitude inside the shear bands is obtained.

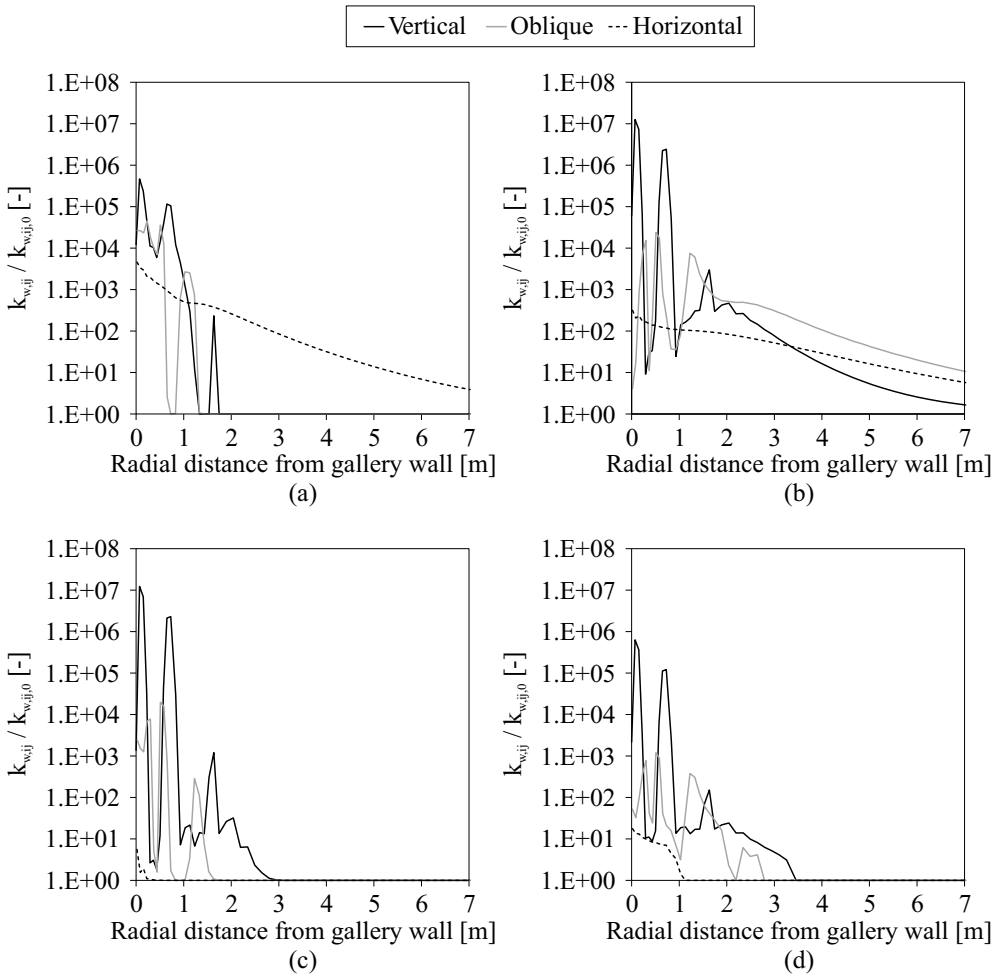

Fig. 6.13: Intrinsic water permeability at the end of excavation for permeability evolutions with: (a) volumetric deformation, (b) deviatoric total strain, (c) deviatoric plastic strain, and (d) deviatoric strain with yield index threshold.

It is to mention that the evolution which is considered in Eq. 6.41 is isotropic and will conserve the initial directions of anisotropy and the permeability ratio $k_{w,\parallel}/k_{w,\perp} = 3$ (Table 6.1). This ratio corresponds to previous measurements from Andra. Nonetheless, the principal directions of anisotropy in the excavation damaged zone do not correspond to the principal directions of the initial anisotropy (Bossart et al., 2002). The permeability increase is indeed more important in the longitudinal direction of the cracks and fractures which engenders an anisotropic modification of the permeability. The fact that the initial directions of anisotropy are kept can be justified by the important increase of permeability in the damaged zone with regard to the low ratio of anisotropy. In fact, the water transfers are principally affected by the important increase of permeability in the EDZ. Consequently, the principal directions of anisotropy should not influence the numerical results significantly.

6.4 Ventilation and air-rock interaction

The next step of the modelling consists in applying, after the excavation, an air ventilation in the underground gallery that corresponds to the SDZ ventilation experiment. In previous modelling of this experiment (section 2.5), the EDZ was *a priori* defined in the numerical model with a higher intrinsic permeability than the undisturbed host rock and without description of the fractures. Now, the fracture description as well as the permeability evolution and inhomogeneity

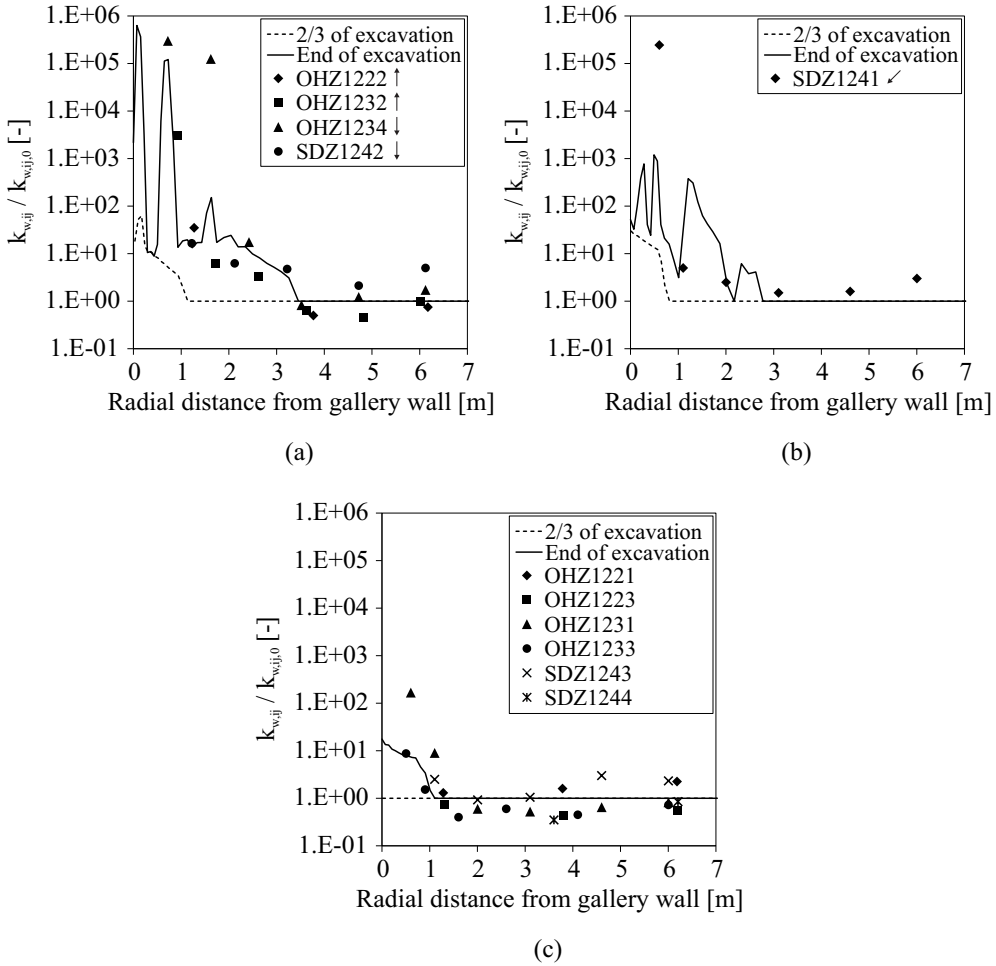

Fig. 6.14: Evolutions of the intrinsic water permeability and comparison to experimental measurements along (a) vertical, (b) oblique at 45°, and (c) horizontal directions.

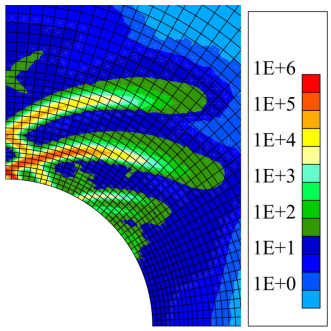

Fig. 6.15: Distribution of the ratio $k_{w,ij}/k_{w,ij,0}$ in logarithmic scale for the intrinsic water permeability at the end of excavation.

in the EDZ have been taken into account. The following challenge is to analyse whether the introduced hydro-mechanical coupling and EDZ description allow to reproduce the drainage and desaturation provoked in the surrounding media by the air ventilation. The principal objectives of the modelling of the SDZ test are to characterise, firstly, the air-rock transfers at gallery wall, and secondly, the influence of a controlled gallery ventilation on the clayey rock behaviour. The same numerical model and material parameters are indeed used hereafter, with the identical configuration of material defects at gallery wall as in Fig. 6.12 (a).

6.4.1 Hydraulic boundary condition at gallery wall

The interaction between air and rock certainly conditions the drainage kinetics in the rock formation. The pore water pressure in the rock decreases during the excavation and the ventilation and, in the long term, a thermodynamic equilibrium is reached between the gallery wall rock and the gallery air. Experimental measurements have shown that the drainage and desaturation are progressive which seems to imply that the vapour transfer between the air and the rock is not instantaneous (section 2.3.2).

Both classical and non-classical flow boundary conditions at gallery wall have been tested for the reproduction of the SDZ experiment in section 2.5. The classical condition assumes an instantaneous equilibrium between the liquid water inside the rock and the water vapour of the gallery air by Kelvin's equilibrium equation:

$$RH = \frac{p_v}{p_v^0} = \frac{\rho_v}{\rho_v^0} = exp\left(\frac{-s^{tot}\ m_v}{\rho_w\ R\ T}\right) \tag{6.44}$$

where RH is the relative humidity of the air inside the cavity, p_v^0 is the pressure of saturated water vapour at the same temperature, p_v is the partial pressure of water vapour, ρ_v^0 is the density of saturated water vapour (Eq. 2.48), ρ_v is the density of water vapour, s^{tot} is the total suction, m_v is the molar mass of the water vapour ($m_v = 0.018\ kg/mol$), ρ_w is the water density ($\rho_w = 1000\ kg/m^3$), R is the universal gas constant ($R = 8.314\ J/molK$), and T is the absolute temperature of the air (expressed in Kelvin). By taking into account only the capillary effects (matric suction) with the capillary pressure being $p_c = p_{atm} - p_w^{cav}$, the water pressure in the cavity p_w^{cav} which is imposed at gallery wall takes the form:

$$p_w^{cav} = \frac{\rho_w\ R\ T}{m_v}\ ln\left(RH\right) + p_{atm} \tag{6.45}$$

The results obtained with this condition indicate that it does not allow a good reproduction of the measurements of pore water pressures around the gallery (Fig. 2.32 in section 2.5.4). The classical imposition at gallery wall is therefore not appropriated to reproduce the water transfers, and a non-classical mixed hydraulic boundary condition at gallery wall is more relevant for the reproduction of large-scale rock-atmosphere interaction problems.

As a consequence, the exchanges between the cavity and the rock are modelled with a non-classical mixed hydraulic boundary condition at gallery wall (Charlier et al., 2013b; Gerard et al., 2008). This condition has been developed previously and is succinctly recalled here; for more details, please refer to section 2.5.1. The condition considers that two types of exchange happen at the gallery wall of ventilated cavities (Ghezzehei et al., 2004): liquid water $\bar{S}$ and water vapour $\bar{E}$. The total water flow is defined as (Fig. 6.16):

$$\overline{q}_w = \bar{S} + \bar{E} \tag{6.46}$$

where $\bar{S}$ and $\bar{E}$ are the seepage and evaporation flows.

The vapour exchange mode assumes the existence of a boundary layer on the porous surface of the cavity (Ghezzehei et al., 2004; Pintado et al., 2009). This exchange occurs when a difference between the vapour density in the rock ρ_v^Γ and in the cavity air ρ_v^{cav} exists (Nasrallah and Perre, 1988):

$$\bar{E} = \alpha_v \left(\rho_v^\Gamma - \rho_v^{cav}\right) \tag{6.47}$$

Moreover, the vapour exchange is not instantaneous and is governed by the external conditions (relative humidity, temperature, and velocity of the air) which are considered in the boundary layer through a vapour mass transfer coefficient α_v.

The exchange of liquid water is an unilateral seepage flow directed towards the gallery. It takes place only when the surface of the material is saturated. That is to say that a seepage flow exists when the pore water pressure in the rock at gallery wall is larger than the water pressure

in the cavity and the atmospheric pressure: $p_w^\Gamma \geq p_w^{cav}$ and $p_w^\Gamma \geq p_{atm}$. This flow is introduced by a unilateral boundary condition on p_w with a ramp function (Bardet and Tobita, 2002; Zheng et al., 2009):

$$\begin{cases} \bar{S} = K^{pen} \left(p_w^\Gamma - p_{atm}\right)^2 & if\ p_w^\Gamma \geq p_w^{cav}\ and\ p_w^\Gamma \geq p_{atm} \\ \bar{S} = 0 & if\ p_w^\Gamma < p_w^{cav}\ or\ p_w^\Gamma < p_{atm} \end{cases} \tag{6.48}$$

where K^{pen} is a numerical penalty coefficient for the seepage that must be as large as possible to respect the unilateral condition (Fig. 6.16). A value of $K^{pen} = 10^{-10}\ s^3/kg$ is assumed.

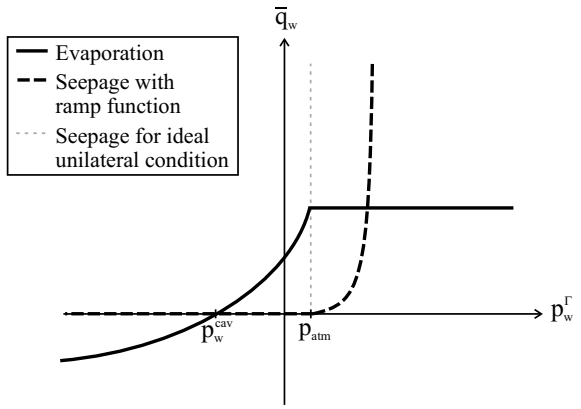

Fig. 6.16: Evaporation and seepage flows at gallery wall for a constant air ventilation (Gerard et al., 2008).

6.4.2 Air ventilation

Once the excavation front has reached the studied section during the drilling, it is assumed that the gallery air remains saturated with water vapour because the gallery is not ventilated yet. It means that the air relative humidity is of 100 % and the water pressure in the cavity corresponds to the atmospheric pressure by Eq. 6.45. The evolution of p_w^{cav} during the excavation phase is illustrated in Fig. 6.10. During the ventilation, the water pressure and the water vapour density in the cavity correspond to the relative humidity of the cavity air by Kelvin's law (Eq. 6.44). The density of water vapour corresponds to:

$$\rho_v^{cav} = RH\ \rho_v^0 \tag{6.49}$$

and the water pressure is obtained by Eq. 6.45. It is calculated from the experimental measurements of the air relative humidity and temperature inside the GED gallery (Fig. 6.5) and is depicted in Fig. 6.17. Finally, the gallery hygrometry is imposed at gallery wall through the non-classical hydraulic boundary condition (Eqs. 6.46 to 6.48).

Moreover, an initiation phase of ventilation is performed after the excavation (between 21 and 50 days) to avoid applying the ventilation instantaneously. During this phase the water pressure in the gallery air decreases from the atmospheric pressure to the first measured value.

6.4.3 Results

The first result that can be analysed is the claystone progressive drainage which occurs due to the ventilation. In Fig. 6.18 is illustrated the comparison between numerical results and experimental measurements of the evolution of the pore water pressure around the drift. The measurements were realised in boreholes drilled around the uncovered SDZ experimental zone and for different distances from gallery wall (Fig. 6.6). A close correspondence is obtained in the different directions for a value of $\alpha_v = 10^{-3}\ m/s$. The pore overpressures observed after the excavation in the vertical direction (Fig. 6.18 (c)) result of hydro-mechanical couplings mainly

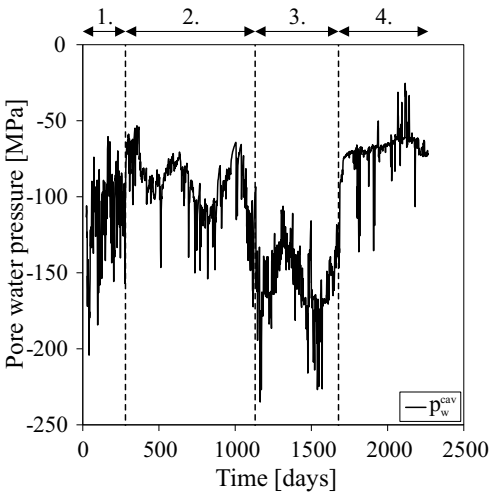

Fig. 6.17: Evolution of water pressure in the SDZ experimental zone.

related to the anisotropy of the initial stress state. In this direction, the matching with the experimental data is slightly less good which may be related to the lower vertical permeability and to the positions of the shear bands that condition the intrinsic permeability evolution. The vapour mass transfer coefficient α_v has indeed an influence on the drainage and its value is chosen to obtain a good reproduction of the experimental data. The chosen value is relatively close to the measurements performed on argillaceous material samples during drying tests (10^{-2} m/s) by Gerard et al. (2010). Moreover, the two controlled ventilation phases (phases (3) and (4) in Fig. 6.17) do not have a visible effect on the numerical results, in the long term.

The pore water pressure sensors being unable to acquire negative measurements, other measurements should be taken into account to characterise the EDZ desaturation. The measurements of water content w performed around the experimental zone can be used (see Fig. 6.19 and section 2.3.2 for more comments on them). The water content is a direct measurement of the degree of water saturation through the relation $S_{r,w} = \frac{\rho_s}{\rho_w}\frac{1-\Phi}{\Phi}\, w$. The numerical and experimental results are illustrated in Fig. 6.19 (a) for eight boreholes drilled shortly after the excavation (less than 220 days) and in Fig. 6.19 (b) for five boreholes drilled later (between 2 and 4.25 years). Even if a quite important dispersion of the experimental measurements is visible, a good reproduction is obtained numerically, especially in the short term. An important evolution of the desaturation close to the cavity is reproduced during the excavation and the ventilation initiation phases (before 50 days). In the long term and because of the gallery ventilation, the numerical results highlight a decrease of the water content corresponding to a progressive desaturation by evaporation at gallery wall. Nonetheless, it is observed experimentally that the desaturation propagation in the rock is limited after the excavation which may be due to low vapour transfers at gallery wall, to fracture closure, or to material sealing / healing. These two last phenomena are not addressed in the present analysis; consequently, the comparison in the long term should be regarded with some reserve.

The evolutions of the degree of saturation and water content at gallery wall, in the horizontal direction, are represented in Fig. 6.20. The numerical results of water content are compared to the experimental measurements performed the closest to the gallery wall for each horizontal borehole. A good reproduction of the desaturation is obtained. Besides, the effect of the controlled ventilation phases is more pronounced on the numerical results of water content at gallery wall than it was on the pore water pressure in the rock mass. In fact, the ventilation effect is more marked closer to the gallery, especially in the damaged zone where the permeability is important and where desaturation occurs. A decrease of $S_{r,w}$ and w is observed on the numerical results during the ventilation phase with $RH = 30$ % (phase (3) between 1130 and 1680 days), with values around $w = 2.8$ % and $S_{r,w} = 0.4$. An increase is observed during the last phase with

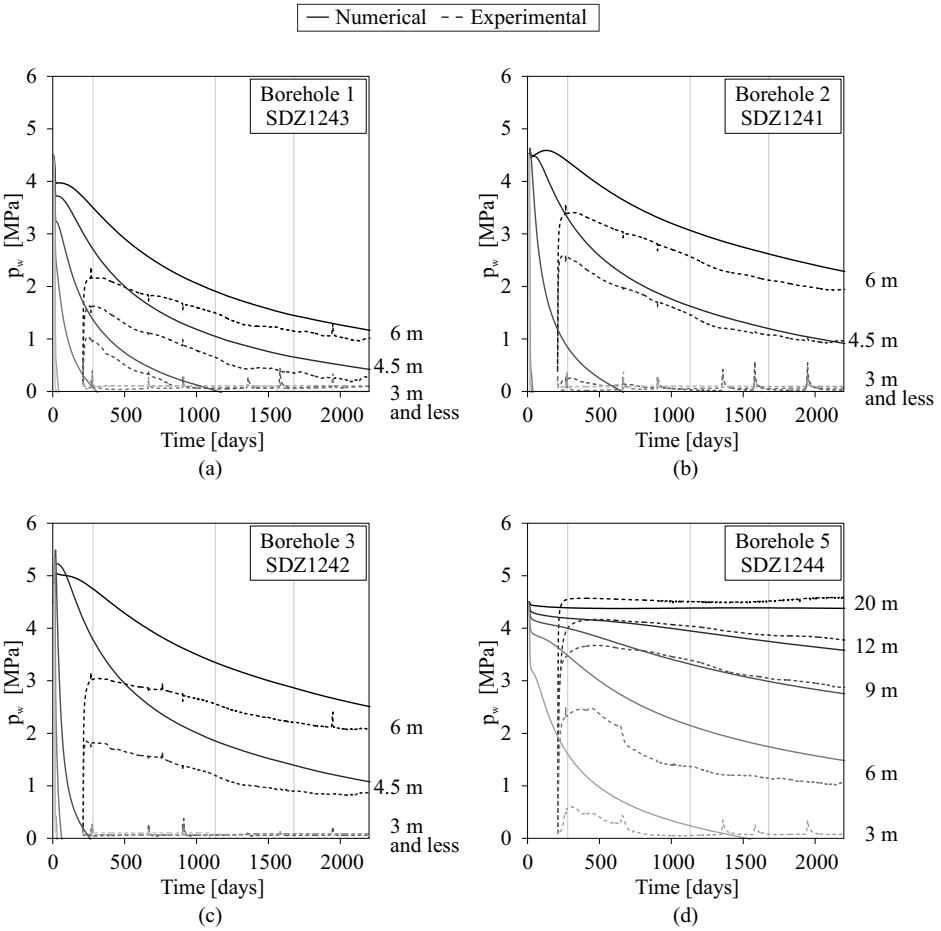

Fig. 6.18: Comparison between experimental and numerical pore water pressure in boreholes for different distances from gallery wall: (a,d) horizontal, (b) oblique at 45°, and (c) vertical boreholes.

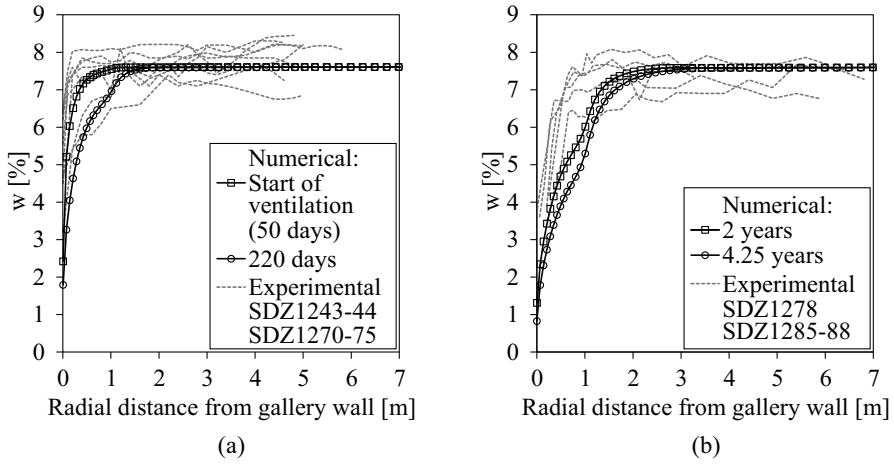

Fig. 6.19: Evolution of water content in the horizontal direction with comparison to experimental measurements in (a) short term up to 220 days and (b) long term from 2 to 4.25 years.

$RH = 60$ % (phase(4)), with values around $w = 3.6$ % and $S_{r,w} = 0.5$. The resaturation of the rock is thenceforward not observed for the considered values of imposed relative humidity.

In addition to the permeability evolution in the EDZ, the drainage kinetics in the rock formation is significantly conditioned by the air-rock interaction and the transfers at gallery

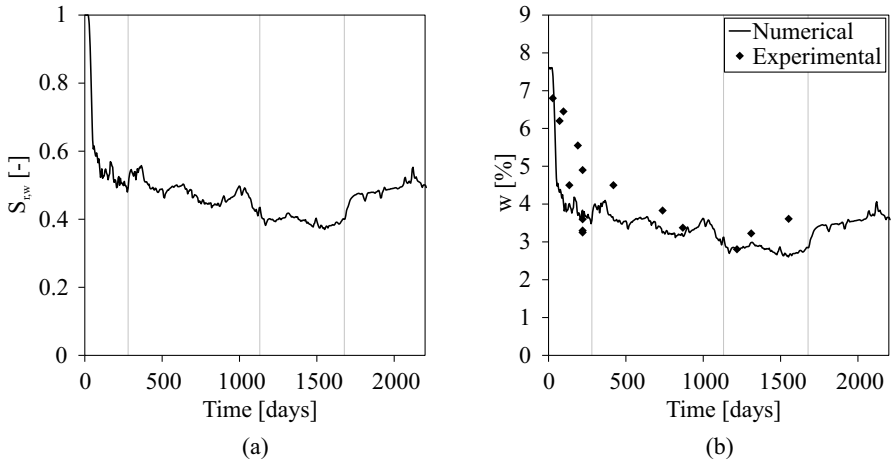

Fig. 6.20: Evolutions of (a) saturation degree and (b) water content at gallery wall in the horizontal direction with comparison to experimental measurements.

wall. The evolutions of the different flows and of the cumulative total flow are represented in Fig. 6.21 for the complete gallery (total circumference). The seepage flow $\bar{S}$ can be considered at first. During the excavation, the claystone is initially fully saturated; then, once the pore water pressure decreases in the gallery air (between 6 and 8 days, Fig. 6.10), it becomes smaller than the pore water pressure in the rock which engenders a seepage flow directed towards the gallery (Fig. 6.21 (a)). After the excavation, the ventilation is applied and the pore water pressure in the rock decreases progressively. It leads to a desaturation of the gallery wall ($p_w^\Gamma < p_{atm}$) which cancels the seepage flow (Fig. 6.21 (a) and (b)). On the other hand, the evaporation flow $\bar{E}$ remains low during the excavation, as long as the rock at gallery wall remains saturated (Fig. 6.21 (a)). Once the ventilation is initiated, the gallery wall desaturates and a vapour flow directed towards the gallery appears to ensure a thermodynamic equilibrium. During the ventilation initiation phase (between 21 and 50 days), the pore water pressure in the gallery air decreases from the atmospheric pressure to about -130 MPa. This generates important gradients and a rapid increase of the evaporation flow. Later, the vapour exchange decreases until the equilibrium is reached between the air and the rock (Fig. 6.21 (b)).

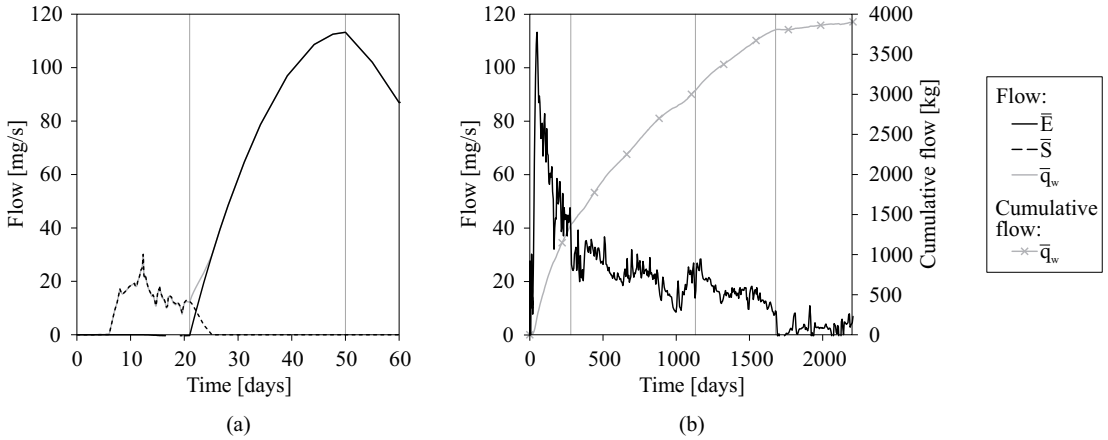

Fig. 6.21: Evolutions of flows and total cumulative flow at gallery wall for the complete gallery: (a) in the short term and (b) in the long term.

The two transfer processes are decoupled in the sense that the total flow $\overline{q}_w$ corresponds to the seepage during the excavation and to the vapour flow during the ventilation. Nevertheless, the evaporation process is dominant and the cumulative total flow is mainly composed of evap-

oration. The vapour mass transfer coefficient α_v controlling the vapour transfer at gallery wall has indubitably a significant influence. A low value implies low vapour transfers and low rock desaturation, while a high value implies important vapour transfers, drainage, and desaturation of the rock.

Once more, the effect of the controlled ventilation phases is noticeable at gallery wall, on the vapour transfers (Fig. 6.21 (b)). The uncontrolled ventilation phase (phase (2) between 280 and 1130 days) displays an average relative humidity of 50 % (Fig. 6.5); then, when the humidity decreases to 30 % in the next ventilation phase, it results in a decrease of ρ_v^{cav} and in an increase of $\bar{E}$ (Eqs. 6.49 and 6.47). The inverse effect is observed for the last ventilation phase when RH increases.

Another result that can be discussed is the gallery convergence (variation of the gallery diameter). It could have been discussed earlier because most part of the convergence is due to the excavation process but the ventilation and the viscoplasticity have an impact on the long-term convergence. For the considered gallery, the convergences that have been measured in several sections are illustrated in Fig. 6.22 (Armand et al., 2013). Three convergence measurement sections are located in the GED gallery and three in the SDZ experimental zone. The measurements indicate that the convergence is anisotropic with a more important vertical convergence, and that it increases in the long term especially in the vertical direction.

The numerical results in Fig. 6.22 (a) reproduce fairly well this anisotropic convergence in the short term, mainly thanks to the strain localisation bands located above the gallery. The increase of vertical convergence in the long term is however not well reproduced. This can be explained by the ventilation of the gallery air and the rock desaturation close to the gallery. In fact, under a constant normal total stress at gallery wall and because of the suction imposed by the air ventilation, the compressive effective stress increases in the vicinity of the gallery by Eq. 6.2. It engenders an elastic unloading close to the gallery which restricts the further plastic deformation (see section 4.3.5, Fig. 4.10, and Fig. 4.17).

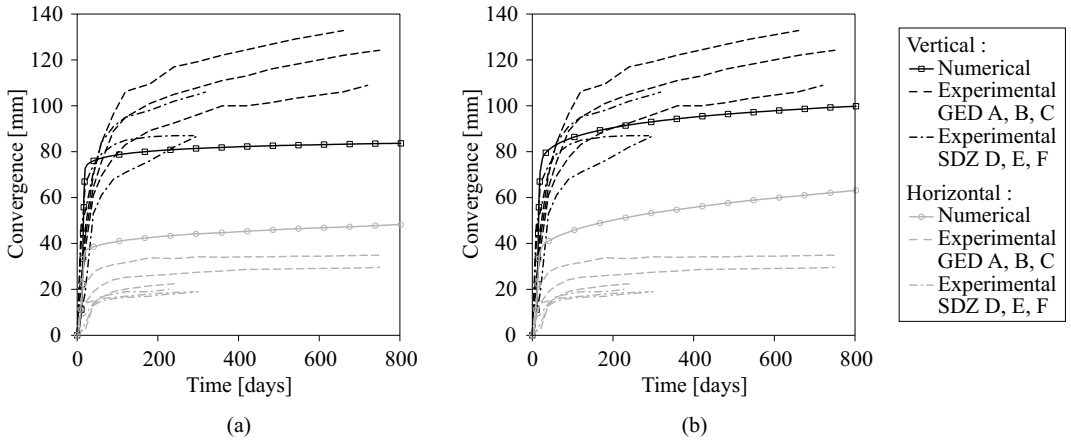

Fig. 6.22: Evolution of the convergence of a gallery parallel to the minor horizontal principal stress with comparison to experimental measurements: (a) viscoplastic parameters of Table 6.1 and (b) increase of viscosity.

During the relatively short excavation period, the creep deformations seem to be negligible, which was also concluded by Jia et al. (2008) for a modelling of shaft excavation in Callovo-Oxfordian claystone. Nevertheless, the viscosity and creep behaviour have an impact on the long-term deformations. This impact has been studied in section 5.4.3 for a gallery (GCS) parallel to the major horizontal principal stress σ_H. It has been shown that it is possible to increase the long-term convergence by adjusting the viscoplastic parameters. Nonetheless, the set of viscoplastic parameters that is used (Table 6.1) has already been adapted to reproduce the long-term convergence of the GCS gallery. The parameters can again be adapted to reproduce

the convergence of the GED gallery parallel to the minor horizontal principal stress σ_h. For instance, setting $\alpha_0^{vp} = 0$ engenders an immediate viscoplastic flow due to the initial deviatoric stress in the rock and leads to larger convergences as illustrated in Fig. 6.22 (b). Unfortunately, from the results of Fig. 6.22 (a), it is clear that amplifying the delayed viscoplastic strain will improve the correspondence with *in situ* measurements in the vertical direction but inevitably deteriorates it in the horizontal direction.

6.5 Conclusions, discussion, and outlooks

6.5.1 Conclusions

The coupled processes that occur during the excavation and ventilation of underground galleries have been addressed in the late modelling. Firstly and similarly to previous representations of the EDZ, the fractures induced by the excavation process in the vicinity of the gallery are reproduced by shear banding, and the strain localisation is properly modelled by means of a regularisation method. The directional development of the excavation damaged zone has been highlighted for a transversely isotropic argillaceous rock with anisotropic initial stress state. Although the influences of the material anisotropy and of the stress anisotropy in the gallery section are in opposition, the stress states anisotropy is the predominant factor leading to the development and orientation of the fractured zone during the drilling.

Secondly, the evolutions of the flow transfer properties have been characterised around the drifts, especially in the excavation damaged zone. The evolution of intrinsic permeability is addressed in correlation with the strain localisation process by using a strain-dependent relation. This relation involves plastic strain as well as a restricted part of the elastic strain to better reproduce the EDZ extent and to avoid underestimating the drainage in the medium. At the end of excavation, the permeability increase is of several orders of magnitude in the shear bands, as measured experimentally.

Thirdly, the flow transfers in the damaged zone and in the undisturbed material are studied through the modelling of a gallery air ventilation experiment performed on a large scale. The air-rock interactions at gallery wall involve both water vapour and liquid water transfers that are implemented with a non-classical hydraulic boundary condition. Such condition is relevant for the reproduction of the transfers because an instantaneous equilibrium between the air and the rock may not be assumed beforehand. An equilibrium is reached in the long term by evaporation process during the gallery air ventilation. It also allows to accurately reproduce the drainage kinetics of the rock outside the EDZ and the rock desaturation within the EDZ. Regarding the different ventilation phases, it has been observed that the applied constant ventilations (constant air hygrometry), with low and high air relative humidity, only have a limited influence on the flow kinetics in the rock and do not induce resaturation. Thus, the progressive drainage of the rock is mostly affected by the long-term ventilation, not by the constant ventilation phases. Longer phases of constant ventilation might have a more important influence on the desaturation and resaturation of the rock.

Furthermore, the reproduction of both mechanical and hydraulic *in situ* measurements is complex because the processes are coupled. The approach aims to highlight the important hydro-mechanical aspects to take into account for the analysis of the EDZ behaviour in unsaturated biphasic media and for the reproduction of experimental measurements. For the reproduction of shear bands and gallery convergence, the regularisation method, the material anisotropy, and the creep effect are crucial. For the reproduction of the water transfers, rock drainage, and desaturation it is the unsaturated properties of the medium, the permeability increase, and the exchanges at gallery wall that are most particularly important.

6.5.2 Discussion

Hereafter, a global discussion is presented to emphasise the possibilities and limitations of the modelling of the excavation damaged zone with shear banding. The arguments are related to the hydro-mechanical results obtained through the different developments and modelling in a general sense.

Onset of strain localisation

The strain localisation and bifurcation phenomena are natural consequences of a strain softening material behaviour. The latter has been considered through the softening of the cohesion which is involved in the strength definition of the material (yield surface with softening plasticity). However, the parameters of the cohesion softening have to be adequately chosen to trigger the strain localisation which may lead to choices that could seem somewhat arbitrary. For the large-scale modelling of gallery drilling, the numerical results have shown that the cohesion softening has to start once the material enters plasticity otherwise strain localisation would not be triggered during the excavation. For small-scale compression test, the deformations are much more important and the start of the softening can be delayed to reproduce the position of the peak stress on the global response curve of the specimen. The softening parameters (especially B_c) have also to be selected in a range that avoids snapback problem and permits computational stability. Thus, choosing the softening parameters to trigger strain localisation in a given material engenders different sets of parameters which depend mainly on the type of solicitation. To go further in the calibration of the strain localisation process, precise information is required about the shear banding structure, including the exact shear band pattern, orientations, number, thickness, and evolution. Unfortunately, such information is rarely available for rocks especially for large-scale problems.

Although softening plasticity is considered, the strain localisation is not automatically triggered for a perfect material. In case of gallery excavation it has been demonstrated that anisotropy, either of the stress state or of the material behaviour, leads to the onset of shear bands. This type of solution has been called the "natural" solution but it is not unique. In fact, even if enhanced models with regularisation methods restore mesh objectivity, the localised solution of an initial boundary value problem remains non-unique. Different methods are possible to force the strain localisation and to generate several possible solutions to an identical boundary value problem. Among them, two have been used for the gallery excavation: a modification of the computational numerical parameters (see Figs. 5.34 and 5.35) and material imperfections (see Figs. 6.11 and 6.12). Various localised solutions could therefore emerge by forcing the strain localisation and, among them, some modes are actually more frequent than others (Marinelli et al., 2014; Sieffert et al., 2009). A study on this particular point would be interesting to realise. Nevertheless, different possible solutions can be of interest when trying to reproduce experimental measurements that may be representative of a particular solution (not of the "natural" solution). For the gallery excavation problem, the drilling damages the rock and creates material defects at gallery wall. Considering various configurations of defects on the wall will inevitably influence the strain localisation process and will impact the solution.

Pattern, number, and width of shear bands

The shape of the EDZ is quite well reproduced by the modelling of the shear bands; nonetheless, the fracturing would be better described if more and thinner shear bands were modelled. The number of shear bands that develop around the galleries is also related to the onset of strain localisation. This number remains quite low and controlling the shear band onset, with material defects for instance, could be appealing. However, the results in Fig. 6.12 indicate that using several defects may allow to control or modify the shear band pattern (location and orientation of the bands) but does not generate much more shear bands. The results of Figs. 4.7 and 4.8 have

shown that the pattern of shear bands of the "natural" solution (without material defects) is related to the rock properties. The differences in the number, orientation, and time of appearance of the shear bands for these particular numerical results are related only to the compressibility of the solid grains, which means to the value of the Biot's coefficient. Other properties of the rock may also influence the shear band pattern (dilatancy angle, final cohesion...).

Another crucial parameter which conditions the pattern, number, and thickness of the shear bands is obviously the elastic modulus D of the second gradient mechanical model. It represents the physical microstructure and the internal length scale relevant for the shear band width is related to it. For granular materials, the thickness of the shear bands depends mainly on the solid grain size (El Bied et al., 2002; Roscoe, 1970; Vardoulakis and Sulem, 1995); thus, the value of D should be evaluated based on experimental measurements. From a numerical perspective, a good precision of the post-localisation plastic behaviour within the shear bands is obtained if a few elements (at least three) compose the shear band width (Bésuelle et al., 2006a). Thus, because the shear bands can be very thin ($<100\mu m$) for fine-grained materials such as clayey rocks or marls (Bésuelle et al., 2006b; Viggiani et al., 2004), very fine meshes must be used to correctly reproduce the small width of the shear bands with finite element methods. They may also allow the development of more shear bands. Such meshes would contain a huge number of finite elements, especially for large-scale applications, which would cause the numerical solving to be time consuming.

Lastly, only circular galleries have been envisaged for the modelling of the EDZ with shear banding, but the galleries in the Andra's URL generally exhibit a shape of "horseshoe" with a concrete slab on the floor (Fig. 2.26). The onset and final pattern of the shear bands can be influenced by different geometries of the problem or by geometrical defects, which could therefore be investigated.

Reproduction of gallery convergence

The mechanical aspects that are considered include mostly the reproduction of the fracturing pattern and gallery diametrical convergence. The latter is strongly affected by the position of the fractures and is much larger in the direction corresponding to the location of the fractured zone (Figs. 6.2 and 2.7). It is clear that the convergence of the galleries and its anisotropy strongly depend on the appearance of shear bands, on their locations, and on the movements of material blocks created by the shear bands. The anisotropy of the convergence can not be reproduced without strain localisation. Nevertheless, other solutions of the gallery excavation problem may generate other shear band patterns and other results in term of convergence. The shear band pattern and convergence could also be modified by the "horseshoe" shape of the galleries.

Creep deformations have been introduced with the purpose of analysing if a viscoplastic mechanism could reproduce the increase of convergence in the long term. It could, but its effect are restricted when an air ventilation is realised in the gallery. The desaturation (suction) of the rock around the gallery, which is implied by the ventilation and the increase of permeability, restricts the deformation after the drilling which comes in opposition to the creep effect. Consequently, reproducing the evolution of the convergence by creep strain and finding one set of parameters that would suit for horizontal and vertical convergences, as well as for both gallery orientations in the Callovo-Oxfodian claystone, are not straightforward. The rock vicosity improve the reproduction of the convergence evolution in the long term, but it may not be efficient to counteract opposite effects such as gallery ventilation.

Reproduction of water transfers

The hydraulic aspects that are considered include mostly the reproduction of the water transfers, the drainage, and the desaturation. They depend on several factors as the increase of permeability in the EDZ, the hygrometry of the air inside the gallery, and the exchanges between the rock and

the air at gallery wall. It is to mention that the reproduction of both mechanical and hydraulic aspects with strain localisation in shear bands is quite complex because the two problems are coupled and influence each other. The permeability variation and the water transfer around the gallery are conditioned by the strain localisation and the shear banding pattern. Consequently, the simultaneous reproduction of all these aspects constitutes a challenge in the context of strain localisation in unsaturated biphasic media.

Concerning the intrinsic permeability in the EDZ, if an increase is considered exclusively inside the shear bands then the drainage in the claystone is underestimated because the rock mass outside the shear bands is not affected (Pardoen et al., 2014a, 2015b). The drainage could be accentuated by increasing the number of shear bands, but it may require to reduce the width of the bands and the permeability increase could remain confined within them. Another possibility, which has been used in the modelling, is to consider a more global increase of the intrinsic permeability in the EDZ, in the shear bands but also in their vicinity. The second method allows a satisfactory reproduction of the drainage and desaturation of the rock (Figs. 6.18 to 6.20).

Material imperfections have also been incorporated in the modelling (Fig. 6.12 (a)) to represent the defects induced by the drilling process at gallery wall. They influence the shear banding pattern and therefore the intrinsic permeability evolution and the water transfers. Different configurations of defects have been tested and both mechanical and hydraulic experimental data have been analysed simultaneously. The results that have been illustrated in sections 6.3 and 6.4 correspond to a configuration that allows a good reproduction of both mechanical and hydraulic measurements.

The exchanges at gallery wall are also of importance regarding the flow kinetics in the rock. Among the two types of exchange involved at gallery wall, the water vapour transfer is controlled by a transfer coefficient α_v. This parameter depends on the external drying conditions (relative humidity, temperature, and velocity of the air) and can be determined from drying flux curves deduced from laboratory drying experiments (Léonard et al., 2005). In the numerical modelling, this parameter has been calibrated to correctly reproduce the experimental measurements of pore water pressure and water content. The used value is lower than the one determined on small-scale samples of argillaceous material during convective drying experiments (Gerard et al., 2010). This difference may be explained by the drying conditions and drying scale in underground galleries that are different than in laboratory. In fact, the kinetics of the air circulation is different than in convective drying tests and the size of the dried material is much larger. A scale effect could possibly help to explain the difference but should be studied in depth.

Following all these arguments, an evident question that can arise is: do other solutions to the second grade boundary value problem of a gallery excavation could have lead to a potential correct reproduction of the experimental data? Due to the non-uniqueness of the solution and to the various choices of parameters, the answer is: probably! Nonetheless, the reproduction of the different hydro-mechanical measurements are not straightforward, and the solution that is obtained is satisfactory. It involves parameter values that are chosen in an acceptable range for the considered rock. It is a fact that the solution is not unique but finding another set of parameters that would also permit to correctly reproduce all the different aspects would not be trivial. It might however be possible for another shear band pattern provided that it is located above the gallery (for the reproduction of the SDZ experiment).

6.5.3 Outlooks

Various perspectives can be extrapolated from the present work on different aspects. Several outlooks are detailed hereafter, without having the pretension of being exhaustive but with the purpose of remaining correlated to the large-scale numerical modelling of the excavation damaged zone.

Mechanical aspects

The proposed approach aims to reproduce the EDZ and the different couplings occurring in it, based on a continuous description of the fractures with strain localisation in shear bands. The material rupture and the fracture discontinuities are not described in a discrete manner, which will consequently not been discussed here. Considering a continuous approach, the strain localisation can be seen as a consequence of material damage by microcracking. In fact, strain localisation appears due to the growth, interaction, and coalescence of microcracks. The material damage could therefore be considered in parallel with strain localisation by considering a degradation of the material strength properties, either with macroscopic or multi-scale approach. The damage could improve the results, as the gallery convergence for instance, but remains to be investigated.

Using shear strain localisation in band mode as a predictor of the fracturing process is an approach that is mostly efficient for the reproduction of shear fractures in materials dominated by this type of failure. As a perspective, the fracture definition can still be improved, and it is evident that additional mechanisms would be necessary for the reproduction of other types of fractures. For instance, modelling tensile fractures in the excavation damaged zone could be of interest. In fact, even if shearing is the predominant fracture mechanism for the considered clayey rock, fractures in extension are also observed in the damaged zone close to the gallery.

The material mechanical behaviour in traction could also be improved by adapting the yield criterion with a resistance criterion in traction. Nevertheless, during the gallery excavation, the total radial stress at gallery wall decreases to zero (or to the atmospheric pressure) for unsupported galleries. Then, tensile effective stress appears only if pore overpressures are generated which is not the case when reproducing gallery air ventilation.

Concerning the compressive material behaviour, rocks can exhibit two principal mechanisms of inelastic deformation: the shear failure and the pore collapse. The shear failure is inherent to frictional materials and appears for predominant deviatoric stresses. It has been modelled with a Van Eekelen yield surface and a slightly dilatant behaviour. The pore collapse is characterised by a contractive plastic behaviour with an important reduction of the porosity due to the collapse of the larger pores, which appears for predominant mean stresses. This second plastic phenomenon might appear for high porosity contractive rocks but not for low porosity dilatant rocks (Fossum and Fredrich, 2000; Issen and Rudnicki, 2001). The considered consolidated rock being of the second type, only the shear failure has been considered with a classical and simple model. For high porosity rocks exhibiting a transition from dilatant to compactive deformation, the pore collapse could be added in the definition of the yield criterion with a cap model expressing the transition from dilatant to contractive pre-failure deformation (Fossum and Fredrich, 2000). The influence of the contractive rock behaviour on the shear bands that develop around galleries would require more investigations. More particularly, it is to recall that bifurcation and strain localisation are eased if a softening plastic behaviour is included in the model, even for the cap part if the development of shear bands is sought at considerable mean stress.

Another aspect that can be improved is the creep behaviour. Firstly, the mechanisms of instantaneous plastic deformation and time-dependent viscoplastic deformation have been separately described with two different constitutive models. Yet, these strains are both related to the plastic behaviour of the material and differ by the time scales at which they develop. Therefore, for this type of approach, the physical explanation of the creep mechanism is not clearly established. In contrast to this classical approach, unified approaches exist. They consist in defining the plastic and viscoplastic surfaces (loading and potential surfaces) with a similar mathematical expression and similar internal variables. Such approach may be adopted to gain coherence in the description of the material behaviour. Moreover, only one viscoplastic mechanism is considered and it is arduous to calibrate its parameters both on the short term (creep tests) and on the long term (gallery convergence). Different vicoplastic processes with different time scales may exist and lead to different mechanisms of creep strain.

Hydraulic aspects

As for the mechanical aspects, additional mechanisms would be required to represent the fractures in opening mode. Experimental measurements indicate that the presence of a network of interconnected extensional fractures close to the gallery significantly contributes to the increase of the hydraulic permeability in the EDZ (Armand et al., 2014). As a consequence, the description of tensile fractures and their influence on the hydraulic kinetics could be incorporated in the description of the EDZ. For the strain localisation approach, one way to proceed could be to link the intrinsic permeability evolution with the tensile strain in the normal direction to the shear bands. The permeability would be more particularly increased in the longitudinal direction of the shear band. This would lead to an anisotropic evolution of the intrinsic permeability whose principal directions would not correspond any longer to the principal directions of the initial material anisotropy. Such anisotropic evolution, with a more pronounced increase in the shear band direction, could be envisaged for any shear band even without taking into account tensile effects. The drawback of this permeability evolution is that the permeability increase in the normal direction to the shear band is limited which restricts the drainage. Therefore, the global drainage of the rock would not necessarily be obtained. Nonetheless, the Rice bifurcation criterion provides two conjugate directions of possible bifurcation and the direction that is actually active is not known. The orientation of the shear bands at macroscale are known only at the end of the computation. Knowing the direction of the shear bands during the computation would require to determine locally in which direction the shear band propagates on a global scale which is not possible.

Other effects of the material drying can also be taken into account. Actually, the effect of drying on the material behaviour is related to the hydro-mechanical coupling inherent to the effective stress definition. The material drying provoked by the air ventilation of the galleries generates a matric suction in the porous rock and an increase of the effective compressive stress. Following the definition of the yield surface, an increase of the mean effective stress strengthens the material, which becomes elastic again (elastic unloading) close to the gallery (Fig. 4.10). Such process does not increase the fracturing by desiccation but, on the contrary, inhibits the strain localisation and the further plastic strains. The expected effect of drying would however be desiccation, shrinkage, and fracturing; consequently, a more complex definition of the hydro-mechanical coupling and of the desiccation fracturing process would be required. The latter could also be related to the description of tensile cracks, to a resistance criterion in traction, and to permeability evolution. The relation to strain localisation requires further studies to be established.

Another aspect that can be influenced by the cracking and damage is the water retention property of the material. The damage process in porous materials such as rocks or concrete can modify the pore network morphology, the permeability, the water retention curve, and the gas breakthrough pressure (Arson and Pereira, 2013; M'Jahad et al., 2015; Pereira and Arson, 2013). A supplementary hydro-mechanical coupling could consequently be introduced by considering an evolution of the retention curve with the deformations (Gerard, 2011; Olivella and Alonso, 2008). For such approach, it is assumed that the increase of the pore size generates a decrease of the air entry pressure. Moreover, experimental studies on concretes performed by M'Jahad et al. (2015) have highlighted that, for the calibrations of retention curves based on the van Genuchten's model, the parameter P_r representing the air entry pressure can reduce significantly after damage. It means that the minimal capillary force needed to desaturate the material pores is lowered by the cracking process, and the desaturation is amplified in the material for a given capillary pressure (matric suction). This would lead to a more rapid decrease of the degree of water saturation around the galleries when they are submitted to air ventilation. The desaturation front would propagate and reach a steady state more rapidly after the excavation. The exchanges of water vapour at gallery wall may therefore be less important during the ventilation phase and may have a lower effect on the drainage of the argillaceous media. Nonetheless, the amplification of

the desaturation will generate a decrease of the relative permeability, by means of the relative permeability curve, and therefore a decrease of the global permeability. This decrease would restrict the advective flows of water and the progressive drainage of the rock, which constitutes an opposite effect to the increase of the intrinsic permeability.

Lastly, the closure of fractures or the sealing and healing of the rock might be considered as well. Their major effects would be a reduction of the intrinsic water permeability and of the flow transfers that would eventually reduce the long-term drainage of the rock.

Other materials and applications

The proposed approach could certainly be extended to other materials and other applications. In the context of nuclear waste repository, two other clayey geological formations that are considered in Europe are the Boom clay (Belgium) and the Opalinus clay (Switzerland). The first is a plastic clay that also exhibits chevron or herringbone fracture patterns around the galleries but no extensional failure (Blümling et al., 2007; Wileveau and Bernier, 2008). More information on the modelling of the EDZ with shear bands in this clay can be found in Salehnia et al. (2015). The second is an indurated clay whose characteristics are comparable to those of the Callovo-Oxfordian claystone but with bedding planes inclined at about 45°. For this material, the extension is the prevailing mechanism of failure; consequently, extensional mechanisms should be included in the fracture description to reproduce the EDZ accurately. The development of the fractures in this indurated clay (Marschall et al., 2008) is however mostly dominated by pre-existing features (tectonic faults) and bedding plane instabilities (bedding slip or buckling) which increase the complexity of the modelling. Other geological formations, such as granite and salt formations, are also envisaged for the deep repository of nuclear wastes.

Moreover, other applications such as tunnelling, petroleum engineering, mining, oversee drilling, fractured reservoirs, geothermal drilling... can be considered especially since the coupled second gradient model has been extended to unsaturated conditions, solid grain compressibility, and anisotropic behaviour. The modelling of the EDZ in different materials would require to analyse their fracturing behaviour and to evaluate if the representation of fractures with shear banding is pertinent for the considered applications.

Chapter 7

Conclusion

7.1 Summary

Among the different sources of energy, the nuclear energy constitutes a significant part of the global production. The long-term management of the most hazardous radioactive wastes is envisaged by deep geological repository. This mode of disposal consists of a repository in stable geological formations that provides good confining characteristics and that insulate the harmful effects of the wastes. Different low-permeability host materials are envisaged and, among them, the Callovo-Oxfordian claystone is studied.

The long-term repository requires a good understanding of the host formation behaviour and of the coupled processes that occur around the underground structures, during the different storage phases. The excavation of the underground galleries and the water transfers resulting of the interaction between the host rock and the gallery air are mostly analysed. It is a fact that the drilling process generates cracks and fractures in the surrounding medium. They concentrate in the gallery's vicinity, in a zone called the Excavation Damaged Zone (EDZ). In this zone, the fracturing engenders important and irreversible modifications of the hydro-mechanical properties of the rock such as a significant increase of the hydraulic permeability. The material behaviour can also be affected by the interaction with the gallery air during maintenance phases due to the air ventilation that is realised inside the galleries. Such ventilation can drain the water from the rock and cause desaturation, especially in the damaged zone. Consequently, the understanding and the prediction of the EDZ hydro-mechanical behaviour are crucial issues for the long-term management of nuclear wastes. The coupled processes that occur during the excavation and ventilation of underground galleries are therefore addressed.

The first objective is to describe the fractures and the EDZ development induced by the excavation process. Among the different possible methods allowing to reproduce the drilling effects and the fracturing process in geomaterials, it is proposed to represent the fractures with strain localisation in shear bands. An appropriate model allowing to properly reproduce the strain localisation in geomaterials with finite element methods is defined. It is an enhanced model for microstructure media called the coupled local second gradient model which involves a regularisation method. To enlarge its application to drilling in unsaturated anisotropic rocks, some improvements of this model are developed to take into account unsaturated conditions, compressibility of the solid grains, anisotropic rock behaviour, and permeability evolution. The numerical modelling of the excavation fractured zone with shear banding provides information about its shape, extent, fracturing structure, and behaviour that are in good agreement with *in situ* measurements. The shear bands develop during the gallery excavation and the modelling exhibits a chevron fracture pattern around the gallery.

At repository scale, experimental measurements have highlighted that the rock anisotropy has an important role in the onset of fractures and in the fractured zone pattern. Then, because sedimentary geomaterials frequently exhibit a transversely isotropic behaviour depending on the direction of loading, a constitutive mechanical model incorporating the rock anisotropy is included. For underground drilling in Callovo-Oxfordian claystone, the fractured zone is controlled by both the anisotropy of the stress state and of the material characteristics. The elliptical shape of the fractured zone as well as its directional development is highlighted with numerical modelling of shear banding. On one hand, the shear banding zone develops preferentially in the direction of the minor principal stress for galleries having an anisotropic stress state in their sections. On the other hand, for galleries having an isotropic stress state in their sections, the development of the strain localisation zone is governed by the anisotropic plastic properties of the rock and develops preferentially in the direction of lower material resistance. The observed pattern and extent of the shear strain localisation zone correspond fairly well to fracture observations and measurements. Furthermore, the numerical results also indicate that the shear bands appearance and pattern have an influence on the convergence of the galleries. A larger convergence is obtained in the direction of the fractured zone according to *in situ* measurements.

Creep deformations may also be important to take into account for the long-term feasibility

analysis of deep geological repository of nuclear radioactive wastes. Such deformations have an impact on the long-term convergence of the underground structures. Viscosity effects are therefore included in the modelling to improve the reproduction of the gallery convergence.

The last major objective is the description of the fluid transfers and of the rock hydro-mechanical behaviour around galleries. In addition to mechanical aspects, the fracture behaviour is dominated by hydro-mechanical property changes. Characterising the impact of the rock fracturing on its hydraulic properties remains a major issue for the EDZ description. It is addressed with a hydro-mechanical coupling for the reproduction of the increase of water intrinsic permeability in the EDZ. To take into account strain localisation effects at the macroscale, the intrinsic permeability evolution is expressed by a strain-dependent relation which engenders a more pronounced increase of permeability inside the fractures (shear bands). A significant permeability increase of several orders of magnitude is reproduced in the excavation damaged zone, in agreement with available experimental measurements.

After gallery excavation, the hydraulic transfers in the rock surrounding the galleries are investigated through the rock interaction with the gallery air. Depending on the air hygrometry, the interaction implies drainage and desaturation of the surrounding material, especially in the EDZ where the permeability is increased. These transfers are studied at large-scale during the reproduction of a gallery air ventilation experiment, namely the Saturation Damaged Zone (SDZ) experiment, conducted in the Andra's Underground Research Laboratory. Its purpose is to investigate, at repository scale, the rock-atmosphere interactions, the effect of drainage and wetting, as well as the desaturation and possible resaturation of the EDZ.

The different transfers depend on the liquid water and water vapour exchanges at gallery wall that are introduced with a non-classical (mixed) hydraulic boundary condition. The latter implies a delayed thermodynamic equilibrium between the gallery wall rock and the gallery air controlled by the water vapour transfer. Such condition is relevant for the reproduction of the transfers and has a significant influence on the reproduction of the experimental measurements performed around the gallery during the test. Based on experimental observations in the claystone, the model prediction successfully captures the drainage kinetics of the undisturbed rock and the desaturation of the EDZ. The effect of the gallery air ventilation on the shear banding development around the galleries is also highlighted. Moreover, it is to mention that the reproduction of both mechanical and hydraulic *in situ* measurements is complex.

The proposed approach aims to highlight the important hydro-mechanical aspects to take into account for the reproduction of the EDZ behaviour in unsaturated biphasic media with shear banding. For the reproduction of the mechanical aspects, the regularisation method, the material anisotropy, and the creep effect are crucial. For the hydraulic aspects it is the unsaturated properties of the medium, the permeability increase, and the exchanges at gallery wall that are most particularly important.

7.2 Contributions

The major contribution is to provide new elements for the prediction and understanding of the hydro-mechanical behaviour of the excavation damaged zone. This behaviour is analysed for partially saturated porous rocks having low-permeability. The new developments concern the characterisation of the fracturing and coupled processes that take place around underground galleries. The approach is innovative in the sense that the fracturing process is predicted on a large scale with shear bands, and that strain localisation effects are taken into account in coupled processes, such as the variation of hydraulic properties.

The developments and applications are oriented towards the numerical modelling of the EDZ. This modelling plays an essential role in the prediction of the rock behaviour related to underground drilling. Numerical applications are realised in parallel to the different developments, improving the complexity of the material behaviour and of the fracture description with shear

banding at each step. This type of modelling constitutes a major novelty because it has not been widely performed at large scale, in partially saturated rock. Concerning the claystone behaviour, the objective is not to develop a complex constitutive model but is to highlight if shear banding can be an adequate numerical tool for the reproduction of the EDZ.

For underground drilling in rocks, the challenges that are addressed in term of strain localisation modelling are multiple. A first challenge consists in investigating if the proposed numerical method is appropriate to reproduce shear bands on a large scale. Secondly, the used approach must be able to represent the impacts of the different material characteristics (unsaturated state, deformability, anisotropy, property modifications) on the post-failure behaviour and on the development of shear bands around galleries. Thirdly, the simultaneous reproduction of mechanical, hydraulic, and coupled aspects is not an easy task when they are all related to strain localisation effects. The last challenge is to capture the drainage and desaturation kinetics in the EDZ and in the surrounding rock, based on *in situ* experimental measurements.

7.3 Outlooks

Diverse perspectives can be considered on several aspects. They are enumerate hereafter, in relation to the large-scale numerical modelling of the excavation damaged zone.

Numerical modelling

The onset of strain localisation is related to various numerical aspects. Firstly, to go further in the calibration of the strain localisation process, precise information is required about the shear banding structure. However, this information is seldom available for rocks especially for large-scale problems. Secondly, enhanced models with regularisation methods are required to properly model the strain localisation by restoring mesh objectivity. The non-uniqueness of the localised solution to the excavation problem could however be studied by generating various solutions. Among these solutions, some modes are more frequent than others (Marinelli et al., 2014; Sieffert et al., 2009) and a study of the most frequent modes around galleries as well as their influence on the reproduction of experimental measurements could be interesting to realise.

The fracturing pattern may be better reproduced. In fact, the shear bands correctly reproduce the shape of the EDZ but thinner bands in a large number would be more appropriated to describe the fracturing. The shear band pattern is related to the rock properties, to material defects, and to the elastic modulus of the second gradient mechanical model. The latter represents the microstructure and is related to an internal length scale and to the shear band width. Reducing its value and the size of the finite elements could allow a better reproduction of the shear band width and number. Additionally, the value of the second gradient elastic modulus should be evaluated based on experimental measurements of shear bands. Moreover, galleries regularly exhibit a "horseshoe" shape which could be reproduced. The influence of such geometry modification or even of geometrical defects on the shear band pattern and gallery convergence could be investigated.

For the hydraulic aspects, increasing the number of shear bands could possibly increase the drainage. Nevertheless, if the shear band width is reduced then the permeability increase could remain confined within the band and restrict the drainage. The cumulated effect of a larger number of shear bands and a thinner width requires further investigations. The hydraulic exchanges at gallery wall may also be analysed more deeply. More particularly, the drying conditions and the drying scale in underground galleries are different than in laboratory which might impact the water transfers. A scale effect and the kinetics of the air circulation could be taken into account.

Rock behaviour

The proposed approach is based on a continuous description of the fractures. For this approach, material damage by microcracking can be considered in parallel with strain localisation by considering a degradation of the material properties. Concerning the description of the fractures in the EDZ, it can be improved by representing other types of fractures, and additional mechanisms would be required for their modelling. Tensile fractures could be particularly interesting to represent since they have an important effect on the hydraulic conductivity of the rock. Linking the evolution of the water permeability with strain localisation effect in opening mode remains an open question. In parallel, the material mechanical behaviour in traction should also be adapted. For the compressive material behaviour, the pore collapse could be added in the definition of the yield criterion for high porosity rocks exhibiting a transition from dilatant to compactive pre-failure deformation. Another mechanical aspect that can be improved is the creep behaviour of the rock. A unified plastic-viscoplastic approach can be envisaged and would provide a better physical explanation of the creep mechanism. Several mechanisms of vicoplastic strain occurring on different time scales may also be incorporated.

Regarding the hydraulic aspects, the anisotropy of the intrinsic permeability variation could be considered in fractured zones. However, reproducing a more important increase of permeability in the direction of the shear bands is not trivial because their orientations at macroscale are known at the end of the computation. The effect of the material drying can also be enlarged with a more complex definition of the fracturing due to desiccation and shrinkage. It could also be related to the description of tensile cracks, traction resistance criterion, and permeability evolution. The link to shear strain localisation needs further investigations. Furthermore, the water retention property may be influenced by the damage and cracking processes. The desaturation of damaged rocks is amplified; consequently, a supplementary hydro-mechanical coupling could be introduced between the retention curve and the deformations. The influence of the fracture closure or of the sealing and healing of the rock on the hydraulic properties might be considered as well.

More broadly, the continuous approach which is used do not actually represent the cracks and a natural representation of the fractures is to consider them in a discrete manner. Various techniques may be used for the modelling of discontinuous fractures with finite element methods.

Applications

The proposed approach could certainly be extended to other materials and other applications. In the context of nuclear waste repository, different clayey media and other types of geological formations, such as granite and salt formations, are envisaged for the deep repository of nuclear wastes. Moreover, other applications such as tunnelling, petroleum engineering, mining, oversee drilling, fractured reservoirs, geothermal drilling... can be considered especially since the coupled second gradient model has been extended to unsaturated conditions, solid grain compressibility, and anisotropic behaviour. The application to any geotechnical problems that engender fractures could even be envisaged. The modelling of fractures, with the proposed approach, in different materials would require to analyse their fracturing behaviour and to evaluate if the representation of fractures with shear banding is pertinent for the considered applications.

Bibliography

Abelev, A. V. and Lade, P. V. (2003). Effects of cross anisotropy on three-dimensional behavior of sand. I: Stress-strain behavior and shear banding. *J Eng Mech*, 129(2):160–166.

Abelev, A. V. and Lade, P. V. (2004). Characterization of failure in cross-anisotropic soils. *J Eng Mech*, 130(5):599–606.

Abramowitz, M. and Stegun, I. A. (1972). *Handbook of Mathematical Functions with Formulas, Graphs, and Mathematical Tables*. Dover Publications, Inc.

Aifantis, E. C. (1984). On the microstructural origin of certain inelastic models. *J Eng Mater Technol*, 106(4):326–330.

Alshibli, K., Batiste, S., and Sture, S. (2003). Strain Localization in Sand: Plane Strain versus Triaxial Compression. *J Geotech Geoenviron Eng*, 129(6):483–494.

Amadei, B. (1983). *Rock anisotropy and the theory of stress measurements*, volume 2. Springer-Verlag, New York. Lecture Notes in Engineering Series.

Anand, L. (1983). Plane deformations of ideal granular materials. *J Mech Phys Solids*, 31(2):105–122.

Andra (2005a). Dossier 2005 Argile. Synthesis: Evaluation of the feasibility of a geological repository in an argillaceous formation, Meuse/Haute Marne site. Technical report, Paris, France.

Andra (2005b). Dossier 2005 Référentiel du site Meuse/Haute-Marne tome 2 : Caractérisation comportementale du milieu géologique sous perturbation. Seconde édition, Paris, France.

Armand, G., Leveau, F., Nussbaum, C., de La Vaissiere, R., Noiret, A., Jaeggi, D., Landrein, P., and Righini, C. (2014). Geometry and properties of the excavation-induced fractures at the Meuse/Haute-Marne URL drifts. *Rock Mech Rock Eng*, 47(1):21–41.

Armand, G., Noiret, A., Zghondi, J., and Seyedi, D. M. (2013). Short- and long-term behaviors of drifts in the Callovo-Oxfordian claystone at the Meuse/Haute-Marne Underground Research Laboratory. *J Rock Mech Geotech Eng*, 5(3):221–230.

Armand, G., Wileveau, Y., and Delay, J. (2007). Analyse des perméabilités mesurées autour des ouvrages du LSMHM au niveau -490 m pour déterminer des lois empiriques utilisables dans des calculs hydromécaniques couplés en milieu continu. Technical Report D.NT.ALS.07.0453, Andra.

Arson, C. and Gatmiri, B. (2012). Thermo-hydro-mechanical modeling of damage in unsaturated porous media: Theoretical framework and numerical study of the EDZ. *Int J Numer Anal Meth Geomech*, 36(3):272–306.

Arson, C. and Pereira, J. M. (2013). Influence of damage on pore size distribution and permeability of rocks. *Int J Numer Anal Meth Geomech*, 37(8):810–831.

Arthur, J. R. F., Chua, K. S., and Dunstan, T. (1977a). Induced anisotropy in a sand. *Géotechnique*, 27(1):13–30.

Arthur, J. R. F., Dunstan, T., Al-Ani, Q. A. J. L., and Assadi, A. (1977b). Plastic deformation and failure in granular media. *Géotechnique*, 27(1):53–74.

Arthur, J. R. F. and Menzies, B. K. (1972). Inherent anisotropy in a sand. *Géotechnique*, 22(1):115–128.

Bardet, J. P. and Tobita, T. (2002). A practical method for solving free-surface seepage problems. *Comput Geotech*, 29(6):451–475.

Barenblatt, G. I. (1962). The mathematical theory of equilibrium cracks in brittle fracture. *Adv Appl Mech*, 7(1):55–129.

Barnichon, J. D. (1998). *Finite Element Modelling in Structural and Petroleum Geology*. PhD thesis, Faculté des Sciences Appliquées, Université de Liège, Belgium.

Barthélémy, J. F. (2009). Effective permeability of media with a dense network of long and micro fractures. *Transp Porous Med*, 76(1):153–178.

Bazant, Z. P., Belytschko, T. B., and Chang, T. P. (1984). Continuum Theory for Strain Softening. *J Eng Mech*, 110(12):1666–1692.

Bäckblom, G. (1991). The Äspö Hard Rock Laboratory-a step toward the Swedish final repository for high-level radioactive waste. *Tunn Undergr Sp Tech*, 6(4):463–467.

Behlau, J. and Mingerzahn, G. (2001). Geological and tectonic investigations in the former Morsleben salt mine (Germany) as a basis for the safety assessment of a radioactive waste repository. *Eng Geol*, 61(2-3):83–97.

Benallal, A. and Marigo, J. J. (2007). Bifurcation and stability issues in gradient theories with softening. *Modelling Simul Mater Sci Eng*, 15(1):283–295.

Bernaud, D. and Rousset, G. (1992). La "nouvelle méthode implicite" pour l'étude du dimensionnement des tunnels. *Rev Franç Géotech*, 60:5–26.

Biot, M. A. (1941). General theory for three-dimensional consolidation. *J Appl Phys*, 12(2):155–164.

Biot, M. A. (1955). Theory of Elasticity and Consolidation for a Porous Anisotropic Solid. *J Appl Phys*, 26(2):182–185.

Biot, M. A. and Willis, D. G. (1957). The Elastic Coefficients of the Theory of Consolidation. *J Appl Mech*, 24:594–601.

Bishop, A. and Donald, I. (1961). The experimental study of partly saturated soil in the triaxial apparatus. In *5th International Conference on Soil Mechanics and Foundation Engineering*, pages 13–21, Paris.

Bishop, A. W. (1959). The principle of effective stress. *Teknisk Ukeblad*, 39:859–863.

Bishop, A. W. and Blight, G. E. (1963). Some aspects of effective stress in saturated and partly saturated soils. *Géotechnique*, 13(3):177–197.

Blümling, P., Bernier, F., Lebon, P., and Martin, C. D. (2007). The excavation damaged zone in clay formations time-dependent behaviour and influence on performance assessment. *Phys Chem Earth*, 32(8-14):588–599.

Boehler, J. P. and Sawczuk, A. (1977). On Yielding of Oriented Solids. 27(1-4):185–204.

Borja, R. I. and Alarcón, E. (1995). A mathematical framework for finite strain elastoplastic consolidation part 1: Balance laws, variational formulation, and linearization. *Comput Methods Appl Mech Engrg*, 122(1-2):145–171.

Bossart, P., Meier, P. M., Moeri, A., Trick, T., and Mayor, J. C. (2002). Geological and hydraulic characterisation of the excavation disturbed zone in the Opalinus Clay of the Mont Terri Rock Laboratory. *Eng Geol*, 66(1-2):19–38.

Bossart, P., Trick, T., Meier, P. M., and Mayor, J. C. (2004). Structural and hydrogeological characterisation of the excavation-disturbed zone in the Opalinus Clay (Mont Terri Project, Switzerland). *Appl Clay Sci*, 26(1-4):429–448.

Bouchard, P. O., Bay, F., and Chastel, Y. (2003). Numerical modelling of crack propagation: automatic remeshing and comparison of different criteria. *Comput Methods Appl Mech Engrg*, 192(35-36):3887–3908.

Bésuelle, P. (2001). Compacting and dilating shear bands in porous rock: Theoretical and experimental conditions. *J Geophys Res*, 106(B7):13435–13442.

Bésuelle, P., Chambon, R., and Collin, F. (2006a). Switching deformation modes in post-localization solutions with a quasibrittle material. *J Mech Mater Struct*, 1(7):1115–1134.

Bésuelle, P., Desrues, J., and Raynaud, S. (2000). Experimental characterisation of the localisation phenomenon inside a vosges sandstone in a triaxial cell. *Int J Rock Mech Min Sci*, 37(8):1223–1237.

Bésuelle, P., Viggiani, G., Lenoir, N., Desrues, J., and Bornert, M. (2006b). *Advances in X-ray Tomography for Geomaterials*, chapter X-ray Micro CT for Studying Strain Localization in Clay Rocks under Triaxial Compression, pages 35–52. ISTE Ltd.

Budiansky, B. and O'connell, R. J. (1976). Elastic moduli of a cracked solid. *Int J Solids Struct*, 12(2):81–97.

Carranza-Torres, C. and Fairhurst, C. (2000). Application of the Convergence-Confinement Method of tunnel design to rock masses that satisfy the Hoek-Brown failure criterion. *Tunn Undergr Sp Tech*, 15(2):187–213.

Casagrande, A. and Carillo, N. (1944). Shear failure of anisotropic materials. *J Boston Soc Civ Eng*, 31(4):74–87.

Chaboche, J. L. and Lemaitre, J. (1985). *Mécanique des matériaux solides*. Dunod, Paris.

Chambon, R. (1986). Bifurcation and shear band localization an approach for incrementally non linear constitutive equations. *J Mec Theor Appl*, 5(2):277–298.

Chambon, R. and Caillerie, D. (1999). Existence and uniqueness theorems for boundary value problems involving incrementally non linear models. *Int J Solids Struct*, 36(33):5089–5099.

Chambon, R., Caillerie, D., and Hassan, N. E. (1998). One-dimensional localisation studied with a second grade model. *Eur J Mech A-Solid*, 17(4):637–656.

Chambon, R., Caillerie, D., and Matsushima, T. (2001a). Plastic continuum with microstructure, local second gradient theories for geomaterials : localization studies. *Int J Solids Struct*, 38(46-47):8503–8527.

Chambon, R., Crochepeyre, S., and Charlier, R. (2001b). An algorithm and a method to search bifurcation points in non-linear problems. *Int J Numer Meth Engng*, 51(3):315–332.

Chambon, R. and Moullet, J. C. (2004). Uniqueness studies in boundary value problems involving some second gradient models. *Comput Methods Appl Mech Engrg*, 193(27-29):2771–2796.

Chapuis, R. P. and Aubertin, M. (2003). On the use of the Kozeny-Carman equation to predict the hydraulic conductivity of soils. *Can Geotech J*, 40(3):616–628.

Charlier, R. (1987). *Approche unifiée de quelques problèmes non linéaires de mécanique des milieux continus par la méthode des éléments finis (grandes déformations des métaux et des sols, contact unilatéral de solides, conduction thermique et écoulements en milieu poreux)*. PhD thesis, Faculté des Sciences Appliquées, Université de Liège, Belgium.

Charlier, R., Collin, F., Gerard, P., Radu, J. P., and Pardoen, B. (2013a). Modélisation numérique de l'expérience SDZ pour l'Andra - Résultats de simulations. Technical report, ULg, Liège, Belgium.

Charlier, R., Collin, F., Pardoen, B., Talandier, J., Radu, J. P., and Gerard, P. (2013b). An unsaturated hydro-mechanical modelling of two in-situ experiments in Callovo-Oxfordian argillite. *Eng Geol*, 165:46–63.

Charlier, R., Radu, J. P., and Barnichon, J. D. (1997). Water movement effect on the strain localisation during a biaxial compression. In Pande, G. and Pietruszczak, S., editors, *Numerical Models in Geomechanics, NUMOG VI*, pages 219–224, Rotterdam. Balkema.

Charlier, R., Radu, J. P., and Collin, F. (2008). Projet HAVL - Argile - Expertise sur les mesures sur échantillons d'argilite du module de déformation et de la résistance à la compression simple. Technical Report C.RP.0ULg.08.001, Université de Liège, Andra.

Chen, L. (2009). *Contribution à la modélisation du comportement hydromécanique des géomatériaux semi-fragiles*. PhD thesis, Université des Sciences et Technologies de Lille, Lille.

Chen, L., Shao, J. F., and Huang, H. W. (2010). Coupled elastoplastic damage modeling of anisotropic rocks. *Comput Geotech*, 37(1-2):187–194.

Chen, Y., Zhou, C., and Sheng, Y. (2007). Formulation of strain-dependent hydraulic conductivity for a fractured rock mass. *Int J Rock Mech Min Sci*, 44(7):981–996.

Cheng, A. H. D. (1997). Material coefficients of anisotropic poroelasticity. *Int J Rock Mech Min Sci*, 34(2):199–205.

Collin, F. (2003). *Couplages thermo-hydro-mécaniques dans les sols et les roches tendres partiellement saturés*. PhD thesis, Faculté des Sciences Appliquées, Université de Liège, Belgium.

Collin, F., Caillerie, D., and Chambon, R. (2009a). Analytical solutions for the thick-walled cylinder problem modeled with an isotropic elastic second gradient constitutive equation. *Int J Solids Struct*, 46(22-23):3927–3937.

Collin, F., Chambon, R., and Charlier, R. (2006). A finite element method for poro mechanical modelling of geotechnical problems using local second gradient models. *Int J Numer Meth Engng*, 65(11):1749–1772.

Collin, F., Levasseur, S., and Chambon, R. (2009b). Numerical post failure methods in multi-physical problems. *Eur J Environ Civ Eng*, 13(7-8):983–1004.

Collin, F. and Pardoen, B. (2013). Excavation damaged zone modelling in claystone with coupled second gradient model. In Yang, Q., Zhang, J. M., Zheng, H., and Yao, Y., editors, *Constitutive Modeling of Geomaterials*, Springer Series in Geomechanics and Geoengineering, pages 313–317, Berlin Heidelberg. Springer. doi: 10.1007/978-3-642-32814-5_42.

Cosserat, E. and Cosserat, F. (1909). *Théorie des Corps Déformables*. Hermann, Paris.

Coulomb, C. A. (1773). Essai sur une application des règles de maximis et minimis à quelques problèmes de statique, relatifs à l'architecture. *Académie Royale des Sciences*, 7:343–382.

Coussy, O. (1995). *Mechanics of Porous Continua*. John Wiley & Sons, Chichester.

Coussy, O. (2004). *Poromechanics*. John Wiley & Sons, Chichester.

Croisé, J., Schlickenrieder, L., Marschall, P., Boisson, J. Y., Vogel, P., and Yamamoto, S. (2004). Hydrogeological investigations in a low permeability claystone formation: the Mont Terri Rock Laboratory. *Phys Chem Earth*, 29(1):3–15.

Cruchaudet, M., Noiret, A., Talandier, J., and Armand, G. (2010a). Expérimentation SDZ - Bilan de la mise en place de l'instrumentation et des premières mesures à fin mars 2010 - Centre de Meuse/Haute-Marne. Technical Report D.RP.AMFS.09.0087, Andra.

Cruchaudet, M., Noiret, A., Talandier, J., Gatmiri, B., and Armand, G. (2010b). OHZ en GED: EDZ initiale et évolution. Technical Report D.RP.AMFS.11.0016, Andra.

de Borst, R. and Mühlhaus, H. B. (1992). Gradient-dependent plasticity: Formulation and algorithm aspects. *Int J Numer Meth Engng*, 35(3):521–539.

de Borst, R., Sluys, L. J., Mühlhaus, H. B., and Pamin, J. (1993). Fundamental issues in finite element analyses of localization of deformation. *Eng Comp*, 10(2):99–121.

Delage, P. and Cui, Y. J. (2000). L'eau dans les sols non saturés. *Techniques de l'ingénieur*, C301:1–20.

Delage, P., Howat, M. D., and Cui, Y. J. (1998). The relationship between suction and swelling properties in a heavily compacted unsaturated clay. *Eng Geol*, 50(1-2):31–48.

Delay, J., Lebon, P., and Rebours, H. (2010). Meuse/Haute-Marne centre: next steps towards a deep disposal facility. *J Rock Mech Geotech Eng*, 2(1):52–70.

Delay, J., Vinsot, A., Krieguer, J. M., Rebours, H., and Armand, G. (2007). Making of the underground scientific experimental programme at the Meuse/Haute-Marne underground research laboratory, North Eastern France. *Phys Chem Earth*, 32(1-7):2–18.

Desrues, J. (1984). *La localisation de la déformation dans les matériaux granulaires*. PhD thesis, Université Joseph Fourier, Institut National Polytechnique, Grenoble.

Desrues, J. (1987). *Manuel de Rhéologie des Géomatériaux*, chapter Naissance des bandes de cisaillement dans les milieux granulaires : expérience et théorie, pages 279–298. Press ENPC.

Desrues, J. (2005). Hydro-mechanical coupling and strain localization in saturated porous media. *Rev Eur Génie Civ*, 9(5-6):619–634.

Desrues, J. and Viggiani, G. (2004). Strain localization in sand: an overview of the experimental results obtained in Grenoble using stereophotogrammetry. *Int J Numer Anal Meth Geomech*, 28(4):279–321.

Detournay, E. and Cheng, A. H. D. (1993). *Comprehensive Rock Engineering: Principles, Practice and Projects*, volume 2 Analysis and Design Method, chapter 5 Fundamentals of Poroelasticity, pages 113–171. Pergamon Press, Oxford.

Diederichs, M. S. (2003). Rock Fracture and Collapse Under Low Confinement Conditions. *Rock Mech Rock Eng*, 36(5):339–381.

Distinguin, M. and Lavanchy, J. M. (2007). Determination of hydraulic properties of the Callovo-Oxfordian argillite at the bure site: Synthesis of the results obtained in deep boreholes using several *in situ* investigation techniques. *Phys Chem Earth*, 32(1-7):379–392.

Dizier, A. (2011). *Caractérisation des effets de température dans la zone endommagée autour de tunnels de stockage de déchets nucléaires dans des roches argileuses*. PhD thesis, Faculté des Sciences Appliquées, Université de Liège, Belgium.

Dormieux, L. and Kondo, D. (2004). Approche micromécanique du couplage permeabilité endommagement. *C R Mecanique*, 332(2):135–140.

Du Bernard, X., Eichhubl, P., and Aydin, A. (2002). Dilation bands: A new form of localized failure in granular media. *Geophys Res Lett*, 29(24):1–4.

Dugdale, D. S. (1960). Yielding of steel sheets containing slits. *J Mech Phys Solids*, 8(2):100–104.

Duveau, G., Shao, J. F., and Henry, J. P. (1998). Assessment of some failure criteria for strongly anisotropic materials. *Mech Cohes-Frict Mat*, 3:1–26.

Ehlers, W. and Volk, W. (1998). On theoretical and numerical methods in the theory of porous media based on polar and non-polar elasto-plastic solid materials. *Int J Solids Struct*, 35(34-35):4597–4617.

El Bied, A., Sulem, J., and Martineau, F. (2002). Microstructure of shear zones in Fontainebleau sandstone. *Int J Rock Mech Min Sci*, 39(7):917–932.

Emsley, S., Olsson, O., Stenberg, L., Alheid, H. J., and Falls, S. (1997). *ZEDEX: A Study of Damage and Disturbance from Tunnel Excavation by Blasting and Tunnel Boring*. Svensk Kärnbränslehantering AB/Swedish Nuclear Fuel and Waste Management Co.

Ewen, J. and Thomas, H. R. (1989). Heating unsaturated medium sand. *Géotechnique*, 39(3):455–470.

Fernandes, R. (2009). *Modélisation numérique objective des problèmes hydromécaniques couplés dans le cas des géomatériaux*. PhD thesis, Université Joseph Fourier, Grenoble.

Finno, R., Harris, W., Mooney, M., and Viggiani, G. (1996). Strain localization and undrained steady state of sands. *J Geotech Engrg*, 122(6):462–473.

Finno, R., Harris, W., Mooney, M., and Viggiani, G. (1997). Shear bands in plane strain compression of loose sand. *Géotechnique*, 47(1):149–165.

Félix, B., Lebon, P., Miguez, R., and Plas, F. (1996). A review of the ANDRA's research programmes on the thermo-hydromechanical behavior of clay in connection with the radioactive waste disposal project in deep geological formations. *Eng Geol*, 41(1-4):35–50.

Fossum, A. F. and Fredrich, J. T. (2000). Cap plasticity models and compactive and dilatant pre-failure deformation.

François, B. (2008). *Thermo-plasticity of fine-grained soils at various saturation states : Application to nuclear waste disposal*. PhD thesis, Ecole Polytechnique Fédérale de Lausanne, Suisse.

François, B., Labiouse, V., Dizier, A., Marinelli, F., Charlier, R., and Collin, F. (2014). Hollow Cylinder Tests on Boom Clay: Modelling of Strain Localization in the Anisotropic Excavation Damaged Zone. *Rock Mech Rock Eng*, 47(1):71–86.

François, B., Laloui, L., and Laurent, C. (2009). Thermo-hydro-mechanical simulation of ATLAS in situ large scale test in Boom Clay. *Comput Geotech*, 36(4):626–640.

Fredlund, D. G. and Rahardjo, H. (1993). *Soil Mechanics for Unsaturated Soils*. John Wiley & Sons, New-York.

Gao, Z. and Zhao, J. (2013). Strain localization and fabric evolution in sand. *Int J Solids Struct*, 50(22-23):3634–3648.

Gaucher, E., Robelin, C., Matray, J. M., Négrel, G., Gros, Y., Heitz, J. F., Vinsot, A., Rebours, H., Cassagnabère, A., and Bouchet, A. (2004). ANDRA underground research laboratory: interpretation of the mineralogical and geochemical data acquired in the Callovian-Oxfordian formation by investigative drilling. *Phys Chem Earth*, 29(1):55–77.

Gawin, D. and Sanavia, L. (2009). A unified approach to numerical modelling of fully and partially saturated porous materials by considering air dissolved in water. *CMES-Comp Model Eng*, 53(3):255–302.

Gawin, D., Schrefler, B. A., and Galindo, M. (1996). Thermo-hydro-mechanical analysis of partially saturated porous materials. *Eng Computation*, 13(7):113–143.

Geankoplis, C. J. (1993). *Transport processes and unit operations*. Prentice-Hall, Englewood Cliffs, New Jersey.

Gens, A., Garcia-Molina, A. J., Olivella, S., Alonso, E. E., and Huertas, F. (1998). Analysis of a full scale in situ test simulating repository conditions. *Int J Numer Anal Meth Geomech*, 22(7):515–548.

Gens, A., Vaunat, J., Garitte, B., and Wileveau, Y. (2007). In situ behaviour of a stiff layered clay subject to thermal loading: observations and interpretation. *Géotechnique*, 57(2):207–228.

Gerard, P. (2011). *Impact des transferts de gaz sur le comportement poro-mécanique des matériaux argileux*. PhD thesis, Faculté des Sciences Appliquées, Université de Liège, Belgium.

Gerard, P., Charlier, R., Chambon, R., and Collin, F. (2008). Influence of evaporation and seepage on the convergence of a ventilated cavity. *Water Resour Res*, 44(5):1–16.

Gerard, P., Léonard, A., Masekanya, J. P., Charlier, R., and Collin, F. (2010). Study of the soil-atmosphere moisture exchanges through convective drying tests in non-isothermal conditions. *Int J Numer Anal Meth Geomech*, 34(12):1297–1320.

Germain, P. (1973). The method of virtual power in continuum mechanics. Part 2 Microstructure. *SIAM J Appl Math*, 25(3):556–575.

Ghezzehei, T. A., Trautz, R. C., Finsterle, S., Cook, P. J., and Ahlers, C. F. (2004). Modeling coupled evaporation and seepage in ventilated cavities. *Vadose Zone J*, 3(3):806–818.

Graham, J. and Houlsby, G. T. (1983). Anisotropic elasticity of a natural clay. *Géotechnique*, 33(2):165–180.

Griffith, A. A. (1921). The Phenomena of Rupture and Flow in Solids. *Philos T R Soc Lond*, 221(582-593):163–198.

Guayacan-Carrillo, L. M., Sulem, J., Seyedi, D. M., Ghabezloo, S., Noiret, A., and Armand, G. (2015). Analysis of Long-Term Anisotropic Convergence in Drifts Excavated in Callovo-Oxfordian Claystone. *Rock Mech Rock Eng*.

Guillon, T. (2011). *Comportement hydromécanique des argilites du Callovo-Oxfordien lors de cycles de désaturation-resaturation*. PhD thesis, Nancy-Université, Institut National Polytechnique de Lorraine, Nancy.

Guy, N., Seyedi, D. M., and Hild, F. (2012). A probabilistic nonlocal model for crack initiation and propagation in heterogeneous brittle materials. *Int J Numer Meth Engng*, 90(8):1053–1072.

Hadamard, J. (1903). *Leçon sur la propagation des ondes et les équations de l'hydrodynamique*. Hermann, Paris.

Hajiabdolmajid, V., Kaiser, P. K., and Martin, C. D. (2002). Modelling brittle failure of rock. *Int J Rock Mech Min Sci*, 39(6):731–741.

Han, C. and Drescher, A. (1993). Shear bands in biaxial tests on dry coarse sand. *Soils Found*, 33(1):118–132.

Hassanizadeh, M. and Gray, W. G. (1979a). General conservation equations for multi-phase systems: 1. Average procedure. *Adv Water Resources*, 2:131–144.

Hassanizadeh, M. and Gray, W. G. (1979b). General conservation equations for multi-phase systems: 2. Mass, momenta, energy, and entropy equations. *Adv Water Resources*, 2:191–203.

Hill, R. (1950). *The Mathematical Theory of Plasticity*. Oxford University Press, Oxford.

Hill, R. (1958). A general theory of uniqueness and stability in elastic-plastic solids. *J Mech Phys Solids*, 6(3):236–249.

Hill, R. and Hutchinson, J. W. (1975). Bifurcation phenomena in the plane tension test. *J Mech Phys Solids*, 23:239–264.

Hoek, E. and Brown, E. T. (1980). Empirical Strength Criterion for Rock Masses. *J Geotech Eng Div, ASCE*, 106(9):1013–1035.

Horii, H. and Nemat-Nasser, S. (1983). Overall moduli of solids with microcracks: Load-induced anisotropy. *J Mech Phys Solids*, 31(2):155–171.

IAEA (1983). Characteristics of Radioactive Waste Forms Conditioned for Storage and Disposal: Guidance for the Development of Waste Acceptance Criteria. Technical Report IAEA-TECDOC-285, International Atomic Energy Agency, Vienna.

IAEA (2003). Scientific and Technical Basis for the Geological Disposal of Radioactive Wastes. Technical Reports Series No. 413, International Atomic Energy Agency, Vienna.

IAEA (2009). Classification of Radioactive Waste, General Safety Guide. Safety Standards Series No. GSG-1, International Atomic Energy Agency, Vienna.

Irwin, G. R. (1948). Fracture dynamics. In *Fracturing of Metals*, pages 147–166, Cleveland. American Society for Metals.

Issen, K. A. and Rudnicki, J. W. (2000). Conditions for compaction bands in porous rock. *J Geophys Res*, 105(B9):21529–21536.

Issen, K. A. and Rudnicki, J. W. (2001). Theory of compaction bands in porous rock. *Phys Chem Earth (A)*, 26(1-2):95–100.

Jaeger, J. C. (1960). Shear failure of anisotropic rocks. *Geol Mag*, 97(1):65–72.

Jaeger, J. C. (1971). Friction of rocks and stability of rock slopes. *Géotechnique*, 21(2):97–134.

Jaumann, G. (1911). *Geschlossenes System physikalischer und chemischer Differentialgesetze*, volume 120, pages 385–530. Sitzgsber. Akad. Wiss. Wien.

Jennings, J. E. (1960). A revised effective stress law for use in the prediction of the behaviour of unsaturated soils. In *Pore Pressure and Suction in Soils*, pages 26–30, London. Butterworths.

Jennings, J. E. B. and Burland, J. B. (1962). Limitations to the use of effective stresses in partly saturated soils. *Géotechnique*, 12(2):125–144.

Jenq, Y. S. and Shah, S. P. (1988). Mixed-mode fracture of concrete. *Int J Fracture*, 38(2):123–142.

Jia, Y., Bian, H. B., Duveau, G., Su, K., and Shao, J. F. (2008). Hydromechanical modelling of shaft excavation in Meuse/Haute-Marne laboratory. *Phys Chem Earth*, 33:S422–S435.

Jia, Y., Song, X. C., Duveau, G., Su, K., and Shao, J. F. (2007). Elastoplastic damage modelling of argillite in partially saturated condition and application. *Phys Chem Earth*, 32:656–666.

Jirásek, M. and Rolshoven, S. (2009). Localization properties of strain-softening gradient plasticity models. part i: Strain-gradient theories. *Int J Solids Struct*, 46(11-12):2225–2238.

Kachanov, L. M. (1958). Time of the rupture process under creep conditions. *Izv Akad Nauk SSR Otd Tech Nauk*, 8:26–31.

Kachanov, M. (1993). *Advances in applied mechanics*, volume 30, chapter Elastic Slids with Many Cracks Related Problems, pages 259–445. Academic Press Inc.

Kanatani, K. I. (1984). Distribution of directional data and fabric tensors. *Int J Eng Sci*, 22(2):149–164.

Khoa, H. D. V., Georgopoulos, I. O., Darve, F., and Laouafa, F. (2006). Diffuse failure in geomaterials: Experiments and modelling. *Comput Geotech*, 33(1):1–14.

Kickmaier, W. and McKinley, I. (1997). A review of research carried out in European rock laboratories. *Nucl Eng Des*, 176(1-2):75–81.

Kim, J. S., Kwon, S. K., Sanchez, M., and Cho, G. C. (2011). Geological storage of high level nuclear waste. *KSCE J Civ Eng*, 15(4):721–737.

Kotronis, P., Collin, F., Bésuelle, P., Chambon, R., and Mazars, J. (2007). Local Second Gradient Models and Damage Mechanics: 1D Post-Localization Studies in Concrete Specimens. In Exadaktylos, G. and Vardoulakis, I., editors, *Bifurcation, Instabilities and Degradation in Geomechanics*, pages 127–142. Springer.

Kotronis, P., Holo, S. A., Bésuelle, P., and Chambon, R. (2008). Shear softening and localization: Modelling the evolution of the width of the shear zone. *Acta Geotechnica*, 3(2):85–97.

Kowalski, S. J. (2003). *Thermomechanics of Drying Processes*, volume 8 of *Lecture Notes in Applied and Computational Mechanics*. Springer, Berlin Heidelberg.

Krajcinovic, D. (1996). *Damage mechanics*. North-Holland.

Labalette, T., Harman, A., Dupuis, M. C., and Ouzounian, G. (2013). Cigéo, the French Geological Repository Project. Phoenix, Arizona, USA. Waste Management Conference.

Lade, P. V. (2007). Modeling failure in cross-anisotropic frictional materials. *Int J Solids Struct*, 44(16):5146–5162.

Lade, P. V., Nam, J., and Hong, W. P. (2008). Shear banding and cross-anisotropic behavior observed in laboratory sand tests with stress rotation. *Can Geotech J*, 45(1):74–84.

Langer, M. (1999). Principles of geomechanical safety assessment for radioactive waste disposal in salt structures. *Eng Geol*, 52(3-4):257–269.

Lasry, D. and Belytschko, T. (1988). Localization limiters in transient problems. *Int J Solids Struct*, 24(6):581–597.

Lekhnitskii, S. G. (1963). *Theory of Elasticity of an Anisotropic Elastic Body*. Holden-Day, San Francisco.

Lenoir, N. (2006). *Comportement mécanique et rupture dans les roches argileuses étudiés par micro tomographie à rayons X*. PhD thesis, Université Joseph Fourier, Grenoble.

Lenoir, N., Bornert, M., Desrues, J., Bésuelle, P., and Viggiani, G. (2007). Volumetric digital image correlation applied to X-ray microtomography images from triaxial compression tests on argillaceous rock. *Strain*, 43(3):193–205.

Levasseur, S., Bésuelle, P., Collin, F., Chambon, R., Charlier, R., and Viggiani, C. (2009). EDZ in clayey rocks: which effect on permeability? In Li, X., Jing, L., and Blaser, P., editors, *Impact of thermo-hydro-mechanical-chemical (THMC) processes on the safety of underground radioactive waste repositories. Proceedings of the European Commission TIMODAZ-THERESA International Conference*, pages 173–183, Luxembourg. European Commission.

Levasseur, S., Charlier, R., Frieg, B., and Collin, F. (2010). Hydro-mechanical modelling of the excavation damaged zone around an underground excavation at Mont Terri Rock Laboratory. *Int J Rock Mech Min Sci*, 47(3):414–425.

Levasseur, S., Collin, F., Charlier, R., and Kondo, D. (2013). A micro-macro approach of permeability evolution in rocks excavation damaged zones. *Comput Geotech*, 49:245–252.

Lewis, R. W. and Schrefler, B. A. (2000). *The Finite Element Method in the Static and Dynamic Deformation and Consolidation of Porous Media*. Wiley, New York.

Lisjak, A., Figi, D., and Grasselli, G. (2014). Fracture development around deep underground excavations: Insights from FDEM modelling. *J Rock Mech Geotech Eng*, 6(6):493–505.

Liu, J., Elsworth, D., and Brady, B. H. (1999). Linking stress-dependent effective porosity and hydraulic conductivity fields to RMR. *Int J Rock Mech Min Sci*, 36(5):581–596.

Léonard, A., Blacher, S., Marchot, P., and Crine, M. (2002). Use of X-ray microtomography to follow the convective heat drying of wastewater sludges. *Dry Technol*, 20(4-5):1053–1069.

Léonard, A., Blacher, S., Marchot, P., Pirard, J. P., and Crine, M. (2003). Image analysis of X-ray microtomograms of soft materials during convective drying. *J Microsc*, 212(Pt2):197–204.

Léonard, A., Blacher, S., Marchot, P., Pirard, J. P., and Crine, M. (2004). Measurement of shrinkage and cracks associated to convective drying of soft materials by X-ray microtomography. *Dry Technol*, 22(7):1695–1708.

Léonard, A., Blacher, S., Marchot, P., Pirard, J. P., and Crine, M. (2005). Convective drying of wastewater sludges: Influence of air temperature, superficial velocity and humidity on the kinetics. *Dry Technol*, 23(8):1667–1679.

Loret, B. and Prevost, J. (1991). Dynamic strain localization in fluid-saturated porous media. *J Eng Mech*, 117(4):907–922.

Love, A. E. H. (1927). *A treatise on the mathematical theory of elasticity*. Cambridge University Press, 4th ed. edition.

Maleki, K. and Poya, A. (2010). Numerical simulation of damage-permeability relationship in brittle geomaterials. *Comput Geotech*, 37(5):619–628.

Malinsky, L. (2009). *Etude expérimentale et modélisation du comportement hydromécanique et de transfert de matériaux argileux saturés et non-saturés*. PhD thesis, Ecole Polytechnique, Laboratoire de Mécanique des Solides, France.

Malvern, L. E. (1969). *Introduction to the mechanics of a continuous medium*. Prentice-Hall, Englewood Cliffs.

Mandel, J. (1966). *Rheology and Soil Mechanics / Rhéologie et Mécanique des Sols*, chapter Conditions de Stabilité et Postulat de Drucker, pages 58–68. Springer, Berlin Heidelberg.

Marinelli, F., Sieffert, Y., and Chambon, R. (2014). Hydromechanical modelling of an initial boundary value problem: Studies of non-uniqueness with a second gradient continuum. *Int J Solids Struct*.

Marschall, P., Trick, T., Lanyon, G. W., Delay, J., and Shao, H. (2008). Hydro-mechanical evolution of damaged zones around a microtunnel in a claystone formation of the Swiss Jura mountains. San Francisco, California. American Rock Mechanics Association. The 42nd US Rock Mechanics Symposium (USRMS).

Martin, C. D. and Lanyon, G. W. (2004). Excavation Disturbed Zone (EDZ) in Clay Shale : Mont Terri. Technical Report 2001-01, Mont Terri Project. with contributions from P Bossart and P Blümling.

Matray, J. M., Savoye, S., and Cabrera, J. (2007). Desaturation and structure relationships around drifts excavated in the well-compacted Tournemire's argillite (Aveyron, France). *Eng Geol*, 90(1-2):1–16.

Matsushima, T., Chambon, R., and Caillerie, D. (2000). Comptes rendus de l'académie des sciences - series iib - mechanics-physics-astronomy. *C R Acad Sci II B*, 328(2):179–186.

Matsushima, T., Chambon, R., and Caillerie, D. (2002). Large strain finite element analysis of a local second gradient model: application to localization. *Int J Numer Meth Engng*, 54(4):499–521.

Mayor, J. C., Velasco, M., and García-Siñeriz, J. L. (2007). Ventilation experiment in the Mont Terri underground laboratory. *Phys Chem Earth*, 32(8-14):616–628.

Mehrabadi, M. M. and Cowin, S. C. (1980). Prefailure and post-failure soils plasticity models. *J Eng Mech Div, ASCE*, 106(5):991–1003.

Mindlin, R. D. (1964). Micro-structure in linear elasticity. *Arch Ration Mech An*, 16(1):51–78.

Mindlin, R. D. (1965). Second gradient of strain and surface-tension in linear elasticity. *Int J Solids Struct*, 1:417–438.

M'Jahad, S., Davy, C. A., Bourbon, X., and Skoczylas, F. (2015). Water retention and gas migration of two high-performance concretes after damage. *J Mater Civ Eng*, 27(2). Special issue: Sustainable Materials and Structures, A4014008.

Mokni, M. and Desrues, J. (1999). Strain localisation measurements in undrained plane-strain biaxial test on Hostun RF sand. *Mech Cohes-Frict Mat*, 4(4):419–441.

Moës, N., Dolbow, J., and Belytschko, T. (1999). A finite element method for crack growth without remeshing. *Int J Numer Meth Engng*, 46(1):131–150.

Mualem, Y. (1976). A new model for predicting the hydraulic conductivity of unsaturated porous media. *Water Resour Res*, 12(3):513–522.

Nadeau, J. P. and Puiggali, J. R. (1995). *Séchage - Des processus physiques aux procédés industriels*. Technique et Documentation - Lavoisier, Paris, France.

Nasrallah, S. B. and Perre, P. (1988). Detailed study of a model of heat and mass transfer during convective drying of porous media. *Int J Heat Mass Transfer*, 31(5):957–967.

NEA (2003). Engineered Barrier Systems and the Safety of Deep Geological Repositories. Sate-of-the-art report, OECD-Nuclear Energy Agency, Paris.

NEA (2008). Moving Forward with Geological Disposal of Radioactive Waste, A Collective Statement by the NEA Radioactive Waste Management Commitee (RWMC). Technical report, OECD-Nuclear Energy Agency, Paris.

Neerdael, B. and Boyazis, J. P. (1997). The Belgium underground research facility: Status on the demonstration issues for radioactive waste disposal in clay. *Nucl Eng Des*, 176(1-2):89–96.

Niandou, H., Shao, J. F., Henry, J. P., and Fourmaintraux, D. (1997). Laboratory investigation of the mechanical behaviour of tournemire shale. *Int J Rock Mech Min Sci*, 34(1):3–16.

Nuth, M. and Laloui, L. (2008a). Advances in modelling hysteretic water retention curve in deformable soils. *Comput Geotech*, 35(6):835–844.

Nuth, M. and Laloui, L. (2008b). Effective stress concept in unsaturated soils: Clarification and validation of a unified framework. *Int J Numer Anal Meth Geomech*, 32(7):771–801.

Ochiai, H. and Lade, P. V. (1983). Three-Dimensional Behavior of Sand with Anisotropic Fabric. *J Geotech Engrg*, 109(10):1313–1328.

Oda, M., Nemat-Nasser, S., and Konishi, J. (1985). Stress-induced anisotropy in granular masses. *Soils Found*, 25(3):85–97.

Olivella, S. and Alonso, E. E. (2008). Gas flow through clay barriers. *Géotechnique*, 58(3):157–176.

Olivella, S., Carrera, J., Gens, A., and Alonso, E. E. (1994). Nonisothermal multiphase flow of brine and gas through saline media. *Transp Porous Med*, 15(3):271–293.

Olsson, R. and Barton, N. (2001). An improved model for hydromechanical coupling during shearing of rock joints. *Int J Rock Mech Min Sci*, 38(3):317–329.

Orowan, E. (1949). Fracture and strength of solids. *Rep Prog Phys*, 12(185).

Panday, S. and Corapcioglu, M. Y. (1989). Reservoir transport equations by compositional approach. *Transp Porous Med*, 4(4):369–393.

Panet, M. and Guellec, P. (1974). Contribution à l'étude du soutènement d'un tunnel à l'arrière du front de taille. In *Advances in rock mechanics, Proceedings of the 3rd International Congress on Rock Mechanics*, volume II, Denver. International Society Rock Mechanics.

Panet, M. and Guenot, A. (1982). Analysis of convergence behind the face of a tunnel. In *Proceedings of the 3rd International Symposium : Tunnelling 82*, pages 197–204, Brighton. Institution of Mining and Metallurgy.

Papanastasiou, P. C. and Vardoulakis, I. G. (1992). Numerical treatment of progressive localization in relation to borehole stability. *Int J Numer Anal Meth Geomech*, 16(6):389–424.

Pardoen, B. and Collin, F. (2016). Modelling the influence of strain localisation and viscosity on the behaviour of underground drifts drilled in claystone. *Comput Geotech.* in press, doi: 10.1016/j.compgeo.2016.05.017.

Pardoen, B., Collin, F., and Charlier, R. (2011). Modélisation de l'argilite perturbée - Localisation des déformations. Technical report, ULg, Liège, Belgium.

Pardoen, B., Collin, F., Levasseur, S., and Charlier, R. (2014a). Andra - GL Geomechanics - Transversal action " Models ", Phase 3: Underground structure modelling. Technical report, ULg, Liège, Belgium.

Pardoen, B., Levasseur, S., and Collin, F. (2014b). Excavation damaged zone modelling including hydraulic permeability evolution in unsaturated argilaceous rock. In Khalili, N., Russell, A. R., and Khoshghalb, A., editors, *Unsaturated Soils: Research and Applications*, pages 1387–1393, London. CRC Press. doi: 10.1201/b17034-203.

Pardoen, B., Levasseur, S., and Collin, F. (2015a). Using Local Second Gradient Model and Shear Strain Localisation to Model the Excavation Damaged Zone in Unsaturated Claystone. *Rock Mech Rock Eng*, 48(2):691–714. doi: 10.1007/s00603-014-0580-2.

Pardoen, B., Levasseur, S., and Collin, F. (2015b). Using shear strain localisation to model the fracturing around gallery in unsaturated Callovo-Oxfordian claystone. In Chau, K. T. and Zhao, J., editors, *Bifurcation and Degradation of Geomaterials in the New Millennium*, Springer Series in Geomechanics and Geoengineering, pages 285–291. Springer. doi: 10.1007/978-3-319-13506-9_41.

Pardoen, B., Seyedi, D. M., and Collin, F. (2015c). Shear banding modelling in cross-anisotropic rocks. *Int J Solids Struct*, 72:63–87. doi: 10.1016/j.ijsolstr.2015.07.012.

Pardoen, B., Talandier, J., Charlier, R., Collin, F., and Radu, J. P. (2012a). Hydro and hydro-mechanical modelling of ventilation test in clayey rocks. In Mancuso, C., Jommi, C., and D'Onza, F., editors, *Unsaturated Soils: Research and Applications*, pages 325–332, Berlin Heidelberg. Springer. doi: 10.1007/978-3-642-31343-1_41.

Pardoen, B., Talandier, J., Charlier, R., Collin, F., and Radu, J. P. (2012b). Modélisation numérique d'un essai de ventilation in situ. In Skoczylas, F., Davy, C. A., Agostini, F., and Burlion, N., editors, *Propriétés de transfert des géomatériaux, Transfert 2012*, pages 420–428. Ecole centrale de Lille.

Pardoen, B., Talandier, J., and Collin, F. (2016). Permeability evolution and water transfer in the excavation damaged zone of a ventilated gallery. *Int J Rock Mech Min Sci*, 85:192–208. doi: 10.1016/j.ijrmms.2016.03.007.

Peerlings, R. H. J., de Borst, R., Brekelmans, W. A. M., and de Vree, J. H. P. (1996a). Gradient enhanced damage for quasi-brittle materials. *Int J Numer Meth Engng*, 39(19):3391–3403.

Peerlings, R. H. J., de Borst, R., Brekelmans, W. A. M., de Vree, J. H. P., and Spee, I. (1996b). Some observations on localisation in non-local and gradient damage models. *Eur J Mech A/Solids*, 15(6):937–953.

Peerlings, R. H. J., Geers, M. G. D., de Borst, R., and Brekelmans, W. A. M. (2001). A critical comparison of nonlocal and gradient-enhanced softening continua. *Int J Solids Struct*, 38(44-45):7723–7746.

Pereira, J. M. and Arson, C. (2013). Retention and permeability properties of damaged porous rocks. *Comput Geotech*, 48:272–282.

Peron, H., Hueckel, T., Laloui, L., and Hu, L. B. (2009a). Fundamentals of desiccation cracking of fine-grained soils: experimental characterisation and mechanisms identification. *Can Geotech J*, 46(10):1177–1201.

Peron, H., Laloui, L., Hueckel, T., and Liang, B. H. (2009b). Desiccation cracking of soils. *Eur J Environ Civ Eng*, 13(7-8):869–888.

Perzyna, P. (1966). Fundamental problems in viscoplasticity. *Adv Appl Mech*, 9:243–377.

Philip, J. R. and de Vries, D. A. (1957). Moisture movement in porous materials under temperature gradients. *Eos, Trans Amer Geophys Union*, 38(2):222–232.

Pietruszczak, S. (2010). *Fundamentals of plasticity in geomechanics*, chapter 7, Description of inherent anisotropy in geomaterials, pages 133–156. CRC Press/Balkema, Leiden, The Netherlands.

Pietruszczak, S., Lydzba, D., and Shao, J. F. (2002). Modelling of inherent anisotropy in sedimentary rocks. *Int J Solids Struct*, 39(3):637–648.

Pietruszczak, S. and Mroz, Z. (2000). Formulation of anisotropic failure criteria incorporating a microstructure tensor. *Comput Geotech*, 26:105–112.

Pietruszczak, S. and Mroz, Z. (2001). On failure criteria for anisotropic cohesive-frictional materials. *Int J Numer Anal Meth Geomech*, 25:509–524.

Pietruszczak, S. and Pande, G. N. (2001). Description of soil anisotropy based on multi-laminate framework. *Int J Numer Anal Meth Geomech*, 25(2):197–206.

Pietruszczak, S. T. and Mróz, Z. (1981). Finite element analysis of deformation of strain-softening materials. *Int J Numer Meth Engng*, 17(3):327–334.

Pijaudier-Cabot, G. and Bazant, Z. P. (1987). Nonlocal damage theory. *J Eng Mech*, 113(10):1512–1533.

Pintado, X., Lloret, A., and Romero, E. (2009). Assessment of the use of the vapour equilibrium technique in controlled-suction tests. *Can Geotech J*, 46(4):411–423.

Plassart, R., Fernandes, R., Giraud, A., Hoxha, D., and Laigle, F. (2013). Hydromechanical modelling of an excavation in an underground research laboratory with an elastoviscoplastic behaviour law and regularization by second gradient of dilation. *Int J Rock Mech Min Sci*, 58:23–33.

Pollock, D. W. (1986). Simulation of fluid flow and energy transport processes associated with high-level radioactive waste disposal in unsaturated alluvium. *Water Resour Res*, 22(5):765–775.

Raniecki, B. and Bruhns, O. T. (1981). Bounds to bifurcation stresses in solids with non-associated plastic flow law at finite strain. *J Mech Phys Solids*, 29(2):153–172.

Rice, J. R. (1976). The localization of plastic deformation. In Koiter, W. T., editor, *Theoretical and Applied Mechanics*, volume 1, pages 207–220. North-Holland Publishing Company.

Rice, J. R. and Rudnicki, J. W. (1980). A note on some features of the theory of localization of deformation. *Int J Solids Struct*, 16:597–605.

Roger, V., Desrues, J., and Viggiani, G. (1998). Experiments on strain localisation in dense sand under isochoric conditions. In Adachi, T., Oka, F., and Yashima, A., editors, *Localization and Bifurcation Theory for Soils and Rocks*, pages 239–248, Rotterdam. Balkema.

Romero, E., Gens, A., and Lloret, A. (2001). Temperature effects on the hydraulic behaviour of an unsaturated clay. *Geotech Geol Eng*, 19(3-4):311–332.

Roscoe, K. H. (1970). The influence of strains in soils mechanics. *Géotechnique*, 20(2):129–170. Tenth Rankine lecture.

Rudnicki, J. W. and Rice, J. R. (1975). Conditions for the localisation of deformation in pressure sensitive dilatant materials. *J Mech Phys Solids*, 23:371–394.

Rutqvist, J., Barr, D., Datta, R., Gens, A., Millard, A., Olivella, S., Tsang, C. F., and Tsang, Y. (2005). Coupled thermal-hydrological-mechanical analyses of the Yucca Mountain Drift Scale Test - Comparison of field measurements to predictions of four different numerical models. *Int J Rock Mech Min Sci*, 42(5-6):680–697.

Salehnia, F., Collin, F., Li, X. L., Dizier, A., Sillen, X., and Charlier, R. (2015). Coupled modeling of Excavation Damaged Zone in Boom clay: Strain localization in rock and distribution of contact pressure on the gallery's lining. *Comput Geotech*, 69:396–410.

Schrefler, B. A. (1984). *The finite element method in soil consolidation (with applications to surface subsidence)*. PhD thesis, University College of Swansea.

Seyedi, D., Poutrel, A., Armand, G., and Plas, F. (2012). Action "Modèles" transverse au GL "Géomécanique" et au Programme de simulation de l'Andra - Phase 2 : cas tests sur des chemins de sollicitation simples. Technical Report CG.RP.AMFS.12.0038, Andra.

Seyedi, D., Poutrel, A., Armand, G., and Plas, F. (2013). Action "Modèles" transverse au GL "Géomécanique" et au Programme de simulation de l'Andra (ups4) - Phase 3 : modélisation des ouvrages. Technical Report CG.RP.AMFS.13.0031, Andra.

Shao, J. F., Chau, K. T., and Feng, X. T. (2006a). Modeling of anisotropic damage and creep deformation in brittle rocks. *Int J Rock Mech Min Sci*, 43(4):582–592.

Shao, J. F., Duveau, G., Bourgeois, F., and Chen, W. Z. (2006b). Elastoplastic damage modeling in unsaturated rocks and applications. *Int J Geomech*, 6(2):119–130.

Shao, J. F., Zhu, Q. Z., and Su, K. (2003). Modeling of creep in rock materials in terms of material degradation. *Comput Geotech*, 30(7):549–555.

Shuttle, D. A. and Smith, I. M. (1988). Numerical simulation of shear band formation in soils. *Int J Numer Anal Meth Geomech*, 12:611–626.

Sieffert, Y., al Holo, S., and Chambon, R. (2009). Loss of uniqueness of numerical solutions of the borehole problem modelled with enhanced media. *Int J Solids Struct*, 46(17):3173–3197.

Sieffert, Y., Buzzi, O., and Collin, F. (2014). Numerical study of shear band instability and effect of cavitation on the response of a specimen under undrained biaxial loading. *Int J Solids Struct*, 51(9):1686–1696.

Simo, J. C., Oliver, J., and Armero, F. (1993). An analysis of strong discontinuities induced by strain-softening in rate-independent inelastic solids. *Comput Mech*, 12(5):277–296.

Skempton, A. W. (1960). Effective stress in soils, concrete and rocks. In *Pore Pressure and Suction in Soils*, pages 4–16, London. Butterworths.

Snow, D. T. (1969). Anisotropic Permeability of Fractured Media. *Water Resour Res*, 5(6):1273–1289.

Suklje, L. (1969). *Rheological Aspects of Soil Mechanics*. Wiley, New York.

Ta, A. N. (2009). *Etude de l'interaction sol-atmosphère en chambre environnementale*. PhD thesis, Ecole Nationale des Ponts et Chaussées, Paris.

Tejchman, J., Bauer, E., and Wu, W. (2007). Effect of fabric anisotropy on shear localization in sand during plane strain compression. *Acta Mech*, 189(1-2):23–51.

Terzaghi, K. (1936). The shearing resistance of saturated soils and the angle between planes of shear. In *International Conference on Soil Mechanics and Foundation Engineering*, pages 54–56, Cambridge, MA. Harvard University Press.

Thakur, V. (2007). *Strain localization in sensitive soft clays*. PhD thesis, Norwegian University of Science and Technology, Trondheim.

Toupin, R. (1962). Elastic materials with couple-stresses. *Arch Ration Mech An*, 11(1):385–414.

Triantafyllidis, N. (1980). Bifurcation phenomena in pure bending. *J Mech Phys Solids*, 28(3-4):221–245.

Tsang, C. F. and Bernier, F. (2004). Definitions of excavation disturbed zone and excavation damaged zone, in Impact of the excavation disturbed or damaged zone (EDZ) on the performance of radioactive waste geological repositories. In *Proceedings European Commission CLUSTER Conference and Workshop on EDZ in Radioactive Waste Geological Repositories*, Luxembourg.

Tsang, C. F., Bernier, F., and Davies, C. (2005). Geohydromechanical processes in the Excavation Damaged Zone in crystalline rock, rock salt, and indurated and plastic clays - in the context of radioactive waste disposal. *Int J Rock Mech Min Sci*, 42(1):109–125.

Valès, F., Minh, D. N., Gharbi, H., and Rejeb, A. (2004). Experimental study of the influence of the degree of saturation on physical and mechanical properties in tournemire shale (france). *Appl Clay Sci*, 26(1-4):197–207.

Van Eekelen, H. A. M. (1980). Isotropic yield surfaces in three dimensions for use in soil mechanics. *Int J Numer Anal Meth Geomech*, 4(1):98–101.

van Genuchten, M. T. (1980). A closed-form equation for predicting the hydraulic conductivity of unsaturated soils. *Soil Sci Soc Am J*, 44(5):892–898.

Vardoulakis, I. (1979). Bifurcation analysis of the triaxial test on sand samples. *Acta Mech*, 32(1-3):35–54.

Vardoulakis, I. (1980). Shear band inclination and shear modulus of sand in biaxial tests. *Int J Numer Anal Meth Geomech*, 4(2):103–119.

Vardoulakis, I. (1981). Bifurcation analysis of the plane rectilinear deformation on dry sand samples. *Int J Solids Struct*, 17(11):1085–1101.

Vardoulakis, I., Goldscheider, M., and Gudehus, Q. (1978). Formation of shear bands in sand bodies as a bifurcation problem. *Int J Numer Anal Meth Geomech*, 2(2):99–128.

Vardoulakis, I. and Sulem, J. (1995). *Bifurcation Analysis in Geomechanics*. Blackie Academic and Professional.

Viggiani, G. and Desrues, J. (2004). *Geotechnical Innovations*, chapter Experimental observation of shear banding in stiff clay, pages 649–658. Verlag Glückauf, Essen.

Viggiani, G., Lenoir, N., Bésuelle, P., Di Michiel, M., Marello, S., Desrues, J., and Kretzschmer, M. (2004). X-ray microtomography for studying localized deformation in fine-grained geomaterials under triaxial compression. *C R Mecanique*, 332(10):819–826.

Walsh, J. B. and Brace, W. F. (1964). A Fracture Criterion for Brittle Anisotropic Rock. *J Geophys Res*, 69(16):3449–5346.

Wang, X. (1993). *Modélisation numérique des problèmes avec localisation de la déformation en bandes de cisaillement*. PhD thesis, Université de Liège, Liège.

Weast, R. C. (1971). *Handbook of Chemistry and Physics*. CRC Press, Cleveland, 51th ed. edition.

Wileveau, Y. and Bernier, F. (2008). Similarities in the hydromechanical response of Callovo-Oxfordian clay and Boom Clay during gallery excavation. *Phys Chem Earth*, 33(1):S343–S349.

Wileveau, Y., Cornet, F. H., Desroches, J., and Blumling, P. (2007). Complete in situ stress determination in an argillite sedimentary formation. *Phys Chem Earth*, 32(8-14):866–878.

Witherspoon, P. A., Wang, J. S. Y., Iwai, K., and Gale, J. E. (1980). Validity of cubic law for fluid flow in a deformable rock fracture. *Water Resour Res*, 16(6):1016–1024.

Wu, S. and Wang, X. (2010). Mesh Dependence and Nonlocal Regularization of One-Dimensional Strain Softening Plasticity. *J Eng Mech*, 136(11):1354–1365.

Xu, X. P. and Needleman, A. (1994). Numerical simulations of fast crack growth in brittle solids. *J Mech Phys Solids*, 42(9):1397–1434.

Yang, D., Chanchole, S., Valli, P., and Chen, L. (2013). Study of the anisotropic properties of argillite under moisture and mechanical loads. *Rock Mech Rock Eng*, 46(2):247–257.

Young, J. F. (1967). Humidity control in the laboratory using salt solutions-a review. *J Appl Chem*, 17(9):241–245.

Zauderer, E. (1989). *Partial Differential Equations of Applied Mathematics*. Wiley, Chichester,UK, second ed. edition.

Zervos, A., Papanastasiou, P., and Vardoulakis, I. (2001a). Modelling of localisation and scale effect in thick-walled cylinders with gradient elastoplasticity. *Int J Solids Struct*, 38(30-31):5081–5095.

Zervos, A., Papanastasious, P., and Vardoulakis, I. (2001b). A finite element displacement formulation for gradient elastoplasticity. *Int J Numer Meth Engng*, 50(6):1369–1388.

Zhang, H. W., Sanavia, L., and Schrefler, B. A. (2001). Numerical analysis of dynamic strain localisation in initially water saturated dense sand with a modified generalised plasticity model. *Comput Struct*, 79(4):441–459.

Zhao, J. and Pedroso, D. (2008). Strain gradient theory in orthogonal curvilinear coordinates. *Int J Solids Struct*, 45(11-12):3507–3520.

Zheng, H., Dai, H. C., and Liu, D. F. (2009). A variational inequality formulation for unconfined seepage problems in porous media. *Comput Geotech*, 33(1):437–450.

Zhong, Z. and Mackerle, J. (1992). Static contact problems - a review. *Eng Computation*, 9(1):3–37.

Zhou, H., Jia, Y., and Shao, J. F. (2008). A unified elastic-plastic and viscoplastic damage model for quasi-brittle rocks. *Int J Rock Mech Min Sci*, 45(8):1237–1251.

Zhu, Q. Z., Shao, J. F., and Kondo, D. (2008). A micromechanics-based non-local anisotropic model for unilateral damage in brittle materials. *C R Mecanique*, 336(3):320–328.

Zienkiewicz, O. C. and Taylor, R. L. (2000). *The Finite Element Method*. Butterworth-Heinemann, Stonchem, MA, fifth edition edition.

Appendices

A Linearisation of the field equations for the coupled local second gradient model

The linearisation of the field equations (Eqs. 4.39, 4.40, and 4.41) of the coupled local second gradient model, leading to the linear auxiliary problem (Eq. 4.63), is detailed hereafter. It accounts for unsaturated conditions, compressibility of the fluid and of the solid grains, permeability anisotropy as well as permeability variation. The theoretical aspects are not recalled, only the linearisation is realised. These novelties are implemented in the non-linear finite element code Lagamine developed at the University of Liège (Charlier, 1987; Collin, 2003). Please refer to sections 3.3 and 4.1 for more details on the coupled local second gradient model for microstructure media and its implementation in finite element methods.

It is to recall that, for finite element formulation, the non-linear balance equation system of the coupled second gradient model is numerically solved by time discretisation, over finite time steps Δt with $\tau = t + \Delta t$, and by iterative procedure. A full Newton-Raphson method and an implicit scheme (finite differences) for the rate of any quantity a, $\dot{a}^\tau = (a^\tau - a^t)/\Delta t$, are used.

In the following developments, the stress and strain fields are defined under the material mechanic convention in which tensile stress and strain are positive. This convention is chosen in accordance with the one of the non-linear finite element code Lagamine in which the equations are implemented.

A.1 Balance equations

The balance equations, the linear auxiliary problem, and the element stiffness matrix are recalled hereafter. The system of non-linear balance equations for the coupled second gradient model is obtained by defining two configurations at the end of the time step ($\Omega^{\tau 1}$ and $\Omega^{\tau 2}$) and non-equilibrium forces ($\Delta_1^{\tau 1}$, $\Delta_2^{\tau 1}$, and $\Delta_3^{\tau 1}$):

$$\begin{aligned}
&\int_{\Omega^{\tau 1}} \frac{\partial u_i^*}{\partial x_l^{\tau 1}} \left(\sigma_{ij}^{\tau 2} \, \frac{\partial x_l^{\tau 1}}{\partial x_j^{\tau 2}} \, det(F) - \sigma_{il}^{\tau 1} \right) + \frac{\partial \upsilon_{ij}^*}{\partial x_l^{\tau 1}} \left(\Sigma_{ijk}^{\tau 2} \, \frac{\partial x_l^{\tau 1}}{\partial x_k^{\tau 2}} \, det(F) - \Sigma_{ijl}^{\tau 1} \right) d\Omega^{\tau 1} \\
&- \int_{\Omega^{\tau 1}} \frac{\partial u_i^*}{\partial x_l^{\tau 1}} \left(\lambda_{ij}^{\tau 2} \, \frac{\partial x_l^{\tau 1}}{\partial x_j^{\tau 2}} \, det(F) - \lambda_{il}^{\tau 1} \right) - \upsilon_{ij}^* \left(\lambda_{ij}^{\tau 2} \, det(F) - \lambda_{ij}^{\tau 1} \right) d\Omega^{\tau 1} \\
&- \int_{\Omega^{\tau 1}} u_i^* \left(\rho^{\tau 2} \, det(F) - \rho^{\tau 1} \right) g_i \, d\Omega^{\tau 1} = -\Delta_1^{\tau 1}
\end{aligned} \tag{1}$$

$$\int_{\Omega^{\tau 1}} \lambda_{ij}^* \left(\left(\frac{\partial u_i^{\tau 2}}{\partial x_k^{\tau 1}} \, \frac{\partial x_k^{\tau 1}}{\partial x_j^{\tau 2}} \, det(F) - \frac{\partial u_i^{\tau 1}}{\partial x_j^{\tau 1}} \right) - \left(\upsilon_{ij}^{\tau 2} \, det(F) - \upsilon_{ij}^{\tau 1} \right) \right) d\Omega^{\tau 1} = -\Delta_2^{\tau 1} \tag{2}$$

$$\int_{\Omega^{\tau 1}} p_w^* \left(\dot{M}_w^{\tau 2} \, det(F) - \dot{M}_w^{\tau 1} \right) - \frac{\partial p_w^*}{\partial x_l^{\tau 1}} \left(f_{w,i}^{\tau 2} \, \frac{\partial x_l^{\tau 1}}{\partial x_i^{\tau 2}} \, det(F) - f_{w,l}^{\tau 1} \right) d\Omega^{\tau 1} = -\Delta_3^{\tau 1} \tag{3}$$

A.2 Linearisation

Variations

By making the two configurations $\Omega^{\tau 1}$ and $\Omega^{\tau 2}$ tend towards each other, the variations between them can be defined by finite differences for any quantity a as:

$$da^{\tau 1} = a^{\tau 2} - a^{\tau 1} \tag{4}$$

They read for the unknown fields:

$$du_i^{\tau 1} = dx_i^{\tau 1} = x_i^{\tau 2} - x_i^{\tau 1} \tag{5}$$

$$d\upsilon_{ij}^{\tau 1} = \upsilon_{ij}^{\tau 2} - \upsilon_{ij}^{\tau 1} \tag{6}$$

$$d\lambda_{ij}^{\tau 1} = \lambda_{ij}^{\tau 2} - \lambda_{ij}^{\tau 1} \tag{7}$$

$$dp_w^{\tau 1} = p_w^{\tau 2} - p_w^{\tau 1} \tag{8}$$

Including the Biot's effective stress definition for unsaturated materials of Eq. 4.24 and the stress-strain constitutive relations of Eqs. 4.5 and 4.6 gives:

$$d\sigma_{ij}^{\tau 1} = \sigma_{ij}^{\tau 2} - \sigma_{ij}^{\tau 1} = d\sigma_{ij}^{'\tau 1} - b\ S_{r,w}^{\tau 1}\ dp_w^{\tau 1}\delta_{ij} \tag{9}$$

$$d\sigma_{ij}^{'\tau 1} = \sigma_{ij}^{'\tau 2} - \sigma_{ij}^{'\tau 1} = C_{ijkl}\ \frac{\partial du_k^{\tau 1}}{\partial x_l^{\tau 1}} \tag{10}$$

$$d\Sigma_{ijk}^{\tau 1} = \Sigma_{ijk}^{\tau 2} - \Sigma_{ijk}^{\tau 1} = D_{ijklmn}\frac{\partial d\upsilon_{lm}^{\tau 1}}{\partial x_n^{\tau 1}} \tag{11}$$

The variations of the phases densities can also be linearised from Eqs. 4.13 and 4.25:

$$d\rho_w^{\tau 1} = \rho_w^{\tau 2} - \rho_w^{\tau 1} = \rho_w^{\tau 1}\frac{dp_w^{\tau 1}}{\chi_w} \tag{12}$$

$$d\rho_s^{\tau 1} = \rho_s^{\tau 2} - \rho_s^{\tau 1} = \rho_s^{\tau 1}\frac{\left(b-\Phi^{\tau 1}\right)S_{r,w}^{\tau 1}\ dp_w^{\tau 1} - d\sigma'^{\tau 1}}{\left(1-\Phi^{\tau 1}\right)\ K_s} \tag{13}$$

they lead to the variations of porosity and mixture density by Eqs. 4.26 and 4.12:

$$d\Phi^{\tau 1} = \Phi^{\tau 2} - \Phi^{\tau 1} = \left(1-\Phi^{\tau 1}\right)\left(\frac{\left(b-\Phi^{\tau 1}\right)S_{r,w}^{\tau 1}\ dp_w^{\tau 1} - d\sigma'^{\tau 1}}{\left(1-\Phi^{\tau 1}\right)\ K_s} + d\varepsilon_v^{\tau 1}\right) \tag{14}$$

$$d\rho^{\tau 1} = \rho^{\tau 2} - \rho^{\tau 1} = d\rho_s^{\tau 1}\ \left(1-\Phi^{\tau 1}\right) - \rho_s^{\tau 1}\ d\Phi^{\tau 1} + dS_{r,w}^{\tau 1}\ \rho_w^{\tau 1}\ \Phi^{\tau 1} + S_{r,w}^{\tau 1}\ d\rho_w^{\tau 1}\ \Phi^{\tau 1} + S_{r,w}^{\tau 1}\ \rho_w^{\tau 1}\ d\Phi^{\tau 1} \tag{15}$$

with:

$$d\varepsilon_v^{\tau 1} = \frac{d\Omega^{\tau 1}}{\Omega^{\tau 1}} = \frac{\partial du_i^{\tau 1}}{\partial x_i^{\tau 1}} \tag{16}$$

The balance equations can be rewritten by taking into account the above variations.

Moreover, the Jacobian matrix $\overline{F}_{ij}$ of the transformation between the two configurations $\Omega^{\tau 1}$ and $\Omega^{\tau 2}$ is approximated by using a Taylor expansion and by retaining only the linear approximation (Chambon and Moullet, 2004), meaning that the terms of degree greater than one are discarded:

$$\overline{F}_{ij} = \frac{\partial x_i^{\tau 2}}{\partial x_j^{\tau 1}} = \frac{\partial\left(x_i^{\tau 1} + du_i^{\tau 1}\right)}{\partial x_j^{\tau 1}} \approx \delta_{ij} + \frac{\partial du_i^{\tau 1}}{\partial x_j^{\tau 1}} \tag{17}$$

The Jacobian determinant becomes:

$$det(F) = \left|\frac{\partial x_i^{\tau 2}}{\partial x_j^{\tau 1}}\right| \approx 1 + \frac{\partial du_i^{\tau 1}}{\partial x_i^{\tau 1}} \tag{18}$$

Similarly and by applying the limit $\tau 2 = \tau 1$, the inverse relation yields:

$$\frac{\partial x_i^{\tau 1}}{\partial x_j^{\tau 2}} = \frac{\partial\left(x_i^{\tau 2} - du_i^{\tau 1}\right)}{\partial x_j^{\tau 2}} \approx \delta_{ij} - \frac{\partial du_i^{\tau 1}}{\partial x_j^{\tau 2}} \approx \delta_{ij} - \frac{\partial du_i^{\tau 1}}{\partial x_j^{\tau 1}} \tag{19}$$

Balance of momentum of the mixture

The development relative to the mixture momentum balance equation 1 are firstly considered. The first term can be rewritten as:

$$\begin{aligned}\sigma_{ij}^{\tau 2}\ \frac{\partial x_l^{\tau 1}}{\partial x_j^{\tau 2}}\ det(F) - \sigma_{il}^{\tau 1} &= \sigma_{ij}^{\tau 2}\ \left(\delta_{jl} - \frac{\partial\left(x_l^{\tau 2} - x_l^{\tau 1}\right)}{\partial x_j^{\tau 2}}\right) det(F) - \sigma_{il}^{\tau 1} \\ &= \sigma_{il}^{\tau 2}\ det(F) - \sigma_{ij}^{\tau 2}\ \frac{\partial\left(x_l^{\tau 2} - x_l^{\tau 1}\right)}{\partial x_j^{\tau 2}}\ det(F) - \sigma_{il}^{\tau 1} \\ &= \left(\sigma_{il}^{\tau 2} - \sigma_{il}^{\tau 1}\right) - \sigma_{ij}^{\tau 2}\ \frac{\partial\left(x_l^{\tau 2} - x_l^{\tau 1}\right)}{\partial x_j^{\tau 2}}\ det(F) + \sigma_{il}^{\tau 2}\left(det(F) - 1\right)\end{aligned} \tag{20}$$

Taking into account the variations defined previously and making the two configurations tend towards each other, which leads to the limit $\tau 2 = \tau 1$, allows to rewrite Eq. 20 as follows:

$$\sigma_{ij}^{\tau 2}\ \frac{\partial x_l^{\tau 1}}{\partial x_j^{\tau 2}}\ det(F) - \sigma_{il}^{\tau 1} = d\sigma_{il}^{\tau 1} - \sigma_{ij}^{\tau 1}\ \frac{\partial du_l^{\tau 1}}{\partial x_j^{\tau 1}} + \sigma_{il}^{\tau 1}\ \frac{\partial du_m^{\tau 1}}{\partial x_m^{\tau 1}} \tag{21}$$

where terms of order higher than one are neglected. The stress definition and the elastoplastic constitutive law can be added, which gives:

$$\sigma_{ij}^{\tau 2}\ \frac{\partial x_l^{\tau 1}}{\partial x_j^{\tau 2}}\ det(F) - \sigma_{il}^{\tau 1} = C_{ilnp}\ \frac{\partial du_n^{\tau 1}}{\partial x_p^{\tau 1}} - b\ S_{r,w}^{\tau 1}\ dp_w^{\tau 1}\ \delta_{il} - \sigma_{ij}^{\tau 1}\ \frac{\partial du_l^{\tau 1}}{\partial x_j^{\tau 1}} + \sigma_{il}^{\tau 1}\ \frac{\partial du_m^{\tau 1}}{\partial x_m^{\tau 1}} \tag{22}$$

The other terms of the mixture momentum balance equation are obtained with similar development as in Eq. 21:

$$\Sigma_{ijk}^{\tau 2}\ \frac{\partial x_l^{\tau 1}}{\partial x_k^{\tau 2}}\ det(F) - \Sigma_{ijl}^{\tau 1} = d\Sigma_{ijl}^{\tau 1} - \Sigma_{ijk}^{\tau 1}\ \frac{\partial du_l^{\tau 1}}{\partial x_k^{\tau 1}} + \Sigma_{ijl}^{\tau 1}\ \frac{\partial du_m^{\tau 1}}{\partial x_m^{\tau 1}} \tag{23}$$

$$\lambda_{ij}^{\tau 2}\ \frac{\partial x_l^{\tau 1}}{\partial x_j^{\tau 2}}\ det(F) - \lambda_{il}^{\tau 1} = d\lambda_{il}^{\tau 1} - \lambda_{ij}^{\tau 1}\ \frac{\partial du_l^{\tau 1}}{\partial x_j^{\tau 1}} + \lambda_{il}^{\tau 1}\ \frac{\partial du_m^{\tau 1}}{\partial x_m^{\tau 1}} \tag{24}$$

$$\lambda_{ij}^{\tau 2}\ det(F) - \lambda_{ij}^{\tau 1} = d\lambda_{ij}^{\tau 1} + \lambda_{ij}^{\tau 1}\ \frac{\partial du_m^{\tau 1}}{\partial x_m^{\tau 1}} \tag{25}$$

$$\rho^{\tau 2}\ det(F) - \rho^{\tau 1} = d\rho^{\tau 1} + \rho^{\tau 1}\frac{\partial du_m^{\tau 1}}{\partial x_m^{\tau 1}} \tag{26}$$

The latter can be developed by including the densities and porosity variations of Eqs. 13 to 15:

$$\begin{aligned}\rho^{\tau 2}\ det(F) - \rho^{\tau 1} = \rho_s^{\tau 1} &\left(\frac{\left(b - \Phi^{\tau 1}\right) S_{r,w}^{\tau 1}\ dp_w^{\tau 1} - d\sigma'^{\tau 1}}{K_s}\right) \\ &- \left(\rho_s^{\tau 1} - S_{r,w}^{\tau 1}\ \rho_w^{\tau 1}\right)\left(1 - \Phi^{\tau 1}\right)\left(\frac{\left(b - \Phi^{\tau 1}\right) S_{r,w}^{\tau 1}\ dp_w^{\tau 1} - d\sigma'^{\tau 1}}{\left(1 - \Phi^{\tau 1}\right)\ K_s} + \frac{\partial du_m^{\tau 1}}{\partial x_m^{\tau 1}}\right) \\ &+ dS_{r,w}^{\tau 1}\ \rho_w^{\tau 1}\ \Phi^{\tau 1} + S_{r,w}^{\tau 1}\ \rho_w^{\tau 1}\ \frac{dp_w^{\tau 1}}{\chi_w}\ \Phi^{\tau 1} + \rho^{\tau 1}\frac{\partial du_m^{\tau 1}}{\partial x_m^{\tau 1}}\end{aligned} \tag{27}$$

By regrouping the different terms, the balance equation is finally rewritten as follows:

$$\begin{aligned}
&\int_{\Omega^{\tau 1}} \frac{\partial u_i^*}{\partial x_l^{\tau 1}} \left[C_{ilnp}\ \frac{\partial du_n^{\tau 1}}{\partial x_p^{\tau 1}} - b\ S_{r,w}^{\tau 1}\ dp_w^{\tau 1}\ \delta_{il} - \sigma_{ij}^{\tau 1}\ \frac{\partial du_l^{\tau 1}}{\partial x_j^{\tau 1}} + \sigma_{il}^{\tau 1}\ \frac{\partial du_m^{\tau 1}}{\partial x_m^{\tau 1}} \right] \\
&\quad + \frac{\partial v_{ij}^*}{\partial x_l^{\tau 1}} \left[d\Sigma_{ijl}^{\tau 1} - \Sigma_{ijk}^{\tau 1}\ \frac{\partial du_l^{\tau 1}}{\partial x_k^{\tau 1}} + \Sigma_{ijl}^{\tau 1}\ \frac{\partial du_m^{\tau 1}}{\partial x_m^{\tau 1}} \right] d\Omega^{\tau 1} \\
&- \int_{\Omega^{\tau 1}} \frac{\partial u_i^*}{\partial x_l^{\tau 1}} \left[d\lambda_{il}^{\tau 1} - \lambda_{ij}^{\tau 1}\ \frac{\partial du_l^{\tau 1}}{\partial x_j^{\tau 1}} + \lambda_{il}^{\tau 1}\ \frac{\partial du_m^{\tau 1}}{\partial x_m^{\tau 1}} \right] - v_{ij}^* \left[d\lambda_{ij}^{\tau 1} + \lambda_{ij}^{\tau 1}\ \frac{\partial du_m^{\tau 1}}{\partial x_m^{\tau 1}} \right] d\Omega^{\tau 1} \\
&- \int_{\Omega^{\tau 1}} u_i^* \left[\rho_s^{\tau 1} \left(\frac{\left(b - \Phi^{\tau 1}\right) S_{r,w}^{\tau 1}\ dp_w^{\tau 1} - d\sigma'^{\tau 1}}{K_s} \right) \right. \\
&\quad - \left(\rho_s^{\tau 1} - \rho_w^{\tau 1} S_{r,w}^{\tau 1}\right) \left(1 - \Phi^{\tau 1}\right) \left(\frac{\left(b - \Phi^{\tau 1}\right) S_{r,w}^{\tau 1}\ dp_w^{\tau 1} - d\sigma'^{\tau 1}}{\left(1 - \Phi^{\tau 1}\right)\ K_s} + \frac{\partial du_m^{\tau 1}}{\partial x_m^{\tau 1}} \right) \\
&\quad \left. + \rho_w^{\tau 1}\ \frac{dp_w^{\tau 1}}{\chi_w}\ \Phi^{\tau 1}\ S_{r,w}^{\tau 1} + \rho_w^{\tau 1}\ \Phi^{\tau 1}\ dS_{r,w}^{\tau 1} + \rho^{\tau 1}\ \frac{\partial du_m^{\tau 1}}{\partial x_m^{\tau 1}} \right] g_i\ d\Omega^{\tau 1} = -\Delta_1^{\tau 1}
\end{aligned} \tag{28}$$

Kinematic constraint

The kinematic constraint corresponding to micro-macro continuity of the deformation gradient fields is solved in Eq. 2. With similar developments, the first term of this equation becomes:

$$\begin{aligned}
\frac{\partial u_i^{\tau 2}}{\partial x_k^{\tau 1}}\ \frac{\partial x_k^{\tau 1}}{\partial x_j^{\tau 2}}\ det(F) - \frac{\partial u_i^{\tau 1}}{\partial x_j^{\tau 1}} &= \left(\frac{\partial u_i^{\tau 1}}{\partial x_k^{\tau 1}} + \frac{\partial du_i^{\tau 1}}{\partial x_k^{\tau 1}} \right) \left(\delta_{jk} - \frac{\partial du_k^{\tau 1}}{\partial x_j^{\tau 2}} \right) det(F) - \frac{\partial u_i^{\tau 1}}{\partial x_j^{\tau 1}} \\
&= \frac{\partial u_i^{\tau 1}}{\partial x_j^{\tau 1}}\ det(F) + \frac{\partial du_i^{\tau 1}}{\partial x_j^{\tau 1}}\ det(F) - \frac{\partial u_i^{\tau 1}}{\partial x_k^{\tau 1}}\ \frac{\partial du_k^{\tau 1}}{\partial x_j^{\tau 2}}\ det(F) \\
&\quad - \frac{\partial du_i^{\tau 1}}{\partial x_k^{\tau 1}}\ \frac{\partial du_k^{\tau 1}}{\partial x_j^{\tau 2}}\ det(F) - \frac{\partial u_i^{\tau 1}}{\partial x_j^{\tau 1}}
\end{aligned} \tag{29}$$

As previously, by making the two configurations tend towards each other ($\tau 2 = \tau 1$) and by neglecting terms of order higher than one, it becomes:

$$\frac{\partial u_i^{\tau 2}}{\partial x_k^{\tau 1}}\ \frac{\partial x_k^{\tau 1}}{\partial x_j^{\tau 2}}\ det(F) - \frac{\partial u_i^{\tau 1}}{\partial x_j^{\tau 1}} = \frac{\partial du_i^{\tau 1}}{\partial x_j^{\tau 1}} + \frac{\partial u_i^{\tau 1}}{\partial x_j^{\tau 1}}\ \frac{\partial du_m^{\tau 1}}{\partial x_m^{\tau 1}} - \frac{\partial u_i^{\tau 1}}{\partial x_k^{\tau 1}}\ \frac{\partial du_k^{\tau 1}}{\partial x_j^{\tau 1}} \tag{30}$$

The second term of the equation reads:

$$v_{ij}^{\tau 2}\ det(F) - v_{ij}^{\tau 1} = dv_{ij}^{\tau 1} + v_{ij}^{\tau 1}\ \frac{\partial du_m^{\tau 1}}{\partial x_m^{\tau 1}} \tag{31}$$

Thus the equation becomes:

$$\int_{\Omega^{\tau 1}} \lambda_{ij}^* \left[\left(\frac{\partial u_i^{\tau 1}}{\partial x_j^{\tau 1}} - v_{ij}^{\tau 1} \right) \frac{\partial du_m^{\tau 1}}{\partial x_m^{\tau 1}} + \frac{\partial du_i^{\tau 1}}{\partial x_j^{\tau 1}} - \frac{\partial u_i^{\tau 1}}{\partial x_k^{\tau 1}}\ \frac{\partial du_k^{\tau 1}}{\partial x_j^{\tau 1}} - dv_{ij}^{\tau 1} \right] d\Omega^{\tau 1} = -\Delta_2^{\tau 1} \tag{32}$$

Water mass balance equation

The water mass balance equation is detailed in Eq. 3. The first term becomes:

$$\dot{M}_w^{\tau 2} detF - \dot{M}_w^{\tau 1} = d\dot{M}_w^{\tau 1} + \dot{M}^{\tau 1} \frac{\partial du_m^{\tau 1}}{\partial x_m^{\tau 1}} \tag{33}$$

The variation of the water mass storage term:

$$d\dot{M}_w^{\tau 1} = \dot{M}_w^{\tau 2} - \dot{M}_w^{\tau 1} \tag{34}$$

can be developed by using Eq. 4.27:

$$\begin{aligned}
d\dot{M}_w^{\tau 1} &= \dot{M}_w^{\tau 2} - \dot{M}_w^{\tau 1} \\
&= d\rho_w^{\tau 1}\ \frac{\dot{p}_w^{\tau 1}}{\chi_w}\ \Phi^{\tau 1}\ S_{r,w}^{\tau 1} + \rho_w^{\tau 1}\ \frac{d\dot{p}_w^{\tau 1}}{\chi_w}\ \Phi^{\tau 1}\ S_{r,w}^{\tau 1} + \rho_w^{\tau 1}\ \frac{\dot{p}_w^{\tau 1}}{\chi_w}\ d\Phi^{\tau 1}\ S_{r,w}^{\tau 1} + \rho_w^{\tau 1}\ \frac{\dot{p}_w^{\tau 1}}{\chi_w}\ \Phi^{\tau 1}\ dS_{r,w}^{\tau 1} \\
&+ d\rho_w^{\tau 1}\ \frac{\left(b-\Phi^{\tau 1}\right)\left(S_{r,w}^{\tau 1}\right)^2\ \dot{p}_w^{\tau 1}}{K_s} - \rho_w^{\tau 1}\ \frac{d\Phi^{\tau 1}\left(S_{r,w}^{\tau 1}\right)^2\ \dot{p}_w^{\tau 1}}{K_s} + \rho_w^{\tau 1}\ \frac{\left(b-\Phi^{\tau 1}\right) 2\ S_{r,w}^{\tau 1}\ dS_{r,w}^{\tau 1}\ \dot{p}_w^{\tau 1}}{K_s} \\
&+ \rho_w^{\tau 1}\ \frac{\left(b-\Phi^{\tau 1}\right)\left(S_{r,w}^{\tau 1}\right)^2\ d\dot{p}_w^{\tau 1}}{K_s} + d\rho_w^{\tau 1}\ \left(\dot{\varepsilon}_v^{\tau 1} - \frac{\dot{\sigma}'^{\tau 1}}{K_s}\right)\ S_{r,w}^{\tau 1} + \rho_w^{\tau 1}\ \left(d\dot{\varepsilon}_v^{\tau 1} - \frac{d\dot{\sigma}'^{\tau 1}}{K_s}\right) S_{r,w}^{\tau 1} \\
&+ \rho_w^{\tau 1}\left(\dot{\varepsilon}_v^{\tau 1} - \frac{\dot{\sigma}'^{\tau 1}}{K_s}\right) dS_{r,w}^{\tau 1} + d\rho_w^{\tau 1}\ \Phi^{\tau 1}\ \dot{S}_{r,w}^{\tau 1} + \rho_w^{\tau 1}\ d\Phi^{\tau 1}\ \dot{S}_{r,w}^{\tau 1} + \rho_w^{\tau 1}\ \Phi^{\tau 1}\ d\dot{S}_{r,w}^{\tau 1}
\end{aligned} \tag{35}$$

where:

$$d\dot{p}_w^{\tau 1} = \frac{dp_w^{\tau 1}}{\Delta t} \quad , \quad d\dot{S}_{r,w}^{\tau 1} = \frac{dS_{r,w}^{\tau 1}}{\Delta t} \quad , \quad d\dot{\sigma}'^{\tau 1} = \frac{d\sigma'^{\tau 1}}{\Delta t} \tag{36}$$

with Δt being the time step and $dS_{r,w}^{\tau 1}$ depending on the choice of the retention curve. Furthermore, $d\dot{\varepsilon}_v^{\tau 1}$ is obtained as follows:

$$\begin{aligned}
d\dot{\varepsilon}_v^{\tau 1} &= d\left(\frac{\dot{\Omega}^{\tau 1}}{\Omega^{\tau 1}}\right) = \frac{\dot{\Omega}^{\tau 2}}{\Omega^{\tau 2}} - \frac{\dot{\Omega}^{\tau 1}}{\Omega^{\tau 1}} = \frac{\dot{\Omega}^{\tau 2}}{\Omega^{\tau 2}} - \frac{\dot{\Omega}^{\tau 1}}{\Omega^{\tau 2}} - \frac{\dot{\Omega}^{\tau 1}}{\Omega^{\tau 1}} + \frac{\dot{\Omega}^{\tau 1}}{\Omega^{\tau 2}} \\
&= \frac{\dot{\Omega}^{\tau 2} - \dot{\Omega}^{\tau 1}}{\Omega^{\tau 2}} - \frac{\dot{\Omega}^{\tau 1}}{\Omega^{\tau 1}}\left(1 - \frac{\Omega^{\tau 1}}{\Omega^{\tau 2}}\right) = \frac{\Omega^{\tau 2} - \Omega^{\tau 1}}{\Omega^{\tau 2}\ \Delta t} - \frac{\dot{\Omega}^{\tau 1}}{\Omega^{\tau 1}}\left(\frac{\Omega^{\tau 2} - \Omega^{\tau 1}}{\Omega^{\tau 2}}\right)
\end{aligned} \tag{37}$$

which becomes by applying the limit $\tau 2 = \tau 1$:

$$d\dot{\varepsilon}_v^{\tau 1} = \frac{d\Omega^{\tau 1}}{\Omega^{\tau 1}\ \Delta t} - \frac{\dot{\Omega}^{\tau 1}}{\Omega^{\tau 1}}\frac{d\Omega^{\tau 1}}{\Omega^{\tau 1}} = \frac{d\Omega^{\tau 1}}{\Omega^{\tau 1}}\left(\frac{1}{\Delta t} - \frac{\dot{\Omega}^{\tau 1}}{\Omega^{\tau 1}}\right) = \frac{\partial du_m^{\tau 1}}{\partial x_m^{\tau 1}}\left(\frac{1}{\Delta t} - \dot{\varepsilon}_v^{\tau 1}\right) \tag{38}$$

After including the different variations, Eq. 33 becomes:

$$\begin{aligned}
&\dot{M}_w^{\tau 2} detF - \dot{M}_w^{\tau 1} = \\
&\rho_w^{\tau 1}\ \frac{dp_w^{\tau 1}}{\chi_w}\ \frac{\dot{p}_w^{\tau 1}}{\chi_w}\ \Phi^{\tau 1}\ S_{r,w}^{\tau 1} + \rho_w^{\tau 1}\ \frac{dp_w^{\tau 1}}{\chi_w\ \Delta t}\ \Phi^{\tau 1}\ S_{r,w}^{\tau 1} \\
&+ \rho_w^{\tau 1}\ \frac{\dot{p}_w^{\tau 1}}{\chi_w}\ \left(1-\Phi^{\tau 1}\right)\left(\frac{\left(b-\Phi^{\tau 1}\right) S_{r,w}^{\tau 1}\ dp_w^{\tau 1} - d\sigma'^{\tau 1}}{\left(1-\Phi^{\tau 1}\right)\ K_s} + \frac{\partial du_m^{\tau 1}}{\partial x_m^{\tau 1}}\right) S_{r,w}^{\tau 1} + \rho_w^{\tau 1}\ \frac{\dot{p}_w^{\tau 1}}{\chi_w}\ \Phi^{\tau 1}\ dS_{r,w}^{\tau 1} \\
&+ \rho_w^{\tau 1}\ \frac{dp_w^{\tau 1}}{\chi_w}\ \frac{\left(b-\Phi^{\tau 1}\right)\left(S_{r,w}^{\tau 1}\right)^2\ \dot{p}_w^{\tau 1}}{K_s} - \rho_w^{\tau 1}\ \frac{\left(S_{r,w}^{\tau 1}\right)^2\ \dot{p}_w^{\tau 1}}{K_s}\left(1-\Phi^{\tau 1}\right)\left(\frac{\left(b-\Phi^{\tau 1}\right) S_{r,w}^{\tau 1}\ dp_w^{\tau 1} - d\sigma'^{\tau 1}}{\left(1-\Phi^{\tau 1}\right)\ K_s} + \frac{\partial du_m^{\tau 1}}{\partial x_m^{\tau 1}}\right) \\
&+ \rho_w^{\tau 1}\ \frac{\left(b-\Phi^{\tau 1}\right) 2\ S_{r,w}^{\tau 1}\ dS_{r,w}^{\tau 1}\ \dot{p}_w^{\tau 1}}{K_s} + \rho_w^{\tau 1}\ \frac{\left(b-\Phi^{\tau 1}\right)\left(S_{r,w}^{\tau 1}\right)^2\ dp_w^{\tau 1}}{K_s\ \Delta t} + \rho_w^{\tau 1}\ \frac{dp_w^{\tau 1}}{\chi_w}\left(\dot{\varepsilon}_v^{\tau 1} - \frac{\dot{\sigma}'^{\tau 1}}{K_s}\right) S_{r,w}^{\tau 1} \\
&+ \rho_w^{\tau 1}\ \left(\frac{\partial du_m^{\tau 1}}{\partial x_m^{\tau 1}}\left(\frac{1}{\Delta t} - \frac{\dot{\Omega}^{\tau 1}}{\Omega^{\tau 1}}\right) - \frac{d\sigma'^{\tau 1}}{K_s\ \Delta t}\right) S_{r,w}^{\tau 1} + \rho_w^{\tau 1}\ \left(\dot{\varepsilon}_v^{\tau 1} - \frac{\dot{\sigma}'^{\tau 1}}{K_s}\right) dS_{r,w}^{\tau 1} + \rho_w^{\tau 1}\ \frac{dp_w^{\tau 1}}{\chi_w}\ \Phi^{\tau 1}\ \dot{S}_{r,w}^{\tau 1} \\
&+ \rho_w^{\tau 1}\ \left(1-\Phi^{\tau 1}\right)\left(\frac{\left(b-\Phi^{\tau 1}\right) S_{r,w}^{\tau 1}\ dp_w^{\tau 1} - d\sigma'^{\tau 1}}{\left(1-\Phi^{\tau 1}\right)\ K_s} + \frac{\partial du_m^{\tau 1}}{\partial x_m^{\tau 1}}\right)\dot{S}_{r,w}^{\tau 1} + \rho_w^{\tau 1}\ \Phi^{\tau 1}\ \frac{dS_{r,w}^{\tau 1}}{\Delta t} + \dot{M}^{\tau 1}\ \frac{\partial du_m^{\tau 1}}{\partial x_m^{\tau 1}}
\end{aligned} \tag{39}$$

The second term of the water mass balance equation, that includes the water flow, becomes:

$$f_{w,i}^{\tau 2}\ \frac{\partial x_l^{\tau 1}}{\partial x_i^{\tau 2}}\ det(F) - f_{w,l}^{\tau 1} = df_{w,l}^{\tau 1} - f_{w,i}^{\tau 1}\ \frac{\partial du_l^{\tau 1}}{\partial x_i^{\tau 1}} + f_{w,l}^{\tau 1}\ \frac{\partial du_m^{\tau 1}}{\partial x_m^{\tau 1}} \tag{40}$$

The variation of the water flow:

$$df_{w,l}^{\tau 1} = f_{w,l}^{\tau 2} - f_{w,l}^{\tau 1} \tag{41}$$

can be developed by using Eq. 4.14:

$$\begin{aligned} df_{w,l}^{\tau 1} &= f_{w,l}^{\tau 2} - f_{w,l}^{\tau 1} \\ &= -d\rho_w^{\tau 1}\ \frac{k_{w,lj}^{\tau 1}\ k_{r,w}^{\tau 1}}{\mu_w}\ \left(\frac{\partial p_w^{\tau 1}}{\partial x_j^{\tau 1}} + \rho_w^{\tau 1}\ g_j\right) - \rho_w^{\tau 1}\ \frac{dk_{w,lj}^{\tau 1}\ k_{r,w}^{\tau 1}}{\mu_w}\ \left(\frac{\partial p_w^{\tau 1}}{\partial x_j^{\tau 1}} + \rho_w^{\tau 1}\ g_j\right) \\ &\quad - \rho_w^{\tau 1}\ \frac{k_{w,lj}^{\tau 1}\ dk_{r,w}^{\tau 1}}{\mu_w}\ \left(\frac{\partial p_w^{\tau 1}}{\partial x_j^{\tau 1}} + \rho_w^{\tau 1}\ g_j\right) - \rho_w^{\tau 1}\ \frac{k_{w,lj}^{\tau 1}\ k_{r,w}^{\tau 1}}{\mu_w}\ \left(d\left(\frac{\partial p_w^{\tau 1}}{\partial x_j^{\tau 1}}\right) + d\rho_w^{\tau 1}\ g_j\right) \end{aligned} \tag{42}$$

where $dk_{w,lj}^{\tau 1}$ and $dk_{r,w}^{\tau 1}$ depend on the chosen intrinsic permeability variation and water relative permeability curve. However, it is noteworthy to mentioned the following development which includes the limit:

$$\begin{aligned} d\left(\frac{\partial p_w^{\tau 1}}{\partial x_j^{\tau 1}}\right) &= \frac{\partial p_w^{\tau 2}}{\partial x_j^{\tau 2}} - \frac{\partial p_w^{\tau 1}}{\partial x_j^{\tau 1}} = \frac{\partial p_w^{\tau 2}}{\partial x_i^{\tau 1}}\ \frac{\partial x_i^{\tau 1}}{\partial x_j^{\tau 2}} - \frac{\partial p_w^{\tau 1}}{\partial x_j^{\tau 1}} = \frac{\partial p_w^{\tau 2}}{\partial x_i^{\tau 1}}\left(\delta_{ij} - \frac{\partial du_i^{\tau 1}}{\partial x_j^{\tau 2}}\right) - \frac{\partial p_w^{\tau 1}}{\partial x_j^{\tau 1}} \\ &= \frac{\partial p_w^{\tau 2}}{\partial x_j^{\tau 1}} - \frac{\partial p_w^{\tau 2}}{\partial x_i^{\tau 1}}\ \frac{\partial du_i^{\tau 1}}{\partial x_j^{\tau 2}} - \frac{\partial p_w^{\tau 1}}{\partial x_j^{\tau 1}} = \frac{\partial dp_w^{\tau 1}}{\partial x_j^{\tau 1}} - \frac{\partial p_w^{\tau 1}}{\partial x_i^{\tau 1}}\ \frac{\partial du_i^{\tau 1}}{\partial x_j^{\tau 1}} \end{aligned} \tag{43}$$

The expression of Eq. 40 can then be rewritten as:

$$\begin{aligned} &f_{w,i}^{\tau 2}\ \frac{\partial x_l^{\tau 1}}{\partial x_i^{\tau 2}}\ det(F) - f_{w,l}^{\tau 1} = \\ &\quad - \rho_w^{\tau 1}\ \frac{dp_w^{\tau 1}}{\chi_w}\ \frac{k_{w,lj}^{\tau 1}\ k_{r,w}^{\tau 1}}{\mu_w}\left(\frac{\partial p_w^{\tau 1}}{\partial x_j^{\tau 1}} + \rho_w^{\tau 1}\ g_j\right) - \rho_w^{\tau 1}\ \frac{k_{w,lj}^{\tau 1}\ k_{r,w}^{\tau 1}}{\mu_w}\left(\frac{\partial dp_w^{\tau 1}}{\partial x_j^{\tau 1}} + \rho_w^{\tau 1}\ \frac{dp_w^{\tau 1}}{\chi_w}\ g_j\right) \\ &\quad - \rho_w^{\tau 1}\ \frac{dk_{w,lj}^{\tau 1}\ k_{r,w}^{\tau 1}}{\mu_w}\left(\frac{\partial p_w^{\tau 1}}{\partial x_j^{\tau 1}} + \rho_w^{\tau 1}\ g_j\right) - \rho_w^{\tau 1}\ \frac{k_{w,lj}^{\tau 1}\ dk_{r,w}^{\tau 1}}{\mu_w}\left(\frac{\partial p_w^{\tau 1}}{\partial x_j^{\tau 1}} + \rho_w^{\tau 1}\ g_j\right) \\ &\quad + \rho_w^{\tau 1}\ \frac{k_{w,lj}^{\tau 1}\ k_{r,w}^{\tau 1}}{\mu_w}\ \frac{\partial p_w^{\tau 1}}{\partial x_k^{\tau 1}}\ \frac{\partial du_k^{\tau 1}}{\partial x_j^{\tau 1}} - f_{w,i}^{\tau 1}\ \frac{\partial du_l^{\tau 1}}{\partial x_i^{\tau 1}} + f_{w,l}^{\tau 1}\ \frac{\partial du_m^{\tau 1}}{\partial x_m^{\tau 1}} \end{aligned} \tag{44}$$

and by regrouping the different terms, the balance equation becomes:

$$
\begin{aligned}
&\int_{\Omega^{\tau 1}} p_w^* \left[\rho_w^{\tau 1} \, \frac{dp_w^{\tau 1}}{\chi_w} \, \frac{\dot{p}_w^{\tau 1}}{\chi_w} \, \Phi^{\tau 1} \, S_{r,w}^{\tau 1} + \rho_w^{\tau 1} \, \frac{dp_w^{\tau 1}}{\chi_w \, \Delta t} \, \Phi^{\tau 1} \, S_{r,w}^{\tau 1} \right. \\
&\quad + \rho_w^{\tau 1} \, \frac{\dot{p}_w^{\tau 1}}{\chi_w} \, \left(1 - \Phi^{\tau 1}\right) \left(\frac{\left(b - \Phi^{\tau 1}\right) S_{r,w}^{\tau 1} \, dp_w^{\tau 1} - d\sigma'^{\tau 1}}{\left(1 - \Phi^{\tau 1}\right) \, K_s} + \frac{\partial du_m^{\tau 1}}{\partial x_m^{\tau 1}} \right) S_{r,w}^{\tau 1} \\
&\quad + \rho_w^{\tau 1} \, \frac{\dot{p}_w^{\tau 1}}{\chi_w} \, \Phi^{\tau 1} \, dS_{r,w}^{\tau 1} + \rho_w^{\tau 1} \, \frac{dp_w^{\tau 1}}{\chi_w} \left(b - \Phi^{\tau 1}\right) \frac{\dot{p}_w^{\tau 1}}{K_s} \, \left(S_{r,w}^{\tau 1}\right)^2 \\
&\quad - \rho_w^{\tau 1} \, \frac{\dot{p}_w^{\tau 1}}{K_s} \left(1 - \Phi^{\tau 1}\right) \left(\frac{\left(b - \Phi^{\tau 1}\right) S_{r,w}^{\tau 1} \, dp_w^{\tau 1} - d\sigma'^{\tau 1}}{\left(1 - \Phi^{\tau 1}\right) \, K_s} + \frac{\partial du_m^{\tau 1}}{\partial x_m^{\tau 1}} \right) \left(S_{r,w}^{\tau 1}\right)^2 \\
&\quad + 2 \, \rho_w^{\tau 1} \left(b - \Phi^{\tau 1}\right) \frac{\dot{p}_w^{\tau 1}}{K_s} \, S_{r,w}^{\tau 1} \, dS_{r,w}^{\tau 1} + \rho_w^{\tau 1} \left(b - \Phi^{\tau 1}\right) \frac{dp_w^{\tau 1}}{K_s \, \Delta t} \, \left(S_{r,w}^{\tau 1}\right)^2 \\
&\quad + \rho_w^{\tau 1} \, \frac{dp_w^{\tau 1}}{\chi_w} \left(\dot{\varepsilon}_v^{\tau 1} - \frac{\dot{\sigma}'^{\tau 1}}{K_s} \right) S_{r,w}^{\tau 1} + \rho_w^{\tau 1} \left(\frac{\partial du_m^{\tau 1}}{\partial x_m^{\tau 1}} \left(\frac{1}{\Delta t} - \frac{\dot{\Omega}^{\tau 1}}{\Omega^{\tau 1}} \right) - \frac{d\sigma'^{\tau 1}}{K_s \, \Delta t} \right) S_{r,w}^{\tau 1} \\
&\quad + \rho_w^{\tau 1} \left(\dot{\varepsilon}_v^{\tau 1} - \frac{\dot{\sigma}'^{\tau 1}}{K_s} \right) dS_{r,w}^{\tau 1} + \rho_w^{\tau 1} \, \frac{dp_w^{\tau 1}}{\chi_w} \, \Phi^{\tau 1} \, \dot{S}_{r,w}^{\tau 1} \\
&\quad + \rho_w^{\tau 1} \left(1 - \Phi^{\tau 1}\right) \left(\frac{\left(b - \Phi^{\tau 1}\right) S_{r,w}^{\tau 1} \, dp_w^{\tau 1} - d\sigma'^{\tau 1}}{\left(1 - \Phi^{\tau 1}\right) \, K_s} + \frac{\partial du_m^{\tau 1}}{\partial x_m^{\tau 1}} \right) \dot{S}_{r,w}^{\tau 1} \\
&\quad \left. + \rho_w^{\tau 1} \, \Phi^{\tau 1} \, \frac{dS_{r,w}^{\tau 1}}{\Delta t} + \dot{M}^{\tau 1} \, \frac{\partial du_m^{\tau 1}}{\partial x_m^{\tau 1}} \right] d\Omega^{\tau 1} \\
&- \int_{\Omega^{\tau 1}} \frac{\partial p_w^*}{\partial x_l^{\tau 1}} \left[-\rho_w^{\tau 1} \, \frac{dp_w^{\tau 1}}{\chi_w} \, \frac{k_{w,lj}^{\tau 1} \, k_{r,w}^{\tau 1}}{\mu_w} \left(\frac{\partial p_w^{\tau 1}}{\partial x_j^{\tau 1}} + \rho_w^{\tau 1} \, g_j \right) \right. \\
&\quad - \rho_w^{\tau 1} \, \frac{k_{w,lj}^{\tau 1} \, k_{r,w}^{\tau 1}}{\mu_w} \left(\frac{\partial dp_w^{\tau 1}}{\partial x_j^{\tau 1}} + \rho_w^{\tau 1} \, \frac{dp_w^{\tau 1}}{\chi_w} \, g_j \right) - \rho_w^{\tau 1} \, \frac{dk_{w,lj}^{\tau 1} \, k_{r,w}^{\tau 1}}{\mu_w} \left(\frac{\partial p_w^{\tau 1}}{\partial x_j^{\tau 1}} + \rho_w^{\tau 1} g_j \right) \\
&\quad - \rho_w^{\tau 1} \, \frac{k_{w,lj}^{\tau 1} \, dk_{r,w}^{\tau 1}}{\mu_w} \left(\frac{\partial p_w^{\tau 1}}{\partial x_j^{\tau 1}} + \rho_w^{\tau 1} \, g_j \right) + \rho_w^{\tau 1} \, \frac{k_{w,lj}^{\tau 1} \, k_{r,w}^{\tau 1}}{\mu_w} \, \frac{\partial p_w^{\tau 1}}{\partial x_k^{\tau 1}} \, \frac{\partial du_k^{\tau 1}}{\partial x_j^{\tau 1}} \\
&\quad \left. - f_{w,i}^{\tau 1} \, \frac{\partial du_l^{\tau 1}}{\partial x_i^{\tau 1}} + f_{w,l}^{\tau 1} \, \frac{\partial du_m^{\tau 1}}{\partial x_m^{\tau 1}} \right] d\Omega^{\tau 1} = -\Delta_3^{\tau 1}
\end{aligned}
\tag{45}
$$

Retention and permeability variations

Among various analytical expressions available in the literature, the van Genuchten's model is used (van Genuchten, 1980) for the retention curve:

$$
S_{r,w} = S_{res} + \left(S_{max} - S_{res}\right) \left(1 + \left(\frac{p_c}{P_r} \right)^{\frac{1}{1-\mathcal{M}}} \right)^{-\mathcal{M}} \tag{46}
$$

with $p_c = -p_w$ in the absence of gaseous phase. The time derivative of the degree of water saturation can be obtained:

$$
\dot{S}_{r,w} = \frac{\partial S_{r,w}}{\partial p_w} \, \dot{p}_w \tag{47}
$$

where:

$$
\frac{\partial S_{r,w}}{\partial p_w} = \frac{\left(S_{max} - S_{res}\right) \, \mathcal{M}}{\left(1 - \mathcal{M}\right) P_r^{\frac{1}{1-\mathcal{M}}} \left(1 + \left(\frac{-p_w}{P_r} \right)^{\frac{1}{1-\mathcal{M}}} \right)^{\mathcal{M}+1}} \, \left(-p_w\right)^{\frac{\mathcal{M}}{1-\mathcal{M}}} \tag{48}
$$

for the van Genuchten's model. The variation form of Eq. 47 is:

$$dS_{r,w}^{\tau 1} = S_{r,w}^{\tau 2} - S_{r,w}^{\tau 1} = \frac{\partial S_{r,w}^{\tau 1}}{\partial p_w^{\tau 1}} \; dp_w^{\tau 1} \tag{49}$$

The water relative permeability curve is defined by Mualem - van Genuchten's model (Mualem, 1976; van Genuchten, 1980):

$$k_{r,w} = \sqrt{S_{r,w}} \left(1 - \left(1 - S_{r,w}{}^{\frac{1}{\mathcal{M}}}\right)^{\mathcal{M}}\right)^2 \tag{50}$$

The time derivative of the water relative permeability reads:

$$\dot{k}_{r,w} = \frac{\partial k_{r,w}}{\partial S_{r,w}} \; \dot{S}_{r,w} = \frac{\partial k_{r,w}}{\partial S_{r,w}} \; \frac{\partial S_{r,w}}{\partial p_w} \; \dot{p}_w \tag{51}$$

where:

$$\frac{\partial k_{r,w}}{\partial S_{r,w}} = \frac{1}{2\sqrt{S_{r,w}}} \left(1 - \left(1 - S_{r,w}^{\frac{1}{\mathcal{M}}}\right)^{\mathcal{M}}\right)^2 + 2\sqrt{S_{r,w}} \left(1 - \left(1 - S_{r,w}^{\frac{1}{\mathcal{M}}}\right)^{\mathcal{M}}\right) \; \left(1 - S_{r,w}^{\frac{1}{\mathcal{M}}}\right)^{\mathcal{M}-1} S_{r,w}^{\frac{1}{\mathcal{M}}-1} \tag{52}$$

for the considered model. The variation form of Eq. 51 is:

$$dk_{r,w}^{\tau 1} = k_{r,w}^{\tau 2} - k_{r,w}^{\tau 1} = \frac{\partial k_{r,w}^{\tau 1}}{\partial S_{r,w}^{\tau 1}} \; dS_{r,w}^{\tau 1} = \frac{\partial k_{r,w}^{\tau 1}}{\partial S_{r,w}^{\tau 1}} \; \frac{\partial S_{r,w}^{\tau 1}}{\partial p_w^{\tau 1}} \; dp_w^{\tau 1} \tag{53}$$

Furthermore, the intrinsic water permeability can also evolves. Its time derivative obviously depends on the chosen evolution law and on the considered parameters. If it varies according to a set of parameters $\overline{m}_i$ and with the pore water pressure, the time derivative of the intrinsic permeability reads:

$$\dot{k}_{w,ij} = \frac{\partial k_{w,ij}}{\partial \overline{m}_k} \; \dot{\overline{m}}_k + \frac{\partial k_{w,ij}}{\partial p_w} \; \dot{p}_w \tag{54}$$

The dependence on the pore water pressure can for instance be linked to the effect of porosity variation if the Biot's coefficient is lower than 1 (Eq. 4.26). Among other possibilities, a strain-dependent isotropic evolution of the hydraulic permeability tensor is taken into account in chapter 6, based on a power (cubic) formulation (Pardoen et al., 2014b). Its general expression reads (Eq. 6.33):

$$k_{w,ij} = k_{w,ij,0} \left(1 + \beta_{per} \; \langle \gamma_{per} \rangle^3\right) \tag{55}$$

where $k_{w,ij,0}$ is the initial intrinsic water permeability tensor, β_{per} is an evolution parameter, and γ_{per} is a deformation parameter for which different expressions are envisaged. For such evolution the time derivative of the permeability reads:

$$\dot{k}_{w,ij} = \frac{\partial k_{w,ij}}{\partial \varepsilon_{kl}} \; \dot{\varepsilon}_{kl} = \frac{\partial k_{w,ij}}{\partial \gamma_{per}} \; \frac{\partial \gamma_{per}}{\partial \varepsilon_{kl}} \; \frac{\partial \dot{u}_k}{\partial x_l} = k_{w,ij,0} \; 3 \; \beta_{per} \; \gamma_{per}^2 \; \frac{\partial \gamma_{per}}{\partial \varepsilon_{kl}} \; \frac{\partial \dot{u}_k}{\partial x_l} \tag{56}$$

with $\frac{\partial \gamma_{per}}{\partial \varepsilon_{kl}}$ depending on the expression of γ_{per}. Moreover, the variation forms of Eqs. 54 and 56 read:

$$dk_{w,ij}^{\tau 1} = k_{w,ij}^{\tau 2} - k_{w,ij}^{\tau 1} = \frac{\partial k_{w,ij}^{\tau 1}}{\partial \overline{m}_k^{\tau 1}} \; d\overline{m}_k^{\tau 1} + \frac{\partial k_{w,ij}^{\tau 1}}{\partial p_w^{\tau 1}} \; dp_w^{\tau 1} \tag{57}$$

$$dk_{w,ij}^{\tau 1} = k_{w,ij}^{\tau 2} - k_{w,ij}^{\tau 1} = \frac{\partial k_{w,ij}^{\tau 1}}{\partial \varepsilon_{kl}^{\tau 1}} \; \frac{\partial du_k^{\tau 1}}{\partial x_l^{\tau 1}} \tag{58}$$

A.3 Element stiffness matrix

The linearisation of the field equations leads to a linear auxiliary problem that can be expressed in matricial form as:

$$\int_{\Omega^{\tau 1}} \left[U^{*,\tau 1}_{(x_1,x_2)}\right]^T \left[E^{\tau 1}\right] \left[dU^{\tau 1}_{(x_1,x_2)}\right] d\Omega^{\tau 1} = -\Delta_1^{\tau 1} - \Delta_2^{\tau 1} - \Delta_3^{\tau 1} \tag{59}$$

where the local stiffness (tangent) matrix of an element is defined as follows:

$$\left[E^{\tau 1}\right]_{25\times 25} = \begin{bmatrix} E^{\tau 1}_{1_{4\times 4}} & 0_{4\times 2} & K^{\tau 1}_{WM_{4\times 3}} & 0_{4\times 8} & 0_{4\times 4} & -I_{4\times 4} \\ G^{\tau 1}_{1_{2\times 4}} & 0_{2\times 2} & G^{\tau 1}_{2_{2\times 3}} & 0_{2\times 8} & 0_{2\times 4} & 0_{2\times 4} \\ K^{\tau 1}_{MW_{3\times 4}} & 0_{3\times 2} & K^{\tau 1}_{WW_{3\times 3}} & 0_{3\times 8} & 0_{3\times 4} & 0_{3\times 4} \\ E^{\tau 1}_{2_{8\times 4}} & 0_{8\times 2} & 0_{8\times 3} & D^{\tau 1}_{8\times 8} & 0_{8\times 4} & 0_{8\times 4} \\ E^{\tau 1}_{3_{4\times 4}} & 0_{4\times 2} & 0_{4\times 3} & 0_{4\times 8} & 0_{4\times 4} & I_{4\times 4} \\ E^{\tau 1}_{4_{4\times 4}} & 0_{4\times 2} & 0_{4\times 3} & 0_{4\times 8} & -I_{4\times 4} & 0_{4\times 4} \end{bmatrix} \tag{60}$$

To compute the current element stiffness matrix it is easier to separate the different parts of the coupled problem. The matrices $\left[E^{\tau 1}_1\right]$, $\left[E^{\tau 1}_2\right]$, $\left[E^{\tau 1}_3\right]$, $\left[E^{\tau 1}_4\right]$, and $\left[D^{\tau 1}\right]$ are not developed because they are identical to those used in the local second gradient model for monophasic medium by Chambon and Moullet (2004) ($\left[D^{\tau 1}\right] = D_{ijklmn}$ in Eqs. 3.78 and 3.80). The matrices that are of interest are: the stiffness matrix of the flow problem, $\left[K^{\tau 1}_{WW}\right]$, the matrices of the coupling between the flow and the mechanical problems, $\left[K^{\tau 1}_{MW}\right]$ and $\left[K^{\tau 1}_{WM}\right]$, as well as the matrices related to the contribution of gravity volume force, $\left[G^{\tau 1}_1\right]$ and $\left[G^{\tau 1}_2\right]$.

Influence of the fluid

To determine the influence of the fluid on the mechanics, an identical geometry for the configurations $\Omega^{\tau 1}$ and $\Omega^{\tau 2}$, a different pore water pressure, and no variation of the effective stress can be assumed. Therefore:

$$dp_w^{\tau 1} = p_w^{\tau 2} - p_w^{\tau 1} \tag{61}$$

$$x_i^{\tau 1} = x_i^{\tau 2} \tag{62}$$

$$\sigma_{ij}^{'\tau 1} = \sigma_{ij}^{'\tau 2} \tag{63}$$

which lead to:

$$du_i^{\tau 1} = 0 \quad , \quad d\varepsilon_v^{\tau 1} = 0 \quad , \quad detF = 1 \quad , \quad d\sigma_{ij}^{'\tau 1} = 0 \tag{64}$$

The balance equations become:

$$\begin{aligned} &\int_{\Omega^{\tau 1}} \frac{\partial u_i^*}{\partial x_l^{\tau 1}} \left(-b\ S_{r,w}^{\tau 1}\ dp_w^{\tau 1}\ \delta_{il}\right) + \frac{\partial v_{ij}^*}{\partial x_l^{\tau 1}}\ d\Sigma_{ijl}^{\tau 1}\ d\Omega^{\tau 1} - \int_{\Omega^{\tau 1}} d\lambda_{il}^{\tau 1} \left(\frac{\partial u_i^*}{\partial x_l^{\tau 1}} - v_{il}^*\right) d\Omega^{\tau 1} \\ &- \int_{\Omega^{\tau 1}} u_i^* \left[\rho_w^{\tau 1} \left(b - \Phi^{\tau 1}\right) \frac{dp_w^{\tau 1}}{K_s} \left(S_{r,w}^{\tau 1}\right)^2 + \rho_w^{\tau 1}\ \frac{dp_w^{\tau 1}}{\chi_w}\ \Phi^{\tau 1}\ S_{r,w}^{\tau 1} + \rho_w^{\tau 1}\ \Phi^{\tau 1}\ dS_{r,w}^{\tau 1}\right] g_i\ d\Omega^{\tau 1} \\ &= -\Delta_1^{\tau 1} \end{aligned} \tag{65}$$

$$\int_{\Omega^{\tau 1}} \lambda_{ij}^* \left(-dv_{ij}^{\tau 1}\right) d\Omega^{\tau 1} = -\Delta_2^{\tau 1} \tag{66}$$

$$
\begin{aligned}
&\int_{\Omega^{\tau 1}} p_w^* \Bigg[\rho_w^{\tau 1} \, \frac{dp_w^{\tau 1}}{\chi_w} \, \frac{\dot{p}_w^{\tau 1}}{\chi_w} \, \Phi^{\tau 1} \, S_{r,w}^{\tau 1} + \rho_w^{\tau 1} \, \frac{dp_w^{\tau 1}}{\chi_w \, \Delta t} \, \Phi^{\tau 1} \, S_{r,w}^{\tau 1} \\
&+ 2 \, \rho_w^{\tau 1} \, \frac{\dot{p}_w^{\tau 1}}{\chi_w} \left(b - \Phi^{\tau 1}\right) \frac{dp_w^{\tau 1}}{K_s} \left(S_{r,w}^{\tau 1}\right)^2 + \rho_w^{\tau 1} \, \frac{\dot{p}_w^{\tau 1}}{\chi_w} \, \Phi^{\tau 1} \, dS_{r,w}^{\tau 1} \\
&- \rho_w^{\tau 1} \, \frac{\dot{p}_w^{\tau 1}}{K_s} \left(b - \Phi^{\tau 1}\right) \frac{dp_w^{\tau 1}}{K_s} \left(S_{r,w}^{\tau 1}\right)^3 + 2 \, \rho_w^{\tau 1} \left(b - \Phi^{\tau 1}\right) \frac{\dot{p}_w^{\tau 1}}{K_s} \, S_{r,w}^{\tau 1} \, dS_{r,w}^{\tau 1} \\
&+ \rho_w^{\tau 1} \left(b - \Phi^{\tau 1}\right) \frac{dp_w^{\tau 1}}{K_s \, \Delta t} \left(S_{r,w}^{\tau 1}\right)^2 + \rho_w^{\tau 1} \, \frac{dp_w^{\tau 1}}{\chi_w} \left(\dot{\varepsilon}_v^{\tau 1} - \frac{\dot{\sigma}'^{\tau 1}}{K_s} \right) S_{r,w}^{\tau 1} \\
&+ \rho_w^{\tau 1} \left(\dot{\varepsilon}_v^{\tau 1} - \frac{\dot{\sigma}'^{\tau 1}}{K_s} \right) dS_{r,w}^{\tau 1} + \rho_w^{\tau 1} \, \frac{dp_w^{\tau 1}}{\chi_w} \, \Phi^{\tau 1} \, \dot{S}_{r,w}^{\tau 1} \\
&+ \rho_w^{\tau 1} \left(b - \Phi^{\tau 1}\right) \frac{dp_w^{\tau 1}}{K_s} \, S_{r,w}^{\tau 1} \, \dot{S}_{r,w}^{\tau 1} + \rho_w^{\tau 1} \, \Phi^{\tau 1} \, \frac{dS_{r,w}^{\tau 1}}{\Delta t} \Bigg] d\Omega^{\tau 1} \\
&- \int_{\Omega^{\tau 1}} \frac{\partial p_w^*}{\partial x_l^{\tau 1}} \Bigg[-\rho_w^{\tau 1} \, \frac{dp_w^{\tau 1}}{\chi_w} \, \frac{k_{w,lj}^{\tau 1} \, k_{r,w}^{\tau 1}}{\mu_w} \left(\frac{\partial p_w^{\tau 1}}{\partial x_j^{\tau 1}} + \rho_w^{\tau 1} \, g_j \right) \\
&- \rho_w^{\tau 1} \, \frac{k_{w,lj}^{\tau 1} \, dk_{r,w}^{\tau 1}}{\mu_w} \left(\frac{\partial p_w^{\tau 1}}{\partial x_j^{\tau 1}} + \rho_w^{\tau 1} \, g_j \right) - \rho_w^{\tau 1} \, \frac{k_{r,w}^{\tau 1}}{\mu_w} \, \frac{\partial k_{w,lj}^{\tau 1}}{\partial p_w^{\tau 1}} \, dp_w^{\tau 1} \left(\frac{\partial p_w^{\tau 1}}{\partial x_j^{\tau 1}} + \rho_w^{\tau 1} \, g_j \right) \\
&- \rho_w^{\tau 1} \, \frac{k_{w,lj}^{\tau 1} \, k_{r,w}^{\tau 1}}{\mu_w} \left(\frac{\partial dp_w^{\tau 1}}{\partial x_j^{\tau 1}} + \rho_w^{\tau 1} \, \frac{dp_w^{\tau 1}}{\chi_w} \, g_j \right) \Bigg] d\Omega^{\tau 1} = -\Delta_3^{\tau 1}
\end{aligned}
\tag{67}
$$

where $\frac{\partial k_{w,lj}^{\tau 1}}{\partial p_w^{\tau 1}} \neq 0$ only if it is considered that the intrinsic permeability evolution depends on the pore water pressure as in Eq. 57.

These equations allow to write the matrix of the flow problem and of the fluid influence on the mechanics. The stiffness matrix of the flow problem is expressed as:

$$
\left[K_{WW}^{\tau 1}\right]_{3\times 3} = \begin{bmatrix}
\rho_w^{\tau 1} \dfrac{k_{w,11}^{\tau 1} k_{r,w}^{\tau 1}}{\mu_w} & \rho_w^{\tau 1} \dfrac{k_{w,12}^{\tau 1} k_{r,w}^{\tau 1}}{\mu_w} & K_{WW_{1,3}}^{\tau 1} \\
\rho_w^{\tau 1} \dfrac{k_{w,21}^{\tau 1} k_{r,w}^{\tau 1}}{\mu_w} & \rho_w^{\tau 1} \dfrac{k_{w,22}^{\tau 1} k_{r,w}^{\tau 1}}{\mu_w} & K_{WW_{2,3}}^{\tau 1} \\
0 & 0 & K_{WW_{3,3}}^{\tau 1}
\end{bmatrix}
\tag{68}
$$

where:

$$
\begin{aligned}
K_{WW_{1,3}}^{\tau 1} = {} & \rho_w^{\tau 1} \frac{k_{w,1j}^{\tau 1}}{\mu_w} \frac{k_{r,w}^{\tau 1}}{\chi_w} \left(\frac{\partial p_w^{\tau 1}}{\partial x_j^{\tau 1}} + 2\rho_w^{\tau 1} g_j \right) + \rho_w^{\tau 1} \frac{k_{w,1j}^{\tau 1}}{\mu_w} \frac{\partial k_{r,w}^{\tau 1}}{\partial S_{r,w}^{\tau 1}} \frac{\partial S_{r,w}^{\tau 1}}{\partial p_w^{\tau 1}} \left(\frac{\partial p_w^{\tau 1}}{\partial x_j^{\tau 1}} + \rho_w^{\tau 1} g_j \right) \\
& + \rho_w^{\tau 1} \frac{k_{r,w}^{\tau 1}}{\mu_w} \frac{\partial k_{w,1j}^{\tau 1}}{\partial p_w^{\tau 1}} \left(\frac{\partial p_w^{\tau 1}}{\partial x_j^{\tau 1}} + \rho_w^{\tau 1} g_j \right)
\end{aligned}
\tag{69}
$$

$$
\begin{aligned}
K_{WW_{2,3}}^{\tau 1} = {} & \rho_w^{\tau 1} \frac{k_{w,2j}^{\tau 1}}{\mu_w} \frac{k_{r,w}^{\tau 1}}{\chi_w} \left(\frac{\partial p_w^{\tau 1}}{\partial x_j^{\tau 1}} + 2\rho_w^{\tau 1} g_j \right) + \rho_w^{\tau 1} \frac{k_{w,2j}^{\tau 1}}{\mu_w} \frac{\partial k_{r,w}^{\tau 1}}{\partial S_{r,w}^{\tau 1}} \frac{\partial S_{r,w}^{\tau 1}}{\partial p_w^{\tau 1}} \left(\frac{\partial p_w^{\tau 1}}{\partial x_j^{\tau 1}} + \rho_w^{\tau 1} g_j \right) \\
& + \rho_w^{\tau 1} \frac{k_{r,w}^{\tau 1}}{\mu_w} \frac{\partial k_{w,2j}^{\tau 1}}{\partial p_w^{\tau 1}} \left(\frac{\partial p_w^{\tau 1}}{\partial x_j^{\tau 1}} + \rho_w^{\tau 1} g_j \right)
\end{aligned}
\tag{70}
$$

$$
\begin{aligned}
K^{\tau 1}_{WW_{3,3}} = & \frac{\rho^{\tau 1}_w}{\chi_w}\,\frac{\dot{p}^{\tau 1}_w}{\chi_w}\,\Phi^{\tau 1}\,S^{\tau 1}_{r,w} + \frac{\rho^{\tau 1}_w}{\chi_w\,\Delta t}\,\Phi^{\tau 1}\,S^{\tau 1}_{r,w} + 2\,\frac{\rho^{\tau 1}_w}{K_s}\,\frac{\dot{p}^{\tau 1}_w}{\chi_w}\left(b-\Phi^{\tau 1}\right)\left(S^{\tau 1}_{r,w}\right)^2 \\
& + \rho^{\tau 1}_w\,\frac{\dot{p}^{\tau 1}_w}{\chi_w}\,\Phi^{\tau 1}\,\frac{\partial S^{\tau 1}_{r,w}}{\partial p^{\tau 1}_w} - \frac{\rho^{\tau 1}_w}{K_s}\,\frac{\dot{p}^{\tau 1}_w}{K_s}\left(b-\Phi^{\tau 1}\right)\left(S^{\tau 1}_{r,w}\right)^3 \\
& + 2\,\rho^{\tau 1}_w\left(b-\Phi^{\tau 1}\right)\frac{\dot{p}^{\tau 1}_w}{K_s}\,S^{\tau 1}_{r,w}\,\frac{\partial S^{\tau 1}_{r,w}}{\partial p^{\tau 1}_w} + \frac{\rho^{\tau 1}_w}{K_s\,\Delta t}\left(b-\Phi^{\tau 1}\right)\left(S^{\tau 1}_{r,w}\right)^2 \\
& + \frac{\rho^{\tau 1}_w}{\chi_w}\left(\dot{\varepsilon}^{\tau 1}_v - \frac{\dot{\sigma}'^{\tau 1}}{K_s}\right)S^{\tau 1}_{r,w} + \rho^{\tau 1}_w\left(\dot{\varepsilon}^{\tau 1}_v - \frac{\dot{\sigma}'^{\tau 1}}{K_s}\right)\frac{\partial S^{\tau 1}_{r,w}}{\partial p^{\tau 1}_w} \\
& + \frac{\rho^{\tau 1}_w}{\chi_w}\,\Phi^{\tau 1}\,\dot{S}^{\tau 1}_{r,w} + \frac{\rho^{\tau 1}_w}{K_s}\left(b-\Phi^{\tau 1}\right)S^{\tau 1}_{r,w}\,\dot{S}^{\tau 1}_{r,w} + \rho^{\tau 1}_w\,\Phi^{\tau 1}\,\frac{1}{\Delta t}\,\frac{\partial S^{\tau 1}_{r,w}}{\partial p^{\tau 1}_w}
\end{aligned}
\tag{71}
$$

The coupled part is:

$$
\left[K^{\tau 1}_{WM}\right]_{4\times 3} = \begin{bmatrix} 0 & 0 & -b\,S^{\tau 1}_{r,w} \\ 0 & 0 & 0 \\ 0 & 0 & 0 \\ 0 & 0 & -b\,S^{\tau 1}_{r,w} \end{bmatrix}
\tag{72}
$$

and a part of the stiffness matrix related to the gravity volume force can be written thanks to the coupling between u^*_i and $dp^{\tau 1}_w$:

$$
\left[G^{\tau 1}_2\right]_{2\times 3} = \begin{bmatrix} 0 & 0 & -\dfrac{\rho^{\tau 1}_w}{K_s}\left(b-\Phi^{\tau 1}\right)\left(S^{\tau 1}_{r,w}\right)^2 g_1 - \dfrac{\rho^{\tau 1}_w}{\chi_w}\Phi^{\tau 1}S^{\tau 1}_{r,w}g_1 - \rho^{\tau 1}_w\Phi^{\tau 1}\dfrac{\partial S^{\tau 1}_{r,w}}{\partial p^{\tau 1}_w}g_1 \\ 0 & 0 & -\dfrac{\rho^{\tau 1}_w}{K_s}\left(b-\Phi^{\tau 1}\right)\left(S^{\tau 1}_{r,w}\right)^2 g_2 - \dfrac{\rho^{\tau 1}_w}{\chi_w}\Phi^{\tau 1}S^{\tau 1}_{r,w}g_2 - \rho^{\tau 1}_w\Phi^{\tau 1}\dfrac{\partial S^{\tau 1}_{r,w}}{\partial p^{\tau 1}_w}g_2 \end{bmatrix}
\tag{73}
$$

Influence of the mechanics

To determine the influence of the mechanics on the fluid, a different geometry for the configurations $\Omega^{\tau 1}$ and $\Omega^{\tau 2}$ as well as an identical pore water pressure can be assumed. Therefore:

$$
du^{\tau 1}_i = x^{\tau 2}_i - x^{\tau 1}_i
\tag{74}
$$

$$
p^{\tau 1}_w = p^{\tau 2}_w
\tag{75}
$$

which lead to:

$$
dp^{\tau 1}_w = 0
\tag{76}
$$

The balance equations become:

$$
\begin{aligned}
& \int_{\Omega^{\tau 1}} \frac{\partial u^*_i}{\partial x^{\tau 1}_l}\left[d\sigma'^{\tau 1}_{il} - \sigma^{\tau 1}_{ij}\frac{\partial du^{\tau 1}_l}{\partial x^{\tau 1}_j} + \sigma^{\tau 1}_{il}\frac{\partial du^{\tau 1}_m}{\partial x^{\tau 1}_m}\right] + \frac{\partial v^*_{ij}}{\partial x^{\tau 1}_l}\left[d\Sigma^{\tau 1}_{ijl} - \Sigma^{\tau 1}_{ijk}\frac{\partial du^{\tau 1}_l}{\partial x^{\tau 1}_k} + \Sigma^{\tau 1}_{ijl}\frac{\partial du^{\tau 1}_m}{\partial x^{\tau 1}_m}\right] d\Omega^{\tau 1} \\
& \quad - \int_{\Omega^{\tau 1}} \frac{\partial u^*_i}{\partial x^{\tau 1}_l}\left[d\lambda^{\tau 1}_{il} - \lambda^{\tau 1}_{ij}\frac{\partial du^{\tau 1}_l}{\partial x^{\tau 1}_j} + \lambda^{\tau 1}_{il}\frac{\partial du^{\tau 1}_m}{\partial x^{\tau 1}_m}\right] - v^*_{ij}\left[d\lambda^{\tau 1}_{ij} + \lambda^{\tau 1}_{ij}\frac{\partial du^{\tau 1}_m}{\partial x^{\tau 1}_m}\right] d\Omega^{\tau 1} \\
& - \int_{\Omega^{\tau 1}} u^*_i\left[-\rho^{\tau 1}_s\frac{d\sigma'^{\tau 1}}{K_s} - \left(\rho^{\tau 1}_s - \rho^{\tau 1}_w\,S^{\tau 1}_{r,w}\right)\left(-\frac{d\sigma'^{\tau 1}}{K_s} + \left(1-\Phi^{\tau 1}\right)\frac{\partial du^{\tau 1}_m}{\partial x^{\tau 1}_m}\right) + \rho^{\tau 1}\frac{\partial du^{\tau 1}_m}{\partial x^{\tau 1}_m}\right] g_i\,d\Omega^{\tau 1} = -\Delta^{\tau 1}_1
\end{aligned}
\tag{77}
$$

$$\int_{\Omega^{\tau 1}} \lambda_{ij}^{*} \left[\left(\frac{\partial u_i^{\tau 1}}{\partial x_j^{\tau 1}} - \upsilon_{ij}^{\tau 1} \right) \frac{\partial du_m^{\tau 1}}{\partial x_m^{\tau 1}} + \frac{\partial du_i^{\tau 1}}{\partial x_j^{\tau 1}} - \frac{\partial u_i^{\tau 1}}{\partial x_k^{\tau 1}} \frac{\partial du_k^{\tau 1}}{\partial x_j^{\tau 1}} - d\upsilon_{ij}^{\tau 1} \right] d\Omega^{\tau 1} = -\Delta_2^{\tau 1} \tag{78}$$

$$\begin{aligned}
&\int_{\Omega^{\tau 1}} p_w^{*} \left[\rho_w^{\tau 1} \frac{\dot{p}_w^{\tau 1}}{\chi_w} \left(-\frac{d\sigma'^{\tau 1}}{K_s} + \left(1 - \Phi^{\tau 1}\right) \frac{\partial du_m^{\tau 1}}{\partial x_m^{\tau 1}} \right) S_{r,w}^{\tau 1} \right. \\
&\quad - \rho_w^{\tau 1} \frac{\dot{p}_w^{\tau 1}}{K_s} \left(-\frac{d\sigma'^{\tau 1}}{K_s} + \left(1 - \Phi^{\tau 1}\right) \frac{\partial du_m^{\tau 1}}{\partial x_m^{\tau 1}} \right) \left(S_{r,w}^{\tau 1}\right)^2 \\
&\quad + \rho_w^{\tau 1} \left(\frac{\partial du_m^{\tau 1}}{\partial x_m^{\tau 1}} \left(\frac{1}{\Delta t} - \frac{\dot{\Omega}^{\tau 1}}{\Omega^{\tau 1}} \right) - \frac{d\sigma'^{\tau 1}}{K_s \, \Delta t} \right) S_{r,w}^{\tau 1} \\
&\quad \left. + \rho_w^{\tau 1} \left(-\frac{d\sigma'^{\tau 1}}{K_s} + \left(1 - \Phi^{\tau 1}\right) \frac{\partial du_m^{\tau 1}}{\partial x_m^{\tau 1}} \right) \dot{S}_{r,w}^{\tau 1} + \dot{M}^{\tau 1} \frac{\partial du_m^{\tau 1}}{\partial x_m^{\tau 1}} \right] d\Omega^{\tau 1} \\
&- \int_{\Omega^{\tau 1}} \frac{\partial p_w^{*}}{\partial x_l^{\tau 1}} \left[\rho_w^{\tau 1} \frac{k_{w,lj}^{\tau 1} \, k_{r,w}^{\tau 1}}{\mu_w} \frac{\partial p_w^{\tau 1}}{\partial x_k^{\tau 1}} \frac{\partial du_k^{\tau 1}}{\partial x_j^{\tau 1}} - \rho_w^{\tau 1} \frac{k_{r,w}^{\tau 1}}{\mu_w} \, dk_{w,lj}^{\tau 1} \left(\frac{\partial p_w^{\tau 1}}{\partial x_j^{\tau 1}} + \rho_w^{\tau 1} \, g_j \right) \right. \\
&\quad \left. - f_{w,i}^{\tau 1} \frac{\partial du_l^{\tau 1}}{\partial x_i^{\tau 1}} + f_{w,l}^{\tau 1} \frac{\partial du_m^{\tau 1}}{\partial x_m^{\tau 1}} \right] d\Omega^{\tau 1} = -\Delta_3^{\tau 1}
\end{aligned} \tag{79}$$

where $dk_{w,lj}^{\tau 1} \neq 0$ only if the intrinsic permeability evolution depends on parameters linked to the displacement field $du_i^{\tau 1}$. It can correspond to the first part of Eq. 57 involving $d\overline{m}_k^{\tau 1}$ or to Eq. 58.

These equations allow to write the matrix of the mechanic influence on the fluid:

$$\left[K_{MW}^{\tau 1}\right]_{3\times 4} = \begin{bmatrix} A_{111}^{\tau 1} & f_{w,2}^{\tau 1} + A_{121}^{\tau 1} & A_{112}^{\tau 1} & -f_{w,1}^{\tau 1} + A_{122}^{\tau 1} \\ -f_{w,2}^{\tau 1} + A_{211}^{\tau 1} & A_{221}^{\tau 1} & f_{w,1}^{\tau 1} + A_{212}^{\tau 1} & A_{222}^{\tau 1} \\ C^{\tau 1} + \dot{M}^{\tau 1} & 0 & 0 & C^{\tau 1} + \dot{M}^{\tau 1} \end{bmatrix} + \left[K_k^{\tau 1}\right] \tag{80}$$

where:

$$A_{ijk}^{\tau 1} = -\rho_w^{\tau 1} \frac{k_{w,ij} \, k_{r,w}^{\tau 1}}{\mu_w} \frac{\partial p_w^{\tau 1}}{\partial x_k^{\tau 1}} \tag{81}$$

and, by assuming poroelasticity (Eqs. 2.57 and 2.62):

$$\frac{d\sigma'^{\tau 1}}{K_s} = (1 - b) \, d\varepsilon_v^{\tau 1} = (1 - b) \frac{\partial du_m^{\tau 1}}{\partial x_m} \tag{82}$$

the term $C^{\tau 1}$ reads:

$$C^{\tau 1} = \rho_w^{\tau 1} \frac{\dot{p}_w^{\tau 1}}{\chi_w} \left(b - \Phi^{\tau 1}\right) S_{r,w}^{\tau 1} - \rho_w^{\tau 1} \frac{\dot{p}_w^{\tau 1}}{K_s} \left(b - \Phi^{\tau 1}\right) \left(S_{r,w}^{\tau 1}\right)^2 + \rho_w^{\tau 1} \left(\frac{b}{\Delta t} - \frac{\dot{\Omega}^{\tau 1}}{\Omega^{\tau 1}} \right) S_{r,w}^{\tau 1} + \rho_w^{\tau 1} \left(b - \Phi^{\tau 1}\right) \dot{S}_{r,w}^{\tau 1} \tag{83}$$

It would be possible to develop the variation of the mean effective stress $d\sigma'^{\tau 1}$ in function of the elastoplastic tensor C_{ijkl} from the constitutive relation Eq. 10. However, the expression of C_{ijkl} is quite complex (Eq. 2.102) and poroelasticity is assumed for simplicity reason.

Moreover, $\left[K_k^{\tau 1}\right]$ in Eq. 80 is a matrix that considers the evolution of the intrinsic permeability. The terms of this matrix differ depending on the intrinsic permeability evolution. By

considering for instance an evolution with the strain tensor, as described in Eq. 58, the matrix is defined as follows:

$$\left[K_k^{\tau 1}\right]_{3\times 4} = \rho_w^{\tau 1}\ \frac{k_{r,w}^{\tau 1}}{\mu_w}\left(\frac{\partial p_w^{\tau 1}}{\partial x_j^{\tau 1}} + \rho_w^{\tau 1}\ g_j\right)\begin{bmatrix} \dfrac{\partial k_{w,1j}^{\tau 1}}{\partial \varepsilon_{11}^{\tau 1}} & \dfrac{\partial k_{w,1j}^{\tau 1}}{\partial \varepsilon_{12}^{\tau 1}} & \dfrac{\partial k_{w,1j}^{\tau 1}}{\partial \varepsilon_{21}^{\tau 1}} & \dfrac{\partial k_{w,1j}^{\tau 1}}{\partial \varepsilon_{22}^{\tau 1}} \\ \dfrac{\partial k_{w,2j}^{\tau 1}}{\partial \varepsilon_{11}^{\tau 1}} & \dfrac{\partial k_{w,2j}^{\tau 1}}{\partial \varepsilon_{12}^{\tau 1}} & \dfrac{\partial k_{w,2j}^{\tau 1}}{\partial \varepsilon_{21}^{\tau 1}} & \dfrac{\partial k_{w,2j}^{\tau 1}}{\partial \varepsilon_{22}^{\tau 1}} \\ 0 & 0 & 0 & 0 \end{bmatrix} \tag{84}$$

where j is a summation index. Finally, the second part of the stiffness matrix related to the gravity volume force is given by:

$$\left[G_1^t\right]_{2\times 4} = \begin{bmatrix} -\rho_w^{\tau 1} S_{r,w}^{\tau 1} g_1 b & 0 & 0 & -\rho_w^{\tau 1} S_{r,w}^{\tau 1} g_1 b \\ -\rho_w^{\tau 1} S_{r,w}^{\tau 1} g_2 b & 0 & 0 & -\rho_w^{\tau 1} S_{r,w}^{\tau 1} g_2 b \end{bmatrix} \tag{85}$$

under poroelasticity assumption.

Simplifications

A few simplifications may be considered in the general problem and simplify the expressions of the stiffness matrices. Firstly, poroelasticity has been assumed for the matrices $\left[K_{MW}^{\tau 1}\right]$ and $\left[G_1^t\right]$ and can be extended to the others by taking into account $\dot{\sigma}'^{\tau 1} = K\ \dot{\varepsilon_v^{\tau 1}}$ in the term $K_{WW_{3,3}}^{\tau 1}$. Secondly, if the gravity is not taken into account, $g_i = 0$, then $\left[G_1^{\tau 1}\right]$ and $\left[G_2^{\tau 1}\right]$ are null matrices because no contribution of the gravity volume force is considered. Moreover, terms including g_i cancel in the other matrices ($\left[K_{WW}^{\tau 1}\right]$ and $\left[K_k^{\tau 1}\right]$). Additionally, if the intrinsic water permeability is independent of the pore water pressure, the terms $K_{WW_{1,3}}^{\tau 1}$ and $K_{WW_{2,3}}^{\tau 1}$ of the stiffness matrix of the flow problem reduce to:

$$K_{WW_{1,3}}^{\tau 1} = \frac{\rho_w^{\tau 1}}{\mu_w}\left(\frac{k_{r,w}^{\tau 1}}{\chi_w} + \frac{\partial k_{r,w}^{\tau 1}}{\partial p_w^{\tau 1}}\right) k_{w,1j}\ \frac{\partial p_w^{\tau 1}}{\partial x_j^{\tau 1}} \tag{86}$$

$$K_{WW_{2,3}}^{\tau 1} = \frac{\rho_w^{\tau 1}}{\mu_w}\left(\frac{k_{r,w}^{\tau 1}}{\chi_w} + \frac{\partial k_{r,w}^{\tau 1}}{\partial p_w^{\tau 1}}\right) k_{w,2j}\ \frac{\partial p_w^{\tau 1}}{\partial x_j^{\tau 1}} \tag{87}$$

Lastly, if no variation of the intrinsic water permeability is considered then $\left[K_k^{\tau 1}\right] = 0$. The coupling matrix $\left[K_{WM}^{\tau 1}\right]_{4\times 3}$ remains unchanged.

Mechanical anisotropy

Anisotropy of the hydraulic properties has been included with the anisotropic intrinsic water permeability tensor $k_{w,ij}$. For mechanical anisotropy, the elastoplastic tensor C_{ijkl} and the Biot's coefficient become anisotropic. The elastoplastic tensor is involved in the definition of the first gradient constitutive law (Eq. 10 in variation form) and in the matrix $\left[E_1^{\tau 1}\right]$ defined by Chambon and Moullet (2004) that remain unchanged. The Biot's anisotropic and symmetric tensor is defined from the Hooke elastic constitutive tensor, under micro-homogeneity and micro-isotropy assumptions, as follows:

$$b_{ij} = \delta_{ij} - \frac{C_{ijkk}^e}{3\ K_s} \tag{88}$$

where δ_{ij} is the Kronecker symbol and K_s is the bulk modulus of the solid phase. For more details about the anisotropy of the Biot's coefficient, please refer to chapter 5. The generalised Biot's coefficient reads:

$$b = \frac{b_{ii}}{3} = 1 - \frac{K}{K_s} \tag{89}$$

where K is the generalised drained bulk modulus of the poroelastic material:

$$K = \frac{C^e_{iijj}}{9} \tag{90}$$

The poroelasticity relations remain valid by considering the above relations.

By taking into account the anisotropy of the Biot's coefficient and the partial saturation effect, the stress definition yields:

$$\sigma_{ij} = \sigma^{'}_{ij} - b_{ij}\ S_{r,w}\ p_w \tag{91}$$

Moreover, the time derivative of the solid density is related to the variations of pore water pressure as well as of mean effective stress, and involves the Biot's coefficient. Nevertheless, the relation

$$\frac{\dot{\rho}_s}{\rho_s} = \frac{(b-\Phi)\, S_{r,w}\ \dot{p}_w - \dot{\sigma}^{'}}{(1-\Phi)\ K_s} \tag{92}$$

remains valid provided that b is the generalised Biot's coefficient. It is also the case for related relationships as the porosity time derivative for instance. Therefore, the different matrices composing $\left[E^{\tau 1}\right]$ remain identical except $\left[K^{\tau 1}_{WM}\right]$ which becomes:

$$\left[K^{\tau 1}_{WM}\right]_{4\times 3} = \begin{bmatrix} 0 & 0 & -b_{11}\ S^{\tau 1}_{r,w} \\ 0 & 0 & 0 \\ 0 & 0 & 0 \\ 0 & 0 & -b_{22}\ S^{\tau 1}_{r,w} \end{bmatrix} \tag{93}$$

due to the effective stress definition.

B Research articles

Charlier, R., Collin, F., Pardoen, B., Talandier, J., Radu, J. P., and Gerard, P. (2013). An unsaturated hydro-mechanical modelling of two in-situ experiments in Callovo-Oxfordian argillite. *Eng Geol*, 165:46-63. doi: 10.1016/j.enggeo.2013.05.021.

Pardoen, B., Levasseur, S., and Collin, F. (2015). Using Local Second Gradient Model and Shear Strain Localisation to Model the Excavation Damaged Zone in Unsaturated Claystone. *Rock Mech Rock Eng*, 48(2):691-714. doi: 10.1007/s00603-014-0580-2.

Pardoen, B., Seyedi, D. M., and Collin, F. (2015). Shear banding modelling in cross-anisotropic rocks. *Int J Solids Struct*, 72:63-87. doi: 10.1016/j.ijsolstr.2015.07.012.

Pardoen, B., Talandier, J., and Collin, F. (2016). Permeability evolution and water transfer in the excavation damaged zone of a ventilated gallery. *Int J Rock Mech Min Sci*, 85:192-208. doi: 10.1016/j.ijrmms.2016.03.007.

Pardoen, B., and Collin, F. (2016). Modelling the influence of strain localisation and viscosity on the behaviour of underground drifts drilled in claystone. *Comput Geotech*, in press, doi: 10.1016/j.compgeo.2016.05.017.